Biological and Medical Physics, Biomedical Engineering

Rodolphe Antoni
Laurent Bourgois

Applied Physics of External Radiation Exposure

Dosimetry and Radiation Protection

Springer

Applied Physics of External Radiation Exposure

More information about this series at http://www.springer.com/series/3740

BIOLOGICAL AND MEDICAL PHYSICS, BIOMEDICAL ENGINEERING

The fields of biological and medical physics and biomedical engineering are broad, multidisciplinary and dynamic. They lie at the crossroads of frontier research in physics, biology, chemistry, and medicine. The Biological and Medical Physics, Biomedical Engineering Series is intended to be comprehensive, covering a broad range of topics important to the study of the physical, chemical and biological sciences. Its goal is to provide scientists and engineers with textbooks, monographs, and reference works to address the growing need for information.

Books in the series emphasize established and emergent areas of science including molecular, membrane, and mathematical biophysics; photosynthetic energy harvesting and conversion; information processing; physical principles of genetics; sensory communications; automata networks, neural networks, and cellular automata. Equally important will be coverage of applied aspects of biological and medical physics and biomedical engineering such as molecular electronic components and devices, biosensors, medicine, imaging, physical principles of renewable energy production, advanced prostheses, and environmental control and engineering.

Rodolphe Antoni · Laurent Bourgois

Applied Physics of External Radiation Exposure

Dosimetry and Radiation Protection

Springer

Rodolphe Antoni
CEA DEN Cadarache
Saint-Paul-lès-Durance
France

Laurent Bourgois
CEA DAM Île de France
Arpajon cedex
France

ISSN 1618-7210 ISSN 2197-5647 (electronic)
Biological and Medical Physics, Biomedical Engineering
ISBN 978-3-319-48658-1 ISBN 978-3-319-48660-4 (eBook)
DOI 10.1007/978-3-319-48660-4

Library of Congress Control Number: 2016955430

Translation from the French language edition: *Physique appliquée à l'exposition externe* by Rodolphe Antoni and Laurent Bourgois, © Springer, 2013. All Rights Reserved.
As per September 1, 2014, copyright belongs to Lavoisier, Paris, France Springer International Publishing has the copyright for the English version only.

Printed on acid-free paper

This Springer imprint is published by Springer Nature
The registered company is Springer International Publishing AG
The registered company address is: Gewerbestrasse 11, 6330 Cham, Switzerland

Preface

This book aims to summarize many years of experience in the field of external dosimetry and protection against ionizing radiation, in the industrial, research, and medical field. It recalls physical concepts and treats a large part of the dosimetry concepts to finally offer a number of tools, for professionals and students, engineers, and technicians to assess radiological risks and to protect themselves in particular by calculating appropriate shielding. It is based on the theory related to the interaction of radiation with matter, empirical formulas, and tables and illustrated by various numerical applications. In addition, it refers continually to the state of the art and particularly in the field of computer codes for external exposure as for a number of medical projects and recent research. Furthermore, it compiles data scattered in many reference works, some of which are hardly available.

The idea came from the authors, involved in the field of radiation protection, which found a lack in terms of practical books and full enough to treat the whole issue of external exposure to ionizing radiation (photons, neutrons, charged particles—electrons, ions etc.).

This book is largely based on a French book by Antoni and Bourgois [1] in which some parts have been added.

This book is dedicated to professionals of radiation protection, dosimetry, and nuclear measurement but also allows to complete the curriculum for students (technician and engineer).

The authors are professionals who have acquired 10 and 20 years of experience in CEA (French Atomic Energy Commission) in different fields of radiation protection: accelerators, X-ray generators, sealed sources, dosimetry, Monte Carlo calculation, etc. They also teach dosimetry and protection against the external radiation exposure in bachelor of science at Cadarache and European Master in radiation protection at Grenoble.

This book is based on two levels of reading: the first affordable by the whole of readers for which elementary physical concepts leading to the understanding of phenomena related to external exposure are supported by simple numerical applications and the second through additional information, available at the end of each chapter, detailing the more complex problems requiring appropriate mathematical

developments. This second level of reading, subsidiary, however, is optional and is for readers eager to deepen aspects of the field.

Regarding the arrangement of the contents, Chap. 1 deals with the definition of fundamental radiometric and dosimetric quantities, for addressing the radiation–matter interaction following an approach dedicated at the dose deposited in biological tissue through Chap. 2 to finally define and apply "protection and operational quantities" related to radiation protection in Chap. 3.

A particular emphasis was placed, in the following Chaps. 4 and 5, on the definition of risk and countermeasures (i.e., biological protection) for sources of conventional radiation: radionuclides, X-ray generators, accelerators (electrons, ions) … but also for "exotic" facility like power laser accelerators … for an energy range that can be classed as medium (0–200 MeV).

The final chapter of the book is entirely devoted to particle transport calculation codes with the Monte Carlo method. The general principles are explained with a specific orientation towards the estimated radiometric and dosimetric quantities described in previous chapters. This part is still littered with numerical applications to enhance understanding. Most of calculation codes used in the radiation protection field are nowadays implemented with algorithms based on this method.

We thank for their various contributions: Nicolas Comte, Laurent Ferreux, Christian Passard, and Murielle Nerbusson.

Arpajon, France

Rodolphe Antoni
Laurent Bourgois

Reference

[1] Antoni, R. & Bourgois, L. (2013). Physique Appliquée à l'exposition externe: Dosimetrie et radioprotection. Springer. ISBN:978-2-8178-0310-4.

Contents

About the Authors

Rodolphe Antoni received a master's degree in radiation protection from the joseph Fourier university of Grenoble in 1998. From 1999 to 2001, he was at the OPRI (French Ancient Governmental Office for Radiation Protection), working on authorizations of radioactive waste release from nuclear plants. From 2001, he joins the radiation protection service at CEA (French Atomic Energy Commission) at Saclay, where he works on dosimetry and radiation protection R&D. Along with this position, he teaches radiation physics and protection in bachelor's and master's degrees at INSTN (Institut National des Sciences et Techniques Nucléaires). Since 2009, he works at LMN (nuclear measurement laboratory) at CEA Cadarache center, on nondestructive essay for radioactive waste with neutron measurement based on differential die-away technique and coincidence. He received his Ph.D. in 2014 on this topic.

Laurent Bourgois After his master's degree, he began his career at the CEA (French atomic energy commission) at Saclay Research Center in the Radiation Protection Department in 1991. He worked in different fields of radiation protection: particle accelerators, X-ray generator, nuclear fuel, and high-activity sealed sources facilities; environment; metrology; dosimetry; radiation shielding; nuclear safety; nuclear intervention; detection; etc. He occupied various management positions. In 2007, he was appointed Radiation Protection Department head at the CEA/DAM Ile de France Research Center (Bruyères-le-Châtel center). He participated in various expertise activities (e.g., expert for French Nuclear Safety Authority), training activities (e.g., lecturer in radiation shielding, European master in radiation protection), various task groups (e.g., evaluation of the radiological and economic consequence of decommissioning particle accelerators, development of methodology for RN material detection, management, and protection of the public for the european commission, and X-ray generator standards). In 2009, he was appointed senior expert at CEA in "Organization and Engineering" with specialization in "Nuclear Safety and Radiation Protection". In 2012, he was appointed senior lecturer at "Institut National des Sciences et Techniques Nucléaires" (INSTN). He is the author of many scientific publications in the fields of radiation protection.

Chapter 1
Quantities and Fundamental Units of External Dosimetry

Abstract In this chapter, the radiation field is characterized in terms of energy and flux at a point of space. These physical datas than make possible to obtain the radiometric and dosimetric quantities of reference for external exposure, such as: fluence, kerma for the indirectly ionizing radiations and the dose. In addition, other quantities such as linear energy transfer and relative biological effectiveness are detailed; they relate to the effect of radiation on biological tissues and to the damage that can occur at the cellular level.

Initially, we will attempt to define the characteristic quantities of dosimetry and radiation fields, called radiometric quantities. The fundamental radiometric and dosimetric quantities are essentially threefold:

- Fluence Φ;
- Absorbed dose D;
- Kerma K.

We will note that these quantities were defined by the ICRU (International Commission on Radiation Units and measurements) as transition variables in obtaining protection and operational quantities (detailed in Chaps. 2 and 3), they are measurable and above all they correspond to punctual concepts. Add to that two other intermediate variables that will be particularly suitable in the dose-biological effects relationship: The linear energy transfer (LET) and the relative biological effectiveness (RBE). All these quantities are detailed in the following.

1.1 Dosimetric Quantities

1.1.1 Total Absorbed Dose and Linear Energy Transfer

Biological dosimetry will consist initially to characterize the physical dose deposited in human tissue. This approach is immediately responsible for a dual problem that

R. Antoni and L. Bourgois, *Applied Physics of External Radiation Exposure*,
Biological and Medical Physics, Biomedical Engineering,
DOI 10.1007/978-3-319-48660-4_1

we will discuss: "typology" of energy deposition as a function of radiation type and size of the volume of tissue in which is characterized this deposition.

In the first approach, for a macroscopic context, i.e. a volume V surrounding a mass m of material sufficiently large (tissue level), subject to radiation responsible for a deposited energy E, the dose is defined by the expression (1.1).

$$\overline{\mathrm{D}} = \frac{\mathrm{E}}{\mathrm{m}} \tag{1.1}$$

In the international system, this quantity is consistent with J kg^{-1} but his unit, the gray (Gy), comes from the name of one of the founding fathers of dosimetry (1 Gy = 1 J kg^{-1}). The bar on the variable D indicates that the result of this calculation is an average: no matter the "topology" of deposited dose. In other words, no matter how the mass m has been irradiated, in homogeneous way or not, the final result is averaged over the total mass. This macroscopic quantity will be called later in the book: "total deposited dose." Without details, we will say that energy depositions are the result of excitations, ionization and generally the setting in motion of any secondary charged particle (e.g. electrons for photons, recoil nuclei for neutrons). The total number of ionizations and excitations can be extremely important and can reach the order of 10^5 for a dose of 1 Gy in a volume the size of the cell nucleus.

Once the dose determined, the "typology" of the deposited dose along the path of the incident particle is then decisive because it greatly influences the response of the medium crossed in this case of human tissues. Indeed, one of the major limitations of the approach leading to such a dose as defined in (1.1) is the failure to take into account the geometry of the energy deposition in the target volume. In particular, it is clear that understanding of the action of radiation on the biological material requires information on the scale of the DNA, that is to say to lower target dimensions less than micron.

It has been found indeed that for equal amount of energy absorbed, the effect depends on the nature of the incident particle. For a certain type of radiation such as photons, electrons and protons to high energies, the location of ionization and excitations are separated in space. However, for low-energy protons, neutrons and ions, ionization are relatively clustered in close proximity of the passage of the particle into tissue. Figure 1.1 shows a schematic view of the difference in density of ionization and excitation to the same sensitive volume and for photons and ions.

The physical quantity to characterise the ionization density disparity depending on the type of radiation and therefore the effects on biological tissues, is the ratio of the deposited energy per unit of path length in the material. For a macroscopic approach, this means, in a given environment, to determine the amount of energy ΔE lost by the particle on a portion of its path Δl.

$$\overline{L} = \left(\frac{\Delta E}{\Delta l}\right) \tag{1.2}$$

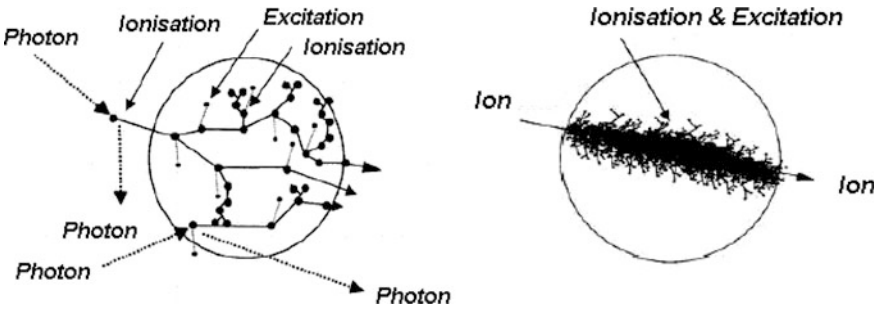

Fig. 1.1 Schematic representation of a photon track and ion through a cell, showing the difference in density of energy deposition in both cases [1], with permission from Springer Heidelberg

In the international system, this quantity is consistent with J m^{-1}, but found in several nuclear units (keV μm^{-1} keV cm^{-1} …). By making infinitesimal terms of the ratio of (1.2) we get the quantity called "linear energy transfer".

$$\lim_{\Delta l \to 0} \overline{L} = L = \left(\frac{dE}{dl} \right) \tag{1.3}$$

This quantity has the same unit as the last. In the literature, we can also find it expressed as a "infinite LET" with the following symbol: L_∞ meaning that the total loss of energy is taken into account through the passage of the particle in matter and not just a fraction confined to the periphery near the passage; by default, L equals L_∞. The LET is a non-stochastic quantity that does not account for the discontinuous nature of energy transfers and statistical fluctuations, as the total deposited dose. It expresses the mean energy loss for a large number of particles. We will see later the incidence of this quantity on cell survival.

Let us add that this quantity is similar to the physical quantity of the "Stopping Power" S for the charged particles and that there are analytical expressions depending on the energy of the incident particle and the type of particle to characterize it that will be detailed in the remainder of this book. By definition, the dose is essentially a deposited energy density. In our initial macroscopic approach leading to the expression (1.1), we can easily make an analogy with the mass density of a material. Recall that the mass density at a point is mathematically considered as the ratio of the mass contained in a element of volume surrounding that point. If the matter was continuous and homogeneous, this ratio does not depend on the size of the element of volume. Against by the fact that a material is composed of discrete entities (atoms, molecules) implies that the volume should contain a sufficiently large number of these entities so that density is a reliable statistical significance. For example, to a volume corresponding to an atom, the concept of density becomes ill-defined and the estimated density at this scale can be very variable.

Microdosimetry focuses precisely quantify the distribution of energy deposition at the microscopic level for sensitive volumes of the order of the cell (10 μm). This discipline has grown significantly to include, among others, how are induced biological effects at the cellular level and in particular to explain the dose-response curves.

The statistical fluctuation of energy deposits was clearly illustrated by Rossi [2] considering, as shown in Fig. 1.2, a set of 150 cells (5 μm diameter) exposed to various types of radiation fields: on the left 1 MeV photons and on the right 1 MeV fission neutrons. The secondary particles from the neutron (mainly the protons of hydrogen from tissues) have a limited path of a few diameters of the cell.

The secondary electrons from the gammas have a greater path than the overall area containing all the cells. The path length traversed in total by the electron is 200 times greater than that of the protons moved by neutrons. Accordingly, the energy deposition actually impacts only very few cells in the case of the interaction of 1 MeV neutrons.

Since the response of a cell depends on the energy absorbed per unit mass, it is essential to consider the fluctuations of the energy per affected cell. An absorbed dose of 10 mGy implies a mean energy per cell equal to the product of 10 mGy by the mass of a cell, but there is a difference in the distribution of energy deposition by cell.

In the case of photon irradiation, fluctuating energy per cell is low and we can consider that we are essentially in a continuous medium. The total deposited dose, as defined by the expression (1.1) as average, takes sense in. for neutrons, fluctuations are significant; 98% of the cells do not get energy and some get significant energy (about 50 times the average). The expression of the total deposited provide this tissue an extremely partial information about the "topology" of déposited dose. In what follows, we will define the microdosimetric concepts enable to understand the dose deposition across the cell.

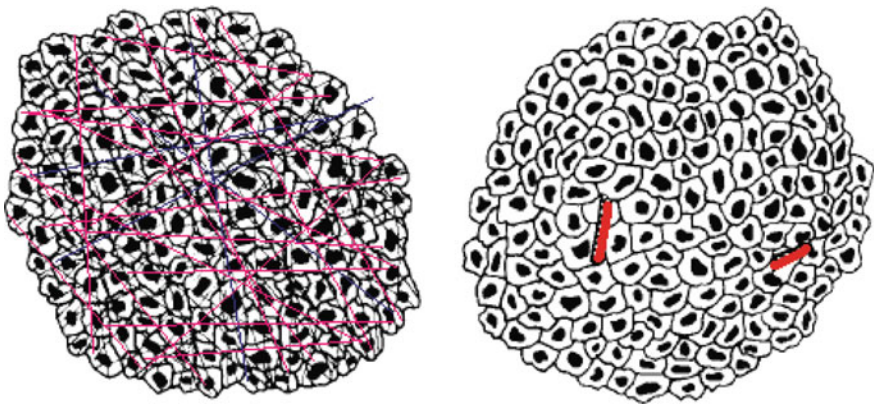

Fig. 1.2 Representation of a 10mGy dose delivered from gamma ^{60}Co (*left*) and the same dose delivered by 1 MeV neutrons (*right*) in a cell volume of 150 cell of 5 μm diameter [2], with permission from Springer Heidelberg

1.1.2 Fundamental Quantities of Microdosimetry and Definition of the Absorbed Dose

Most physical microdosimetry quantities were defined and standardized by the International Commission on Radiation Units and Measurement in the report of the ICRU report 36 [3]. First, the term "event", written the meaning of microdosimetry, represents the whole of energy deposition in the sensitive volume considered, produced by the incident particle and all its secondary particles being moved. "The energy imparted" is defined by the expression (1.4).

$$\varepsilon = \sum \mathrm{E_e} - \sum \mathrm{E_s} + \sum \mathrm{Q_{\Delta m}} \tag{1.4}$$

In other words, for a given volume V, ε is given by the whole of energies of all incoming particles (E_e), which is subtracted from all the energies of all outgoing particles (E_s). The heat reaction term $Q_{\Delta m}$ reflects the change in mass of all particles and nuclei involved in nuclear interactions in the sensitive volume. In human tissue, this term is substantially negligible. Note that ε is a stochastic quantity subject to statistical fluctuations of the interactions of incident particles with secondary particles being moved. To reach a mean value of the energy imparted, it should be to perform a large number of measures or to consider a large enough volume to make these significant statistical fluctuations. From this quantity, a stochastic variable is defined similar to the dose defined by the expression (1.1), but this time for a microscopic approach adapted to dimensions of the order of the cell. This is the "specific energy". It is calculated by the ratio of the energy imparted and the mass of the sensitive volume according to expression (1.5).

$$z = \frac{\varepsilon}{m} \tag{1.5}$$

It is also expressed in gray (Gy); m is the mass of the sensitive site; from the point of microscopic view we prefer to speak of "sensitive site" rather than sensitive volume because of the small dimensions likely to be affected (e.g. cell nucleus). This quantity characterizes the local energy deposition.

The total deposited dose $\overline{D}$ is a non-stochastic quantity: when the measurement is repeated, the values obtained are in each case identical with deviation due to measurement accuracy. However, fluctuations in z are important and originate from the fact that energy deposition are due to discrete events, the number decreases as the size of the sensitive site decrease.

Figure 1.3 shows the field of the microdosimetry, which is located in the part where the fluctuations in energy deposition are significant. This section relates to sensitive sites of low mass, so small size.

To go from the specific energy to the total deposited dose D expression (1.1) a "distribution of the specific energy dependent D" is defined.

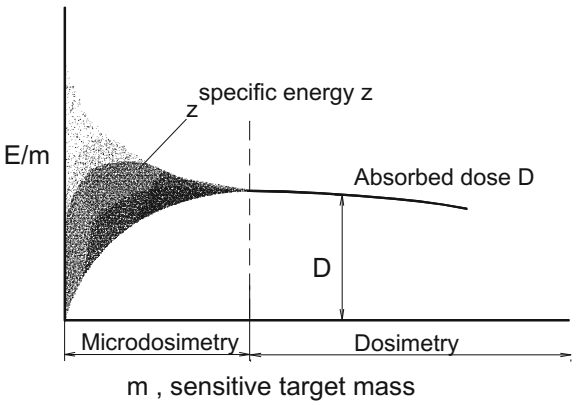

Fig. 1.3 Representation of the variation of the specific energy z depending on the mass m sensitive site

When a small sensitive volume (in the range of one nanometer or micrometer) receives the energy deposition of several events (single or multiple) different values of the specific energy are recorded. For a large number of consecutive events, fluctuations of the specific energy can be represented by a probability density function, $f\left(z,\overline{D}\right)$, where $\overline{D}$ represents the total dose deposited to a small volume. The cumulative probability density associated $F\left(z,\overline{D}\right)$ is the probability that the specific energy is less than or equal to z.

$$\mathrm{F}\left(\mathrm{z},\,\overline{\mathrm{D}}\right)=\mathrm{P}\quad\left(0\leq \mathrm{z}'\leq \mathrm{z},\,\overline{\mathrm{D}}\right) \tag{1.6}$$

$$\mathrm{f}\left(\mathrm{z},\,\overline{\mathrm{D}}\right)=\frac{\mathrm{dF}\left(\mathrm{z},\,\overline{\mathrm{D}}\right)}{\mathrm{dz}} \tag{1.7}$$

The total deposited dose, corresponding *de facto* to a specific mean energy, is then obtained by average of the distribution as (1.8).

$$\overline{D}=\overline{z}=\int z\cdot f\left(z,\overline{D}\right)dz \tag{1.8}$$

By performing this average, we pass from a stochastic quantity subject to statistical fluctuations to a mean macroscopic quantity consistent with the expression (1.1).

$$\overline{\mathrm{D}}=\frac{\bar{\varepsilon}}{\mathrm{m}} \tag{1.9}$$

Finally, if we reach the mass of this object to a negligible amount, we get the "absorbed dose", this time corresponding to a punctual characterization of the dose.

$$\lim_{\mathrm{m}\to 0}\overline{\mathrm{D}}=\frac{\mathrm{d}\bar{\varepsilon}}{\mathrm{dm}}=\mathrm{D} \tag{1.10}$$

This quantity is a fundamental dosimetric variable. while punctual in nature, we will show later that it is measurable and calculable. It is obvious that in an irradiated macroscopic inhomogeneous medium the value of the absorbed dose varies from one point to another in the volume. The latter therefore overcomes, in part, the "topology" of the deposited dose. From this quantity, we define a "absorbed dose rate" (1.11) homogeneous to Gy s^{-1}.

$$\dot{D} = \frac{dD}{dt} \tag{1.11}$$

This variable is also a point-quantity. Now, let us get back to the "typology" of energy deposition mentioned above. The LET, while calculated with varying degrees of simplifying assumptions (e.g. linear stopping power for charged particles), has the drawback of not being accessible to the measure. To overcome this limitation, as to the specific energy for the total deposited dose, there is a similar stochastic variable for LET. This variable is calculated using the ratio of the energy imparted to the sensitive site by a single event, to the mean length of the chord in the sensitive site in question according (1.12).

$$y = \frac{\varepsilon}{\bar{l}} \tag{1.12}$$

This quantity is called "lineal energy". As it relates to sensitive sites of the order of microns, it will be expressed in keV μm^{-1}. The microscopic site where happens the energy transfer can be likened to a sphere. The mean chord is then obtained by the ratio of the volume *V* of the sphere to that of the surface at equatorial disk of the sphere (see Chap. 2, Further Details 2.2).

$$\bar{l} = \frac{2}{3}d \tag{1.13}$$

with *d* the diameter of the sensitive site. Unlike the specific energy, we note that this quantity is meaningful only for a single event and not for multiple events. Then, we can readily express the specific energy as a function of that quantity. For material with density of 1 (of the order of that of human tissue), *z* expressed in Gy, *d* in microns and *there* in keV μm^{-1} we obtain equality (1.14).

$$z = \frac{0.204}{d^2}y \tag{1.14}$$

Since the mean lineal energy represents discrete energy deposition, it is more significant than LET to characterize the "topology" of energy deposition of radiation. However, the ICRP publication 60 [4] recommends the use of LET, more accessible quantity, in particular, we will see in Chap. 2, for obtaining a transfer quantity called quality factor *Q*. LET and lineal energy can however be linked considering whether the TLE match the value of the mean lineal frequency energy

$\overline{y}_f$ or at the value of the mean lineal energy dose $\overline{y}_D$ (see Further Details 1.1). We can also talk in the literature of "mean LET". Table 1.1 gives the values of LET and the number of ionizations per μm in water and for various radiations.

Adding that, a class of detectors: "tissue equivalent proportional counters" (TEPC) measure the lineal energy y and specifically his distribution variable (recalling that it is a stochastic variable) for a given radiation flux (see Further Details 1.1) which is also called "microdosimetric spectrum." These chambers recreate an environment and a sensitive volume close to that of a cell. They deliver an electrical pulse proportional to the energy deposited in the detector volume by the heavy secondary charged particles set in motion in the tissue equivalent wall, by the incident radiation. Note that this is not the photon or neutron that deposit dose, but the secondary particles set in motion by the primary radiation. This distinction, we shall see, is the origin of the definition of dosimetric variables specific to these two types of radiation.

This wall in equivalent tissue material is composed by elementary constituents of human: carbon, hydrogen, oxygen and nitrogen. Secondary particles set in movement in this wall are the electrons to photons. For neutrons, according to the energy of the latter: the recoil protons, hydrogen nuclei, the alpha and proton (n, α) and (n, p) and a more marginally heavy nuclei C, O and N. Microdosimetric spectra are characteristic of incident radiation and may have recognizable peaks, indicating the contribution of a particular secondary particle set in motion in the wall. Figure 1.4 shows the general shape of a microdosimetric spectrum obtained in a mixed radiation field (neutron-photon).

- Region A ($y < 15$ keV μm^{-1}): the dose is due to photons (see Fig. 1, Further Details 1.1).
- Region B (1 keV μm^{-1} < y < 100 keV μm^{-1}): This region corresponds to the proton contribution from neutron-material interactions.
- Region C ($y > 100$ keV μm^{-1}): a significant peak appears in this region for neutron energies above 1 MeV. It is the contribution of heavy recoil nuclei (carbon, nitrogen, oxygen), and the (n, α) whose importance increases with the neutron energy (except for boron and lithium).

Table 1.1 Mean LET and number of ionizations per range unit for different radiations, according [15], with the permission of ATSR

Radiance	Particle charge of the ionization	Means TLE (keV μm^{-1})	Number of ionisations by μm
Electrons > 1 MeV photons	Secondary electrons	0.28	8.5
RX 30–180 kV	Secondary electrons	3.2	100
8 kV RX	Secondary electrons	4.7	145
5 MeV alpha	Alpha	120	3700
400 keV neutron	p + e	35.8	1100
12 MeV neutron	p	9.5	290
1 MeV proton	p	54	2000
10 MeV proton	p	8	250

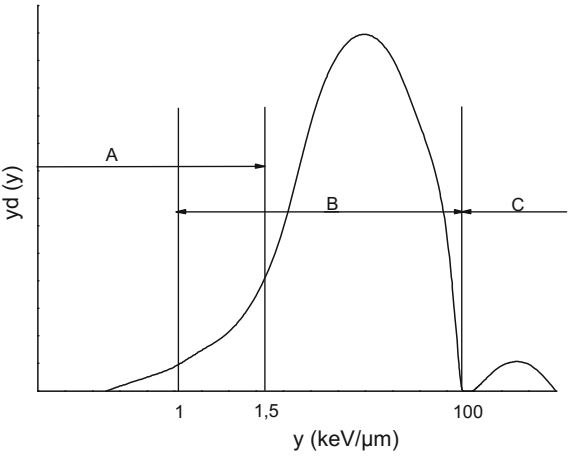

Fig. 1.4 Distribution of typical lineal energy function for a mixed neutron-photon radiation field adapted from [5]

Recovery of spectra for neutrons and photons, between 1 and 15 keV μm^{-1}, encourage to define a threshold at 3.5 keV μm^{-1}. This threshold is effective only in the case of real mixed fields. The check-out of high linear energy beyond 20 keV μm^{-1}, indicates the presence of neutrons. Thus, TEPC allows, to have in real time and with a single measure, a usable information for neutrons and photons; this is one of its main advantages.

Figure 1.5 given a differentiated representation of micro-dosimetric spectra of a TEPC.

For 1 MeV protons, almost only recoil, protons formed by the hydrogen nuclei moved by elastic collision, deposit their energy in the sensitive volume. The maximum energy of the lineal spectrum is around 130 keV μm^{-1}; it is the peak 1, which limits zone 1 and corresponds to the maximum energy deposited by this process when the range of the recoil proton is substantially equal to the diameter of the sensitive volume of the detector (here 2 μm). We note that this peak is common to all three spectra of incident energy. This type of interaction taking place at three energies but with different probabilities of occurrence (cross section inversely proportional to the square root of the energy in this energy range).

Zone 2 is due to inelastic capture (n, α) most likely being the following: $^{14}N(n, \alpha)$ $^{16}O(n, \alpha)$ and $^{12}C(n, \alpha)$ with the following respective response thresholds: 0.16; 2.35 and 6.18 MeV. This explains for 1 MeV neutrons a small contribution in the area 2, a more important for those of 5 MeV, since both reactions are possible. Finally a greater at 15 MeV, because this time the three capture reactions are possible. The optimum of lineal energy, marked by the peak 2, around 300 keV μm^{-1}.

Zone 3 is due to the energy deposition in the sensitive volume of heavy nuclei set in motion in the wall, that is to say: oxygen, carbon and nitrogen. Note that their very small path in the wall limits the number of those entering the gas-sensitive volume, this explains the low amplitude of the area. The maximum peak 3 is around 1000 keV μm^{-1} for neutrons 5 MeV and 1500 keV μm^{-1} for 15 MeV neutrons and indicated by peak 4.

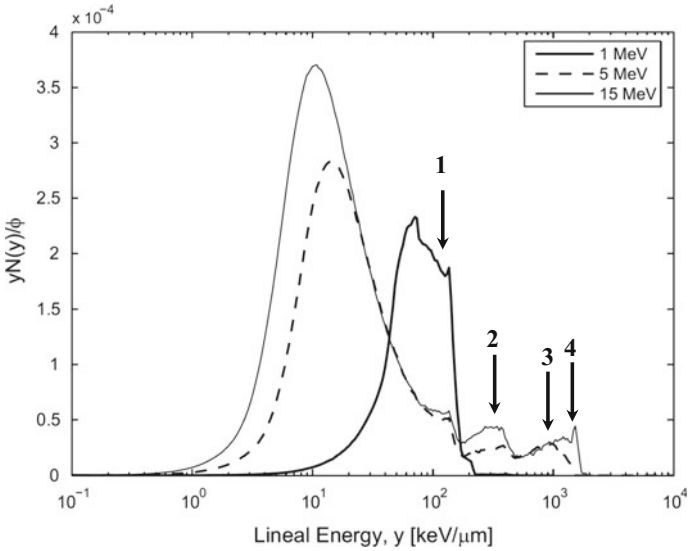

Fig. 1.5 Spectra in a TEPC microdosimetric type detector for different neutron energies: 1, 5 and 15 MeV, reproduced with permission from Elsevier [6]

The spectrum is much larger than in the case of photons. These curves therefore clearly highlight the "mapping" of secondary particles set in movement and the part of energy they deposit in the sensitive volume of the detector supposed to simulate tissue environment cell. At this point, a fundamental distinction in dosimetry related to the type of radiation is involved.

In the case of electrically neutral radiation: photons and neutrons, as briefly mentioned, the secondary particles set in movement are responsible for deposition, electrons in the first and recoil nuclei for the latter. The energy is de facto "indirectly" deposited. This is called "indirectly ionizing radiation." Conversely, the charged particles are called "direct ionizing radiation", since from their penetration into a material medium, they deposit energy "directly" by Coulomb interaction and excitation.

1.1.3 Kerma Calculation for Radiation Indirectly Ionizing

This major difference above is the source of an physical quantity intermediate described as "energy transferred" E_{tr}. It is, this time, not to characterize the deposited energy confined to a sensitive site (ε) but the energy "transferred" to the secondary particles at the point of interaction in the target volume.

To understand the difference between energy imparted ε and energy transferred E_{tr}, consider a photon and an electron microscopic entering a sensitive volume of the dimension of a cell, as shown in Fig. 1.6.

Considering that the path of the electron in the tissue is much greater than the dimensions of the sensitive site, it is possible to assess the mean energy imparted $\overline{\varepsilon}$ on the length of chord through the linear energy transfer TLE. We have recognized that it was possible to define the mean specific energy and thus to the total deposited dose as shown in the expression (1.15).

$$\overline{\mathrm{D}} = \overline{\mathrm{z}} = \frac{\overline{\varepsilon}}{\mathrm{m}} = \frac{1}{\mathrm{m}} \int_{\overline{\mathrm{l}}} \mathrm{L}\,\mathrm{dx} = \frac{1}{\mathrm{m}} \int_{\overline{\mathrm{l}}} \left(\frac{\mathrm{dE}}{\mathrm{dx}}\right) \mathrm{dx} \tag{1.15}$$

Setting the mass to a negligible amount, the absorbed dose D (punctual) is assessable.

Consider by assuming that the incident photon interacts with Compton reaction (scattering of the incident photon with a degraded energy and a deflection angle and transferring energy to an electron in the collision) which is the essential reactions in human tissue for photons in the field of energy which we are concerned in this book. We are able to assess the probability with which this interaction will raise in the sensitive volume and the mean energy transferred to the electron of the sensitive volume (effective and classical physics section). Depending on the size of the sensitive volume, we can also estimate the mean number of interactions therein. However, when these interactions take place, we are unable to determine precisely where this interaction will occur in the sensitive volume, nor with what angle will be emitted secondary electrons set in motion. Consequently, it is impossible to determine the energy imparted ε, by the latter, in the sensitive volume, since we cannot know exactly the track that this emerging electron will perform in this sensitive volume. At this stage, the calculation of the dose is therefore not possible. However, the physical quantity available in this configuration is the energy transferred to the secondary particle that is at the origin of a dedicated quantity to indirectly ionizing radiation (photons and neutrons): it is the "Kerma" which is defined by the ratio of the total energy transferred to the secondary particles into a mass m by the same mass (1.16).

$$\overline{K} = \frac{\overline{E}_{tr}}{m} \tag{1.16}$$

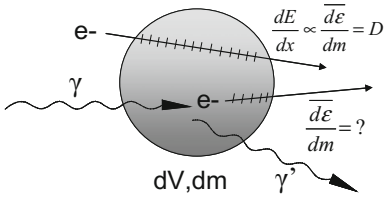

Fig. 1.6 Scheme of the distinction between energy imparted and energy transferred

This quantity is not appropriated for stochastic and a macroscopic context. His unit Gy remains as homogeneous to J kg^{-1}. Like the absorbed dose calculated with (1.10) we obtain the "kerma" by setting the mass m to a negligible amount (1.17).

$$K = \lim_{m \to 0} \overline{K} = \frac{\overline{dE_{tr}}}{dm} \tag{1.17}$$

As the absorbed dose, a kerma rate is defined according (1.18).

$$\dot{K} = \frac{dK}{dt} \tag{1.18}$$

Its unit is the same as the absorbed dose rate, the Gy s^{-1}. To illustrate the conceptual distinction between both fundamental dosimetric quantities that are kerma and absorbed dose, Troesh and Choudens [7] propose a count of energies transferred and imparted in Fig. 1.7.

Consider a mass of infinitesimal element m. In the proposed case in this figure, all of the kinetic energies of the secondary charged particles—electrons—transferred by photon radiation, that is to say the term E_{tr} kerma, is: $E_{tr} = E_1 + E_2$. However, the energy imparted into m, ε allowing access to the calculation of the

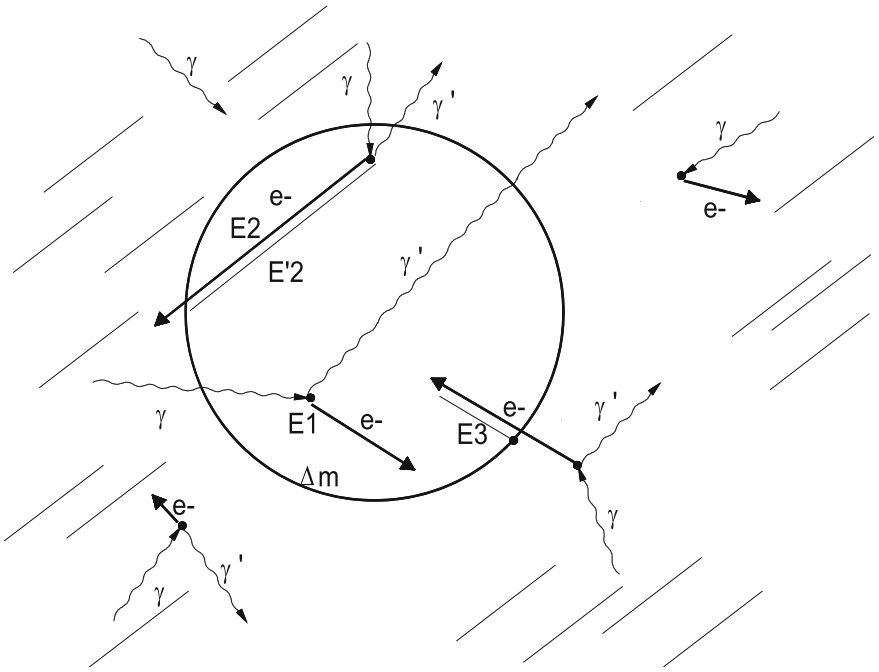

Fig. 1.7 Scheme of the distinction between absorbed dose and kerma in elementary volume, [7]. © Technical Documentation and 1997

absorbed dose is equal to: $\varepsilon = E_1 + E_2' + E_3$. It finally comes $E_{tr} \neq E_{at}$ and therefore for the same elementary mass element m : $D \neq K$. However, we will show in Chap. 2 that under certain conditions and assumptions (equilibrium of secondary charged particles set in motion), equivalence between kerma and absorbed dose for indirectly ionizing radiation is possible. Finally, let's add that the kerma is systematically measurable, while the absorbed dose is so only measurable under certain conditions.

1.2 Biological Damage and Relative Biological Effectiveness (RBE)

1.2.1 Radiation Injury on DNA of the Cell

Upon exposure to directly or indirectly ionizing radiation the cells are impacted and in particular the element most radioreactive thereof: the nucleus and its DNA molecule. The DNA damage may be caused either directly, that is to say, by ionization of the molecule by the passage of the ionizing radiation, or indirectly following a chemical interaction with a free radical produced by irradiation. A radical is a very reactive molecule with a non-bet valence electron. A free radical is a wandering radical which has not yet reacted and thereby threatening its neighbors. Their lifetime is about 10^{-5} s. For example, the ionization of a water molecule will create after several successive chemical reactions, the radical OH (hydroxyl radical) highly reactive, able to damage the DNA molecule in its vicinity. This indirect action via radicals, is the dominant mechanism of damage for low LET radiation, like X-rays.

The human body is composed of 70% water, so most of the damage will raise via OH radical. This justifies the widespread use of water as a irradiated medium in radiobiology studies. Radiation-induced lesions in the DNA consecutive to exposure are of several types: single break or double-stranded DNA-protein bypass formation. Figure 1.8 illustrates the different possible DNA damages by direct and indirect effect.

Among all of these lesions, double-strand breaks are considered as the major responsible for cell inactivation.

Repair mechanisms are triggered by these types of attacks; elimination by excising the lesion and restoration of the original information by resynthesis. However, in some circumstances, they are ineffective against the alteration of the cell structure.

The effects of radiation depend on the spatial distribution of energy deposited in the cell (LET). If the number of fractures formed in a small area of the molecule increases, these cracks can form complexes damage difficult to repair by the cell.

The results of there ineffective repair mechanisms, and chromosomal aberrations it can cause, lead to two outcomes for injured cell: the genetic mutation or death.

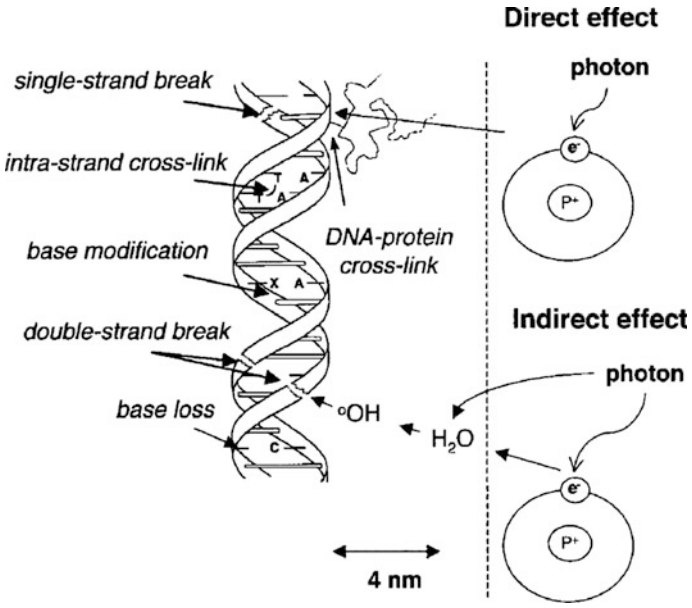

Fig. 1.8 Radiation-induced damage by direct and indirect effect of ionizing radiation on DNA, according to [1], with permission from Springer Heidelberg

Note that this inability is increased when the dose, instead of being spread over time, is instantly distributed; the repair mechanism is then "Swamped". This nuance is essential on the concept of dose rate. Adding that this issue becomes an asset when the aim is to destroy cancer cells: it is entirely appropriate in this context, to deliver a maximum dose in a short time at the tumor to kill most tumor cells as possible.

1.2.2 Cell Survival Rate and RBE

One way to characterize the "dose-effect" at the cellular level is for a given cell type, to observe the cell survival rate in accordance with the increase of the dose. To compare this effect for different types of radiation, radiation biologists have defined "relative biological effectiveness" RBE, which is defined as the ratio between the dose of a reference radiation and studied radiation inducing the same effect, that is to say the cell survival rate S_u. The reference radiation for which the RBE is arbitrarily set to 1 is an X-radiation of 250 keV, 1 MeV gamma, and an absorbed dose rate of 0.1 Gy.min^{-1}. The exposure rate is also important in quantifying biological damage, but we will not go into that level of detail. For any radiation R_i and a cell survival rate S_u, the RBA is calculated according to the expression (1.19).

$$\mathrm{RBE} = \frac{\mathrm{D}(\mathrm{S_u}, \mathrm{X}(250\ \mathrm{keV})}{\mathrm{D}(\mathrm{S_u}, \mathrm{R_i})} \tag{1.19}$$

For example, Fig. 1.9 gives a representation of the cell survival rate for gamma and neutrons.

In Fig. 1.9, to a cell survival rate of 0.1, the RBE obtained according to the expression (1.19) is:

$$\mathrm{RBE} = \frac{\mathrm{D}(0.1; \mathrm{X}(250\ \mathrm{keV})}{\mathrm{D}(0.1; \mathrm{n}[\mathrm{d}(50) + \mathrm{Be}])} = \frac{7.5\ \mathrm{Gy}}{3.8\ \mathrm{Gy}} \cong 2$$

1. 2.5 MeV alpha (Curve 1—LET = 166 keV μm^{-1})
2. 4 MeV alpha (Curve 2—LET = 110 keV μm^{-1})
3. 5.1 MeV alpha (Curve 3—LET = 88 keV μm^{-1})
4. 8.3 MeV alpha (Curve 4—LET = 61 keV μm^{-1})
5. 26 MeV alpha (Curve 5—LET = 25 keV μm^{-1})
6. 3 MeV deuteron (Curve 6—LET = 20 keV μm^{-1})
7. 14.9 MeV deuterons (Curve 7—LET = 5.6 keV μm^{-1})
8. 250 kVp X-rays (Curve 8—LET ≈ 1.3 keV μm^{-1}).

As mentioned above, the damage caused by ionizing radiation leading to cell death are related to the distribution of energy deposition in the cell and thus, for the same dose deposited at LET radiation considered. Figure 1.10 gives a

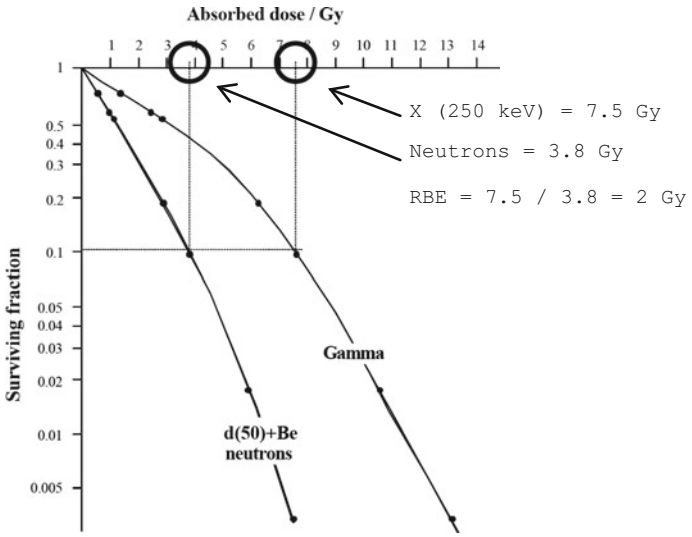

Fig. 1.9 Cell survival rate depending on the dose of gammas and neutrons from the reaction of 50 MeV deuteron on beryllium target—sample calculation RBE, adapted from [8]

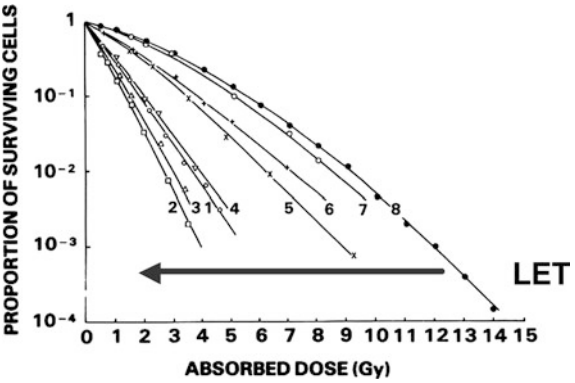

Fig. 1.10 Effect of LET on cell survival curves. Cell survival curves in vitro for human kidney cells exposed to different types of radiation, adapted from [9]

representation of the cell survival rates for renal cells, for different types of decreasing LET radiation.

1. 2.5 MeV alpha (Curve 1—LET = 166 keV μm^{-1})
2. 4 MeV alpha (Curve 2—LET = 110 keV μm^{-1})
3. 5.1 MeV alpha (Curve 3—LET = 88 keV μm^{-1})
4. 8.3 MeV alpha (Curve 4—LET = 61 keV μm^{-1})
5. 26 MeV alpha (Curve 5—LET = 25 keV μm^{-1})
6. 3 MeV deuteron (Curve 6—LET = 20 keV μm^{-1})
7. 14.9 MeV deuterons (Curve 7—LET = 5.6 keV μm^{-1})
8. 250 kVp X-Rays (Curve 8—LET ≈ 1.3 keV μm^{-1}).

Note that the RBE increases with the increase of LET (since the deposited dose required for the same effect decreases [denominator (1.19)]. However, this applies to a LET about 110 keV $\mu m\ m^{-1}$ (curve 2, 4 MeV alpha), beyond the RBE decreases (curve 1, 2.5 MeV alpha). Figure 1.11 gives the RBE as a function of LET microscopic equivalent: the lineal energy y. From it are determined "transfer factors" needed to obtain protection and operational quantities, respectively the weighting factor for radiation w_R and the quality factor Q we will detail later in Chap. 3.

We can admit that a cell is killed when it has accumulated a certain amount of damage. Consider this occurrence takes place arbitrarily when three ionization takes place (ionization = black dots). The three configurations of the illustration proposed in Fig. 1.12 are lethal to the cell.

Configuration (1). For low LET radiation, below 15 keV μm^{-1}, the amount of energy deposition (and thus damage) by passing a weak trajectory is generally to cause cell death and more paths are required to accumulate enough damage and kill the cell. The amount of energy increases with LET and it takes less track to kill the cell, it results in an increase of the RBE between 15 keV μm^{-1} and up to about 50 keV μm^{-1}.

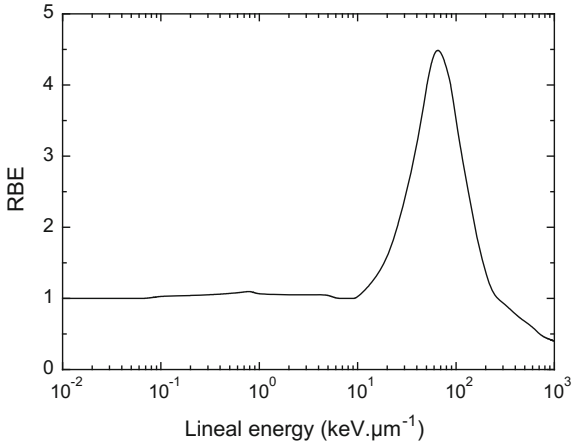

Fig. 1.11 Relative biological effectiveness (RBE) based on the lineal energy, adapted from [10]

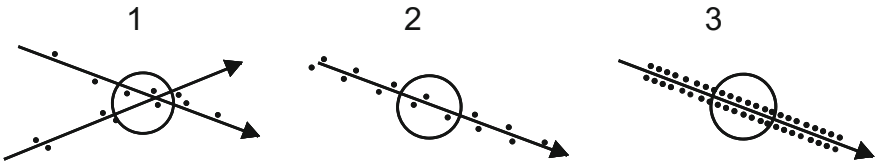

Fig. 1.12 Diagram of three lethal configurations for the cell—black dots are the successive ionization along the path, according to [8]

Configuration (2). RBE maximum is reached when a single path delivers on average just enough energy to kill the cell between 50 and 100 keV μm^{-1}.

Configuration (3). Beyond, the passage of a single path expends more energy than necessary to kill the cell, there is a "waste of energy" and in fact decrease the RBE since the definition is the ratio of doses required to produce a given effect. Furthermore, with a massive energy deposition over a short distance, the following cells will be made more "spared" at equal dose than in the case of particles with lower LET; we speak of an "energy cluster" effect.

Figure 1.13 adds to this RBE microdosimetric curves, spectra of three types of particles: gamma, protons and neutrons.

Strictly speaking, with a LET $\overline{L}$ approach, the RBE value is partially incorrect. In particular, as shown in Fig. 1.13 for the interval of microdosimetric spectrum located in the region of strongest RBE: 50 and 100 keV μm^{-1}. The method of calculation of the mean RBE incorporates this strong RBE area. if $r(y)$ is RBE

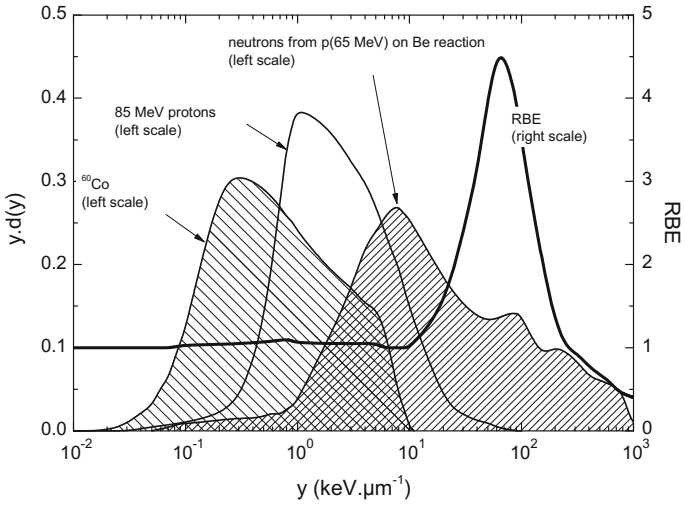

Fig. 1.13 Curve RBE and microdosimetric spectra gamma ^{60}Co, 85 MeV proton and neutron from the bombardment of a beryllium target with protons of 65 MeV, adapted from [10]

in respect with given lineal energy, mean EBR is calculated using the expression (1.20).

$$\overline{\mathrm{EBR}} = \int_{y_{min}}^{y_{max}} r(y)\, d(y)\, dy \tag{1.20}$$

It is recalled that the dose distribution in the lineal energy $d(y)$ is normalized to 1 (see Further Details 1.1). We will see in Chap. 2 that is with mean of this approach that is calculated the mean quality factor for a radiation field.

1.3 Radiometric Quantities

Dosimetric quantities of reference, punctual concepts, are absorbed dose D and Kerma K respectively defined by the expression (1.10) and (1.17). In the above, we have clearly established link between these specific quantities and ionizing radiation density in the sensitive volume. We therefore propose in this part to define the physical quantities to characterize directly and indirectly ionizing radiation field, called "radiometric quantities." From some of them, it will be possible to assess the dose quantities previously described.

1.3.1 Radiation Field Characterization

To determine at point P in space the action of radiation in a given environment, we define the radiation field characterized by the mathematical function to six variables: $\varphi_u\left(\vec{r},\vec{u},E,t\right)$. This function is the number of particles propagating at a point P of the spatial coordinate $\vec{r}$, in the direction $\vec{u}$, In a solid angle Ω, around $\vec{u}$, with an energy E, at time t according to the diagram of Fig. 1.14. This is called "angular distribution of fluence."

In Cartesian coordinates, the unit vector $\vec{u}$ is defined by (1.21).

$$\vec{u}\begin{cases}\sin\theta\cdot\cos\varphi\\ \sin\theta\cdot\sin\varphi\\ \cos\theta\end{cases} \tag{1.21}$$

Prior to the practical definition of this quantity, it should define a number of tools and intermediate quantities.

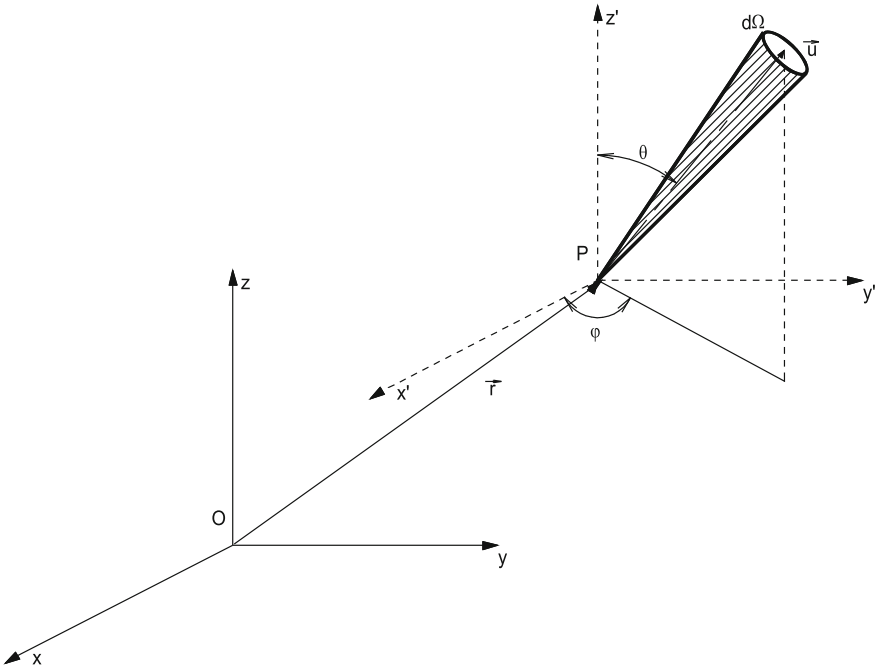

Fig. 1.14 Representation of an angular distribution of fluence

1.3.2 Radiant Energy and Flux

The number of particles emitted transferred or received at a point is characterized by the variable N (Dimensionless). The "radiant energy R" is defined as the total energy of the particles (excluding the rest energy) transferred or received in a point; his unit is the joule. To illustrate these terms, consider that a point in space, cross N particles and that they have 4 discrete possible energies: E_1, E_2, E_3 or E_4. We can then represent "the energy distribution" of these N particles according to Fig. 1.15.

The number of particles N is the sum of all the particles, regardless of their energy, and is given by (1.22). The radiant energy R also a sum, but this time the number of particles N *is* weighted by respective energy *Ei* (1.23).

$$\mathrm{N} = \sum_{\mathrm{i}} \mathrm{N}(\mathrm{E_i}) \tag{1.22}$$

$$\mathrm{R} = \sum_{\mathrm{i}} \mathrm{N}(\mathrm{E_i}) \cdot \mathrm{E_i} \tag{1.23}$$

We can then calculate a weighted average of the mean energy this energy distribution according (1.24).

$$\overline{E} = \frac{R}{N} = \frac{\sum_i N(E_i) \cdot E_i}{\sum_i N(E_i)} \tag{1.24}$$

In the case of 4 rays emission, shown in Fig. 1.15, the ratio of the radiant energy by the number of particles emitted, leading to the result of the mean energy would be:

$$\overline{E} = \frac{R}{N} = \frac{N_1E_1 + N_2E_2 + N_3E_3 + N_4E_4}{N_1 + N_2 + N_3 + N_4}$$

While this trivial approach is applicable, for example, de-excitation photons emitted during radioactive decay, most distributions encountered in the nuclear environment (particle accelerator, reactors, cosmic …) are continuous. More readily we speak of "spectral energy distribution" or "energy spectra."

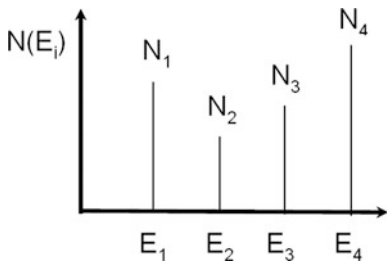

Fig. 1.15 Example of discrete energy distribution

In the context of continuous distribution, if N is the number of particles passing through a point in space whose energy distribution is continuous, it is necessary to define "the spectral energy distribution" characterized by the ratio of the increase in the number dN in the energy interval between infinitesimal E and E + dE (1.25).

$$\mathrm{N_E} = \left(\frac{\mathrm{dN}}{\mathrm{dE}}\right) \tag{1.25}$$

This variable dimension is an inverse of energy: keV^{-1} or MeV^{-1}. Thus, in this continuous distribution context, the term (1.23) becomes (1.26).

$$\mathrm{R} = \int_0^{\mathrm{E_{Max}}} \left(\frac{\mathrm{dN}}{\mathrm{dE}}\right) \mathrm{E}\,\mathrm{dE} = \int_0^{\mathrm{E_{Max}}} \mathrm{N_E E}\,\mathrm{dE} \tag{1.26}$$

Similarly, the mean energy obtained previously by the expression (1.24) is obtained by this time (1.27).

$$\overline{\mathrm{E}} = \frac{\int_0^{\mathrm{E_{Max}}} \mathrm{N_E E}\,\mathrm{dE}}{\int_0^{\mathrm{E_{Max}}} \mathrm{N_E}\,\mathrm{dE}} \tag{1.27}$$

In order to integrate the time component, we define the "flux" or "emission" in the case of a source that emits N particles per unit time according (1.28).

$$\dot{\mathrm{N}} = \left(\frac{\mathrm{dN}}{\mathrm{dt}}\right) = \lim_{\mathrm{t}\to 0}\left(\frac{\mathrm{N}}{\mathrm{t}}\right) \tag{1.28}$$

The size of this variable is (s^{-1}). In the literature, particularly in the standards, this variable is sometimes symbolized by *B (for Beam)*. We will actually not difficult to be convinced of the similarity there may be between a point source which emits radiation with a certain flux $\dot{N}$ and a point in space crossed with a flux $\dot{N}$. If both situations are not physically the same, the quantity that characterizes the number of radiation emerging at a time t is the same in both cases: $\dot{N}$.

Finally, note that there is also the quantity "radiant energy flux" $\dot{R}$, according to (1.29).

$$\dot{\mathrm{R}} = \left(\frac{\mathrm{dR}}{\mathrm{dt}}\right) \tag{1.29}$$

This quantity is the ratio of increase of the radiant energy R over a time interval t in a point of space. Its unit is typically the MeV s^{-1}. We have just defined punctual radiometric quantities applicable to continuous spectral distributions. In practice, the lack of analytical expression or precision in the experimental

information requires treating the representations of these quantities by histograms of energy bins and performing a sampling of the energy distribution.

If $\dot{N}$ is particles flux in a point in space whose energy distribution is continuous, it is necessary to define the spectral energy distribution characterized by the ratio of the increase in transmission the source $d\dot{N}$ in the energy interval between infinitesimal E and $E + dE$ (1.30).

$$\dot{N}_E = \left(\frac{d\dot{N}}{dE}\right) \tag{1.30}$$

This variable has the typical size: $MeV^{-1}\ s^{-1}$. This distribution is used to determine the part of emission or particle flux within the energy range between E_1 and E_2 according to (1.31), as shown in Fig. 1.16.

$$\dot{N}(E_1; E_2) = \int_{E_1}^{E_2} \dot{N}_E \, dE \tag{1.31}$$

Indeed, across the spectrum, we get the total value of particle flux (1.32)

$$\dot{N} = \int_0^{E_{Max}} \dot{N}_E \, dE \tag{1.32}$$

As a simple example, consider the spectral distribution characteristic of the source emission or a flux of 1000 (n) s^{-1} whose energy is between 1 and 10 MeV. This is thus defined by:

$$\begin{aligned} \dot{N}_E &= 1000/10 = 100\ MeV^{-1}\ s^{-1} && E \in [1\ MeV;10\ MeV] \\ \dot{N}_E &= 0 && E \notin [1\ MeV;10\ MeV] \end{aligned}$$

that may be represented by Fig. 1.17.

In some very rare cases, it is possible to assess the analytical expression, true or approaching, the spectral energy distribution of the emission of a source or a stream of particles. For example, this is the case for the neutron emission by spontaneous fission,

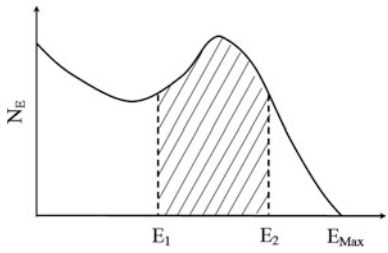

Fig. 1.16 Spectral energy distribution of a source emission or a particle flux for a continuous distribution

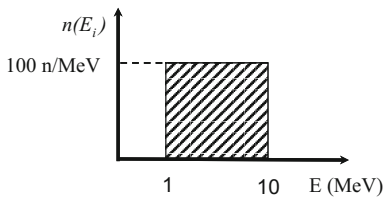

Fig. 1.17 Energy distribution of a flux of 1000 (n) s^{-1}, the neutron energy is between 1 and 10 MeV

as will be illustrated later in this paragraph by the spontaneous fission spectrum of ^{252}Cf radionuclide.

1.3.3 Application to Neutron Spectrum of ^{252}Cf

The probability that a neutron is emitted with an energy E during fission is described by an analytical expression of type "Maxwell" (1.33).

$$\mathrm{p(E)} = \frac{2}{\sqrt{\pi}\mathrm{T}^{3/2}}\left(\sqrt{\mathrm{E}}\right)\exp\left(-\frac{\mathrm{E}}{\mathrm{T}}\right) \tag{1.33}$$

With T a parameter of the spectrum (T = 1.42 MeV for the ^{252}Cf [11]). The spectral distribution by weighting this probability density by issuing $\dot{N}$ Source is accessed (1.34).

$$\dot{N}_E = p(E)\dot{N} \tag{1.34}$$

For example, let's determine the emission rate of 0.6 MeV neutron by a ^{252}Cf source for a total neutron emission $\dot{N}$ normalized to 1(n) s^{-1}.

$$\dot{N}_{0.6} = p(0.6)\dot{N} = \frac{2}{\sqrt{\pi}(1.42)^{3/2}}\left(\sqrt{0.6}\right)\exp\left(-\frac{0.6}{1.42}\right) \times 1 = 0.338\ \mathrm{s}^{-1}$$

In what follows, we describe how are represented practically the data of this type of energy distribution, first in a table and then graphically.

1.3.4 Representation of Data to an Energy Distribution in an Array

In Table 1.2, The spectral energy distribution is given in the form of groups $\dot{N}_i$ according to energy bins, meaning that the emission of neutrons having an energy between E_i and E_{i+1} is obtained according to (1.35).

Table 1.2 Example of an energy bin distribution for the ^{252}Cf source [11] data from NF ISO 8529-1 March 2002 © AFNOR 2002

Ei (MeV)	N_i (s^{-1})	Ei (MeV)	N_i (s^{-1})	Ei (MeV)	N_i (s^{-1})	Ei (MeV)	N_i (s^{-1})
4.14×10^{-7}	3.10×10^{-10}	4.00×10^{-2}	2.80×10^{-3}	6.00×10^{-1}	3.38×10^{-2}	3.50×10^{0}	4.68×10^{-2}
1.00×10^{-6}	1.11×10^{-8}	6.00×10^{-2}	3.29×10^{-3}	7.00×10^{-1}	3.39×10^{-2}	4.00×10^{0}	3.49×10^{-2}
1.00×10^{-5}	2.76×10^{-7}	8.00×10^{-2}	3.68×10^{-3}	8.00×10^{-1}	3.37×10^{-2}	4.50×10^{0}	2.58×10^{-2}
5.00×10^{-5}	2.76×10^{-7}	1.00×10^{-1}	1.05×10^{-2}	9.00×10^{-1}	3.33×10^{-2}	5.00×10^{0}	3.30×10^{-2}
1.00×10^{-4}	7.82×10^{-7}	1.50×10^{-1}	1.21×10^{-2}	1.00×10^{0}	6.46×10^{-2}	6.00×10^{0}	1.74×10^{-2}
2.00×10^{-4}	2.21×10^{-6}	2.00×10^{-1}	1.33×10^{-2}	1.20×10^{0}	6.12×10^{-2}	7.00×10^{0}	9.01×10^{-3}
4.00×10^{-4}	4.53×10^{-6}	2.50×10^{-1}	1.42×10^{-2}	1.40×10^{0}	5.73×10^{-2}	8.00×10^{0}	4.61×10^{-3}
7.00×10^{-4}	5.68×10^{-6}	3.00×10^{-1}	1.49×10^{-2}	1.60×10^{0}	5.31×10^{-2}	9.00×10^{0}	2.33×10^{-3}
1.00×10^{-3}	5.51×10^{-5}	3.50×10^{-1}	1.55×10^{-2}	1.80×10^{0}	4.88×10^{-2}	1.00×10^{1}	1.17×10^{-3}
3.00×10^{-3}	1.28×10^{-4}	4.00×10^{-1}	1.60×10^{-2}	2.00×10^{0}	6.55×10^{-2}	1.10×10^{1}	5.83×10^{-4}
6.00×10^{-3}	2.30×10^{-4}	4.50×10^{-1}	1.63×10^{-2}	2.30×10^{0}	5.67×10^{-2}	1.20×10^{1}	2.88×10^{-4}
1.00×10^{-2}	7.74×10^{-4}	5.00×10^{-1}	1.66×10^{-2}	2.60×10^{0}	6.33×10^{-2}	1.30×10^{1}	1.42×10^{-4}
2.00×10^{-2}	2.17×10^{-3}	5.50×10^{-1}	1.68×10^{-2}	3.00×10^{0}	6.21×10^{-2}	1.40×10^{1}	6.94×10^{-5}
						1.50×10^{1}	–

$$\dot{\mathrm{N}}_{\mathrm{i}} = \int_{\mathrm{E_i}}^{\mathrm{E_{i+1}}} \dot{\mathrm{N}}_{\mathrm{E}}\,\mathrm{dE} \tag{1.35}$$

In this case of the spontaneous fission emission of the ^{252}Cf source, $\dot{N}_i$ groups are calculated by numerical integration using the analytic function (1.34). For other sources—e.g. ^{241}Am (α, n)Be—this type of expression is not accessible and experimental data are used. More generally, for any flux particles, at a point in space, process would be the same; accessed by measurement or by numerical simulation (e.g. type of transport code Monte Carlo) with results by energy bins. In Table 1.2, the energy given to each $\dot{N}_i$ is the lower limit, *Ei* of the energy interval index *i*, the last energy index specified in each table is the upper limit of the last energy interval index. In the case of Table 1.2, energy bins are normalized to a total emission: $\dot{N}_i = 1\ \mathrm{s}^{-1}$. The sum leads to unity (1.36).

$$\sum_{\mathrm{i=1}}^{\mathrm{n}} \dot{\mathrm{N}}_{\mathrm{i}} = 1\ \mathrm{s}^{-1} \tag{1.36}$$

For example, to calculate the flux part of the 25th energy bin in Table 1.2 (the lower bound *Ei* = 0.6 MeV), the numerical calculation leads to the result in accordance with that announced by Table 1.2.

$$\dot{N}_{25} = \int_{0.6}^{0.7} \frac{2}{\sqrt{\pi}(1.42)^{3/2}} \left(\sqrt{E}\right) \exp\left(-\frac{E}{1.42}\right) dE \cong 0.038\ \mathrm{s}^{-1}$$

The values given in the table allow to calculate the flux part between the energies E_a and E_b by simply adding the corresponding emission groups (1.37).

$$\dot{N}(E_a; E_b) = \sum_{i=a}^{i=b-1} \dot{N}_i \tag{1.37}$$

Note that this expression is a "sampled" approach to the expression of a continuous distribution (1.31).

Thus, to know the ^{252}Cf neutron emission between 0.6 and 1.2 MeV: 25th group (i.e. lower bound *Ei* = 0.6 MeV) up to 29th group (i.e. lower bound *Ei* = 1 MeV), the sum (1.37) with the values in Table 1.2 gives:

$$\dot{\mathrm{N}}(0.6; 1.2) = \sum_{\mathrm{i=25}}^{\mathrm{i=29}} \dot{\mathrm{N}}_{\mathrm{i}} \approx 0.2\ \mathrm{s}^{-1}$$

Obtaining the mean energy of the spectral energy distribution of this "histogram approach", while the expression (1.27) for the continuous approach, is obtained according to (1.38).

$$\bar{E} = \frac{\sum_{i=1}^{n} \dot{N}_i \, E_i}{\sum_{i=1}^{n} \dot{N}_i} \tag{1.38}$$

In the case of normalization, in Table 1.2, the previous expression becomes (1.39) and we obtained for ^{252}Cf:

$$\bar{E}\left(^{252}Cf\right) = \sum_{i=1}^{n} \dot{N}_i E_i \approx 2.13 \text{ MeV} \tag{1.39}$$

The size of flux intervals necessarily influences the value of the mean energy and its deviation from its true value.

1.3.5 Graphical Representation Distribution Energy

While the values of flux bins are the fundamental data from physical measurements or calculations and serving in other integration calculations, they are inappropriate for the graphic representation of the spectra because their values depend on the width (arbitrary) energy intervals. For sources, the most common graphic representations are the spectral emission $\dot{N}_E = \mathrm{d}\dot{N}/\mathrm{d}E$ in terms of E when the energy is in linear scale and represented by (1.40) when E is a logarithmic scale.

$$\frac{d\dot{N}}{d(\ln(E/E_o))} \tag{1.40}$$

Historically this term comes from the neutron and is known as "plotted lethargy". Arbitrary parameter E_0 is necessary to ensure that the argument of the logarithm is of dimension 1, and mathematically as: d(ln x) = dx/x. It results from the equality (1.41).

$$\frac{\mathrm{d}\dot{N}}{\mathrm{d}(\ln(E/E_o))} = E\left(\frac{\mathrm{d}\dot{N}}{\mathrm{d}E}\right) = E\dot{N}_E \tag{1.41}$$

So for energy, x-axis, expressed in logarithmic scale, it will be common to see one of the three formalisms equality (1.41). Based on these assumptions, it is possible to draw curves so that equal areas under the curves represent equal particle flux.

$$\int_{E_1}^{E_2} \dot{N}_E \, \mathrm{d}E = \int_{E_1}^{E_2} E\dot{N}_E (\mathrm{d}E/E)$$

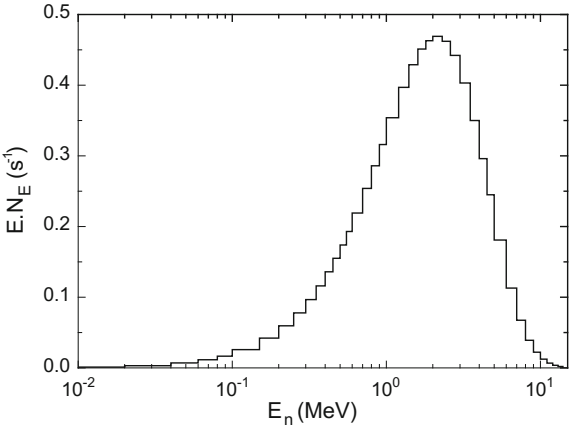

Fig. 1.18 Energy distribution of spontaneous fission neutron emission for ^{252}Cf with the graduated abscissa in logarithmic scale, from Table 1.2

Note that $E\dot{N}_E$ has again the dimension of a particle flux (s^{-1}), while a curve with graduated abscissa linearly, the ordinates of values would be calculated from the approach "sampled" by (1.42).

$$\dot{N}_E = \frac{\Delta\dot{N}}{\Delta E} = \frac{\dot{N}}{(E_{i+1} - E_i)} \tag{1.42}$$

They must be for a plot with the graduated abscissa logarithmically calculated according to (1.43).

$$E_n\dot{N}_E = \frac{\dot{N}_i}{\ln(E_{i+1}/E_i)} \tag{1.43}$$

Let us add that because of spectra that can be spread over ten decades logarithmic representation is required. Figure 1.18 gives a product of the histogram $E\dot{N}_E$ of ^{252}Cf on a linear axis, as a function of neutron energy *En* on a logarithmic x-axis.

1.3.6 Fluence Definition and Interest in Dosimetry and Radiation Protection

The question we can ask at this stage is: the particle flux $\dot{N}$ at a point of the space it is sufficient to characterize the radiation field and, consequently, the absorbed dose at a point? The answer is no. We have been clear, in previous paragraphs that the greater the spatial density of radiation is important for a same time interval and the absorbed dose or kerma increased. If we consider two sensitive sites with slightly different volumes, crossed by three radiations, the flux of particles in these two sites

is the same: $\dot{N}_1 = \dot{N}_2$. Volumes are different however: this necessarily leads to an absorbed dose or kerma in the case of indirectly ionizing radiation, different in both cases (Fig. 1.19).

In addition to increasing the amount of radiation which passes through a point in space during the time interval we are obliged to use a variable that takes into account the spatial density of radiation. This quantity is called "fluence". We can for example characterize it considering a microscopic sphere of radius r, Volume V and section a (area describing the boundary between the two half-spheres) and counting the radiation which pass through the section a as shown in Fig. 1.20.

There is a simple calculation method, which is also used in the Monte Carlo transport code, to achieve this radiant quantity. The latter is to recognize all radiation entering the volume of sphere V and radius r and to weight the latter by the mean length of chord, while dividing the final result by the volume V. If N is the number of particles counted, the "mean fluence" in Volume V is then described by the expression (1.44)

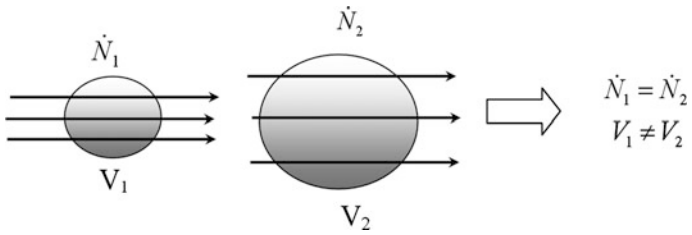

Fig. 1.19 Illustration of use limit of flux for an application in dosimetry and radiation protection

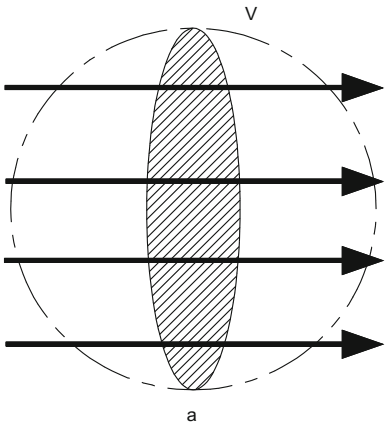

Fig. 1.20 Illustration of the fluence calculation in a sensitive site comparable to a sphere of radius r and section a

$$\bar{\Phi} = \frac{N\bar{l}}{V} \tag{1.44}$$

This is a mean result; we assumes indeed that on average, an incoming particle performs in Volume V a path length equal to the mean chord. Knowing the value of the previously calculated mean chord ($\bar{l} = (4/3)r$). In the case of a sensitive volume theoretically materialized by a sphere, we deduce a trivial result for expression (1.45).

$$\bar{\Phi} = \frac{N(4/3)r}{(4/3)\pi r^3} = \frac{N}{\pi r^2} = \frac{N}{a} \tag{1.45}$$

This amounts to counting the number of particles that cross the section (a) of the sphere. The practical unit of this quantity is cm^{-2}. From this mean microscopic quantity, it comes to getting a punctual quantity that can be connected to punctual dose quantities previously defined. This is achieved by setting the section to a negligible amount, according to (1.46).

$$\lim_{a\to 0} \bar{\Phi} = \frac{dN}{da} = \Phi \tag{1.46}$$

This quantity is called "particle fluence at a point in space" and is linked to most dose quantities and radiation related to external exposure. From this quantity, we define a "fluence rate" according (1.47).

$$\dot{\Phi} = \frac{d\Phi}{dt} \tag{1.47}$$

His unit is $cm^{-2}\ s^{-1}$. Thus, with the knowledge of the energy of radiation and of this quantity, all data are now available to characterize the radiation field at a point in space from which it is possible to obtain fundamental dosimetric quantities by means of a correlation coefficient. Below, from the fluence and with the knowledge of the energy of the incident radiation (for simplicity, we consider here only one possible energy E). It will be possible to determine the absorbed dose and kerma by simple proportionality relationship (1.48).

$$\begin{cases} K = k_\Phi(E)\Phi(E) \\ D = d_\Phi(E)\Phi(E) \end{cases} \tag{1.48}$$

The challenge in Chap. 2 will consist of determining precisely these correlation coefficients, with the knowledge of the energy transfer phenomena during the interaction of different types of radiation with matter.

As with the particle flux for a continuous spectrum, it is possible to define a spectral distribution of the fluence called "differential energy fluence" and

translating increasing fluence Φ on a range of the spectrum between energies E and $E + dE$ (1.49).

$$\Phi_E = \frac{d\Phi}{dE} \tag{1.49}$$

Its typical unit is cm^{-2} MeV^{-1}. As before, for the contribution to the total fluence Φ to an energy interval between E_1 and E_2. Calculation is performed according (1.50).

$$\Phi(\mathrm{E}_1;\mathrm{E}_2) = \int_{\mathrm{E}_1}^{\mathrm{E}_2} \Phi_{\mathrm{E}} \mathrm{dE} \tag{1.50}$$

Again, by integrating over the full spectrum, we obtain complete fluence Φ for the radiation field at the point considered. Another variable is likely to interest dosimetry, it is the "energy fluence" used to summon the energies of N particles that cross section *at* of Fig. 1.20. It is expressed in infinitesimal manner from the radiant energy and differential energy fluence as expressed in (1.51).

$$\Psi = \frac{\mathrm{dR}}{\mathrm{da}} = \int_{\mathrm{E}} \left(\frac{\mathrm{d}^2\mathrm{N}}{\mathrm{da}\,\mathrm{dE}}\right) \mathrm{EdE} = \int_{\mathrm{E}} \Phi_{\mathrm{E}} \mathrm{E}\,\mathrm{dE} \tag{1.51}$$

His unit is expressed typically in MeV cm^{-2}. We define the "energy fluence rate" in the words (1.52)

$$\dot{\Psi} = \int_E \dot{\Phi}_E E\, dE \tag{1.52}$$

whose unit is expressed in MeV in cm^{-2} s^{-1}. We also calculate these quantities from the mean energy of a radiation spectrum as (1.53).

$$\bar{E} = \frac{\int_0^\infty \Phi_E E\, dE}{\int_0^\infty \Phi_E dE} = \frac{\Psi}{\Phi} \tag{1.53}$$

All that has been previously discussed for the bin setting in the graphical representation of source emission can be applied to the particle fluence. Thus, when the abscissa is set to logarithmic scale, it will be common to read one of the three formalisms given below, for the ordinate of the differential energy fluence Φ_E.

$$\frac{d\Phi}{d(\ln(E/E_o))} = E\left(\frac{d\Phi}{dE}\right) = E\Phi_E \tag{1.54}$$

Let's finally mention two other quantities of interest for isotropic or rotationally symmetrical source (e.g. target irradiated by beam accelerator). The "angular fluence rate" characterize the number of particles spreading in a solid angle Ω during a

time t (1.55) whose unit is the Sr^{-1} s^{-1} and the angular energy fluence rate (1.56), whose unit is the MeV Sr^{-1} s^{-1}.

$$\omega = \frac{d^2N}{dt\, d\Omega} \tag{1.55}$$

$$\omega_E = \frac{d^2R}{dt\, d\Omega} \tag{1.56}$$

Although discrete radiation is encountered in conventional radiation sources: de-excitation photon during decays, conversion electrons, secondary particles of energy secured in the event of special nuclear reactions (e.g. 14 MeV neutron to the fusion reaction) … in most situations shielding, interposition or structural elements of facility affect these discrete energy which results in continuous energy spectrum. We'll develop it extensively in the following chapters. For now, to illustrate how to practice fluence, we propose to study the properties related to the calculation of the fluence induced by isotropic point source, that is to say, emitting the same way in all directions of space.

1.3.7 Calculating the Fluence Induced by an Isotropic Point Source

Let's apply the expression (1.45) of the particles fluence rate in case of an isotropic point source. Beforehand, let's determine by which surface it's necessary to divide the particles flux to get the fluence rate at a distance r from an isotropic source. An isotropic source transmits with equal probability in all directions in space and consequently provide a spherical symmetry for the emission of particles. This property allows to assume that in a virtual sphere centered on the source of radius r_1, each cm^2 of the sphere is crossed by the same number of particles. If we increase the radius to a value r_2, we can intuitively convince us that this property remains true, but in this case the number of particles passing through each cm^2 decrease, since the distance from the source. Figure 1.21 shows schematically this basic concept.

Indeed, one can figure out that three particles emitted by the source spaced from each other with the same angle—because of the spherical symmetry—cross 1 cm^2 of the sphere of radius r_1; because of the path divergence, only one particle pass through 1 cm^2 of the sphere of radius r_2. Thus, to the distance r_1, we have a fluence of three particles per cm^2 and to the distance r_2, a fluence of one particle per cm^2. Thus, the larger the radius of the sphere increases, the lower the fluence rate of particles will be important in a point thereof. The expression of the particle fluence at a distance r of the source in the case of an isotropic source in space is given by the ratio of the number of particles emitted by the source, on the surface of the "virtual" sphere of radius r as expressed by (1.57).

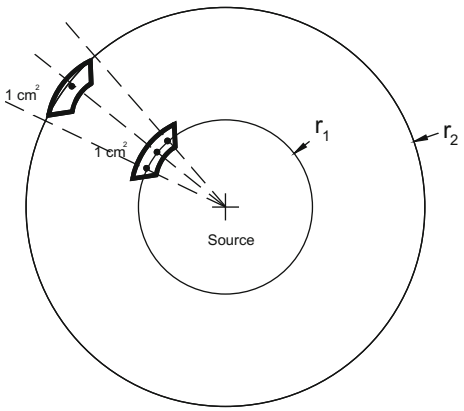

Fig. 1.21 Fluence rate of an isotropic source in space and impact of the distance of calculation point

$$\Phi = \frac{N}{4\pi r^2} \tag{1.57}$$

Note that the fluence can be likened to a spatial density of current flowing through a sphere at a distance r to the source.

By taking up the case of the previous two spheres and a number of particles N, we get the following fluence of particles:

$$\Phi_1 = \frac{N}{4\pi r_1^2} \quad \text{and} \quad \Phi_2 = \frac{N}{4\pi r_2^2}$$

We can spontaneously notice the following property:

$$\frac{\Phi_1}{\Phi_2} = \left(\frac{r_2}{r_1}\right)^2.$$

and yet that:

$$\Phi_1 = \left(\frac{r_2}{r_1}\right)^2 \Phi_2$$

So it is possible to spontaneously get a fluence of particles at any distance from the source, if you know the value of the fluence at another distance. More generally for two distances d_1 and d_2 responsible for respective influences Φ_1 and Φ_2, the relationship between all of these terms is given by (1.58).

$$\frac{\Phi_1}{\Phi_2} = \left(\frac{d_2}{d_1}\right)^2 \tag{1.58}$$

Note, finally, that this law is necessarily valid for the ratio of particle fluence rates:

$$\frac{\dot{\Phi}_1}{\dot{\Phi}_2} = \left(\frac{d_2}{d_1}\right)^2$$

To illustrate concretely some of the variables described below, apply these concepts to simple cases. For example, consider a point source that emits isotropically, $\dot{N} = 5 \cdot 10^6$ particles per second, calculate the angular fluence rate, fluence rate to 1 and 3 m. For this calculation, divide the number of particles emitted per unit of time by the total solid angle around the source, i.e. 4π; we are getting then:

$$\omega = \frac{\dot{N}}{4\pi} = \frac{5 \cdot 10^6}{4\pi} \cong 4 \cdot 10^5 \text{ Sr}^{-1} \text{ s}^{-1}$$

Note that from the angular fluence rate, we can get directly the fluence rate at any distance from the source: it is sufficient to divide ω by the squared distance. Thus we get the fluence rates at 1 and 3 m, as following:

$$\dot{\Phi}_{1\,\text{m}} = \frac{\omega}{d^2} = \frac{N}{4\pi d^2} = \frac{4 \cdot 10^5}{100^2} = 40\,\text{cm}^{-2}\text{s}^{-1} \quad \text{and}$$
$$\dot{\Phi}_{3\,\text{m}} = \frac{\omega}{d^2} = \frac{N}{4\pi d^2} = \frac{4 \cdot 10^5}{300^2} = 4.4\,\text{cm}^{-2}\,\text{s}^{-1}$$

Now consider an isotropic point source in space, whose flux is $3 \cdot 10^5$ particles per second, with isotropic energy and emitting a single energy ray of 0.6 MeV. Calculate the angular energy fluence rate and energy fluence rate at 0.5 m.

$$\omega_E = \frac{\dot{N}E}{4\pi} = \frac{3 \cdot 10^5 \cdot 0.6}{4\pi} = 1.4 \cdot 10^4 \text{ MeV Sr}^{-1} \text{ s}^{-1}$$

was obtained, similarly to previously, the energy fluence rate to 0.5 m:

$$\left(\dot{\Phi}E\right)_{0.5\,\text{m}} = \frac{\omega_E}{d^2} = \frac{NE}{4\pi\, d^2} = \frac{1.4 \cdot 10^4}{50^2} = 5.6\,\text{MeV cm}^{-2}\,\text{s}^{-1}$$

A 1 MBq point source of ^{65}Ni emits through the decay β, 366, 1116 and 1482 keV gamma-rays, respectively with the emission rates: 5, 15 and 24% [12]; we get the energy fluence rate 0.5 m, in the void:

$$\psi_{0.5\,\text{m}} = \frac{A\sum_{i=1}^{3}\Gamma_i E_i}{4\pi\, d^2} = \frac{1 \cdot 10^6 \times (0.366 \times 5 \cdot 10^{-2} + 1.116 \times 0.15 + 1.482 \times 0.24)}{4\pi(50)^2}$$
$$= 17.2 \text{ MeV cm}^{-2} \text{ s}^{-1}$$

1.3.8 Calculation of the Fluence Induced by a No Punctual Source

For non-point object, let it a density of activity corresponding to the ratio of the total activity of the radiating object on length, area or volume depending on the number of dimensions that characterizes it. The calculation of the fluence at a point then is provided by an integration on all the dimensions of the object. This approach physically equivalent to considering the object as a sum of independent point sources.

To illustrate the case of calculating the fluence for a non-point source, consider a linear source of flux $\dot{N}$ and length L. Figure 1.22 represents the studied geometry.

Considering the flux volume density $n_L = \dot{N}/L$, the expression of flux density due to an infinitesimal element "dl" is given by the following expression:

$$d\dot{\Phi} = \frac{n_L}{4\pi\rho^2} dl$$

we have mathematically:

$$\text{h.tan}(\theta) = 1 \quad \text{so} \quad \text{h}\frac{d\theta}{\cos^2\theta} = dl$$

$$\text{and } \rho = \frac{h}{\cos\theta}$$

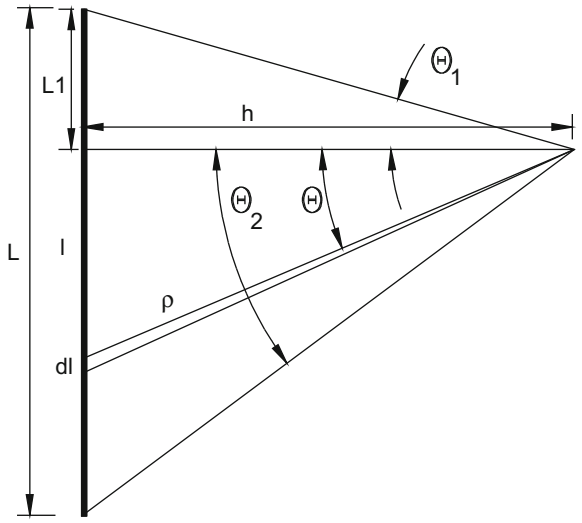

Fig. 1.22 Geometry for the calculation of the fluence of a line

we can deduce

$$d\dot{\Phi} = \frac{n_L\left(\frac{h}{\cos^2\theta}\right)}{4\pi\left(\frac{h}{\cos\theta}\right)^2} d\theta$$

to consider all of geometry, then it should be integrated across the line. hence:

$$\dot{\Phi} = \int_L d\dot{\Phi} = \frac{\dot{N}}{4\pi Lh} \int_{-\theta_1}^{\theta_2} d\theta = \frac{\dot{N}}{4\pi Lh}\left(Arc\tan\left(\frac{L_1}{h}\right) + Arc\tan\left(\frac{L-L_1}{h}\right)\right) \quad (1.59)$$

Note that when L is very small in front h, angles θ_1 and θ_2 are small and we have in this case $\arctan(\theta) \approx \theta$ when θ is small. The (1.59) becomes:

$$\dot{\Phi} = \frac{\dot{N}}{4\pi Lh}\left(Arc\tan\left(\frac{L_1}{h}\right) + Arc\tan\left(\frac{L-L_1}{h}\right)\right) \cong \frac{\dot{N}}{4\pi Lh}\left(\frac{L_1}{h} + \frac{L-L_1}{h}\right) = \frac{\dot{N}}{4\pi h^2}$$

then we find the fluence rate of a point source.

Further Details 1.2 presents an approach leading to the calculation of the fluence for a surface source.

In Chap. 2 below, we will aim at determining, for different types of conventional radiation, correlation factors "fluence-dosimetric quantity" defined by the expressions (1.48). Thereafter, metrology elements for measuring devices with suitable three quantities that are Φ, K and D will be provided.

Further Details 1.1: Distribution frequency and dose for the calculation of microdosimetric spectra

The specific energy z may be deposited via a single or multiple events. A unitary distribution is a distribution that only record the energy deposition of a single event, i.e. when a single particle and its secondary particle set in movement deposit their energy in the sensitive site. The "unitary frequency distribution" is denoted $f_1(z)$. Note that unlike $f_1(z = 0, \bar{D})$ the singularity $f_1(z = 0)$ is not defined, since by definition, for each event corresponds a deposit of energy. This distribution as the previous (1.7) is normalized to 1. The cumulative probability density $F_1(z)$ reflects the probability that the specific energy z is less than z.

$$F_1(z) = P(0 < z' \le z, n = 1) \Rightarrow f_1(z) = \frac{dF_1(z)}{dz} \quad (1)$$

Note that this distribution of simple events is independent of the dose (i.e. the mean number of ionizations and excitations in matter), but it depends on the "typology" of energy deposition induced by radiation, the shape, size and composition of the target volume. The distribution $f_1(z)$ while discrete, can be viewed as a histogram of frequency of specific energies during the passage of a particle in the

sensitive volume. We can thus obtain a mean value called "mean specific energy frequency" as expressed by (2).

$$\bar{z}_f = \int_0^\infty z f_1(z) dz \tag{2}$$

As the value of $\bar{z}_f$ is the mean specific dose deposited by event. For a total deposited dose $\bar{D}$, the number of events can be estimated by the expression (3).

$$\bar{n} = \frac{\bar{D}}{\bar{z}_f} \tag{3}$$

These distributions are calculated by a uniform sampling of many spheres (sensitive sites) centered on the deposit points in the middle. This amounts to a uniform sampling of irradiated environment and results in "frequency distribution". This method is costly in computation time, especially for high doses.

Using a weighted sampling method, the deposited energy, as expressed in the integration, reduces the computation time and then we get the "dose distributions." In this case, the random sampling of the spheres is done with probability proportional to the energy deposited in these spheres.

The integrand of the expression (2) $zf_1(z)\mathrm{d}z$ reflects the contribution to the total deposited dose $\bar{D}$ of events depositing a specific energy between z and $z + \mathrm{d}z$. The dose distribution is then expressed in terms of the unitary frequency distribution of the expression (2) above.

$$\frac{z f_1(z)}{\bar{z}_f} dz \tag{4}$$

It reflects the fraction of the total deposited dose $\bar{D}$ which contribute to the deposits of specific energy between z and $z + \mathrm{d}z$. In other words, it is an infinitesimal increment of the total deposited dose. This relationship allows to introduce a new distribution of the specific energy, "unitary dose distribution" $d_1(z)$ defined by the expression (5).

$$d_1(z) = \frac{z f_1(z)}{\bar{z}_f} \tag{5}$$

From this distribution, which is normalized, we can calculate a second average called "mean specific energy in dose" $\bar{z}_D$.

$$\bar{z}_D = \int z\, d_1(z) dz = \int \frac{z^2 f_1(z)}{\bar{z}_f} dz = \frac{\overline{z_f^2}}{\bar{z}_f} \tag{6}$$

The index D indicates that it is an mean dose. The two calculated average $\bar{z}_f$ and $\bar{z}_D$ express two different views: $\bar{z}_f$ is the average of the specific energy deposited by each event, but events that contribute most to the dose deposit around a specific energy $\bar{z}_D$. These distributions can be calculated by simulating tracks by Monte Carlo particle transport code.

To illustrate the differences between all these microdosimetric variables, Dabli [13] offers the following schematic numerical application.

The disks in Fig. 1 represent the six spheres (sensitive sites) of an irradiated medium, randomly sampled, and the lines represent the paths of the particles (event).

If we consider that the specific energy distributed in the figure have the following values:

$$z_1 = 0.1 \text{ Gy}, \quad z_2 = 0.3 \text{ Gy}, \quad z_3 = 0.5 \text{ Gy}$$

The probability distribution of $f(z, \bar{D})$ expression (1.7) is discrete and can be summerize as follows:

$$f(0, \bar{D}) = 2/6, \quad f(z_1, \bar{D}) = 2/6, \quad f(z_2, \bar{D}) = 0/6, \quad f(z_3, \bar{D}) = 1/6,$$
$$f(z_1 + z_2, \bar{D}) = 1/6$$

Then the total deposited dose $\bar{D}$ is obtained by the expression (1.8):

$$\bar{D} = \bar{z} = \sum_i z_i f(z_i, \bar{D}) = [(3z_1 + z_2 + z_3)/6] = 0.183 \text{ Gy}$$

For the calculation of the unitary frequency distribution $f_1(z)$, only the spheres containing an energy deposition are recognized and the deposited specific energy stems from a single event. Therefore the components $f_1(0)$ and $f_1(z_1 + z_2)$ do not exist. This distribution thus can be summerize as follows:

$$f_1(z_1) = 3/5, \quad f_1(z_2) = 1/5, \quad f_1(z_3) = 1/5$$

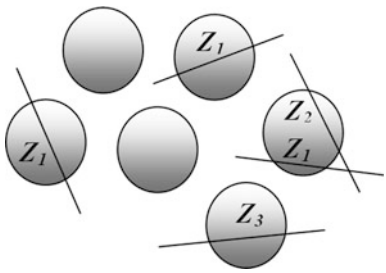

Fig. 1 Illustration for calculating distributions of specific energy [13]

the number of total events is 5. The mean specific energy frequency $\bar{z}_f$ is obtained in the discrete expression:

$$\bar{z}_f = \sum_i z_i f_1(z_i) = \frac{3z_1 + z_2 + z_3}{5} = 0.22 \text{ Gy}$$

we deduce using the expression (1.16) the mean number of events:

$$\bar{n} = \frac{\bar{D}}{\bar{z}_f} = \frac{0.183}{0.22} = \frac{5}{6}$$

Note that the mean number of events is simply the ratio of the number of events by the number of spheres. The mean specific energy dose is then obtained by discrete expression:

$$\bar{z}_D = \sum_i \frac{z_i^2 f_1(z_i)}{\bar{z}_f} = \frac{z_1^2 f_1(z_1) + z_2^2 f_1(z_2) + z_3^2 f_1(z_3)}{\bar{z}_f} = 0.336 \text{ Gy}$$

We see clearly that although we have three events to 0.1 Gy, the mean specific energy dose is at 0.336 Gy, that is to say between the single events z_2 = 0.3 and z_3 = 0.5 Gy. These events that contribute most to the dose.

Note that the methods of average calculation and distributions of specific energy z detailed above also apply to energy lineal since the latter is also subject to statistical fluctuation. However, it is notable that, by definition, the probability density function is a unitary distribution, because the values of y result only from a single event. By analogy, then, the following relations are obtained:

$$\text{Frequency unitary distribution}: f_1(y) = \frac{dF_1(y)}{dy} \tag{7}$$

$$\text{Mean lineal energy Frequency}: \bar{y}_f = \int_0^\infty y f_1(y) dy \tag{8}$$

$$\text{Dose distribution}: d(y) = \frac{y f_1(y)}{\bar{y}_f} \tag{9}$$

$$\text{Mean lineal energy dose}: \bar{y}_D = \int_0^\infty y d_1(y) dy = \int_0^\infty \frac{y^2 f_1(y)}{\bar{y}_f} dy = \frac{\overline{y_f^2}}{\bar{y}_f} \tag{10}$$

As we mentioned, this microdosimetric quantity is measured by tissue equivalent proportional counter (CPET) for example. As in the case of the specific energy, the dose distribution for lineal energy reflects the increment of the total deposited dose $\bar{D}$. Moreover, for each energy value lineal y will match a deposited dose value $D(y)$ in the medium. Knowing therefore the microdosimetric spectrum of the

distribution in dose $d(y)$, we can thus access ultimately the total dose deposited $\bar{D}$ as indicated in expression (11).

$$\bar{D} = \int_0^\infty d(y)D(y)dy = \int_0^\infty \frac{yf_1(y)}{\bar{y}_f} D(y)dy \tag{11}$$

To illustrate this approach, refer to Further Details 2.11, Chap. 2, in the section on Neutron Dosimetry.

Figure 2 shows examples of lineal energy distributions [14], represented as a frequency distribution in the left diagram or a dose distribution in the right diagram.

The lineal energy is distributed exponentially $f_1(y) = \text{Exp}\ (-y)$ with $\bar{y}_f = 1$ keV μm^{-1}. These distributions are not very different from those measured for single events in a spherical counter of 2 mm diameter simulating tissue and irradiated with ^{60}Co. In the lower part of the figure, the ordinates were multiplied by y so that the area under the curve is proportional to the fraction of events (or dose) in the considered air. Finally, we will note that, as with the digital application, the value of the mean frequency $\bar{y}_f$ is less than the mean dose $\bar{y}_D$.

Further Details 1.2: Calculating the fluence of a disk

Calculate the fluence of a disc emitting homogeneously N particle per second, of radius R at a distance D. Figure 1 shows the geometry considered.

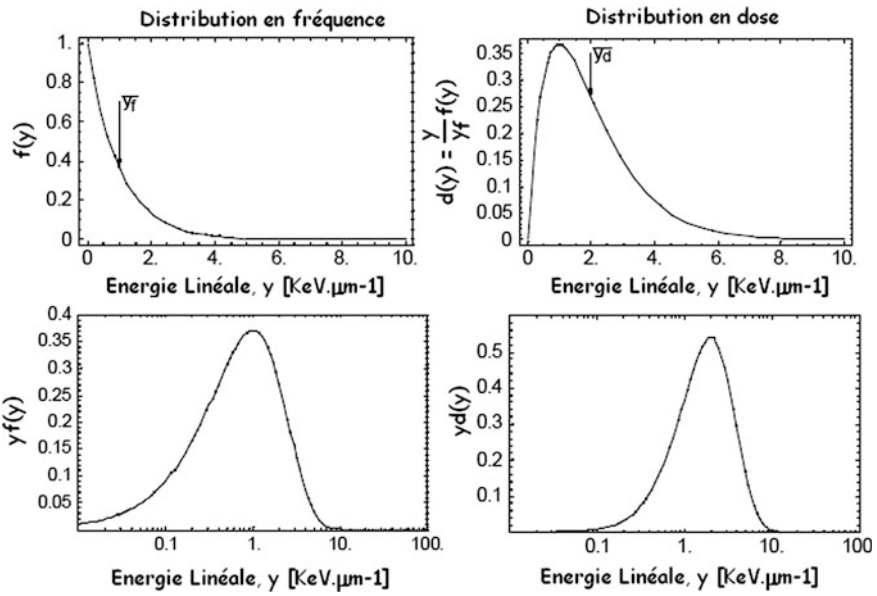

Fig. 2 Illustration of distributions and dose frequency, according [14]

At first, the disc is divided into infinitesimal elements of surface dS, so that each element dS is punctual toward the measurement point. Surface dS flux density is given as follows:

$$n_s = \frac{\dot{N}}{S} = \frac{\dot{N}}{\pi R^2}$$

The differential element fluence is expressed, toward this surface let flux density, according to:

$$d\dot{\Phi} = \frac{n_s}{4\pi\rho^2} dS$$

For a total fluence due to disk, you must integrate this equation over the full surface S:

$$\dot{\Phi} = \iint_S \frac{n_s}{4\pi\rho^2} dS \tag{1}$$

Looking at Fig. 1, the following three equations are obtained:

$$dS = r\, dr\, d\alpha, \tag{2}$$

$$\rho = \frac{D}{\cos\theta} \tag{3}$$

and

$$D\tan(\theta) = r \tag{4}$$

Differentiating on both side (4) leads to:

$$\frac{D}{\cos^2(\theta)} d\theta = dr \tag{5}$$

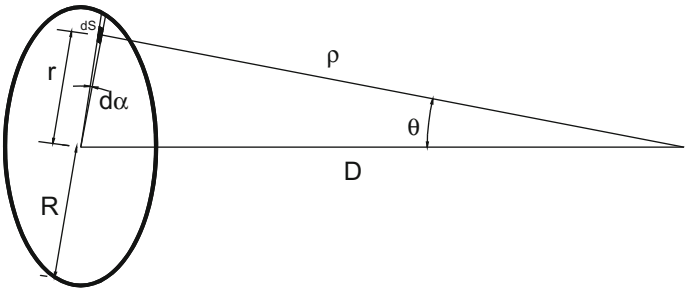

Fig. 1 Geometric consideration for exercise: calculate the fluence of a disk

Injecting (2), (4) and (5) into (1) we have:

$$\dot{\Phi} = \frac{n}{4\pi}\iint_S r\left(\frac{D}{\cos\theta}\right)^{-2} d\alpha\, dr = \frac{n}{4\pi}\iint_S \left[D\tan(\theta)\times\frac{D}{\cos^2(\theta)}\right]\left(\frac{D}{\cos\theta}\right)^{-2} d\alpha\, d\theta$$

$$= \frac{n}{4\pi}\int_0^{2\pi} d\alpha \int_0^{\arctan\left(\frac{R}{D}\right)} \tan(\theta)d\theta = \frac{n}{2}\left[-\ln\left|\cos(\theta)\right|\right]_0^{\arctan\left(\frac{R}{D}\right)}$$

finally:

$$\dot{\Phi} = \frac{N}{2\pi R^2}\left(-\ln\left|\cos\left(\arctan\left(\frac{R}{D}\right)\right)\right|\right)$$

Note that $\arctan(\theta) = \arccos\left(\left(\sqrt{(1+\theta^2}\right)^{-1}\right)$, we obtain:

$$\dot{\Phi} = \frac{\dot{N}}{2\pi R^2}\left[-\ln\left(\left(\sqrt{1+\left(\frac{R}{D}\right)^2}\right)^{-1}\right)\right] = \frac{\dot{N}}{4\pi R^2}\ln\left|\left(1+\left(\frac{R}{D}\right)^2\right)\right|$$

It is relevant to determine how for the disk can be likened to a point: remember that $\lim_{x\to 0}(\mathrm{Ln}(1+x)) = x$ (for $x = 0.1$, this approximation results in a relative error of less than 5%), which reduces the previous expression as follows:

$$\lim_{R/D\to 0}\dot{\Phi} = \frac{\dot{\mathrm{N}}}{4\pi\,\mathrm{R}^2}\left(\frac{R}{D}\right)^2 = \frac{\dot{\mathrm{N}}}{4\pi\,\mathrm{D}^2}$$

We observe the same fluence rate of a point source at a distance D. So, for a disc comparable to a point, it is necessary that $R/D \leq 0.1$ and therefore $D \geq 10\ R$.

References

1. Pouget, J. P., & Mather, S. J. (2001). General aspect of the cellular response to low and high-LET radiation. *European Journal of Nuclear Medicine, 28*, 541–561.
2. Rossi, H. H. (1979). The role of microdosimetry in radiobiology. *Radiation and Environmental Biophysics, 17*, 29–40.
3. ICRU. (1983). Microdosimetry, international commission on radiation units and measurements. Report 36.
4. ICRP. (1991). 1990 Recommendations of the international commission on radiological protection. ICRP Publication 60.

5. Bordy, J. (1992). Contribution à la réalisation d'un compteur proportionnel à dérive équivalent-tissu destiné à la dosimétrie individuelle et la radioprotection. Rapport CEA-R-5603.
6. Hanu, A., Byun, S. H., & Prestwich, W. V. (2010). A Monte Carlo simulation of the microdosimetric response for thick gas electron multiplier. *Nuclear Instruments and Methods A, 622*(1), 270–275.
7. De Choudens, H., Troesch, G. (1997). *Radioprotection dans les installations nucléaires*. Technique & Documentation.
8. Tubiana, M., Dutreix, J., Wambersie, A. (1986). *Radiobiologie*. Hermann.
9. Barendsen, G. W. (1968). Responses of cultured cells, tumours and normal tissues to radiations of different linear energy transfer. In M. Ebert & A. Howard (Eds.), *Current Topics in Radiation Research Quarterly* (Vol. IV, pp. 293–356). New York: John Wiley and Sons, Inc.
10. Wambersie, A., Menzel, H. G., Gahbaur, R. A., et al. (2002). Biological weighting of absorbed dose in radiation therapy. *Radiation Protection Desimetry, 99*, 445–452.
11. ISO. (2002). Norme internationale 8529-1. Rayonnements neutroniques de référence. Partie 1: Caractéristiques et méthode de production.
12. Delacroix, D., Guerre, J. P., Leblanc, P. (2006). *Guide pratique. Radionucléides et radioprotection. Manuel pour la manipulation de substances radioactives dans les laboratoires de faible et moyenne activité.* EDP Sciences.
13. Dabli, D. (2010). Utilisation d'un modèle microdosimétrique cinétique (MKM) pour l'interprétation d'irradiations cellulaires dans le cadre de l'hadronthérapie: Application de simulations Monte-Carlo. *Thèse Université de Clermont-Ferrand II*.
14. Francis, Z. (2007). Simulations Monte-Carlo et étude microdosimétrique pour des irradiations cellulaires à faibles doses en neutrons de 14 MeV. *Thèse Université de Clermont-Ferrand II*.
15. Faussot, A. (2009). Grandeurs et unités dosimétriques. *ATSR, 4*.
16. ICRU. (2000). Nuclear data for neutron and proton radiotherapy and for radiation protection. Report 63.

Chapter 2
Ionizing Radiation Interaction in Tissues: Kerma and the Absorbed Dose

Abstract In previous chapter, the basic concepts of dosimetry and all elements for the characterization of a radiation field in a point in space, have been defined. This chapter attempts to detail the physical concepts to estimate the mean energy transferred to secondary particles for indirectly ionizing particles and energy locally imparted for directly ionizing particles. These estimates allow then analytical approaches, under certain conditions, for basic dosimetric quantities that are respectively: kerma and absorbed dose. These two variables and fluence are the primary quantities which are connected to protection and operational and quantities that are defined in the next chapter. The principles and techniques of measurements of these primary dosimetric quantities are discussed in this chapter.

We established in Chap. 1 that the energy transferred or imparted to the secondary charged particles to tissues, is of fundamental importance in determining the dose quantities. In this chapter, an analysis of physical processes leading to these energy exchanges should allow, where possible, to analytically characterize reference quantities previously defined: Φ, K, D.

Moreover, for obvious practical reasons, special emphasis is placed on the explanation of metrological concepts to instantly access these values by measurement (e.g. absolute dosimeter).

2.1 Electrons and Heavy Charged Particles (HCP)

The charged particles interact mainly by two processes: by Coulomb interaction responsible for electrons ionization and excitation through the medium and inelastic collisions with the medium nuclei, causing release of photon called "bremsstrahlung".

For a Coulomb interaction quite intense, the energy transfer is sufficient (>10 eV) to pull the electron from the atom to which it is linked. There then create a "electron-hole pair"; if the energy imparted to the secondary electron is important, it

R. Antoni and L. Bourgois, *Applied Physics of External Radiation Exposure*,
Biological and Medical Physics, Biomedical Engineering,
DOI 10.1007/978-3-319-48660-4_2

ionizes in turn the medium of electrons. However, for an insufficient transfer of energy to ionize, an excitation process on orbital electrons can take place. In this effect, the excited electron transits from an orbital bond energy state E_0 to a final energy state less bound E_1. X-radiation energy $h\nu = E_1 - E_0$ is then transmitted to compensate for the energy imbalance caused by this transition. Both interactions are also inelastic, since they alter the initial state of target atom.

For the bremsstrahlung, resulting from the deceleration of an electron in the periphery of a medium nucleus, there is a value of energy of incident electrons, called "critical", below which this radiative phenomenon is not significant. The empirical formula (2.1), according to [1], Allows access to this value within 10% based on Z medium:

$$T_c(\text{MeV}) = \frac{610}{Z + 1.24} \tag{2.1}$$

Thus, considering hydrogen, constituting a majority of tissues, the calculation of the "critical enerengy" leads to an energy of 272 MeV. For the energy range studied in this work, not exceeding a few hundred MeV, this effect will be neglected for tissues. However, it will prove to be significant in the context of interaction of electrons with high Z atomic number materials we meet in Chaps. 4 and 5 of this book.

If the physical process of Coulomb interaction is similar to electrons and heavy charged particles (HCP), however it differs in its effects, due to the intrinsic characteristics of charged particles, such as their charge or their mass. These features are responsible for a different energy deposition typology, having a direct consequence a RBE characteristic of charged particle type (see Chap. 1).

2.1.1 *Physical Characteristics of Electrons and HCP During Transport in Matter*

These include, first, a common feature of electrons and HCP: the notion of slowdown due to a loss of energy throughout the path in the matter. This feature is different from the attenuation concept with energy transfer to secondary charged particles for indirectly ionizing particles such as neutrons or photons. First consequence: if the thickness of crossed material is sufficient, the slowing down led to the complete stop of charged particle.

We will detail the major physical characteristics responsible for "typology" of different energy deposition between HCP and electrons. For the energy range studied in this book (i.e. from 0 to a hundred MeV), the kinetic energy of the HCP, because of their high mass, is great for velocity that reach only a small part of celerity c (e.g. $T\alpha = 10$ MeV $\Rightarrow$ $v = 1/15c$, $T_p = 100$ MeV $\Rightarrow$ $v = 0.4c$). As a result, the HCP can be treated by classical mechanics instead of electrons, relativistic from fifty keV.

To understand the behavior of the matter in distinction between both types of particles, let's consider an electron and a HCP, e.g. alpha, moved both with same kinetic energy at the entrance of a biological tissue. Due to the mass specificity, a first consequence arise on the velocity of both projectiles:

$$T_{e-} = T_{\alpha} \Leftrightarrow m_{e-}(v_{e-})^2 = m_{\alpha}(v_{\alpha})^2 \quad \text{or} \quad m_{\alpha} \approx 7200\, m_{e-} \Leftrightarrow \quad v_{e-} = 84 v_{\alpha}$$

At equivalent kinetic energy, the electron is 84 times faster than alpha. By extension, we can also say that with equal kinetic energy, the proton would go twice as fast as alpha. In contrast, for the same velocity, the electron kinetic energy is about 2000 times lower than that of proton and 8000 times lower than that of alpha.

Accordingly, the alpha is much slower than the electron in the same environment and we can roughly assume that it spends more time in the vicinity of surrounding orbital electrons, than an incident electron of same energy. This relative slowness is responsible for a direct effect on the energy transferred to orbital electrons that can be described as a simplistic physical approach: let's remind that in the absence of external force, the orbital electron is responsible for a momentum constant due to its orbital movement around the nucleus.

$$\sum \vec{F} = m\vec{a} \Leftrightarrow \vec{F} = m\frac{d\vec{v}_{e-}}{dt} \Leftrightarrow \vec{F} = \frac{d\vec{p}_{e-}}{dt} \Rightarrow \text{if } F = 0 \Rightarrow \vec{p}_{e-} = m\vec{v}_{e-} = \text{cste}$$

If a charged particle (electron or alpha) passes in the vicinity of orbital electron, we can easily, using a simplified physical approach, set the momentum transferred to the orbital electron by the Coulomb force and consequently the energy released in the medium by the electron and alpha incident:

$$d\,\vec{p}_{e-} = \vec{F}_c dt \quad \approx \Delta p_{e-} = F_c \Delta t \Leftrightarrow \Delta p_{e-} = F_c \left(\frac{L}{v}\right)$$

as accepted $v_{e-} \gg v_{\alpha}$, that implies that $\Delta p_{e-}(\alpha) \gg \Delta p_{e-}(e-)$ or the kinetic energy is expressed in terms of momentum as follows:

$$T_{e-} = \left(\frac{(\Delta p_{e-})^2}{2m_{e-}}\right) \Rightarrow \quad T_{e-}(\alpha) \gg T_{e-}(e-)$$

We therefore conclude that the energy transferred by the alpha to the orbital electron is much higher than that yielded by the electron. Adding that alpha has twice the electron charge, which impacts the effect of Coulomb force whose shape is given by (2.2).

$$F_c \propto \frac{ze^2}{r^2} \tag{2.2}$$

With r the distance between the incident particle and the orbital electron, e the electric charge, z the number of charges of the incident charged particle. The previous development shows that: $T_{e-} \propto (F_c)^2 \propto (z)^2$; this difference in charge therefore causes an increase by a factor 4 on the energy transferred. This approach must be nuanced. Actually, the energy transferred to the heavy charged particles is limited by the conservation laws of momentum and kinetic energy (see Further Details 2.1): the electron can not take more than 1/2000 of alpha energy. Therefore, the high kinetic energy transferred to the medium by the heavy charged particle will be in small quantities through a large number of collisions on the electron cloud surrounding the charged particle track. Remind, also, that the electron has the possibility to give all his energy in a single Coulomb interaction (see Further Details 2.1); this scenario is likely significantly at the end, so to low energy, made with extremely low energy transfer to the medium electron.

A microscopic effect on the cells of biological environment is the strands break densities on DNA depending on the type of incident charged particles: we have previously admitted that more breaks are close together (e.g. double-strand breaks) less repair mechanisms are effective. The physical reasoning suggested above makes it clear that the ionization density increases with mass, charge and energy of particle, explaining a typology of dose deposition difference absorbed and hence on RBE. We will see in Chap. 3, dedicated to sanitary radiation protection quantities, that this biological harmfulness is taken into account through weighting factors related to types of radiation and their energy (i.e. $W_R(\alpha) \gg W_R(e)$ in Chap. 3).

A consequence on alpha path can be deduced from classic cinematic approach (see Further Details 2.1):

$$\begin{aligned} M_\alpha v_1 \cos\theta_1 &= M_\alpha v_o - m_{e-} v_2 \cos\theta_2 \\ \Rightarrow \cos\theta_1 &= \frac{M_\alpha v_o - m_{e-} v_2 \cos\theta_2}{M_\alpha v_1} \cong \frac{M_\alpha v_o}{M_\alpha v_1} \approx 1 \Rightarrow \theta_1 \approx 0 \end{aligned}$$

Reflecting an approximately straight track for alpha in the matter; it would be the same for the proton or other HCP.

For electrons, the more the particle passes slowly and proximity to an orbital electron, the greater the energy transfer by Coulomb interaction and its deflection are important. For over 500 keV energy ($v > 0.9c$), the electron is widely relativistic, which induces little interaction, almost no deflection and likened to phenomenon to a shock wave in which the material is as condensed; the electron is far from the cloud and deposits only very little energy locally. For energy less than 500 keV, the electron approaches the cloud at a slower velocity; the large energy transfers probability with large deflection increases and the number of interactions is amplified as the energy decreases.

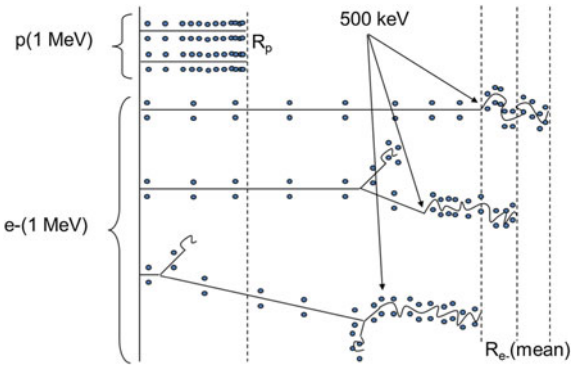

Fig. 2.1 Schematic view of 1 MeV electrons and protons path in tissues

At very low energy, the electron deflection is substantially isotropic, which explains the appearance of totally erratic track at the very end of the track and the increasing probability of backscattering.

Figure 2.1 gives a schematic view of path and medium ionization density (points couple on both sides of path) for an electron and a proton of same energy.

We admitted that for similar kinetic energy, due to its very low velocity, CHP will release on his track more energy that the electron on a path much shorter. This scheme also illustrates that the HCP range R is substantially equal to the path length L_t since we have shown that the transport of these was substantially straight. Let us add that the influence of HCP remains the same until the path end with a few statistics microfluctuations. Table 2.1 gives to alphas and protons path in water (to which soft tissue can be assimilated) to 1, 10 and 100 MeV.

Note that later in this chapter, tissues are frequently treated as water, due to a medium Z and a similar density.

Figure 2.2 shows a numerical simulation using the Monte Carlo code for 1 MeV Electron transport in water [2]. Several informations can be learned: as observed in Fig. 2.1 the path beginning is rather straight and slightly accompanied by ionization, whereas at the end of trajectory there has been an erratic path with many collisions accompanied by strong deflections. Consequently, unlike the HCP, the electron range, R, is very much less than the track length: $R \ll L_t$. Furthermore, the electron fluence remains substantially the same throughout the range, but in the end, it decreases less sharply than for HCP. This is due to a statistical distribution of each electron path of the initial beam around a mean value $\overline{R}_{e-}$ because of substantial difference in track. Usefully, this mean value is considered as effective for assess the electron range. While it is theoretically possible to access analytically the range value of charged particles, this approach need a complex calculation. It is possible

Table 2.1 Protons and α range in water

Energy (MeV)	R_p (μm)	R_α (μm)
1	50	5
10	1000	100
100	100000	10000

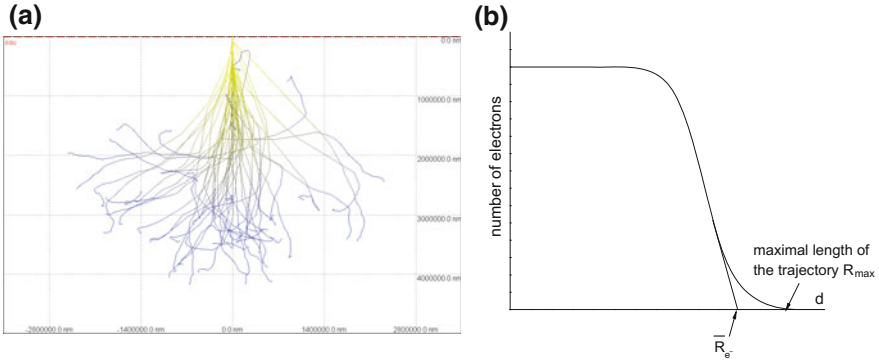

Fig. 2.2 Transport simulation of 1 MeV electron in water using a Monte Carlo code (**a**) shape of mono-energetic electrons fluence in matter and the range R (**b**)

to determine the value of electron range, for example, by the mean of Katz and Penfold semi-empirical formula (2.3) [3] of light Z medium (up to aluminum $Z = 13$).

$$\begin{aligned} &\text{For } 0.01 \leq \mathrm{E} \leq 3\,\mathrm{MeV}: \\ &\mathrm{R}\left(\mathrm{mg\,cm^{-2}}\right) = 412.\mathrm{E^n} \\ &n = 1.265 - 0.0954 \cdot \ln(E) \quad \text{with } E \text{ in MeV} \\ &\text{for } 1 \leq E \leq 20\,\mathrm{MeV}: \\ &R\left(\mathrm{mg\,cm^{-2}}\right) = 530E - 106 \quad \text{with } E \text{ in MeV} \end{aligned} \tag{2.3}$$

These relationships also allows to calculate the thickness shield required for complete electrons stop in light Z materials. We note that the thickness is given in mg cm^{-2}, it should be weighted by the density of medium to obtain a quantity homgeneous to the unit length. This will be a recurring process in this work and will permit to overcome variations in density related to fluctuations in pressure and temperature. Add a few orders of magnitude can be used as the 1 MeV electron range: approximately 4 mm in water and 3.2 m in the air.

2.1.2 Mass Stopping Power of Charged Particles

We admitted the slow of charged particles in matter. It is therefore necessary to assess the amount of energy transferred to the medium per length unit. The LET, defined in Chap. 1, which characterizes the energy lost on an infinitesimal increase dx of range, performs this function. For the same reasons mentioned above, it is necessary to define a new quantity, independent of medium density and derived from LET: the mass stopping power defined in (2.4).

$$\frac{S}{\rho} = \frac{1}{\rho}\left(\frac{dT}{dx}\right) \quad (\text{MeV cm}^2\,\text{g}^{-1}) \tag{2.4}$$

This expression comes in two parts: one relating to the slowing down by Coulomb electron interaction or collision (coll)[1] the other by bremsstrahlung (rad) according to expression (2.5). As admitted, bremsstrahlung can be considered negligible for electrons due to light z material discussed in this chapter and for HCP because of their large mass (see Chap. 4). Thus it can be assumed that only the Coulomb component remains in the tissue.

$$\frac{S}{\rho} = \frac{1}{\rho}\left[\left(\frac{dT}{dx}\right)_{coll} + \left(\frac{dT}{dx}\right)_{rad}\right] \cong \frac{1}{\rho}\left(\frac{dT}{dx}\right)_{coll} = \left(\frac{S}{\rho}\right)_{coll} \tag{2.5}$$

The mass stopping power per collision depends on the characteristics of particle and crossed medium. A simplified relationship of the different physical parameters involved can be expressed according to (2.6).

$$\left(\frac{S}{\rho}\right)_{coll} = \frac{z^2 Z}{AT}\left[\ln\left(\frac{f(T)}{I}\right) + g(T)\right] \tag{2.6}$$

with T the kinetic energy of incident charged particle, z the charge carried by the incident particle, A and Z the molar mass and atomic number of crossed medium and I the mean excitation potential (almost equal to the mean orbital frequency $\overline{v}$ multiplied by Planck's constant h: $I \approx h\overline{v}$). In practice, this amount is difficult to assess; it is deduced by measuring the stopping power for each material. It is accessible by means of empirical formula (2.7) according to the Z medium as:

$$I(eV) = \begin{cases} 12Z + 7 & for \quad Z < 13 \\ 9.76Z + 58.8Z^{-0.19} & for \quad Z \geq 13 \end{cases} \tag{2.7}$$

This term has a significant influence on the result of mass stopping power. In fact, for aluminum (Z = 13) the calculation gives $I_{alu} \approx 163$ eV. To air, whereas the latter is almost exclusively composed of nitrogen (Z = 7), it is equal to $I_{air} \approx 91$ eV. This term located in the denominator of logarithm of expression (2.6) strongly influences the result of calculation and explains for example that, whatever energy T the incident charged particle, inequality (2.8) is always verified.

[1] In 2011, the ICRU 85a [4] adopts the term (dT/ dx)el to set the mass stopping power by Coulomb electron interaction instead of commonly used term (dT/ dx)col for the mass stopping power by collision. However, the notation "col" is maintained to ensure confirmity with the tables of mass stopping power cited therein.

$$\left(\frac{S}{\rho}\right)_{coll}^{air} > \left(\frac{S}{\rho}\right)_{coll}^{alu} \quad \forall T \tag{2.8}$$

The tissue mass stopping power is systematically greater than that of air, due to the presence in its composition of a significant number of hydrogen atoms. This effect decrease the value of mean excitation potential.

Bethe-Block formulas [5] for HCP and Rohrlish-Carlson [6] for electrons give full expressions of mass stopping power by Coulomb interaction (see Further Details 2.12). Note that for electrons the term I is squared and energies are preferentially expressed in terms of ratio β:

$$\beta = v/c = \sqrt{T(T + 2m_{e-}c^2)}/(T + m_{e-}c^2)$$

It reports relativistic effects felt from a hundred keV.

Figure 2.3 gives the mass stopping power as a function of energy in water, aluminum and gold for protons and electrons.

Regarding electrons, we notice in accordance with expression (2.6) that the more the energy decreases and the more the energy transferred to the medium increases. Moreover, the water curve supports the idea accepted that beyond 500 keV little energy is transferred and the stopping power by collision has a flat behaviour up to 100 MeV. Finally, the curve also confirms that the bremsstrahlung stopping power can be neglected, for the energy range studied in this work and in water, substantially equivalent medium to biological tissues.

Regarding ions (e.g. protons), we note the importance of deposited energy with respect to that of equivalent energy electrons and a permanent increase of deposition as the energy decreases to about 100 keV; below, the process is reversed. Indeed, low energy (about 100 keV/nucleon), formula (2.6) is no longer valid, this particle "present" an effective charge $z_{\text{eff}}e < ze$ which decreases continuously as the

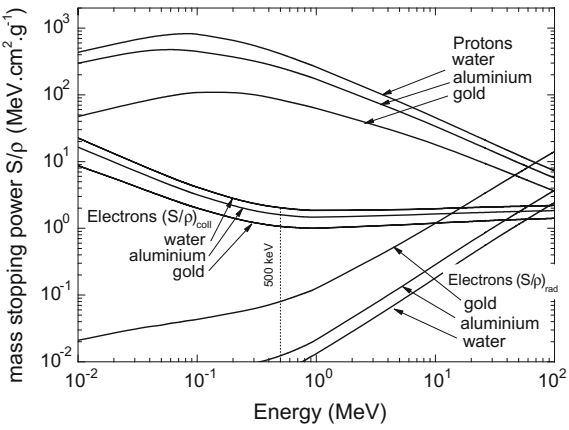

Fig. 2.3 Mass Stopping power in water, aluminum, and gold for protons and electrons (according to the data [7] for electrons and [8] for protons)

energy decreases. Indeed, as the velocity decreases, free orbital electrons tend to pair with incident ion, reducing its effective charge in the medium.

Finally adding that for material compound of *i* body, we access the value of mass stopping power for a given energy as the average (2.9).

$$\left(\frac{S}{\rho}\right)_c = \sum_i \left(\frac{S}{\rho}\right)_i \cdot w_i \tag{2.9}$$

with w_i and $(S/\rho)_i$ respectively the mass percentage and the mass stopping power of constituent *i.*

2.1.3 Scattering of Electrons

As seen, electrons are scattered as they pass through a medium mostly through elastic 'collisions' with atom nuclei. Scattering is more pronounced at lower beam energies and with higher atomic numbers. As electrons move through a medium, they lose energy through attenuation. Electrons at lower energy are more likely to scatter laterally. This is seen for high energy electron beams, where the penumbra is relatively narrow near the surface and broadens significantly at depth. As for loss of energy, the "mass scattering power", dependent on the incident electron energy as well as the material, is given by expression (2.10):

$$\frac{\theta_s^2}{\rho} = \frac{1}{\rho}\left(\frac{d\overline{\theta^2}}{dl}\right) \tag{2.10}$$

where θ is the mean scattering angle and ρ is the density of material. The scattering power is proportional to the square of the atomic number Z Inversely proportional to the square of the kinetic energy of electron. Therefore, low energy electrons will be scattered more readily than high energy electrons; and high Z materials will cause more scattering than low Z material.

This explains two important concepts in physics: Electrons passing through an inhomogeneity can be backscattered if the inhomogeneity is of higher atomic number than the medium. This can lead to increased dose on the low Z side of the inhomogeneity boundary. Electrons generated from a linear accelerator have high energy and travel in a pencil beam. By passing them through a scattering filter, they will be scattered in numerous directions. Scattering filters are made from thin, high Z material to produce the required scattering.

On the condition that product ρl is small the previous expression (2.10) leads to the "mean square scattering angle" at depth l and electron energy E (2.11):

Table 2.2 Radiation length X_O (g/cm^2) for different element (data from ICRU 35 [9])

Element	C	H	O	N	Tissue	Air	Water	PMMA
X_0 (g/cm^2)	4.270	6.305	3.424	3.799	4.176	3.661	3.608	4.054

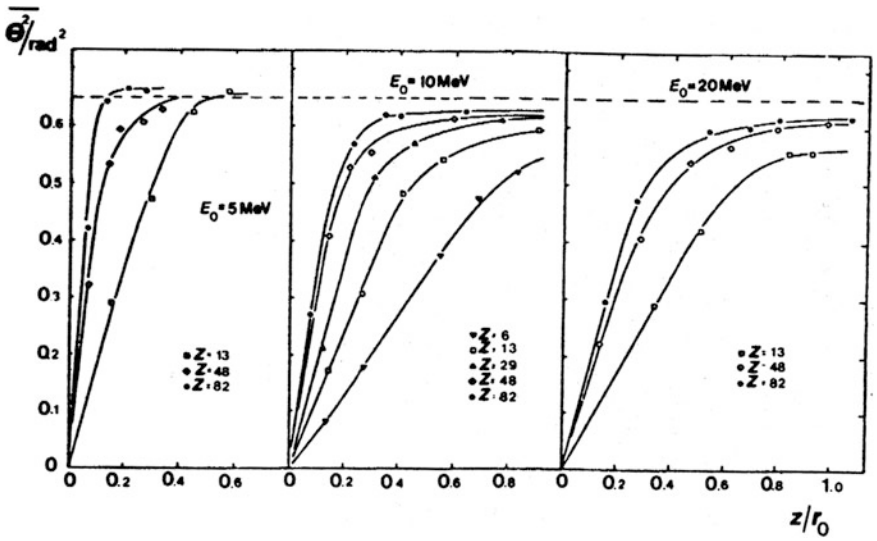

Fig. 2.4 The variation of the mean square scattering angle, $\overline{\theta_S^2}$, with depth (z) measured in fraction of the mean range (r_0) for materials of different atomic number (Z) (from ICRU 35 [9])

$$\overline{\theta_S^2}(l) = \frac{\rho l}{\beta^4 X_0}\left(\frac{E_S}{E}\right)^2 \tag{2.11}$$

where E_s has a constant value of 21.2 MeV and X_o in different materials is given in Table 2.2.

Figure 2.4 shows the variation of the mean square scattering angle with depth for materials of different atomic numbers according to ICRU 35 [9].

2.1.4 Calculation of the Absorbed Dose for the Electrons in the Tissues

We established in Chap. 1 that the energy imparted ε of electrons in the medium was suitable for the characterization of the absorbed dose in a point of medium, which can be applied to tissues and energy range considered in this book. Thus, a simplistic approach allows to characterize the absorbed dose in tissue due to a

primary electron beam. consider N electrons with energy E entering an area bounded by a surface a, the front side of a thin tissue layer Δx which is negligible in respect with electron range $(\Delta x \ll R_{e-})$, So that the number of electrons is not changed and remains the same once the crossed layer. we can assume that each electron is responsible for the deposit of an energy imparted $\Delta\varepsilon$. The absorbed dose in the irradiation area can then be expressed as (2.12).

$$\overline{D}_t = \frac{\overline{\varepsilon}}{m} = \frac{N\,\Delta\varepsilon}{\rho\, a\, \Delta x} \tag{2.12}$$

If we reach the mass m to an infinitesimal amount (equivalent operation on a and Δx), recalling that the absorbed dose is a punctual concept, we deduce the theoretical expression for absorbed dose (2.13).

$$D_t = \lim_{m\to 0} \overline{D}_t = \lim_{m\to 0} \frac{1}{\rho}\left(\frac{\Delta\varepsilon}{\Delta x}\right)\left(\frac{N}{a}\right) = \frac{1}{\rho}\left(\frac{dT}{dx}\right)\Phi = \left(\frac{S}{\rho}\right)_{coll}\Phi \tag{2.13}$$

So, theoretically, we access the absorbed dose by the product of the fluence $\Phi(x)$ of electrons at a x point, within the medium by the mass stopping power to the energy of electrons considered. This approach is also valid for the dose rate connected the fluence rate. Regarding an energy spectrum of charged particles, the dose rates due to each energy component are added (2.14).

$$\dot{D}_t = \sum_i \left(\frac{S}{\rho}\right)_{coll,i} \dot{\Phi}_i \tag{2.14}$$

Table 2.3 gives values of mass stopping power for collision energies between 10 keV and 2 MeV, for basic chemical elements and the following compounds: water, air and tissues.

There is a relationship to express the absorbed dose to a medium interface M_1 and M_2. In a medium interface, both side absorbed doses are:

$$D_{M1} = \overline{\left(\frac{S}{\rho}\right)}_{M_1}\Phi_{M_1} \quad and \quad D_{M_2} = \overline{\left(\frac{S}{\rho}\right)}_{M_2}\Phi_{M_2}$$

By taking the ratio of both values and assuming that the incoming fluence is equivalent to that outgoing $\Phi_{M_1} \approx \Phi_{M_2}$, We obtain the expression (2.15).

$$\frac{D_{M_1}}{D_{M_2}} = \frac{\overline{(S/\rho)}_{M_1}}{\overline{(S/\rho)}_{M_2}} = \overline{\left(\frac{S}{\rho}\right)}_{M_2}^{M_1} \tag{2.15}$$

Table 2.3 Mass stopping power (S/ρ) in MeV cm^2 g^{-1} for electrons (adapted from [56])

E (keV)	H	C	N	O	F	Al	Fe	Cu	Water	Air	Tissue
10	51.24	19.99	19.96	19.37	17.62	16.5	13.9	13.19	22.56	19.76	22.57
15	36.82	14.61	14.59	14.19	12.95	12.21	10.41	9.917	16.47	14.45	16.47
20	29.16	11.69	11.68	11.38	10.41	9.851	8.468	8.08	13.18	11.58	13.17
25	24.39	9.852	9.842	9.6	8.79	8.345	7.213	6.892	11.1	9.757	11.09
30	21.1	8.575	8.568	8.363	7.666	7.294	6.33	6.055	9.657	8.495	9.647
35	18.7	7.635	7.629	7.452	6.836	6.516	5.672	5.431	8.596	7.566	8.586
40	16.87	6.911	6.908	6.75	6.197	5.916	5.163	4.947	7.781	6.852	7.771
45	15.42	6.337	6.335	6.193	5.689	5.437	4.756	4.56	7.134	6.284	7.124
50	14.24	5.869	5.868	5.739	5.275	5.046	4.422	4.242	6.607	5.822	6.597
55	13.27	5.481	5.481	5.362	4.931	4.721	4.144	3.977	6.17	5.438	6.16
60	12.45	5.153	5.154	5.044	4.64	4.446	3.908	3.753	5.801	5.114	5.791
70	11.14	4.629	4.632	4.535	4.174	4.005	3.529	3.392	5.211	4.597	5.202
80	10.15	4.229	4.233	4.146	3.819	3.668	3.238	3.114	4.761	4.201	4.753
90	9.368	3.913	3.918	3.839	3.538	3.401	3.007	2.894	4.407	3.889	4.398
100	8.738	3.657	3.664	3.591	3.31	3.185	2.82	2.715	4.119	3.637	4.111
150	6.82	2.874	2.885	2.831	2.614	2.521	2.242	2.164	3.242	2.865	3.235
200	5.852	2.476	2.491	2.446	2.261	2.183	1.947	1.881	2.798	2.474	2.791
250	5.276	2.238	2.256	2.217	2.05	1.981	1.771	1.711	2.533	2.241	2.527
300	4.899	2.081	2.103	2.067	1.913	1.849	1.656	1.601	2.36	2.089	2.354
350	4.637	1.971	1.996	1.963	1.818	1.757	1.576	1.524	2.241	1.984	2.234
400	4.447	1.891	1.92	1.889	1.75	1.691	1.519	1.469	2.154	1.908	2.148
450	4.305	1.831	1.863	1.833	1.699	1.642	1.477	1.428	2.09	1.852	2.084
500	4.196	1.785	1.82	1.791	1.661	1.604	1.445	1.398	2.041	1.809	2.034
550	4.111	1.749	1.787	1.759	1.632	1.576	1.421	1.375	2.003	1.776	1.995

(continued)

Table 2.3 (continued)

E (keV)	H	C	N	O	F	Al	Fe	Cu	Water	Air	Tissue
600	4.044	1.72	1.761	1.734	1.609	1.554	1.402	1.357	1.972	1.751	1.963
700	3.949	1.678	1.725	1.7	1.578	1.522	1.376	1.333	1.926	1.715	1.917
800	3.887	1.65	1.703	1.679	1.559	1.503	1.362	1.319	1.896	1.694	1.886
900	3.846	1.631	1.69	1.666	1.548	1.492	1.354	1.312	1.876	1.681	1.865
1000	3.821	1.619	1.683	1.659	1.542	1.486	1.35	1.309	1.862	1.674	1.851
1500	3.796	1.6	1.688	1.667	1.552	1.491	1.365	1.327	1.841	1.68	1.829
2000	3.835	1.61	1.719	1.699	1.584	1.518	1.4	1.364	1.85	1.711	1.838

The expression (2.13) has the following dimensions:

$$\dot{\mathrm{D}} = \left(\frac{\mathrm{S}}{\rho}\right) \times \dot{\Phi} \propto \left[\mathrm{MeV\,cm^2\,g^{-1}}\right] \times \left[\mathrm{cm^{-2}s^{-1}}\right] \equiv \left[\mathrm{MeV\,g^{-1}\,s^{-1}}\right]$$

To set it in a typical unit of radiation protection devices, either mGy h^{-1}, we put the equation with dimensions with conversion factors unities as following

$$[\mathrm{MeV/g/s}] \times [\mathrm{J/MeV}] \times [\mathrm{g/kg}] \times [\mathrm{s/h}] \times [\mathrm{mGy/Gy}] = [\mathrm{mGy/h}]$$

and

$$[\mathrm{MeV/g/s}] \times \left[1 \cdot 10^6 \cdot 1.6 \cdot 10^{-19}\right] \times [1000] \times [3600] \times [1000] = \left[\mathrm{MeV \cdot g^{-1} \cdot s^{-1}}\right] \times 5.76 \cdot 10^{-4}$$

This equality set to dimensions involves the practical expressions (2.16) and (2.17).

$$\mathrm{D(mGy)} = 1.6 \cdot 10^{-7} \left(\frac{\mathrm{S}}{\rho}\right)_{\mathrm{coll}} \Phi \tag{2.16}$$

$$\dot{D}(\mathrm{mGy\,h^{-1}}) = \sum_E 5.76 \cdot 10^{-4} \left(\frac{S}{\rho}\right)_{coll} \dot{\Phi}_E \tag{2.17}$$

with $(S/\rho)_{\mathrm{col}}$ in MeV $\mathrm{cm^2\ g^{-1}}$, $\dot{\Phi}_E$ in $\mathrm{cm^{-2}\ s^{-1}}$, Φ_E $\mathrm{cm^{-2}}$.

For a parallel beam of monoenergetic electrons of energy Te_- = 2 MeV, let's determine the fluence of electrons responsible of 1 mGy absorbed dose in tissues. Referring to Table 2.3 we get an energy of 2 MeV and a mass stopping power of 1.8 MeV cm g^{-1}, therefore the fluence is:

$$\Phi = \frac{D_t}{1.6 \cdot 10^{-7}(S/\rho)_{coll}} = \frac{1}{1.6 \cdot 10^{-7} \times 1.8} = 3.4 \cdot 10^6\,\mathrm{cm^{-2}}$$

Now let's calculate what would be the fluence rate that would produce a 1 mGy h^{-1} absorbed dose rate in tissues; by taking the formula (2.17), we get:

$$\dot{\Phi} = \frac{\dot{D}_t}{5.76 \cdot 10^{-4}(S/\rho)_{coll}} = \frac{\dot{D}_t}{5.76 \cdot 10^{-4} \times 1.8} = 965\,\mathrm{cm^{-2}s^{-1}}$$

Notice that the formula, just established, is valid since fluence or density electrons at a point in space are precisely known. In the case of electron beam, we can, for example, calculate with certainty the absorbed dose rate at the entrance of medium, but it gets complicated as electrons penetrate the material. We assumed previously that the electrons can undergo a significant number of large angle scattering, especially at low energies, which coincides with "erratic" trajectory in the medium. This specificity makes it difficult to assess the fluence rate at any point

upstream of range. At this stage, Monte Carlo type calculations become necessary to take over the deterministic analytical approach and estimate the electron fluence, or the absorbed dose in depth (see Chap. 6). Grosswendt [10] Provides calculated values of dose absorbed fluence unit (nGy cm^2) for monoenergetic electrons in a tissue-equivalent phantom ICRU composed of four chemical constituents of tissues (C–H–O–N). The absorbed dose or absorbed dose rate in the tissue is then obtained by weighting a single conversion factor "fluence-absorbed dose in tissue" at energy of primary electrons, by the fluence or the fluence rate electrons at the tissue entrance according to (2.18).

$$D_t(d) = d_\Phi \Phi = \left(\frac{D_t(d)}{\Phi}\right)_{T_o} \Phi \tag{2.18}$$

The set of values calculated for energies between 60 keV and 10 MeV is provided for slices of 0.05 times the path of the energy of primary electron seen in Table 2.4.

For example, let's consider a parallel beam of 2 MeV monoenergetic electrons with 5 nA whose section has a 10 cm^2 surface and estimate the absorbed dose rate under 0.5 cm tissues. The Katz and Penfold formula (2.3) estimate the range for 2 MeV electrons in water to ensure that the depth of 0.5 cm is well below this range and that the dose calculation has a physical sense:

$$n = 1.265 - 0.0954 \ln(2) = 1.198 \text{ for } 0.01 < E \leq 3 \text{ MeV}$$
$$\Rightarrow R_o = 412 \times (2)^{1.198} = 945.21 \text{ mg cm}^{-2}$$

With water density, the range is 0.94 and the 0.5 cm point is below that depth. It remains to be done the ratio d depth, on R_0 range previously calculated:

$$\frac{d}{R_o} = 0.53$$

In Table 2.4, for the "0.50–0.55" bin, we get the value of corresponding conversion coefficient:

$$\left(\frac{D_t(d)}{\Phi}\right) = 0.458 \text{ nGy cm}^2$$

Calculate the fluence rate of primary electrons in the beam:

$$\dot{\Phi} = \frac{\mathrm{i}}{\mathrm{a\,e}} = \frac{5 \cdot 10^{-9}}{10 \times 1.6 \cdot 10^{-19}} = 3.12 \cdot 10^9 \text{ cm}^{-2}\text{s}^{-1}$$

The absorbed dose rate in tissue at this depth is finally:

Table 2.4 "Fluence of electron-absorbed dose" Conversion factor at a depth d in a tissue phantom ICRU D_t (d) Φ, according to the ratio d/R_0 with R_0 the electron path of in the water, for electron energies between 60 keV and 10 MeV, in nGy cm^2 (based [10], With permission from Oxford University Press)

d/R_0	T (MeV)													
	0.06	0.07	0.08	0.09	0.10	0.113	0.125	0.15	0.20	0.30	0.40	0.50	0.60	0.70
0.00–0.05	1.083	0.980	0.896	0.842	0.787	0.732	0.699	0.624	0.541	0.467	0.427	0.398	0.349	0.335
0.05–0.10	1.296	1.165	1.076	1.000	0.939	0.875	0.832	0.739	0.642	0.544	0.506	0.469	0.413	0.391
0.10–0.15	1.556	1.381	1.276	1.197	1.112	1.036	0.987	0.882	0.758	0.641	0.586	0.546	0.481	0.455
0.15–0.20	1.856	1.655	1.523	1.431	1.327	1.235	1.162	1.038	0.901	0.742	0.667	0.620	0.545	0.519
0.20–0.25	2.117	1.898	1.738	1.645	1.522	1.414	1.323	1.191	1.028	0.833	0.741	0.684	0.601	0.578
0.25–0.30	2.339	2.106	1.910	1.783	1.664	1.557	1.442	1.301	1.110	0.911	0.794	0.736	0.641	0.618
0.30–0.35	2.493	2.217	2.028	1.867	1.731	1.618	1.522	1.350	1.156	0.940	0.822	0.763	0.667	0.636
0.35–0.40	2.568	2.291	2.085	1.899	1.770	1.651	1.550	1.371	1.163	0.939	0.821	0.755	0.674	0.634
0.40–0.45	2.567	2.275	2.062	1.890	1.752	1.638	1.523	1.355	1.152	0.927	0.803	0.734	0.658	0.629
0.45–0.50	2.508	2.219	2.010	1.843	1.706	1.583	1.470	1.305	1.095	0.876	0.759	0.687	0.629	0.606
0.50–0.55	2.384	2.113	1.907	1.734	1.620	1.478	1.376	1.224	1.025	0.809	0.701	0.634	0.573	0.550
0.55–0.60	2.192	1.939	1.761	1.583	1.482	1.332	1.253	1.122	0.927	0.727	0.611	0.555	0.517	0.497
0.60–0.65	1.920	1.720	1.552	1.418	1.324	1.178	1.098	0.979	0.795	0.614	0.516	0.466	0.451	0.432
0.65–0.70	1.644	1.462	1.311	1.178	1.092	0.993	0.909	0.808	0.644	0.486	0.409	0.354	0.378	0.355
0.70–0.75	1.291	1.170	1.040	0.947	0.860	0.779	0.709	0.622	0.489	0.359	0.291	0.255	0.293	0.280
0.75–0.80	0.957	0.855	0.765	0.700	0.645	0.565	0.516	0.441	0.343	0.236	0.188	0.161	0.214	0.205
0.80–0.85	0.625	0.571	0.508	0.444	0.416	0.368	0.329	0.279	0.202	0.139	0.104	0.085	0.140	0.133
0.85–0.90	0.366	0.320	0.287	0.262	0.232	0.205	0.188	0.147	0.103	0.066	0.048	0.037	0.078	0.074
0.90–0.95	0.179	0.162	0.142	0.129	0.114	0.094	0.086	0.067	0.043	0.024	0.016	0.011	0.037	0.034
0.95–1.00	0.072	0.064	0.054	0.045	0.045	0.035	0.031	0.025	0.013	0.006	0.004	0.003	0.013	0.011
1.00–1.05	0.022	0.017	0.013	0.013	0.012	0.009	0.008	0.006	0.003	0.001	0.001	0.000	0.003	0.003
1.05–1.10	0.005	0.004	0.003	0.002	0.002	0.003	0.002	0.001	0.001	0.000	0.000	0.000	0.000	0.000

(continued)

Table 2.4 (continued)

d/R_0	T (MeV)													
	0.06	0.07	0.08	0.09	0.10	0.113	0.125	0.15	0.20	0.30	0.40	0.50	0.60	0.70
d/R_0	0.80	1.00	1.25	1.50	1.75	2.00	2.50	3.00	3.50	4.00	5.00	6.00	8.00	10.00
0.00–0.05	0.327	0.311	0.300	0.293	0.290	0.288	0.283	0.281	0.283	0.282	0.283	0.285	0.287	0.289
0.05–0.10	0.379	0.356	0.338	0.328	0.323	0.317	0.309	0.306	0.305	0.302	0.301	0.301	0.302	0.305
0.10–0.15	0.436	0.408	0.386	0.368	0.356	0.347	0.334	0.329	0.324	0.318	0.316	0.314	0.314	0.315
0.15–0.20	0.498	0.463	0.434	0.413	0.396	0.386	0.364	0.357	0.347	0.339	0.332	0.328	0.324	0.324
0.20–0.25	0.551	0.514	0.479	0.458	0.439	0.426	0.402	0.387	0.373	0.365	0.352	0.344	0.336	0.334
0.25–0.30	0.589	0.550	0.522	0.496	0.478	0.462	0.434	0.418	0.402	0.392	0.373	0.363	0.350	0.343
0.30–0.35	0.611	0.573	0.546	0.521	0.507	0.487	0.463	0.444	0.431	0.420	0.398	0.382	0.366	0.355
0.35–0.40	0.612	0.574	0.552	0.529	0.513	0.503	0.483	0.466	0.451	0.441	0.419	0.402	0.383	0.368
0.40–0.45	0.601	0.567	0.542	0.524	0.510	0.501	0.485	0.471	0.465	0.453	0.434	0.421	0.398	0.381
0.45–0.50	0.571	0.543	0.517	0.508	0.494	0.486	0.476	0.470	0.464	0.455	0.442	0.430	0.409	0.391
0.50–0.55	0.331	0.504	0.486	0.473	0.468	0.458	0.454	0.448	0.451	0.444	0.441	0.429	0.411	0.400
0.55–0.60	0.477	0.460	0.441	0.433	0.428	0.424	0.423	0.421	0.420	0.422	0.419	0.417	0.407	0.401
0.60–0.65	0.418	0.404	0.386	0.377	0.378	0.375	0.378	0.382	0.382	0.388	0.390	0.393	0.392	0.389
0.65–0.70	0.346	0.332	0.319	0.317	0.316	0.322	0.325	0.327	0.336	0.340	0.350	0.357	0.369	0.370
0.70–0.75	0.270	0.259	0.254	0.251	0.250	0.255	0.264	0.270	0.274	0.283	0.304	0.311	0.327	0.336
0.75–0.80	0.192	0.190	0.185	0.187	0.186	0.188	0.202	0.206	0.212	0.219	0.240	0.254	0.276	0.288
0.80–0.85	0.125	0.124	0.121	0.121	0.123	0.126	0.137	0.143	0.151	0.157	0.175	0.191	0.217	0.236
0.85–0.90	0.071	0.068	0.069	0.070	0.073	0.076	0.083	0.087	0.093	0.100	0.115	0.129	0.152	0.173
0.90–0.95	0.033	0.032	0.032	0.033	0.034	0.036	0.042	0.043	0.047	0.054	0.063	0.074	0.092	0.111
0.95–1.00	0.012	0.011	0.011	0.011	0.011	0.013	0.016	0.017	0.019	0.022	0.027	0.033	0.047	0.060
1.00–1.05	0.003	0.003	0.003	0.003	0.003	0.003	0.004	0.004	0.005	0.006	0.008	0.011	0.018	0.025
1.05–1.10	0.000	0.000	0.000	0.001	0.001	0.001	0.001	0.001	0.001	0.001	0.002	0.003	0.005	0.008

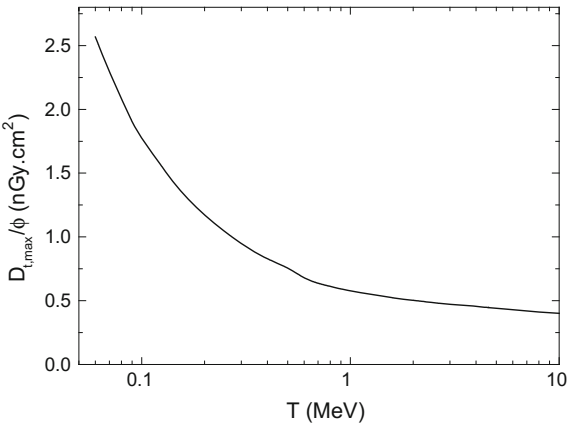

Fig. 2.5 Maximal absorbed dose per unit fluence of primary electrons in water, adapted from [10]

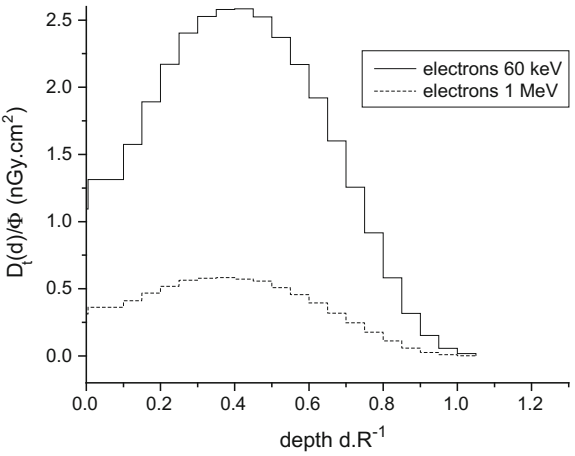

Fig. 2.6 $(D_t(d)/\ \Phi)_T$ factors in terms of d/R_0 for 60 keV and 2 MeV electrons, adapted from [10]

$$\dot{D}_t(0.5\,\text{cm}) = \left(\frac{D_t(d)}{\Phi}\right)_T \dot{\Phi} = 0.458 \cdot 10^{-9} \times 3.12 \cdot 10^{9} \times 3600 = 5.1 \cdot 10^{3}\ \text{Gy/h}$$

Figures 2.5 and 2.6 show on the one hand the maximum absorbed dose per unit fluence of primary electrons in water and on the other hand, absorbed dose plots for 100 keV and 10 MeV monoenergetic electrons.

2.1.5 Calculation of the Tissue Dose for Particles β

Remind that for β disintegration, electrons or positrons are emitted with energies covering a continuous energy spectrum. In this context, it is possible to determine a

mean mass stopping power $\overline{(S/\rho)}_{\text{coll}}$ by taking a weighted average of $(S/\rho)_{\text{al}}$ on the full spectral energy distribution according to (2.17).

$$\overline{\left(\frac{S}{\rho}\right)}_{coll} = \frac{\int_0^{T_{\beta\max}} \left(\frac{S}{\rho}\right)_{coll} \Phi_E \, dE}{\int_0^{T_{\beta\max}} \Phi_E \, dE} = \frac{D_\beta}{\Phi_\beta} \tag{2.19}$$

So numerator is the absorbed dose induced by a β spectrum and the denominator is the fluence of charged particles, hence the basic relationship of the absorbed dose (2.19) for a β spectrum.

$$\dot{D}_\beta = \overline{\left(\frac{S}{\rho}\right)}_{el} \dot{\Phi}_\beta \tag{2.20}$$

where $\overline{(S/\rho)}_{\text{coll}}$ can be considered as the mass stopping power for the mean energy of β spectrum: $\overline{T}_\beta$. (Note: for convenience from now we stop setting "coll" for mass stopping power).

While crossing the medium changes the spectrum, we consider that the mean value of energy remains constant. Thus in a first approach, the dose can be calculated by (2.20) considering that the β fluence in terms of depth roughly responds to a decreasing exponential attenuation. However, it is not trivial to obtain rigorously this fluence without Monte Carlo methods [11]. Loevinger et al. [12] proposed semi-empirical expressions for a β source point in a semi-infinite medium. These expressions selected by Cross [13] are given in (2.21) that the dose (Gy) to the depth x (g cm^{-2}) in a semi-infinite homogeneous material.

$$\mathrm{D(x)} = \begin{cases} \frac{\mathrm{k}}{(\upsilon.\mathrm{X})^2}\left[\mathrm{C} - \upsilon.\mathrm{x}.\exp(1 - \upsilon.\mathrm{x/C}) + \upsilon.\mathrm{x}.\exp(1 - \upsilon.\mathrm{x}) - \mathrm{A}\right] & \text{if } \mathrm{x} \le \mathrm{C}/\upsilon \\ \frac{\mathrm{k}}{(\upsilon.\mathrm{X})^2}\left[\upsilon.\mathrm{x}.\exp(1 - \upsilon.\mathrm{x}) - \mathrm{A}\right] & \text{if } \mathrm{C}/\upsilon < \mathrm{x} < \mathrm{R} \\ 0 & \text{if } x > R \end{cases} \tag{2.21}$$

coefficients ν are given depending on the environment by:

$$\upsilon(\mathrm{cm}^2 \cdot \mathrm{g}^{-1}) = \frac{18.6}{(E_{\beta Max} - 0.036)^{1.37}} \quad \text{for water} \tag{2.22}$$

$$\upsilon(\mathrm{cm}^2 \cdot \mathrm{g}^{-1}) = \frac{16}{(E_{\beta Max} - 0.036)^{1.4}} \quad \text{for air} \tag{2.23}$$

The value of coefficient k is given by relationships (2.24).

$$k(Gy) = 1.6 \cdot 10^{-10} \left(\frac{\upsilon^3 E_{\beta moy.} \alpha}{4\pi\rho} \right) \tag{2.24}$$

$$\alpha = \left(3C^2 - \left(C^2 - 1\right) \cdot \exp(1) - \left(1 + \upsilon R + \upsilon^2 R^2\right) \cdot \exp(1 - \upsilon R)\right)^{-1} \tag{2.25}$$

the coefficient C depends on the maximum energy, the spectrum nature and whether it is an electron or a positron.

$$C = \begin{cases} 1.349 - 0.416\ \ln(E_{\max}) & simple\ spectrum \\ 1.637 - 0.496\ \ln(E_{\max})\ multi - composant\ spectrum \\ 1.135 - 0.1086\ \ln(E_{\max}) - 0.0861(\ln E_{\max})^2 positrons \end{cases} \tag{2.26}$$

$$A = \upsilon R\ \exp(1 - \upsilon R)\ and\ \overline{R} = 0.74 \times R_{\max} \tag{2.27}$$

with $R_{\max}$ the maximum range of β particles.

Note that the expression (2.21) although semi-empirical gives a satisfactory approximation of the β dose in depth. Bourgois [14] compares the results of the dose distribution of β point-source in water obtained by the expression (2.19) with those of Monte Carlo code (MCNPX [15]) for four radionuclides (Fig. 2.7). A good agreement is observed.

Apply this approach to assess the dose rate at contact with ^{32}P point source of 4 MBq activity under 70 μm of water. ^{32}P emits a maximum β energy of 1.71 and 0.696 MeV mean β energy. Intermediate parameters for (2.19) calculation are:

$$\upsilon = \frac{18.6}{(1.71 - 0.036)^{1.37}} = 9\ \mathrm{cm^2\ g^{-1}} = 9\,\mathrm{cm}\ \ \text{for water},$$

$$C = 1.349 - 0.416 \ln(E_{\max}) = 1.12$$

$$R_{\max} = 0.412 E^{1.265 - 0.0954\ Ln(1.71)} = 0.8\,\mathrm{cm}$$

$$\text{Is}: \overline{R} = 0.74 \times R_{\max} = 0.58$$

$$\alpha = \left(3C^2 - \left(C^2 - 1\right) \cdot \exp(1) - \left(1 + \upsilon R + \upsilon^2 R^2\right) \cdot \exp(1 - \upsilon R)\right)^{-1} = 0.32$$

$$k = 1.6 \cdot 10^{-10} \left(\frac{\upsilon^3 E_{\beta moy.} \alpha}{4\pi\rho} \right) = \frac{9^3 \times 0.696 \times 0.32}{4\pi \times 1} = 2.1 \cdot 10^{-9} Gy$$

$$A = \upsilon R \times \exp(1 - \upsilon R) = 9 \times 0.58 \times \exp(1 - 9 \times 0.58) = 7.7 \cdot 10^{-2}$$

$$C/\upsilon = 0.12\,\mathrm{cm\ so}\ x \leq C/\upsilon$$

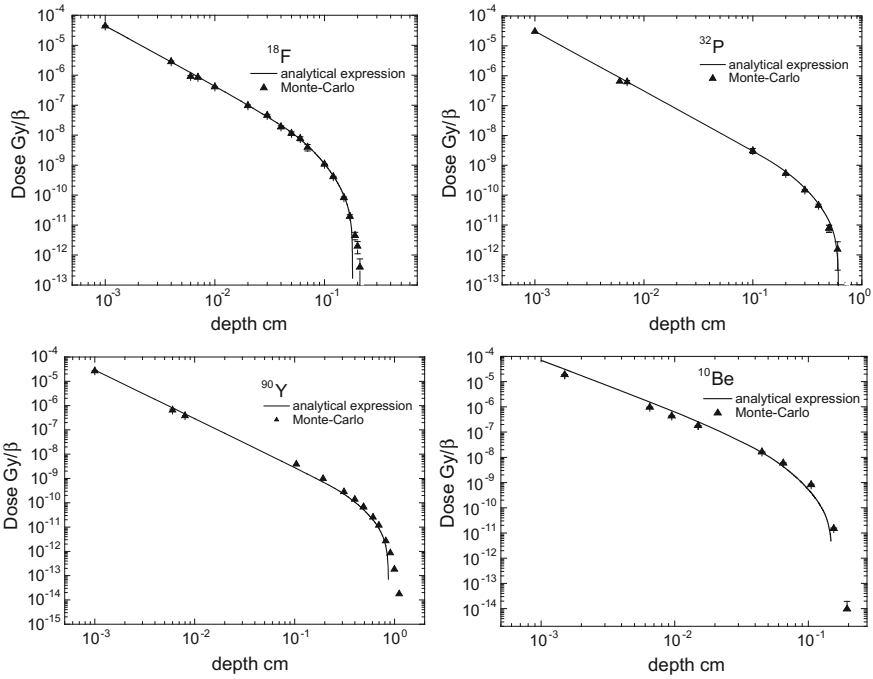

Fig. 2.7 β doses comparison calculated by the analytical expression (2.19) and by MCNPX in water (after [14], with the permission of EDP Sciences)

It is therefore:

$$D(x) = \frac{\mathrm{k}}{(\upsilon \cdot \mathrm{x})^2}\left[\mathrm{C} - \upsilon \cdot \mathrm{x} \cdot \exp(1 - \upsilon \cdot \mathrm{x/C}) + \upsilon \cdot \mathrm{x} \cdot \exp(1 - \upsilon \cdot \mathrm{x}) - \mathrm{A}\right]$$

$$D(x) = \frac{2.10.10^{-9}}{(9 \times 7 \cdot 10^{-3})^2}\left[1.12 - 9 \times 7 \cdot 10^{-3} \cdot \exp(1 - 9 \times 7 \cdot 10^{-3}/1.12)\right.$$

$$\left. + 9 \times 7 \cdot 10^{-3} \cdot \exp(1 - 9 \times 7 \cdot 10^{-3}) - 7.7 \cdot 10^{-2}\right]$$

$$D = 5.6 \cdot 10^{-7}\mathrm{Gy} \quad \text{for a } \beta$$

hence: $\dot{D} = 5.14 \cdot 10^{-7} \times 4 \cdot 10^{6} \times 3600 = 8060\,\mathrm{Gy/h}$. The dose rate in source vicinity is therefore extremely large.

2.1.6 *Calculation of the Dose in the Tissue for HCP*

We have shown that the more ion energy decreases and the more the stopping power significantly increases to a minimum energy corresponding to a change in the

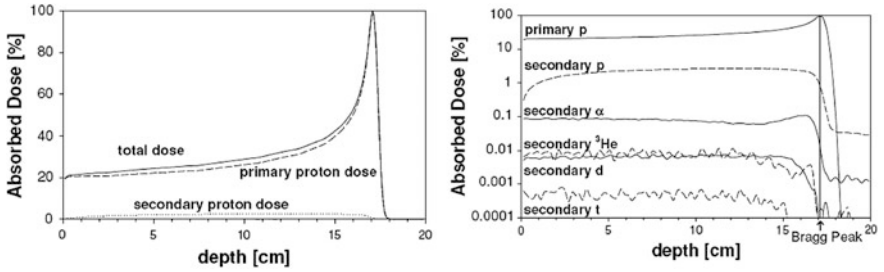

Fig. 2.8 The absorbed dose distribution in water phantom for a 160 MeV proton beam from [5], with permission from IOP Publishing. *Note* left curve in lin-lin, right curve in lin-log

effective charge for the HCP. So at the end path of ion, there is a rapid increase in energy deposition which reaches its maximum in a "Bragg peak".

For high-energy ions, in addition to energy deposition by Coulomb interactions, it should also take into account nuclear interactions responsible for the production of secondary charged particles (e.g. (p,t), (p,α) …). The energy imparted to the medium, in these processes, is due the set in movement of these created particles and by resulting recoil nuclei. Paganetti [5] simulated the absorbed dose due to primary protons and these secondary particles as a function of depth in a water phantom for a 160 MeV proton beam. This is observed in Fig. 2.8. The total dose is due to different types of particles: protons primary and secondary particles: p, α, ^{3}He, t and d.

Gunzert Marx et al. [16] performed the same type of simulation (in terms of ionization) for high energy ^{12}C ions at 200 MeV/u. Figure 2.9 represents this simulation. Notice that such particle is now useful in particle therapy.

Figures 2.8 and 2.9 show that the absorbed dose increases until the Bragg peak and the latter is mainly due to the primary beam ion until peak. Beyond that, it is due to the secondary ions. Golovachik et al. [17] estimated that the absorbed dose due to protons beam of energy between 2 and 600 MeV is slightly influenced by the secondary particles produced during nuclear interactions.

Absorbed dose calculations in the ICRU sphere of 30 cm diameter using a Monte Carlo code for high-energy protons, has been performed. Figure 2.10, from Pelliccioni [18], gives "fluence-dose absorbed in tissue" conversion factors, depending on the depth of the ICRU sphere for various energy protons.

2.1.7 Measurement of the Absorbed Dose for the Electron and β Radiation

Beforehand, a fundamental concept related to ionizing radiation metrology should be defined: the notion of absolute dosimeter. This is the property of certain detector devices which directly return a dosimetric quantity by directly proportional to a

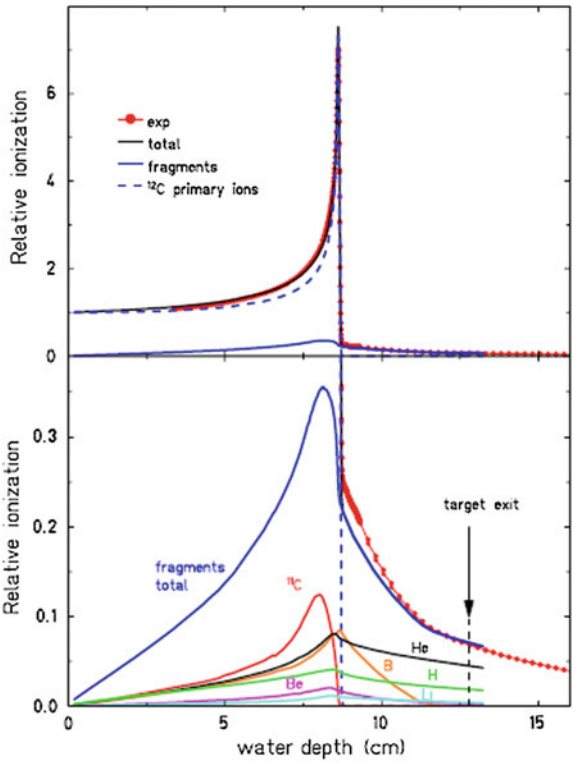

Fig. 2.9 Ionization of ^{12}C ion beam at 200 MeV/u in water. The total ionization is caused by different particles: primary ions and secondary particles (from [16], with permission from IOP Publishing). *Note* the *bottom curve* is a zoom of the *top one*

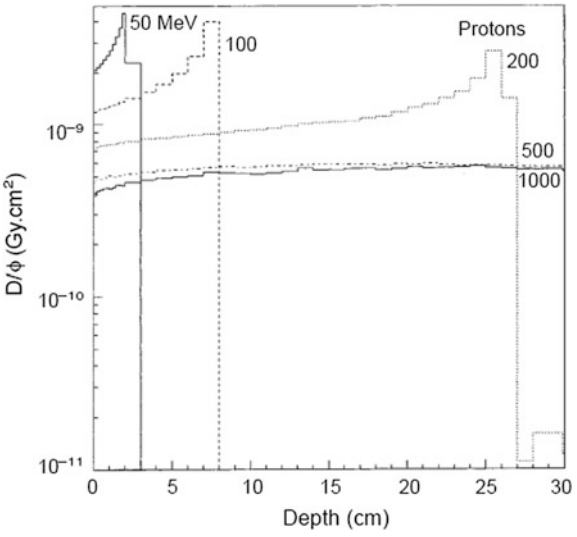

Fig. 2.10 "Fluence-dose absorbed" conversion factors as a function of the depth of the ICRU sphere for energy incident proton monokinetic 50, 100, 200, 500 and 1000 MeV (after [18], with permission from Oxford University Press)

measured physical quantity. So if G_D is the desired dosimetric quantity, and that the m_g is the value of a physical quantity measured by the detector in the presence of an absolute dosimeter, there is a proportionality coefficient N_D such as simple equality (2.28) holds.

$$G_D = N_D m_g \tag{2.28}$$

The N_D term, as we will see in Chap. 3, can be described as calibration coefficient. We access the measurement of the absorbed dose in tissue D_t (more pricisely at 0.07 mm depth i.e. Dt(0.07)) by an extrapolation chamber for β radiation. It is a ionization chamber with flat geometry which has a volume of variable collection. The latter is obtained by the movement of the back electrode by means of a valve. This device allows, by realizing measures for smaller and smaller volumes, to extrapolate the density of ionization by volume unit of which would be measured in a zero-collection volume. The absorbed dose at a skin depth of 0.07 mm can be expressed as fellows (2.29).

$$\mathrm{D}_{\mathrm{tissu}}(0.07) = \frac{\overline{W}_{air}}{e} \frac{1}{\rho_{air} a} \overline{\left(\frac{S}{\rho}\right)}_{air}^{tissu} k' \left(\frac{d(kI)}{dl}\right) \tag{2.29}$$

With the effective surface of collection electrode, ratio between mean mass stopping power for air and tissue, *d(kI)/dl* limit value of current slope as a function of depth l of ionization chamber when *l* tends to 0, *k* the product of the correction factors, which vary with the depth of the chamber (density of the air according to weather conditions, attenuation and particle distribution in the collection volume, not uniformity of radiation fields according to chamber axis, recombination, disturbance of side walls) and k′ the product of the correction factors, which are independent, from the chamber depth radial no-uniformity of the radiation field, the electrostatic attraction of the input window as a function of electric field, and difference between tissues and the constituting materials chamber.

Concerning mono-energetic electrons, two types of absolute dosimetry devices provide access to the absorbed dose in tissue: calorimeter and chemical dosimeters.

The calorimeter

This is the technique providing most direct access to the energy imparted by radiation to matter, so to the absorbed dose. Indeed, the ultimate degradation of this energy leads to a simple increase of thermal agitation of the medium. The application of this technique is mainly limited by its low sensitivity, on the order of mK/Gy. The solid calorimeter consists of a block of reference material (graphite or tissue-equivalent), in which an absorber (sensitive element) of the same composition and weight of the order of one gram is thermally isolated from the rest of the instrument with empty succession of gaps and shields. In the absorber, the amount of heat resulting from the irradiation is measured with thermistor constituting one of the branches of a Wheatstone bridge. The system calibration is performed by injecting a known amount of heat by Joule effect. This mode is called

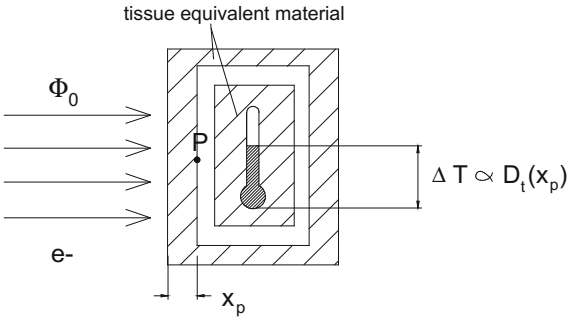

Fig. 2.11 Scheme of a calorimeter irradiated by electron field

"quasi-adiabatic". A new mode, called "constant temperature", was developed in recent years LNHB [19]. Its principle is to keep the shields at a fixed temperature and dissipate into the absorber an electrical power Joule to achieve thermal equilibrium. During irradiation, the power required to maintain this equilibrium is reduced in proportion to the energy deposition by radiation. The value of the dose rate is proportional to the difference of electrical power with and without radiation (Fig. 2.11).

Adding that there is also a water calorimetry whose interest is to measure the absorbed dose in water,—reference variable in radiotherapy—the most direct way possible. The proportionality coefficient is the following: Knowing that the heat amount Q provided to a specific heat capacity medium cp (J kg^{-1} K^{-1}) is related to the temperature change ΔT (K) as follows: $Q = mcp\Delta T$, with m the mass transfer medium. The mean dose delivered in a mass m is indeed related to the temperature measurement by (2.30).

$$\overline{D} = \frac{\overline{\varepsilon}}{m} = \frac{Q}{m} = c_p \Delta T \tag{2.30}$$

By analogy with expression (2.28), the proportionality coefficient of this absolute dosimeter is $N_D = c_p$ and the measured physical quantity $m_g = \Delta T$, for the dosimetric quantity $\overline{D}$. For example, consider a 2 MeV primary electron field with fluence $\Phi = 6.5 \cdot 10^9$ cm^{-2} to the front side of a calorimeter whose screen has a thickness of 0.5 cm of tissue-equivalent material, the absorber is constituted by a 2 cm diameter disc of 0.3 cm thickness Also in tissue-equivalent which will be likened to water density (i.e., weight of about 1 g). Let's determine the change in temperature caused by such a fluence. The previous calculation for a given monokinetic energy of 2 MeV gave a range of $R_{e-} = 0.94$ cm greater than the thickness screen added to that of absorber (i.e. 0.8 cm), which implies that a constant fluence will range the sensitive area. The mean energy distributed in absorber should be determined by means of Table 2.4 for range intervals between: $d/R_0 = 0.5/\ 0.94 = 0.53$ and $d/R_0 = (0.5 + 0.3)/0.94 = 0.85$. In this area, dose coefficients in nGy cm^2 reported in Table 2.4 for 2 MeV are:

d_Φ (0.5–0.55) = 0.458, d_Φ (0.55–0.6) = 0.424, d_Φ (0.6–0.65) = 0.375, d_Φ (0.65–0.7) = 0.322, d_Φ (From 0.7–0.75) = 0.255, d_Φ (0.75–0.8) = 0.188, d_Φ (0.8–0.85) = 0.126.

As each range interval has the same length, we can perform an arithmetic average over all of these coefficients to obtain an mean dose coefficient in the absorber: $\overline{d}_\Phi - 0.306$ nGy cm^2. At fluence considered, the mean deposited dose in the absorber and therefore in tissue is:

$$\overline{D}_t = \overline{d}_\Phi \Phi = 0.306 \cdot 10^{-9} \times 6.5 \cdot 10^9 \approx 2\,\text{Gy}$$

Temperature variation corresponding to this dose, knowing that the specific heat capacity for the tissue is 0.83 cal/g/K, i.e. $3.55 \cdot 10^3$ J/kg/K, is taken from (2.30).

$$\Delta T = \frac{\overline{D}_t}{c_p} = \frac{2}{3.55 \cdot 10^3} = 0.56\,\text{mK}$$

Note the need to measure this variation with highly sensitive thermometers, due to its weakness. Furthermore, if the absorber dimension is small compared to the thickness x_p of block screen, it can be postulated that the mean dose measured is equal to the absorbed dose—punctual—in a depth corresponding to this thickness: $D_t(x_p) \cong \overline{D}_t$.

Fricke chemical dosimeter

In an irradiated environment, initial atomic and molecular ionization and excitation cause chemical changes that can, in some cases, allow dosimetric measurement. The most widely used chemical system is the Fricke dosimeter, based on the oxidation of a ferrous sulfate acid aqueous solution. The specified entity is ferric ion resulting from this oxidation, the concentration is measured spectrophotometrically. There is a proportionality relationship between concentration and dose absorbed in the medium. The proportionality coefficient N_D here is the chemical ferric ions yield $G(Fe^{3+})$ which varies according to the nature and energy of the radiation and is typically of the order of 10^{-6} mol/kg/Gy. This system has the advantage of being almost identical to the water. If the sensitivity of the dosimeter operating according to this technology is low, namely an acceptable minimum dose of 20 Gy for metrological use, performance on the uncertainty of order of 0.1% makes this dosimeter compatible with primary laboratories for calibration.

2.2 Photons

Photons are “indirectly ionizing” radiation type and will transmit their energy to secondary particles, electrons, which deposit thereafter some or all of their energy into the medium. The goal of this section will therefore be to assess theoretically what energy $\overline{E}_{tr}$ is transferred, on average, to electrons of tissue by each photon

collision with electrons of medium. This will allow, as seen in the previous chapter, the assessment of the only dosimetric quantity systematically accessible for photons: kerma.

First, a few reminders on the physical characteristics of photons: the photon is a particle linked to a wave of frequency ν and energy $E = h\nu$. However, although its mass is zero, it is animated by a non-zero momentum p. Indeed, by connecting the energy to mass, we obtain an expression of the momentum dependent upon the total energy E of particle:

$$E = mc^2 \Leftrightarrow m = \frac{E}{c^2} \Leftrightarrow p = \frac{E\nu}{c^2}$$

As the velocity ν of the photon is equal the celerity, the momentum can be expressed as $p = h\nu/c \neq 0$, with h Planck's constant worth $6.62 \cdot 10^{-34}$ J s. Conservation of momentum in a collision will contribute to the determination of energy of particles emerging during interaction. From a practical standpoint, the energy range of interest for photon dosimetry and radiation protection is for wavelengths below 100 nm. For this wavelength, the corresponding energy is:

$$E = h\nu = \frac{hc}{\lambda} = \frac{6.62 \cdot 10^{-34} \times 3 \cdot 10^{8}}{100 \cdot 10^{-9} \times 1.6 \cdot 10^{-19}} = 12\,\text{eV}$$

This value corresponds substantially to the smallest possible ionization energy in tissues. Regarding the interaction of photons with matter, there are three main processes: the photoelectric effect, the Compton effect and pair production effect with different consequences on the transfer of energy. We will omit, in this chapter, another type of interactions to strong energy: "Photonuclear" reactions that will take all their essence in Chap. 4 dedicated to secondary radiation sources.

2.2.1 The Photoelectric Effect

An orbital electron is stripped, taking the energy of incident photon minus W_i, Orbital bond energy of electron to the layer i. These photoelectrons are monoenergetic with well-defined energies according to expression (2.31).

$$T_{ph} = E_{\gamma} - W_i \tag{2.31}$$

This loss of orbital electron leads to an electron rearrangement to more bonded layers. This leads to the release of X radiation fluorescence or Auger electrons, in accordance with detailed energy exchange process in Fig. 2.12.

Considering that the mean ionization energy in the tissue $\overline{W}_t$ is negligible compared to the energy of incident photons, the energy transferred to the photoelectron is substantially the energy of primary photon. In addition, this energy

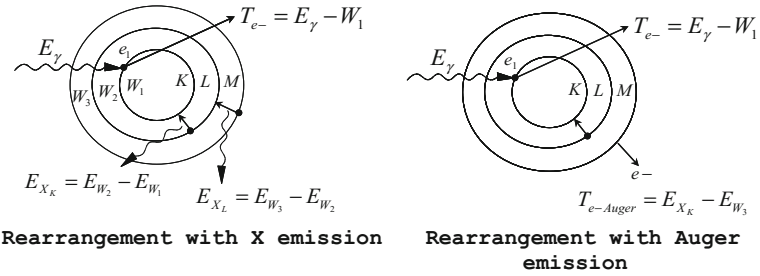

Fig. 2.12 Interaction with photoelectric release of radiation or X Auger electron

transferred can be regarded as mean since it is the only possible result for the photoelectric effect to a considered energy of primary photon.

$$\overline{E}_{tr} = T_{ph} \cong E_\gamma \tag{2.32}$$

Note: We neglect the binding energy in the case of light environments such as water or human tissues (~ 10 eV); However, for dense media (Pb) the most probable binding energy is that of the K layer and can make tens of keV. This nuance will make sense in Chap. 5 on designing calculations of biological shielding.

In terms of the angular distribution of photoelectrons, at low energy ($\beta \ll 1$), photoelectrons are ejected mainly at 90° to the axis of incidence of the primary photon, while in the highest energy ($\beta \cong 1$), they are emitted in the same direction as the primary photon, as observed in the beam curves of Fig. 2.13.

Note that this effect is all the more significant that the medium Z is high and the photon energy is low. That is translated by the cross section through the proportional relationship (2.33).

$$\sigma_{ph} \propto Z^5 E^{-(7/2)} \tag{2.33}$$

In tissues, this effect can be considered to be predominant for the energies of photons below 50 keV and substantially non-existent beyond 100 keV.

2.2.2 *The Compton Effect*

It is a inelastic scattering with decrease of photon energy on the orbital electron. This electron is ejected carrying a part of energy of primary photon, as shown in Fig. 2.14.

It is possible to access an expression linking the energy of Compton scattered photon to the initial energy through momentum and kinetic energy conservation laws (see Further Details 2.4). This relationship is given by the expression (2.34).

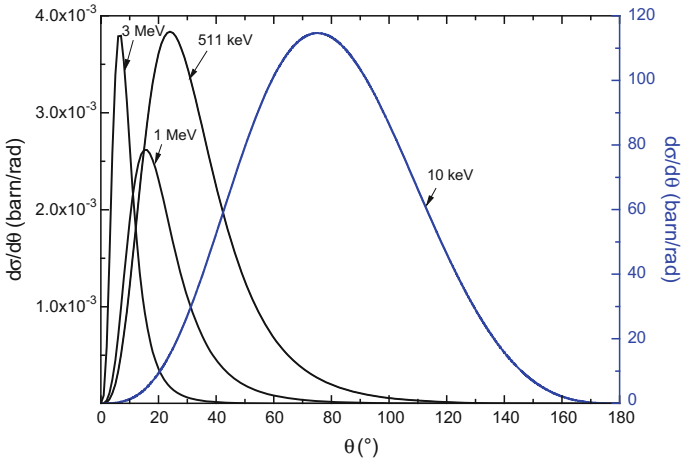

Fig. 2.13 Angular distribution of photoelectrons for photon energies between 10 keV and 3 MeV, for Z_{eq} = 7.7 (for tissues)

$$E'_{\gamma} = \frac{E_{\gamma}}{1 + \frac{E_{\gamma}}{m_o c^2}(1 - \cos\theta)} \tag{2.34}$$

First learning: it is a spectrum for which the energy of scattered photon is maximum in forward direction and minimum in backward direction. Moreover, it will be noted that the energy of a scattered photon at right angles is less than 0.511 MeV and that a backscattered photon at 180° is less than 0.255 MeV, regardless of incident photon energy. This property at extreme angles will be used for shielding calculations related to the scattered radiation discussed in Chap. 5. The energy transferred to the Compton electron is obtained by subtracting this energy to the photon of primary energy according to (2.35).

$$T_c = E_{\gamma} - E'_{\gamma} \quad \Leftrightarrow \quad T_c = \frac{E_{\gamma}^2(1 - \cos\theta)}{m_o c^2 + E_{\gamma}(1 - \cos\theta)} \tag{2.35}$$

Thus this energy is minimum in forward direction and maximum to backward direction and results in the expression (2.36).

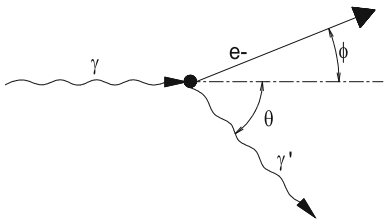

Fig. 2.14 Scheme of Compton scattering

$$T_{c\,\max} \approx \frac{4E_\gamma^2}{4E_\gamma + 1} \quad with \quad E_\gamma(\text{MeV}) \tag{2.36}$$

Table 2.5 provides the evolution of the maximum transferable energy to an electron in the Compton process.

Note that most of the energy of incident photon increases, the maximum energy that can be carried by the Compton electron becomes large; this property is illustrated in the curve of Fig. 2.15. At high energy, the minimum energy carried by the Compton photon ($E'_{\gamma\min} = E_\gamma - T_{c\,\max}$) in the boundary condition where it scatters (θ = 180 °) is bounded by an asymptote at 0.255 MeV.

A relationship can be defined (2.37) derived from the kinematic equations (cf. Further Details 2.4), for connecting the angle θ of the scattered photon at the angle ϕ of the Compton electron, depending on the energy of primary photon.

$$\cot\,\phi = \left(1 + \frac{E_\gamma}{0.511}\right)\tan\left(\frac{\theta}{2}\right) \tag{2.37}$$

Figure 2.16 proposed a set of curves relating to (2.37) for energies between 0.511 and 10 MeV. Figure 2.16b provides a basic scheme of the limiting cases of Compton scattering.

Table 2.5 Variation of the energy of the maximum Compton electron as a function of the incident photon energy

E_γ (MeV)	0.05	0.1	0.2	0.5	1	2	5	10
$t_{c\max}$ (MeV)	0.0085	0.028	0.088	0.33	0.8	1.78	4.76	9.75
$t_{c\max}/E_\gamma$	0.17	0.28	0.45	0.66	0.8	0.9	0.95	0.975

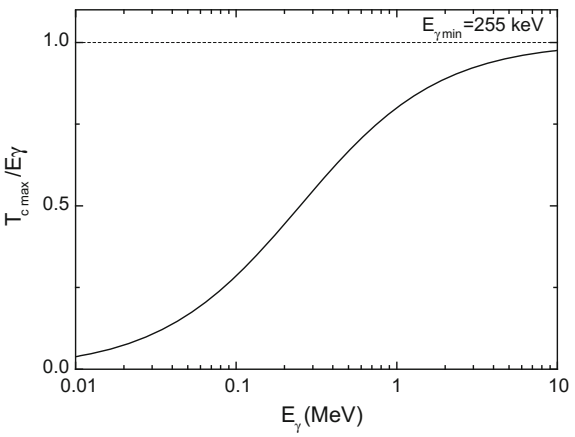

Fig. 2.15 Change in quotient of the maximum energy of the Compton electron energy of the incident photon

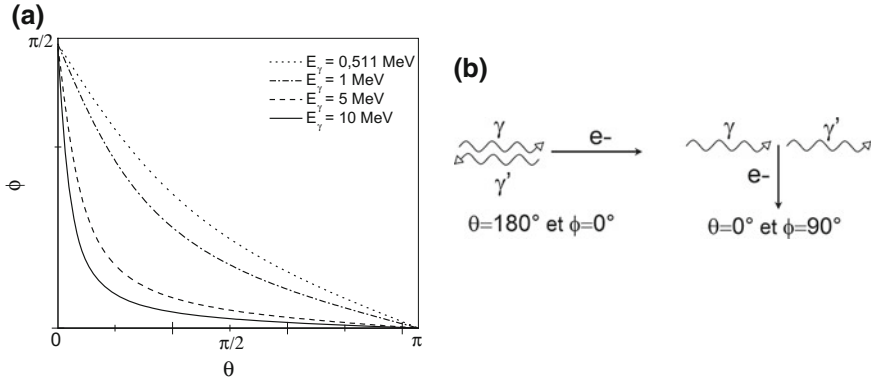

Fig. 2.16 **a** Relationship curve for scattering angle between photon and electron in a Compton interaction. **b** Limit configurations in terms of angles at a Compton interaction

Learnings from these curves are: the Compton electron is always thrown forward in an angle between 0° and 90°. Furthermore, when θ varies from 0° to 180°, ϕ varies from 90° to 0° and the angle θ is even greater than the angle ϕ is small.

Let us add that the energy imparted to the Compton electron is so much greater than the angle ϕ is small; it is up to ϕ = 0 and approaches 0 for ϕ = 90°.

From a statistical standpoint, the differential cross section for solid angle, which reflects the probability that a photon is scattered by an electron in the solid angle between Ω and Ω + dΩ having a polar angle between θ and θ + dθ (Fig. 2.17), provides information on the scattering trend of photons and Compton electrons as a function of energy.

The differential cross section is expressed through the relationship of Klein and Nishina [20] according to (2.38)

$$\left(\frac{d\sigma_c}{d\Omega}\right)_{E_\lambda} = \frac{r_o^2}{2}\left(\frac{E'_\gamma}{E_\gamma}\right)^2\left(\left(\frac{E_\gamma}{E'_\gamma}\right) + \left(\frac{E'_\gamma}{E_\gamma}\right) - \sin^2\theta\right) \tag{2.38}$$

with r_o the classical electron radius 2.818 fm. Replacing E'_γ by its expression (2.38), differential cross section is obtained only in terms of θ and E_γ.

$$\left(\frac{d\sigma_c}{d\Omega}\right)_{E_\lambda} = f(E_\gamma, \theta) \tag{2.39}$$

Figure 2.18 provides the probability distribution, derived from the cross section of Klein and Nishina [20], for scattered photons in a polar angle direction θ relative to the direction of initial incident photon, in function of energy E_γ.

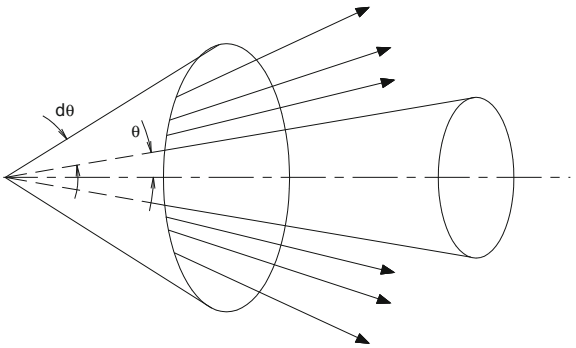

Fig. 2.17 Photon scattering for Compton interaction in a solid angle between Ω and Ω + dΩ and with polar angle between θ and θ + dθ

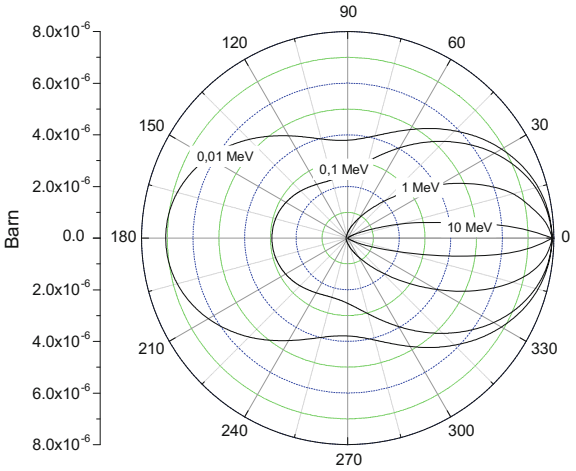

Fig. 2.18 Probability distribution of the scattering angle θ derived from the differential cross section of Klein-Nishina, for incident energies of photon between 10 keV and 10 MeV

The more energy is large, the less scattering is isotropic and in forward direction. Notice that the total effective Compton cross section $\sigma_{c,total}$ is determined by integrating over all space and by weighting by the Z of the medium in order to take into account all orbital electrons:

$$\sigma_{c,total} = Z \int_{\Omega} \left(\frac{d\sigma_c}{d\Omega} \right)_{E_\gamma} d\Omega$$

This nontrivial term derives from a sum of terms (see Further Details 2.5); first idea, we can specify that this cross section is inversely proportional to the energy of incident photon, it tends to 0 for infinite energy and it is directly proportional to Z of the crossed medium:

$$\sigma_{c,total} \propto \frac{Z}{E_\gamma}$$

We also can access, from the expression (2.38), the differential cross section of energy reflecting the probability that Compton photon is emitted with energy between E'_γ and $E'_\gamma + \mathrm{d}\,E'_\gamma$. For this, it is necessary to express θ in terms of E_γ et E'_γ and modify the differential element $d\,\Omega = 2\pi\, r^2 \sin\theta\, d\theta$ in terms of $\mathrm{d}\,E'_\gamma$. Thus it is possible to assess the mean energy E'_γ carried by released photon with integral (2.40).

$$\overline{E}'_\gamma = \frac{1}{\sigma_c} \int_{E'_\gamma} E'_\gamma \left(\frac{d\sigma_c}{dE'_\gamma} \right) dE'_\gamma \tag{2.40}$$

The mean energy carried away (2.41) by the Compton electron corresponds to the mean energy transferred to the medium in each collision of this type:

$$\overline{E}_{tr} = \overline{T}_c = E_\gamma - \overline{E}'_\gamma \tag{2.41}$$

Table 2.6 shows the cross section evolution, the mean energy of Compton electrons and the mean energy fraction transferred to the Compton electron, for primary photon energies between 10 keV and 10 MeV.

Obviously, the more the energy of incident photon increases, the more the proportion of mean energy transferred to the Compton electron increases. Figure 2.19 provides curves of the energy distribution of Compton electrons for energies of incident photon for set values 0.5, 1 and 2 MeV. The mean energy transferred is represented for each of these distributions.

Finally, regarding this effect, we can summarize the behavior of emergent particle, mentioning that for low energies ($E_\gamma < 100$ keV) the scattered photons are emitted in all directions (isotropic), their mean energy is close to the primary photon one, Compton electrons are projected uniformly in all directions in the half space before and their mean energy is a small part of the primary photon one. At higher energies ($E_\gamma > 100$ keV), the scattered photons are emitted forward in a cone whose opening decreases as E_γ increases. Their energy is small part of E_γ (on average). Compton electrons are projected within a cone whose the opening angle becomes smaller when E_γ increases and their mean energy is a fraction increasingly wide of E_γ. Figure 2.20 schematically illustrates these differences in behavior.

We can consider that the Compton interaction takes effect from 50 keV in the tissues and is the main process of energy transfer in this medium for energies between 50 keV and 10 MeV.

Table 2.6 Evolution of the mean energy transferred to Compton electrons for energies of incident photon between 10 keV and 10 MeV

E_γ (MeV)	σ_c (Barn/e$^-$)	$\overline{E}_{tr} = \overline{T}_c$ (MeV)	$\overline{E}_{tr}/E_\gamma$ (%)	E_γ (MeV)	σ_c (Barn/e$^-$)	$\overline{E}_{tr} = \overline{T}_c$ (MeV)	$\overline{E}_{tr}/E_\gamma$ (%)
0.01	0.64	$2.00 \cdot 10^{-4}$	2.00	0.5	0.29	0.17	34.00
0.015	0.63	$4.00 \cdot 10^{-4}$	2.67	0.6	0.27	0.22	36.67
0.02	0.62	$7.00 \cdot 10^{-4}$	3.50	0.8	0.24	0.33	41.25
0.03	0.60	$1.60 \cdot 10^{-3}$	5.33	1	0.21	0.44	44.00
0.04	0.58	$2.70 \cdot 10^{-3}$	6.75	1.5	0.17	0.74	49.33
0.05	0.56	$4.00 \cdot 10^{-3}$	8.00	2	0.15	1.06	53.00
0.06	0.55	$5.60 \cdot 10^{-3}$	9.33	3	0.12	1.73	57.67
0.08	0.52	$9.40 \cdot 10^{-3}$	11.75	4	0.10	2.43	60.75
0.1	0.49	$1.38 \cdot 10^{-2}$	13.80	5	0.08	3.14	62.80
0.15	0.44	$2.72 \cdot 10^{-2}$	18.13	6	0.07	3.86	64.33
0.2	0.41	$4.32 \cdot 10^{-2}$	21.60	8	0.06	5.34	66.75
0.3	0.35	$8.09 \cdot 10^{-2}$	26.97	10	0.05	6.83	68.30
0.4	0.32	0.12	31.00				

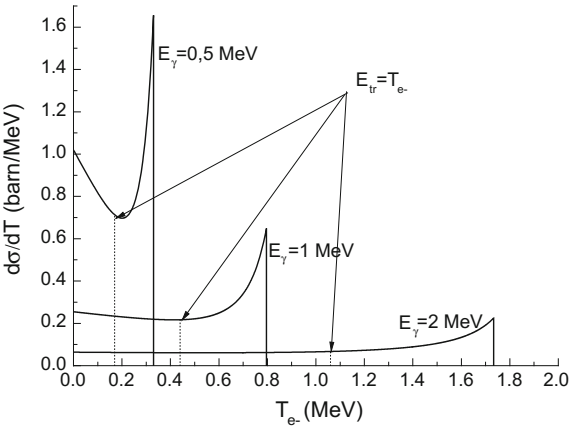

Fig. 2.19 Energy distribution of Compton electrons and mean energy transferred for 0.5, 1 and 2 MeV photons

2.2.3 The Pair Production Effect

In the vicinity of nucleus, this effect is the annihilation of a photon whose energy is converted into creation of electron–positron pair. At the end of slowdown, the positron annihilates in turn with orbital electron to create two 511 keV photons, as observed in Fig. 2.21.

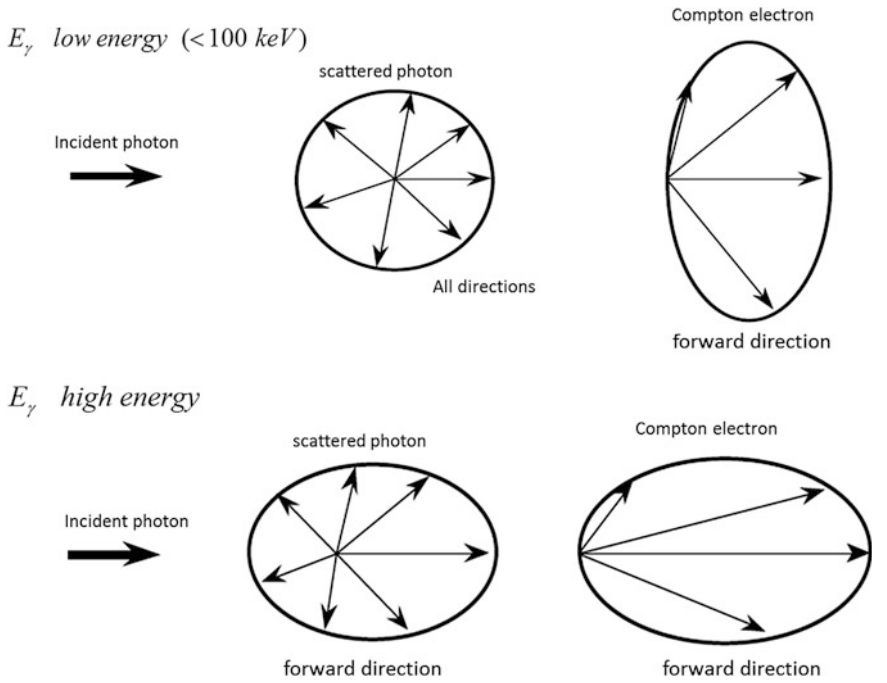

Fig. 2.20 Summary of differences in behavior of scattered electron and Compton photon, for low and high energies of photon

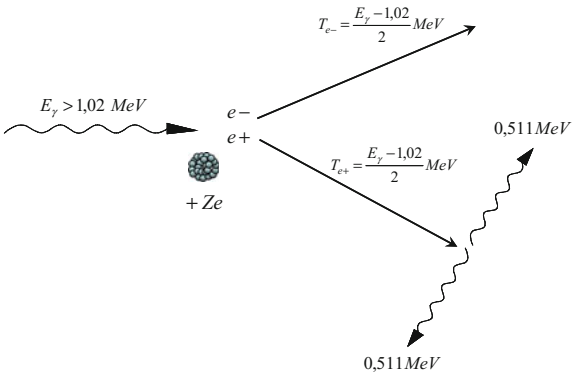

Fig. 2.21 Pair production in the vicinity of a nucleus for a photon of energy greater than 1.022 MeV

It is a threshold reaction: this requires an energy of incident photon at least equal to the sum of the mass of electron and positron, it means: 1.022 MeV. Once the effect is occured, we can consider that the mean residual energy is distributed in equiprobable way between electron and positron.

$$T_{e+} = T_{e-} \approx \frac{E_\gamma - 1.022}{2} (\text{MeV}) \tag{2.42}$$

Accordingly, the energy transferred E_{tr} in the medium is the sum of both contributions. Note that it also corresponds to the mean energy transferred $\overline{E}_{\text{tr}}$ since it is the only possible result for a given energy for primary photon.

$$\overline{E}_{tr} = E_\gamma - 1.022 \tag{2.43}$$

The cross section is proportional to Z, squared, weighted by the logarithm of the energy of incident photon.

$$\sigma_{pp} \propto Z^2 \ln\left(E_\gamma\right) \tag{2.44}$$

This effect is marginal in tissues for common range of energy and can be considered significant from about 10 MeV in these medium.

2.2.4 *Effective Macroscopic Section and Transmission of Photons in Tissue*

The macroscopic cross section of photon interaction with matter characterizing the probability per unit length for a photon to interact in medium (see Further Details 2.3) is the sum of macroscopic cross sections of three effects detailed above:

$$\mu = N\left(\sigma_{pe} + \sigma_{c,total} + \sigma_{pp}\right) \quad (\text{cm}^{-1}) \tag{2.45}$$

with N the atomic density obtained as follows: $N(\text{cm}^{-3}) = \eta_A \rho / A$, where η_A is Avogadro's number: $6.02 \cdot 10^{23}$ atoms/mol, ρ the density (g/cm^3) and A the atomic mass (g/mol). The term μ is the "linear attenuation coefficient". The inverse of this quantity is the "mean free path" and reflects the distance covered on average by the photon in a given medium before interacting as one of three effects.

$$\lambda = \frac{1}{\mu} \quad (\text{cm}) \tag{2.46}$$

We insisted on the property related to the photon attenuation in a medium, in comparison to that of slowdown for charged particles.

Consider a parallel beam (i.e. collimated source at long distance) of N photons penetrating the front side of tissue layer, through a surface section a. A thickness Δx small enough to consider that the number of interactions of photons is small, and consequently the N primary photons is not diminished. Also, the number of photons, ΔN interacted and lost for the primary beam (even if it gives rise to a secondary photon) is expressed according to (2.47).

$$\left(\frac{\Delta N}{a}\right) = -\mu\left(\frac{N}{a}\right)\Delta x \tag{2.47}$$

As before, by considering a distance Δx and the infinitesimal surface a, we obtain the following differential equation of first degree:

$$d\Phi = -\mu\,\Phi\,dx$$

regarding the incoming initial fluence Φ_0, the equation resolution provides the fluence in tissue depth x according to (2.48).

$$\Phi(x) = \Phi_o \exp(-\mu x) \tag{2.48}$$

For convenience, to overcome the fluctuations due to temperature and pressure, mass attenuation coefficient (μ/ρ) is difined. Its unit is $cm^2\ g^{-1}$. The transmission coefficient is defined by the ratio of fluence at point x to initial fluence:

$$T(\mu x) = \frac{\Phi(x)}{\Phi_o} = \exp(-\mu x);\ T(\mu, x) = \frac{\Phi(x)}{\Phi_o} = \exp\left(-\left(\frac{\mu}{\rho}\right)\rho\, x\right) \tag{2.49}$$

For a non-parallel beam (i.e. a non-collimated source), the transmission coefficient which estimates the population of photons in a desired depth, must be modulated by taking into account the increase of the fluence at point x due to the secondary compton photons near that point. There is a need to weight this result by a coefficient called *build-up* noted $B(\mu x, E_\gamma)$ depending on the material crossed, the calculation point depth and the energy of incident photon. The expression (2.49) should be written strictly according to the formulation (2.50).

$$T\left(\mu x, E_\gamma\right) = \frac{\Phi(x)}{\Phi_o} = B\left(\mu x, E_\gamma\right)\exp\left(-\left(\frac{\mu}{\rho}\right)\rho\, x\right) \tag{2.50}$$

However, due to the low Z for studied media (essentially air and tissue) and depths, not exceeding a few mean free paths in these medium, this term can be neglected: $B(\mu x, E_\gamma) \cong 1$. Let us add that this factor will have great significance in Chap. 5 for the calculation of biological protections with higher Z materials and significant thicknesses.

Figure 2.22 provides mass attenuation coefficient curves as a function of energy with each of 3 components in soft tissues.

Adding that like the mass stopping power, for a compound material, the mass attenuation coefficient is calculated using the weighted average of (2.51).

$$\left(\frac{\mu}{\rho}\right)_{comp.} = \sum_i \left(\frac{\mu}{\rho}\right)_i w_i \tag{2.51}$$

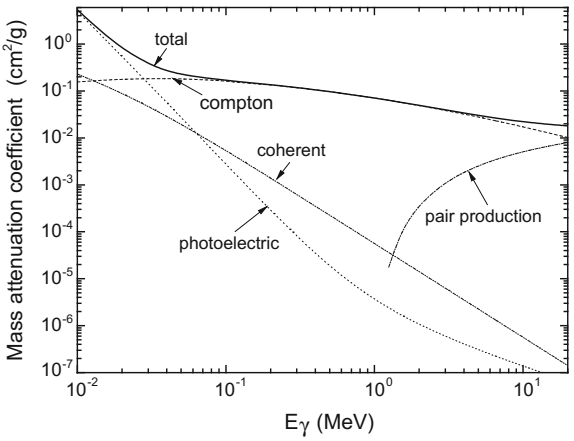

Fig. 2.22 Mass attenuation coefficient in water (according to the data [21])

with $(\mu/\rho)_i$ the mass attenuation coefficient of the compound i and w_i the mass fraction for this one. Table 2.6 provides a number of mass attenuation coefficients for various materials (these are available on the internet link [22]) (Table 2.7).

2.2.5 *Kerma Calculation for Photons*

For the reasons mentioned in the previous chapter, the only dosimetric quantity instantly accessible by calculation for indirectly ionizing radiation is the kerma that characterizes tissue at a point the mean energy transferred per unit mass. We have established in the previous sections, relationships to calculate the mean energy transferred according to photon interaction. However, typically between 50 and 100 keV, two of them have higher probability to occur in tissues: photoelectric and Compton. The mean transferred energy will be a composition of energy transferred with both effects, more exactly a weighted average of microscopic cross sections for each effect expressed by (2.52).

$$\overline{E}_{tr} = \frac{\sigma_{c,total}\overline{E}_{trc} + \sigma_{pe}\overline{E}_{trpe}}{\sigma_{c,total} + \sigma_{pe}} \tag{2.52}$$

this mean transferred energy is actually the mean energy of secondary electrons set in motion during photon collisions in the medium.

$$\overline{E}_{tr} = \overline{T}_{e-}$$

Figure 2.23 gives a schematic diagram of the energy spectrum of secondary electrons set in motion and the mean transferred energy for this energy range.

Table 2.7 Mass attenuation coefficients μ/ρ ($Cm^2\ g^{-1}$) for energies from 10 keV to 20 MeV, adapted from [22]

E (KeV)	H	C	O	F	Al	Cr	Fe	Or	Cu	Mg	Water	Air	Tissues
10	0.3854	2.373	5.952	8.205	26.23	138.6	170.6	209	215.9	21.05	5.329	5.12	4.937
15	0.3764	0.8071	1.836	2.492	7.955	45.71	57.08	70.81	74.05	6.358	1.673	1.614	1.558
20	0.3695	0.442	0.8651	1.133	3.441	20.38	25.68	32.2	33.79	2.763	0.8096	0.7779	0.7616
30	0.357	0.2562	0.3779	0.4487	1.128	6.434	8.176	10.34	10.92	0.9306	0.3756	0.3538	0.3604
40	0.3458	0.2076	0.2585	0.2828	0.5685	2.856	3.629	4.6	4.862	0.4881	0.2683	0.2485	0.2609
50	0.3355	0.1871	0.2132	0.2214	0.3681	1.55	1.958	2.474	2.613	0.3292	0.2269	0.208	0.2223
60	0.326	0.1753	0.1907	0.192	0.2778	0.9639	1.205	1.512	1.593	0.257	0.2059	0.1875	0.2025
80	0.3091	0.161	0.1678	0.1639	0.2018	0.4905	0.5952	0.7306	0.763	0.1951	0.1837	0.1662	0.1813
100	0.2944	0.1514	0.1551	0.1496	0.1704	0.3166	0.3717	0.444	0.4584	0.1686	0.1707	0.1541	0.1688
150	0.2651	0.1347	0.1361	0.1298	0.1378	0.1788	0.1964	0.2208	0.2217	0.1394	0.1505	0.1356	0.149
200	0.2429	0.1229	0.1237	0.1176	0.1223	0.1378	0.146	0.1582	0.1559	0.1245	0.137	0.1233	0.1356
300	0.2112	0.1066	0.107	0.1015	0.1042	0.1067	0.1099	0.1154	0.1119	0.1065	0.1186	0.1067	0.1175
400	0.1893	0.09546	0.09566	0.09073	0.09276	0.09213	0.094	0.09765	0.09413	0.09492	0.1061	0.09549	0.1051
500	0.1729	0.08715	0.08729	0.08274	0.08445	0.08281	0.08414	0.08698	0.08362	0.08647	0.09687	0.08712	0.09593
600	0.1599	0.08058	0.0807	0.07649	0.07802	0.07598	0.07704	0.07944	0.07625	0.07988	0.08956	0.08055	0.0887
800	0.1405	0.07076	0.07087	0.06717	0.06841	0.0662	0.06699	0.06891	0.06605	0.07008	0.07865	0.07074	0.07789
1000	0.1263	0.06361	0.06372	0.06037	0.06146	0.0593	0.05995	0.0616	0.05901	0.06296	0.07072	0.06358	0.07003
1250	0.1129	0.0569	0.05697	0.05399	0.05496	0.05295	0.0535	0.05494	0.05261	0.05629	0.06323	0.05687	0.06262
1500	0.1027	0.05179	0.05185	0.04915	0.05006	0.04832	0.04883	0.05015	0.04803	0.05129	0.05754	0.05175	0.05699
2000	0.08769	0.04442	0.04459	0.04228	0.04324	0.04213	0.04265	0.04387	0.04205	0.04426	0.04942	0.04447	0.04893
3000	0.06921	0.03562	0.03597	0.03422	0.03541	0.03559	0.03621	0.03745	0.03599	0.03613	0.03969	0.03581	0.03929
4000	0.05806	0.03047	0.031	0.0296	0.03106	0.03235	0.03312	0.03444	0.03318	0.03159	0.03403	0.03079	0.03367
5000	0.05049	0.02708	0.02777	0.02663	0.02836	0.03057	0.03146	0.03289	0.03177	0.02873	0.03031	0.02751	0.02998

(continued)

Table 2.7 (continued)

E (KeV)	H	C	O	F	Al	Cr	Fe	Or	Cu	Mg	Water	Air	Tissues
6000	0.04498	0.02469	0.02552	0.02457	0.02655	0.02956	0.03057	0.0321	0.03108	0.02681	0.0277	0.02522	0.02739
8000	0.03746	0.02154	0.02263	0.02195	0.02437	0.02869	0.02991	0.03164	0.03074	0.02445	0.02429	0.02225	0.024
10000	0.03254	0.01959	0.02089	0.02039	0.02318	0.02855	0.02994	0.03185	0.03103	0.02313	0.02219	0.02045	0.02191
15000	0.02539	0.01698	0.01866	0.01846	0.02195	0.0292	0.03092	0.0332	0.03247	0.02168	0.01941	0.0181	0.01913
20000	0.02153	0.01575	0.0177	0.01769	0.02168	0.03026	0.03224	0.03476	0.03408	0.02127	0.01813	0.01705	0.01785

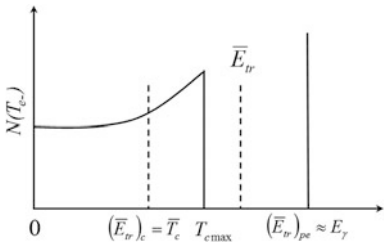

Fig. 2.23 Schematic diagram of the energy transferred in a tissue for photon energy between about 50 and 100 keV

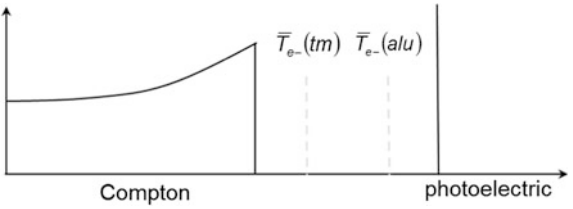

Fig. 2.24 Schematic diagram of mean energy behavior for secondary electrons set in motion in soft tissue and aluminum

In comparison, the mean energy spectrum of secondary electrons is greater in aluminum than in soft tissues; for a 80 keV photon energy: $\overline{T}_{e-}(alu) \cong 2\overline{T}_{e-}(st)$. This reflects the significance of photoelectric effect for aluminum having a higher Z: $\left(\sigma_{pe}(alu) \gg \sigma_{pe}(st)\right)$. This fact is reflected in the diagram of Fig. 2.24 by a shift of mean energy transferred within aluminum, towards the photoelectron energy.

To assess the part of energy of primary photon that is transferred to secondary electrons per unit length, we define the "energy-transfer coefficient" μ_{tr} whose unit is cm^{-1}.

$$\frac{\Delta \overline{E}_{tr}}{\Delta x} = \mu_{tr} E_\gamma \tag{2.53}$$

If Δx tends to zero, we can be convinced that the above ratio is the part of the energy of primary photon that is transferred to the electron of the medium. Once again, to overcome pressure and temperature issue, a derived quantity is defined, called "mass energy-transfer coefficient" independent of density (μ_{tr}/ρ) whose unit is $cm^2\ g^{-1}$. We demonstrate in Further Details 2.6 that the relationship between kerma at a point and the fluence of primary photons at same point, for a given energy, is expressed as (2.54).

$$K = \left(\frac{\mu_{tr}}{\rho}\right) \Phi\, E_\gamma \tag{2.54}$$

Note that a part of the kinetic energy carried by secondary particles set in motion will not be absorbed locally. Indeed, if secondary electrons are emitted with high energy within large Z medium, they lose a part of their energy by bremsstrahlung.

This is why, most frequently in the publications the tabulated values of "mass energy-absorption coefficients" are found and defined as (2.55).

$$\frac{\mu_{en}}{\rho} = \frac{\mu_{tr}}{\rho}(1-g) \tag{2.55}$$

where g is the energy loss of secondary charged particles by bremsstrahlung in the material. Now, for low Z media, as seen above, the bremsstrahlung radiation is negligible, that is the case for light media studied here. Therefore, We can assume the equivalence (2.55).

$$\frac{\mu_{en}}{\rho} \cong \frac{\mu_{tr}}{\rho} \tag{2.56}$$

Table 2.8 provides the mass energy-absorption coefficients: μ_{en}/ρ (Data available on internet [22]).

In the following, we systematically assimilate the mass energy-transfer coefficient with mass energy-absorption coefficient in energy $\mu_{en}/\rho = \mu_{tr}/\rho$.

For a set of discrete rays emitted by a source, kerma in depth x, taking account of unit homogeneity is expressed in formula (2.57).

$$K(x) = 1.6 \cdot 10^{-7} \sum_{E_\gamma} \left(\frac{\mu_{tr}}{\rho}\right)_{E_\gamma} \Phi_{E_\gamma}(x) E_\gamma \,(\text{mGy}) \tag{2.57}$$

Formula (2.58) provides kerma rate as a function of fluence rate for photon of energy E_γ.

$$\dot{K}(x) = 5.76 \cdot 10^{-4} \sum_{E_\gamma} \left(\frac{\mu_{tr}}{\rho}\right)_{E_\gamma} \dot{\Phi}_{E_\gamma}(x) E_\gamma \,(\text{mGy/h}) \tag{2.58}$$

with (μ_{tr}/ρ) in cm^2g^{-1}, $\dot{\Phi}_{E_\gamma}$ in cm^2s^{-1} and E_γ in MeV. For an isotropic point source with activity A (Bq) with multi-ray emission, kerma at a distance d is expressed as (2.59).

$$\dot{K}(d) = 5.76 \cdot 10^{-4} \frac{A}{4\pi d^2} \sum_{E_\gamma} \left(\frac{\mu_{tr}}{\rho}\right)_{E_\gamma} \Gamma(E_\gamma) E_\gamma \,(\text{mGy/h}) \tag{2.59}$$

By extension, for the same source, the kerma in the air at a distance d (cm) crossing i material of thickness x_i is given by 60.

$$\dot{K}(d) = 5.76 \cdot 10^{-4} \cdot \frac{A}{4\pi d^2} \sum_{E_\gamma} \Gamma(E_\gamma) E_\gamma \left(\frac{\mu_{tr}}{\rho}\right)_{E_\gamma} \prod_i T_i(E_\gamma, x) \,(\text{mGy/h}) \tag{2.60}$$

with $T_i(E_\gamma,x)$ transmissions calculated using the formula (2.49).

Table 2.8 Mass energy-absorption Coefficients μ_{en}/ρ ($cm^2\ g^{-1}$) for energies from 10 keV to 20 MeV, adapted from [22]

E (KeV)	H	C	O	F	al	Cr	Fe	Or	Cu	Mg	Water	Air	Tissues
10	0.009849	2.078	5.565	7.776	25.43	119.3	136.9	152.4	148.4	20.36	4.944	4.742	4.564
15	0.01102	0.5627	1.545	2.186	7.487	40.93	48.96	57.34	57.88	5.925	1.374	1.334	1.266
20	0.01355	0.2238	0.6179	0.8796	3.094	18.46	22.6	27.22	27.88	2.432	0.5503	0.5389	0.507
30	0.01863	0.06614	0.1729	0.2451	0.8778	5.78	7.251	8.982	9.349	0.6855	0.1557	0.1537	0.1438
40	0.02315	0.03343	0.0753	0.1036	0.3601	2.482	3.155	3.967	4.163	0.2815	0.06947	0.06833	0.06474
50	0.02709	0.02397	0.04414	0.05747	0.184	1.278	1.638	2.078	2.192	0.1451	0.04223	0.04098	0.03987
60	0.03053	0.02098	0.03207	0.03903	0.1099	0.742	0.9555	1.219	1.29	0.0882	0.0319	0.03041	0.03051
80	0.0362	0.02037	0.02468	0.02676	0.05511	0.3182	0.4104	0.5259	0.5581	0.04671	0.02597	0.02407	0.0253
100	0.04063	0.02147	0.02355	0.02394	0.03794	0.1701	0.2177	0.2781	0.2949	0.0341	0.02546	0.02325	0.02501
150	0.04813	0.02449	0.02506	0.02417	0.02827	0.06536	0.07961	0.09812	0.1027	0.02766	0.02764	0.02496	0.02732
200	0.05254	0.02655	0.02679	0.02554	0.02745	0.04211	0.04825	0.05649	0.05781	0.02761	0.02967	0.02672	0.02936
300	0.05695	0.0287	0.02877	0.02729	0.02816	0.0316	0.03361	0.03659	0.03617	0.02871	0.03192	0.02872	0.03161
400	0.0586	0.0295	0.02953	0.028	0.02862	0.02938	0.03039	0.03209	0.03121	0.02928	0.03279	0.02949	0.03247
500	0.059	0.02969	0.02971	0.02815	0.02868	0.02849	0.02914	0.03036	0.02933	0.02938	0.03299	0.02966	0.03267
600	0.05875	0.02956	0.02957	0.02801	0.02851	0.02788	0.02836	0.02937	0.02826	0.02921	0.03284	0.02953	0.03252
800	0.05739	0.02885	0.02887	0.02734	0.02778	0.0268	0.02714	0.02795	0.02681	0.02848	0.03206	0.02882	0.03175
1000	0.05556	0.02792	0.02794	0.02645	0.02686	0.02576	0.02603	0.02674	0.02562	0.02753	0.03103	0.02789	0.03073
1250	0.05311	0.02669	0.02669	0.02527	0.02565	0.0245	0.02472	0.02536	0.02428	0.02629	0.02965	0.02666	0.02937
1500	0.05075	0.02551	0.02551	0.02416	0.02451	0.0234	0.0236	0.0242	0.02316	0.02514	0.02833	0.02547	0.02806
2000	0.0465	0.02345	0.0235	0.02226	0.02266	0.02178	0.02199	0.02257	0.0216	0.02322	0.02608	0.02345	0.02582
3000	0.03992	0.02048	0.02066	0.01964	0.02024	0.02011	0.02042	0.02107	0.02023	0.02067	0.02281	0.02057	0.02258
4000	0.03523	0.01849	0.01882	0.01797	0.01882	0.01947	0.0199	0.02066	0.01989	0.01915	0.02066	0.0187	0.02044
5000	0.03174	0.0171	0.01757	0.01685	0.01795	0.01929	0.01983	0.0207	0.01998	0.01819	0.01915	0.0174	0.01894
6000	0.02905	0.01607	0.01668	0.01607	0.01739	0.01933	0.01997	0.02094	0.02027	0.01756	0.01806	0.01647	0.01785
8000	0.02515	0.01468	0.01553	0.01508	0.01678	0.0197	0.0205	0.02163	0.021	0.01683	0.01658	0.01525	0.01638
10000	0.02247	0.0138	0.01483	0.01451	0.0165	0.02016	0.02108	0.02234	0.02174	0.01646	0.01566	0.0145	0.01546
15000	0.01837	0.01258	0.01396	0.01382	0.01631	0.02112	0.02221	0.02368	0.02309	0.01614	0.01441	0.01353	0.0142
20000	0.01606	0.01198	0.0136	0.01357	0.01633	0.02174	0.02292	0.02446	0.02387	0.01609	0.01382	0.01311	0.0136

For example, let's calculate the kerma in the air from a Co-60 point source ($E_{\gamma 1}$ = 1.17 MeV, Γ_1 = 1 and $E_{\gamma 2}$ = 1.33 MeV, Γ_1 = 1) of 3.2 GBq activity, at 1 m. For convenience, we consider a 1.25 MeV mean photon energy with an emission intensity of 2. For this single energy, the following parameters for the air are obtained in Tables 2.6 and 2.8:

$$\left(\frac{\mu_{tr}}{\rho}\right)_{air}^{1.25\,\mathrm{MeV}} = 0.0267\,g^{-1}\cdot\mathrm{cm}^2 \text{ and } \left(\frac{\mu}{\rho}\right)_{air}^{1.25\,\mathrm{MeV}} = 0.0568\,g^{-1}\cdot\mathrm{cm}^2$$

And consequently, by the expression (2.49), the following result:

$$\begin{aligned}\dot{K}_a &= 5.76\cdot 10^{-4}\cdot\left(\frac{A\Gamma}{4\pi d^2}\right)\cdot E_\gamma\cdot\left(\frac{\mu_{tr}}{\rho}\right)_{air}^{1.25\,\mathrm{MeV}}\cdot\exp\left(-\left(\frac{\mu}{\rho}\right)_{air}^{1.25\,\mathrm{MeV}}\rho_{air}d\right)\\ &= 5.76\cdot 10^{-4}\cdot\left(\frac{3.2\times 10^9\times 2}{4\pi\times(100)^2}\right)\times 1.25\times 0.0267\times\exp(-0.0568\times 0.00122\times 100)\\ \dot{K}_a &\cong 1\ \mathrm{mGy/h}\end{aligned}$$

Also regarding that the fluence of photons is substantially constant at the interface between two media M_1 and M_2, we can assume that at a point of this interface is verified:

$$\begin{aligned}&K_1 = \left(\frac{\mu_{tr}}{\rho}\right)_{m_1}\Phi_1 E_\gamma,\ K_2 = \left(\frac{\mu_{tr}}{\rho}\right)_{m_2}\Phi_2 E_\gamma \text{ and}\\ &\Phi_1 = \Phi_2 \Rightarrow \frac{K_1}{K_2} = \left(\frac{\mu_{tr}}{\rho}\right)_{m_2}^{m_1}\end{aligned} \tag{2.61}$$

Like charged particles (i.e. d_Φ), it is now possible to establish a "fluence-kerma" conversion coefficient k_Φ according to the following ratio:

$$k_\Phi(E_\gamma) = \left(\frac{K}{\Phi}\right)_{E_\gamma} = \left(\frac{\mu_{tr}}{\rho}\right)_{E_\gamma} E_\gamma \tag{2.62}$$

Figure 2.25 gives a plot of this kerma coefficient in air and tissue-equivalent material from ICRU [23] whose the mass composition of each four elements are: H 0.101—C 0.111—0.026 N—O 0.761 for a density of 1. Table 2.9 provides the discrete values of "Fluence-kerma" conversion factor k_Φ (pGy cm^2) for air.

A similar behaviour of kerma depending on the photon energy is observed, in the air and tissues. This property and others, such as the easy access to the material medium "air", contribute to defining the air kerma as measurable reference quantity for the metrology of photons; we will talk more later.

Another allowed application of formula (2.53) is the possibility to determine the mean energy of electron spectrum set in motion in the medium by primary photons.

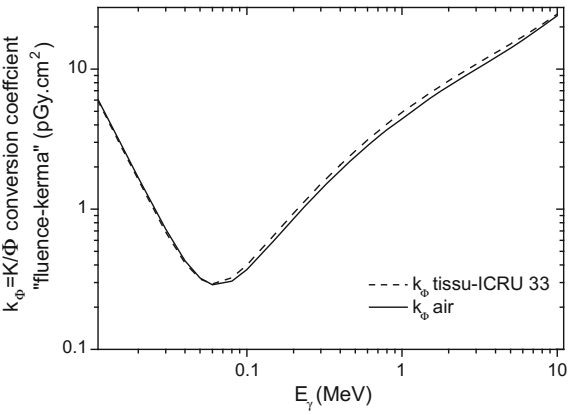

Fig. 2.25 "Fluence-kerma" Conversion factor k_Φ (pGy cm^2) for air and tissue-equivalent material [23], for energies between 10 keV and 10 MeV

Table 2.9 "Fluence-kerma" Conversion factor k_Φ (pGy cm^2) for air, for energies between 10 keV and 10 MeV, adapted from [23]

Energy photon keV	k_Φ pGy cm^2	Energy photon keV	k_Φ pGy cm^2	Energy photon keV	k_Φ pGy cm^2
10	7.6	100	0.372	1000	4.47
15	3.21	150	0.6	1500	6.12
20	1.73	200	0.856	2000	7.51
30	0.739	300	1.38	3000	9.89
40	0.438	400	1.89	4000	12
50	0.328	500	2.38	5000	13.9
60	0.292	600	2.84	6000	15.8
80	0.308	800	3.69	8000	19.5
				10000	23.2

this quantity is equivalent to the mean energy transferred to electrons of medium. According to a macroscopic approach, we can consider that in a thin layer Δx, the total energy transferred in an amount of mass Δm is equal to the number of photons that have interacted in this thickness weighted by the mean electron energy set in motion during the collision. Thus, the kerma can be written in this context:

$$\overline{K} = \frac{\Delta N \, \overline{T}_{e-}}{\Delta m}$$

With expression (2.47) describing the attenuation process of photons in the matter and when the surface a tends to 0 having an effect to make appear the photon fluence at any point within medium, we end upto the expression kerma based on the mean energy of electrons set in motion:

$$\lim_{a\to 0}\overline{K}=\lim_{a\to 0}\frac{\mu N\,\Delta x\,\overline{T}_{e-}}{\rho\,a\,\Delta x}=\lim_{a\to 0}\left(\frac{\mu}{\rho}\right)\left(\frac{N}{a}\right)\overline{T}_{e-}\Rightarrow K=\left(\frac{\mu}{\rho}\right)\Phi_{\gamma}\overline{T}_{e-}$$

expressing K by means of expression (2.54), we obtain the following equation:

$$\overline{T}_{e-}(E_{\gamma})=\overline{E}_{tr}(E_{\gamma})=\left(\left(\frac{\mu_{tr}}{\rho}\right)\Big/\left(\frac{\mu}{\rho}\right)\right)_{E_{\gamma}}E_{\gamma} \tag{2.63}$$

For example, the calculation of mean energy transferred to secondary electrons, set in motion by 1 MeV photons in tissues, leads to 438.5 keV.

2.2.6 *Relationship Between the Absorbed Dose and Photon Kerma*

Consider a small enough volume in material, to be considered as a point, in which a 50 keV photon interacts according to the photoelectric effect, predominant in this energy field. The energy carried by the electron is then approximately 50 keV. The electron range in the tissues at that energy, calculated with Katz and Penfold (2.3), for such energy, is 40 μm and can be considered as negligible and limited to the target volume.

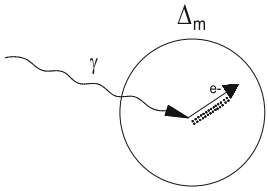

In other words, the energy transferred in collision can be considered locally absorbed by the medium. In this case, kerma is spontaneously assimilated to the absorbed dose:

$$\Delta E_{tr}\approx\overline{\Delta\varepsilon}\Rightarrow\quad K=D$$

Consider, now, a 1 MeV photon for which the predominant reaction in tissue is the Compton effect, the maximum transferable energy to an electron of the medium is from formula (2.34):

$$T_{c\,\max}\approx\frac{4\times(1)^2}{(4\times 1)+1}=0.8\,\text{MeV}$$

For such an energy, according to the Katz and Penfold formulation (2.3), the range would be 3.1 mm in tissue. we can postulate that the energy transferred is not

deposited locally because of range in medium is no longer limited to the target volume.

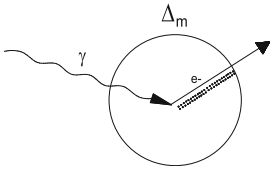

Consequently, the kerma can not be considered equal to the dose:

$$\Delta E_{tr} \neq \overline{\Delta\varepsilon} \Rightarrow \quad K \neq D$$

However, we will see that even in this second case, under certain conditions, it is possible to achieve equality between kerma and absorbed dose.

Considering a medium M preceded by the vacuum, with initial fluence Φ_0 of photons at energy E_γ. At the interface, at vacuum side, there is initially $K = D = 0$. Theoretically, we consider that incident photons cause, at each crossing of elementary thickness dx *in* material, the set in motion of two secondary electrons whose range would be four thicknesses dx. Intuitively, we notice that the kerma corresponds to eight units of energy transferred; since this value corresponds to the total energy transferred by the photons to secondary electrons.

Let's account the deposited energy in each of dx thick layer, considering that an arbitrary unit of deposited energy graphically corresponds to the length of electronic path in a thickness dx (Fig. 2.26).

We easily see that, in the first layer, 2 units of energy are deposited, in the second 4, the third 6 and the fourth, as well as in all the following, we have 8. This shows that as the depth increases the dose is growing to be equal to kerma in the fourth. From this depth, which is actually equal to path $R = 4\mathrm{d}x$ of secondary electron, so we have equality between kerma and dose: $K = D$. Thus, beyond the range of most energetic electrons set in motion, considering a target volume of small size, it is as if every deposited energy outside the volume was compensated by the deposited energy of another secondary electron as shown in Fig. 2.27.

So that, there is systematically equality between transferred and imparted energy into the target volume: $\Delta E_{\mathrm{tr}} = \Delta\varepsilon \Rightarrow K = D$. We can also postulate that beyond this limit, there are as many electrons moved as annihilated. This property is called "electron equilibrium" (EE). Consequently, the following rule can be stated: a medium M with photon field, at electron equilibrium (EE), meaning from the depth corresponding to the range of most energetic secondary electron, the absorbed dose due to photons is equal to kerma at the same point. Below this depth, the absorbed dose can not be determined analytically and only kerma is accessible to the deterministic analytical calculation and measurement.

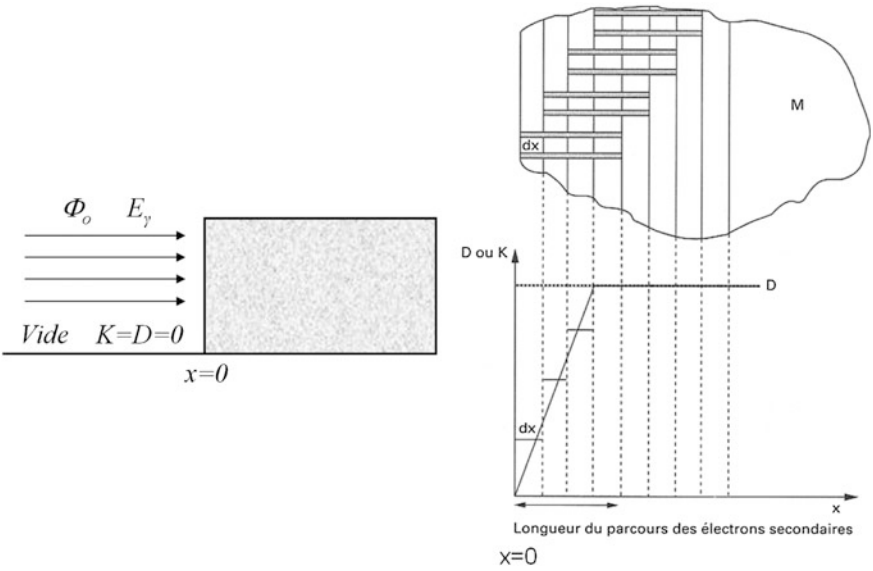

Fig. 2.26 Schematic illustration of the electron equilibrium (after [24], and Technical Documentation © 1997)

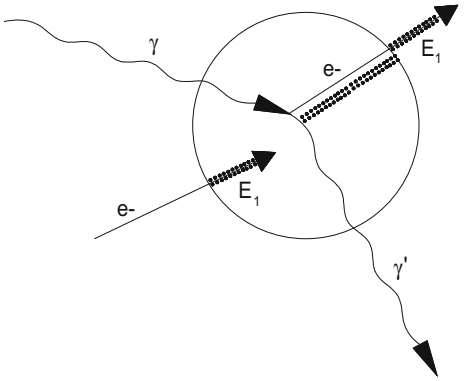

Fig. 2.27 Principle of deposited energy compensation outside the volume by electrons moved upstream, at electron equilibrium

2.2.7 Kerma and Absorbed Dose in Successive Light Media

It is theoretically possible to plot kerma and absorbed dose curve as a function of depth in light media and a for small number of mean free paths, so for a small depth (no scattering). Let's study the evolution of these dosimetric quantities for a parallel beam of monoenergetic photons, and successively crossing two light media M_1 and M_2 as shown in Fig. 2.28.

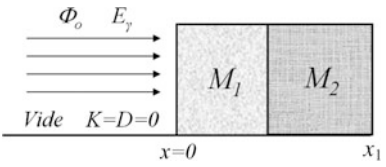

Fig. 2.28 Scheme of parallel beam towards two adjacent light media

For this application, we will consider that arbitrarily R_1 and R_2 are range of most energetic electrons moved by the photons of primary beam in the materials M_1 and M_2, from which the electron equilibrium conditions are observed in both materials. We also postulate that at the energy of incident photons, media present following differences:

$$\left(\frac{\mu}{\rho}\right)_{M_2} > \left(\frac{\mu}{\rho}\right)_{M_1} \quad \left(\frac{\overline{S}}{\rho}\right)_{M_2} > \left(\frac{\overline{S}}{\rho}\right)_{M_1} \quad \left(\frac{\mu_{tr}}{\rho}\right)_{M_2} > \left(\frac{\mu_{tr}}{\rho}\right)_{M_1}$$

First, in a vacuum, in the absence of electron, the fluence of secondary electrons is zero and no energy is transmitted, inducing zero-kerma and zero-absorbed dose anywhere in the vacuum upstream of M_1. In M_1, the photon fluence follows the attenuation law:

$$\Phi_{\gamma M_1}(x) = \Phi_o \exp\left(-\mu_{M_1} x\right)$$

Kerma at a point x of M_1 is accessible by theoretical calculation:

$$K_{M_1}(x) = \left(\frac{\mu_{tr}}{\rho}\right)_{M_1} \Phi_{\gamma M_1}(x) E_\gamma$$

In particular, at the interface "vacuum—M_1 front side" (i.e. $x = 0$), we obtain:

$$K_{M_1}(0) = \left(\frac{\mu_{tr}}{\rho}\right)_{M_1} \Phi_o E_\gamma$$

The fluence of secondary electrons increases as x increases to the value $x = R_1$ and decreases with same law as photon fluence for $x > R_1$. From this depth, the electron equilibrium condition is verified, hence there is equality between kerma and dose according to the rule defined in previous section. Substituting both values by their theoretical expressions, it is shown that the primary photon-to-secondary electrons fluence ratio is constant:

$$D = K \quad \Leftrightarrow \quad \left(\frac{\overline{S}}{\rho}\right)_{\overline{T}_{e-}} \Phi_{e-}(x) = \left(\frac{\mu_{tr}}{\rho}\right)_{E_\gamma} \Phi_\gamma(x) E_\gamma \quad \Rightarrow$$
$$\frac{\Phi_{e-}(x)}{\Phi_\gamma(x)} = \left[\left(\frac{\mu_{tr}}{\rho}\right)_{\overline{T}_{e-}} \Big/ \left(\frac{\overline{S}}{\rho}\right)_{E_\gamma}\right] E_\gamma = cste$$

It is considered in the theoretical formula for fluence of secondary electrons, the mean mass stopping power to mean energy secondary electrons moved in M_1: $\overline{T}_{e-}(M_1)$ which is calculated by expression (2.63). Finally, concerning the absorbed dose $D_{M_1}(x)$, both cases of the rule are presented: for $x < R_1$ We can not access the calculated value of absorbed dose, a Monte Carlo calculation should be used to determine the fluence of secondary electrons $\Phi_{e-M_1}(x)$ and the dose should be as follows:

$$D_{M_1}(x) = \left(\frac{\overline{S}}{\rho}\right)_{\overline{T}_{e-}(M_1)} \Phi_{e-M_1}(x)$$

however, for $x \geq R_1$ the condition of electron equilibrium is met, the absorbed dose is directly equal to the Kerma:

$$D_{M_1}(x) = K_{M_1}(x)$$

At the interface of the adjacent media M_1 and M_2, the photon fluence is the same in x_1 on both sides of the border between both media: $\Phi_{\gamma M_2}(x_1) = \Phi\gamma M_1(x_1)$, the same goes for the fluence of secondary electrons that can be considered constant at the intersection: $\Phi_{e-M_2}(x_1) = \Phi_{e-M_1}(x_1)$. M_2 Kerma is obtained by the boundary property described by (2.61):

$$K_{M_2}(x_1) = \left(\frac{\mu_{tr}}{\rho}\right)_{M_2}^{M_1} KM_1(x_1)$$

At this point, the absorbed dose is calculated according to the ratio law of mass stopping powers described by the expression (2.15).

$$D_{M_2}(x_1) = \left(\frac{\overline{S}}{\rho}\right)_{M_2}^{M_1} D_{M_1}(x_1)$$

Mean mass stopping powers are then taken at the mean energy of secondary electrons moved in the medium M_1: $\overline{T}_{e-}(M_1)$.

Once in M_2, the behavior of all quantities is substantially the same as the upper medium, regarding intrinsic physicochemical M_2 characteristics. Thus the photon fluence at any point x in M_2 is described by the following exponential:

$$\Phi_{\gamma M_2}(x) = \Phi_o \exp\left(-\mu_{M_1} x_1\right) \exp\left(-\mu_{M_2}(x - x_1)\right)$$

Note, however, that unlike the M_1 treatment, the curve of the fluence of secondary electrons $\Phi_{e-M2}(x)$, in the area between the interface and R_2, has a different shape. The electrons fluence is composed of persistent secondary electrons moved in M_1. These are annihilated as they progress through second medium to disappear

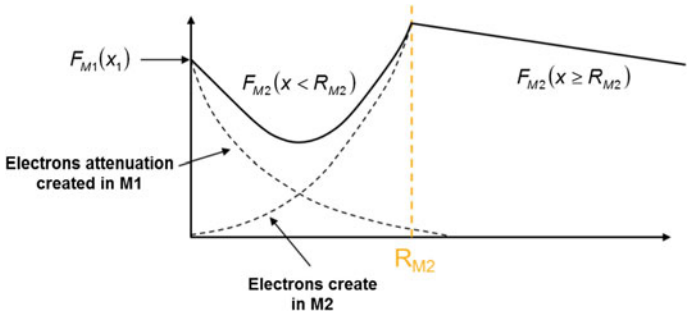

Fig. 2.29 Possible shape for the fluence of secondary electrons in crossing media case

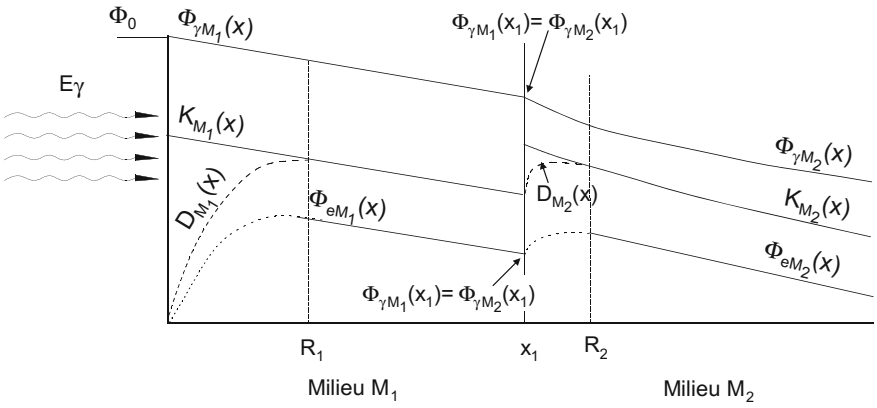

Fig. 2.30 Theoretical curve of the fluence of primary photons, secondary electrons moved by initial photons, kerma and absorbed dose, in two adjacent light media

completely at a depth corresponding to the range in M_2 for energy of electrons set in motion in M_1. In this component are added the electrons moved by the photon beam progressing in M_2 and for which the number increases to reach its maximum at R_2 depth. The curve in Fig. 2.29 gives a potential shape of electronic fluence in this intermediate zone.

So between x_1 and R_2 we can not quantify the fluence of secondary electrons using a simple analytical approach. In the curve of Fig. 2.29 the fluence reach arbitrarily a minimum, but in some cases it could involve a maximum. To overcome this issue a monte-carlo calculation should be used. Finally, curves of Fig. 2.30 summarize the shape profiles of all studied quantities for both media, taking into account the underlying assumptions.

Consequently, we can state the following law: for fluence of initial photon Φ_0 to energy E_γ, there are as many electron equilibrium as media crossed (Fig. 2.31) if the thickness of the media is greater than the range of the most energetic electron in each medium.

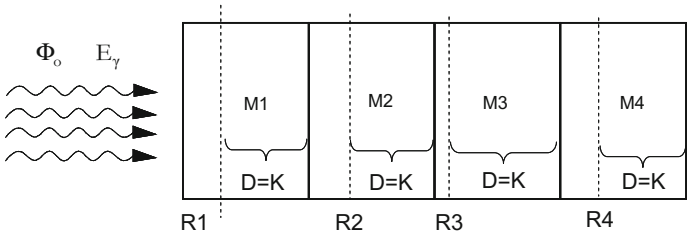

Fig. 2.31 Concept of electron equilibrium for each medium crossed. *Note* An issue resulting from the law ignorance, for example, is to assume for a source sealed by plexiglas for which EE is verified in plexiglas, it is the same at any point of the air outside plexiglas. This assumption as demonstrated above is absolutely untrue!

2.2.8 Measurement of Air Kerma and Absorbed Dose in Tissue for Photons

While detection methods for accessing dose quantities related to photon fields are numerous, the ionization chamber has significant adaptability properties to nuances of dosimetric quantities: K_a, K_t, D_t… and allows, under certain conditions, direct access to these. The principle of detection process consist in collection of charges produced by ionization that is proportional to the energy deposition by particle in the detector volume by application of a suitable high voltage. For a given medium, there is an analytic relationship to link this charge, by extension this current, to dose rate in the sensitive area.

In a target volume of mass m_g in gas, considering that a fluence of secondary electrons moved in material upstream of the gas volume deposit a mean energy imparted $\overline{\varepsilon}$ in mass m_g. We postulate that this energy imparted is responsible for the creation of ΔN ion-electron pairs. If $\overline{W}$g is the mean ionization energy for the creation of each pairs, the mean dose absorbed in the gas can be expressed by (2.64).

$$\overline{D}_g = \frac{\overline{\varepsilon}}{m} = \frac{\Delta N}{m}\overline{W}_g \tag{2.64}$$

Indeed, the number of ion-electron pairs is responsible for the electronic charge: $\Delta Q = \Delta N e$, with e the electron charge. By developing the mass term in numerator, we obtain the relationship between the absorbed dose in this gas and charge created in the gas volume, and consequently that of dose rate in the gas as a function of the current generated (2.65).

$$\overline{D}_g = \frac{\Delta Q}{e}\frac{\overline{W}_g}{\rho_g V_g} \quad \Rightarrow \quad \dot{\overline{D}}_g = \left(\frac{\Delta Q}{\Delta t}\right)\frac{1}{e}\frac{\overline{W}_g}{\rho_g V_g} = \frac{i}{e}\frac{\overline{W}_g}{\rho_g V_g} \tag{2.65}$$

For air, easy available medium often used, not taking into account the correction due to bremsstrahlung (negligible in this case): $\overline{W}_{\text{air}} = 33.97 \pm 0.06$ eV. We will round later in the book that value to 34 eV. In solid medium, due to reduced charge mobility, the charge collection is not a simple method (need to use doped-semiconductor materials as detectors junction), however the electricity produced by ionization in a gas volume by anode-cathode subjected to tension electric field is easily measurable. In the Bragg-Gray approach, this property is exploited.

Narrow cavity and Bragg-Gray relationship

To overcome the inability to measure, at any point, produced charges in solid medium, a volume of gas is juxtaposed to the measurement point. the measured current in this volume is then connected to the dose absorbed at that point, as shown in Fig. 2.32.

If cavity sizes are small compared to the range of secondary electrons, the introduction of this gas-filled cavity within a solid homogeneous medium does not change the spectrum of these electrons in medium. This leads to the so-called "narrow cavity" and we demonstrate that for electron equilibrium conditions, there is a proportional relationship between the deposited dose at material point and that deposited in the gas cavity (see Further Details 2.7); it is the "Bragg-Gray relationship":

$$D_M = \left(\frac{\overline{S}}{\rho}\right)_g^M D_g \tag{2.66}$$

The material-to-gas ratio of mean mass stopping power for the mean energy of secondary electron spectrum, is therefore obtained by the expression (2.60). This relation (2.65) also can be applied to dose rates with charge replaced by intensity (2.67):

$$\dot{D}_M(\text{mGy/h}) = 3.6 \cdot 10^9 \left(\frac{\overline{S}}{\rho}\right)_g^M \frac{i}{\rho_g V_g} \overline{W}_g \tag{2.67}$$

with i A, ρ_g g cm^{-3}, V_g cm^{-3} and $\overline{W}_g$ in eV.

In practice, it is considered that a cavity is narrow and allows the application of Bragg-Gray theory, since, for the mean energy spectrum of secondary electrons

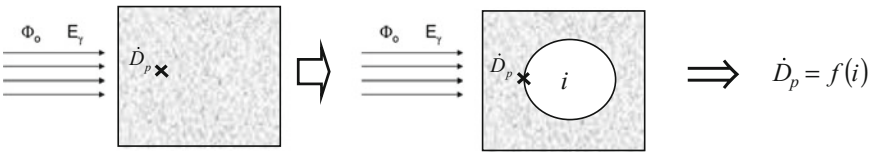

Fig. 2.32 Scheme of measurement of intensity in gas volume as a transfer quantity for calculating the absorbed dose rate at a point on a solid medium

moved in the solid medium above, the electron range in the gas cavity is at least five times greater than the largest size of cavity:

$$R_g\left(\overline{T}_{e-}(M)\right) \geq 5x_{cavity} \tag{2.68}$$

At this point, it is important to emphasize that in this cavity, these are secondary electrons that create the dose in the sensitive gas volume and not photons for which the mean free path is several thousand times higher than electrons in the gas.

Moreover, adding that it is imperative for the application of Bragg-Gray relationship, that the secondary electron field is homogeneous throughout the cavity; otherwise, significant errors in the predicted value of absorbed dose can occur.

In support of this, let's consider a detector with narrow cavity for applying the Bragg-Gray rule. Two cases are considered: a homogeneous field of primary photons that moves N_1 electrons which penetrate into the cavity and a beam whose section is much less than the input cavity surface, but which due to a higher fluence also generates N_1 electrons into the cavity as shown in Fig. 2.33.

The Bragg-Gray rule leads to $D_M(1) = D_M(2)$. In reality, the difference in electronic fluence due to difference in two beams input sections causes the following inequality:

$$\Phi_{e-}(1) < \Phi_{e-}(2) \Leftrightarrow \left(\frac{S}{\rho}\right)_M \Phi_{e-}(1) < \left(\frac{S}{\rho}\right)_M \Phi_{e-}(2) \quad \Rightarrow \quad D_M(1) < D_M(2)$$

Then there is inconsistency between results. This issue can typically be met when measuring collimated beam of X radiation: measuring, with higher cavity size compared to beam cavity, causes underestimation of absorbed dose.

Absorbed dose measurement in tissue D_t by ionization chamber with equivalent-tissue wall

A direct application of narrow cavity theory lies in the possible absorbed dose measurement in tissue at depth x: $D_t(x)$. To achieve such a measure through an ionization chamber, it is necessary that the solid medium component of the detector wall responds similarly to the energy transfered from primary photons in tissue. This results in the requirement of equality (2.69) for mass energy-transfer coefficients of the solid medium versus tissue for the photon energy considered:

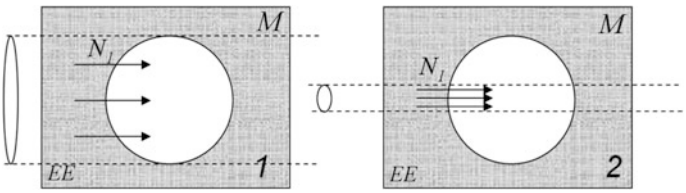

Fig. 2.33 Schematic diagram of a narrow cavity operating according to the Bragg-Gray rule subjected to a field of homogenous and inhomogeneous fluence of secondary electrons

$$\left(\frac{\mu_{tr}}{\rho}\right)_{tissu}^{M} = 1 \tag{2.69}$$

In this case, this is an "equivalent-tissue wall detector". The "Babyline", a type of radiation survey meter, can work typically in this mode.

For example, let's calculate the mass composition for a wall consisting of mixture of polyethylene $(CH_2)_n$ and magnesium fluoride MgF to achieve the condition of equivalent-tissue wall for ^{60}Co photons (i.e. mean photon energy of 1.25 MeV). Mass energy-transfer coefficients for elementary chemical elements of wall, to energy considered, are provided in Table 2.8 and are worth:

$$\left(\frac{\mu_{tr}}{\rho}\right)_{C} = 0.0267 \quad \left(\frac{\mu_{tr}}{\rho}\right)_{H} = 0.0531 \quad \left(\frac{\mu_{tr}}{\rho}\right)_{F} = 0.0253$$
$$\left(\frac{\mu_{tr}}{\rho}\right)_{Mg} = 0.0263$$

First mass energy-transfer coefficients for polyethylene and magnesium fluoride are calculated by a mass composition law similar to expression (2.51).

$$\left(\frac{\mu_{tr}}{\rho}\right)_{CH_2} = \left(\frac{\mu_{tr}}{\rho}\right)_{C} w_c + \left(\frac{\mu_{tr}}{\rho}\right)_{H} w_H = 0.0267 \times \left(\frac{12}{14}\right) + 0.0531 \times \left(\frac{2}{14}\right) = 0.0304$$
$$\left(\frac{\mu_{tr}}{\rho}\right)_{MgF} = \left(\frac{\mu_{tr}}{\rho}\right)_{Mg} w_{Mg} + \left(\frac{\mu_{tr}}{\rho}\right)_{F} w_F = 0.0263 \times \left(\frac{24}{43}\right) + 0.0531 \times \left(\frac{19}{43}\right) = 0.0258$$

For an energy of 1.25 MeV, the mass energy-transfer coefficient to tissue is 0.0294. According to the expression (2.69), to obtain percentages for both compounds, we solve the two equations system, as follows:

$$\left(\frac{\mu_{tr}}{\rho}\right)_{tissu} = \left(\frac{\mu_{tr}}{\rho}\right)_{CH_2} w_{CH_2} + \left(\frac{\mu_{tr}}{\rho}\right)_{MgF} w_{MgF} = 0.0304\, w_{CH_2} + 0.0258\, w_{MgF} = 0.0294$$
$$w_{CH_2} + w_{MgF} = 100\%$$

This relationship leads to following percentages: $w_{CH_2} = 78.3\%\, and \quad w_{MgF} = 21.7\%$, and for such a wall the behavior of 1.25 MeV photons is the same as for soft tissue. Note that due to a small variation of the various (μ_{tr}/ρ) for the energy range between 50 keV and 2 MeV, it can be postulated that this wall is "tissue-equivalent" for energy photons within this range.

Consider now a radiation survey meter performed with 1000 mg cm^{-2} thick wall of this tissue-equivalent compound, with a density of 1, exposed to Co-60 source of 3.2 GBq located at 1 m. Its cavity is a 15 cm length and 3 cm radius cylinder, filled with air at atmospheric pressure. Determine the absorbed dose rate $\dot{D}_t(10)$ at

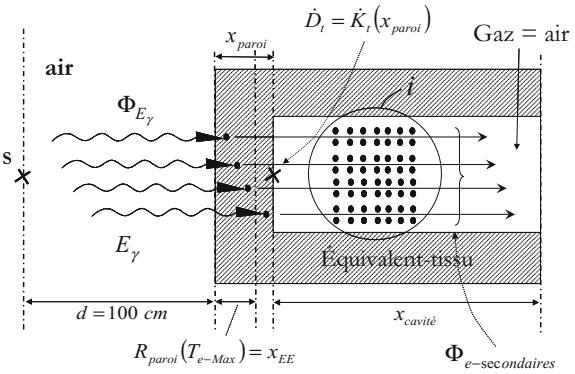

Fig. 2.34 Principle of a narrow cavity

1000 mg cm^{-2} (10 mm) depth, meaning at the internal wall boundary of the detector as shown in Fig. 2.34.

Beforehand, it must be considered if for this depth, the medium respects electron equilibrium condition to assimilate the dose to kerma, and also respect requirements for the application of Bragg-Gray rule. At this energy, we can assume that only Compton interaction takes place in the wall. Thus determining the energy of the most energetic electron by means of expression (2.36).

$$T_{c\,Max} = \frac{4E_\gamma^2}{4E_\gamma + 1} = \frac{4 \times (1.25)^2}{(4 \times 1.25) + 1} = 1.04\,\text{MeV}$$

For such electron energy, the Katz and Penfold formula (2.3) gives the following result:

$$n = 1.265 - 0.0954 \times \ln(1.04) = 1.6125$$
$$\Rightarrow R_{wall}(T_{c\,Max}) = 412 \times (1.04)^{1.6125} = 432\,\text{mgcm}^{-2}$$

So 432 mg cm^{-2} < 1000 mg cm^{-2}; at this depth electron equilibrium condition is verified. The absorbed dose rate at x_{wall} = 1000 mg cm^{-2} = 10 mm depth (Similar in this case to an equivalent depth of tissue) is equal to the kerma. This can be deduced from the previous kerma calculation in air (Sect. 2.2.5) at 1 m from a Co-60 source of same activity, using the transmission properties and change of medium. For convenience, we consider the origin of the system at the kerma calculation point in the air: $\dot{K}_{\text{air}}(0) \cong 1$ mGy/h. Eventually, the absorbed dose rate in the tissue at the wall depth of the chamber is expressed with following expression:

$$\dot{D}_t(x_{cavity}) = \dot{K}_t(x_{wall}) = \left(\frac{\mu_{tr}}{\rho}\right)_{air}^{tissu} \dot{K}_{air}(0) \exp\left(-\left(\frac{\mu}{\rho}\right)_{tissu} \rho_{wall}\, x_{wall}\right)$$

Considering the previous result for $\dot{K}_{\text{air}}$ and the mass attenuation coefficient in the tissue to the energy of 1.25 MeV that is equal to 0.0626 $\text{cm}^2\ \text{g}^{-1}$, we obtain:

$$\Rightarrow \dot{D}_t(10) = \dot{K}_t(10) = \left(\frac{0.0294}{0.0267}\right) \times 1 \times \exp(-0.0626 \times 1 \times 1) = 1.03\,\text{mGy/h}$$

Determine the current generated in the cavity by such absorbed dose rate. Beforehand, it is necessary to check if the chamber meets the specifications of narrow cavity, allowing the application of Bragg-Gray. So check inequality (2.69) by first determining the mean energy of electrons moved in the tissue-equivalent wall by means of expression (2.63).

$$\overline{T}_{e-}(E_\gamma) = \left(\left(\frac{\mu_{tr}}{\rho}/\left(\frac{\mu}{\rho}\right)\right)\right)_{tissu} E_\gamma = \left(\frac{0.0294}{0.0626}\right) \times 1.25 = 587\,\text{keV}$$

In this energy range in air calculated with Katz and Penfold (2.3) gives:

$$R\left(\overline{T}_{e-} = 0.587\,\text{MeV}\right) = 205\,\text{mg cm}^2 \Rightarrow R_{air} = \frac{R}{\rho_{air}} = \frac{205.10^{-3}}{1.22.10^{-3}} = 168\,\text{cm}$$

What does satisfy the rule:

$R_g\left(\overline{T}_{e-}(M)\right) \geq 5x_{cavité} \Leftrightarrow 168 \geq 5 \times 15 = 75\,\text{cm}$. Since this condition and the electron equilibrium are respected, and moreover the source is sufficiently distant from the cavity to assume that the photon field homogeneously exposes the cavity, it is possible to apply the expression (2.64). by linear interpolation Table 2.3, mass stopping powers in tissue and air are obtained to $\overline{T}_{e-} = 0.587\,MeV : (\overline{S}/\rho)_{tissu} = 5.94$ and $(\overline{S}/\rho)_{air} = 5.18$. The current generated by the dose rate is derived from (2.67).

$$i = \frac{\rho_g V_g}{3.6 \cdot 10^9 \left(\frac{\overline{S}}{\rho}\right)_{air}^{tissu} \overline{W}_g} \dot{D}_M = \frac{1.22 \cdot 10^{-3} \times \pi \times (3)^2 \times 15}{3.6 \cdot 10^9 \times \left(\frac{5.94}{5.18}\right) \times 34} \times 1.03 = 4 \cdot 10^{-12}\,A$$

Thus, we are therefore able to determine the current related to the absorbed dose in tissue under depth, induced by exposure to a photon source. However, this analytical approach would deserve comment: we have assumed that the chamber wall behaved in a manner substantially similar in terms of energy transfer in tissues for an energy range between 50 keV and 2 MeV. The measurement at wall depth is similar to absorbed dose in tissue through electron equilibrium conditions for this energy range. However, we notice that the measured current is subject to the mass stopping power ratio between the wall and the gas cavity, since it is different from 1.

$$\left(\frac{\overline{S}}{\rho}\right)_g^{wall} \neq 1 \tag{2.70}$$

So there is no direct relationship between the measured transferred quantity (i.e. current) and the dosimetric quantity, this detector is then called "relative dosimeter" in this case it's more accurate to speak of "tissue-equivalent wall chamber" which is typically the case of Babyline dedicated to the measurement of absorbed dose at the wall depth if the latter is in tissue-equivalent material. However, we will note that the ratio does not differ more than 10% of the unit for the energy range specified above.

It is possible to ensure that this ratio is equal to unity, especially for the measurement of a dosimetric quantity which has many properties with respect to the metrology of photons: air kerma.

Measurement of air kerma K_{air} by an equivalent-air chamber

As previously admitted, the air kerma is close to that in the tissues and does not need to check the electron equilibrium conditions to measure at any point in space. Another property is that if the previous chamber is design with equivalent-air wall, the above stopping powers ratio (2.70) is equal to unity since the cavity is filled with air.

The Fano theorem [26] specifies that the secondary radiation is not changed by the "compression" of medium, thus by strength of atoms settlement in medium. Considering a chamber with same behavior as air with respect of the primary radiation, but of larger density, the absorbed dose in the air can be measured in depth with correct conditions. For the mass composition of such a wall, the process is the same as for determining that of a tissue-equivalent wall by verifying (2.69). Typically, the above mixed composition consisting of CH_2 and MgF respective weight percentages of 19.5 and 80.5% responds equally to air for an energy of 1.25 MeV. By resuming expressions related to the medium change, air kerma at wall input can be correlated to the delivered current within the cavity:

$$\dot{K}_{air}(\text{mGy/h}) = 3.6 \cdot 10^9 i \left(\frac{\overline{S}}{\rho}\right)_g^{wall} \left(\frac{\mu_{tr}}{\rho}\right)_{wall}^{air} \frac{1}{\rho_g V_g} \overline{W}_g \exp\left(\left(\frac{\mu}{\rho}\right)_{wall} \rho_{wall} x_{wall}\right) \tag{2.71}$$

Care should be taken in advance to ensure that the electron equilibrium is achieved at the thickness of the air-equivalent wall in order to apply the Bragg-Gray theory. Which is achieved for the announced composition and a unity density. This detector design leads to both following equalities:

$$\left(\frac{\overline{S}}{\rho}\right)_g^M = 1 \quad and \quad \left(\frac{\mu_{tr}}{\rho}\right)_M^{air} = 1$$

The kerma rate is directly proportional to the delivered current in the gas cavity. Knowing that $(\mu/\rho)_{Wall} = (\mu/\rho)_{air} = 0.0568–1.25$ MeV, the relationship is:

$$\dot{K}_{air}(\text{mGy/h}) = \frac{3.6 \cdot 10^9 \times 34 \times \exp(0.0568 \times 1 \times 1)}{1.22 \cdot 10^{-3} \times \pi \times (3)^2 \times 15} i = 2.5 \cdot 10^{11}\, i$$

Therefore, this equivalent air chamber whose cavity is filled with air, also called air-equivalent chamber, operates as absolute dosimeter in respect with photons between 50 keV and 2 MeV (we assume that the response of air-equivalent wall is the same throughout this energy range) like the calorimeters and Fricke dosimeters for electrons. Indeed, the detector response in respect with dosimetric quantity (i.e. Air Kerma) is directly proportional to the physical transfer quantity (i.e. current). By repeating the previous formalism, the proportionality coefficient (or calibration) is achieved: $N_D = 2.5 \cdot 10^{11}$ mGy h^{-1} A^{-1}. Figure 2.35 gives a picture of such absolute dosimeter.

We will see later that this class of dosimeter is a transfer device for measuring the air kerma related to the calibration process in the case of radiation protection equipment. Adding that it is also possible in practice to achieve absolute dosimeter to measure absorbed dose in tissue below the depth of wall; in this case, the cavity gas must be "tissue-equivalent". The dosimeter is then called "tissue-equivalent chamber" (in comparison to "tissue-equivalent **wall** chamber"). It is also recommended for the measurement of primary spectrum β fields for a wall thickness of 70 mg cm^{-2} (70 μm) with extrapolation chamber (see Sect. 2.1.6).

Note that there are also more voluminous devices whose wall are directly made of air, so called "air chamber". These allow the measurement of air kerma and absorbed dose in the air under sufficient depth to respect the electron equilibrium condition. Figure 2.36 gives a view in section of half the ionization chamber with toroidal air-wall. The calibration source is located at the circle center.

This chamber, for obvious reasons of size, can not be practically used only in primary dosimetry laboratories and a limited range of energy because of the large range of secondary electrons in the air.

Fig. 2.35 Absolute dosimeter to measure kerma in the air, air-equivalent ionization chamber PTW

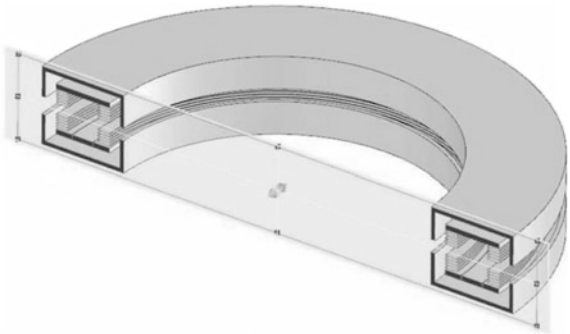

Fig. 2.36 Ionization chamber with toroidal air-wall, according [25], with permission of EDP Sciences

Measurement of the absorbed dose profile in a multilayer wall ionization chamber

The ionization chamber multilayer wall allows the measurement of absorbed dose at different depths of a material. For example, the chamber described by Wall et al. [27] consists of a series of metal sheets, parallel, separated by an insulator 0.08 cm polystyrene. Between each pair of plate, a narrow air cavity of 4.8 cm diameter is located at the center of the insulator. An input wall has a thickness of 0.5 g/cm^2 and the successive sheets, within the device, a thickness of about ten mg/cm^2 (Fig. 2.37). The ionization measured in each air cavity are proportional to the deposited dose in the sheet before it. The dose-depth profile is sampled at a bin corresponding to the thickness of each sheet.

Sequence of metal sheets of different materials can be arranged in order to reproduce conditions of a change in medium in respect with dose.

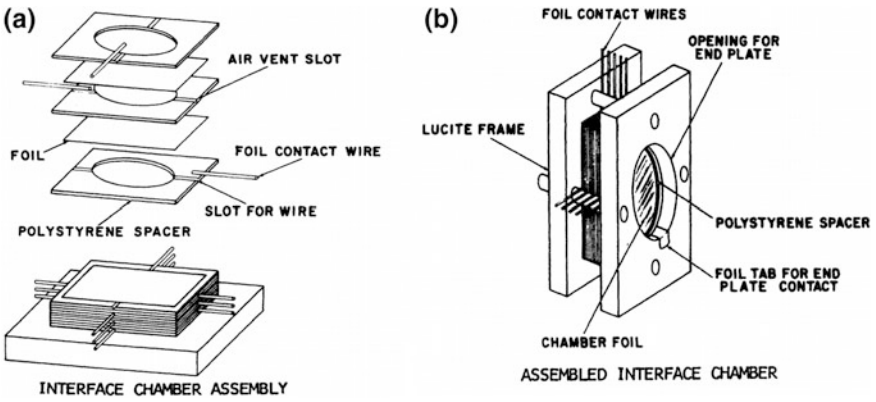

Fig. 2.37 Multi-layer ionization chamber—**a** Construction of the chamber. **b** completely assembled set-up [28]

Principle of the large and intermediate cavity

We described the case of the range of secondary electrons is large enough to apply the principle of the narrow cavity allowing the Bragg-Gray law. Let's study now the opposite case in which the range of secondary electrons is small compared to cavity sizes. For this case, there is a metrological approach so called "large cavity". As it is not possible to take into account the ionization of secondary electrons substantially absorbed by the wall, this time the main ionizer becomes primary photons, whose energy deposition is significant in the cavity gas. If the development of physical model differs from that of Bragg-Gray (see Further Details 2.8), the large cavity model leads to an analytical expression with the ratio of mass energy-transfer to the energy of primary photons.

$$\begin{aligned} \dot{D}_M(\text{mGy/h}) &= 3.6 \cdot 10^9 i \frac{1}{\rho_g V_g} \overline{W}_g \left(\frac{\mu_{tr}}{\rho}\right)_g^{wall} A \\ \text{with } A &= \frac{\mu_g x_{cavity}}{1 - \exp\left(-\mu_g x_{cavity}\right)} \approx 1 \end{aligned} \tag{2.72}$$

Like the narrow cavity, a empirical rule is defined to allow large cavity model. It is necessary that the larger size of cavity is greater than five times the range in gas for secondary electrons moved in the wall.

$$x_{cavity} \geq 5 R_g\left(\overline{T}_{e-wall}\right) \tag{2.73}$$

It remains "mixed" configurations where two photon energies can be measured, one consistent with large cavity model, other with narrow cavity model. For example, Cs-137 emits a 662 keV gamma and a 38.7 keV Xk-ray. for a cavity with 5 cm thick for major size, after having checked empirical rules (2.68) and (2.72), the first is consistent with narrow cavity property and the second with large cavity property. The absorbed dose rate is therefore based on the composition of the two approaches through the sum of the expressions (2.64) and (2.70).

Without even considering a situation of multi-photon release, it is possible that a single primary radiation does not obey neither empirical rules; typically, the 60 keV energy of Am-241 with respect to a 5 mm size cavity compound with aluminum wall (aluminium regarded as light medium) does not meet either of both rules. To energy of the secondary electrons moved in the wall $\overline{T}_{e-wall} = 25\,\text{keV}$, the range in cavity air, calculated with Katz and Penfold, is 8 mm; thus, neither empirical rules is not verified! There is however a possibility to separate inization into two components: one resulting of Compton interactions and responsible for a mean energy spectrum $\overline{T}_c = 5.6\,\text{keV}$ (See Table 2.6) And the other from the photoelectric process with energy: $\overline{T}_{ph} \approx 60\,\text{keV}$. For the first component, the range in air is $R_{air}\left(\overline{T}_c\right) = 0.4\,\text{mm}$ and the large cavity rule is met: (5×0.4 mm < 5 mm). For the second $R_{air}\left(\overline{T}_{ph}\right) = 4.2\,\text{cm}$ and the narrow cavity can be applied (4.2 cm ≥ 5×5 mm). Thus, The calculation of the absorbed dose rate proceeds from a

narrow and large cavity composition, also called "intermediate cavity" and defined in its analytical formalism by the Burlin's theorem [29].

$$\dot{D}_M(\text{mGy/h}) = 3.6 \cdot 10^9 \frac{i}{\rho_g V_g} \overline{W}_g \left[\left(\frac{\overline{S}}{\rho} \right)_g^{wall} + j \left(\frac{\mu_{tr}}{\rho} \right)_g^{wall} \right] \tag{2.74}$$

with ratios of means mass stopping powers to $\overline{T}_{\text{ph}} = 60\,\text{keV}$ and mass energy-transfers to the energy of primary incident photons: 60 keV. In the formalism of expression (2.74), the current i is due to the narrow cavity therefore the photoelectric effect: $i = i_{\text{pe}}$ and the term j represents the ratio of current component related to the Compton on the photoelectric effect: $j = i_c/i_{\text{pe}}$.

2.3 Neutron Interaction with Matter and Calculating the First Collision Kerma

These neutral and uncharged particles interact with nuclei of crossed medium, according to two different types of collisions: elastic and inelastic. The elastic collision (n,n) is a simple mechanical shock similar to collisions that occur in billard. This collision mode does not induce any internal change within target nucleus. In the inelastic collision, however, this internal change occurs. This type of collision is accompanied by several output ways:

- Inelastic scattering (n,n′) in which the neutron penetrate the nucleus. It follows a re-emission of neutron n′ and the deexcitation of the target nucleus with emission of one or more photons, whose energy we will see can be significant;
- Capture (n,X) where the neutron also enters the nucleus, with various type of particle emerging from the target nucleus: photon in the case of radiative capture (n,γ) or charged particle, proton or alpha, respectively in the case of nuclear (n, p) or (n,α) reactions type.

Like what we showed for photons, also neutral particles, the challenge for dosimetry will consist in characterize the energy transferred E_{tr} to secondary charged particles set in motion during interactions. This characterization allows the determination of dosimetric quantities. This *modus operandi* applied to photons and neutrons thus refers to the concept of "indirectly ionizing particles": this is not neutron or photon that generates the dose, but the secondary charged particles set in motion during the various interactions. Moreover, as for photons, the stochastic nature of energy deposition of neutrons in the material will involve the characterization of the mean energy transferred to secondary charged particles.

2.3.1 Elastic Collision (n,n)

In this collision, a part of the initial energy of the incident neutron is carried by the nucleus, commonly known as "recoil nucleus" (Fig. 2.38).

The conservation law of kinetic energy involves: $E_n(i) = E_n(f) + E_{tr}$. Like the calculation for photons with conservation law of momentum, the relation (2.75 and 2.73) is obtained, linking the incident neutron energy to that transferred to the recoil nucleus.

$$E_{tr} = E_n(i)\frac{4A}{(A+1)^2}\cos^2\varphi \tag{2.75}$$

The angle φ varies from 0 to π/2 and θ varies π at 0°. The maximum energy transferred to the recoil nucleus is obtained when θ = π and so φ = 0 with expression (2.76).

$$E_{tr,\max} = \frac{4A}{(A+1)^2}E_n(i) \tag{2.76}$$

The value of energy transferred to the recoil nucleus has equal probability from 0 to the maximum value previously calculated. The energy distribution for the transferred energy is shown in Fig. 2.39.

We then deduce the mean energy transferred to the recoil nucleus (2.77).

$$\overline{E}_{tr} = \frac{E_{tr,\max}}{2} = \frac{2A}{(A+1)^2}E_n(i) \tag{2.77}$$

Note that the loss of energy by elastic shock is greater when the nucleus is lighter and is maximum for hydrogen. For this chemical element, the mean energy transferred to the recoil proton is:

$$E_{tr,\max} = E_n(i) \quad et \quad \overline{E}_{tr} = \frac{E_n(i)}{2}$$

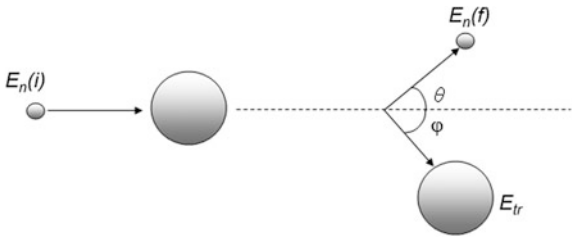

Fig. 2.38 Principle of elastic scattering for neutrons

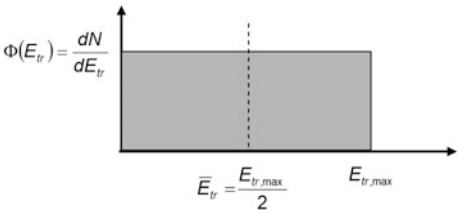

Fig. 2.39 Distribution of energy transferred to the recoil nucleus during the elastic neutron scattering

After N successive shocks on hydrogen protons, an initial neutron of energy E_n (i) will be set at mean final energy:

$$\overline{E}_n(f) = \frac{E_n(i)}{2^N}$$

To thermalize a 2 MeV neutron, it will require therefore, in average:

$$N = \ln\left(\frac{2.10^6}{0.025}\right) \times \frac{1}{\ln(2)} = 26\, collisions$$

The macroscopic cross section of elastic collision Σ_s similar to the linear attenuation coefficient μ for photons, provides the mean free path λ_s that the neutron cross in medium before an elastic collision. the path necessary to achieve, on average, this slowdown can be calculated. In water, for which the mean free path for elastic scattering is 0.65 cm [30], The mean path would be:

$$\overline{l} = \overline{N}\lambda_s = \frac{\overline{N}}{\Sigma_s} = 26 \times 0.65 = 17\,\text{cm}$$

As the path is not straight, since each neutron is scattered with an angle of deflection θ, most of neutrons are thermalized in the order of 10 cm thick. In this regard, it is observed that more nuclei are lighter and the scattered angle of neutrons are reduced. Indeed, the angle is roughly related to the atomic weight as follows:

$$\overline{\mu} = \overline{\cos\theta} = \frac{2}{3A}$$

Finally, notice that the general law to estimate the mean energy of neutron having passed through depth x:

$$\overline{E}_n(x) = E_n(i)\exp\left[-\frac{\Sigma_s(1-\alpha)x}{2}\right] \quad with \quad \alpha = \left(\frac{A-1}{A+1}\right)^2$$

From the viewpoint of dosimetry, elastic scattering is the most probable interaction in human tissues. Cross sections are of the order of 10 barns for oxygen,

carbon and nitrogen up to about 100 keV, and then beyond it behaves according to $1/\sqrt{E}$ shape with resonances. For protons of hydrogen, the cross section is 20 barns to about 100 keV, and then beyond it behaves $1/\sqrt{E}$ without resonance. We remind that hydrogen nuclei comprise 63.2% of nuclei in human tissue. Finally, we note that the energy of the recoil nucleus is even lower than this nucleus is heavy and that in any case its energy will be imparted locally because of its small range in matter. This last point is significant for characterization of absorbed dose.

The reaction of neutron-proton elastic scattering is predominant in terms of dosimetry in human body, for neutrons of energy higher than a few tens of eV.

2.3.2 *Inelastic Scattering (n,n')*

This nuclear reaction is passing through a transitional step in which the neutron enters the target nucleus to temporarily create what is commonly called a "compound nucleus" very excited and thus unstable. The output way will consist of emitting a new neutron n′ with energy decreased compared to that of incident neutron. The residual nucleus, identical to the initial nucleus, remain excited after the emergence of neutron then emits a photon γ:

$$n + {}^{A}_{Z}X \rightarrow {}^{A+1}_{Z}X^{*}_{NC} \rightarrow n' + {}^{A}_{Z}X* \rightarrow {}^{A}_{Z}X + \gamma$$

The emitted photons have discreet spectrum consistent with excitation levels of compound nucleus. In this reaction, the secondary charged particle set in motion is also the target nucleus. The energy of emitted photon is the energy of an excited state of compound nucleus. The mean energy transferred to the recoil nucleus is approximately equal to the difference between energy of incident neutron and energy of deexcitation photon:

$$\overline{E}_{tr} \cong E_n(i) - E_\gamma = E_n(i) - E^{*}_{NC}$$

This inelastic scattering is a threshold reaction. A detailed example of calculation of the various components of energy for this reaction is supplied in Further Details 2.9. Other reactions of this type, in addition to the ^{12}C treated in Further Details likely to occur in human tissues, are:

$$\begin{aligned} &{}^{14}\mathrm{N}(\mathrm{n},\mathrm{n}')^{14}\mathrm{N}*, \text{ with } E_\gamma = 1.63 \text{ MeV}(\sigma = 30 \text{ mb}) \\ &E_\gamma = 5.1 \text{ MeV}(\sigma = 80 \text{ mb}) \\ E_\gamma &= 10 \text{ MeV}(\sigma = 90 \text{ mb}); \\ &{}^{16}\mathrm{O}(\mathrm{n},\mathrm{n}')^{16}\mathrm{O}*, \text{ with } E_\gamma \end{aligned}$$

The reactions of inelastic scattering only appear at very high energies and are fairly marginal for generating dose in tissues except from a dozen MeV. For neutrons close to 100 MeV, it becomes highly significant in particular on oxygen and nitrogen and higher than the elastic scattering on tissues. In addition, there is a significant contribution of secondary photons of deescitation to energy deposit.

2.3.3 Radiative Capture (n,γ)

For this inelastic reaction, the incident neutron remains "trapped" in the compound nucleus and the deexcitation occurs with release of a photon:

$$n + {}^{A}_{Z}X \rightarrow {}^{A+1}_{Z}X^{*}_{NC} \rightarrow \gamma + {}^{A+1}_{Z}X$$

The consequence of such a reaction is the possible release of a high energy photon up to 8 MeV for light nuclei (Fig. 2.40).

This reaction gets no threshold and is very likely for thermal neutrons. The mean energy carried by the recoil nucleus, considering a zero-energy for incident neutron, is achieve through the conservation of momentum:

$$\sum \vec{p} = 0 \Rightarrow \vec{p}_{\gamma} + \vec{p}_{r} = 0 \Leftrightarrow \frac{E_{\gamma}}{c} - M'v = 0 \Leftrightarrow \left(\frac{E_{\gamma}}{c}\right)^{2} = M'^{2}v^{2} \Leftrightarrow E_{tr} = \frac{E_{\gamma}^{2}}{2M'c^{2}}$$

Thus, in the case of N-14 for which the radiative capture involves the release of a 10.83 MeV photon, the energy of recoil nucleus is:

$$E_{tr}({}^{14}C) = \frac{E_{\gamma}^{2}}{2M'c^{2}} = \frac{(10.83)^{2}}{2 \times 938 \times (14+1)} = 4\,\text{keV}$$

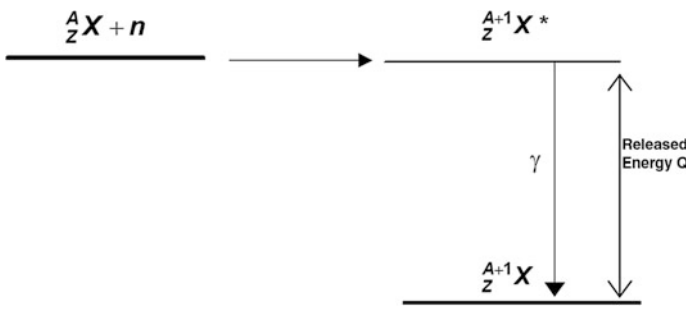

Fig. 2.40 Energy diagram of a radiative capture

The energy transferred is low. In biological tissues, this reaction takes place in the field of thermal neutrons, on hydrogen with a small cross section. The excited hydrogen nucleus then releases a characteristic photon of 2.2 MeV. The radiative capture contribute much to the energy transferred in the field of energy between 0 and a dozen eV only the tiny recoil energy of the target nucleus will be absorbed locally.

Note that high-energy gamma rays emitted during radiative capture (few MeV) will later interact with tissues and contribute increasing the absorbed dose in thick medium.

2.3.4 (n,p) and (n,α) Capture

For these inelastic reactions, the compound nucleus is de-excited by releasing a charged particle: a proton or an alpha.

$$n + {}^{A}_{Z}X \rightarrow {}^{A+1}_{Z}X^{*}_{NC} \rightarrow p + {}^{A}_{Z-1}X$$
$$n + {}^{A}_{Z}X \rightarrow {}^{A+1}_{Z}X^{*}_{NC} \rightarrow \alpha + {}^{A-4}_{Z-2}X$$

These reactions are characterised in being both exoenergetic, so with positive heat reaction ($Q > 0$), and with threshold, due to the Coulomb barrier to cross. Further Details 2.10 provides a detailed explanation. These reactions can also be accompanied by the release of de-excitation gamma (Fig. 2.41).

(n,α) thresholds on oxygen and carbon are of the order of 8 MeV. For these types of reactions, this time, the energy transferred is divided between the recoil nucleus and released charged particle. The total energy transferred is:

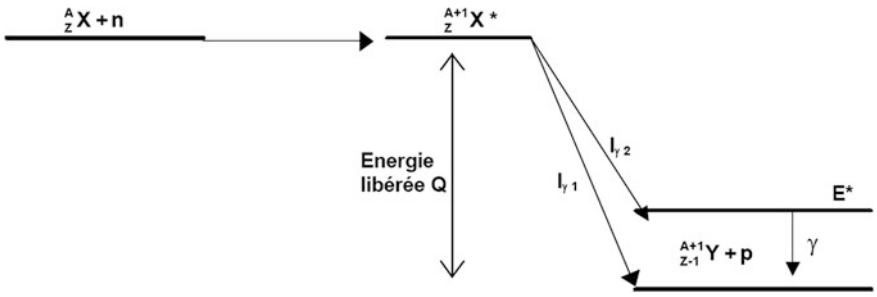

Fig. 2.41 Energy diagram of a capture with release of heavy charged particle

$$\overline{E}_{tr} = \overline{E}_{tr}(nucleus) + \overline{E}_{tr}(\alpha\, or\, p) = Q + E_n$$

For reasons of classic cinematic, most of the energy is carried away by the charged particle released. In human tissue, only the reaction ${}^{14}_{7}N(n,p){}^{14}_{6}C$ has no energy threshold and the positive heat thereof is 0.6 MeV. In other words, the energy of the incident neutron plus 0.6 MeV will be systematically transferred.

More marginally, other (n,α) captures may occur: ^{14}N(n,α), ^{16}O(n,α) and ^{12}C(n,α) with respective thresholds: 0.16, 2.35 and 6.18 MeV.

The predominant reaction in terms of energy transferred into the tissue to energies between 0 to about 10 eV is ${}^{14}_{7}N(n,p){}^{14}_{6}C$. Once again, the energy of released secondary particles will be absorbed locally.

2.3.5 *Microscopic Cross Sections in the Chemical Constituents of Human Tissue*

In what follows, all the microscopic cross sections of different nuclear reactions described above are given in Fig. 2.42. Hydrogen represents 63.2% of atoms in the human tissue or a mass percentage of 10%; oxygen (99.76% of ^{16}O) represents 29.8% of nuclei or a mass percentage of 76.2%; carbon (98.89% of ^{12}C) represents 5.8% of nuclei or a mass percentage of 11%; finally, nitrogen (99.63% ^{14}N) represents 1.16% of nuclei or a mass percentage of 2.6%.

Question: We have admitted that from 0 to about 10 eV almost all of the energy transferred into the tissue, and therefore the absorbed dose is due to the ^{14}N(n,p) reaction. For the lowest energy available on the graph above, i.e. 0.01 eV, this reaction has a microscopic cross section of about 3 barns for 1.16% of the total number of nuclei. At the same time, the cross section for elastic scattering (also without threshold reaction) hydrogen presents a cross section of about 50 barns for an atomic percentage of 63.2%. At first sight, regarding these values, we might be tempted to assume that most of energy transferred comes from elastic scattering on hydrogen, but this is wrong conclusion. What is the reason? The answer lies in the amount of energy transferred for each of these interactions. For elastic scattering, the energy transferred to the recoiling nucleus is worth, on average, half the energy of the incident neutron, hence:

$$\overline{E}_{tr} = \frac{E_n}{2} = \frac{0.01}{2} eV = 0.005\,\text{eV}$$

In contrast, in the case of (n,p) capture on the ^{14}N, we know that the heat of reaction is positive and is about 0.6 MeV. The energy transferred is then:

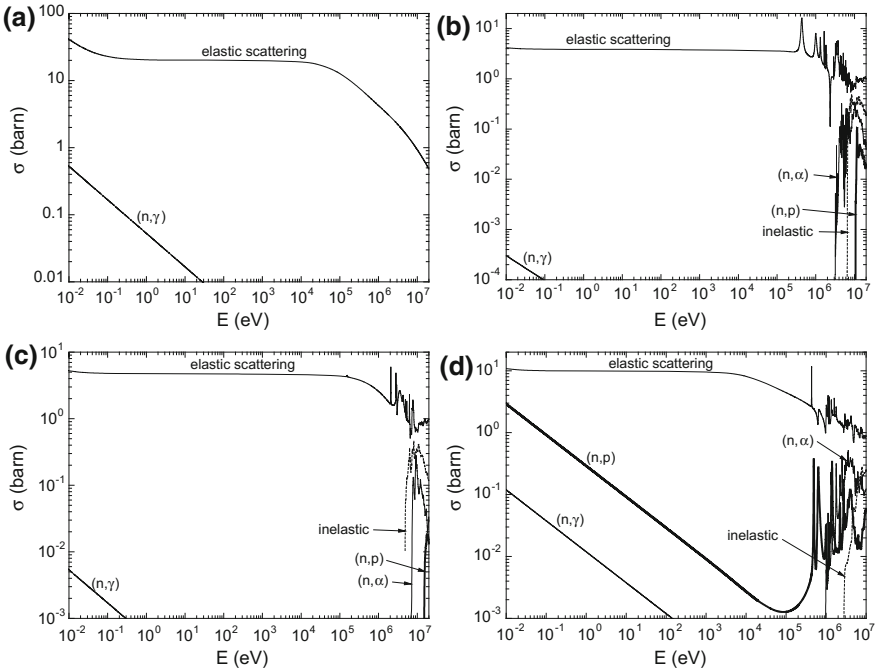

Fig. 2.42 Cross-sections of the hydrogen (**a**), oxygen (**b**), carbon (**c**) and nitrogen (**d**), based on data from http://www-nds.iaea.org/Exfor/endf.htm

$$E_{tr} = Q + E_n = 0.6\,\text{MeV} + 0.01\,\text{MeV} \approx 0.6\,\text{MeV}$$

We therefore find that there are 8 decades of discrepancy for the energy transferred between both reactions to the incident energy of 0.01 eV. Hence, this effect annihilates both effects of gap on the cross section and atomic density.

2.3.6 *Calculation of the First Collision Kerma*

As with photons, the energy deposition process for neutrons is stochastic by nature. If we consider an elementary volume of mass m and volume V in which a neutron interacts, we can not know where exactly this collision occurs in the volume. It is therefore not possible to predict the energy imparted ε by secondary particles set in motion, in this sphere. Like the photon treatment, it is therefore necessary to characterize the mean energy transferred to secondary charged particles at collision point. This approach is therefore to define a neutron kerma. However, equality $K = D$, this time, turns out much more difficult than in photon case. By analogy with photon, in first idea, if Σ_t is the total macroscopic cross section of neutron

interaction in human tissues (equivalent to μ for photons), we can consider that at depth x, the fluence of transmitted neutrons describes an exponential decay:

$$\Phi_t(x) = \Phi(x_o)\exp(-\Sigma_t x)$$

The issue is that "real" fluence $\Phi_R(x)$ can be higher than the estimated value provided by this simple model, due to the large neutron scattering. Remind that neutrons tend to spread elastically forward on protons of hydrogenated media. Unlike photons, a significant build-up factor $B_n = \Phi_R(x)/\Phi_t(x)$ can be generated in human tissues. Moreover, the equilibrium of secondary charged particles (protons in hydrogenated media) is never fully realized. Calling Φ_{cp} the fluence of secondary charged particles, the ratio between Φ_{cp} and the "real" neutron fluence in depth x is never constant:

$$\frac{\Phi_{cp}(x)}{\Phi_R(x)} \neq cste$$

Remind that for photons this ratio is constant as long as the electronic equilibrium is reached.

There is, however, a region of space to which the equilibrium of secondary charged particles is substantially constant and the previous ratio is constant. In this thin tissue thickness, just one collision occurs and we can neglect neutron scattering accumulation and electromagnetic secondary radiation (e.g. from radiative capture). In this zone, the absorbed dose is substantially equal to kerma: $D \approx K$. This is called region of "first collision kerma". The thickness at which this approximation can be made is determined by the mean free path in the tissues. For example, for previous case with neutrons of energy greater than 10 eV and less than 1 MeV, where the energy deposition is attributable to the elastic scattering on hydrogen nuclei, the maximum thickness on which applies first collision kerma and bounds the $D \approx K$ area is:

$$\lambda_t = \frac{1}{\Sigma_t} \approx \frac{1}{\Sigma_s(H)} = 0.65\,\text{cm}$$

Throughout the area bounded by the mean free path, the approximation $D \approx K$ can be made since, unlike photons, there is no need to define a minimum thickness (path of the most energetic secondary charged particles) from which the approximation is valid. Indeed, the path of the secondary charged particles is small enough that we can consider that all the energy transferred is deposited at the collision point and therefore, equivalent to the imparted energy: $\overline{\Delta E_{tr}} = \overline{\Delta\varepsilon}$. It is possible to determine a theoretical formulation of the first collision kerma. The expression that gives the number of neutrons interacting in the medium, in a volume element dV is given by (2.78).

$$dN_n = \Phi_n \Sigma_t dV \tag{2.78}$$

The total macroscopic cross section Σ_t is the sum of all cross sections σ_i of possible reactions i weighted by the number of target nuclei per unit volume.

$$dN_n = \Phi_n \cdot \sum_i N\sigma_i \cdot dV = dN_n = \Phi_n N \cdot \sum_i \sigma_i \cdot \left(\frac{dm}{\rho}\right) \tag{2.79}$$

As for photons, the differential element characterizing the energy transferred in the elementary volume dV and mass dm is the product of the energy transferred by dN_n the differential number of neutrons interacting in the elementary volume:

$$dE_{tr} = \overline{E}_{tr} dN_n$$

With the above expression (2.79) the differential element of the transferred energy can be written as (2.80).

$$dE_{tr} = \Phi_n N \cdot \sum_i \sigma_i \overline{E}_{tr,i} \cdot \left(\frac{dm}{\rho}\right) \tag{2.80}$$

For the expression (2.81) kerma, then just divide by the elementary mass dm.

$$K = \frac{dE_{tr}}{dm} = \frac{\Phi_n}{\rho} N \cdot \sum_i \sigma_i \overline{E}_{tr,i} \tag{2.81}$$

N is the atomic density and reminding that: $N = \rho(\eta_A/A)$ with $\eta_A = 6.2 \cdot 10^{23}$ atoms mol^{-1}, A in g mol^{-1} and ρ in g cm^{-3}. Expression (2.81) above can thus be written as (2.82).

$$K = \frac{\Phi_n}{\rho}\left(\frac{\eta_A \rho}{A}\right) \cdot \sum_i \sigma_i \overline{E}_{tr,i} = \Phi_n \left(\frac{\eta_A}{A}\right) \cdot \sum_i \sigma_i \overline{E}_{tr,i} \tag{2.82}$$

The ratio (η_A/ρ) is homogeneous to atom/g of material and can be described as "mass density atom". Beware that expression of kerma (2.82) is valid for media composed by single chemical species. In the case of a molecule composed of several chemical elements, the expression becomes (2.83).

$$K = \Phi_n \left(\frac{\eta_A}{A}\right) \cdot \sum_i n_i \cdot \sum_j \sigma_{i,j} \overline{E}_{tr_{i,j}} \tag{2.83}$$

n_i is the number of atoms of material i constituting the molecule. For example, for polyethylene $(CH_2)_n$: $A = 14$, $n_C = 1$ and $n_H = 2$. Indeed, in the case of a CH_2 molecule, the mass density of atoms N_m (atoms g^{-1}) is:

$$N_m(CH_2) = \frac{atoms(CH_2)}{g} = \frac{\eta_A}{A_{CH_2}} = \frac{\eta_A}{14} \text{ atoms } \text{g}^{-1}$$

We deduce the atomic density of each chemical species:

$$N_m(C) = \frac{atoms(C)}{g} = n_C \frac{atoms(CH_2)}{g} = 1 \times \frac{\eta_A}{14} \text{ atoms } \text{g}^{-1}$$

$$N_m(H) = \frac{atoms(H)}{g} = n_H \frac{atoms(CH_2)}{g} = 2 \times \frac{\eta_A}{14} \text{ atoms } \text{g}^{-1}$$

There is a third form for the expression of first collision kerma, since in the calculation assumptions, this time, the material is characterized by weight percentages (e.g. ICRU sphere). Expressions of first collision Kerma and first collision kerma rate for a molecule are given by (2.84).

$$\begin{aligned} K(mGy) &= 1.6.10^{-7} \cdot \Phi_n \sum_i N_m(i) \sum_j \sigma_{i,j} \overline{E}_{tr_{i,j}} \\ \dot{K}(\text{mGy/h}) &= 5.76.10^{-4} \cdot \dot{\Phi}_n \sum_i N_m(i) \sum_j \sigma_{i,j} \overline{E}_{tr_{i,j}} \end{aligned} \tag{2.84}$$

with Φ_n in cm^{-2}, $\dot{\Phi}_n$ in $\text{cm}^{-2}\ \text{s}^{-1}$, σ in cm^2 and $\overline{E}_{tr}$ in MeV. The first collision kerma is the only dosimetric quantity that can be calculated analytically for neutrons. Caswell et al. [31] have calculated values of first collision kerma for human body, for each type of nuclear reaction and its components. The curves of Fig. 2.43 provide conversion factors "fluence-first collision kerma" in ICRU tissue-equivalent and for the four chemical elements.

As mentioned above, although we observed a preponderance of energy transfered due to interactions with nitrogen $\left({}_7^{14}N(n,p){}_6^{14}C\right)$ for neutron energies below 10 eV. For energies above 10 eV, the reaction of elastic scattering (n,n) on hydrogen protons is almost exclusively responsible for the first collision kerma. We note however that at very high energies (from 50 MeV), inelastic reactions (n,α) And (n,n′) on ^{16}O become significant. To be convinced of the importance of reaction ${}_7^{14}N(n,p){}_6^{14}C$ at low energy, let's calculate theoretically the first collision kerma in the ^{14}N for a fluence of thermal neutrons (0.025 eV) of $1 \cdot 10^{10}\ \text{cm}^{-2}$. Accordance cross sections of neutron reactions on ^{14}N, three reactions that can occur are:

1. $^{14}N + n \rightarrow p + {}^{14}C$
2. $^{14}N + n \rightarrow \gamma + {}^{15}N$
3. $^{14}N + n \rightarrow n + {}^{14}N$

First, we neglect the third reaction (n,n) due to the negligible mean energy transferred: $\overline{E}_{tr} = E_n/2 = 0.01$ eV. The cross sections of the two first reactions are

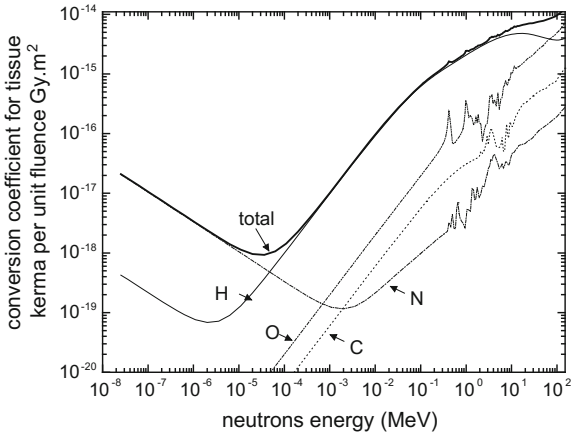

Fig. 2.43 First collision kerma factors for neutrons in a ICRU tissue-equivalent (total) and four component parts, weighted with the following mass fractions: 0.101 H, 0.111 C, 0.026 N, 0.762 O (according to the data [32] and [21])

respectively $\sigma_1 = 1.8$ barn and $\sigma_2 = 7.5 \cdot 10^{-2}$ barn, the heat for the first reaction is $Q_p = 0.626$ MeV and during the radiative capture (second reaction), a photon is released with an energy $E_\gamma = 10.83$ MeV. We are here in the presence of a single chimical element, so the formula (2.82) is used.

$$\sum_i \sigma_i \overline{E}_{tr,i} = \sigma_1 \cdot \left(Q_p + E_n\right) + \sigma_2 \cdot \left(\frac{E_\gamma^2}{2M'c^2}\right) \approx \sigma_1 \cdot Q_p + \sigma_2 \cdot \left(\frac{E_\gamma^2}{2M'c^2}\right)$$

$$K_N = 1.6 \cdot 10^{-7} \cdot \frac{\Phi \eta_A}{A} \cdot \left[\sigma_1 \cdot Q_p + \sigma_2 \cdot \left(\frac{E_\gamma^2}{2M'c^2}\right)\right]$$

The numerical application then gives:

$$K_N = 1.6 \cdot 10^{-7} \cdot \frac{1 \cdot 10^{10} \times 6.02 \cdot 10^{23}}{14} \cdot \left[\left(1.8 \cdot 10^{-24} \times 0.624\right) + 7.5 \cdot 10^{-2} \cdot 10^{-24} \cdot \left(\frac{10.83^2}{2 \times 938 \times (14+1)}\right)\right] = 0.077\,\text{Gy}$$

We observe, in brackets, that the right term is negligible compared to the left: the reaction ${}^{14}_{7}N(n,p){}^{14}_{6}C$ is therefore predominant for the calculation of the first collision kerma on nitrogen.

In addition, the tabulated values of ICRU [32] Indicate for thermal energy in tissues, a conversion coefficient "fluence-kerma first collision" equal to $0.788 \cdot 10^{-15}$ Gy m^2. Hence, the first collision kerma is accessed trivially as follows:

$$K_{tissu}(mGy) = \left(\frac{K_{tissu}}{\Phi}\right) \cdot \Phi = 0.788 \cdot 10^{-15} \times 1 \cdot 10^{10} \times 10^{4} = 0.0788\,\text{Gy}$$

Finally, we observe that for this energy $K_{\text{tissu}} \approx K_{\text{N}}$.

2.3.7 Calculation of Multi-collision Kerma and Mean Absorbed Dose

Beyond the thickness for which the calculation of the first collision kerma is valid (typically the mean free path of the neutron) and for which $D \approx K$, it is not possible to calculate analytically kerma, which in the circumstances is so called "multi-collision kerma", and by extension to access the absorbed dose. This is attributable in particular to the difficulty of assessing accurately the neutron fluence at a point in medium. Strictly speaking, as already suggested, the "transmitted" fluence term should incorporate a Build-up factor B_{n} due to neutron scattering in medium. This factor depends on the geometry, material, neutron energy, as well as the crossing depth. Consequently, it can only be quantified on a case-by-case basis.

That is why, at this stage, experiments and more recently the use of particle transport calculation codes based on the Monte Carlo method (Chap. 6) takes over the deterministic analytical approach. It is possible to calculate the depth absorbed dose beyond first mean free path using the statistical estimator "point-detector" that we will detail later in the book. The absorbed dose in tissue $D_{\text{t}}(10)$ under 10 mm will be the intermediate dosimetric quantity for the definition of operational quantities in neutron case (see Chap. 3). This quantity is also available in the ICRU report [33] through fluence conversion coefficients.

$$d_{\Phi}(10) = \left(\frac{D_t(10)}{\Phi}\right)_{E_n} \tag{2.85}$$

Furthermore, in developing protections quantities that we will detail in Chap. 3, for convenience, the concept of one-point dosimetric calculation, used until now, is dropped in favor of mean macroscopic quantity. Kerma is now estimated by the ratio of the energy transferred to a macroscopic volume V on the mass of the same volume. The dimensions of the volumes considered are greater than the path of secondary charged particles set in motion in the medium. Also, the approximation of equilibrium of secondary charged particles is made. All the energy transferred is considered as deposited very close to point collision. We can then write the expression (2.86).

$$\overline{D} \approx \overline{K}_{mc} \cong \frac{E_{tr}}{m} \tag{2.86}$$

We can now touch on the whole idea of mean multi-collision Kerma and mean absorbed dose. As such, the ICRU [34] gives the value of the mean absorbed doses to the critical organs for different direction of human body depending on the energy of incident neutrons, also as fluence conversion factors:

$$\left(\frac{D_T}{\Phi}\right)_{E_n} (\mathrm{Gy\,cm^2})$$

Note: The horizontal bar above the variable dose is not retained for mean dose to the organ nomenclature D_T.

Calculations in the ICRU report [34] are also made, among others, using the Monte Carlo code MCNP4b [35] on an anthropomorphic phantom simulating the human body. To estimate the potential gap between the theoretical calculation of the first collision kerma and values of mean doses to organs obtained through computer code, as well as the absorbed dose $D_t(10)$ in tissues, reference [36] propose the following example: exposing, with AP geometry (parallel radiation beam on frontside of the body), an anthropomorphic phantom to a point-source of Am–Be, placed in air, located at 1 m of the frontside of phantom. We consider an activity $A = 9.25 \cdot 10^{11}$ Bq. The Neutron flux is $6.6 \cdot 10^7$ (n) s^{-1} in 4π steradians with mean energy $\overline{E}_n = 4.5$ MeV. The mass composition of human tissues is as follows: 10.2% H, 72.9% O, 12.3% C and 3.5% N. The first collision kerma in tissue is calculated and compared to the values of the mean absorbed dose D_T provided by ICRU data to the following organs: breast, bladder, stomach, thyroid, and the absorbed dose in 10 mm tissue $D_t(10)$.

First, let's calculate the fluence rate at 1 m of the source as shown in the diagram of Fig. 2.44.

The fluence rate of neutron fluence is given by the following expression:

$$\dot{\Phi}_n = \frac{\dot{N}}{S} = \frac{6.6.10^7}{4\pi \times (100^2)} = 525(n).\mathrm{cm^{-2}s^{-1}}$$

Then, let's calculate the first collision kerma rate (in mGy h^{-1}) in tissue by limiting the elastic collisions reactions on hydrogen and oxygen (we assume that the tissues are located 100 cm to the source). Cross sections for both reactions are respectively: $\sigma_H = 1.8$ barn and $\sigma_O = 0.9$ barn. For the atomic density of a chemical element on the basis of mass percent, the simple following reasoning can be made:

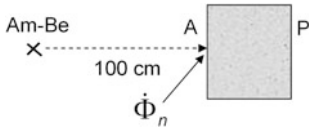

Fig. 2.44 Am-Be point-source at 1 m a phantom in tissue-equivalent material

in 1 g oxygen, there's $\eta_A/16$ (atoms) g^{-1}; in 1 g tissue, if W_i is the weight percentage of element i, there is: 1 g × W_o = 1 × 0.729 = 0.729 g oxygen. Finally, the atomic oxygen density in tissue is therefore:

$$N_m(O) = W_o \frac{\eta_A}{A_o} = 0.729 \times \frac{6.02 \cdot 10^{23}}{16} = 2.8.10^{22} \text{atomes g}^{-1}$$

Similarly, for the hydrogen of the polyethylene:

$$N_m(H) = W_H \frac{\eta_A}{A_H} = 0.123 \times \frac{6.02 \cdot 10^{23}}{1} = 6.14 \cdot 10^{22} \text{ atomes g}^{-1}$$

Thus, the first collision kerma will be:

$$\begin{aligned}\dot{K} &= 5.76 \cdot 10^{-4} \dot{\Phi}_n \left(N_m(O) \sigma_o \overline{E}_{tr}(O) + N_m(H) \sigma_H \overline{E}_{tr}(H) \right) \\ &= 5.76 \cdot 10^{-4} \times 525 \times \left(\left(2.74 \cdot 10^{22} \times 0.9 \cdot 10^{-24} \times \frac{2 \times 16}{(16+1)^2} \right) \right. \\ &\quad \left. + (6.14 \cdot 10^{22} \times 1.8 \cdot 10^{-24} \times 2.25) \right) \\ \dot{K} &= 78\, \mu\text{Gy/h}\end{aligned}$$

Now we compare that value to the value of $\dot{D}_{tissu}(10)$ obtained in [33], and the mean absorbed dose calculated in [34] to various organs. By linear interpolation between 4 and 5 MeV, the conversion factor "fluence-absorbed dose in tissue" is $d_\Phi(10)$ = 42 pGy cm^{-2}, hence the absorbed dose rate is:

$$\dot{D}_{tissu}(10) = d_\Phi(10) \cdot \dot{\Phi} = \left(\frac{D_{tissu}(10)}{\Phi} \right)_{E_n} \cdot \dot{\Phi} = 79\, \mu\text{Gy/h}$$

So $\dot{K} \approx \dot{D}_{tissu}(10)$. This can be explained by the fact that for energy of 4.5 MeV, the mean free path is of the order of 15 mm and therefore to 10 mm depth the approximation "first collision kerma equal to mean absorbed dose" is still valid. The effect of scattering and thus neutron increase in the fluence is not met. The Fig. 2.45 gives the neutron energy from which $\dot{K} \approx \dot{D}_{tissu}(10)$.

As regards now the mean absorbed doses, all the results from the ICRU [34] is summarized in Table 2.10.

As suggested above, two phenomena are opposed as the neutron enters matter: attenuation due to the transmission (exp ($\Sigma_s x$)) which tends to decrease the dose and scattering which induces an increase in the fluence depth (Build-up factor B_n). As seen, the more the incident is energetic and the more scattering occurs in forward direction. For 4.5 MeV energy, this involves few backscattering on organs located

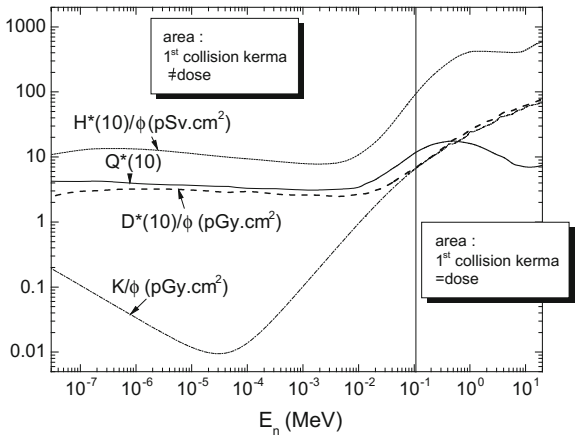

Fig. 2.45 Dosimetric quantities as a function of neutron energy (from the data of [32, 34, 37])

Table 2.10 Value of coefficients "mean absorbed dose to the organ-fluence" and mean absorbed dose to different organs and for an 4.5 MeV energy of neutron

	Breast	Bladder	Stomach	Thyroid
$D_T/\phi(pGy.cm^2)$	45.15	43.25	43	45.2
$\dot{D}_T(mGy.h^{-1})$	$8.5 \cdot 10^{-2}$	$8.2 \cdot 10^{-2}$	$8.1 \cdot 10^{-2}$	$8.5 \cdot 10^{-2}$

forward in body, hence no additional dose. Consequently, the first collision kerma is substantially equal to the mean dose in the anteroposterior exposure organs. Low build-up factor is responsible for the slight underestimation.

By changing the incident energy, we can emphasize this "duality" between transmission and scattering: the cross section for elastic scattering shows little variation between 1 keV and a few MeV; the major change, over this interval, is the mean energy transferred $\overline{E}_{tr} = E_n/2$ and scattering-backscattering. For example, for "breasts" if we consider 0.1 MeV energy, it comes for anteroposterior geometry AP:

$$D/\Phi = 5.16\,\text{pGy cm}^2 \Rightarrow \dot{D}_T = 9.7 \cdot 10^{-3}\text{mGy h}^{-1}$$
$$\text{or} \quad \dot{K} = 1.4 \cdot 10^{-2}\text{mGy h}^{-1}$$
$$\Rightarrow \dot{D}_T < \dot{K}$$

So in this case, the transmission is clearly dominant. The first collision kerma majorises the mean absorbed dose in the body. If the same component is subjected to 1 MeV energy, results are as follows:

$$\dot{D}_T = 4.38 \cdot 10^{-3}\,\text{mGy h}^{-1}$$
$$\text{and} \quad \dot{K} = 1.8 \cdot 10^{-3}\text{mGy h}^{-1}$$
$$\Rightarrow \dot{D}_T > \dot{K}$$

So here is the backscattering dominates. The first collision kerma underestimates the mean absorbed dose in entire body.

2.3.8 *Measurement of the Fluence and Neutron Spectra*

Previously, it has been clearly established that the intermediate physical quantity associated with neutron field for access to dosimetric quantities was fluence. For applications related to the first collision kerma only case of monoenergetic neutrons was studied. In practice, these situations are marginal and the source terms frequently encountered are polyenergetics. Therefore, in addition to the total fluence, the energy distribution must be described. The detection devices dedicated to the determination of this quantity or its spectral distribution, are described in the following sections.

Measuring the fluence by "fission chamber"

The "fission chamber" works on the principle of the ionization chamber with fissile material deposition on the electrode. The neutrons cause fissions on fissile material deposit, inducing ionization of the gas in the sensitive volume generated by fission products. Figure 2.46 gives a vue of a fission chamber.

Two fissile isotopes are used for deposits on the electrodes: ^{238}U or ^{235}U. For ^{235}U electrode, the deposit is 201.4 mg ^{235}U (99.91% enrichment). For an electrode ^{238}U, the deposit is 197.8 mg of ^{238}U (99.999% enrichment) [38].

An international interlaboratory [38] shows that for monoenergetic neutrons at 0.144, 0.565, 2.5, 5 and 14.8 MeV, fluence is measured with less than 1% of uncertainty. Nonetheless, this process include a difficulty in calibrating this type of detector when determining their response function.

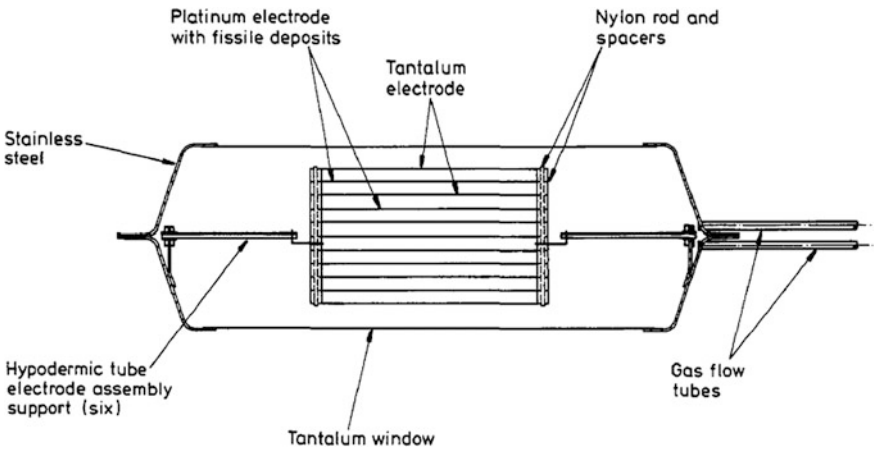

Fig. 2.46 Fission chamber (after [38], With permission from IOP Publishing)

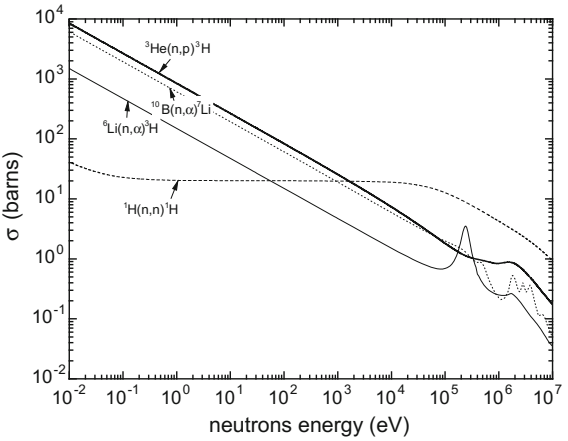

Fig. 2.47 Cross sections of neutron capture reactions, according to the data of the site http://www-nds.iaea.org/exfor/endF.htm

Absolute measure of fluence with a "long counter"

The detection principle of proportional gaz counters ^{3}He and BF_3 is based on the exploitation of nuclear reactions respectively $^{3}H(n,p)^{3}H$ and $^{10}B(n,\alpha)^{7}Li$. These capture reactions are particularly suitable for neutron energies less than 1 MeV and more at very low energies of the order of thermal (i.e. 0.025 eV) as shown by the cross sections curves in Fig. 2.47.

However, the best way for measuring the neutron fluence is to provide a detector with constant response over a wide range in energy. For this, the proportional counter is introduced into a hydrogenated medium to slow fast neutrons and only count neutrons of thermal energy field. Hydrogenated moderator is arranged such that the response is substantially independent of energy; this detector is called "long counter". Figure 2.48 gives a view of two long counters: first is the "counter Hanson" [39] which provides an independent response to the energy range between 10 keV and 1 MeV. The second is an improved version by De Pangher et al. [40] "De Pangher counter".

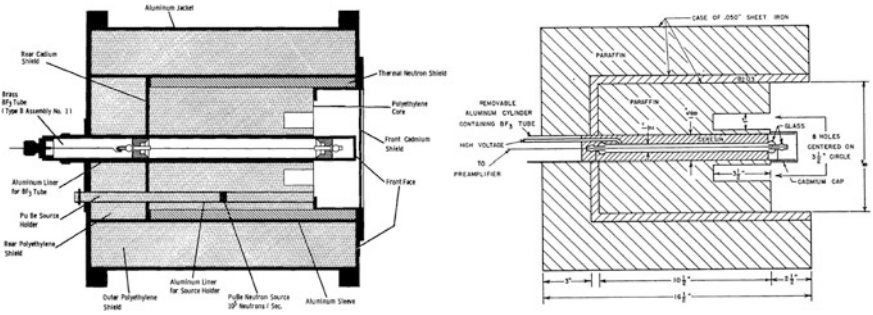

Fig. 2.48 View of long counters. On the *left*, long counter From Pangher [40], the *right* of Hanson [39], authorized by the American Physical Society

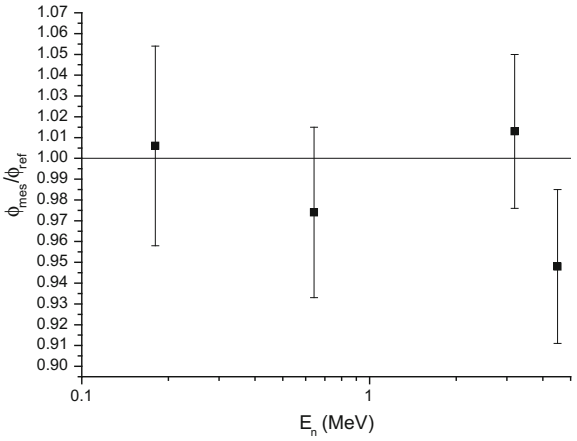

Fig. 2.49 The ratio of the measured fluence and the reference fluence on a long counter, according to the data [42]

The recent use of Monte Carlo code has increased the performance related to energy response [41]. These advances allow measuring the neutron fluence with an uncertainty of about 3% to an energy of a few keV to a few MeV and an efficiency of around 30% [42]. Figure 2.49 shows the response of the detector for a few monokinetic neutron emissions.

As suggested in introduction, to estimate the dose quantities related to neutron, in addition to fluence, it is important to access the energy distribution of the fluence. However, for the neutrons produced by sources of known spectra (e.g. ^{252}Cf source, Am–Be or nuclear reactions known), the energy spectrum can be overcome and the only knowledge of the neutron fluence at the measuring point allows the estimation of dosimetric quantity of interest. Also, because of its performance, this class of instrument is commonly used to measure the neutron fluence for neutron cross section assessment and to measure reference fluences of neutron in calibration facilities [43].

Measuring the fluence by a passive sensor "activation pellets"

Passive detector of the class "activating pellet" work on the principle of materials activation subjected to a neutron flux. The activity of radionuclides and products depends on the neutron fluence and energy (activation phenomena are described in Chap. 4). Exothermic reactions are used to measure low energy neutrons and endothermic reactions (threshold) for areas of higher energy.

The advantages of this measuring technique are [44]: No electronics are required and the detectors can be used in hostile environments, it can be used in pulsating

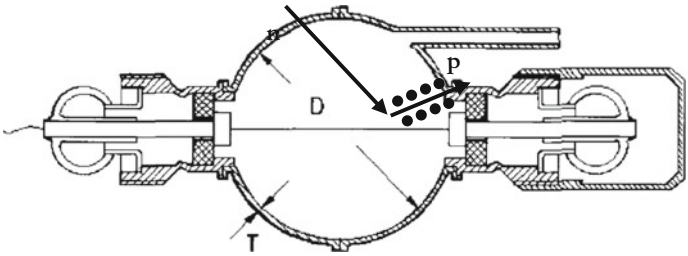

Fig. 2.50 Sectional vue of a spherical proportional counter recoil protons (D = 40 mm, T = 0.5 mm) [45], with the permission of EDP Sciences

fields, the size of the detector can be adapted to the measurement, it can measure very intense fields, it is insensitive to photonic radiation. Its disadvantages are that the sensitivity is extremely low, the spectrum can be determined by the response thresholds but remains imprecise. Using a plurality of pellets of different materials, each having a different response depending on the neutron energy, the energy spectrum of the fluence is obtained by deconvolution matrix.

Recoil proton spectrometer

Neutron detection working on elastic scattering is effective because of significant cross sections and well known between 200 keV and 22 MeV. This measurement technique is based on discrimination of the energy of the end recoil nucleus of the elastic neutron scattering in condensed gaseous medium of a proportional counter. Remind that this energy varies from 0 to a maximum of $[4A/(A + 1)^2] \cdot E_n$. According to (2.77). As the gaseous medium is often hydrogenated, the energy of recoil proton range over 0 and E_n. This is then measured either by direct ionization in the gas volume of sensitive proportional counter or by left traces in a solid organic medium. The disadvantage of this type of detector lies in a significant sensitivity to photons as well as the potential complexity of the post-processing steps.

For neutron energies between 0.05 and 5 MeV, proportional counters to H_2 and CH_4 are used [45]. For 1 MeV neutrons, the energy resolution is then of the order of 10% and efficiency of 3% [46]. Figure 2.50 gives a sectional view of proportional counter based on the measurement of the recoil proton.

For Higher energies, up to 20 MeV, solid scintillators (plastic) or liquids (NE 213) are used [45]. For 8 MeV neutron, the energy resolution is then 4% and efficiency of 20% [46].

Measurement M of the detector is given by (2.87) with $R(E)$ the fluence response of the device depending on the energy.

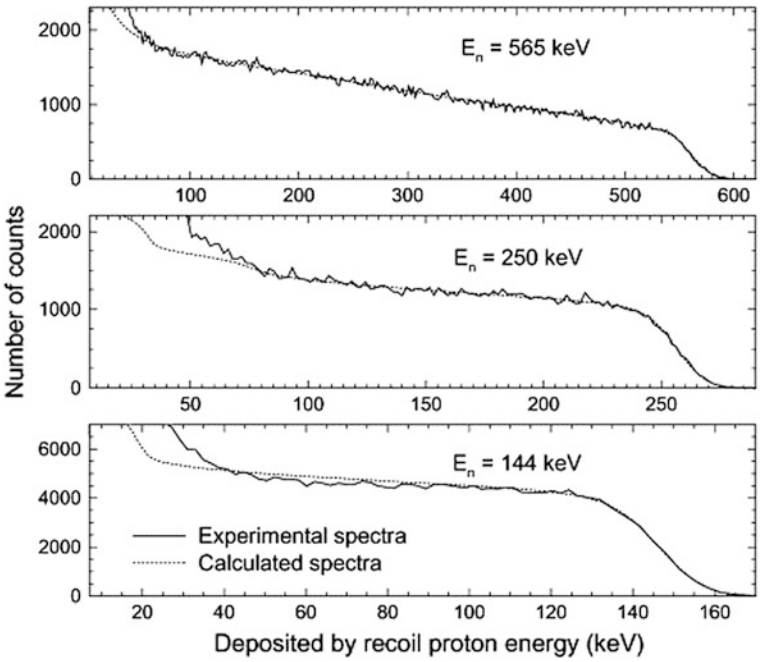

Fig. 2.51 Response of the energy distribution of the recoil protons for neutrons of different energies interacting in a spherical gas counter (H_2) [47], With permission from Elsevier

$$M = \int R(E)\Phi_E dE \tag{2.87}$$

When the integral of (2.85) is replaced by a discrete sum with fluence spectrum divided into n_E energy bins, the answer is obtained in n_C channels of a multichannel analyzer according to (2.88) [45].

$$M(k) = \sum_{i=1}^{n_E} R_i(k)\,\Phi_E(E_i)\Delta E_i \quad (k = 1.2, \ldots, n_C) \tag{2.88}$$

In a proton recoil spectrometer, the spectrum measurement is made by the height of the pulse. The response fluence $R_i(k)$ is then subtracted from the height of the pulse corresponding to the recoil protons produced by neutron energy E (see Fig. 2.51). Note that the expression (2.88) can be written in matrix form as (2.89). This expression describes a system of n_C equations with n_E unknowns. Then,

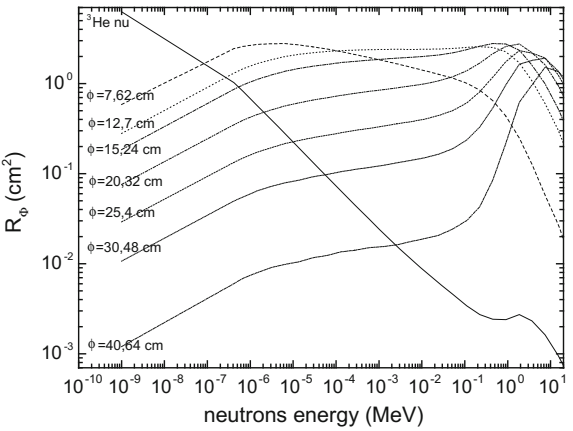

Fig. 2.52 Response in fluence of ^{3}He detector in $(CH_2)_n$ spheres of different sizes (according to the data [49])

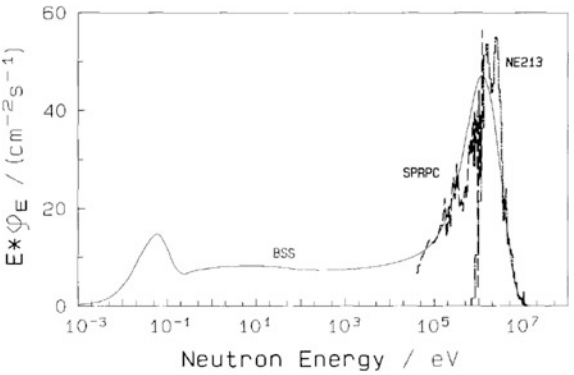

Fig. 2.53 Fluence Spectrum for PuO_2 measured by different spectrometers: BSS, Bonner sphere; SPRPC, spherical recoil proton counter; NE213, scintillator recoil protons [45], with the permission of EDP Sciences

fluence distribution Φ_E by energy band can be deduces with matrix mathematical treatment.

$$M = R\,\Phi \tag{2.89}$$

Multi-sphere spectrometer ("Bonner sphere")

Detectors containing ^{6}Li, ^{3}He or ^{10}B, as admitted, have huge efficiency for detection of thermal neutrons. To make them sensitive to fast neutrons, these are introduced in very hydrogenated medium (e.g. polyethylene). This slows neutrons to thermal energies as in the case of long counters described above. Bramblett, Ewing and Bonner [48] have designed a system of isocentric spheres of different sizes for splitting the answer to a neutron fluence. Figure 2.52 gives the response of a detector ^{3}He into spheres of different sizes depending on the neutron energy ("Bonner sphere"). Equation (2.88) for recoil proton detector remains valid and Φ_E is calculated by energy bins, resolving a matrix system.

Table 2.11 Compositions and characteristics of the detectors component "ROSPEC" [57]

Detector	Radius (2.4 cm)	Gas	Pressure (kPa)	Energy range
^{3}He bare	2.54	^{3}He/Kr	83	0.01–1 eV
^{3}He boron	2.54	^{3}He/Kr	216	1 eV–0.05 MeV
Spherical SP2-1	2.54	H2	76	0.05, 0.25 MeV
Spherical SP2-4	2.54	H2	400	0.15, 0.75 MeV
Spherical SP2-10	2.54	H2	1000	0.4, 1.5 MeV
Spherical SP6	7.62	CH4/Ar	500	1.2–5 MeV
Scintillator	2.8 cm radius	–	–	4–16.6 MeV

Fig. 2.54 Visualization of six proportional counters ROSPEC

This system allows to provide neutron spectra for energies of a few eV to 20 MeV. Figure 2.53 compares PuO_2 neutron spectrum for different types of spectrometers. Note that spectra are similar except that the low energy region is obtained only by the Bonner sphere spectrometer.

Neutron spectrometer "ROSPEC"

Ing et al. [50] designed a neutron spectrometer "ROSPEC" (*Rotating Spectrometer*) compound of ^{3}He proportional counters, recoil proton gas detector (H_2 and CH^4) at different pressures and a plastic scintillator. The number of detectors allows a neutron spectrometry with a measuring range between 0.01 eV and 17 MeV. The characteristics of the detectors and their performance are given in Table 2.11. The set of detectors being placed on a rotating platform, the fluence spectrum is given to the center of all the detectors. A photograph of ROSPEC device is given in Fig. 2.54 and technical characteristics of the different detectors component thereof are shown in Table 2.11.

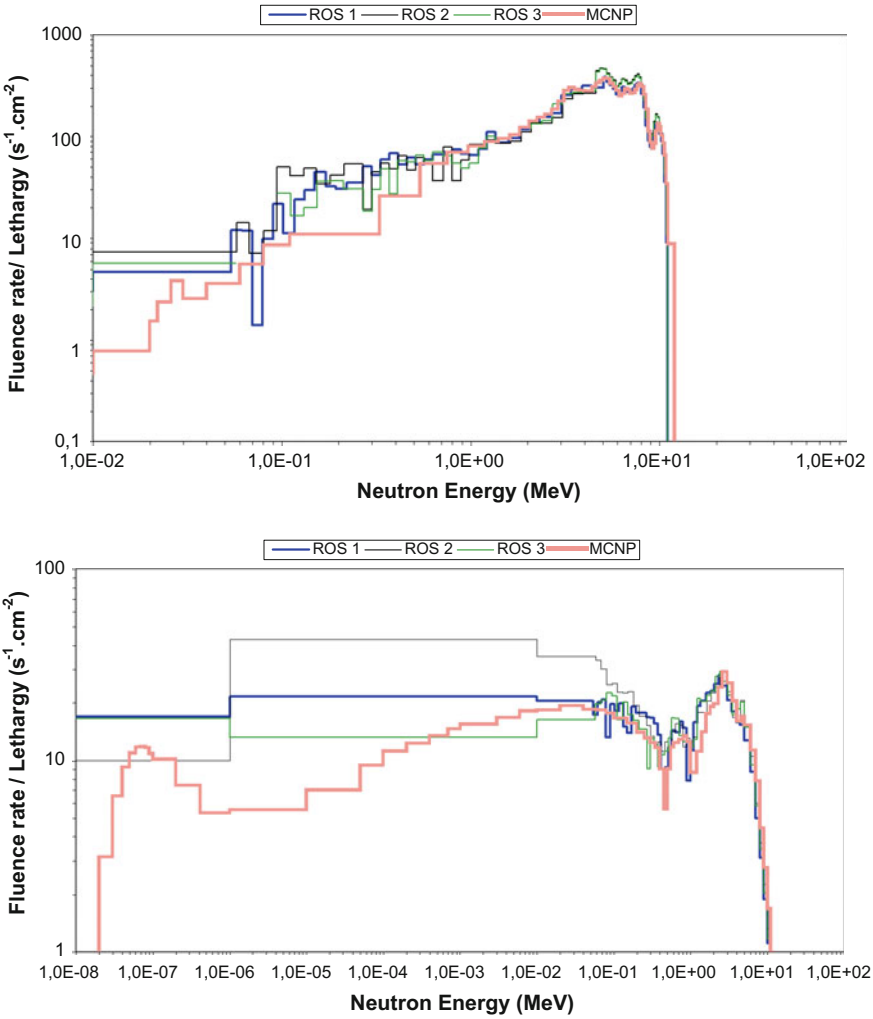

Fig. 2.55 Neutron spectra measured by ROSPEC. Top naked AmBe spectrum; down, ^{252}Cf spectrum + D_2O [51], with permission from Oxford University Press

Figure 2.55 gives neutron spectra measured by ROSPEC for an AmBe bare source and a ^{252}Cf source Moderate by D_2O.

Further Details 2.1: Charged particles—energy transferred to electron of target atom

According to conservation of kinetic energy and momentum laws: $T_o = T_1 + T_2$ et $\vec{p}_o = \vec{p}_1 + \vec{p}_2$ and setting $T_o = \left(M_1 v_o^2\right)/2$ and $p^2 = 2MT$

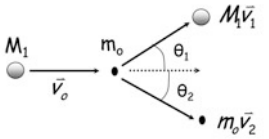

Projections on ordinate and abscissa provide following equalities system:

$$\vec{p}_0 - \vec{p}_2 = \vec{p}_1 \quad \Rightarrow \quad p_0^2 + p_2^2 - 2p_0p_2\cos\theta_2 = p_1^2$$

with $p^2 = 2MT$ follows $T_2(m_0 + M_1) = p_0p_2 \cos\theta_2$ and:

$$T_2 = 4\frac{m_oM_1}{(m_o + M_1)^2}T_o\cos\theta_2$$

θ_2 is always lower than $\pi/2$. The maximum value for T_2 is reached when the electron is projected in incident axis of particle, that is, when $\theta_2 = 0$, which results in

$$T_{2\,Max} = 4\frac{m_oM_1}{(m_o + M_1)^2}T_o$$

For alpha, as $m_0 \ll M_1 \Rightarrow T_{2\,Max} = 4\frac{m_o}{M_1}T_o$ so if $T_0(\alpha) = 5$ MeV, the electron carries a maximum $T_{2\max} = 2.7$ keV, hence a maximum energy transferred 2,000 times lower.

For an electron, $m_0 = M_1 \Rightarrow T_{2\max} = T_0$ all the energy can be imparted at once (*Knock-on*); this case is marginal, but shows, however, that for electron, large energy can be communicated at once.

Further Details 2.2: Calculation of the absorbed dose in a medium for electrons

Here after is presented the relationship between absorbed dose and fluence of charged particles at a point in medium. For this, let's consider an elementary sphere centered on the point M whose diameter is much less than the path of the particles. The absorbed dose is the limit of Z, Mean specific energy imparted to a mass volume of material, m when m tends to 0:

$$D = \lim_{m\to 0}\overline{Z} = \lim_{m\to 0}\frac{\overline{\varepsilon}}{m} \text{ with } \overline{Z} = \frac{\overline{\varepsilon}}{m}$$

The mean energy imparted ε by ionizing radiation to a volume of material is $\overline{\varepsilon} = \overline{R_e - R_s}$ assuming $\Sigma Q = 0$. Substituting R, the radiant energy by its definition:

$$R = \int_E \left(\frac{dN}{dE}\right) \cdot E \cdot dE \Rightarrow \overline{\varepsilon} = \int_E \left(\frac{dN}{dE}\right) \cdot E \cdot dE - \int_E \left(\frac{dN}{dE}\right) \cdot \left(E - \overline{\Delta E}\right) \cdot dE$$

ΔE is the energy part lost on average by each charged particle with energy $E \cdot \Delta E$. This quantity is equal to the product of linear stopping power S_{coll} by l, mean chord of the elementary sphere—we consider low loss of energy compared to energy of the incident charged particle. Note that only collision linear stopping power is considered: the loss of energy by bremsstrahlung occurs outside the sphere. The absorbed energy concept involves that energy is deposited locally to matter. $\Delta\overline{E} = S_{\text{coll}} \cdot \overline{l}$. The mean sphere chord is equal to $4R/3$ (R radius of the sphere), it is obtained by taking the ratio of volume on surface of the sphere:

$V = \frac{4}{3}\pi R^3$ and $at = \pi R^2$ so $\overline{l} = \frac{V}{a} \Rightarrow \Delta\overline{E} = S_{coll} \cdot \frac{V}{a}$
so: $\overline{\varepsilon} = \int_E \left(\frac{dN}{dE}\right) \cdot \overline{\Delta E} \cdot dE = \int_E \left(\frac{dN}{dE}\right) \cdot \frac{V}{a} \cdot S_{coll} \cdot dE$

Knowing that $V = m/\rho$ with ρ the medium density, the mean specific energy is written as follows:

$$\overline{Z} = \int_E \left(\frac{dN}{dE}\right) \cdot \frac{1}{a} \cdot \left(\frac{S}{\rho}\right)_{coll} \cdot dE = \int_E \frac{d(N/a)}{dE} \cdot \left(\frac{S}{\rho}\right)_{coll} \cdot dE$$

By definition, as seen before, D is the limit of Z when m tends to 0, so when a tends to 0, expression becomes:

$$D = \int_E \frac{d}{dE}\left[\lim_{a \to 0} \frac{N}{a}\right] \cdot \left(\frac{S}{\rho}\right)_{coll} \cdot dE$$

However, the limit of N/a, in terms of E, when a tends to 0, is the differential energy fluence:

$$\Phi_E = \frac{d^2N}{da\, dE}$$

Finally, the expression of the dose as a function of is as follows:

$$D = \int_E \left(\frac{S}{\rho}\right)_{coll} \Phi_E \cdot dE$$

Similarly, the energy distribution of fluence rate provides expression of dose rate:

$$\dot{D} = \int_E \left(\frac{S}{\rho}\right)_{coll} \dot{\Phi}_E \cdot dE$$

Further Details 2.3: Concept of Microscopic and macroscopic cross sections
Let's consider that all particles of beam I cause a reaction (*a*) on a target nucleus when they reach a distance less than the center of the target *d*. The probability *P(a)* that a particle causes event (*a*), in a target, is proportional to the following ratio:

$$P(a) = \frac{\text{effective area}}{\text{total target area}} = \frac{\text{number of center} \times \text{apparent surface of a center}}{\text{total surface of a center}}$$

Basically, as shown in the figure below, let's imagine a cuboid with apparent frontside surface (*S*) and thickness (*e*), and consider that cuboid material is composed of 6 atoms that can cause reaction (*a*) in collision case.

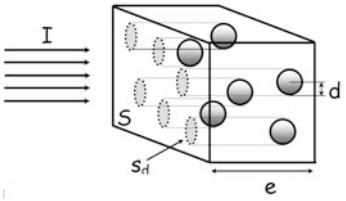

Schematic view of geometrical cross section concept.

If we consider that S_d is the projected area of each atoms on apparent surface (*S*), the reaction probability *P(a)* becomes:

$$P(a) = \frac{6 \times s_d}{S} = \frac{6 \times \pi d^2}{S}$$

If we extend this approach to a large number of target atom, the previous expression becomes:

$$P(a) = \frac{n \times \pi d^2}{S} = \frac{n \times \sigma_a}{S} = Ne\sigma_a \quad (1)$$

With *N* the atomic density obtained as follows: $N\,(\mathrm{Cm}^{-3}) = \eta_{AT}/A$, where η_{AT} is the Avogadro number $6.02 \cdot 10^{23}$ atoms/mol, ρ the density ($\mathrm{g/cm}^3$) and A the atomic mass (g/mol). σ_a is the "geometric cross section" of the reaction (*a*) and means the probability that an incident particle meets only a single nucleus located on 1 cm^2 area. It is homogeneous to a surface, but, for convenience, it is expressed in barns (1 barn = 10^{-24} cm), which corresponds approximately to the apparent surface of the uranium nucleus. The *d* term is also called "impact parameter". To a cross section much higher than the barn, an event can occur even when the incident partilce pass some distance away from the nucleus, it is the case for Coulomb scattering for charged particles. The cross sections are determined for the physical

processes involved. Consequently, and for convenience, it is necessary to define a macroscopic cross section (μ for photons and Σ for neutrons) obtained from the Expression (2.1) as follows:

$$\frac{P(a)}{e} = N\sigma_a = \mu\left(\mathrm{cm}^{-1}\right)$$

its unit, as indicated, is inverse of dictance. The latter reflects the probability of interacting according to reaction (*a*) per unit length of crossed medium. From the inverse of this quantity, the mean free path is defined (*mean free path*):

$$\lambda = (\mu)^{-1}(\mathrm{cm})$$

which translates the mean length reached in the medium before causing the reaction (*a*).

Further Details 2.4: Expression of energy of the scattered photon according to the incident energy for a Compton interaction

The conservation of kinetic energy provides:

$$E_\gamma = E'_\gamma + T_{e-} \tag{1}$$

The conservation of momentum gives:

$$\left(\vec{E}_\gamma/c\right) = \left(\vec{E}'_\gamma/c\right) + \vec{p}_{e-} \tag{2}$$

Both terms of the total energy of the electron are:

$$E_{e-}^2 = p^2c^2 + m_o^2c^4 \tag{3}$$

$$E_{e-} = T_{e-} + m_oc^2 \tag{4}$$

Laws (3) and (4) leads to the following equation:

$$p^2c^2 = E^2 - m_o^2c^4 = m^2c^4 - m_o^2c^4 = \left(T + m_oc^2\right)^2 - m_o^2c^4 = T_{e-}^2 + 2m_oc^2T_{e-} \tag{5}$$

Then expression (2) is squared:

$$E_\gamma^2 - 2E_\gamma E'_\gamma\cos\theta + E_\gamma'^2 = p^2c^2 = T_{e-}^2 + 2m_oc^2T_{e-} = E_\gamma^2 - 2E_\gamma E'_\gamma + 2m_oc^2\left(E_\gamma - E'_\gamma\right)$$

$$\Leftrightarrow \quad E_\gamma E'_\gamma - E_\gamma E'_\gamma\cos\theta = m_oc^2E_\gamma - m_oc^2E'_\gamma$$

$$\Leftrightarrow \quad E'_\gamma\left(E_\gamma(1-\cos\theta) + m_oc^2\right) = m_oc^2E_\gamma$$

So finally: $E'_\gamma = \dfrac{E_\gamma}{1 + \dfrac{E_\gamma}{m_oc^2}(1-\cos\theta)}$

Further Details 2.5: Expression of the Klein and Nishina differential cross section [20] and the Compton cross section

The Klein-Nishina differential cross section can be expressed as a sum of independent terms as follows:

$$\frac{d\sigma_c}{dx} = K\left(A + \frac{B}{x} + \frac{C}{x^2} + \frac{D}{x^3}\right) \tag{1}$$

with: $x = \frac{E_\gamma}{E'_\gamma}, K = \pi\frac{r_o^2}{\alpha_o}, \alpha_o = \frac{E_\gamma}{0.511}$ where r_0 is the electron radius: $r_o^2 = \left(\frac{\mu_o e^2}{4\pi m_e}\right)^2 = 7.94077 \cdot 10^{-26}$

Remind that the energy of Compton photon is bounded as follows:

$$\left(1 + \left(2E_\gamma / m_e c^2\right)\right)^{-1} \leq E'_\gamma \leq E_\gamma$$

which, by the formalism of the expression (1) above, amounts to the following rule: $1 \leq x \leq 1 + 2\alpha_0$.

The four coefficients of the expression (1) are:

$$A = \frac{1}{\alpha_o^2}, B = 1 - 2\frac{(\alpha_o + 1)}{\alpha_o^2}, C = \frac{(1 + 2\alpha_o)}{\alpha_o^2} \text{ and } D = 1$$

The total Compton cross section is given by integration of the *KN* differential cross section across the range of validity $1 \leq x \leq 2\alpha_0$:

$$\sigma_c = \int_1^{1+2\alpha_o} \left(\frac{d\sigma_c}{dx}\right) dx = K'\left[\frac{4}{\alpha_o} + \left(1 - \left(\frac{1+\beta}{\alpha_o^2}\right)\right)\ln(\beta) + \frac{\gamma}{2}\right] barn/e-$$

with $K' = K \times 10^{-24}$, $\beta = 1 + 2\alpha_0$ and $\gamma = 1 - \beta^{-2}$. We note that the expression of the total cross section Compton is only dependent on the energy of incident photon (α_0).

Further Details 2.6: Kerma calculation in a medium for photons

Let's determine the relationship between the fluence of primary photons at a point in material and energy transferred at the same point by the primary photons to secondary electrons. Let's consider a photon of energy E entering an elementary sphere whose diameter is much greater than the mean free path of the photon in medium. This photon, after interaction, transfer a mean energy $\overline{E}_{tr}(E)$ in sphere. Thus, throughout the elementary distance *dl* in sphere, the variation of energy transferred E_{tr} can be postulated as follows:

$$dE_{tr} = \mu_{tr}(E_\gamma) E_\gamma \, dx$$

If the mean transferred value $\overline{E}_{tr}(E_\gamma)$ is searched, the quantity dx represents the mean chord length l reached by the photon through the elementary sphere. So we can write:

$$\overline{E}_{tr}(E_\gamma) = \mu_{tr}(E_\gamma) \, E_\gamma \overline{l}$$

The total energy transferred for energies distributed over a photon spectrum is given as follows:

$$E_{tr} = \int_{E_\gamma} \left(\frac{dN(E_\gamma)}{dE} \right) \overline{E}_{tr}(E_\gamma) \, dE$$

d$N(E)$ represents the number of photons entering the sphere of energy between E and dE. $\overline{E}_{tr}(E)$ is replacing by its value, and:

$$E_{tr} = \int_{E_\gamma} \left(\frac{dN(E_\gamma)}{dE} \right) \mu_{tr}(E_\gamma) E_\gamma \overline{l} . dE$$

The mean sphere chord is:

$$\overline{l} = \frac{4}{3} R = \frac{V}{a}$$

with V volume and a the surface of the sphere. It comes then:

$$E_{tr} = \int_{E_\gamma} \left(\frac{dN(E_\gamma)}{dE} \right) \frac{V}{a} \mu_{tr}(E_\gamma) E_\gamma \, dE$$

then dividing by m to show kerma (setting $m = \rho V$ with ρ density):

$$K = \lim_{m \to 0} \left(\frac{E_{tr}}{m} \right) = \lim_{m \to 0} \left(\frac{E_{tr}}{\rho V} \right) = \lim_{m \to 0} \int_E \left(\frac{dN(E)}{dE} \right) \frac{E}{a} \frac{\mu_{tr}(E)}{\rho} dE$$

As m tends to 0, then the sphere surface a also tends to 0:

$$K = \int_{E_\gamma} \frac{d}{dE} \left[\lim_{m \to 0} \frac{N(E_\gamma)}{a} \right] E_\gamma \frac{\mu_{tr}(E_\gamma)}{\rho} dE$$

Now we have: $\lim_{m \to 0} \left(\frac{N(E_\gamma)}{a} \right) = \frac{dN(E_\gamma)}{da} = \Phi(E_\gamma)$

so $K = \int_{E_\gamma} \frac{d\Phi(E_\gamma)}{dE} E_\gamma \frac{\mu_{tr}(E_\gamma)}{\rho} dE$

with $(d\Phi(E)/dE) = \Phi_E$ the energy distribution of fluence, it finally comes:

$$K = \int_E \Phi_E E \left(\frac{\mu_{tr}(E)}{\rho} \right) dE$$

Thus, for a discrete distribution, the expression above is:

$$K = \sum_E \left(\frac{\mu_{tr}}{\rho} \right) \Phi E$$

Further Details 2.7: Demonstration of the Bragg-Gray relationship

If the geometric dimensions of the gas cavity are small compared to the path of the secondary electrons moved in the solid medium, the introduction of the cavity does not disturb the electron spectrum present in the solid. We now consider a homogeneous secondary electrons field moved at point respecting electron equilibrium in medium. If we insert at this point a small cavity filled with a gas which does not disturb the flux of secondary electrons, we attempt to determine the relationship between the absorbed dose in medium and that measured in gas. We consider that a secondary electron crosses two elementary volumes of similar geometry; let's determine what should be the respective dimensions of the two volumes so that the energy imparted ε is the same:

$$(\mathrm{d}\varepsilon) = \mathrm{G}(\mathrm{d}\varepsilon)\mathrm{M} \tag{1}$$

we defined S_g^m as the ratio of linear stopping power for both media:

$$\overline{S}_g^M = \frac{(dE/dx)_M}{(dE/dx)_g}$$

to verifiy equality (1), it is necessary that $\Delta x_g = \overline{S}_g^M \Delta x_M$. In other words, the ratio of the linear dimensions of the two volumes is $\overline{S}_g^M$. Similarly, if V represents the volume of the medium, both volumes are linked by the following proportionality:

$$V_g = \left(\overline{S}_g^M \right)^3 V_M$$

As the mean energy imparted to the volume is directly proportional to the number of electrons that enter each volume, the number of those entering the gas cavity is greater than that which would be within the volume of medium; this

number is proportional to the input surface. So, considering that for each collision, electrons deposit, on average, the same energy $\overline{\varepsilon}$; that they are in the gas or the medium M, the number of electrons that enter the volume of the gas cavity is $\left(\overline{S}_g^M\right)^2$ times greater than that in the volume of the medium M, so we get:

$$\overline{d\varepsilon}_g = \overline{\varepsilon} dN_g = \left(\overline{S}_g^M\right)^2 \overline{\varepsilon} dN_M = \left(\overline{S}_g^M\right)^2 \overline{d\varepsilon}_M$$

From this equality can be deduced the mean energy imparted per unit volume:

$$\left(\frac{\overline{d\varepsilon}}{dV}\right)_g = \frac{\left(\overline{S}_g^M\right)^2 \overline{d\varepsilon}_M}{\left(\overline{S}_g^M\right)^3 dV_M} = \frac{1}{S_g^M}\left(\frac{\overline{d\varepsilon}}{dV}\right)_M$$

By making appear infinitesimal mass elements: $dm_g = \rho_g dV_g$ and $dm_M = \rho_M dV_M$, the Bragg-Gray relationship between both absorbed doses is getting:

$$\left(\frac{\overline{d\varepsilon}}{dm}\right)_g = \left(\frac{\overline{S}}{\rho}\right)_M^g \left(\frac{\overline{d\varepsilon}}{dm}\right)_M \Leftrightarrow D_M = \left(\frac{\overline{S}}{\rho}\right)_g^M D_g$$

Further Details 2.8: Demonstration of large cavity relationship

Ionizations measured in the cavity are caused this time by secondary electrons moved in the sensitive gas volume of the cavity by the primary photons.

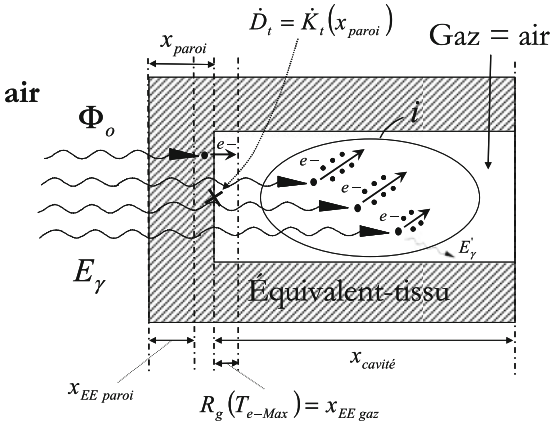

From the depth in the cavity to which the electron equilibrium is achieved for the primary photons $x_{EE}(g)$ which can be considered negligible due to the low range of the secondary electrons compared to cavity depth: x_{cavity}, at any point x in the gas cavity, the dose is:

$$D_{cavité}(x) = \Phi(0)E_\gamma \left(\frac{\mu_{en}}{\rho}\right)_g \exp(-\mu_g x)$$

We consider an initial fluence Φ_0 to the frontside of the wall:

$$\Phi(0) = \Phi_o \exp(-\mu_{wall} x_{wall})$$

The delivered current is directly proportional to integration of the cavity dose throughout the depth of the cavity: x_{cavity}. For the mean absorbed dose in the cavity, the result of this integrated dose is divided by the depth of the cavity:

$$\overline{D}_{cavity}(x) = \frac{1}{x_{cavity}} \int_0^{x_{cavity}} D_{cavity}(x)dx$$

$$\Rightarrow \overline{D}_{cavity}(x) = \Phi_o E_\gamma \left(\frac{\mu_{en}}{\rho}\right)_g \left[\frac{1 - \exp(-\mu_g x_{cavity})}{\mu_g x_{cavity}}\right] \exp(-\mu_{wall} x_{wall})$$

This dose in the cavity is equal to that in wall at depth x_{wall}, ensuring that, at this measurement point, necessarily electron equilibrium is achieved. We can write:

$$D_M(x_{wall}) = \Phi_o E_\gamma \left(\frac{\mu_{en}}{\rho}\right)_{wall} \exp(-\mu_{wall} x_{wall})$$

Thus, both quantities are related by the following relationship:

$D_M = \left(\frac{\mu_{en}}{\rho}\right)_g^{wall} \overline{D}_{cavity}(x)A$ with $A = \frac{\mu_g x_{cavity}}{1-\exp(-\mu_g x_{cavity})}$

With the setting dimensions, we finally obtain the expression of the absorbed dose rate in the depth of the wall to a large cavity. In practice, the factor A is close to 1.

Further Details 2.9: Calculation of energy transferred to the recoil nucleus for inelastic scattering on ^{12}C

First, let's determine the reaction threshold on ^{12}C; the incident neutron must have substantially equal energy to the first excited state of collisioned nulceus. For ^{12}C, the first level is 4.43 MeV. Thus, the threshold energy obtained from the heat of reaction for the neutron must be:

$$E_n(threshold) = -\left(\frac{A+1}{A}\right)Q = \left(\frac{13}{12}\right) \times 4.43 = 4.8\,\text{MeV}$$

Consider a neutron whose energy is greater than this threshold value: e.g. 6 MeV. Therefore the neutron enters the ^{12}C to become a ^{13}C excited with energy:

$$E*(C13) = B(n) + \left(\frac{A}{A+1}\right)E_n = 4.95 + \frac{12}{13} \times 6 = 10.5\,\text{MeV}$$

with B(N) the binding energy of the last neutron. ^{13}C in turn release a neutron with energy between 0 and:

$$\left(\frac{A}{A+1}\right)E_n + Q = \left(\frac{12}{13}\right) \times 6 - 4.43 = 1.1\,\text{MeV}$$

The probability of a particular energy between 0 and 1.1 MeV for released neutron n′ is directly released to the level of excitation ^{13}C.

Then happens the de-excitation of the residual excited ^{12}C. this loses energy by realising a γ whose energy is:

$$E_\gamma = -Q = 4.43\,\text{MeV}$$

Finally, the recoil nucleus, on average, carry away the following energy transferred [21]:

$$\overline{E}_{tr} = \frac{2E_nA}{(A+1)^2}\left[1 + \frac{|Q|(A+1)}{2AE_n}\right] = \frac{2 \times 6 \times 12}{13^2} \times \left[1 + \frac{4.43 \times 13}{2 \times 12 \times 6}\right] = 1.2\,\text{MeV}$$

That is consistent with: $\overline{E}_{tr} \cong E_n(i) - E_\gamma = E_n(i) - E^*_{NC}$

Further Details 2.10: Why an energy threshold for positive heat reaction ($Q > 0$)?

Let's study, for example, the ^{235}U(n,α) reaction leading to the ^{232}Th creation and calculate the heat of reaction:

$$\begin{aligned} Q &= B\left(^{232}Th\right) + B(\alpha) + B\left(^{235}U\right) \\ &= 1766.691 + 28.295 - 1783.87 = 11.1\,\text{MeV} \Rightarrow Q > 0 \end{aligned}$$

Although the heat is positive and the reaction present an energy threshold. In fact, the compound nucleus must have sufficient excitation energy to break-up the charged particle by communicating the potential energy necessary for break-up. This energy is therefore used to overcome the Coulomb barrier. Let's calculate it.

Beforehand, it should be considered the most "expensive" configuration modeled by alpha sticking to thorium nucleus, as represented in the scheme below:

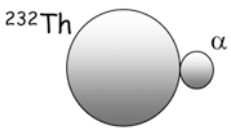

The Coulomb barrier to overcome is thus determined by the work resulting from the application of the Coulomb force, considering that the entire charge is centered in each nucleus. In this model, the distance between the centered charge of both nuclei is given by: $r = R_o\left(A_{Th}^{1/3} + A_{\alpha}^{1/3}\right)$

With R_0 = 1.4 fm, knowing that $m_0c^2 \approx 0.5$ MeV and the classical electron radius is:

$$r_o = \frac{e^2}{4\pi\varepsilon_o m_o c^2} = 2.8\,\text{fm}$$

The calculation of the Coulomb barrier gives the following result:

$$B_c = \frac{1}{4\pi\varepsilon_o}\frac{e^2 Z_\alpha Z_{Th}}{r} = \frac{e^2}{4\pi\varepsilon_o m_o c^2}\frac{m_o c^2 Z_\alpha Z_{Th}}{R_o\left(A_{Th}^{1/3} + A_\alpha^{1/3}\right)} \cong \frac{Z_\alpha Z_{Th}}{\left(A_{Th}^{1/3} + A_\alpha^{1/3}\right)} \approx 23\,\text{MeV}$$

We thus observe that $Q - B_c < 0$, which involves the presence of energy threshold. The energy of the incident neutron to cause such reaction must be:

$$E_{seuil} = \left(\frac{A_{^{235}U} + 1}{A_{^{235}U}}\right)(Q - B_c) \approx 12\,\text{MeV}$$

Further Details 2.11: Method for measuring Kerma factors according to the Report No. 63 of the ICRU [32]

Factors Kerma k_Φ are obtained by calculating the following ratio: $k_\Phi = K/\Phi$ for neutrons with energy less than 20 MeV. Cross sections are well known and can be calculated using the formula:

$$k_\Phi = \frac{1}{\rho} \cdot \sum_i N\sigma_i \overline{E}_i$$

In practice, these calculations are made using a Monte Carlo code.

Beyond 20 MeV, the cross sections are not as accurate, so we have to determine at first neutron fluence Φ at a point in space, for example by means of a recoil protons telescope. Then the kerma is assessed using the following method: using a low pressure proportional counter filled with a gas (LPPC), surrounded by a material of interest, for example carbon—remind that carbon is a human tissues constituent. The equilibrium of secondary charged particles is produced in this carbon wall, so the secondary charged particles—recoil nuclei, protons, α…—will ionize the gas detector. The absorbed dose in this gas is obtained from the charges produced:

$$D_g = \frac{\Delta q}{\Delta m_g}\frac{\overline{W}_g}{e}$$

Figure 1 below provides curves of absorbed dose for 34 and 66 MeV monoenergetic neutrons in the gas cavity of the LPPC per unit neutron fluence. This curve is a function of the linear energy transfer y (keV μm^{-1}):

This representation of microdosimetric spectrum reveals the contributions of different secondary charged particles set in motion by the neutron field. We can indeed see that the first bump is due to protons, the second to α and the last to recoil nuclei. Moreover, it is clear that the difference in energy mostly causes an increase of absorbed dose from protons; which is not the case for other types of charged particles set in motion, where we have a substantially overlap of the two spectra at those locations. For the absorbed dose in the gas cavity by fluence unit for both energies, we must integrate these dose distribution curves on all y:

$$D_g\Phi^{-1} = \int_0^\infty yd(y)D_g(y)\Phi^{-1}dy$$

From a practical point of view, to get a "quasi monoenergetic" ray, neutrons of 66 MeV are provided bombarding a thick beryllium target with protons of 71 MeV. It appears a peak at 66 MeV, once collimated, allows a beam onto a small solid angle of the order of 10^{-5} sr. However, when measuring, it will be important to subtract the absorbed dose due to photonic noise due to initial neutron beam. Then the expression of the absorbed dose in the carbon is deduced with the following expression: $D_C = D_g r_{C,g}$. Now, if the cavity is small enough that the energy lost by the charged particles is low and the interaction of indirectly ionizing radiation with the gas cavity is negligible, the law of Bragg-Gray shows that:

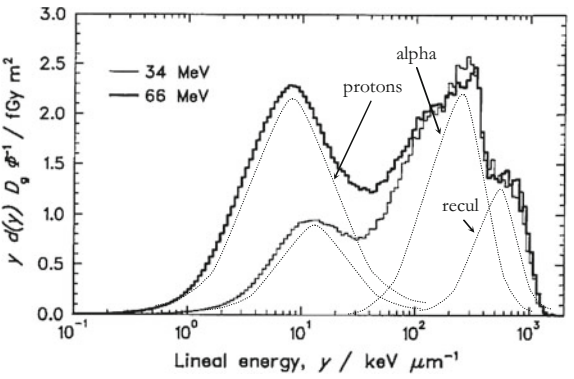

Fig. 1 Absorbed dose in the gas cavity of the LPPC per unit fluence $yd(y)D_g\Phi^{-1}$ As a function of linear energy transfer, y, measured with a LPPC wall atoms with a neutron beam of 34 and 66 MeV, adapted to [32]

$$r_{C,g} = \left(\frac{\overline{S}}{\rho}\right)_g^C = \frac{(\overline{S}/\rho)_C}{(\overline{S}/\rho)_g}$$

And, finally, in the equilibrium conditions of the charged particles, the kerma expression for carbon is as follows:

$$K_C = c_w c_c D_C$$

where the correction factor c_w considers neutrons attenuation and scattering in the carbon wall of the cavity and c_c takes into account the fact that the neutron beam is not exactly monoenergetic. In our example, these calculations, for 34 and 66 MeV energies, lead respectively to following dose factors: 4.21 fGy m^2 and 5.53 fGy $m^{2.}$

Further Details 2.12: Bethe-Block Formulas [5] for heavy charged particles and Rohrlish-Carlson [6] For electrons

The Coulomb force applied between two charged particles of charges q_1 and q_2 spaced apart a distance r is (Fig. 2):

$$\vec{F}_{1\to 2} = -\vec{F}_{2\to 1} = \frac{1}{4\pi\varepsilon_o}\frac{q_1 q_2}{r^2}\vec{u}$$

The momentum provided by the incident particle of charge z to an orbital electron of mass m_e is reduced, for reasons of symmetry, to the expression of the integral of the coulomb force to the y component shown Fig. 3.

This is written as follows:

$$P_e = \int_{-\infty}^{+\infty} F_y dt = \int_{-\infty}^{+\infty} F\,\sin\theta\, dt = \int_{-\infty}^{+\infty} \frac{1}{4\pi\varepsilon_o}\frac{ze^2}{r^2}\sin\theta\, dt$$

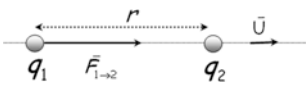

Fig. 2 Coulomb force between two charged particles

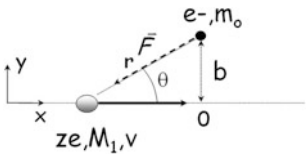

Fig. 3 Coulomb interaction between a heavy charged particle and an orbital electron of the irradiated areas

with $r = \frac{b}{\sin\theta}$, $dt = \frac{dx}{v}$ $x = \frac{b}{\tan\theta}$ and like: $d\left(\frac{1}{\tan\theta}\right) = \frac{1}{\sin^2\theta}$ it comes:

$$P_e = \frac{1}{4\pi\varepsilon_o}\frac{ze^2}{bv}\int_0^{\pi}\sin\theta\, d\theta = \frac{1}{4\pi\varepsilon_o}\frac{2ze^2}{bv}$$

Thus, for an electron, the transmitted kinetic energy is:

$$T_e = \frac{P_e^2}{2m_e} = \left(\frac{1}{4\pi\varepsilon_o}\right)^2\frac{2z^2e^4}{b^2v^2m_e} \tag{1}$$

Assuming that the electron distribution is uniform in the irradiated areas, the charged particle actually will transfer a part of its energy to all the electrons in the volume described in Fig. 4: dV = 2πbdbdx. Thus, if N is the atomic density, there will be 2πb NZdb dx electron impacted during the path of the charged particle.

The energy lost to all of these electrons will be:

$$dT = \int_{b_{\min}}^{b_{Max}}\left(\frac{1}{4\pi\varepsilon_o}\right)^2\frac{4\pi z^2e^4}{m_ev^2}NZ\frac{db}{b}dx$$

or:

$$\left(\frac{dT}{dx}\right)_c = \frac{1}{4\pi\varepsilon_0^2}\frac{z^2e^4}{m_ev^2}NZ\,\ln\left(\frac{b_{max}}{b_{\min}}\right) \tag{2}$$

It remains to determine the impact parameters $b_{\max}$ and $b_{\min}$, that is to say the minimum and maximum radial distance where the effect of the Coulomb interaction is felt by the particle during its passage. concerning $b_{\min}$ we have seen that, typically, the maximum energy that can be imparted to an electron by a heavy charged particle is given by the expression (1) and:

$$T_{eMax} = \frac{4m_e}{M}T_o \Leftrightarrow T_{eMax} = \frac{4m_e}{M_1}\times\frac{1}{2}Mv^2 = 2\mathrm{m}_ev^2$$

In relativistic mechanics, as $p = \gamma mv$ we would get: $T_{\mathrm{emax}} = 2\gamma^2MeV^2$. Thus, by injecting this expression in expression (1), we get: $b_{\min} = ze^2/4\pi\varepsilon_o\gamma\, v^2m_e$. For the

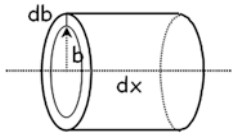

Fig. 4 Volume between the impact parameter b and b + db

maximum distance for which the charged particle interacts with the electron medium, we take the minimum energy which can be transmitted to an electron to move it to an excited state. This energy is called mean potential of excitation and depends on the environment, we note *I*. Again using the expression (1) we get this time:

$$I = \left(\frac{1}{4\pi\varepsilon_o}\right)^2 \frac{2z^2e^4}{b^2v^2m_e} \Leftrightarrow b_{max} = \frac{1}{4\pi\varepsilon_o}\sqrt{\frac{2z^2e^4}{v^2m_eI}}$$

Thus, by inserting the two expressions of impact parameters in (2) and expressing the atomic density *N* depending on the medium density ρ and its atomic number *A,* We finally obtain the expression of Bohr:

$$\left(\frac{dT}{dx}\right)_c = \frac{1}{8\pi\varepsilon_0^2}\frac{z^2e^4}{m_ev^2}\frac{\rho N_A Z}{A}\ln\left(\frac{2\gamma^2m_ev^2}{I}\right)$$

Moreover, we can directly determine the value of $\beta = v/c$ depending on the kinetic energy of the particle. Moreover, this transformation has the benefit to make appear c^2 for expressing directly the electron mass m_e in atomic mass unit MeV. Thus we write:

$$\left(\frac{dT}{dx}\right)_c = \frac{1}{8\pi\varepsilon_0^2}\frac{z^2e^4}{m_ec^2\beta^2}\frac{\rho N_A Z}{A}\ln\left(\frac{2\gamma^2m_ec^2\beta^2}{I}\right) \tag{3}$$

This expression is approximate, but is relatively valid to very heavy particles like α or heavy ions. Observing the expression (3) shows that it is linearly proportional to the medium density. This defines the expression of the mass stopping power as follows:

$$\left(\frac{S}{\rho}\right)_c = \frac{1}{\rho}\left(\frac{dT}{dx}\right)_c$$

This is expressed in MeV g cm^{-2} and allows for a given material multiplied by its density to get the linear stopping power. A refined calculation based on relativistic quantum mechanics led to the Bethe-Bloch:

$$\left(\frac{S}{\rho}\right)_c = \frac{1}{4\pi\varepsilon_0^2}\frac{z^2e^4}{m_ec^2\beta^2}\frac{N_A Z}{A}\left[\ln\left(\frac{2m_ec^2\beta^2}{I}\right) - \ln\left(1-\beta^2\right) - \beta^2 - \frac{\delta}{2}\right] \tag{4}$$

The correction factor for the charge density effects δ reflects the fact that the electric fields of the incident particle polarize the atoms near its trajectory. This reduces the polarization effect of the electric field on the farthest electrons, which is a screening effect. This effect is especially important at high energy and as the irradiated medium density increase. This effect is of little importance for energies below 100 MeV. Beyond this energy, the effect is significant, and is described

empirically [52]. The δ factor taking into account the effect of charge density becomes significant above 100 MeV. Sternheimer [52] proposed an empirical method to characterize this effect:

$$\begin{cases} \delta = 0 & X < X_o \\ \delta = X - C_1 + a\,(X_1 - X)^m & X_o < X < X_1 \\ \delta = X - C_1 & X_1 < X \end{cases}$$

or:

$$X = \log\left(\sqrt{\frac{\beta^2}{1-\beta^2}}\right)$$

X_0, X_1, C and a are parameters that must be determined for each target material, they are provided by Sternheimer in tables and used in stopping power calculations for the particles from proton to alpha of 50 keV to 500 MeV energies (Williamson 1963). To simplify expression (3), we can calculate the value of the factor K as following:

$$K = \frac{e^4 N_A}{4\pi\varepsilon_0^2 m_e c^2} \approx 0.307075\ \text{MeV g}^{-1}\ \text{cm}^2$$

The expression (3) is then written as follows:

$$\left(\frac{S}{\rho}\right)_c = K\frac{z^2}{\beta^2}\frac{Z}{A}\left[\ln\left(\frac{2m_e c^2\beta^2}{I}\right) - \ln\left(1-\beta^2\right) - \beta^2 - \frac{\delta}{2}\right] \tag{5}$$

This formula is valid for heavy particles with energies above about 200 keV/nucleon. It applies for example for a proton whose energy is greater than 200 keV and for an alpha whose energy is greater than 1 MeV. Below this energy the semi-empirical formula of the Williamson et al. can be used [53]. For energies below 200 keV/nucleon, the expression of the Bethe-Bloch formula becomes:

$$\left(\frac{S}{\rho}\right)_c = K\frac{z_{eff}^2}{\beta^2}\frac{Z}{A}\left[\ln\left(\frac{A(E)}{\left[1-\exp\left(-A(E)^{1/b}\right)\right]^b}\right) - \beta^2 - \frac{\delta}{2}\right]$$

with:

$$A(E) = \sqrt{\frac{2m_e c^2 \beta^2 W_m}{(1-\beta^2)I^2}}\, b = 1 + 0.035\left(z_{eff}^{3/2} - Z^{1/2}\right)$$

$$b = 1 + 0.035\left(z_{eff}^{3/2} - Z^{1/2}\right)$$

$$I = 11.8.10^{-6} Z \exp\left[Z^{-2/3} - 8.33Z^{-2} + 26.04Z^{-3} - 18.38Z^{-4}\right] \cdot \left[1 - 0.25 \exp\left(-\frac{100}{E}\right)\right]$$

In this expression, energy is expressed in MeV. The term W_{m} is the maximum transferable energy to an orbital electron of the medium irradiated by the charged particle. Its expression as a function of the incident energy of the particle is as follows:

$$W_m = \frac{2m_e c^2 \beta^2}{\left(1-\beta^2\right)\left(1+\frac{1}{1835A}\right)^2\left[1 + 4.635.10^{-3}\left(\frac{E}{A}\right)\left(\frac{1}{1+1835A}\right)\right]}$$

E.g. calculate successively the mass stopping power and linear by collision of a 50 MeV proton in aluminum: for such energy, the proton is considered as relativistic—energy is greater than 45 MeV. Therefore, the value of β^2 is determined as follows:

$$\beta^2 = \frac{T(T + 2m_p c^2)}{\left(m_p c^2 + T\right)^2} = \frac{50(50 + 2 \times 938)}{(938 + 50)^2} = 0.0986$$

For aluminum: A = 27, Z = 13, ρ = 2.7 g cm^{-3}. From (2.7) (Sect. 2.1.2), the mean potential of excitation I = 9.76 × 13 + 58.8 × (13) −0.19 ≈ 163 eV. Finally, the mass stopping power is provided by the expression (5) by neglecting the effect of charge density:

$$\begin{aligned}\left(\frac{S}{\rho}\right)_c &= 0.307075 \times \frac{1}{0.0986} \\ &\quad \times \frac{13}{27}\left[\ln\left(\frac{1.022 \times 0.0986}{163.10^{-6}}\right) - \ln(1 - 0.0986) - 0.0986\right] \\ &= 9.65\,\mathrm{MeV g^{-1} cm^2}\end{aligned}$$

We deduce directly the Linear stopping power multiplying it by the aluminum density: $S_{\mathrm{coll}} = \rho(S/\rho)_{\mathrm{c}}$ = 2.7 × 9.65 = 26 MeV cm^{-1}. A low energy noticeable effect is that of "effective charge" seen by the irradiated medium: indeed, as the energy decreases, the incident charged particles are increasingly neutralized by electrons that gravitate around them, which actually limits the Coulomb interaction. Northcliffe [54] offers a semi-empirical formula to account for this, that is expressed directly as a function of the energy T for nonrelativistic particle:

$$z_{eff}(E) = z \cdot \tanh\left(\frac{\beta}{\alpha z}\sqrt{\frac{\pi}{2}}\right) = z \cdot \tanh\left(\frac{1}{\alpha z}\sqrt{\frac{\pi T}{m_o c^2}}\right) \tag{6}$$

α is the fine structure constant and its inverse is 137.

Take, e.g., alpha ($z = 2$) and see the behavior of the charge as function of energy. The expression (6) becomes:

$$z_{eff}(E) = 2 \cdot \tanh\left(0.125\sqrt{T}\right) \tag{7}$$

with T Energy alpha in keV. Figure 5 shows the representation of the expression (7).

We note that, from 1 keV, the effective charge of alpha decreases until it becomes substantially zero close to 0.01 eV.

From the Bethe continuous slowingdown theory that leads to the expression (4), Rohrlish and Carlson established a formula to calculate the loss of energy by collision. This expression is given below however with the addition of a term δ taking into account the Density effect [55]. Note that this expression differs slightly for positrons.

$$\frac{1}{\rho}\left(\frac{dT}{dx}\right)_c = \frac{K}{2\beta^2}\frac{Z}{A}\left[Ln\left(\frac{T^2(T+2)}{2I^2}\right) + \frac{\left(T^2/8\right) - (2T+1)\ln 2}{(T+1)^2} + \left(1-\beta^2\right) - \delta\right] \tag{8}$$

the density effect reduces energy loss by collision due to the dielectric properties of the crossed medium. A theoretical expression developed by Sternheimer quantifies this. Table 2.12 provides for various elements and energies the decreasing percentage brought to the mass-transfer energy.

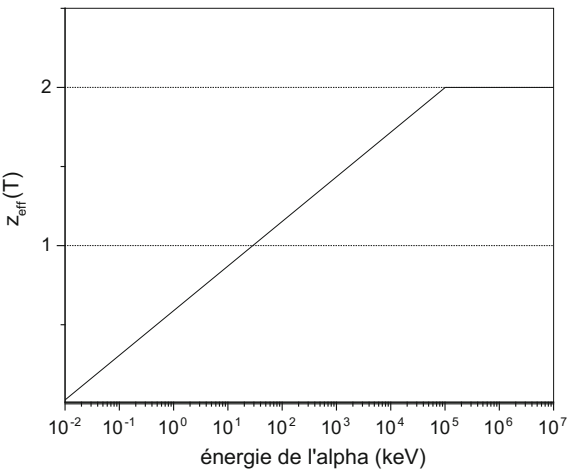

Fig. 5 Effective charge in number of charges, according to the alpha energy

Table 2.12 Percentage reduction in the mass stopping power for electrons by collision of 1.10 and 100 MeV for different materials [55]

Electron energy (MeV)	Through material							
	H	O	Born	A	C	Al	Cu	Pb
1	0	0	0	0	3.53	2.09	3.78	0.85
10	0	0	0	0	14.3	10.4	12.8	7.44
100	3.55	4.23	1.21	2.25	29.2	24.8	25.7	19.7

Let's calculate, e.g., the collision stopping power for electrons of 100 MeV in aluminum. The mean potential of excitation for aluminum is about 163 eV. Moreover, at this energy as the electrons are widely relativistic, we can assume that: $\beta^2 \cong 1$. Without the term density effect we then determine yields:

$$\left(\frac{S}{\rho}\right)_c = \frac{0.307075}{2\times 1}\frac{13}{27}\left[Ln\left(\frac{(100)^2(102)}{2\times(163.10^{-6})^2}\right) + \frac{(100^2/8) - 201\times \ln 2}{101^2}\right]$$
$$\cong 2.33 \quad \text{MeV}\,\text{g}^{-1}\text{cm}^2$$

now calculate the term: $\Delta = -KZ\delta/2\beta^2 A$ which decreases the stopping power by referring to Table 2.12. This gives for 100 MeV electrons a decrease percentage of 24.8%. Finally, The mass stopping power taking into account this effect is:

$$\left(\frac{S}{\rho}\right)_c \cong 2.33 - \Delta \approx 2.33 - \left(\frac{2.33\times 24.8}{100}\right) \approx 1.75\,\text{MeV}\,\text{g}^{-1}\text{cm}^2$$

Further Details 2.13: Mass scattering power Formulas (2.11) for electrons [icru 35]

The formula of mass scattering power (Rossi 1952 and Brahme 1971) includes screening effect.

$$\frac{\theta_s^2}{\rho} = \pi\left(\frac{2r_e Z}{(\tau+1)\beta^2}\right)^2 \frac{N_A}{A}\left\{\begin{array}{c}\ln\left[1+\left(\frac{\theta_m}{\theta_\mu}\right)^2\right] - 1 + \\ \left[1+\left(\frac{\theta_m}{\theta_\mu}\right)^2\right]^{-1}\end{array}\right\} \qquad (1)$$

In this expression θ_m is the cut-off angle due to the finite size of the nucleus. It is given by the ratio of the reduced de Broglie wave length of the electron to the nuclear radius ans is

$$\theta_m = \frac{2A^{-1/3}}{\alpha\beta(\tau+1)}$$

where τ is the ratio of the kinetic energy of the electron to its rest mass energy. For θ_m larger than unity, θ_m should be set equal to 1 (Rossi 1952). The screening angle θ_μ, is due to the screening of the nucleus by the orbital electrons. This angle is given by the ratio of the reduced de Broglie wave length of the electron to the atomic radius and can be written as

$$\theta_\mu = 1.13 \frac{\alpha Z^{1/3}}{\beta(\tau + 1)}$$

The masse scattering power must be used with care for thin absorbers where single large-angle scattering events can be important. This the case when the mean number of scattering events is less than about 20 (Moliere 1947, 1948), i.e., when the thickness is less than approximately 1 mg cm^{-2}. In addition, for thick absorbers, the mean energy loss of the electrons must be considered. according to experimental results in Fig. 2.4, the proportionality of the mean square scattering angle with thickness is useful over a fairly wide range of absorber thickness in low atomic number materials. However, the proportionality observed in Fig. 2.4 is not entirely due to the mass scattering power at the initial energy because the energy loss of electrons and the consequent gradual increase in scattering power has to be taken into account in thick absorbers. In the first approximation, this increase is given by (Eyges 1948; Brahme 1975)

$$\overline{\theta_S^2}(l) = \left(\frac{\theta_s^2}{\rho}\right)\left\{1 - \left(\frac{S}{\rho}\right)_{tot}\frac{\rho l}{E_0 + m_e c^2}\right\}^{-1}\rho l$$

Furthermore, at larger depths, the angular distribution reaches an equilibrium shape (Bethe et al. 1938), as is seen, because electrons that are scattered at large angles are rapidly lost from the beam. When the value of ρl in previous equation is small, this reduces to:

$$\overline{\theta_S^2}(l) = \left(\frac{\theta_s^2}{\rho}\right)\rho l$$

An approximate estimation of the scattering power for electrons of kinetic energy E can be made using the following formula (Rossi 1952)

$$\frac{\theta_s^2}{\rho} = \frac{1}{\beta^4 X_0}\left(\frac{E_S}{E}\right)^2$$

where E_s has a constant value of 21.2 MeV and X_O in different materials is given in Table 2.2 and these values were calculated with the use of Z(Z + 1) instead of Z^2 which was used in the expression of scattering power.

References for Further Details 2.13

Bethe, H. A., Rose M. E. Smith L.P. (1938). The multiple scattering of electron Proc. Am. Philos. Soc. 78, 573.

Brahme, A. (1975). Simple relations for the penetration of high energy electron beams in matter, SSI: 1975-011, Dep. Radiation Physics, Karolinska Institutet, Stockholm, Sweden.

Eyges, L. (1948). Multiple scattering with energy loss Phys. Rev. 74, 1534

Moliere, G. (1947). Theorie der Streuung schneller geladener Teilchen. I. Einzelstreuung am abgeschirmten Comlomb-field Z. Naturforsch. 2a, 133.

Moliere, G. (1948). Theorie der Streuung schneller geladener Teilchen. II. Mehrfach und vielfachstreuung, Z. Naturforsch. 3a, 78.

Rossi, B. B. (1952). High energy particles (Prentice Hall, New York)

References

1. Collot, J. (2001). *Cours de physique expérimentale des hautes énergies du DEA de physique théorique Rhône-Alpes*.
2. Drouin, D., Réal Couture, A., Joly, D., Tastet, X., Aimez, V., & Gauvin, R. (2007). CASINO V2.42—A fast and easy-to-use modeling tool for scanning electron microscopy and microanalysis users. *Scanning, 29*(3), 92–101.
3. Katz, L., & Penfold, A. S. (1952). Range energy relations for electrons and the determination on beta–ray end point energies by absorption. *Reviews of Modern Physics, 24*(1), 28–44.
4. ICRU (2011) *Fundamental quantities and units for ionizing radiation (revised)*. Publication 85a.
5. Paganetti, H. (2002). Nuclear interactions in proton therapy: dose and relative biological effect distributions originating from primary and secondary particles. *Physics in Medicine & Biology, 47*, 747–764.
6. Rohrlish, C. (1953). Positron-electron differences in energy loss and multiple scattering. *Physical Review, 93*(1954), 38–44.
7. ICRU (1984) *Stopping powers for electrons and positrons*. Publication 37.
8. ICRU (1993) *Stopping powers and ranges for protons and alpha particles*. Publication 49.
9. ICRU (1984). *Radiation dosimetry: Electron beams with energies between 1 and 50 MeV*. Report 35.
10. Grosswendt, B. (1994). Determination of electron depth-dose curves for water, ICRU tissue, and PMMA and their application to radiation protection dosimetry. *Radiation Protection Dosimetry, 54*(2), 85–97.
11. Profio, A. E. (1979). *Radiation shielding and dosimetry*. New York, NY: Wiley.
12. Loevinger R, Japha EM, Brownwell G (1956) L. Discrete radioisotope sources. In Hine, G. J., Brownell, G. L. (Eds.) *Radiation dosimetry* (pp. 693–799). Academic Press.
13. Cross, W. G. (1997). Empirical expression for beta ray point source dose distributions. *Radiation Protection Dosimetry, 69*(2), 85–96.
14. Bourgois, L. (2011). Estimation de la dose extrémité due à une contamination par un radionucléide émetteur β: l'équivalent de dose est-il un bon estimateur de la grandeur de protection? *Radioprotection, 46*(2), 175–187.
15. Pelowitz, D. B. (2005). *MCNPX user's manual version 2.5.0*. LA–CP–05–0369.

16. Gunzert-Marx, K., Iwase, H., Schardt, D., Simon, R. S. (2008). Secondary beam fragments produced by 200 MeV.u^{-1} ^{12}C ions in water and their dose contributions in carbon ion radiotherapy. *New Journal of Physics*, *10*(075003), 21 p.
17. Golovachik, V. T., Kustarjov, V. N., Savitskaya, E. N., & Sannikov, A. V. (1989). Absorbed dose and dose equivalent depth distributions for protons with energies from 2 to 600 MeV. *Radiation Protection Dosimetry, 28*(3), 189–199.
18. Pelliccioni, M. (1998). Fluence to dose equivalent conversion data and radiation weighting factors for high energy radiation. *Radiation Protection Dosimetry, 77*(3), 159–170.
19. Daures, J., & Ostrowsky, A. (2005). New constant-temperature operating mode for graphite calorimeter at LNE-LNHB. *Physics in Medicine & Biology, 50*, 4035–4052.
20. Klein, O., & Nishina, Y. (1929). Die Streuung von Strahlung durch freie Elektronen nach der neuen relativistischen Quantendynamik von Dirac. *Zeitschrift für Physik, 52*(11–12), 853–869.
21. Shultis, J. K., Faw, R. E. (2000). *Radiation shielding*. American Nuclear Society, Inc.
22. Hubbell, J. H., Seltzer, S. M. (1996). *Tables of X–ray mass attenuation coefficients and mass energy–absorption coefficients from 1 keV to 20 MeV for elements Z = 1 to 92 and 48*, Additional Substances of Dosimetric Interest Ionizing Radiation Division, Physics Laboratory, NIST. Disponible sur le site http://physics.nist.gov/PhysRefData/XrayMassCoef/tab3.html et http://physics.nist.gov/PhysRefData/XrayMassCoef/tab4.html.
23. ICRU (1980) *Radiation quantities and units*. Publication 33.
24. Gambini, D. J., Granier, R. (1997). *Manuel pratique de radioprotection*. 2^{e} éd, Tec & Doc.
25. Barthe, J., Chauvenet, B., & Bordy, J. M. (2006). La métrologie de la dose au CEA: le Laboratoire National Henri Becquerel. *Radioprotection, 41*(5), 9–24.
26. Fano, U. (1956). Note on the Bragg-Gray cavity principle for measuring energy dissipation. *Radiation Research, 1*, 237–240.
27. Wall, J. A., & Burke, E. A. (1974). *Dose distributions at and near the interface of different materials exposed to Co-60 gamma radiation, report AFCRL-TR-0004*. NM: Sandia National Laboratory.
28. Wall, J.A., Burke, E.A. (1970). Gamma dose distributions at and near the interface of different materials nuclear science. IEEE Transactions on Nuclear Science, vol. 17.
29. Burlin, T. E. (1966). A general theory of cavity ionisation. *The British Journal of Radiology, 39*(466), 727–734.
30. Lefort M (1966) *La chimie nucléaire: étude des noyaux radioactifs et des réactions nucléaires*. Dunod.
31. Caswell, R. S., Coyne, J. J., & Randolph, M. L. (1980). Kerma factors for neutron energies below 30 MeV. *Radiation Research, 83*(2), 217–254.
32. ICRU (2000) *Nuclear data for neutron and proton radiotherapy and for radiation protection*. Publication 63.
33. ICRU (2001) *Determination of operational dose equivalent quantities for neutrons*. Publication 66.
34. ICRU (1998) *Conversion coefficients for use in radiological protection against external radiation*. Publication 57.
35. Briesmeister, J. F. (1997). *MCNP—A general Monte-Carlo N- Particle Transport Code version 4B LA-12625-M*.
36. Faussot, A., Antoni, R. (2008). *Cours de dosimétrie fondamentale du Brevet de technicien supérieur en radioprotection*.
37. Veinot, K. G., Hertel, N. E. (2005). Effective quality factor for neutrons based on the revised ICRP/ICRU recommendations. *Radiation Protection Dosimetry*, *115*(1–4), 536–541.
38. Gayther, (1990). International intercomparison of fast neutron fluence-rate measurements using fission chamber transfer instruments. *Metrologia, 27*, 221–231.
39. Hanson, A. O., & McKibben, J. L. (1947). A neutron detector having uniform sensitivity from 10 KeV to 3 MeV. *Physical Review, 72*(8), 673–677.
40. De Pangher, J., Nichols, L. L. (1966). *A precision long counter for measuring fast neutron flux density, BNML-260*.

41. Lacoste, V. (2010). Design of a new long counter for the determination of the neutron fluence reference values at the IRSN AMANDE facility. *Radiation Measurements, 45*, 1250–1253.
42. Lacoste, V., & Gressier, V. (2010). Experimental characterisation of the IRSN long counter for the determination of the neutron fluence reference values at the AMANDE facility. *Radiation Measurements, 45*, 1254–1257.
43. Roberts, N. J., Douglas, D. J., Lacoste, V., Böttger, R., & Loeb, S. (2010). Comparison of long counter measurements of monoenergetic and radionuclide source-based neutron fluence. *Radiation Measurements, 45*, 1151–1153.
44. Holt, P. D. (1985). Passive detectors for neutron fluence measurement. *Radiation Protection Dosimetry, 10*(1–4), 251–264.
45. Alevra, A. V. (1999). Neutron spectrometry. *Radioprotection, 34*(3), 304–333.
46. Brooks, F. D., & Klein, H. (2002). Neutron spectrometry – historical review and present status. *Nuclear Instruments and Methods A, 476*, 1–11.
47. Pichenot, G., Guldbakke, S., Asselineau, B., Gressier, V., Itié, C., Klein, H., et al. (2002). Characterisation of spherical recoil proton proportional counters used for neutron spectrometry. *Nuclear Instruments and Methods A, 476*, 165–169.
48. Bramblett, R. L., Ewing, R. I., & Bonner, T. W. (1960). A new type of neutron spectrometer. *Nuclear Instruments and Methods, 9*, 1–12.
49. Vega-Carrillo, H. R., Manzanares-Acuña, E., Hernández-Dávila, Mercado Sánchez, G. A. (2005). Response matrix of a multisphere spectrometer with an ^{3}He proportional counter. *Revista Mexicana de Fisica*, *51* (1), 45–52.
50. Ing, H., Clifford, T., McLean, T., Webb, W., Cousin, T., & Dhermain, J. (1997). A simple reliable high resolution neutron spectrometer. *Radiation Protection Dosimetry, 70*(1–4), 273–278.
51. Crovisier, P., Asselineau, B., Pelcot, G., Van-Ryckeghem, L., Cadiou, A., Truffert, H., et al. (2005). French comparison exercise with the rotating neutron spectrometer, "ROSPEC". *Radiation Protection Dosimetry, 115*(1–4), 324–328.
52. Sternheimer, R. M. (1966). Density effect for the ionization loss of charged particles. *Physical Review, 145*(1), 247–250.
53. Williamson, C., Boujot, J. P., Picard, J. (1966). *Tables of range and stopping power of chemical elements for charges particles of energy 0,5 to 500 MeV*. Rapport CEA R 3042.
54. Northcliffe, L. C. (1960). Energy loss and effective charge of heavy ions in aluminum. *Physical Review, 120*, 1744–1757.
55. Pagès L, Bertel E, Joffre H, Sklavenitis L (1972) Energy loss range, and bremsstrahlung yield for 10 keV to 100 MeV electrons. Atomic Data and Nuclear Data, *4*(1).
56. Berger, M. J., Coursey, J. S., Zucker, M. A., Chang, J. Stopping-power and range tables for electrons, protons, and helium ions. http://physics.nist.gov/PhysRefData/Star/Text/ESTAR.html.
57. Heimbach, C. (2006). NIST calibration of a neutron spectrometer ROSPEC. *Journal of research of the National Institute of Standards and Technology, 111*, 419–428.

Chapter 3
Protection and Operational Dosimetric Quantities and Calibration

Abstract This chapter is devoted to protection and operational dosimetric quantities. These quantities are of paramount importance for radiation protection problems: The limit exposure of workers and public are in term of protection quantity while measurement with radiation device is in term of operational quantity. In what follows, these quantities are defined, compared and calculated for major radiation field. A final part is dedicated to the calibration of radiation protection devices.

We have seen that a tissue exposed to ionizing radiation leads the ionization of atoms that can cause impairment or death of the affected cells. Depending on the intensity of the irradiation, the risk for the body is quite different:

- At high doses, the effect is immediate and sure for an exposition to a higher dose than effect threshold, this is called deterministic effect;
- At low doses, the effect is delayed and does not appear necessarily to each person irradiated. It is a stochastic phenomenon for which there is no occurrence threshold.

Note that in the case of high-dose irradiation, besides the immediate effects, it is also observed the delayed effects with a high probability.

To assess the risks associated with ionizing radiation and consequently specify dose limits, ICRP has defined specific dose quantities. Moreover, the ICRU has defined other set of quantities to estimate ICRP quantities by measurement. This chapter describes the whole of these quantities.

3.1 Stochastic Effects

After exposure to ionizing radiation, if the alteration of a somatic cell (ordinary) causes the change in its DNA, it can remain viable. After successive cell divisions, a longer or shorter period called latency period, cancer can arise. The probability of cancer occurrence increases as the dose increases like a substantially linear

R. Antoni and L. Bourgois, *Applied Physics of External Radiation Exposure*,
Biological and Medical Physics, Biomedical Engineering,
DOI 10.1007/978-3-319-48660-4_3

relationship and probably with no threshold. This notion of probability gives a random character to that effect: two persons from same age and identical constitution having been subjected to the same dose will not react the same way, it is what we call "stochastic effects". These radiation-induced cancers take an average of several years to appear. The feedback of Hiroshima and Nagasaki shows that the maximum rate of leukemia was reached after 7 years and other cancers arised after 40 years.

A second delayed effect of random nature is the induction of malformations in the offspring of the irradiated person.

Note that the severity of the cancer is independent of the dose. Finally, let's add that we usually connect these effects at moderate and low doses, even if the probability, as said before, is increasing as the dose increases.

3.2 Deterministic Effects

Beyond a threshold, substantial damage occurs reproducibly and cause massive destruction of cells. Large-scale effects occur, which can lead to partial or permanent loss of biological function of the tissue or organ. Severity increases as the dose increases and can lead to death of the individual beyond the level of lethal dose.

These effects occur after few days or weeks, not immediately but quickly compared to the appearance of stochastic effects (medium and low doses).

Because of this reproducibility, the effects at the high doses used in radiation therapy to destroy cancer cells, focusing the dose on the tumor to be treated. This class of effect is associated indeed at high doses and in what is called the "acute radiation".

3.3 Protections Quantities

To quantify the stochastic risks related to exposure to ionizing radiation described above, ICRP [1] provides a number of quantities called "protections quantities." The radiological protection system is based on these ones. The limits are defined to keep the risk due to ionizing radiation in the same order of magnitude as the overall risks of everyday life.

3.3.1 Organ Absorbed Dose

In radiation protection, the fundamental quantity is the absorbed dose D expressed in gray (see expression 3.1). In practice, use will be made of the mean dose to the

organ or tissue (D_T). By considering a homogeneous irradiation of that organ or tissue, we can deduct the radiological contribution of each organ during exposure.

For the organ or tissue T, the absorbed dose noted D_T is obtained according to the ratio of total deposited energy E_T considered for radiation R on the total mass of the organ m_T (3.1).

$$D_T = \frac{E_T}{m_T} \tag{3.1}$$

Its SI unit is joule per kilogram (J/kg), but is given in gray (Gy). If the distribution of absorbed dose D is available (see previous chapters), then an analytical approach can be used and to be distributed on the whole of the organ or tissue considered as written (3.2).

$$D_T = \frac{1}{m_T}\int_{m_T} D\,dm = \frac{1}{m_T}\int_{m_T}\left(\frac{d\bar{\varepsilon}}{dm}\right)dm \tag{3.2}$$

$D = (\mathrm{d}\bar{\varepsilon}/\mathrm{d}m)$ is the absorbed dose distribution in the element volume dm. The mean dose to the organ or tissue (T) is the reference value from which are calculated other protection parameters: the equivalent dose to an organ and effective dose on the entire body.

3.3.2 *Radiation Weighting Factor W_R and Equivalent Dose in an Organ or Tissue*

The absorbed dose in the body is not sufficient to characterize the harmfulness of radiation. Indeed, for the same absorbed dose, we showed in Chap. 2 that high LET radiation have a greater probability of generating a biological impairment linked to the RBE. Also, to take account of this "radiation quality", ICRP 60 [1] introduced weighting factors (w_R) applicable to the absorbed dose in a tissue or organ and based on the type and quality of the radiation field.

In fact, there is a direct correspondence between the RBE at the radiation energy in presence and the value of the weighting factor w_R.

To account for this "typology" of radiation, ICRP [1] has introduced a quantity called "equivalent dose in a tissue or organ T" $H_{T,R}$ for a radiation R and given by the relation (3.3).

$$H_{T,R} = w_R\, D_{T,R} \tag{3.3}$$

When the radiation field is composed of several types of radiation having different w_R, the absorbed dose should be accordingly subdivided into different dose components, which are multiplied by their own value w_R and are added to determine the total equivalent dose according (3.4).

$$H_T = \sum_R w_R \, D_{T,R} \tag{3.4}$$

If in the SI system the results are in joules per kilogram (J/kg), the unit assigned to that quantity is the sievert (Sv).

At this stage, it should be noted the switch from a purely physical quantity D_T to this health type quantity. The values of the weighting coefficient w_R prescribed in ICRP 60 [1] are given in Table 3.1.

The choice of radiation weighting factor is directly related to the value of the maximum RBE for considered radiation (this value is obtained for the exposure of a cell, subjected to a particular dose value and a dose rate, as shown in Chap. 1).

Indeed, although the RBE varies with the dose and the dose rate, we can not in daily practice of radiation protection change its value depending on the dose. It therefore appeared necessary to choose fixed values for each type of radiation based on those of the maximum RBE in the dose range and biological effects expected. This same approach, we shall see, led to the definition of an intermediate quantity so-called "quality factor Q" for characterizing "operational quantities".

Note that for radiation whose characteristics do not match those in Table 3.1, the value w_R must be calculated from the value of a mean quality factor $\overline{Q}$ that we will define later in the section related to the operational quantities.

Finally, add that ICRP 60 [1] also provides a weighting factor for neutrons on the basis of an analytical expression involving neutron energy E_n and defined in expression (3.5).

$$w_R(E_n) = 5 + 17 \exp\left[\frac{-(\ln(2E_n))^2}{6}\right] \tag{3.5}$$

Table 3.1 Value of radiation weighting factor w_R [1]

Type and energy field	Radiation weighting factor, w_R
Photons all energies	1
Electrons and muons all energies	1
Neutron energy <10 keV	5
Neutron energy between 10 and 100 keV	10
Neutron energy of 100 keV–2 MeV	20
Neutron energy of 2–20 MeV	10
Neutron energy >20 MeV	5
Protons, other than recoil protons, energy >2 MeV	5
Alpha particles, fission fragments, heavy nuclei	20

3.3.3 Tissue Weighting Factor and Effective Dose

The relationship between the probability of stochastic effects (cancer occurrence probability) and equivalent dose also varies depending on the organ or tissue irradiated. It is therefore appropriate to define an additional factor, coupled with the equivalent dose to represent the contribution of that organ or tissue to overall radiation detriment from stochastic effects for an uniform irradiation of the whole body.

This factor by which the equivalent dose is weighted is called "tissues weighting factor" (w_T). The sum of the weighted equivalent doses expressed by expression (3.6) is called "effective dose" and noted E. The unit is the sievert (Sv).

$$E = \sum_T w_T H_T = \sum_T w_T \sum_R w_R D_{T,R} \tag{3.6}$$

The recommended values ICRP 60 [1] for the tissue weighting factors are given in Table 3.2.

The reader will infer that the sum of all tissue weighting factors w_T is 1. To illustrate an instantaneous result of this feature, let's consider a person exposed uniformly on the whole body with a highly penetrating radiation, offering little attenuation in the human body. We can assume that each organ is then subjected to the same value of mean dose D_T at the organ. In addition, if the radiation field is composed exclusively with photons, the radiation weighting factor w_R is 1 and the equivalent dose H_T to each organ is equal to the mean dose value D_T. Finally, as the sum of weighting factors w_T is 1, the effective dose E is in fact equal to D_T. Thus, for a highly penetrating radiation with $w_R = 1$, we can approximate the effective dose by the organ dose regardless of the organ.

$$E \cong \sum_T w_T D_T = D_T \sum_T w_T = D_T \quad \forall T \tag{3.7}$$

In this case, there is direct correspondence between the physical quantity and the health quantity, namely 1 gray is substantially equal to 1 Sv. Accordingly, in

Table 3.2 Value of the tissue weighting factor w_T adapted from [1]

Tissue or organ	Tissues weighting factor, w_T	Tissue or body	Tissues weighting factor, w_T
Gonads	0.2	Liver	0.05
Bone marrow (red)	0.12	Esophagus	0.05
Colon	0.12	Thyroid	0.05
Lungs	0.12	Skin	0.01
Stomach	0.12	Bone surface	0.01
Bladder	0.05	Other	0.05
Breast	0.05		

practice, when an operator performs a measurement in a homogeneous field of high-energy photons with a radiation meter calibrated in absorbed dose (Gy), he assesses fairly accurately the effective dose (Sv).

Add that the term "whole body dose" is commonly associated with to the effective dose quantity, even if this designation do not exist right now in any standard.

Note that this trivial demonstration becomes completely wrong with radiation field whose $w_R \neq 1$ or weakly penetrating. In fact, they are strongly attenuated and organs position are asymmetric in the body (mostly situated forward thereof) induces a substantially equivalent dose different from one organ to another.

Finally, the mean absorbed dose to an organ D_T can not reflect in any way the effective dose E. It can be a source of confusion for unwary people, especially in radiological incidents or accidents in radiotherapy contexts related to the cancer treatment. Indeed, in the field of radiotherapy, the mean dose delivered to an organ target, is absolutely not representative of the whole body dose; all organs do not undergo the same exposure, none, for some. However, by assigning the weighting factor w_T ad hoc to target organ, and those on the periphery that have undergone "collateral" irradiation, it is possible to assess the effective dose from this medical process. The effective dose that results is, indeed, very lower in absolute terms, compared with the mean dose to the target organ. This distinction can be extrapolated to radiological accidents or incidents: a localized dose of 10 Gy at the basal layer of the skin during an accidental exposure is absolutely not representative of the whole body dose, especially if it is caused by weakly penetrating radiation (e.g. β radiation).

While the whole of protection quantities and values of tissue or radiation weighting factor are currently based on those established in ICRP 60 [1], they can be subject to changes, in particular over the new publications ICRP. The recommendations in publications 103 [2] and 116 [3] of ICRP commission could, in the medium-term, be included in the regulations (see Sect. 3.9). Thus, as with any regulations related to safety, it is fundamental to maintain a regulatory monitoring in order to integrate new requirements.

3.3.4 Quantifying Risks for Stochastic Effects

ICRP 60 [1] and more recently ICRP 103 [2] propose a number of datas linking levels of effective dose *E* to the probability of cancer occurrence, especially in a context of low and medium doses. These datas are largely based on the consequences of experience feedback of Hiroshima and Nagasaki.

Cancer rates for a population subjected to irradiation of 1 mSv is about 4 cases per 100 000, i.e. an occurrence probability of $4 \cdot 10^{-5}$.

The second effect that may arise, even if, until now, it has never been observed, is the induction of malformations for the offspring of the irradiated person, that is termed "hereditary effect". It is assumed that the risk of genetic mutation leading to

this effect is 1 per 100 000 parents exposed to a dose of 1 mSv. This time which corresponds to a probability of 10^{-5}.

For example, in France, knowing that the natural and medical exposure level are respectively 2.4 and 1.3 mSv [4] for a population of 60 million inhabitants, it is assessed that for 120,000 reported cancer per year, 7500 and 3000 are due to these exposures, without being able to prove it. Indeed, it is difficult to disentangle these effects from those caused by other types of risk such as exposure to chemicals, for example.

Although we admit that there is no threshold for the occurrence of these effects, no identification of these diseases has been made, below an effective dose of 100 mSv delivered with a high dose rate.

3.3.5 *Recommended Limits for Radiological Exposure*

In its publication 60 [1], ICRP considers the acceptability of risk radiation-induced in absolute way and not by comparison with other types of risks. Thus, as described above, based on a lethal cancer risk of 4% per sievert for workers (aged 18–65) and 5% per sievert for the population (all ages) ICRP considers that the tolerable maximum limit is 1 Sv for workers and 70 mSv for public. The annual dose limits are deducted from this approach: either 20 mSv for the workers (with excess authorized up to 50 mSv in 1 year but less than 100 mSv per 5 years) and 1 mSv for the public. These limits are also included in ICRP 103.

The Table 3.3 displays the whole of exposure limits recommended by ICRP 103.

The new European directive 2013/59 [6] laying down basic standards for health protection against ionizing radiation has taken into account the recommendations of ICRP 103 incorporating the recommendation of the new limits for the lens equivalent dose. European countries will have to incorporate these limits in their future regulations. These limits are summarized in Table 3.4.

Table 3.3 Limit exposure of workers and the public from the recommendations of ICRP 103 [2]

Organ exposure	Quantities	Limit worker	Public
Full body	Effective dose E	20 mSv per year[a]	1 mSv per year
Hands, feet	Equivalent dose $H_{T,R}$	500 mSv per year	50 mSv per year
Skin	Equivalent dose $H_{T,R}$	500 mSv per year[b]	50 mSv per year[b]
Lens	Equivalent dose $H_{T,R}$	150 mSv per year[c]	15 mSv per year[c]

[a]With excess authorized up to 50 mSv in 1 year but less than 100 mSv per 5 years

[b]This limit applies to the dose averaged over any area of 1 cm^2 regardless of the exposed surface. It is assessed now by the local skin dose

[c]Note that in 2011 ICRP [5], following epidemiological studies, reviewed the dose limit to the lens and recommends, for workers 20 mSv per year (with excess authorized up to 50 mSv in 1 year but less than 100 mSv per 5 years)

Table 3.4 Workers Exposure Limits and the public based on the recommendations of the new European directive 2013/59 [6]

Type exposure	Quantities	Workers[a] limit	Public
Full body	Effective dose E	20 mSv per year[b]	1 mSv per year
Hands, feet	Equivalent dose $H_{T,R}$	500 mSv per year	–
Skin	Equivalent dose $H_{T,R}$	500 mSv per year[c]	50 mSv per year[c]
Lens	Equivalent dose $H_{T,R}$	20 mSv per year[b]	15 mSv per year

[a]The workers belong to two categories: those that may exceed an effective dose of 6 mSv per year (or more than 15 mSv/year in Lens or over 150 mSv/year hand or skin) are category A, others category B

[b]On average over 5 years with excess authorized up to 50 mSv year

[c]This limit applies to the dose averaged over any area of 1 cm^2 regardless of the exposed surface. It is now assessed by the local skin dose

Let us add that these limits apply to combine the whole of exposure, namely external and internal. For internal exposure, which is not addressed in this book, there is a dedicated coefficient "Effective dose coefficients for ingested and inhaled particulates" whose unity is the Sv/Bq, which links the amount of radionuclide inhaled or ingested (Bq) to the effective dose.

Moreover, the protection quantity to which are attached the exposure limits in the case of the extremities—hands, skin …—is the equivalent dose to the organ. It is relevant to figure out this specification and, in particular, when applied for the skin.

The value of 500 mSv is the deterministic effects threshold and it is necessary to consider that, this time, the limit is prescribed, not for stochastic effects, but to prevent acute radiation syndrome (e.g., erythema for the skin).

In the case of the skin, this approach is accompanied by the obligation to compare this limit to the 1 cm^2 area of the most exposed skin and not on the 2 m^2 area of skin that covers the body in the calculation of the equivalent dose to the skin. Remember that this latest intermediate calculation take part in the determination of the effective dose E to the whole body.

3.3.6 Calculation of Protection Quantities

A fundamental characteristic of the protection quantities is that they are only calculable. This specificity immediately raises the issue of measurement, particularly since the exposure limits are based on the protection quantities. We will discuss later that ICRU physicists have offset this inconsistency, offering measurable operational quantities.

Let's focus on the various assumptions and techniques to calculate the protection quantities.

Geometries' irradiation

The human body can be subjected to radiation from all directions. Conventionally, a number of radiation geometries were chosen to perform theoretical calculations needed to determine the reference value which is the mean absorbed dose in the organ or tissue. Note that the organs in a human body are not arranged symmetrically (bone marrow is closer to the back side than the front side and vice versa for the gonads). It is clear that if an individual is exposed on the front side of the body (geometry anteroposterior or AP by ICRP 74 [7]), on the back side of the body (posteroanterior or PA) or from either side of the body (lateral or LAT when it is necessary to be more specific, two following symbols are used LLAT from the left side to the right side of the body and RLAT from the right side to the left side of the body). Note that, for weakly penetrating radiation (highly attenuated by the human body) the mean doses to organs and therefore equivalent doses will differ significantly.

In general, we will retain that the organs are located preferentially forward. Irradiation in anteroposterior geometry, in a first approach, involves more exposure than its opposite posterior-anterior.

In all cases, for different irradiation geometries, a large and homogeneous incident beam is considered. Six Geometries are recommended by ICRP:

- Antero-posterior geometry (AP). The irradiation geometry in which the ionising radiation is incident on the front side of the body in a orthogonal direction to the long axis of the body.
- Poster-anterior geometry (PA). The irradiation geometry in which the ionising radiation is incident on the back side of the body in a direction orthogonal to the long axis of the body.
- Lateral geometry (LAT). The irradiation geometry in which the ionising radiation is incident from either side of the body in a direction orthogonal to the long axis of the body. When it is necessary to be more specific, the following symbols are used: RLAT (from the right side to the left side of the body) or LLAT (from the left side to the right side of the body).
- Rotational geometry (ROT). The geometry in which the body is irradiated by a parallel beam of ionising radiation, from a direction orthogonal to the long axis of the body, which rotates at a uniform rate around the long axis. Alternatively, this geometry may be defined by rotating the body at a uniform rate about its long axis, while irradiating the body by a broad beam of ionising radiation from a stationary source located on an axis at right angles to the long axis of the body.
- Isotropic geometry (ISO). Defined by a radiation field in which the particle fluence per unit of solid angle is independent of direction.

Figure 3.1 displays these different configurations of irradiation.

Protection quantities computational techniques

As mentioned above, the effective dose E and organ equivalent dose H_T are accessible by calculation and not by measure. To access these two protection

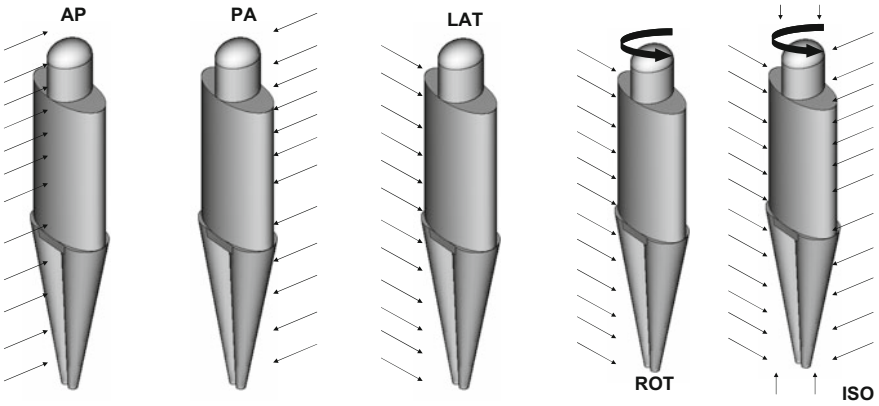

Fig. 3.1 Irradiation geometries for the calculation of the effective dose E

quantities, first, the reference value that is the mean absorbed dose D_T for each organ or tissue (T) must be determined.

Initially, this quantity was determined using a solid phantom tissue-equivalent materials, modeled on a standard human, in which were incorporated dosimeters (e.g. LiF) to volumes of tissue-equivalent material embodying each organ. The phantom was then subjected to different irradiation geometries described above. A weighted average based on the weight of the organ allowed the obtaining of the mean absorbed dose D_T. This method had the disadvantage to estimate the mean absorbed dose depending on the number and location of embedded dosimeters, for an experimental device more binding.

In recent years, virtual anthropomorphic phantom (MIRD), also called mathematical phantom, modeled with Monte Carlo codes is substituted for this process. The mean absorbed dose in various organs is rigorously obtained using appropriate statistical estimator (see Chap. 6). The phantom of simplified model used is composed of simple geometric shapes, which does not induce significant differences on dosimetric quantities sought, compared with an accurate representation of the human body.

Note that two MIRD phantom are available depending on sex: ADAM (male) and EVA (female). Figure 3.2 gives a mathematical phantom (MIRD) representation used for the calculations of protection quantities. The ICRP publication 74 [7] rely on this phantom for the whole of calculations.

Figure 3.2b shows the materialization of the transport of the particles from a point source in a MIRD phantom calculated with a Monte-Carlo code. For calculations of the mean doses to the organ, different geometries presented above are modeled; in addition of point sources, it is possible to simulate unidirectional emission planar sources or volume sources (Chap. 6). Note that the release of 116 ICRP [3] changes the geometry phantom advocating "voxelised" phantom (cf. Sects. 3.4.6 and 3.9).

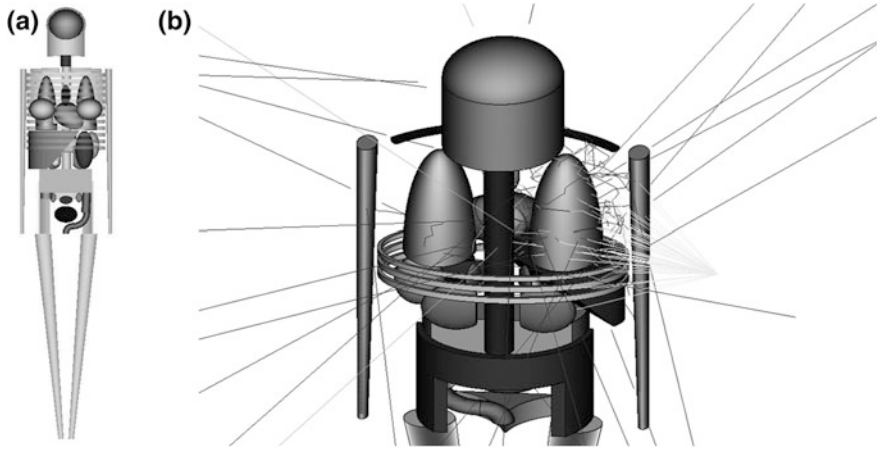

Fig. 3.2 **a** View of an anthropomorphic phantom type MIRD (defined in ICRP). **b** Example of calculation Monte Carlo with materialization of the path of the transported particles [8]

Special case: calculating the skin equivalent dose

The skin equivalent dose calculation is a special case with two possible numerical models: a model for effective dose—on the whole body—another for extremities exposure.

For effective dose calculation, the tissue "skin" is characterized by a surface of about 2 m^2 in the anthropomorphic phantom MIRD. For skin thickness, the Shultz and Zoetellief approach [9], adopted by the publication of 74 ICRP [7], recommends a "sensitive skin" thickness of 0.193 cm between the depths of 0.007 cm (70 μm) and 0.2 cm. Upstream of 70 μm, the model specifies the presence 'thick dead skin'. Both layers have the same density of 1.105. Downstream of the thickness of "sensitive skin", a layer of "soft tissue" of 2 cm is attached whose essential function is to take into account the backscattering radiation of electrons and neutrons; its density is 0.987. Figure 3.3 illustrates this model.

Thus, we can roughly calculate the total mass m_T of this tissue. This data is necessary to calculate the absorbed dose to the organ D_T of expression (3.2) as following:

$$m_T = m_{skin} = (\rho\, V)_{\text{sensitive skin}} = (\rho \times S)_{\text{sensitive skin}} \cong 1.105 \times 0.193 \times 2 \cdot 10^4 \cong 4\,\text{kg}$$

with x the "sensitive skin" thickness and S the area covered. With the total energy imparted in the skin $E_{T,skin}$ and the knowledge of radiation weighting factor w_R, we deduce the equivalent dose to the skin H_{skin}. For example, for photons, i.e. $w_R = 1$, and an energy imparted in the skin volume of 0.2 J, we get the following result:

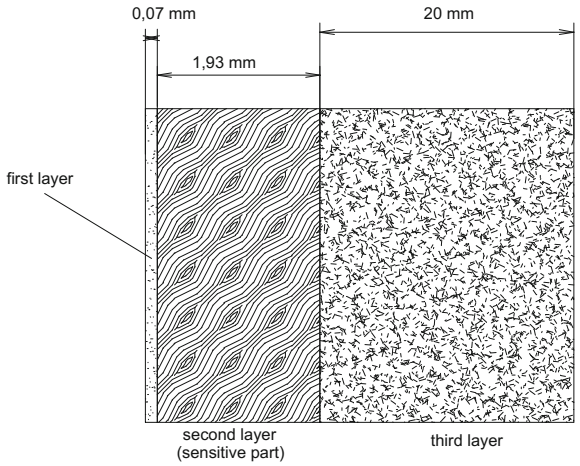

Fig. 3.3 Skin Model in MIRD phantom for calculating the equivalent dose to the skin H_{skin} retained by ICRP 74

$$H_{skin} = w_R(\gamma)\, D_{skin,\gamma} = w_R(\gamma)\left(\frac{E_{T,skin}}{m_{skin}}\right)_{\gamma} = 1 \times \left(\frac{0.2}{4}\right) = 0.05\ \text{Sv}$$

As a consequence, by weighting the result by $w_{skin} = 0.01$ (Table 3.2) we deduce the skin equivalent dose to calculate the effective dose E:

$$w_{skin} H_{skin} = 0.01 \times 0.05 = 0.5\ \text{mSv}$$

For the extremities, the approach is significantly different. As stated in the Table 3.3, the skin limit corresponds to the threshold value of the equivalent dose at which deterministic effects arise: 500 mSv. It must be considered the most exposed area of the skin to prevent not stochastic risks but deterministic associated with intensive exposure of the skin (erythema, pigmentation …). This maximum exposure area can not be punctual, also a maximum of 1 cm^2 exposed area was adopted as shown schematically in Fig. 3.4.

The estimated skin dose constituted a problem for radiation protection, especially for reconstruction dose in accident context. Either this dose was estimated using the model adopted by ICRP 74 [7] described above, or from the calculation at a 70 μm depth of skin to estimate the skin dose by the operational quantity $H_p(0.07)$ (see Sect. 3.5.4). But Bourgois [10] showed that both approaches give, for the β particles, significantly different values.

To overcome this issue, ICRP 116 introduced a new protection quantity: the "Local skin dose," in which a 10 × 10 × 10 cm^3 cube is exposed to a circular parallel beam of radius 3.5 cm. The mean absorbed dose is calculated in a cylindrical volume of 1 cm^2 area and 50 μm height, centred on the cube and located 50 μm from its surface.

Fig. 3.4 Illustration of the region of greatest exposure for the calculation of the equivalent dose to the organ H_{skin} in the context of extremities exposure

An absorbed dose profile D_t is provided by Bourgois [10], deepending on the depth to radiation β of a ^{18}F punctual source in contact with the skin (Fig. 3.5). This profile is calculated in two ways: by means of the Monte Carlo MCNPX code and using the semi-empirical dose equations from Cross [11], as described in Chap. 2.

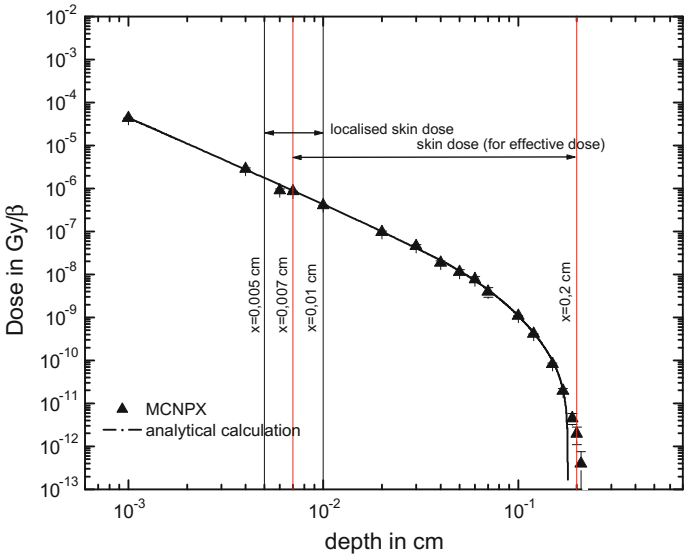

Fig. 3.5 Profile of the absorbed dose point $D_t(x)$. In the region of "sensitive skin" obtained by Monte-Carlo computation and by analytical calculation, for a punctual source ^{18}F (β^+) (according to the data [10]). Also shown the scoring geometry for the skin dose and local skin dose calculation

The calculation scoring geometry are shown in Fig. 3.5: Shultz and Zoetellief's Model (between 70 μm and 2 mm) and the ICRP 116's model for "Localised skin dose" (between 50 and 100 μm).

Conversion Factors

The mean absorbed dose to the organs can be calculated by a Monte-Carlo method described above. Also it becomes relevant to define conversion factors that allow converting physical quantities (K_a, ϕ …) in mean organ dose.

Thus, for each type of external radiation (photons and neutrons), for each radiosensitive organ (Table 3.2), for each irradiation geometry and depending on the incident radiation energy, the theoretical calculation has determined a conversion factor which is the ratio of the reference D_T to the radiation field physical quantity.

The characteristic physical quantity for photons field is the air kerma (as specified in Chap. 1); the conversion factor, for an energy E, is the "Kerma air-mean organ dose" and expressed as: $(D_T/K_a)_E$ in Gy/Gy. Figure 3.6 provides the conversion factor curves "kerma air-mean organ dose" versus photon energy.

The characteristic physical quantity for neutrons field is the fluence; the conversion factor, for an energy E, is: D_T/Φ in pGy cm^2. Figure 3.7 gives the conversion coefficient curves as a function of neutron energy.

The considered geometry for the "Local skin absorbed dose" for α and β, introduced by ICRP 116, is a 10 × 10 × 10 cm^3 cube exposed to a circular parallel beam of 3.5 cm radius. The mean absorbed dose is calculated in a cylindrical volume of 1 cm^2 cross section area and 50 μm height, centred on the cube and located 50 μm from its surface. The Figs. 3.8, 3.9 and 3.10 give the values of the fluence-local skin dose respectively for electrons, alphas and positrons.

To assess the conversion factors of "characteristic physical quantity-mean organ dose", it is necessary to know the characteristics of the incident radiation field; this one is idealized and considered as homogeneous on the organ. Note that this assumption is realistic for highly penetrating radiation, but less reliable for weakly

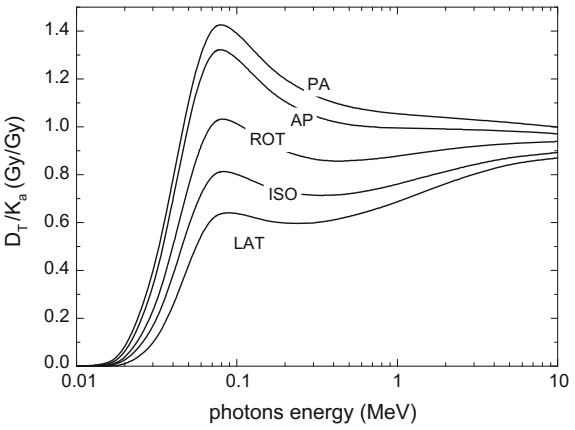

Fig. 3.6 Conversion factor "Kerma air-mean organ dose" for the lungs, according to the photon energy, for all irradiation geometries calculated using a Monte Carlo code on the anthropomorphic phantom (MIRD), from data [7]

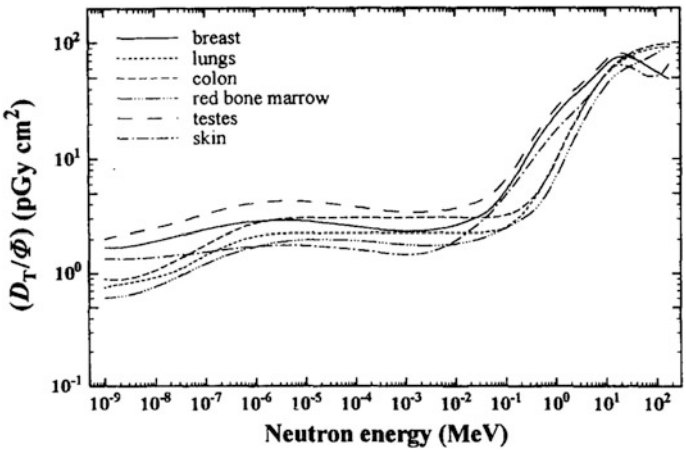

Fig. 3.7 Conversion factor "fluence-mean organ dose" based on the neutron energy, anteroposterior geometry, calculated using a Monte Carlo code on the anthropomorphic phantom (MIRD), from [7]. Reproduced by permission of Michiya Sasaki on behalf of ICRP

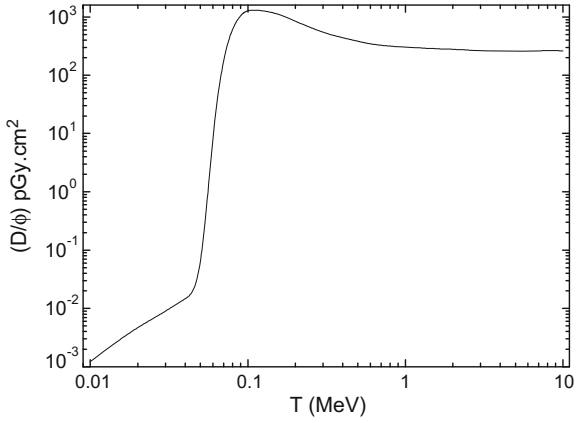

Fig. 3.8 Fluence-local skin dose conversion coefficient (D/ϕ) in pGy cm^2 for mono-energetic electrons (from ICRP 116 datas)

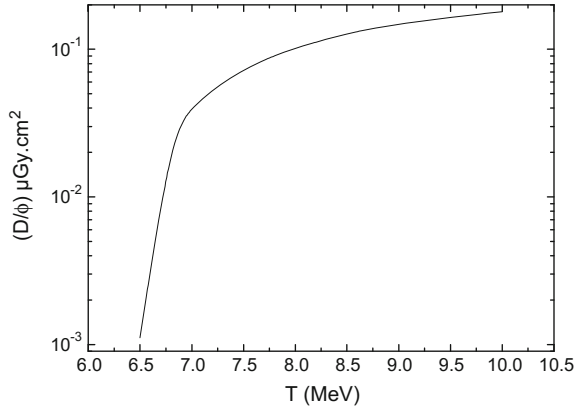

Fig. 3.9 Fluence-local skin dose conversion coefficient (D/ϕ) in pGy cm^2 for mono-energetic alpha particles (from ICRP 116 datas)

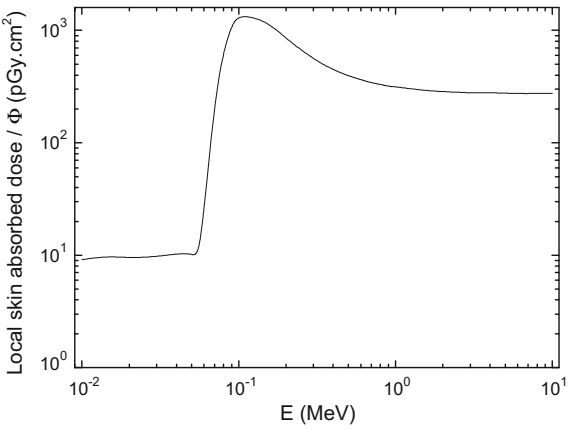

Fig. 3.10 Fluence-local skin dose conversion coefficient (D/ϕ) in pGy cm^2 for mono-energetic positrons (from Bourgois and Antoni datas [50])

penetrating radiation field (low energy radiation). The fluence and the air kerma are calculated at each energy at a "mid-point" located in barycentric center of the phantom, representative of the radiation field through the whole body. Calculating the mean absorbed dose to various organs is achieved by Monte Carlo calculations. The conversion coefficient is, finally, the ratio of the calculated value to the physical quantity of the "middle point" beam, in the absence of phantom, as shown in the diagram of Fig. 3.11.

So now, knowing the characteristic physical quantity, let's determine the value of the mean dose D_T to organ T by the appropriate conversion factor.

For mono-energetic electrons, the conversion factor provides the ratio of the mean dose D_T to electron fluence for each radiation-sensitive organ for a single geometry: the AP geometry. Only this geometry is relevant for low penetration particles.

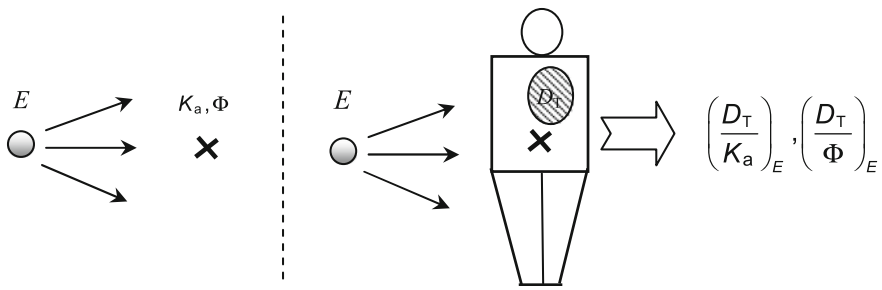

Fig. 3.11 Schematic diagram of conversion coefficients calculation for a energy particles *E*

For the other two protection quantities (organ equivalent dose H_T and effective dose E), once the mean absorbed dose is calculated for each of the organs, the calculations become fairly simple. All these conversion factors are available in ICRP 74.

Protection quantities calculation from the ICRP 74 [7] conversion factors

For example, let's consider the simple case of AP exposure of a photon field, characterized by a mono-energetic fluence $\phi_\gamma = 2 \cdot 10^6$ (γ) cm^{-2} with $E_\gamma = 1$ MeV. ICRP 74 provides the conversion coefficients $(D_T/K_a)_{E\gamma}$ "air kerma-mean organ dose" for each organ. At this point, we could calculate the air kerma at the calculation point caused by the fluence ϕ_γ for 1 MeV photons (see Chap. 2). However, this same ICRP 74 provides factors air kerma to fluence at a point $(K_a/\Phi)_{E\gamma}$; these were calculated in Chap. 2. We therefore deduce the value of the mean dose to organ from the fluence of the radiation field in each organ depending on the product (3.8).

$$\left(\frac{D_T}{K_a}\right)_{E_\gamma}\left(\frac{K_a}{\Phi}\right)_{E_\gamma} = \left(\frac{D_T}{\Phi}\right)_{E_\gamma} \Rightarrow \quad D_T = \left(\frac{D_T}{\Phi}\right)_{E_\gamma} \Phi(E_\gamma) \tag{3.8}$$

The Table 3.5 provides the mean absorbed dose calculated for each organ with energy and fluence of this example.

Each organ equivalent doses, and effective dose for the same incident beam are obtained according to the expressions (3.4) and (3.6). For photons, the weighting factor w_R is 1. The tissue weighting factors for each organ are provided in Table 3.2.

Table 3.6 gives, for the example above, the organs equivalent doses, the tissue weighting factor w_T and the product of both.

Finally the effective dose is obtained by summing the whole of products of the right column:

$$E = \sum_{organe} w_T H_T = 8\,\mu Sv$$

Table 3.5 Mean absorbed doses to the organ calculated from the conversion factors "fluence-mean absorbed dose to an organ" from ICRP 74 [7], for 1 MeV photons and $2 \cdot 10^6$ (γ) cm^{-2} fluence

Organ	D_T/Φ (pGy/cm^2)	D_T (μGy)	Organ	D_T/Φ (pGy/cm^2)	D_T (μGy)
Gonads	4.65	9.30	Liver	4.42	8.84
Bone-marrow (red)	3.47	6.94	Oesophagus	3.69	7.37
Colon	4.45	8.91	Thyroid	5.49	1.10
Lung	4.39	8.78	Skin	4.29	8.57
Stomach	4.73	9.46	Bone surface	3.82	7.64
Bladder	4.78	9.56	Rest of the body	4.02	8.04
Breast	4.95	9.90			

Table 3.6 Organs equivalent dose calculation H_T, and product $H_T w_T$ for 1 MeV and $2 \cdot 10^6$ (γ) cm^{-2} photons

Organ	D_T (μgy)	H_T (Sv)	w_T	$H_T \cdot w_T$ (Sv)
Gonads	9.30	9.30	0.20	1.86
Bone marrow (red)	6.94	6.94	0.12	0.83
Colon	8.91	8.91	0.12	1.07
Lung	8.78	8.78	0.12	1.05
Stomach	9.46	9.46	0.12	1.14
Bladder	9.56	9.56	0.05	0.48
Breast	9.90	9.90	0.05	0.50
Liver	8.84	8.84	0.05	0.44
Oesophagus	7.37	7.37	0.05	0.37
Thyroid	1.10	1.10	0.05	0.55
Skin	8.57	8.57	0.01	0.09
Bone surface	7.64	7.64	0.01	0.08
Remainder	8.04	8.04	0.05	0.40

The conversion factors for both quantities are also available in ICRP 74 [7]. Figures 3.12 and 3.13 give ratios of the effective dose to air kerma (Sv/Gy) for photons and the effective dose to the fluence (pSv cm^2) for neutrons and this for various irradiation geometries.

For neutron and photon radiation, the anteroposterior (AP) geometry is responsible of the highest effective dose. This geometry is the most penalizing irradiation, because the critical organs are located, for most of them, to the front side of the body.

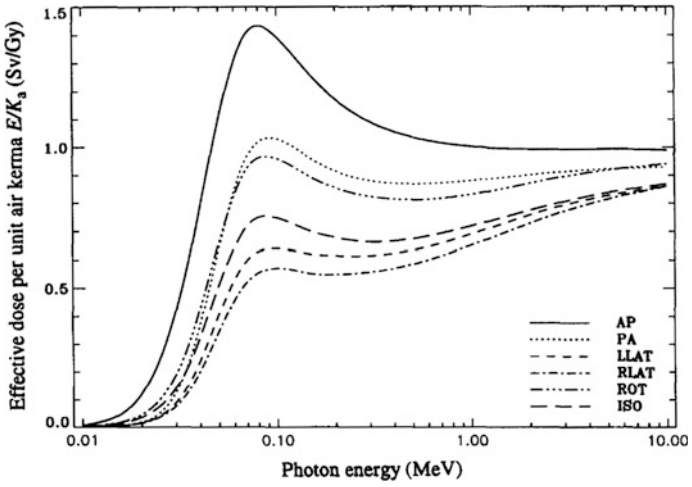

Fig. 3.12 Effective dose E per air kerma (K_{air}) according to [7]. Reproduced by permission of Michiya Sasaki on behalf of ICRP

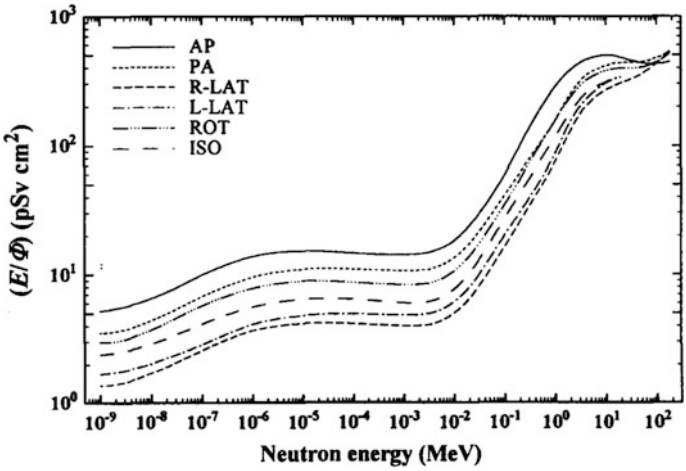

Fig. 3.13 Effective dose E per unit neutron fluence Φ. According to [7]. Reproduced by permission of Michiya Sasaki on behalf of ICRP

Note that in ICRP 74 all data relating to the conversion factors are tabulated, allowing easier access to the coefficient values.

Regarding the previous example, so it is possible to get an effective dose E immediately without passing through the previous steps. Thus, for an 1 MeV energy, using the composition of previous factors: $(E/K_a)(K_{at}/\phi)_{E\gamma}$, the effective dose is obtained by means of a single calculation, as follows:

$$E = \left(\left(\frac{E}{K_{air}}\right)\left(\frac{K_{air}}{\Phi}\right)\Phi\right)_{1\,\mathrm{MeV}}$$
$$= 1.003\,\mathrm{Sv/Gy} \times 4.11 \cdot 10^{-12}\,\mathrm{Gy\ cm^2} \times 2 \cdot 10^6\,\mathrm{cm^{-2}} = 8\,\mu\mathrm{Sv}$$

It provides the same value than the previous calculation. For strongly penetrating radiation, the expression (3.7) is reliable, indeed, D_T averaged over all organs is about 8 μGy and as w_R = 1:

$$E \cong D_T = 8\,\mu\mathrm{Sv} \quad \forall T$$

We are, therefore, in the unique configuration, where physical unit can be substituted by the health unit: Gy = Sv.

Finally, for comparison, Fig. 3.14 gives a representation of the variation of the photons conversion factor "air kerma-effective dose" (E/K_a), depending on the incidence angle of a photons parallel beam, for three energies 1.25 MeV, 90 keV and 45 keV, calculated on the MIRD phantom.

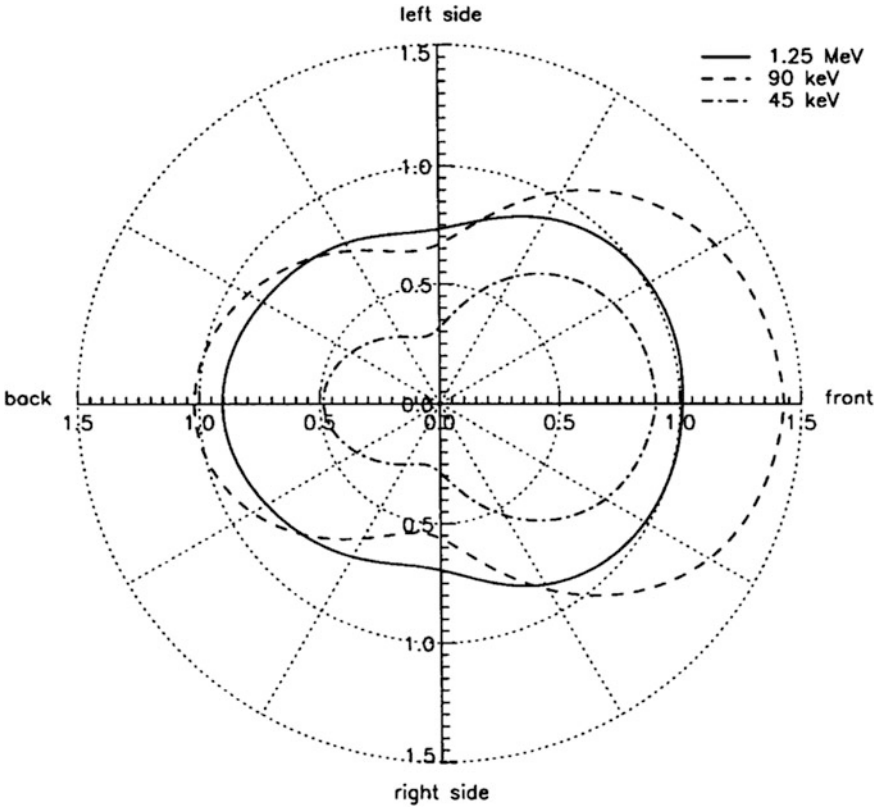

Fig. 3.14 The angular variation of effective dose for photons (ii): effective dose per unit air kerma in free air, (E/Kat) for monoenergetic parallel proton beams at various angles on an adult anthropomorphic computational model. The direction of incidence is orthogonal to the long axis of the body (according to [7]). Reproduced by permission of Michiya Sasaki on behalf of ICRP

We have established the methods and assumptions for calculating the protection quantities effective dose context or equivalent doses to the extremities. These quantities must be now compared to the exposition limit for a worker.

Effective doses during medical procedures

It is relevant to provide orders of magnitude of organ doses and effective doses during medical procedures. The Table 3.7 gives the values of organ doses and effective doses (according to ICRP 103) for scanning acts and Table 3.8 for radiography acts. These values are derived from [12].

In what follows, we will strive to detail computational techniques, also largely based on the Monte Carlo method, for contexts of radiological incidents and accidents. If these methods are quite similar to those used to characterize the dose in radiotherapy and nuclear medicine, these scopes will not be treated in this book.

Table 3.7 Effective dose values for CT exams [12]

Computed tomography (CT)	Mean effective dose (mSv)	Average organs absorbed dose in the explored area (mGy)
Skull with CI	2.4	70
Skull without CI	1.7	50
Thorax with CI	7.9	20
Thorax without CI	6.9	20
Abdomen and pelvis with CI	15.5	35
Abdomen and pelvis without CI	9.6	20
Thorax, abdomen and pelvis with CI	18.3	25

CI contrast injection

Table 3.8 Effective dose values for radiology examinations [12]

Radiology (adults)	Mean effective dose (mSv)	Organs average absorbed dose in the explored area (mGy)
Thorax	0.05	Breasts: 0.05, lungs: 0.2
Thorax with chest skeleton	0.75	Breast: 3, lungs: 1
Abdomen without preparation	1.1	stomach, colon, uterus: 2, ovary: 1.5
Lumbar segment of the spine by 1–3 impacts	2	stomach: 3, colon: 5, uterus, ovaries: 6
Pelvic (pelvis) by 1 impact	0.75	colon, uterus: 1.5, ovary: 1, testes: 5
Coxo-femoral articulation by 1 or 2 impact	0.2	ovary, uterus: 1, testes: 3, colon: 0.5

3.4 Absorbed Dose Calculation for Deterministic Risk Evaluation

3.4.1 Quantifying for Deterministic Effects

For high doses, it is ensured that beyond an effective dose threshold of 500 mSv, deterministic effects appear. Their severity is directly connected to the absorbed dose level. Due to the high level Exposure, these effects are also called “acute radiation syndrome”.

Beyond this threshold, the importance of biological damage becomes substantially independent of the nature and the type of radiation. Acute radiation syndromes are then directly connected to the physical dose distributed in the organ or tissue. Dosimetric variables related to deterministic effects are therefore absorbed dose to the organ D_T obtained according to the expressions (3.1) and (3.2), or in the case of heterogeneous biological medium, the absorbed dose (which is the punctual

quantity for the dose characterization), whose units are Gy instead of the Sv. In the case of the whole body, if it is uniformly exposed and acutely, we may assume that this is an average of the set of absorbed doses to each organs.

It should distinguish syndromes for irradiation of whole body of those affecting an organ or a given tissue.

3.4.2 Deterministic Effects for Acute Radiation

Occurrence thresholds for deterministic effects for acute exposure of the body are substantially the following:

- Below an effective dose of 500 mSv, no appearance of deterministic effects;
- A mean absorbed dose on whole body between 500 mGy and 2 Gy, there is little temporary changes in blood count, vomiting, fatigue;
- from 3 Gy, appearance of the hematopoietic syndrome, characterized by the destruction of the bone marrow. Whereas between 4 and 6 Gy, the effect may be reversible, destruction is complete from 8 Gy;
- At 5 Gy, the semi-lethal dose (LD_{50}) is reached and without medical treatment led to a 50% risk of death;
- Since 10 Gy, the gastrointestinal syndrome appears, which is characterized by destruction of the intestinal mucosa, and leads to death within weeks after radiation;
- Beyond 15 Gy, central nervous system injury characterized by a general disruption of vital functions. Death is unavoidable in the hours following the irradiation.

3.4.3 Deterministic Effects for Acute Radiation on Organ and Tissue

A acute radiation from about 3 Gy on skin generates redness, called erythema or radiodermatitis. At higher doses, the irradiation generates successively, depending on doses: pigmentation, hair removal, ulceration and necrosis.

In the gonads, for male, the syndrome is temporary sterility. The higher the dose, the greater the infertility period is long (several years for a 6 Gy dose); and in female, ovarian irradiation at a dose greater than about 6 Gy also produces sterilization.

Irradiation from about 5 Gy on eye may produce a cataract.

Embryo is particularly radiosensitive. The damage produced depends on the stage of development. During the organogenesis period (organs' formation, from the 8th to 60th day), irradiation can induce malformations. Later, the malformation

risk decreases, but a risk of delayed mental development occurs mainly for radiation occuring between the 8th and the 17th week.

In the field of deterministic effects, the damage severity to health increases with dose. In case of an accidental strong dose irradiation, the absorbed dose (Gy) value to the most exposed location on human body must be estimated, instead of the equivalent dose to an organ or the effective dose (Sv). From this estimate, we can then determine deterministic effects that may occur and the best medical countermeasures to apply.

3.4.4 Absorbed Dose Calculation for a ^{18}F Contamination

For instance, let's consider the problem of an incident during handling involving vials containing a solution of ^{18}F (β^+). An operator, following a handling error, is contaminated with two drops of this solution, fallen on his forearm.

To assess the absorbed dose in forearm and its distribution, a numerical simulation of the scene is carried out using a Monte Carlo (MCNP) code. The model chosen is simplified: forearm modeled by a cuboid soft tissue. Figure 3.15 gives a overview of the scene as modeled in the code.

The model, as faithful as possible, is taking into account the shape of the contamination spots. These two spots are the sources geometry considered for the simulation. Figure 3.16 provides the calculated isodose curves with a dose estimator in a mesh grid in 3D on a sectional plane passing through the center of two contamination spots.

The results are here provided in absorbed dose rate (Gy/h). The isodose curves representation shows how the absorbed dose is distributed in depth and how it decreases. There is a substantial and rapid reduction of the absorbed dose in function of depth of tissue exposed: the high deposited dose generated by the both contamination spots, on a superficial thickness, is due to the β^+ slowing down. The deposition of significantly lower dose is attributable to the annihilation photons of these β^+.

This computational approach is required to determine the deposited dose at the most exposed cm^2, which would be compared to the extremity limits.

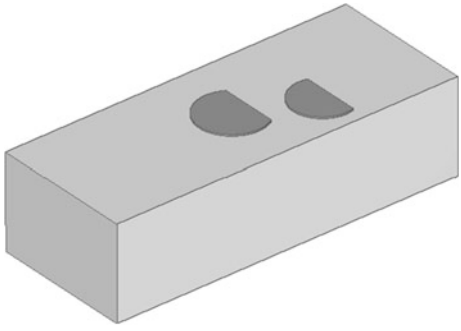

Fig. 3.15 Simplified forearm model for a isodose calculation with MCNP, with two spots ^{18}F contamination [13]

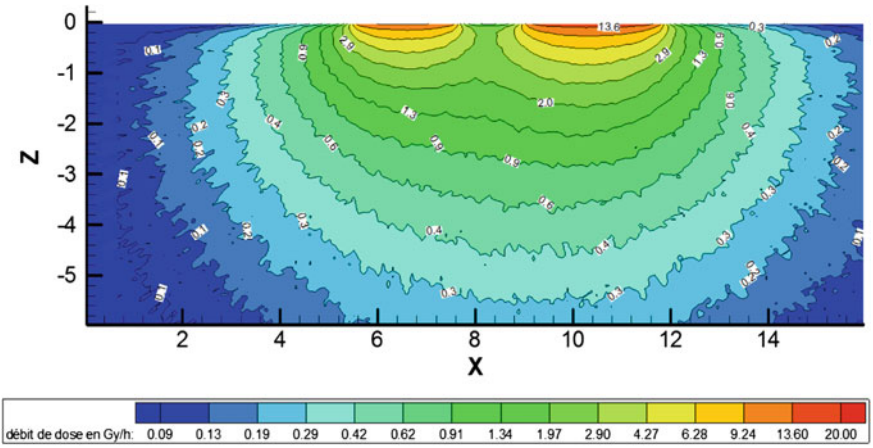

Fig. 3.16 Isodose curves calculated with MCNP for a simplified model visualized in TECPLOT [13]

3.4.5 Absorbed Dose Calculation in the Case of a Proton Beam

It may also be necessary to determine the absorbed dose in certain conditions for characterizing the deterministic risk. The following result provides a Monte Carlo calculation for a proton and helium accelerator (Aglae Louvre). Figure 3.17 gives the absorbed dose rate profile in a water phantom used as beam stopper.

As the beam intensity increases, the absorbed dose rate increases to a peak and then decreases abruptly (due to the Bragg peak, see Chap. 2). The high dose that is delivered in depth, but with limiting the upstream organ exposure, is of interest for radiotherapy: this property is typically exploited in hadron therapy.

3.4.6 Absorbed Dose Calculation Using a Complex Model: Voxelized Phantom

We have seen, in the previous case, a simplified model to characterize the absorbed dose distribution in case of radiation exposure accident. In this model, an important approximation is made on the geometry irradiation. It is possible to significantly smooth the calculation results using a more complex model: the voxelized phantom.

The voxelized phantom principle is to transcribe from cutting plans of collection of medical computed tomographic images, a 3D phantom in a readable formalism by a Monte Carlo code. For this purpose, a software "transfers" stacks the cut planes in a 3D mesh composed of voxels (small elementary cubes constituting the 3D grid). At each voxels is then assigned a material (bone, soft tissue, air …) and a

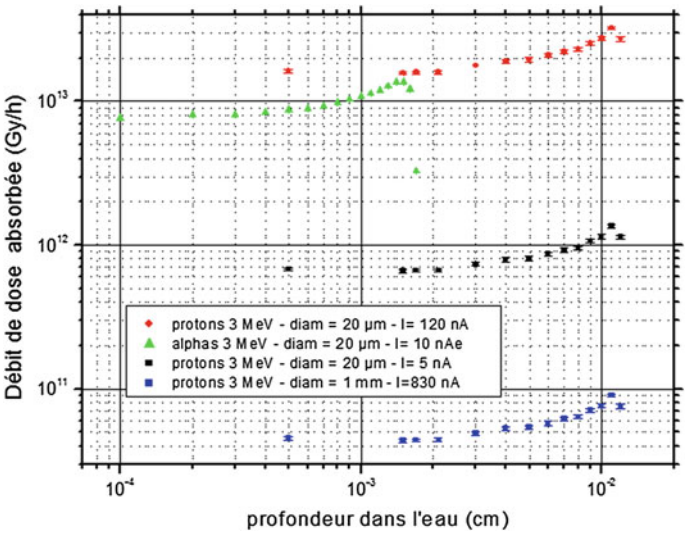

Fig. 3.17 Profile of absorbed dose at depth in a water phantom for different configurations of Aglae accelerator (musée du Louvre) [14]

density measured with a density analyzer. The next step is to recode the grid in the language readable by the Monte Carlo code. Then a phantom almost identical to the scanned subject is defined. Each voxels are calculation's cells, which can cause significant computing time.

For example, we will describe a radiation exposure accident which occurred in Chile in 2005. A person has been exposed for ten minutes to a ^{192}Ir gamma radiography source with an 3.3 TBq activity ($\overline{E}_{\gamma} = 350\,\text{keV}$). The reconstitution of the absorbed dose associated with exposure was carried out as follows [15]: The source has been present for ten minutes in the left back pocket of the trousers of a worker, a scanner of 163 cuts from the middle of the abdomen to mid-thigh was performed. These cuts were then processed using the SESAME preprocessing software [16] to create a voxelized phantom compatible with the code MCNPX 2.4.0; this software also allows to define and locate the source in the input file. Figure 3.18 summarizes the different modeling step.

Isodose curves are calculated with MCNPX, using an appropriate dosimetric estimator (see Chap. 6), with the aim of characterizing the possible deterministic consequences associated with such exposure. Figure 3.19 gives the voxelized phantom cuts with isodose curves representation.

This type of modeling, because of heavy pretreatment time (scanner and voxelized phantom creation) and calculation in many cells, is only recommended for applications that require significant levels of accuracy: radiological accidents, radiotherapy …

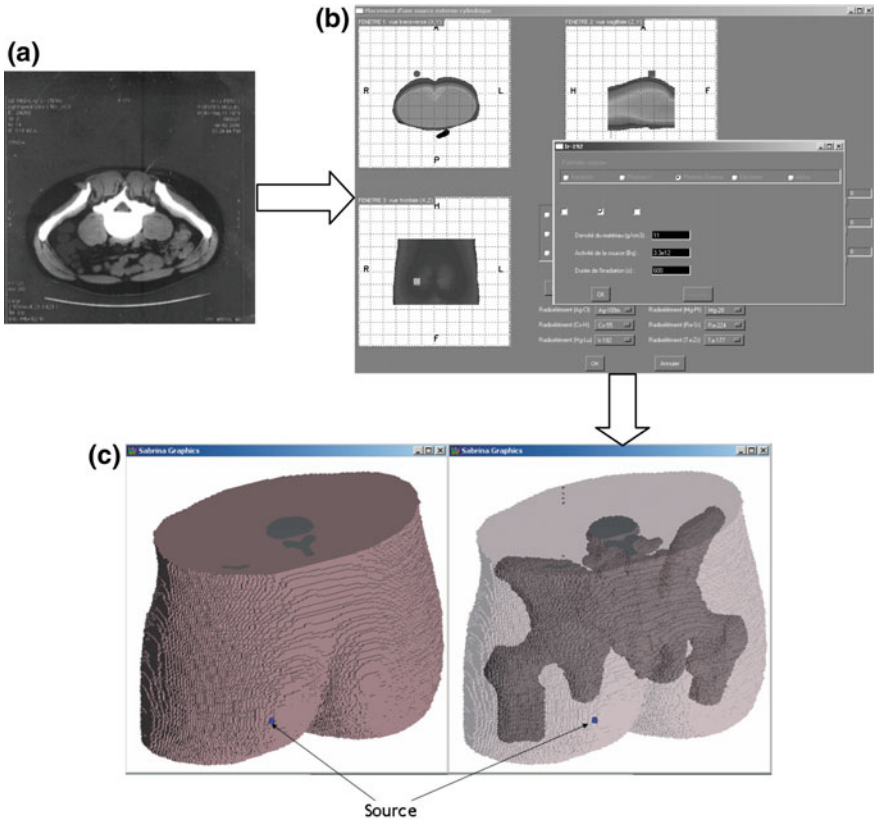

Fig. 3.18 **a** One of the 163 scanner cuts. **b** HMI SESAME preprocessing software in the definition phase and positioning the ^{192}Ir source. **c** Voxelized phantom created in SESAME, from the input file compatible with MCNPX [15], with the permission of EDP Sciences

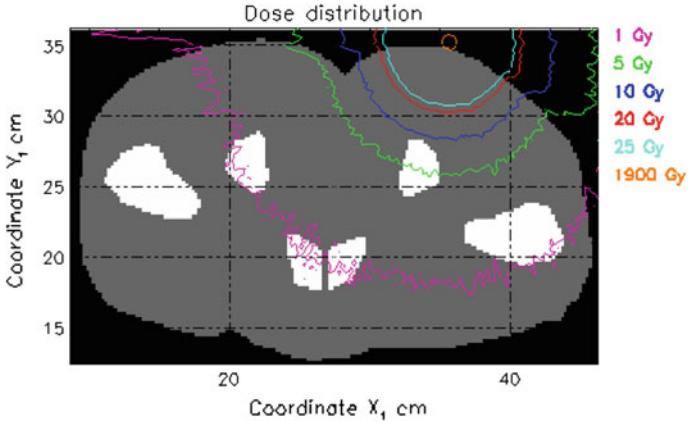

Fig. 3.19 Representation on a cut of a voxelized phantom of calculated isodose curves using the Monte Carlo code MCNPX [15], with the permission of EDP Sciences

3.5 The Operational Quantities

If the calculation methods leading to the determination of the protection quantities are fairly simple (see example), the methodology suggests to clear up the following points.

Calculations based on the use of conversion coefficients "dosimetric quantities—protection quantities" are given to geometries and irradiation conditions very specific that are rarely found in practical situations. Furthermore, the use of these factors require an accurate characterization of the incident energy; But typically the monokinetic energy neutron case remains marginal (e.g. fusion reaction, some nuclear reactions e.g. (p, n) …). Radiation neutron sources are generally spectra difficult to characterize (see Chap. 4). Let us add that these protection quantities, on which are determined the regulatory limits, are calculated and not measurable by definition! The challenge will therefore be to define the measurable quantities called "operational" which will allow to estimate these protection quantities. The following section details these estimators.

We established in Chap. 2, with the use of suitable measuring devices, that it is possible to access the punctual reference physical quantities, characterizing the radiation field: air kerma for photon, fluence for neutron, absorbed dose in tissue for β. The International Commission on Radiation Units and Measurements (ICRU) is based on the "know-how" to define experimental variables to estimate the protection quantities (H_T and E). The ICRU reports 39 [17], 43 [18], 47 [19] and 51 [20] explicit these quantities, used in practical applications to monitor and investigate situations involving external exposure. They are defined to slightly overestimate the protection quantities, according to a conservative approach related to radiation protection. The values of each of these quantities are additive for radiation energies and different angles of incidence.

3.5.1 Quality Factor and Definition Dose Equivalent

The operational quantities are defined from the concept of "dose equivalent", offering a "equivalency" to the dose. This "dose equivalent" is characterized by the product of the absorbed dose to the point of interest in the tissue, by a factor taking into account the energy deposition and thus radiation energy biological harmfulness typology considered, therefore its RBE. This factor already briefly mentioned is called "quality factor" with symbol Q. The generic expression of the dose equivalent for a single radiation type and single energy is given by (3.9).

$$H = DQ \tag{3.9}$$

His unit, by analogy to protection quantities, remains the sievert. While the quality factor Q is relatively close to the radiation weighting factor w_R, it should be

noted an important distinction: it is a direct function of linear energy transfer L in the water, while the latter is directly related to the EBR but indirectly linked to L. The relationship between the quality factor $Q(L)$ and the linear energy transfer of charged particles in water: L (or LET), specified by the report 33 [21] ICRU, hold in three equation (3.10) depending on the level of importance of the linear energy transfer.

$$\begin{cases} Q(L) = 1 & (L < 10\,\text{keV}/\mu\text{m}) \\ Q(L) = 0.32L - 2.2 & (10 \leq L \leq 100\,\text{keV}/\mu\text{m}) \\ Q(L) = 300/\sqrt{L} & (L > 100\,\text{keV}/\mu\text{m}) \end{cases} \tag{3.10}$$

When the radiation field is mixed at the point in the tissue (several radiation type moving different secondary charged particles with various energies), which is the case for neutrons, for example, (i.e. scattered neutrons, recoil protons, alpha), it is necessary to calculate a "mean quality factor" by integrating over the spectrum according to the TLE (or L) of the absorbed dose at the point, as proposed in the expression (3.11).

$$\overline{Q} = \frac{1}{D}\int_L Q(L)\, D_L\, dL \quad with \quad D_L = \left(\frac{dD}{dL}\right) \tag{3.11}$$

where DL = dD/ dL is the absorbed dose distribution in the tissue at the point, for charged particles with LET in water is between L and L + dL. The variable D is the value of the total absorbed dose at the same point, due to all the particles. The expression (3.9) and dose equivalent are expressed as (3.12).

$$H = D\,\overline{Q} \tag{3.12}$$

Note that in the neutrons case, there is a similarity between the mean quality factor as a function of the energy $\overline{Q}(E_n)$ at a thickness of 10 mm tissue [22] and the weighting factor for the radiation at the same energy $w_R(E_n)$, both for the histogram approach (cf. Table 3.1) and for the analytical approach proposed by ICRP 60 through expression (3.5). Figure 3.20 gives the comparative curves of both factors.

From a practical standpoint, it is possible to determine the quality factor by the mean of a TEPC proportional counter type 'Rossi' with tissue-equivalent wall whose the operating principle is detailed in Chap. 1. From the single event spectrum $f_1(y)$, by assimilating the linear energy transfer L to the lineal energy y and so $Q(L)$ at $Q(y)$, we assess the mean quality factor $\overline{Q}$ according to the relation (3.13).

$$\overline{Q} = \int Q(y)\,\frac{y f_1(y)}{\bar{y}_f}\,dy \tag{3.13}$$

with $Q(y)$ subdivided in three parts according to the three expressions $Q(L)$ presented in (3.10). The term $y f_1(y)/\bar{y}_f$ is the fraction of energy (or absorbed

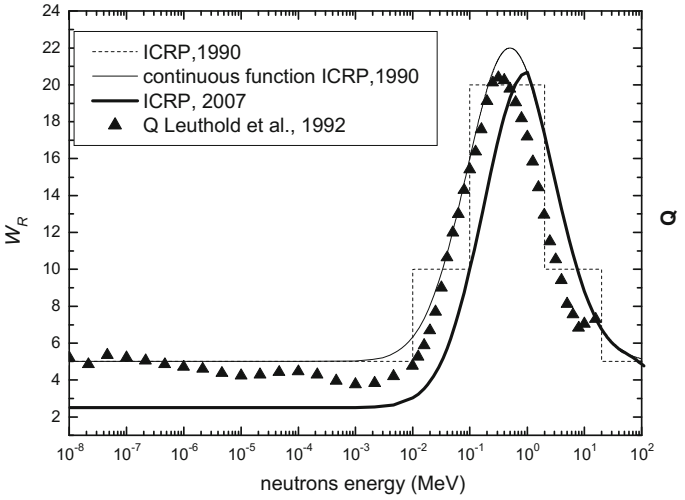

Fig. 3.20 Comparison between the mean quality factor as a function of neutron energy $\overline{Q}(E_n)$ and the weighting factor for the radiation $w_R(E)$. For the histogram and analytical approaches, according to data [1, 2, 23]

dose) having been impacted by energy events lineal y; this term is called dose distribution in linear energy $d(y)$ (See Chap. 1). Then we note the following equivalence between deterministic approaches (3.12) and stochastic (3.13) of the dose distribution according to (3.14).

$$d(y) \cong \frac{D_L}{D} = \frac{1}{D}\left(\frac{dD}{dL}\right) \tag{3.14}$$

where the absorbed dose D is a normalization term for the dose distribution on the linear energy transfer spectrum.

Note that for the radiation outside Table 3.1, ICRP 74 recommends to estimate the radiation weighting factor w_R by the mean quality factor $\overline{Q}$ obtained by the expression (3.11) for an absorbed dose D under 10 mm on the ICRU sphere.

The dose equivalent application is the "area monitoring" and "personal monitoring" with specific quantities for each. Moreover, the distinction between high and low penetrating radiation is of major importance for defining the parameters depending on the type of radiation involved.

3.5.2 Expanded and Aligned Fields

For the definition of variables associated with the dose equivalent concept, as they relate to area monitoring or individual monitoring, ICRU has defined radiation

fields derivative of the actual field at the reference point. The terms "expanded" and "unidirectional" are given in the ICRU report 39 [17] to characterize these derivatives radiation fields.

An expanded radiation field is defined as a hypothetical field where the fluence and its angular and energy distributions have the same value throughout the volume of interest as that in the actual field at the point of reference. An expanded and aligned radiation field is a hypothetical field where the fluence and its energy distribution are the same as an expanded field, but the fluence is unidirectional.

3.5.3 *Operational Quantities for Area Monitoring*

As previously mentioned, the definition of variables related to the dose equivalent concept differs with the presence of a weekly or strongly penetrating radiation.

Ambient dose equivalent *H*(d)*

The ambient dose equivalent, H^*(d), at a point, in a radiation field, is the dose equivalent ($H = D_t\overline{Q}$) that would be produced by the corresponding expanded and aligned field in the ICRU sphere at a depth, d, on the radius opposite to the direction of the aligned field. The recommended value of d is 10 mm for penetrating radiation and 0.07 mm for low-penetrating radiation.

The ICRU type sphere is composed with tissue equivalent material with following mass composition: 76.2% oxygen, 10.1% hydrogen, 11.1% carbon and 2.6% nitrogen for a density of 1; its diameter is 30 cm. Figure 3.21 gives a schematic representation of the specific conditions of irradiation to obtain the ambient dose equivalent $H^*(10)$ with the ICRU sphere.

Add that for the highly penetrating radiation, the incident direction at a depth of 10 mm in the ICRU sphere is insignificant on the calculation. The use of unidirectional expanded field in which radiation fields must be added in the direction of

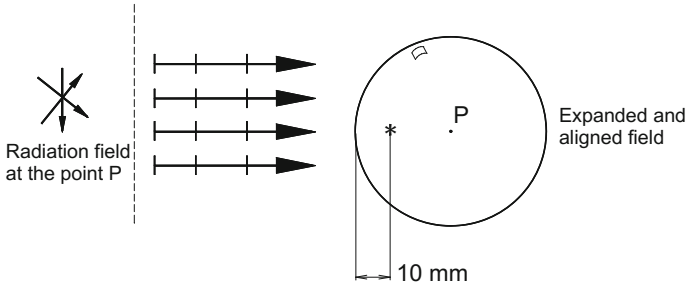

Fig. 3.21 Irradiation protocol and calculation of the ambient dose equivalent $H^*(10)$ for strongly penetrating radiation by means of an expanded and aligned field in the ICRU sphere

the calculation overestimates the equivalent dose in relation to the protection quantity: the effective dose E. To better understand the protocol for estimating the effective dose by the ambient dose equivalent $H^*(10)$ for a highly penetrating radiation, let's consider the calculation for a 1 MeV photon and a fluence $\phi_\gamma = 2 \cdot 10^6 \text{cm}^{-2}$ example done to calculate the protection quantities (p. 167).

It is reminded that $E \cong w_R D_{T,R} = D_T = 8\,\mu\text{Sv}\ \forall T$. Let us calculate $H^*(10)$: we know that $Q = 1$ for photons, so this calculation can be summed to determine the dose value absorbed in 10 mm tissue. Beforehand, it is necessary to determine if the electronic equilibrium is reached at the depth of 10 mm in the tissue. At this photon energy, the most energetic electrons reach the maximum Compton electron energy; this energy is obtained by the expression (see Chap. 2):

$$T_{c\,Max} = \frac{4E_\gamma^2}{4E_\gamma + 1} = \frac{4}{5} = 0.8\ \text{MeV}$$

For this energy, the electrons range in tissue is given by Katz and Penfold [24]:

$$n = 1.265 - 0.0954 \times \ln(0.8) = 1.28$$
$$R_{\max} = 0.412 \times (0.8)^{1.28} = 0.3\,\text{g}\,\text{cm}^{-2}$$

With a density equal to 1, the electrons range in tissue is 3 mm, lower than the depth of 10 mm required for calculation. Thus, the calculation of the absorbed dose in 10 mm in the ICRU sphere is obtained from the theoretical expression of tissue kerma (in mGy) (see Chap. 2), considering the attenuation of the fluence at a 10 mm depth of tissue.

$$D_t(x) = K_t(x) = 1.6 \cdot 10^{-7} \Phi_\gamma \left(\frac{\mu_{tr}}{\rho}\right)_{tissue}^{1\,\text{MeV}} E_\gamma \exp\left(-\left(\frac{\mu}{\rho}\right)_{tissue}^{1\,\text{MeV}} \rho_{tissue} x\right)$$
$$\text{D}_\text{t}(10) = 1.6 \cdot 10^{-7} \times 2 \cdot 10^6 \times 0.0307 \times 1 \times \exp(-0.07 \times 1 \times 1) = 9.1\,\mu\text{Sv}$$

We show that $H^*(10) \geq E$ and also the dose equivalent in 10 mm depth slightly overestimates of the effective dose protection quantity. If this approach can be extended to an energy range of 10 keV–10 MeV for photon, we will see, in the case of neutrons, for some energy, this approach may no longer works and the estimator may be lower than the protection quantity.

Directional dose equivalent $H'(d, \Omega)$

The directional dose equivalent, $H'(d, \Omega)$, at a point, in a radiation field, is the dose equivalent that would be produced by the corresponding expanded field in the ICRU sphere at a depth, $\boldsymbol{d}$, on a radius in a specified direction Ω.

This dose equivalent is suitable for weakly penetrating radiation. The ICRU specifies a depth d of 70 μm (70 mg cm^{-2}) in the ICRU sphere in any direction $H'(0.07)$ to estimate the dose equivalent protection quantity to the extremities

(e.g. H_{skin}). Figure 3.22 provides an illustration of the irradiation protocol and calculation of the operational quantity.

In this approach that the radiation field is multidirectional, unlike irradiation conditions $H^*(d)$. Note that, for weakly penetrating radiation, the angle of incidence is significant for the absorbed dose calculation in the ICRU sphere depth. Indeed, if we consider for example electrons, it is clear that the decrease in the energy when they penetrate in the ICRU sphere implies that their direction of arrival in the ICRU sphere must be considered: The derived field preserves the directions of the actual radiation field at the reference point.

However, this dose equivalent variation for unidirectional fields exist: $H'(d, \alpha)$; the direction can be specified in terms of an angle α between the radius passing through the measurement point and the radiation inlet direction in the sphere as shown in Fig. 3.23.

When α is 0°, the quantity $H'(d, 0°)$ can be written as $H'(d)$; it is equal, in the particular case of unidirectional fields, at the ambient dose equivalent in a depth d: $H^*(d)$.

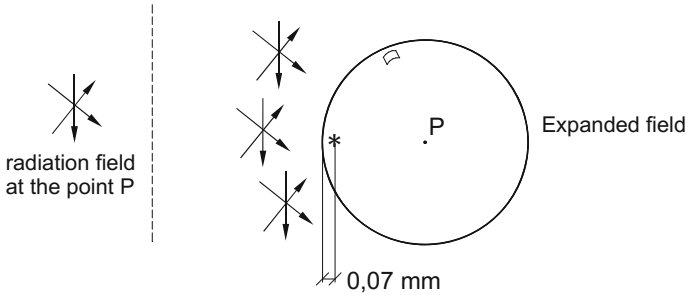

Fig. 3.22 Irradiation protocol and calculation of directional dose equivalent $H'(0.07)$ for weakly penetrating radiation by means of a expanded field on the ICRU sphere

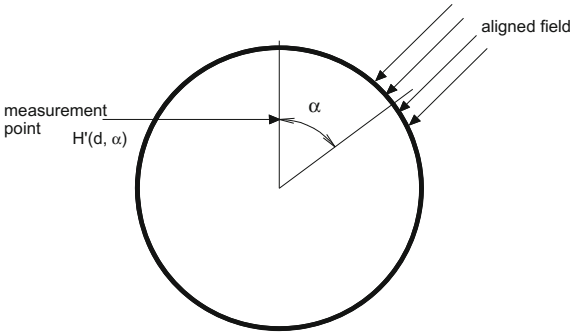

Fig. 3.23 Angle definition α for directional dose equivalent $H'(d, \alpha)$

Figure 3.24 provides the curves of the ratio $R(0.07, \alpha) = H'(0.07, \alpha)/H'(0.07, 0)$ for the directional dose equivalent $H'(0.07, \alpha)$, for electron between 0.1 and 2 MeV. These values are available in a table in Appendix 1.

We note a significant impact of the angle, depending on energy, on the directional dose equivalent response. This variation is attributable to the absorbed dose value under 70 μm, $D_t(0.07)$, which strongly depends on the electron energy. It is due to path and angular straggling of electrons within the ICRU sphere before reaching the measurement point; it is directly related to the incidence angle.

Let us add that for weakly penetrating radiation, because of these quantities principle, the directional dose equivalent under 70 μm at a zero angle of incidence can be likened to the personal dose equivalent under the same thickness: $H'(0.07, 0°) \approx H_p(0.07)$.

3.5.4 *Operational Quantities for Individual Monitoring*

To take into account the backscattered radiation within the human body, especially when wearing a personal dosimeter, ICRU was driven to define a "personal dose equivalent". It is based on the use of phantom simulating all or part of the human body.

Personal dose equivalent $H_p(d, \alpha)$

The personal dose equivalent $H_p(d, \alpha)$ is the dose equivalent in soft tissue at a depth d in the body. The unit of personal dose equivalent is the sievert (Sv). Like the directional dose equivalent, the personal dose equivalent also depends on the incident direction of the radiation field (Fig. 3.25).

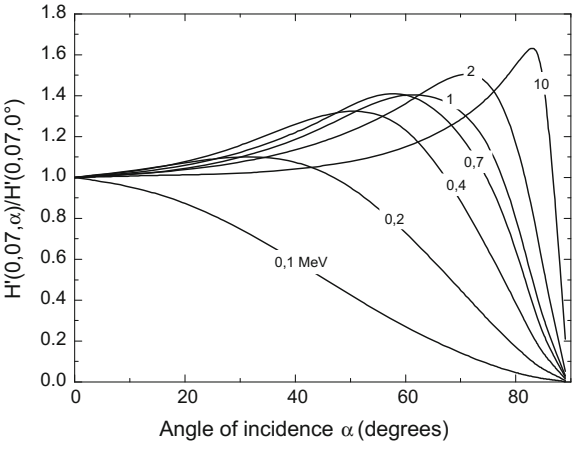

Fig. 3.24 Angular response $R(0.07, \alpha)$ for directional dose equivalent $H'(0.07, \alpha)$, for electron energy between 0.1 and 2 MeV, according to the data [7]; values available in Appendix 1

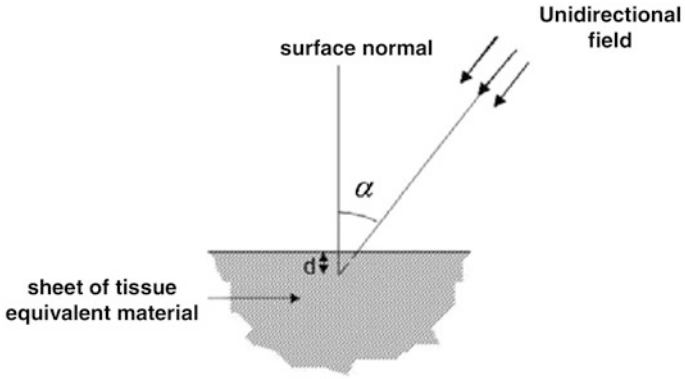

Fig. 3.25 Theoretical definition of personal dose equivalent $H_p(d, \alpha)$, according to [25]

In practice, this quantity is essentially useful for a radiation field penetrating the tissue with a same direction as the surface normal ($\alpha = 0$) and to the specified depths for weakly and strongly penetrating radiation, namely $H_p(0.07, 0°)$ and $H_p(10, 0°)$ commonly called $H_p(0.07)$ and $H_p(10)$. The phantoms recommended to determine the dose equivalents are different according to the dosimetric context.

Note that it is possible to calculate analytically the dose equivalent rate $\dot{H}_p(0.07)$ for the β with the detailed relationships in Chap. 2 for the calculation of the absorbed dose to the β. Hereafter, the dose equivalent rate $\dot{H}_p(0.07)$ is calculated for a contamination of 1 Bq cm^{-2} of ^{18}F. For this radionuclide the maximum energy is 633 keV and the mean energy is 243 keV (from Lund/LBNL Nuclear Data Search 1999 [26]).

Figure 3.26 represents the geometry of calculation. To calculate the dose equivalent $\dot{H}_p(0.07)$, the dose under $d = 70$ µm of soft tissue, approximated here by water needs to be calculated. We know that beyond a distance R representing the maximum range of β, the dose is vanished. Thus, the area of interest for the calculation can be defined by a radius equal to disk $\sqrt{R^2 - d^2}$ (see Fig. 3.26). We must divide the disk into infinitesimal elements of surface dS, so that each element dS can be considered as punctual for the observer. So we get for 1 Bq cm^{-2} the following expression:

$$D_{disc}(d) = \iint_{dS} D(\rho) dS = 2\pi \int_{d}^{R} \rho\, D(\rho)\, d\rho$$

with $D(\rho)$ given in Chap. 2; if $d \leq C/\upsilon$ the expression get the following form:

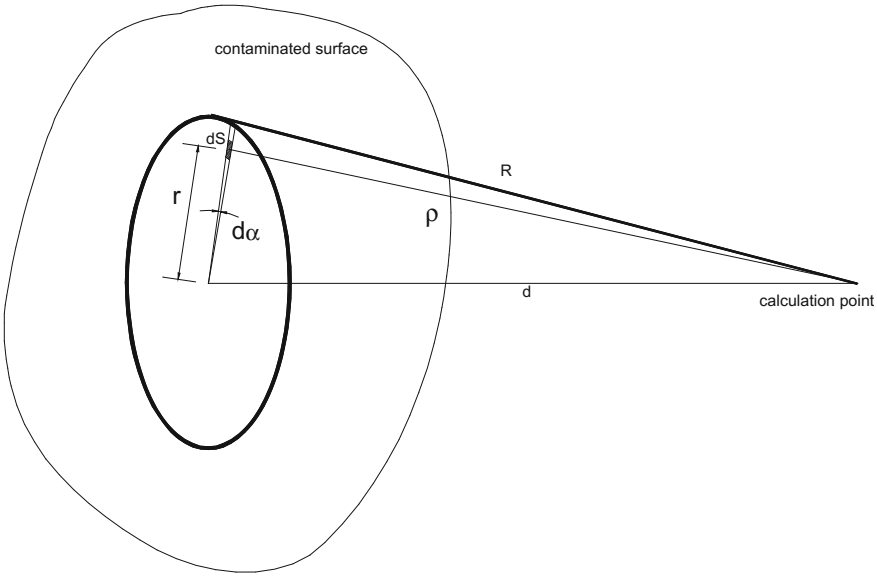

Fig. 3.26 Mathematical scheme for calculating the personal dose equivalent rate $H_p(0.07)$ for a surface contamination

$$D_{disk}(d) = \frac{2\pi k}{\upsilon^2}\left[\int_d^{C/\upsilon}\left(\frac{C - \upsilon\cdot\rho\cdot\exp(1-(\upsilon\cdot\rho/C)) + \upsilon\cdot\rho\cdot\exp(1-\upsilon\cdot\rho) - A}{\rho}\right)d\rho + \int_{C/\upsilon}^{R}\left(\frac{\upsilon\cdot\rho\cdot\exp(1-\upsilon\cdot\rho) - A}{\rho}\right)d\rho\right]$$

$$D_{disk}(d) = \frac{2\pi k}{\upsilon^2}\left[\begin{array}{l} C[1-\exp(1-\upsilon\cdot d/C) - \ln(\upsilon\cdot d/C)] \\ +\exp(1-\upsilon\cdot d) - \exp(1-\upsilon\cdot R) - A\times\ln(R/d)\end{array}\right]$$

If $C/\upsilon < d < R$:

$$D_{disk}(d) = \frac{2\pi k}{\upsilon^2}\left[\int_d^R\left(\frac{\upsilon\cdot\rho\cdot\exp(1-\upsilon\cdot\rho) - A}{\rho}\right)d\rho\right]$$
$$= \frac{2\pi k}{\upsilon^2}[\exp(1-\upsilon\cdot d) - \exp(1-\upsilon\cdot R) - A\times\ln(R/d)]$$

Numerical application: For the ^{18}F, datas are (see Chap. 2) $\upsilon = 37.7\ cm^2\ g^{-1} = 37.7$ cm for water, $C = 1.16$, $\overline{R} = 0.74 \times R_{max} = 0.17$ cm, $\alpha = 0.32$, $k = 5.38\cdot 10^{-8}$ and $A = 0.03$. $C/\upsilon = 0.03$ cm, so $d \le C/\upsilon$. The integration of the above expression leads to:

$$D_{disk}(d) = \frac{2\pi k}{\upsilon^2}\left[\begin{array}{l} C[1-\exp(1-\upsilon\cdot d/C) - \ln(\upsilon\cdot d/C)] \\ +\exp(1-\upsilon\cdot d) - \exp(1-\upsilon\cdot R) - A\times\ln(R/d)\end{array}\right]$$

And consequently: $D_{disk}(7 \cdot 10^{-3}) = 5.63 \cdot 10^{-10}$ Gy to 1 β cm^{-2}.

It follows that $D_{disk}(7 \cdot 10^{-3}) = 5.63 \cdot 10^{-10}$ Gy/s per Bq/cm^2 (2 μGy h^{-1} per Bq cm^{-2}). As $Q = 1$, for $L_\infty < 10\,keV/\mu m$ finally $\dot{H}_p(0.07) = \dot{D}(0.07) = 2\,\mu Sv/h$.

Finger Phantom for personal dose equivalent $H_p(0.07)$

The skin equivalent dose (H_{skin}) assessment for finger is done using the personal dose equivalent dedicated to weakly penetrating radiation $H_p(0.07)$ with a phantom "finger" relied on the Schultz and Zoetelief's [9] model described above (Fig. 3.3) is used. This phantom consists of a "soft tissue" central cylinder of 2cm diameter, surrounded by 2 layers: 0.193 cm of "sensitive skin" and 70 μm of "dead skin" (basal layer); this model allows to take into account the scattered radiation in the soft tissue (Fig. 3.27). The absorbed dose for the calculation of $H_p(0.07)$ is calculated under 70 μm depth.

The absorbed dose $D_t(0.07)$ that allows to calculate $H_p(0.07)$ is estimated at a point under 70 μm, namely the interface between the "dead skin" and "sensitive skin".

Phantom for personal dose equivalent $H_p(10)$

The ICRU [17] also specified an ISO-PMMA phantom to simulate the human torso, especially for the personal dose equivalent for monitoring strongly penetrating radiation $H_p(10)$ and for calibration personal dosimeters.

The device is a slab in PMMA (polymethyl methacrylate "Plexiglas"), tissue-equivalent material of dimensions 30 cm × 30 cm × 15 cm. This phantom is relevant for personal dose equivalent measurement with a personal dosimeter.

Figure 3.28 presents a schematic view of the experimental setup used to access the response $H_p(10, \alpha)$ depending on the angle of incidence in the presence of a slab phantom ISO-PMMA.

The ratio $R(10, \alpha)$, $H_p(10, \alpha)/H_p(10, 0°)$, for different photon energies and angles of incidence is proposed in Fig. 3.29.

For low energy radiation (e.g. 15 keV), as the angle of incidence α grows and therefore the distance to the measurement point, the beam attenuation effect is prominent and absorbed dose in 10 mm, and $D_t(10)$ is greatly reduced in this

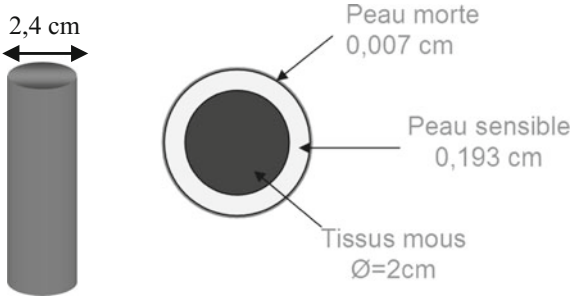

Fig. 3.27 Finger phantom model to calculate the dose equivalent $H_p(0.07)$ recommended by the ICRP 74 [7]—density skin: 1.105 and soft tissue: 0.987

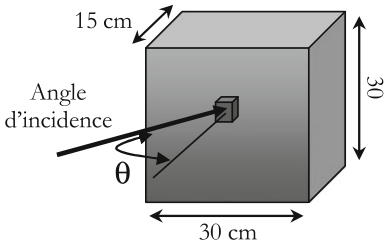

Fig. 3.28 Basic scheme of the experimental setup for accessing $H_p(10, \alpha)$ depending on the angle of incidence in the presence of a PMMA phantom slab

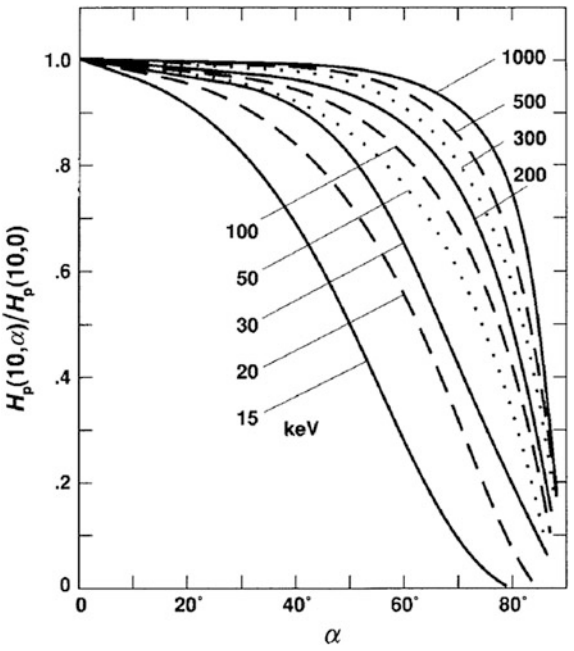

Fig. 3.29 Angular dependence Factor $R(10, \alpha)$ defined by the ratio of $H_p(10, \alpha)/H_p(10, 0°)$ for photon energies between 15 keV and 1 MeV, and for different angles of incidence, calculated by a Monte Carlo code [7], values provided in Appendix 2

energy field, the photoelectric interaction is dominating and Compton scattering is almost nonexistent.

For higher energies, the Compton scattering becomes significant and the incident beam attenuation less significant. The scattered photons increase the dose at the measurement point under 10 mm and offset the attenuation of the primary beam. This explains the flattening of the angle response curve.

Estimate the equivalent dose to the eye-lens $H_p(3)$

In 2011, ICRP [5] proposed a new limit on equivalent dose to the eye-lens of 20 mSv (instead of 150 mSv currently) [5]. This reduction is based on new epidemiological studies that has demonstrated the occurrence of tissue reactions from lower dose limits. The new EU Directive 2013/59, laying down basic standards for

health protection against the risks arising from exposure to ionizing radiation was inspired by this recommendation [6].

Furthermore, ICRP recommends that the dose equivalent to the eye-lens must be estimated at a depth of 3 mm of tissues.

It should be noted, right now, the ICRU or ICRP does not offer a conversion factor to estimate Hp(3). Also, a European working group, ORAMED (Radiation Optimization of protection for medical staff) has defined a new phantom to characterize this estimator. It consist of a cylinder 20 cm high for 20 cm diameter. The conversion factors for this quantity were calculated using Monte Carlo simulations. The results are available for example by Gualdrini et al. [27].

Response of absolute dosimeter (LiF) in terms of $H_p(0.07)$ and $H_p(10)$

Regarding the previous case, a dosimeter which measure absorbed dose under 70 μm of tissue, actually directly measures the personal dose equivalent $H_p(0.07)$ (with the assumption that the quality factor Q is equal to 1). Indeed, it incorporates in the measurement result, in addition to the dose deposited at this depth by primary radiation, the scattered radiation component. It is the case with the use of a "ring LiF" around the finger for measurement for photons and high energy β dose. Indeed, the LiF^7, composed of fluorine and lithium, sensitive to photons in the detector, is a good tissue-equivalent for photons and electrons (only 50% maximum error for 50 keV photons). Furthermore for a LiF ring, the sensitive volume of the detector (pellet) is contained in a heat-shrinkable plastic of thickness 70 μm corresponding to the basal layer of the skin: we are clearly in the presence of an "absolute dosimeter" measuring directly $H_p(0.07)$ without using a conversion coefficient. Moreover, the quality factor photons and electrons is 1, we obtain spontaneously without calibration $H_p(0.07)$.

This feature remains marginal: for most personal dosimeters technologies, we will need to perform a calibration for access to operational quantity.

3.5.5 Difference Between Strongly and Weakly Penetrating Radiation in Terms of Operational Dosimetry

If the difference between weakly and strongly penetrating radiation can be better understood by the penetrating power of a given particle in matter, differentiation adopted by the ICRU rely on health approach. The ICRU 51 [20] report specifies this distinction in these terms: "a radiation will be weakly penetrating if the nearest equivalent dose limit is the equivalent dose to the eye-lens or defined for the skin. It will be strongly penetrating if the dose equivalent for "whole body" is closest to the effective dose limit." To illustrate this health approach, let's consider two distinct radiation: ^{60}Co photons and β radiation ^{32}P. Regulatory limits related to this classification are: effective dose E = 20 mSv and a equivalent dose for the extremities H_T = 500 mSv. Arbitrarily, but realistic, let's postulate that exposure to photons is

responsible for a dose equivalent $H_p(10) = 10$ mSv and the skin level $H_p(0.07) = 2$ mSv; in this case, the nearest equivalent dose limit of the relevant protection quantity is the dose equivalent of "whole body". Consequently, this type of radiation can be described as "highly penetrating." Let's consider this time that exposure β has led to the following dose equivalents: $H_p(10) = 0.01$ mSv and $H_p(0.07) = 300$ mSv, this time the equivalent dose to the skin is clearly the nearest to the limit of H_{skin} and this radiation can be described as "weakly penetrating."

3.5.6 *"Physical Quantity—Dose Equivalent" Conversion Factors*

From a practical standpoint, the challenge now is to link the operational quantities to the reference physical quantities that can be measured using appropriate devices, like fluence, Φ, air kerma, K_a, or absorbed dose in tissue, D_t. Adding that besides being measurable, these reference physical quantities are also calculable using either deterministic calculation or stochastic Monte Carlo transport code.

A joint working group between the ICRU 57 and ICRP 74 [7] specifies a number of "physical quantity reference—dose equivalent" conversion factors for photons, neutrons and electrons and of extended energy ranges.

These conversion factors are particularly suitable for the calibration of radiation protection devices in the "secondary laboratory" (i.e. calibration laboratory dosimeters in a nuclear facility). First, the physical quantity of reference must be measured at a point P and secondly this conversion factor must be applied at this same point.

The other major advantage of these factors concerns in the numerical simulation of radiological scenes (e.g. rooms accelerator, reactor building, glovebox …) by means of numerical codes. Numerical simulations allow an instant access to the operational quantity sought by simple weighting of these factors by the calculation result of the estimator of the physical quantity.

Calculation protocol conversion coefficients

Calculations are made using particle transport code such Monte Carlo code as follows: an initial calculation is run for assessing the physical reference value at a reference point P at a given energy. A second calculation is to locate at this point P a ICRU sphere and calculate the absorbed dose in the sphere at the specified depth. The conversion factor obtained by ratio of both calculation results; its symbol is "*h*". Figure 3.30 shows the process for determining conversion factors "Air Kerma-ambient dose equivalent" $h^*_{K_a}(10) = (H^*(10)/K_a)_{E_\gamma}$ and "fluence-ambient dose equivalent" $h^*_\Phi(10) = (H^*(10)/\Phi)_{E_\gamma}$ for photons.

Note that, in the second step of the calculation for the assessment of $H^*(10)$, the simulation of radiation field has been changed to unidirectional and expanded according to the above definition of the dose equivalent.

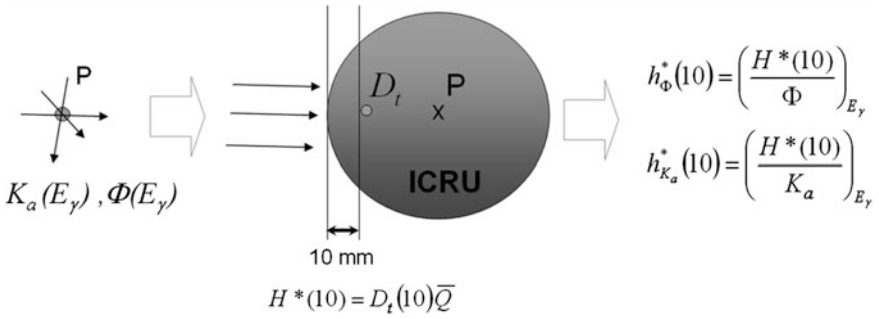

Fig. 3.30 Protocol of Monte Carlo calculation for "fluence-dose-equivalent" and "air Kerma-ambient dose-equivalent" conversion factors for photons

Conversion factors for photons

The following figures show the curves ICRP 74 [7] of the main conversion factors "reference physical quantity—dose equivalent" for photons. Figure 3.31 provides conversion factors "fluence-ambient dose equivalent" to strongly penetrating radiation and "fluence-directional dose equivalent" for weakly penetrating radiation $h^*_\Phi(10) = (H^*(10)/\Phi)_{E_\gamma}$ and $h'_\Phi(0.07) = (H'(0.07)/\Phi)_{E_\gamma}$. These factors are shown in a table in Appendix 3.

The conversion coefficient $h^*_\Phi(10)$ from 10 to 20 keV increases. The transmission decrease as the energy increases in the region where the photoelectric process is almost exclusive. At 20 keV, the curve reaches a front shoulder before to flex and decrease until 100 keV. In this region, as the energy increases, the Compton process increases and is responsible for a tiny fraction of energy transferred to the secondary electrons. In this same region, this process compete with the photoelectric process in which all the energy of the photon is transferred to the medium.

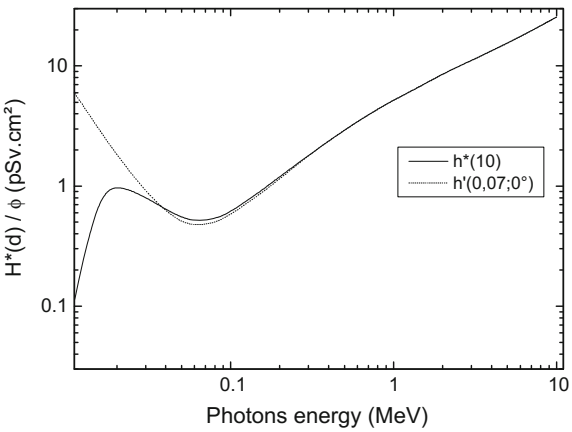

Fig. 3.31 Conversion factors "fluence-ambient dose equivalent" to strongly penetrating radiation and "fluence-directional dose equivalent" for weakly penetrating radiation for photons, according to data ICRP 74 [7]. Values provided in Appendix 3

A consequence of this curve profile can be illustrated by calculating the dose equivalent of a punctual source of ^{241}Am at a distance d (in air or vacuum). This radionuclide emits a photon of 15 keV substantially located at the aforementioned shoulder and a photon of 60 keV located in the zone of inflection. These photons are emitted with the following respective intensities: 43 and 36%. It is common in the calculations for this type of source—without biological protection—to omit the component related to photon radiation of 14 keV, while in this calculation configuration, it is responsible for a major component of the dose.

Regarding the comparison of the $h^*_\Phi(10)$ curves with respect to $h'_\Phi(0.07)$, note that, at low energy (<50 keV) a significant increase of $h'_\Phi(0.07)$ compared to $h^*_\Phi(10)$: below these energies, the high value of photoelectric interaction cross section in tissues significantly attenuates the photons of the incident beam at the depth of 10 mm; Consequently: $h'_\Phi(0.07) \gg h^*_\Phi(10)$. This observation refers also to the character of "strongly" and "weakly" penetrating radiation, previously established.

From 100 keV to 10 MeV, the two curves are substantially identical: beyond this energy of 100 keV, the incident beam becomes "strongly penetrating", the primary photons fluence is slightly altered and we can then apply that in any point of the ICRU sphere: $D_t(x)$ is a constant, which induces $h'_\Phi(0.07) = h^*_\Phi(10)$ reminding that Q = 1. From 100 keV, the constant progression of the curve is due to the dominant Compton interaction in the tissues, as demonstrated in Sect. 3.2: the more the energy of the incident photon is high, the more the energy Compton electron is high. The energy transferred into the medium then increases.

If we consider the example developed in Sect. 3.3.6, with a fluence $\phi = 2 \cdot 10^6$ (γ) cm^{-2} of 1 MeV photons, it is now possible to access the operational quantity of the ambient dose equivalent $H^*(10)$ dedicated to the estimation of the protection quantity E, by the following trivial calculation:

$$H*(10) = \left(\frac{H^*(10)}{\Phi}\right)_{E_\gamma} \Phi\left(E_\gamma\right) = 5.2 \cdot 10^{-12} \times 2 \cdot 10^6 = 1.04 \cdot 10^{-5} \text{ Sv} = 10.4 \text{ µSv}$$

The effective dose calculation for this case led to a value of 8 µSv. The result is therefore consistent with expectations: the ambient dose equivalent overestimates slightly the effective dose.

$$H^*(10) \geq E$$

In other words, using a single calculation, we can access an estimation, slightly upper bound, of protection quantity.

Although the challenge of these conversion factors lies in the connection to a measurable physical quantity, in some trivial cases, for which the source term is clearly identified, the physical quantity can be obtained by analytical calculation. As a result, the conversion factor ad hoc allows almost immediate access to operational quantity. For example, for a ^{131}I punctual source of 1 Bq emitting several photons with different emission intensities: 284 keV to 6%, 365 keV to 637 keV and 82% to 7%, we can determine the ambient dose equivalent rate at a distance of 30 cm thereof. The conversion factors "fluence-ambient dose equivalent" are respectively for these energies: 1.5, 2 and 4 pSv cm^2. The ambient equivalent dose is then obtained by summing according to (3.15).

$$\dot{H}^*(10) = \sum_{E_\gamma} h^*_\Phi(10)\,\dot{\Phi}(E_\gamma) = \sum_{E_\gamma} h^*_\Phi(10)\left(\frac{A\,\Gamma\,(E_\gamma)}{4\pi\,d^2}\right) \tag{3.15}$$

$$\begin{aligned}\dot{H}*(10) &= \frac{3600\ \times 10^{-6}}{4\pi \times 30^2}((0.06 \times 10.5) + (0.82 \times 2) + (0.07 \times 4)) \\ &= 6.4 \cdot 10^{-7}\,\mu\mathrm{Sv\,h^{-1}}\end{aligned}$$

We will notice that it may be convenient to have a single conversion factor for that source and, in particular, for calibration operations in a secondary laboratory, from a standard source emitting more rays. We access this coefficient with the ratio of expression (3.15) to the total fluence rate $\dot{\Phi}$ according to (3.16).

$$\left(\frac{H^*(10)}{\Phi}\right)_{^{131}I} = \frac{1}{\dot{\Phi}} \sum_{E_\gamma} h^*_\Phi(10)\ \dot{\Phi}(E_\gamma) \tag{3.16}$$

This relationship defines a mean conversion coefficient for the radionuclide. The fluence of this problem is:

$$\dot{\Phi} = \frac{0.06 + 0.82 + 0.07}{4\pi \times 30^2} = 8.4 \cdot 10^{-5}\ (\gamma) \cdot \mathrm{cm^2\,s^{-1}}$$

The conversion factor "fluence-ambient dose equivalent" for the I-131 is finally:

$$h^*_\Phi(10) = \left(\frac{H*(10)}{\Phi}\right)_{^{131}I} = \frac{6.4 \cdot 10^{-7} \cdot 10^{-6}}{3600 \times 8.4 \cdot 10^{-5}} = 2.11\ \mathrm{pSv\ cm^2}$$

To further illustrate this computational approach for operational quantity, we refer to the case of the linear source discussed in Chap. 1, considering a source of 1 GBq of ^{137}Cs emitting a single photon of 662 keV with a intensity of 85%. The conversion factor "fluence-ambient dose equivalent" is 3 pSv cm^2. The ambient dose equivalent rate is then obtained as follows (cf. the fluence calculation for a line in Chap. 1):

$$\dot{H}^*(10) = h^*_{\Phi}(10)\ \dot{\Phi} = h^*_{\Phi}(10)\frac{\Gamma A}{4\pi L h}\left(\arctan\left(\frac{L_1}{h}\right) + \arctan\left(\frac{L_2}{h}\right)\right)$$

$$\Rightarrow \quad \dot{H}^*(10) = 3\cdot 10^{-12}\times\frac{3600\ \times 0.85\times 10^9}{4\pi\ \times 10\times 3}\left(\arctan\left(\frac{1}{3}\right) + \arctan\left(\frac{9}{3}\right)\right) = 38\ \text{mSv h}^{-1}$$

Note that in these calculations, because of the propagation medium, air and distance "source-observer", the fluence attenuation and the build-up factor were not taken into account.

Let us add that for high energy photons, the values of these coefficients are available for energies up to 10 GeV [28].

Finally, Fig. 3.32 provides conversion factors "Air Kerma-ambient dose equivalent" to strongly penetrating radiation and "Air Kerma-directional dose equivalent" for weakly penetrating radiation $h^*_{K_a}(10) = (H*(10)/K_a)_{E_\gamma}$ and $h'_{K_a}(0.07) = (H'(0.07)/K_a)_{E_\gamma}$. These factors are displayed in a table in Appendix 4.

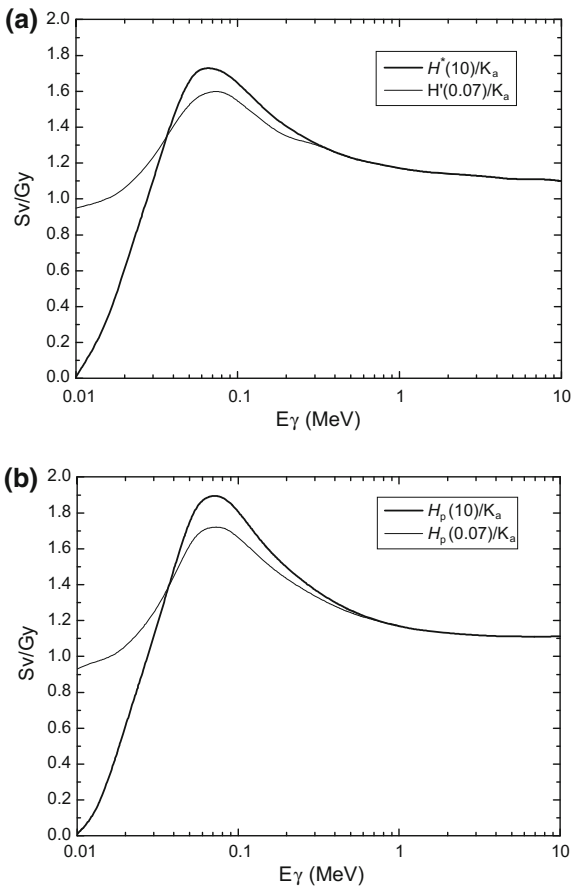

Fig. 3.32 **a** Conversion factors "air Kerma—ambient dose equivalent" to strongly penetrating radiation and "Air Kerma-directional dose equivalent" for weakly penetrating radiation for photons. **b** Conversion factors "air Kerma—individual dose equivalent" for strongly penetrating radiation and weakly penetrating radiation for photons, according to data [7]—the values are provided in Appendix 4

The curves of Fig. 3.32 are particularly relevant to the calibration operation in a secondary laboratory for photon radiation protection devices. The air Kerma is the physical quantity of reference recommended for transfer instruments dedicated to photons (e.g. PTW chamber).

The calibration of personal dosimeters is performed on appropriate phantoms simulating all or part of the body. The conversion coefficients "Kerma-personal dose equivalent" $h_{pK}(10)$ and $h_{pK}(0.07)$ allow the switch of the physical quantity K_a to the operational quantities $H_p(10)$ and $H_p(0.07)$.

$H_p(3)/K_a$ conversion factors, allowing the estimation of the dose equivalent to eye-lens $H_p(3)$, from [27], are given in Fig. 3.33.

Conversion factors for neutrons

The fluence is the physical quantity of reference for neutrons since the energy spectrum of this quantity can be measured with different detection techniques detailed in Chap. 2. Figure 3.34 provides the conversion factors "fluence-ambient dose equivalent" $h^*_\Phi(10) = (H*(10)/\Phi)_{E_n}$ from ICRP 74 [7] for energies below 200 MeV. These factors are given in a table in Appendix 4. Added that Ferrari and Pelliccioni [22] have calculated values for energies up to 10 TeV related to the use of high-energy particle accelerators.

Remind that for energies above 200 keV, the curve follows the first collision kerma in tissues (only dosimetric quantity of reference calculable for neutrons) to the nearest quality factor. Below this energy, it overestimates this quantity (see Chap. 2).

As previously admitted, monoenergetic neutron emissions are marginal. We will see that for a workstation subject to polyenergetic neutron exposure, it may be necessary to calculate of fluence energy spectrum ϕ_E. A Monte Carlo transport code is used to best characterize the radiation field or this spectrum is measured in situ. Then, each histogram contributions to fluence $\phi(E_i; E_{i+1})$ is weighted by the conversion factor $h^*_\Phi(E_i)$ to the lower bound, and the set of values is summed according (3.17).

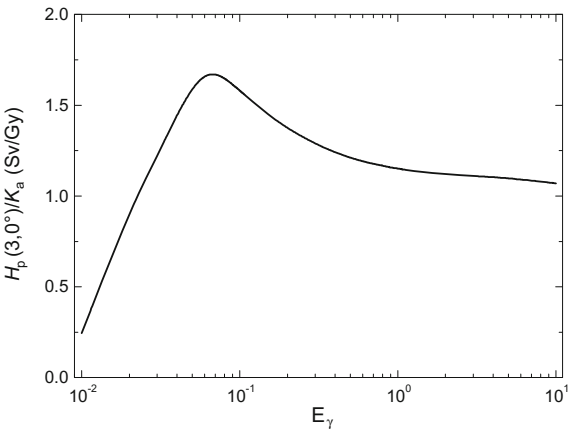

Fig. 3.33 Conversion factor $H_p(3)/K_a$ (according to data from [27])

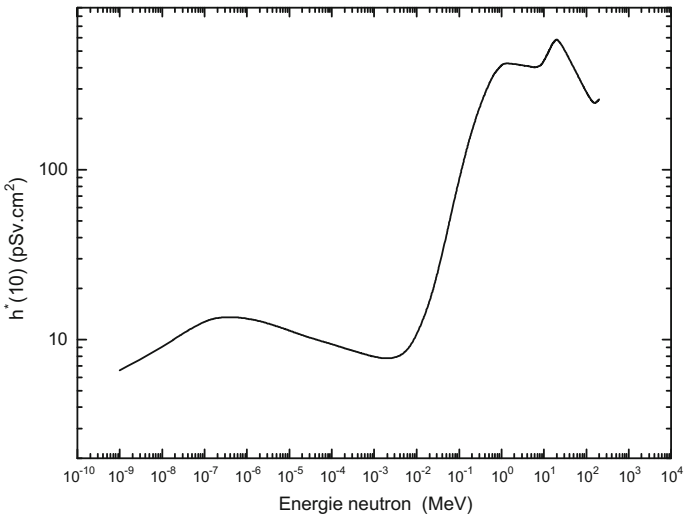

Fig. 3.34 Conversion factor fluence-ambient equivalent dose $H^*(10)$ from the data [7]—values provided in Appendix 5

$$H^*(10) = \sum_{E_i} h^*_{\Phi}(10)_{E_i}\, \Phi(E_i; E_{i+1}) \tag{3.17}$$

Similarly, for the calibration of neutrons radiation device in a secondary laboratory, using a standard source, it is necessary to have a unique conversion factor. Inspired by the expression (3.16), this coefficient for a continuous spectrum is theoretically obtained by the expression (3.18).

$$\bar{h}^*_{\Phi} = \frac{1}{\Phi} \int_0^{E_{\max}} h^*_{\Phi}(E_n)\, \Phi(E_n)\, dE_n \tag{3.18}$$

In practice, the fluence energy spectrum of a ^{252}Cf source is sampled (see histogram representation of a ^{252}Cf source, Chap. 1). Expression (3.19) is discritized (3.19).

$$\bar{h}^*_{\Phi} = \frac{1}{\Phi} \sum_{E_i} h^*_{\Phi}(E_i)\, \Phi(E_i; E_{i+1}) \tag{3.19}$$

This approach leads for a ^{252}Cf source at a mean conversion factor "fluence-ambient dose equivalent" of $\bar{h}^*_{\Phi}(10) = 385$ pSv cm^2. Thus, if we consider a neutron source emitting 100 (n) s^{-1}, the dose equivalent at 1 m is:

$$H*(10) = \bar{h}^*_{\Phi}(10)_{^{252}Cf}\frac{\dot{N}}{4\pi d^2} = 3600 \times 385 \cdot 10^{-12} \times \frac{100}{4\pi \times (100^2)} = 1.1 \text{ nSv h}^{-1}$$

So the operational quantity for a continuous spectrum source is provided by a fairly simple calculation.

Let's consider a typical mixed case of neutrons and photons yield by a punctual source of AmBe. Let's determine the ambient dose equivalent rate at 50 cm form an AmBe source with a active mass of 0.88 g. ISO 8529. The [29] (see Chap. 4) announces a specific emission source of $6.6 \cdot 10^{-5}$(n) s^{-1} Bq^{-1} due to (α, n) reaction. For the AmBe spectrum a mean conversion coefficient "fluence-ambient dose equivalent" equal to 391 pSv cm^2 is applied (see Chap. 4). Beforehand, it is necessary to calculate the activity corresponding to such a mass; it is obtained from the specific activity of a radionuclide as follows:

$$A_m = \frac{\lambda \eta_A}{\mathrm{A}}$$

with λ the radioactive decay constant in s^{-1}, η_A Avogadro's number and A the atomic mass. The ^{241}Am half life is 432.6 years, the specific activity is therefore:

$$A_m = \frac{\left[\ln(2)/T_{1/2}\right]\ \eta_A}{A} = \frac{[\ln(2)/(432.6 \times 365 \times 24 \times 3600)] \times 6.02 \cdot 10^{23}}{241} = 1.269 \cdot 10^{11} \text{ Bq/g}$$

Accordingly, a mass of 0.88 g ^{241}Am has an activity of 111 GBq. The ambient dose equivalent is obtained in the same way as for the ^{252}Cf source.

$$\dot{H}^*_n(10) = \bar{h}^*_{\Phi}(10)_{AmBe}\left(\frac{\dot{N}_n}{4\pi d^2}\right) = \bar{h}^*_{\Phi}(10)_{AmBe}\left(\frac{Y_A A}{4\pi d^2}\right) = 3600 \times 391 \cdot 10^{-12} \times \frac{6.6 \cdot 10^{-5} \times 111 \cdot 10^9}{4\pi \times (50^2)} = 330 \text{ μSv h}^{-1}$$

Do remember to take into account the component related to the photon emission of ^{241}Am. The latter, as mentioned above, is responsible for the emission of a 60 keV photon to 36% and a 15 keV photon to 43%. Conversion factors "fluence-ambient dose equivalent" are provided in Appendix 3 and are respectively 0.51 and 0.83 pSv cm^2. If in previous calculations, we have omitted the transmission factor related to the medium interposed between the source and the calculation point, and the self shielding of the source (see Chap. 5), rigorously this parameter must be taken into account. In this case the medium considered is air. Thus, the ambient dose equivalent, in respect with a negligible build-up in air, is given by:

$$\dot{H}^{*}_{\gamma}(10) = \sum_{E_\gamma} h^{*}_{\Phi}(10) \left(\frac{A\,\Gamma\left(E_\gamma\right)}{4\pi\, d^2}\right) T_{air}\left(\mu x, E_\gamma\right)$$

The results of transmission factors obtained from the mass attenuation coefficients given in Chap. 2, are:

$$T_{air}(\mu x,\ 15\,\text{keV}) = \exp\left(-1.615 \times 1.3 \cdot 10^{-3} \times 50\right) = 0.9 \cong 1$$
$$T_{air}(\mu x,\ 60\,\text{keV}) = \exp\left(-0.187 \times 1.3 \cdot 10^{-3} \times 50\right) = 0.98 \cong 1$$

Finally, with $\left[h^{*}_{\Phi}(10)\right]_{15\,\text{keV}} = 0.83\,\text{pSv cm}^2$ and $\left[h^{*}_{\Phi}(10)\right]_{60\,\text{keV}} = 0.51\,\text{pSv cm}^2$. From this, we infer the following ambient dose equivalent rate:

$$\dot{H}^{*}_{\gamma}(10) \cong 3600 \times \left(\frac{1.11 \cdot 10^{11}}{4 \times \pi \times 50^2}\right) \times \left[\left(0.43 \times 0.83 \cdot 10^{-12} \times 0.9\right) + \left(0.36 \times 0.51 \cdot 10^{-12} \times 0.98\right)\right]$$
$$\dot{H}^{*}_{\gamma}(10) \cong 2.28 \cdot 10^{-3} + 4.08 \cdot 10^{-3}\ \text{Sv/h} = 6.4\ \text{mSv/h}$$

Several lessons can be learned from this problem: first, as mentioned on the commentary of Fig. 3.29, the contribution of 15 keV photon is twice higher than that of 60 keV photon dose equivalent of ^{241}Am in the air (i.e. in the vacuum). In this same medium, it appears that the photonic component is 22 times greater than that related to the neutron emission. However, this finding must be qualified by the non-inclusion of any source self-shielding or outer shell thereof, which would limit the photonic component. Furthermore, we will show in Chap. 5 that the interposition of shielding causes a reversal of contributions: as the thickness of the shielding increases, the neutron contribution to the dose equivalent, for the AmBe Source becomes widely predominant and those related to γ negligible.

Note that Chap. 4, a section is devoted to detail "fluence ambient dose equivalent" factors for different neutron sources.

3.5.7 *Conversion Factors for Electrons*

For electrons, the physical quantity of reference is the fluence at a point. Because of their low penetration in matter, the recommended operational quantity is the directional dose equivalent $H'(d,\ \alpha)$. The curves of Fig. 3.35 display these coefficients for depths, 70 μm, 3 and 10 mm. These values are given in a table in Appendix 6.

With knowledge of electron fluence, the conversion factors $h'_{\Phi}(0.07)$, $h'_{\Phi}(3)$ and $h'_{\Phi}(10)$ allows to calculate the respective estimators of equivalent dose to the skin H_{skin}, the equivalent dose to the eye-lens H_{eye} and the "whole body" effective dose. We can observe a energy limit below which these coefficients are zero: this is the minimum energy to reach the depth of tissue for the

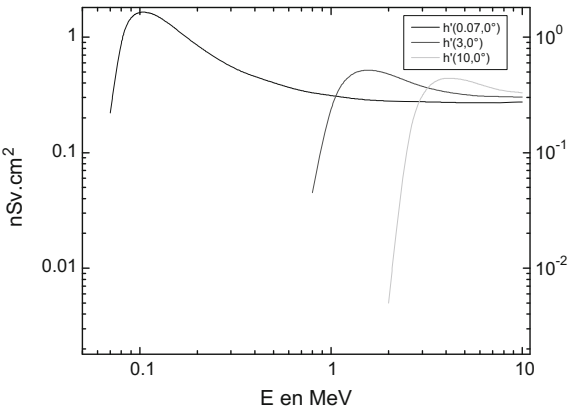

Fig. 3.35 Conversion coefficients from fluence to directional dose equivalent for monoenergetic electron and normal incidence according to the data [7]—values provided in Appendix 6

desired operational quantity. It can be estimated by focusing on the curve $h'_{\Phi}(10)$: an electron must have a minimum energy of about 2 MeV to reach the depth of 10 mm. This is corroborated by the range calculation provided by Katz and Penfold's formula (2.3), leading to the value of 9.5 mm.

Moreover, for each of the conversion factors, the peak corresponding to maximum energy deposition is linked to the "Bragg peak" previously studied for the energy deposition of charged particles.

In the case of the emission spectra of β, a calculation by energy bin can be performed according to the expression (3.15). But to a first approximation, a calculation from the conversion coefficient to the mean energy spectrum $\overline{E}_{\beta}$ can be understood in two different ways: for a typical Maxwellian spectrum (e.g. ^{32}P), it is considered a mean energy equal to one third of the maximum energy

$$\overline{E}_{\beta} = \frac{E_{\beta Max}}{3}$$

For "less typical" spectrum shape, the mean energy is derived from nuclear database (e.g. www.oecd-nea.org/janis) or empirical approximation such as the Joffre's method [30] according to the atomic number of the radionuclide and $E_{\beta\max}$ (Table 3.9).

Table 3.9 Weight factor of $E_{\beta\max}$ to get $\overline{E}_{\beta}$ depending on the atomic number radionuclide [30]

$E_{\beta\max}$ in MeV radionuclide atomic number	0.2	0.5	1	2
4	0.15	0.16	0.20	0.21
10	0.12	0.13	0.18	0.20
20	0.12	0.13	0.16	0.19
40	0.11	0.12	0.14	0.18
80	0.09	0.09	0.11	0.15

By focusing on the shape of the $h'_{\Phi}(0.07)$ curve, beyond an energy of 300 keV, the curve presents a constant shelf, whose value is 0.32 nSv cm^2. Thus, we can approximate the dose equivalent rate $\dot{H}'(0.07)$ for a source of activity A; intensity Γ; higher energy electrons to 300 keV; at a distance d cm, below 30 cm, by the following relationship:

$$\dot{H}'(0.07)_{\mathrm{Sv/h}} = 9 \cdot 10^{-8} \cdot \frac{A\Gamma}{d^2}$$

For example, let's calculate the dose equivalent rate at 30 cm of a punctual 37 GBq ^{32}P source. The Maxwellian shape of spectrum allows us to approach the mean energy to 1/3 of the maximum energy, i.e.: with $E_{\beta\max}$ = 1.71 MeV, it comes $\overline{E}_{\beta} = 700\,\mathrm{keV}$ and for an intensity of 100%:

$$\dot{\mathrm{H}}'(0.07)_{\mathrm{Sv/h}} = 9 \cdot 10^{-8} \cdot \frac{\mathrm{A}\Gamma}{\mathrm{d}^2} = 9 \cdot 10^{-8} \times \frac{37 \cdot 10^9}{30^2} = 3.7\ \mathrm{Sv/h}$$

A special care have to be taken on the reliability of this formula below 30 cm. Beyond this distance, the attenuation in the air becomes significant for β, as well as the loss of energy for monoenergetic electrons, which significantly alter the primary assumption. Note, finally, that ICRP provides these coefficients up to 10 MeV. Pelliccioni [28] extends the "fluence-ambient dose equivalent in 10 mm" factors up to 10 GeV.

Note: If these conversion factors for electrons are used in numerical or analytical calculations, however they are not used during calibration of radiation protection devices, given that the physical quantity reference for electrons and β remains D_t, the absorbed dose in tissue.

Conversion factors for heavy charged particles

To calculate "fluence-ambient dose equivalent" factors, Pelliccioni [31] has achieved absorbed dose calculations within the ICRU sphere using a Monte Carlo code (see Chap. 2). Similarly, the quality factors Q in the ICRU sphere for light ions at energies up to 1 GeV were calculated. Figure 3.36 show the calculated depth distributions of absorbed dose or dose equivalent for incident proton for an energy range between 50 MeV and 1 GeV.

Thus, two variables can then be deduced from above results: the ambient dose equivalent at depth 10 mm which is the value for depth 10 mm in the ICRU sphere and the maximum dose equivalent, namely the value of the maximum dose equivalent in ICRU sphere. This latest quantity provides the maximum dose equivalent regardless of the depth where the maximum is. Indeed, in the case of protons and more generally light ions, it is roughly located at the Bragg peak depth.

Figure 3.37 displays, "fluence-dose equivalent" factors for monoenergetic protons at a 10 mm depth, i.e. h*(10), and of $h_{\max}$ as a function of energy.

For example, let's consider a 200 MeV protons beam of 10 cm^2 section and intensity $1 \cdot 10^{10}$ (protons) s^{-1}. The ambient dose equivalent rate in the protons beam should be:

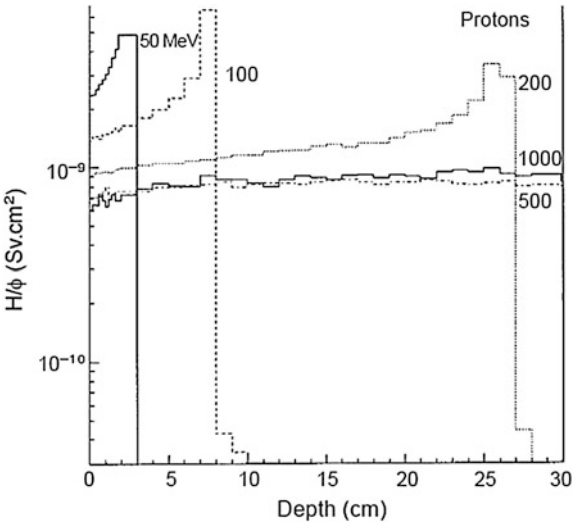

Fig. 3.36 Absorbed dose plotted versus depth in the ICRU sphere for a parallel beam of monoenergetic incident protons of various energies (after [31], with permission from Oxford University Press)

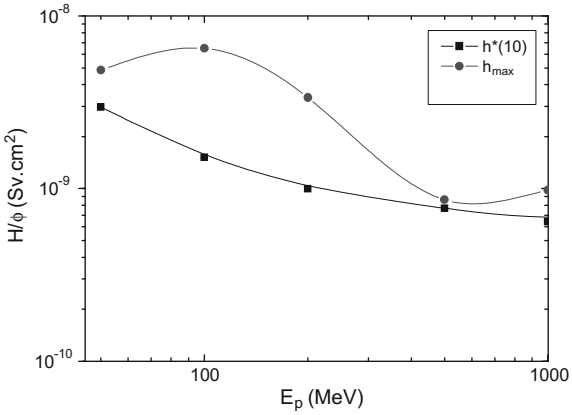

Fig. 3.37 "Fluence-equivalent dose in 10 mm tissue" factors and "fluence-maximum equivalent dose" factors (according to the data [31])

$$\dot{H}^*(10) = \frac{1 \cdot 10^{-9}}{10} \times 1 \cdot 10^{10} = 1 \text{ Sv s}^{-1}$$

The equivalent maximum dose rate in the beam should be:

$$\dot{H}_{\max} = \frac{3.4 \cdot 10^{-9}}{10} \times 1 \cdot 10^{10} = 3.4 \text{ Sv s}^{-1}$$

Note that no consensus is adopted by authors on the value of the conversion factors for protons. Indeed, the absorbed dose varies hugely around the Bragg peak; as the calculation is performed by assessing the mean energy deposition in an element of volume of the sphere ICRU, the size of this volume for calculation affects the result.

3.6 Comparison Between Operational Quantities and Protection Quantities

As mentioned, the operational quantity is established in order to slightly overestimate the protection quantity, hence to always ensure that the exposed worker is below the legal exposure limits. Thus, ideally, inequality given in (3.20) should be checked.

$$\begin{aligned} &H_p(10),\ H^*(10) \geq E \\ &H'(0.07),\ H_p(0.07) \geq H_{extremity} \end{aligned} \tag{3.20}$$

However, in its Report 57, ICRU has calculated the differences between protection and operational variables, and showed that, in some specific configurations, the first is underestimated by the second. Figure 3.38 gives ratios $E/H_p(10)$ $E/H^*(10)$ and $E/H'(10)$ for different radiation field, and energy for photons and neutrons.

For photons, in geometry AP, the ratio highlights a significant underestimation of the effective dose for energies below 0.1 MeV.

For neutrons, this underestimation of the protection quantity by the operational quantity is noteworthy for energy range between 10^{-6} MeV and 0.04 MeV.

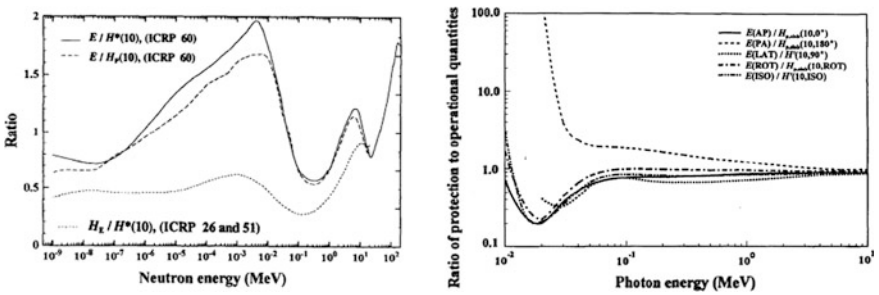

Fig. 3.38 Ratio $E/H_p(10)$ $E/H^*(10)$ and $E/H'(10)$ for various configurations of radiation, and energy for photons and neutrons, according to [7]. Reproduced by permission of Michiya Sasaki on behalf of ICRP

However, as mentioned earlier, the monoenergetic neutron situations are marginal. As such, ICRP in its publication 74 specifies that for most of neutron spectra encountered at the workstations, the dose equivalent overestimates the effective doses. However, we will see in Chap. 4 below, this rule does not hold for a number of neutron sources (e.g. AmBe).

Furthermore, we have previously admitted a significant variation for the dosimeters response in terms of individual dose equivalent based on the angle of incidence. Hence, the question is: what is the impact of this observation on the estimated effective dose? In particular, when a dosimeter calibrated in $H_p(10)$ is subjected to an irradiation field with various incident angle? This reflection led Chumak and Bakhanova [32] to simulate an anthropomorphic phantom and a dosimeter worn at the front of the phantom, to the location where it is carried by a worker. By calculating Monte Carlo, they assessed, for different polar and azimuthal angles, the effective dose provided by the operational quantity when the dosimeter is located on the trunk. They observed substantial underestimates of the effective dose according to the angle (Fig. 3.39).

These underestimations are the consequence of radiation attenuation by the thickness of the trunk to reach the dosimeter. They are mainly present for azimuthal angles from 60° to 180°.

In conclusion, for a side irradiation with photons of about 50 keV, by accumulating the differences related to the intrinsic model of dose equivalent (Fig. 3.38) and the high angular dependency of the response (Fig. 3.39), the underestimation of the effective dose by the operational quantity can reach about a factor of 5.

Conversely, Bourgois [10] showed, using the model of ICRP 74, a significant overestimation of the equivalent dose to the skin H_{skin} by its estimator: the personal

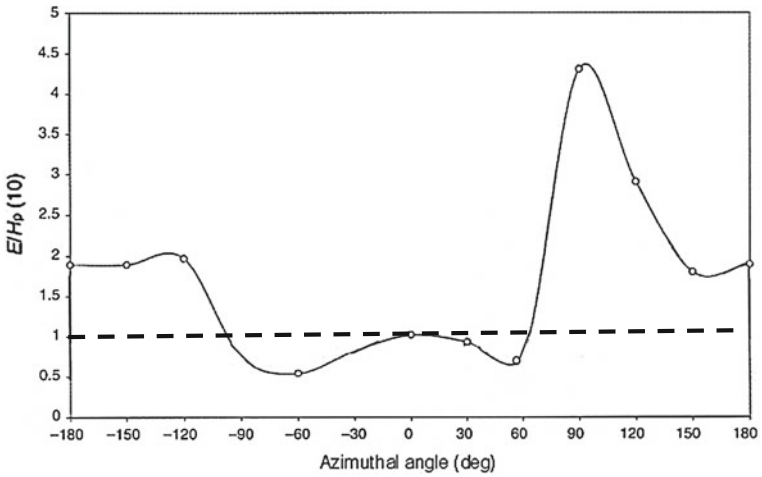

Fig. 3.39 Angular dependence of the report $E/H_p(10)$ depending on the azimuth angle for a photon energy of 200 keV. Adapted from [32]

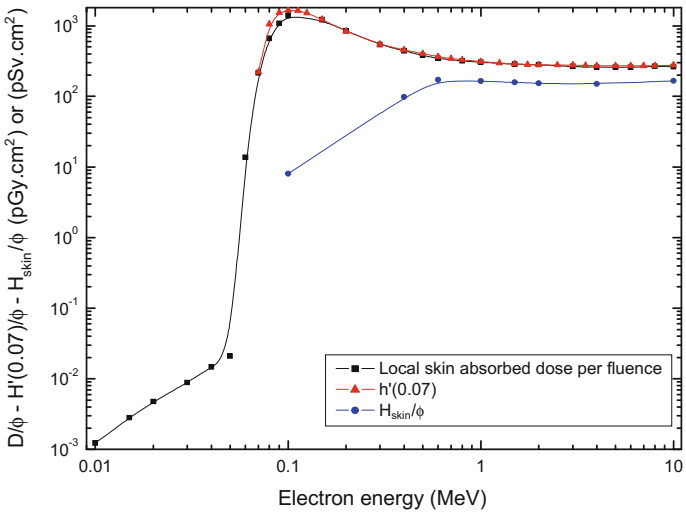

Fig. 3.40 Protection and operational quantities for electrons. Local skin absorbed dose (ICRP 116); H_{skin} (ICRP 74 for effective dose calculation) and the directional dose equivalent $H'(0.07)$ as a function of electron energy (from [3] and [7] datas)

dose equivalent, $H_p(0.07)$ for punctual radiation sources β in contact with the skin and for surface contamination spots. However the introduction into ICRP 116 of the concept of the local skin dose overcomes this overestimation.

The Fig. 3.40 compares, for monoenergetic electrons, protection quantities: equivalent dose to the skin (to calculate the effective dose) and local skin dose (allowing compliance with the dose limit equivalent to the skin of 500 mSv) and operational quantity the dose equivalent at a depth 0.07 mm $H'(0.07)$. Then it is noted that, for the electrons, local skin dose is substantially superimposed on the dose equivalent $H'(0.07)$. A significant lesson concerns the energies below 65 keV: The values of this new protection quantity are non-zero below this energy, unlike the estimator $H'(0.07)$. This is explained by the decrease in depth from which the calculation region of the mean dose is achieved.

3.7 Calibration of Radiation Devices

Even if in very few cases, dosimeters allow instant access to the desired operational quantity (e.g. case of dose equivalent $H_p(0.07)$ for a LiF ring for photons and electrons) in most cases, it is necessary to use a calibration to connect the measurement to the operational quantity. The principle of the calibration of radiation protection devices (ambient and individual) is developed later in this section.

3.7.1 Definition of Reference Fields

The primary metrology laboratories (e.g. LNHB in France) own "standard beams" for each type of directly or indirectly ionizing radiation, whose characteristics in terms of physical quantities of reference are clearly identified. These "primary fields," must represent a wide range of energy sources to cover a wide response domain of dosimeters. The dosimeter response as a function of energy $R'(E)$ according to the operational quantity, may vary significantly from one energy to another. Moreover, this variety allows a broader characterization of "source terms" of external exposure that may be present in radiological exposure areas. These fields of primary radiation and energy areas covered are further specified through standards to ensure reproducibility of the calibration parameters. The standards, ISO 4037 [33], ISO 6980 [34] and ISO 8529 [29] define the primary fields respectively for photons (X and γ) β and neutrons.

A number of these primary fields, due to their heavy mode of production, are available only in specialized laboratories namely primary laboratories. For instance, for X and photons, the use of filtered generators X at constant voltage is recommended for energies below 250 keV and reactor or accelerator for photon energies above 4 MeV. Similarly, for neutrons, accelerators allow the production of monoenergetic neutrons via specific reactions: $^{7}Li(p, n)^{7}Be$, $^{48}Ti(p, n)^{48}V$, $^{45}Sc(p, n)^{45}Ti$, $^{3}H(d, n)^{4}He$.

Radioactive sources are less binding devices than those of primary radiation emission fields:

- for photons, sources ^{241}Am, ^{137}Cs and ^{60}Co primarily emitting energy rays 59.5 keV, 662 keV, 1173 keV and 1332 keV are recommended;
- for neutrons, ^{252}Cf, ^{252}Cf moderated by heavy water (D_2O) and $^{241}AmBe$ are the standards for sources of neutron emission spectra.

Finally, the use of pure β emission sources can cover a energy range between 0.156 MeV for ^{14}C and 3.54 MeV for $^{106}Ru/^{106}Rh$.

3.7.2 Transfer Dosimeters in Primary Laboratories

As mentioned, the primary radiation are fully characterized toward the physical quantities of reference (e.g. air kerma for photonic primary radiation). Thus, a transfer device located at a reference point of the primary field, must measure precisely the reference quantity at this point. If this instrument provides a measured value m_0, it must match the value G_0 of the physical quantity at the same point. The calibration factor N_0 of this transfer instrument, in the primary laboratory is then given by the ratio (3.21).

$$N_o = \frac{G_o}{m_o} \tag{3.21}$$

Thus, as a result, for any measured value m, we access to the reference value G according to this calibration factor by the relationship of proportionality $G = N_0 m$. For example, let's consider a ionization chamber as a transfer instrument without special dosimetric property (nor equivalent air chamber nor air equivalent wall chamber) for photon radiation measurement. The reference quantity is the air kerma and more specifically a rate of this quantity. To characterize the response of the device at low energies, the choice to use a standard source of 1 TBq ^{241}Am is done to generate a primary field of 60 keV photons. Consider a reference point at 1 m of the source. With an exact knowledge of the source activity (to uncertainty about, given by the manufacturer, the impact is limited), the kerma in the air can be perfectly determined (absence of scattered radiation in air and due to large irradiation area to limit the scattered radiation on the walls). At 1 m the Air Kerma is determined by the theoretical expression of Chap. 2, available for both energies of ^{241}Am as follows:

$$\dot{K}_a\left(^{241}Am\right) = \dot{K}_a(15\,\mathrm{keV}) + \dot{K}_a(60\,\mathrm{keV})$$

$$\dot{K}_a\left(E_\gamma\right) = 5.76 \cdot 10^{-4}\left(\frac{A\Gamma_{E_\gamma}}{4\pi\, d^2}\right) E_\gamma \left(\frac{\mu_{tr}}{\rho}\right)_{E_\gamma}^{air} B_{air}\left(\mu x, E_\gamma\right) \exp\left(-\left(\frac{\mu}{\rho}\right)_{E_\gamma}^{air} \rho\, d\right)$$

with $B_{air}(\mu x, 15\ \mathrm{keV}) = B_{air}(\mu x, 60\ \mathrm{keV}) \approx 1$;
$(\mu_{tr15\ keV}/\rho)_{air} = 1.334\ g^{-1}\ cm^2$, $(\mu_{15\ keV}/\rho)_{air} = 1.614\ g^{-1}\ cm^2$
$(\mu_{tr60\ keV}/\rho)_{air} = 0.0287\ g^{-1}\ cm^2$, $(\mu_{60\ keV}/\rho)_{air} = 0.178\ g^{-1}\ cm^2$.

$$\dot{K}_a(60\,\mathrm{keV}) = 5.76 \cdot 10^{-4} \cdot \left(\frac{0.36 \times 10^{12}}{4\pi \times (100)^2}\right) \times 0.06 \times 0.0287$$
$$\times \exp(-0.178 \times 0.00122 \times 100) = 2.93\ \mathrm{mGy\ h^{-1}}$$

$$\dot{K}_a(15\,\mathrm{keV}) = 5.76 \cdot 10^{-4} \cdot \left(\frac{0.36 \times 10^{12}}{4\pi \times (100)^2}\right) \times 0.015 \times 1.334$$
$$\times \exp\left(-1.614 \times 1.3 \cdot 10^{-3} \times 100\right)$$
$$= 31.97\ \mathrm{mGy\ h^{-1}}$$

$$\dot{\mathrm{K}}_\mathrm{a}\left(^{241}\mathrm{Am}\right) = \dot{\mathrm{K}}_\mathrm{a}(15\ \mathrm{keV}) + \dot{\mathrm{K}}_\mathrm{a}(60\ \mathrm{keV}) = 31.97 + 2.93 = 35\ \mathrm{mGy\ h^{-1}}$$

At this reference point, the transfer instrument is disposed and the measurand considered is the current delivered by the latter. The measured intensity is $i = 5 \cdot 10^{-13}$ A. The calibration factor of the transfer instrument in the primary laboratory is determined by the expression (3.21).

Table 3.10 Physical quantities and transfer device used for the different types of reference fields, according to [35]

Type of radiation	Physical quantity of reference	Transfer equipment
X and gamma	Air Kerma (Gy)	Absolute air wall ionization chamber
		Absolute type Bragg-Gray ionization chamber
Beta	Absorbed dose in tissue (Gy)	Extrapolation ionization Chamber with a tissue-equivalent material 7 mg cm^{-2} (70 μm) window
Electrons	Absorbed dose in tissue (Gy)	Calorimetry
		Chemical dosimetry
Neutrons	Fluence (m^{-2})	Spectrometry chain
		scintillator
		Proton recoil counters
		Bonner Sphere Spectrometer (BSS)

With the permission of ATSR

$$N_o = \frac{G_o}{m_o} = \frac{\dot{K}_{air}}{i} = \frac{35}{5 \cdot 10^{-13}} = 7 \cdot 10^{13}\ \text{mGy h}^{-1}\ \text{A}^{-1}$$

The three aforementioned ISO standards define for different types of radiation, the physical quantity of reference and transfer equipment recommended. The set of these data is summarized in the Table 3.10.

We find in the Table 3.10 various metrological equipment detailed in Chap. 2 for characterization of radiometric and dosimetric physical quantities. We will note also, especially in the case of photon and electron radiation, the use of absolute dosimeters as transfer device.

3.7.3 Connecting Process and Transition to the Operational Quantity in a Secondary Laboratory

The purpose of calibrating a radiation protection device is to measure an appropriate operational quantity, for an area or a personal dosimetry.

Beforehand, a connecting process can be performed which consists, in the calibration laboratory of a nuclear facility to recreate the reference fields conditions of the primary laboratory (e.g. previous ^{241}Am source). In this facility, the transfer dosimeter (e.g. PTW chamber) is set at a reference point P, and the measurement of the "true value" of the physical quantity of reference is performed (e.g. air kerma for PTW chamber). Figure 3.41 shows a picture of a calibration bench of a secondary laboratory in the presence of the ^{241}Am source and an ionization chamber (PTW chamber) as transfer dosimeter.

Fig. 3.41 Secondary laboratory bench during a connecting process for the measurement of air kerma with PTW chamber and a point-source

For example, let's consider that the transfer dosimeter indicates an intensity of $2 \cdot 10^{-14}$ A at the reference point P. The relationship of the calculated calibration factor previously used to access the results of the Air Kerma, gives

$$c\dot{K}_{air} = N_0 I = 7 \cdot 10^{13} \times 2 \cdot 10^{-14} = 1.4 \text{ mGy h}^{-1}$$

the next step includes providing the operational quantity to point P, here an ambient dose equivalent rate using "physical quantity-operational quantity" conversion factors we have detailed in Sect. 3.5.6; so, in this case, the "Air Kerma-ambient dose equivalent" factor $h^*_{K_a}(10) = (H^*(10)/K_a)_{E_\gamma}$ for ^{241}Am. It shall be here a composition of coefficients for 15 and 60 keV through a weighted average of:

$$\left[h^*_{K_a}(10)\right]_{^{241}Am} = \frac{\sum\limits_{E_\gamma}\left[h^*_{K_a}(10)\right]_{E_\gamma} K_a(E_\gamma)}{\sum\limits_{E_\gamma} K_a(E_\gamma)}$$

$$= \frac{\left[h^*_{K_a}(10)\right]_{15\,\text{keV}} K_a(15\,\text{keV}) + \left[h^*_{K_a}(10)\right]_{60\,\text{keV}} K_a(60\,\text{keV})}{K_a(15\,\text{keV}) + K_a(60\,\text{keV})}$$

The elements of calculation in Sect. 3.7.2 and the table provided in Annex 4, lead to the following result:

$$\left[h^*_{K_a}(10)\right]_{^{241}Am} = \frac{(31.97 \times 0.26) + (2.93 \times 1.74)}{35} = 0.383 \text{ Sv/Gy}$$

Note that for ^{137}Cs and ^{60}Co, the factors 1.202 and 1.158 Sv/Gy are respectively obtained. At the point P, the ambient dose equivalent rate connected to the kerma rate previously calculated would be:

$$\dot{H} * (10) = h^*_{K_a}(10)\, \dot{K}_{air} = 1.4 \times 0.383 = 0.54 \,\text{mSv h}^{-1}$$

Once the operational quantity perfectly characterized at the point P, a final step is to calibrate the radiation protection device (γ operating ionization chamber for area dosimetry) at this point. The latter is therefore located at the point P in place of the transfer dosimeter as shown in Fig. 3.42 and a measurement is then performed.

Let's consider, for example, that the previous device indicates at the point P: $5 \cdot 10^3$ units of measurement. The calibration coefficient N_H for this device for ambient dose equivalent H*(10) and for low energy is finally obtained according to the ratio (3.22).

$$N_H = \frac{H * (10)}{m_u} = \frac{0.54}{5 \cdot 10^3} = 1.1 \cdot 10^{-4} \text{ mSv h}^{-1}\left(\text{u}^{-1}\right) \tag{3.22}$$

Regarding the calibration of personal dosimeters, they substantially follow the whole process with the exception of this last step.

First, remind that the operational quantities to be measured are supposed to simulate the scattering in any part of the body: $H_p(10)$ for strongly penetrating and $H_p(0.07)$ for weakly penetrating. The "Air Kerma-personal dose equivalent" conversion factors are then used in accordance with the second step. In the last step, devoted to the determination of the calibration coefficient to be applied to the dosimeter, the dosimeter will this time not be set isolated at P but located on an

Fig. 3.42 Calibration of the radiation protection device on the calibration bench, here γ ionizing chamber in a secondary laboratory

appropriate phantom (e.g. ISO-PPMA phantom) to recreate scattering conditions of the radiation field, necessary for the characterization of the personal dose equivalent. This class of device is shown in the picture Fig. 3.43.

Let us add that the choice of the point P location is not insignificant: according to the fluence rate of the radiation field, the calibration point is required to meet the homogeneity of the field in the sensitive volume of detector to avoid statistical errors on the count rate for source of low activity, the effects of scattering …

3.7.4 Calibration with a Standard Source in a Secondary Laboratory

We admitted that "standard sources" can be used to ensure the conditions of the primary fields specified by the standards. Accordingly, it is possible to "bypass" the step of the connecting process in a second laboratory using a transfer dosimeter, by the use of "standard sources" whose the activity itself constitutes a physical quantity of reference, since linearly related to the fluence. The example below shows the calibration process performed at the CEA Cadarache center (France) to calibrate neutrons dosimeters.

A standard source of ^{252}Cf, is the primary field whose the activity is well known and therefore his fluence is well characterized at the point P. Through the knowledge of the mean "fluence-ambient dose equivalent" factor, so it is perfectly

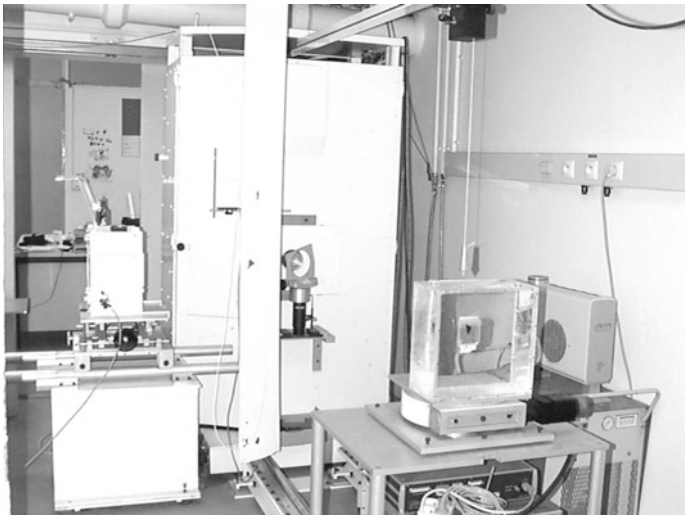

Fig. 3.43 Calibration of a personal dosimeter on a phantom ISO-PPMA for personal dose equivalent $H_p(10)$ in a primary field of fluorescent X-ray

possible to estimate at this point the ambient dose equivalent. In the specific case of neutrons, the influence of the neutrons scattering on the result, which induces the need to a raw measurement and a secondary measurement through a polyethylene "shadow cone" for only measure the scattered component on calibration laboratory facility. Figure 3.44 gives a schematic representation of both measurements.

The area dosimeter calibration factor is then obtained by means of a variant of the expression (3.23).

$$N_H = \frac{H^*(10)}{m_t - m_s} = \bar{h}^*_{\Phi}(10)\ \frac{\dot{N} F_1(\theta)}{4\pi d^2} \frac{1}{(m_t - m_s)} \exp(-\Sigma d) \tag{3.23}$$

with $\bar{h}^*_{\Phi}(10) = 385$ pSv cm^2 the mean "fluence-ambient dose equivalent" conversion factor for the ^{252}Cf source, $\dot{N} = Y_A A$ the neutron flux (s^{-1}), d the distance "detector-source", $F_1(\theta)$ the isotropic source factor taking into account the decrease over time of the effective emission of the source (e.g. effect of irradiation on alphas sources AmBe), m_t is the raw measurement, m_s is the scattering measurement with the shadow cone.

Figure 3.45 gives histograms of spectral distribution of a ^{252}Cf source with and without "shadow cone" used in the calibration process for area dosimeters.

Note that previous approach using conversion factors is not used for β area dosimetry. The dosimeters are directly calibrated in terms of absorbed dose under 7 mg cm^{-2} of tissue-equivalent material $D_t(0.07)$, which, with quality factor of 1, is equal to the directional dose equivalent at this depth $H'(0.07)$ measured by extrapolation chamber.

3.7.5 *Area and Personal Dosimeters Responses in Energy* R*(*E*), in Angular* R*(Ω) and Flux Rate*

Most of calibration process for dosimeters consists to connect to one energy or a spectrum the associated operational quantity. However, dosimeters may respond differently depending on the radiation energy. This raises the issue of the possible deviation between the measured value of the dose equivalent for energy other than that used during calibration and the one we should theoretically get. This gap can be

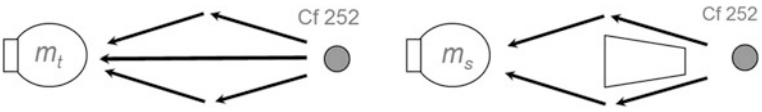

Fig. 3.44 Raw and scattering measurements for neutron device calibration using the "shadow cone" technique

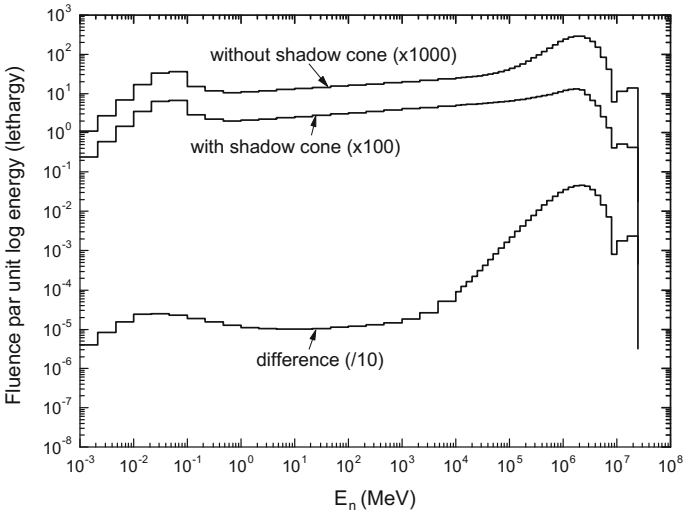

Fig. 3.45 Energy distribution of ^{252}Cf spectrum with and without shadow cone for the calibration process, from to the data [36]

evaluated by a ratio of the measured response to the theoretical response, called "energy response" of the dosimeter for a given dosimetric quantity.

$$R(E) = \frac{R_m(E)}{R_{th}(E)}$$

Obviously, if this ratio is 1 whatever the energy the response of the dosimeter is ideal. This case, we shall see, although existing, is marginal. A variant of this "energy response" is to consider the gap between the dosimeter response to the calibration energy E_0 and the response to a given energy E.

$$R'(E) = \frac{R(E)}{R(E_o)}$$

The IEC (International Electrotechnical Commission) and ISO recommend acceptable deviation levels depending on the type of radiation and the energy range for individual dosimeters (e.g. IEC 1525 [32] sets a tolerance for electronic dosimeters sensitive to photons ±30% compared to the response of ^{137}Cs, for a range of photon energy between 50 keV and 1.5 MeV).

Similarly, the "angular response" of an individual dosimeter which reflects the gap of the response for an incidence angle $\alpha = 0$, to an angle of incidence α, must be taken into account.

$$R'(\alpha) = \frac{R(\alpha)}{R(\alpha = 0)}$$

In the case of the area dosimetry, for measuring $H^*(10)$, for which we have broadly described above calibration process, the response must be "isotropic", that is the same response regardless of the angle of incidence. The ratio above is then ideally 1. Standards also set for these ratio the tolerated deviation (e.g. between 0° and 30° ±20% compared to the response of the ^{137}Cs to 0°).

In contrast, in the case of directional quantities (e.g. $H'(0.07, \alpha)$ and $H_p(0.07)$), the response must be isodirectional, that is to say, the dosimeter response should vary according to the angle, ideally along the theoretical curve calculated in the ICRP 74: $R(0.07, \alpha) = H'(0.07, \alpha)/H'(0.07, 0°)$ (Fig. 3.24 for electrons).

Similarly, specifications exist for tolerance on dose equivalent rate measurements (e.g. less than 20% deviation for the measurement of 1 Sv h^{-1} for a ^{137}Cs source).

Answers of some area dosimeters

Consider a Babyline ionization chamber type, with a sensitive volume of 515 cm^3 filled with air, working on a absorbed dose in tissue rate range from 10 μGy/h to 1000 mGy/h. This ionization chamber works with tissue equivalent wall in accordance with Bragg-Gray's law (see Chap. 2). According to the manufacturer a constant response for photons between about 8 keV and 2 MeV is provided, so independent of the energy over the same energy range, as shown in Fig. 3.46.

This independent energy response of the absorbed dose may be explained regarding the expression of the Bragg-Gray law for the absorbed dose in the wall with a stopping power ratio $\left(\overline{S}/\rho\right)_{air}^{tissue} \approx 1.14$ for all energies between 60 keV and 2 MeV (see Chap. 2). Thus we can assume that:

$$R'(E) = \frac{R(E)}{R(E_o)} = \frac{D_t(60\,\text{keV})}{D_t(1.25\,\text{MeV})} = \frac{D_t(2\,\text{MeV})}{D_t(1.25\,\text{MeV})} \approx 1$$

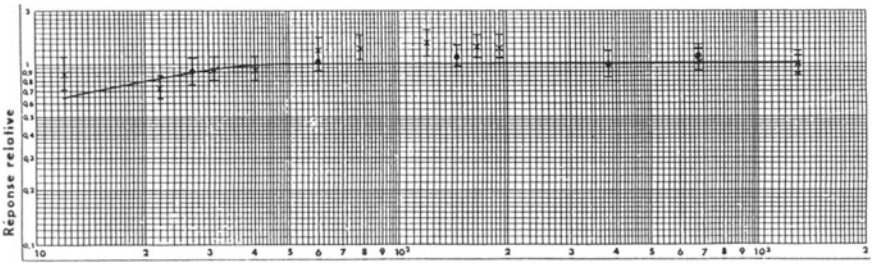

Fig. 3.46 Certificate of the manufacturer for the energy response of the absorbed dose in tissue under 300 mg cm^{-2} for Babyline calibrated with a primary field of ^{60}Co

However, if we keep in mind that the quantity to be measured for this area radiation device is the ambient dose equivalent $H^*(10)$, the energy response $R(E)$ is, this time, not constant over the energy range. Let's consider that under the wall thickness of 300 mg cm^{-2}, the absorbed dose rate is the same (e.g. 1 mGy h^{-1}) for both successive incoming energies: 60 keV and 2 MeV. The air kerma Calculation at the wall inlet differs as evidenced by the results of the following calculations:

$$\dot{K}_{air}(60\ \text{keV}) = \dot{D}_t \left[\exp\left(\left(\frac{\mu}{\rho}\right) \rho \cdot \mathrm{x}_{\text{wall}} \right) \left(\frac{\mu_{tr}}{\rho}\right)_{tissue}^{air} \right]_{60\ \text{keV}}$$

$$= 1 \cdot \exp(0.195 \cdot 1 \cdot 0.3) \cdot \left(\frac{0.0287}{0.031}\right) = 0.98$$

$$\dot{K}_{air}(2\ \text{MeV}) = \dot{D}_t \left[\exp\left(\left(\frac{\mu}{\rho}\right) \rho \cdot \mathrm{x}_{\text{wall}} \right) \left(\frac{\mu_{tr}}{\rho}\right)_{tissue}^{air} \right]_{2\ \text{MeV}}$$

$$= 1 \cdot \exp(0.048 \cdot 1 \cdot 0.3) \cdot \left(\frac{0.0234}{0.0258}\right) = 0.92$$

Using the "Air Kerma-ambient dose equivalent" factors $h^*_{K_a}(10)$, ICRP 74 [7] (Given in Annex 4) gives the following dose equivalent rates:

$$\dot{K}_{air}(60\,\text{keV}) = \dot{D}_t \left[\exp\left(\left(\frac{\mu}{\rho}\right) \rho\, x_{wall} \right) \left(\frac{\mu_{tr}}{\rho}\right)_{tissue}^{air} \right]_{60\,\text{keV}} = 1 \times \exp(0.195 \times 1 \times 0.3) \times \left(\frac{0.0287}{0.031}\right) = 0.98$$

$$\dot{K}_{air}(2\,\text{MeV}) = \dot{D}_t \left[\exp\left(\left(\frac{\mu}{\rho}\right) \rho\, x_{wall} \right) \left(\frac{\mu_{tr}}{\rho}\right)_{tissue}^{air} \right]_{2\,\text{MeV}} = 1 \times \exp(0.048 \times 1 \times 0.3) \times \left(\frac{0.0234}{0.0258}\right) = 0.92$$

If the dose equivalent is substantially equal to the absorbed dose under 300 mg cm^{-2} for an energy of 2 MeV, this would be in contrast for an energy of 60 keV. The calculation leads to an undervaluation of 70% of the real ambient dose equivalent. The energy response $R'(E)$ in term of ambient dose equivalent varies this time significantly, especially at low energies; it is shown in Fig. 3.47.

Moreover, as previously admitted, according to the prescription of the standard, this class of area dosimeter must respond isotropically (i.e. $R'(\alpha) = 1$), Fig. 3.48 shows clearly the angular anisotropy at weak energies, for 60 keV of ^{241}Am and 10 keV of ^{71}Ge.

However, some dosimeters present an energy response $R(E) = R_m(E)/R_{th}(E)$ substantially constant. The proportional counter Stusvik 2202D is one of them. It works on the principle of the detection of thermal neutrons in a sensitive volume filled with BF_3 ($^{10}B(n_{th}, \alpha)^7Li$) placed at the center of a cylindrical moderator of 21.5 cm diameter and 23 cm long. This device has satisfactory energy response $R(E)$ with respect to ambient dose equivalent, as shown in Fig. 3.49.

In the context of measuring the directional equivalent dose for β, we can also mention, the PTW extrapolation chambers of a thickness of 7 mg cm^{-2} (70 μm in

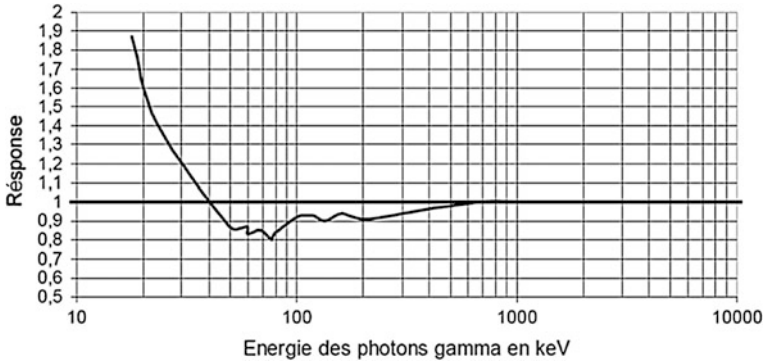

Fig. 3.47 Babyline response in $H^*(10)$ with a tissue-equivalent wall 300 mg/cm^2, normalized to 1 for ^{137}Cs (from [37])

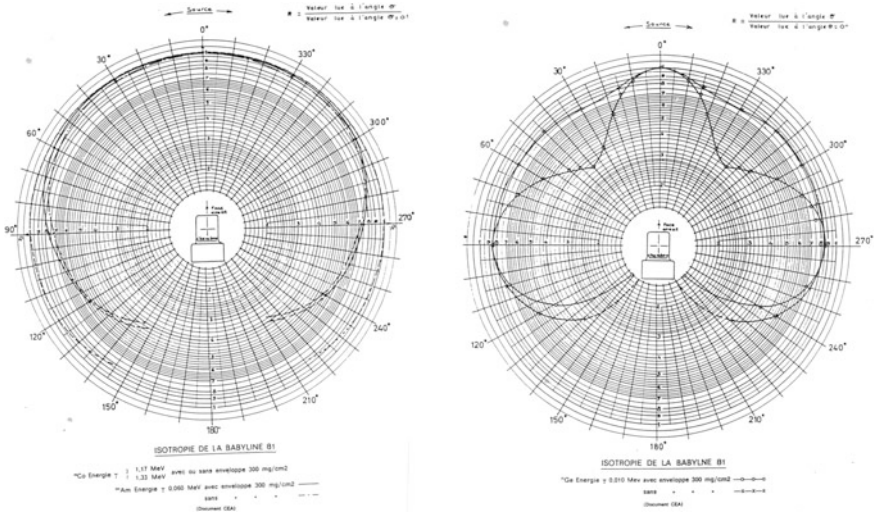

Fig. 3.48 On the *left*, depending on the angle response $R'(\alpha)$ for energies of ^{241}Am (60 keV) and ^{60}Co (1.17 and 1.33 MeV); to the *right*, to an energy source of ^{71}Ge (10 keV)

tissues) which provide isodirectional response function of the angle that substantially follows the curves ICRP 74: $R(0.07, \alpha) = H'(0.07, \alpha)/H'(0.07, 0°)$.

Response of personal dosimeters

Personal dosimeters are classified into two classes: passive personal dosimeters which record the dose with no immediate readout and no alarm and electronic personal dosimeters, allowing instant reading, access to operational quantity rate, as well as the possibility of applying alarm thresholds.

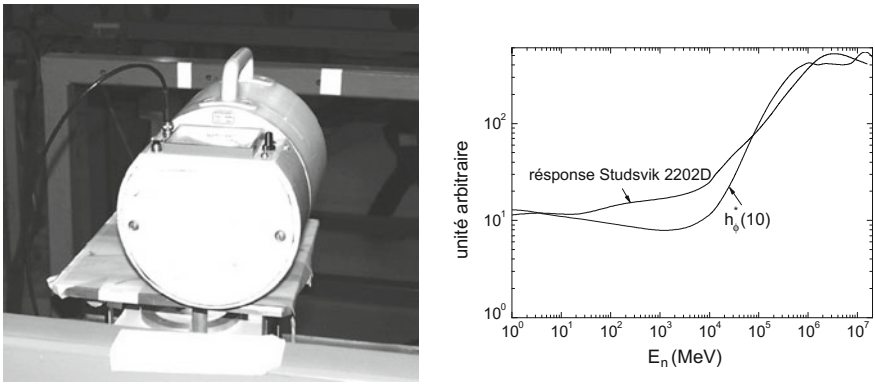

Fig. 3.49 Energy Response Curve $R(E)$ for the proportional counter neutron Stusvik 2202D, compared to the ambient dose equivalent $H^*_n(10)$ (according to the data [36])

The principle of personal dosimeters, although technologies differ, remains the same: a relationship between dose and ideally a dose equivalent, and the energy transferred by the incident radiation in a sensitive volume of small size unlike the area dosimeters (Fig. 3.50).

Among all the techniques of detections used for passive dosimeters, characteristics of TLD (LiF), radiophotoluminescents (RPL) and solid track detectors (NTA, CR39 …) are detailed below. For electronic personal dosimeters, the diode sensor technology being the most widespread, will also be described.

Thermoluminescent dosimeters (TLD type LiF)

In crystal structures of materials, energy ionizing radiation can be absorbed to create defects in the structure. When the material is heated, the thermal agitation eventually destroys the defects and crystal structure is restored. During these repair, light is emitted: the phenomenon of thermoluminescence. The amount of light, under given conditions, is proportional to the received dose.

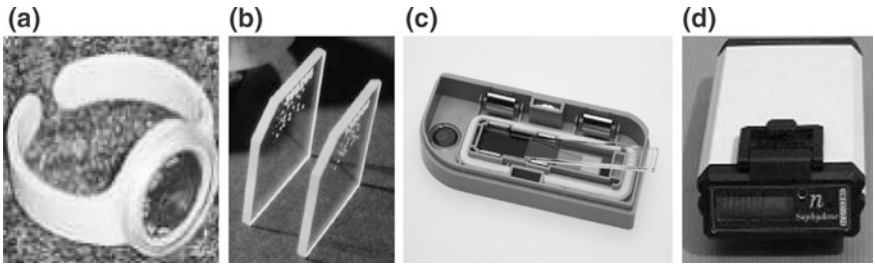

Fig. 3.50 Personal dosimeters: **a** ring Lif, **b** trace detector PN_3, **c** RPL detector, **d** semiconductor detector Saphydose-n

In theory, the thermoluminescent crystals are sensitive to all common types of radiation (X, γ, β, E-, α, P, n).

Although several thermoluminescent compounds exist, the most commonly used, for convenience reasons of use and embodiment, is lithium fluoride: LiF. As assumed above, this compound is a satisfactory tissue equivalent including through its low *Z*. With the addition of a thick tissue-equivalent material of 70 mg cm^{-2}, it can allow direct access to operational quantities $H'(0.07, 0°)$ and $H_p(0.07)$.

When it is calibrated in term of absorbed dose in tissue with ^{60}Co, its energy response $R'(E)$ significantly approaches to the unity up to about 100 keV; below 100 keV, at low energy, LiF overestimates the quantity (typically a deviation $R'(E)$ of the order of 50% to 50 keV).

For X-radiation, γ, electron and β, the majority of application relate to individual monitoring for extremities $H_p(0.07)$. However, it is possible to measure the personal dose equivalent $H_p(10)$.

As part of a working group Eurados (European Radiation Dosimetry Group), 26 laboratories have provided information on the energy dependence of TLD they use [38]. The reference, denoted $H_p(10)$ true, was calculated from the measurement of air kerma (made by standard instruments) convolved with the appropriate conversion factors. All the responses of dosimeters was grouped anonymously in Fig. 3.51.

The reference radiation, as shown in the figure, is ^{137}Cs ($R(E) = 1$). We can then observe that below 50 keV, the response with respect to dose equivalent is outside the limits of ±20% for several dosimeters.

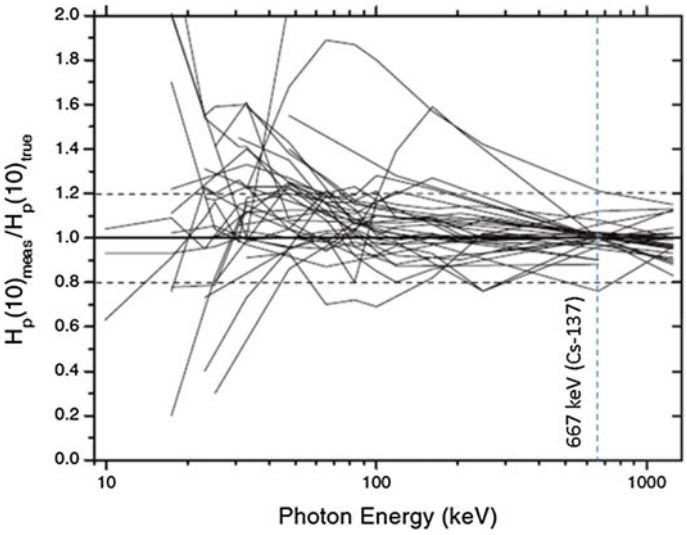

Fig. 3.51 Response, $R(E) = H_p(10)_{measured}/H_p(10)_{true}$ as a function of energy for whole-body photon thermoluminescent dosimeters for normal incidence, from [38]

The absorbed dose in tissue, for the measurement of X, γ, electrons, and β, extended over 0.1 mGy and 10^3 mGy for this class of dosimeter.

Let us add, that the energy response performance for electrons and β, with respect to $H_p(0.07)$, largely depends on dimensions of the sensitive volume reported to the range of this radiation therein.

For the neutron measurement, the ^{6}LiF, also sensitive to thermal neutrons (i.e. ^{6}Li(n, α), ^{3}H with energy deposition of α and ^{3}H, newt in the crystal) is associated with the ^{7}LiF, an isotopic compound sensitive to X, γ, electrons and β. Note that a dose equivalent of 1 mSv due to thermal neutron responds similarly to 100 mSv due to γ. To expand the spectral range of use, thermalizing property of the human body is used; after multiple scattering, neutrons may be reissued by the body with energy in the thermal region and interact with the ^{6}LiF: this process is called "albedo neutrons." By differentiation of the measurement results of both isotopic compounds, we can separately access to the component due to neutrons and photons. The measuring range for the neutron component is from 0.2 mSv to 4 Sv.

Solid trace detectors (NTA emulsion, CR39 ...)

In polymeric materials (CR39 type) heavy charged particles (fission nucleus, α, p …) can cause damage at atomic scale during their path in this environment. A chemical etching using an appropriate reagent allows to make salient the defect which are present as trace amounts. These are then recorded by reading means such as optical microscope. This approach is particularly suitable for neutron dosimetry: by applying a layer of doped material to ^{6}Li or ^{10}B, α from capture reaction permits to account the dose due to the thermal neutron field. The use of a uranium enriched in ^{235}U converter or a polyethylene converter allows the characterization of the dose for epithermal and fast neutrons, respectively, through the fission products and recoil protons on hydrogen. The solid trace detector energy response depends of the linear energy transfer and the angle of incidence of the detected particle and the nature of the detector material. A detection threshold have to be reached: only a higher deposited energy of 200 keV, gives rise to detectable levels. Therefore, in the case of a converter recoil protons, neutrons of energy less than 200 keV are not detected.

The study and track counts allows measurement of the fluence of incident particles. By calibration, it is possible to connect the number of traces measured by cm^2 to dose equivalent. The background noise, characterized by the number of traces in the absence of intentional radiation, is extended over 0.1 and 2 mSv depending on the type of material. The sensitivity is of the order of 10^4 traces/cm^2 for a dose equivalent of 1 mSv.

Radiophotoluminescents detectors (RPL)

These dosimeters use of radiophotoluminescence property (RPL) of specific glasses: during manufacture or by the action of ionizing radiation, electrons are stripped away from atoms and trapped in defects within the glass structure. When illuminating the glass with ultraviolet light, these electrons become excited and then

produce deexcitation by a characteristic orange luminescence. The intensity thereof is proportional to the number of defects in the sample and its measurement allows, to estimate the received dose. The arrival on the specific UV lasers market has permitted to develop this technique. Figure 3.52 gives the operating principle diagram.

These dosimeters have different answers according to energy γ, which can be corrected with appropriate shields. They are more sensitive than film and present high dynamic (i.e. 20 mSv to 10 Sv). They are used as dosimeters regulatory liabilities.

The photoluminescent glasses have components of relatively high atomic number, which results in hypersensitivity to low energies gamma: 3.6 times more sensitive to 50 keV than the γ of ^{60}Co. It is possible to overcome the hypersensitivity by lowering the Z of the glass by incorporation of beryllium for example (case of the dosimeter CEC) and covering the glass with shields. These compensated glasses have an energy response $R'(E)$ relatively constant (±15% between 12 keV and 1.2 MeV for a photons radiation on a phantom).

The angular response $R'(\alpha)$, in particular for low energy photons, depends on the shape and size of the dosimeter and shield system. The flat glasses have a roughly constant angular response (±30%) between 0 and 60° for energies higher than 12 keV; property due to the geometry of the filters completely wrapping the detector more efficient than filtration sandwiched used on other types of dosimeters. Figure 3.53 gives the angular response and energy to the RPL.

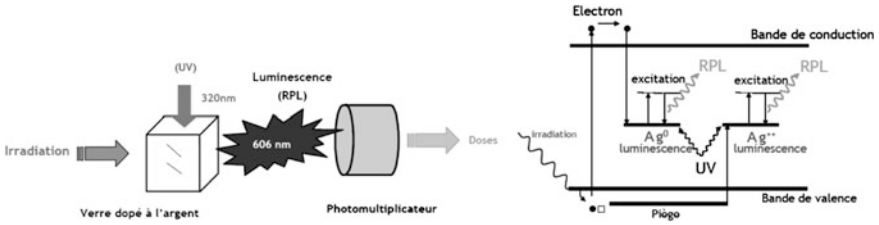

Fig. 3.52 Schematic diagram of a dosimeter radiophotoluminescent by UV excitation, according to [39]

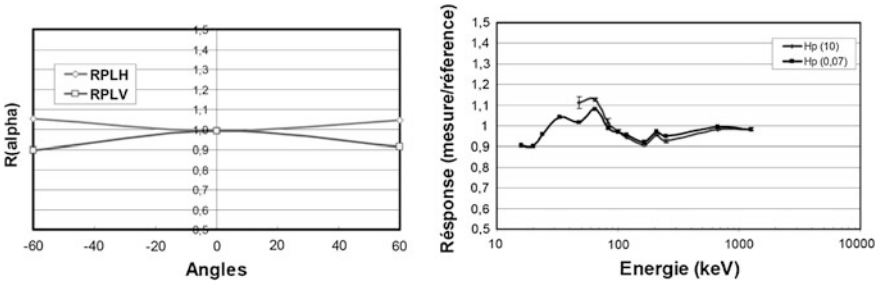

Fig. 3.53 $R(\alpha)$ and $R'(E)$ response for radiophotoluminescent dosimeter (RPL), according to [39]

This relative isotropy of the angular response allows their use also as area dosimeters for neutrons. Girod et al. [40] ascend the latter, surrounded by a moderator $(CH_2)_n$ and a cadmium converter allows a measurement of the ambient dose equivalent for neutrons $H_n^*(10)$ on an energy range between 0.25 and 9 MeV with an energy response $R'(E)$ constant ± nearly 30% (see Chap. 6).

Let us add that the RPL dosimeter is also sensitive to β (mean energy between 100 keV and 3 MeV); in the same way as a silver film, this detector is capable of producing real images of the dose.

Electronic semiconductor dosimeter

The depleted area of the space charge region of a diode is used as a sensitive detection region. The incident radiation causes electron-hole pair that induces a signal processed by a electronic measurement system. Unlike gas of ionization chamber, the high density of semiconductor materials (e.g. 2.3 for silicon) allows the detection of X with energy less than 30 keV. Furthermore, the high mobility of charges allows significant count rates (of the order of 10^7 c/s) and, consequently, with appropriate electronics, an important maximum dose rate. Finally, the mean energy of ionization of the order of 3 eV, 10 times less than that of a gas, allows a high number of collected charges, which increases the detection performance, and energy resolution. All of these properties provides satisfactory sensitivity to this class of detector despite the narrow dimensions of sensitive volume. The Table 3.11 summarize the characteristics of different diode detectors and radiations detected.

Due to a high density and a high mean Z (e.g. $Z = 14$ for Si), semiconductors are poor equivalent tissue, unlike LiF for example. However, they meet the specifications recommended by the IEC-61526 standard [42] related to the energy response $R'(E)$ for this class of detector, setting a tolerance ±30% for a photon response to the personal dose equivalent $H_p(10)$ in the energy range between 60 keV and 3 MeV.

The response with respect to personal dose equivalent $H_p(10)$ for a lot of electronic dosimeter was tested under the energy response $R'(E)$ Normalized at a photon energy of 662 keV is represented in Fig. 3.54. In this figure, the horizontal lines give the tolerance of ±30% compared to ^{137}Cs.

Table 3.11 Main characteristics of semiconductor detectors, according to [41]

Detector	Features and applications	Radiation detected
Junction N-P or P-N	Good energy resolution	α, Proton, β
	Contamination measurement	
PIN Si (Li)	Good energy resolution	X, γ
Ge (Li)	Fine spectrometry	
AuGe ultrapure	Fixed or mobile	X, γ
	Good energy resolution	
CdTe type or HgI2	Portable, operates at 300 K	X, γ
	High efficiency for X or γ	

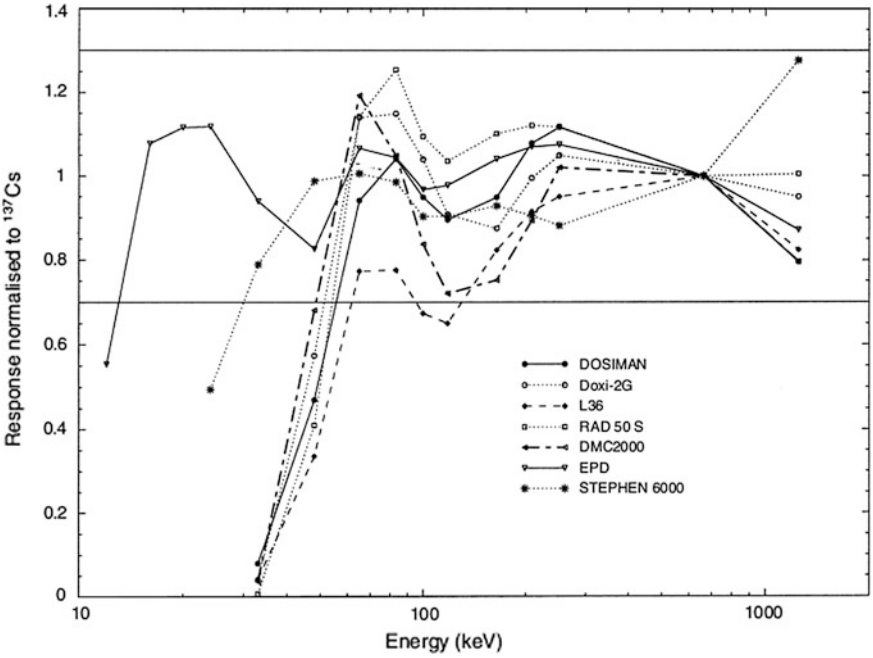

Fig. 3.54 Energy response $R'(E)$ in terms of $H_p(10)$ normalized to the energy of ^{137}Cs for marketed semiconductors, according to [43], with permission from Oxford University Press

Below 50 keV, the response of most dosimeters drops. It exceeds the limit of ±30% error permitted by the standard IEC-61526 [42]. Beyond 50 keV, although the response of the whole of dosimeters is within ±30%, there is a large variability of responses.

The energy dependence of the studied electronic dosimeters demonstrates that special attention should be paid to the choice of dosimeter based on the energy distribution of this field at the workstation. For example, for the hospital field (radiography X) or Pu workshops, where the photon radiation are mainly of low-energy, low number of dosimeters seems capable to provide a satisfactory estimate of the personal equivalent dose.

For to the angular response $R(\alpha) = H_p(0.07, \alpha)/H_p(10.0°)$, the standard specifications recommended a tolerance of ±30% for the ^{137}Cs and 50% for an energy of 65 keV, for incidence angles between ±60°. Conveniently, the variation of the response $R(\alpha)$ dosimeter must follow that calculated in ICRP 74 (see Fig. 3.29). However, a similar comparative study to that of the energy response above tends to show that some of these personal dosimeters have a substantially isotropic response, responsible for deflections larger than those prescribed by the standard; the latter would therefore have a required efficiency for area dosimetry, but here are inappropriate for personal dosimetry [43].

In addition, for the photon dosimetry, in some dosimeters, a further diode may be added to the estimate of dose equivalent $H_p(0.07)$, from a 15 keV photon energy.

Finally, note that it is also possible to measure the neutrons by adding a polyethylene moderator doped with boron, surrounding the diode, which allows through α issued by capture reaction (n, α) on the ^{10}B to promote measurement of neutrons whose energy range from thermal to fast (15 MeV). The measurement range is typically extended over 1 μSv up to 1 Sv, for an personal dose equivalent rate between 10 and 0.1 Sv/h.

The IEC-1323 standard [44] specifics recommendations related to the energy response of electronic dosimeters for neutrons in an energy range between 100 keV to 15 MeV, the gap must be limited to ±50% of the reference response.

Figure 3.55a displays the difference between $H_p(10)_{ref}$ and that measured for different monoenergetic energies (e.g. 14.8 MeV neutron accelerators), thermal neutrons, the spectrum of the AmBe set at its mean energy (i.e. 4.4 MeV), and a realistic workstation spectrum product on the CANEL device at IRSN (France) [46] for the Saphydose-n dosimeter. We remind that for these measurements, the dosimeter is located at the center of the front side of a phantom ISO-PMMA, simulating the human trunk and the irradiation conditions specified in the ISO-8529 standard [29].

The differences on the energy response comply with the standards prescriptions. This same standard also sets requirements on the differences of the angular response $R(\alpha)$ in $H_p(10, \alpha)$ for angles between 0° and ±75°: the variation does not exceed ±30% of the reference value. Figure 3.55b represents $R(\alpha) = H_p(10, \alpha)_{mes}/H_p(10, \alpha)_{ref}$ for angles between 0 and ±75° on the horizontal and vertical planes passing through the reference center of the detector. The horizontal angular Saphydose-n responses comply with IEC 1323 (±30%). Only the point + 60° from the vertical angular response shows a gap of 34%.

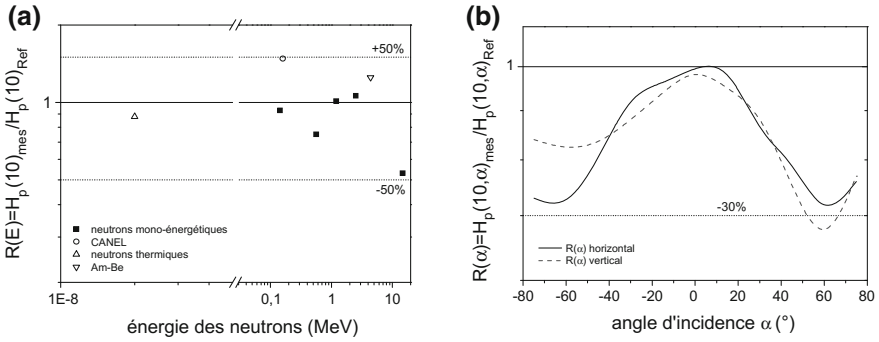

Fig. 3.55 **a** Response $R(E) = H_p(10)_{mes}/H_p(10)_{ref}$ for various neutron energies (adapted from [45]). **b** Angular response $R(\alpha) = H_p(10, \alpha)_{mes}/H_p(10, \alpha)_{ref}$ for angles between 0 and ±75° on a horizontal and vertical plane passing through the reference center of the detector, for the Saphydose-n semiconductor dosimeter

Add that the response of the dosimeter with respect to integrated personal equivalent dose for photonic radiation fields is less than 5% (test carried out with ^{60}Co, ^{137}Cs, X 164 and 250 keV). Where appropriate, in mixed field, the nature of the transmitted pulse allows the discrimination of photons and neutrons by the means of a suitable electronic treatment.

Finally, note that dosimeters are appropriate to specific radiological contexts: we will include the activation detectors used for criticality accidents (e.g. SNAC 2), composed of different activatable materials (see Chap. 2, Sect. 2.3.8). this class is insensitive to γ, enabling to characterize to the energy spectrum of the fluence rate and neutron emission, by the mean of a matrix algorithm.

3.7.6 *Realistic Spectra of Neutrons for Calibration*

The calibration process of radiation protection device as described above introduce a major limitation: the standards define primary fields of single energy or spectral distribution that are partially simulating the actual radiation field present at workstation. This approach can lead, in some cases, to significant deviation on energy responses $R(E)$ and $R(\alpha)$ for actual operational quantity at the workstation. To overcome this risk of incorrect assessment, three alternatives are possible. In order to consider the best the radiation field at the workstation, the ideal approach is to measure the fluence energy spectrum at a point P of the workstation. We described, in Chap. 2, various measurement techniques to access the energy distribution—ROSPEC, Bonner spheres, proton recoil counters …—for neutrons, with a convolution by "fluence-dose equivalent" conversion factors, we determine the dose equivalent to the workstation. Figure 3.56 shows the results in spectrum by Bonner spheres and a ROSPEC near a spent nuclear fuel cask NTL 11 type (Krümmel, Germany), according to [47].

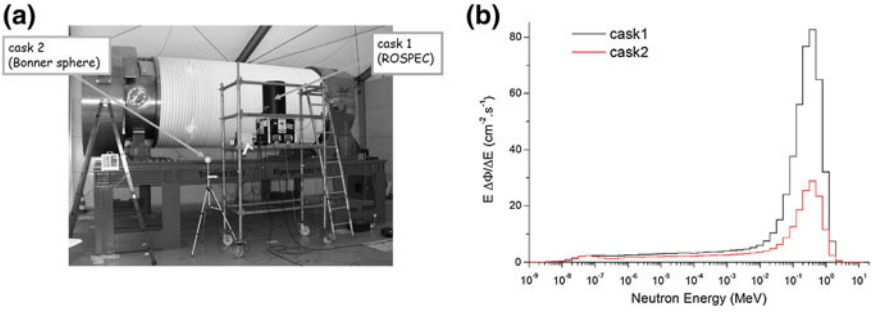

Fig. 3.56 **a** Experimental determination of the energy distribution of the neutron fluence by Bonner spheres and a ROSPEC around a spent nuclear package type NTL 11 (Krümmel-Germany). **b** Spectra neutron emission obtained by the two detectors (according to [47])

We note in Fig. 3.56, "hard" neutron spectra with a typical low thermal component of the neutron emission by spontaneous fission reaction or (α, n) on fluorinated compounds or oxidized Pu and U (see Chap. 4).

Then, the dosimeter is amounted at this measurement point and the "true" calibration coefficient is calculated according to the ratio (3.24).

$$N_H = \frac{(H^*(10))_{true}}{m_u} \tag{3.24}$$

While this approach constitutes the appropriate calibration method, it provide a number of disadvantages: access to the workstation, implementation of binding measurement devices, calibration time per workstation …

An alternative to these drawbacks is then the use of laboratory devices to recreate radiations conditions close to those likely to be encountered on workstations. The facility CANEL/T400 of IRSN [46] is devoted to this process: an deuterons accelerator produced mono-energetic neutrons of 2.4 MeV on a deuterium target (D(d, n)^{3}He), issued on a target depleted uranium ^{238}U, to generate induced fissions. This source of fission neutrons is surrounded by different moderators and absorbing elements (Fe + H_2O + $(CH_2)_n$) for recreating the energy spectra of neutrons, degraded by shielding, providing typical source terms of external exposure to neutrons, in the fuel cycle. Figure 3.57a gives a sectional view of the calibration device.

In Fig. 3.57b, we observe the two characteristic bumps (i.e. thermal and fast) for neutron spectra of nuclear spent fuels. Note that the mean "fluence-ambient dose equivalent" conversion factor for the CANEL spectrum is $\bar{h}^*_\Phi(10) = H*(10)/\Phi = 43.3$ pSv cm^2 distributed up to 14% for the thermal zone, 6% for intermediate and 80% for the fast. The disadvantages of this method are related to the deployment of the device in a laboratory and in nature may be too "stereotyped" of the energy spectrum produced.

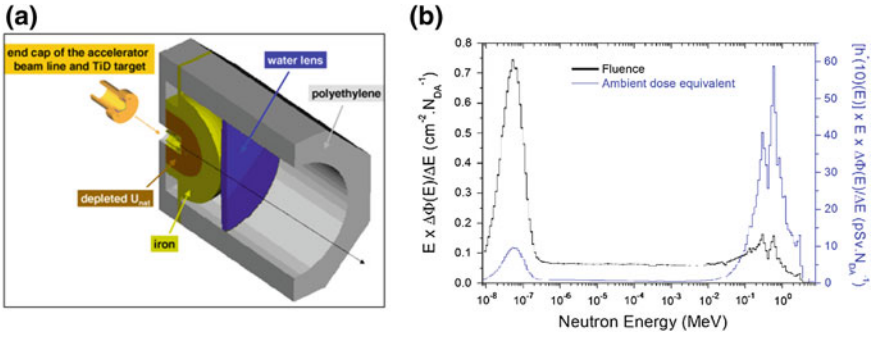

Fig. 3.57 **a** Longitudinal view of neutron calibration device CANEL/T400 as modeled in MCNP. **b** Emission spectrum and neutron spectrum of ambient dose equivalent $H^*(10)$, adapted from [46]

One last method, less restrictive than previous, consists in the modeling of the source term and surrounding structures of the workstation in a transport code particles. We will see later that the particle transport code based on the Monte Carlo method provides access to the distribution of the fluence energy spectrum ϕ_E. The histogram of the spectral energy response allows *ultimately* the weighting of each answer by energy bin $\phi(E_i; E_{i+1})$ by the corresponding conversion factor (e.g. $h^*_\Phi(10)_{E_i}$). The summation of each of these partial terms provides the desired operational quantity (e.g. $H^*(10)$) according to the expression (3.17).

This approach for determining operational quantities by numerical calculation code using the "physical quantity-operational quantity" conversion factors is nowadays the most common method of estimating external radiation risk.

Regarding the calibration of dosimeters, like the first method, the calibration coefficient N_H is obtained at the point of interest, as the ratio of the calculated value of the operational quantity by the measured value at that point in the facility.

However, this method also has drawbacks: the partial modeling of the facility or the source term can induce bias in consideration of scattering or attenuated components, or problems of "statistical convergence" related to the method of calculation. Especially for thick shielding, physical models and cross sections that may not be accurate for some materials and energy ranges.

3.8 Radiological Zoning

It appears a great diversity of national rules and practices to define the radiological zoning; the international recommendations (like ICRP) focus only on defining the workers/public annual dose limits and not on the facilities.

Eventhough international scope of texts, such as the European Directive 2013/59/Euratom, introduces notions of controlled area and monitored area, it does not specify quantitative limits (this text only defines access rules, signalization of these zones …).

Thus, the radiological zoning specificities, different from one country to another, will not be detailed in this book. Note finally, the current rules of radiological zoning in European countries are likely to change for implementing the new regulation of 2013/59/Euratom.

3.9 Evolution of Protection Quantities

ICRP continues to evolve the protection quantities field inspired by permanent changes due to enhancement in research in radiation biology and epidemiological studies. Remember that most of the recommendations in the publications are set by European directives; the current reference document related to external exposure is

Publication 60 [1]. The ICRP recommendation which will refer future regulatory guidelines is ICRP 103 [2].

For instance, this publication reassesses the values of coefficients w_R. We notice a significant change in the w_R coefficient passing from 5 to 2 for protons. In addition, the w_R for neutrons move from a discrete value depending on the energy range to a continuous value according to equations by energy intervals (3.25)

$$w_R = \begin{cases} 2.5 + 18.2\, e^{-[\ln(En)]^2/6} & En < 1\,\text{MeV} \\ 5 + 17\, e^{-[\ln(2En)]^2/6} & 1\,\text{MeV} \le En \le 50\,\text{MeV} \\ 2.5 + 3.25\, e^{-[\ln(0.04\,En)]^2/6} & En > 50\,\text{MeV} \end{cases} \tag{3.25}$$

Figure 3.57 provides this factor according to the neutron energy. This new approach has been empirically obtained and is consistent with existing biological knowledge (Fig. 3.58).

Note that for most of the usual known neutron spectra, the change in the effective dose does not result in more significant difference with the operational quantity of the ambient dose equivalent [48]. Figure 3.59 gives this comparison.

It should be mentioned here that the recommendations of ICRP 60 have been taken into account in the Euratom Directive (96/29) after 6 years and transposed to French law after 10 years.

Note that the concept of ambient dose equivalent is still valid and that Pellicioni [49] shows that for neutrons, it remains a good conservative estimate of the effective dose up energies of 100 MeV.

A noteworthy change in Publication 103 of ICRP [2] is the reassessment of the weighting factor for tissues: 14 weighting factors specified instead of 12 in ICRP 60 (adding the brain and salivary glands) and "remaining tissue" about 15 instead of 10. These values are given in the Table 3.12.

With respect to the quality factor Q, publication 103 provides a relationship between the weighting factor for the radiation and means quality factor, averaged

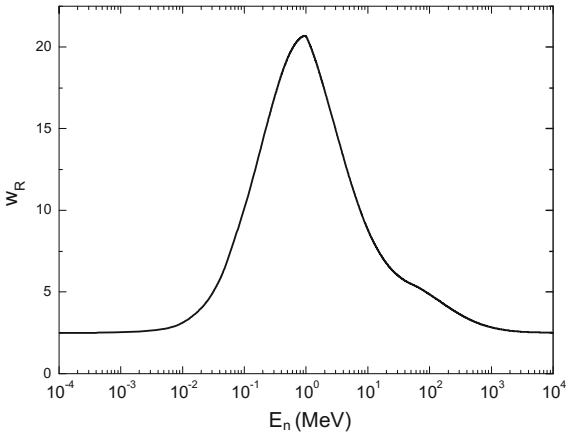

Fig. 3.58 Weighting factor for radiation w_R for neutrons as a function of energy (3.26)

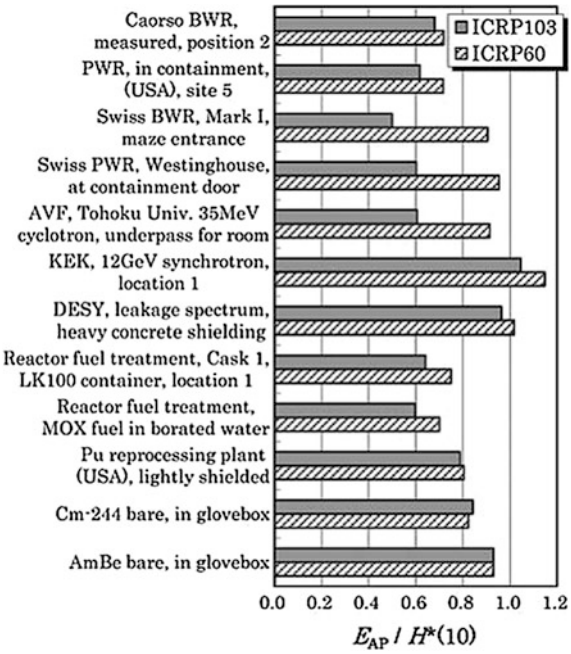

Fig. 3.59 Comparison of the effective dose defined in the ICRP 60 and 103 and the ambient dose equivalent $H^*(10)$, after [48], with permission from Oxford University Press

Table 3.12 Values recommended ICRP 103 for the weighting factors for fabrics, adapted from [2]

Tissue	W_T	Σw_T
Bone marrow (red), colon, lung, stomach, breast, remaining tissue[a]	0.12	0.72
Gonads	0.08	0.08
Bladder, esophagus, liver, thyroid	0.04	0.16
Bone surface, brain, salivary glands, skin	0.01	0.04
	Total	1.00

[a]Adrenal, extrathoracic region (ET), gall bladder, heart, kidneys, lymph nodes, muscle, oral mucosa, pancreas, prostate, small intestine, spleen, thymus, uterus/cervix

over the human body and for calculating an isotropic exposure. The relationship between this mean quality factor to the human body q_E and the weighting factor w_R is given by the function:

$$w_R = 1.6(q_E - 1) + 1$$

This equation retains value $w_R = 20$ approximately at energies near 1 MeV neutrons. Calculations of parameter q_E were performed taking into account the dose distribution in the human body and use factors weighting w_T for different organs and tissues by the equation:

$$q_E = \sum_T w_T \overline{Q}_T D_T / \sum_T w_T D_T$$

where $\overline{Q}_T$ is the mean quality factor in the tissue or organ T and D_T the mean dose corresponding to this body. As the different values of w_T to organs and tissues are not distributed symmetrically in the human body, the value of q_E depends on the directional incidence of the radiation on the body.

This relationship presents interest to bring out more clearly the common scientific basis of the weighting concept for radiation and the quality factor used in defining the operational quantities.

ICRP 116 [3] reassess the whole of effective doses considering the new factors of weights ICRP 103. In this publication, in addition to the factors w_R and w_T, new anthropomorphic phantoms, based on voxelised phantoms are introduced for calculations. Figure 3.60 shows these new phantoms introduced into ICRP.

Fig. 3.60 New voxelised phantom (male *left*, female *right*) to calculate effective doses, according to [3]. Reproduced by permission of Michiya Sasaki on behalf of ICRP

Figure 3.61 compares to photon effective dose in AP geometry with new factors ICRP 103 (Data ICRP 116) and the operational quantity $H^*(10)$ (Fig. 3.62).

Note that the conclusions of Sect. 3.6 comparing the protection quantities and operational quantities remain the same with this new ICRP.

Let us add, that, in April 2011, ICRP has released a recommendation concerning the limit on equivalent dose to the eye-lens for workers. This recommendation sets the limit at 20 mSv per year, averaged over periods of 5 years, not to exceed 50 mSv per year. The current regulatory and value is 150 mSv per year.

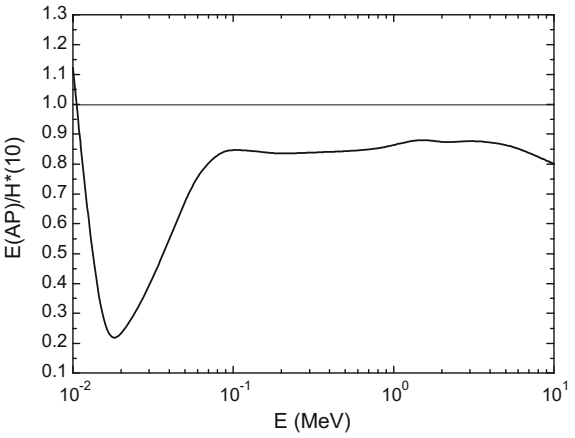

Fig. 3.61 Ratio of the effective dose E geometry AP following ICRP 116 and the operational quantity $H^*(10)$ for the photons (according to the data ICRP 116 [3] and ICRP 74 [7])

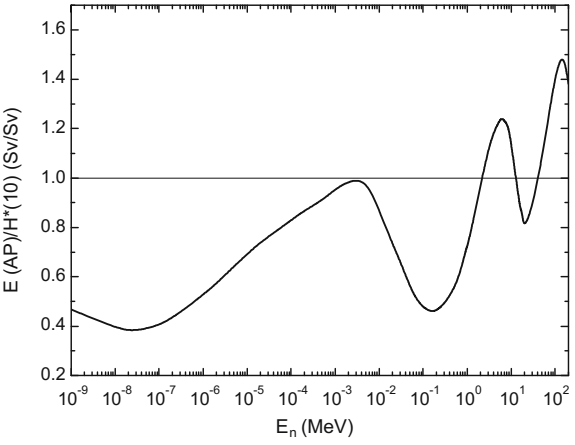

Fig. 3.62 Ratio of the effective dose E in AP from geometry ICRP 116 and the operational quantity $H^*(10)$ for neutrons (according to the data ICRP 116 [3] and ICRP 74 [7])

Appendix 1

Photon angular response $R(0.07, \alpha)$ for directional dose equivalent $H'(0.07, \alpha)$ for electron energy between 0.1 and 2 MeV—ICRP 74 [7]. Reproduced by permission of Michiya Sasaki on behalf of ICRP.

E (MeV)	$R(0.07, \alpha)$									
	0°	15°	30°	45°	60°	67.5°	75°	82.5°	85°	89°
0.07	1	0.813	0.471	0.17	0.041	–	0.005			
0.08	1	0.903	0.645	0.348	0.132	–	0.028	0.007	0.003	
0.09	1	0.926	0.709	0.445	0.201	–	0.055	0.017	0.01	0.001
0.1	1	0.938	0.76	0.509	0.258	–	0.081	0.027	0.016	0.002
0.15	1	0.989	0.945	0.771	0.486	–	0.18	0.064	–	–
0.2	1	1.046	1.12	1.072	0.751	–	0.295	0.106	0.06	0.008
0.4	1	1.039	1.143	1.33	1.348	1.083	0.661	0.245	0.133	0.015
0.7	1	1.028	1.11	1.266	1.517	1.502	1.085	0.426	0.216	0.023
1	1	1.017	1.087	1.227	1.469	1.583	1.308	0.552	0.294	0.03
1.5	1	1.027	1.075	1.191	1.401	1.574	1.572	0.756	–	–
2	1	1.022	1.066	1.163	1.338	1.51	1.654	0.95	0.53	0.053
3	1	1.004	1.038	1.113	1.264	1.39	1.612	1.277	0.731	0.072
4	1	1.007	1.042	1.097	1.239	1.369	1.546	1.479	0.952	0.093
7	1	1.005	1.019	1.071	1.18	1.274	1.419	1.736	1.412	0.151
10	1	1.01	1.016	1.05	1.126	1.22	1.345	1.661	1.646	0.21

Appendix 2

Photon angular dependence factor $R(10, \alpha)$ defined by the ratio of $H_p(10, \alpha)$ on $H_p(10, 0°)$ for photon energies between 15 keV and 1 MeV, and for different angles of incidence, calculated by a Monte Carlo code—ICRP 74.

Photon energy (MeV)	$H_p(10, 0°)/K_a$ (Sv/Gy)	Ratio $H_p(10, \alpha)/H_p(10, 0°)$					
		0°	15°	30°	45°	60°	75°
0.010	0.009	1.000	0.889	0.556	0.222	0.000	0.000
0.0125	0.098	1.000	0.929	0.704	0.388	0.102	0.000
0.015	0.264	1.000	0.966	0.822	0.576	0.261	0.030
0.0175	0.445	1.000	0.971	0.879	0.701	0.416	0.092
0.020	0.611	1.000	0.982	0.913	0.763	0.520	0.167
0.025	0.883	1.000	0.980	0.937	0.832	0.650	0.319
0.030	1.112	1.000	0.984	0.950	0.868	0.716	0.411

(continued)

(continued)

Photon energy (MeV)	$H_p(10, 0°)/K_a$ (Sv/Gy)	Ratio $H_p(10, \alpha)/H_p(10, 0°)$					
		0°	15°	30°	45°	60°	75°
0.040	1.490	1.000	0.986	0.959	0.894	0.760	0.494
0.050	1.766	1.000	0.988	0.963	0.891	0.779	0.526
0.060	1.892	1.000	0.988	0.969	0.911	0.793	0.561
0.080	1.903	1.000	0.997	0.970	0.919	0.809	0.594
0.100	1.811	1.000	0.992	0.972	0.927	0.834	0.612
0.125	1.696	1.000	0.998	0.980	0.938	0.857	0.647
0.150	1.607	1.000	0.997	0.984	0.947	0.871	0.677
0.200	1.492	1.000	0.997	0.991	0.959	0.900	0.724
0.300	1.369	1.000	1.000	0.996	0.984	0.931	0.771
0.400	1.300	1.000	1.004	1.001	0.993	0.955	0.814
0.500	1.256	1.000	1.005	1.002	1.001	0.968	0.846
0.600	1.226	1.000	1.005	1.004	1.003	0.975	0.868
0.800	1.190	1.000	1.001	1.003	1.007	0.987	0.892
1	1.167	1.000	1.000	0.996	1.009	0.990	0.910
1.5	1.139	1.000	1.002	1.003	1.006	0.997	0.934
3	1.117	1.000	1.005	1.010	0.998	0.998	0.958
6	1.109	1.000	1.003	1.003	0.992	0.997	0.995
10	1.111	1.000	0.998	0.995	0.989	0.992	0.966

Appendix 3

Photon conversion factors "fluence-ambient dose equivalent at 10 mm" and "fluence-directional dose equivalent at 0° under 70 μm," according to the photon energy [7]. Reproduced by permission of Michiya Sasaki on behalf of ICRP.

E (MeV)	$h^*_\Phi(10)$ (pSv cm^2)	$h'_\Phi(0.07)$ (pSv cm^2)	E(MeV)	$h^*_\Phi(10)$ (pSv cm^2)	$h'_\Phi(0.07)$ (pSv cm^2)
0.01	0.061	7.2	0.5	2.93	2.93
0.015	0.83	3.19	0.6	3.44	3.44
0.02	1.05	1.81	0.8	4.38	4.38
0.03	0.81	0.9	1	5.2	5.2
0.04	0.64	0.62	1.5	6.9	6.9
0.05	0.55	0.5	2	8.6	8.6
0.06	0.51	0.47	3	11.1	11.1
0.08	0.53	0.49	4	13.4	13.4
0.1	0.61	0.58	5	15.5	15.5

(continued)

(continued)

E (MeV)	$h^*_\Phi(10)$ (pSv cm^2)	$h'_\Phi(0.07)$ (pSv cm^2)	E(MeV)	$h^*_\Phi(10)$ (pSv cm^2)	$h'_\Phi(0.07)$ (pSv cm^2)
0.15	0.89	0.85	6	17.6	17.6
0.2	1.2	1.15	8	21.6	21.6
0.3	1.8	1.8	10	25.6	25.6
0.4	2.38	2.38			

Appendix 4

Photon conversion factors "Air Kerma-ambient dose equivalent at 10 mm" conversion factors "Air Kerma-directional dose equivalent at 0° under 70 μm," conversion factors "Air Kerma individual dose-equivalent under 10 mm" conversion factors "air kerma-personal dose equivalent under 70 μm" [7]. Reproduced by permission of Michiya Sasaki on behalf of ICRP.

E (MeV)	$H^*(10)/K_a$ (Sv/Gy)	$H'(0.07)/K_a$ (Sv/Gy)	$H_p(10, 0°)/K_a$ (Sv/Gy)	$H_p(0.07, 0°)/K_a$ (Sv/Gy)
0.005				0.750
0.01	0.008	0.95	0.009	0.947
0.0125			0.098	
0.015	0.260	0.99	0.264	0.981
0.0175			0.445	
0.02	0.610	1.05	0.611	1.045
0.025			0.883	
0.03	1.100	1.22	1.112	1.230
0.04	1.470	1.41	1.490	1.444
0.05	1.670	1.53	1.766	1.632
0.06	1.740	1.59	1.892	1.716
0.08	1.720	1.61	1.903	1.732
0.1	1.650	1.55	1.811	1.669
0.125			1.696	
0.15	1.490	1.42	1.607	1.518
0.2	1.400	1.34	1.492	1.432
0.3	1.310	1.31	1.369	1.336
0.4	1.260	1.26	1.300	1.280
0.5	1.230	1.23	1.256	1.244
0.6	1.210	1.21	1.226	1.220
0.8	1.190	1.19	1.190	1.189

(continued)

(continued)

E (MeV)	$H^*(10)/K_a$ (Sv/Gy)	$H'(0.07)/K_a$ (Sv/Gy)	$H_p(10, 0°)/K_a$ (Sv/Gy)	$H_p(0.07, 0°)/K_a$ (Sv/Gy)
1	1.170	1.17	1.167	1.173
1.5	1.150	1.15	1.139	
2	1.140	1.14		
3	1.130	1.13	1.117	
4	1.120	1.12		
5	1.110	1.11		
6	1.110	1.11	1.109	
8	1.110	1.11		
10	1.100	1.10	1.111	

Appendix 5

Neutron conversion factors "fluence-ambient dose equivalent at 10 mm" depending on the neutron energy [7]. Reproduced by permission of Michiya Sasaki on behalf of ICRP.

E (MeV)	$h^*_\Phi(10)$ (pSv cm^2)	E (MeV)	$h^*_\Phi(10)$ (pSv cm^2)	E (MeV)	$h^*_\Phi(10)$ (pSv cm^2)
2.00E-05	10.6	0.3	233	14	520
5.00E-05	9.9	0.5	322	15	540
1.00E-04	9.4	0.7	375	16	555
2.00E-04	8.9	0.9	400	18	570
5.00E-04	8.3	1	416	20	600
1.00E-03	7.9	1.2	425	30	515
0.002	7.7	2	420	50	400
0.005	8	3	412	75	330
0.01	10.5	4	408	100	285
0.02	16.6	5	405	125	260
0.03	23.7	6	400	150	245
0.05	41.1	7	405	175	250
0.07	60	8	409	201	260
0.1	88	9	420		
0.15	132	10	440		
0.2	170	12	480		

Appendix 6

Conversion factors "fluence-directional dose equivalent to 0" [7] depending on electron energy. Reproduced by permission of Michiya Sasaki on behalf of ICRP.

Energy (MeV)	$H'(0.07, 0°)/\Phi$ (nSv cm^2)	$H'(3, 0°)/\Phi$ (nSv cm^2)	$H'(10, 0°)/\Phi$ (nSv cm^2)
0.07	0.221		
0.08	1.056		
0.09	1.527		
0.10	1.661		
0.11	1.627		
0.13	1.513		
0.15	1.229		
0.20	0.834		
0.30	0.542		
0.40	0.455		
0.50	0.403		
0.60	0.366		
0.70	0.344		
0.80	0.329	0.045	
1.00	0.312	0.301	
1.25	0.296	0.486	
1.50	0.287	0.524	
1.75	0.282	0.512	
2.00	0.279	0.481	0.005
2.50	0.278	0.417	0.156
3.00	0.276	0.373	0.336
3.50	0.274	0.351	0.421
4.00	0.272	0.334	0.447
5.00	0.271	0.317	0.43
6.00	0.271	0.309	0.389
7.00	0.271	0.306	0.36
8.00	0.271	0.305	0.341
10.00	0.275	0.303	0.33

References

1. ICRP. (1991). Publication 60. Recommendations of the ICW. *Annals of ICRP, 21*(1–3).
2. ICRP. (2007). Publication 103. Recommandations 2007 de la Commission internationale de Protection radiologique.
3. ICRP. (2010). Publication 116. Conversion coefficients for radiological protection quantities for external radiation exposures. *Annals of ICRP, 40*(2–5).
4. ASN. (2011). Revue contrôle n°192. Imagerie médicale, maîtriser les expositions aux rayonnements ionisants.
5. ICRP. (2012). ICRP statement on tissue reactions/early and late effects of radiation in normal tissues and organs—threshold doses for tissue reactions in a radiation protection context. ICRP Publication 118. *Annals of ICRP*, *41*(1/2).
6. Council Directive 2013/59/Euratom. (2013). Laying down basic safety standards for protection against the dangers arising from exposure to ionising radiation, and repealing directive 89/618/Euratom, 96/29/Euratom, 97/43/Euratom and 2003/43/Euratom.
7. ICRP. (1996). Publication 74. Conversion coefficients for use in radiological protection against external radiation.
8. Antoni, R., & Bourgois, L. (2005). communication privée.
9. Schultz, F. W., & Zoetelief, J. (1996). Organ and effective doses in the male phantom ADAM exposed in AP direction to broad beams of monoenergetic electrons. *Health Physics, 70*(4), 498–504.
10. Bourgois, L. (2011). Estimation de la dose extrémité due à une contamination par un radionucléide émetteur β: l'équivalent de dose est-il un bon estimateur de la grandeur de protection? *Radioprotection, 46*(2), 175–187.
11. Cross, W. G. (1997). Empirical expression for beta ray point source dose distributions. *Radiation Protection Dosimetry, 69*(2), 85–96.
12. IRSN. (2010). Doses délivrées aux patients en scanographie et en radiologie conventionnelle Résultats d'une enquête multicentrique en secteur public - Rapport DRPH/SER N°2010–12.
13. Ferreux, L., & Bourgois, L. (2005). Communication privée.
14. Antoni, R. (2006). *Calculs de débits de dose pour l'accélérateur Aglae du Louvre*. CEA Saclay: Rapport interne.
15. Huet, C., Clairand, I., Trompier, F., Bey, E., & Bottollier-Depois, J. F. (2007). Reconstitution de dose par calcul Monte-Carlo en cas d'accident radiologique : application à l'accident du Chili. *Radioprotection, 42*(4), 489–500.
16. Lemosquet, A., Clairand, I., de Carlan, L., Franck, D., Aubineau-Lanièce, I., & Bottollier-Depois, J. F. (2004). A computational tool based on voxel geometry for dose reconstruction of a radiological accident due to external exposure. *Radiation Protection Dosimetry, 110*, 449–454.
17. ICRU. (1985). Détermination des équivalents de dose dus aux sources externes de rayonnement. Publication 39.
18. ICRU. (1988). Determination of dose equivalents from external radiation sources-Part II. Publication 43.
19. ICRU. (1992). Measurement of dose equivalents from external photon and electron radiations. Publication 47.
20. ICRU. (1993). Quantities and units in radiation protection dosimetry. Publication 51.
21. ICRU. (1980). Radiation quantities and units. Publication 33.
22. Ferrari, A., & Pelliccioni, M. (1998). Fluence to dose equivalent conversion data and effective quality factors for high energy neutrons. *Radiation Protection Dosimetry, 76*(4), 215–224.
23. Leuthold, G., Mares, V., & Schraube, H. (1992). Calculation of the neutron ambient dose equivalent on the basis of the ICRP revised quality factors. *Radiation Protection Dosimetry, 40*(2), 77–84.
24. Katz, L., & Penfold, A. S. (1952). Range energy relations for electrons and the determination on beta-ray end point energies by absorption. *Reviews of Modern Physics, 24*(1), 28–44.

25. Furstoss, C. (2006). Conception et développement d'un fantôme anthropomorphe équipé de détecteurs dans le but d'évaluer la dose efficace à un poste de travail: étude de faisabilité. Thèse de l'Université de Paris XI.
26. Lund/LBNL Nuclear Data Search 1999.
27. Gualdrini, G., Bordy, J. M., Daures, J., Fantuzzi, E., Ferrari, P., Mariotti, F., et al. (2013). Air kerma to HP(3) conversion coefficients for photons from 10 keV to 10 MeV, calculated in a cylindrical phantom. *Radiation Protection Dosimetry, 154*(4), 522–525.
28. Pelliccioni, M. (2000). Overview of fluence-to-effective dose and fluence-to-ambient dose equivalent conversion coefficients for high energy radiation calculated using the FLUKA code. *Radiation Protection Dosimetry, 88*(4), 279–297.
29. ISO 8529. (1989). Neutron reference radiation for calibrating neutron-measuring devices used for radiation protection purposes and for determining their response as a function of neutron energy (Genève).
30. Joffre, H. (1963). Les problèmes physiques de la radioprotection. Génie atomique tome I.
31. Pelliccioni, M. (1998). Fluence to dose equivalent conversion data and radiation weighting factors for high energy radiation. *Radiation Protection Dosimetry, 77*(3), 159–170.
32. Chumak, V. V., & Bakhanova, E. V. (2003). Relationship between protection and operational quantities in dosimetry of photon external exposure—Deficiencies of $H_p(10)$. *Radiation Protection Dosimetry*, *104*(2), 103–111.
33. ISO 4037. (1992). X and gamma reference radiations for calibrating dosimeters and dose ratemeters and for determining their response as a function of photon energy, Part 1 et 2.
34. ISO 6980. (1992). Reference beta radiations for calibrating dosimeters and doserate meters and for determining their response as a function of beta radiation energy.
35. Faussot, A. (2010). Étalonnage du matériel de radioprotection ATSR.
36. IAEA. (2001). *Compendium of neutron spectra and detector responses for radiation protection purposes*. Technical Reports Series No. 403. Supplement No. 318.
37. Martel, P. (2009). Évaluation technique d'un débitmètre/dosimètre dans le cadre du contrôle réglementaire des générateurs électriques de Rayons X utilisés en radiodiagnostic Congrès de la Société Française de Radioprotection - La Hague.
38. Lopez Ponte, M. A., Castellani, C. M., Currivan, L., et al. (2004). A catalogue of dosemeters and dosimetric services within Europe—an update. *Radiation Protection Dosimetry, 112*(1), 45–68.
39. Fraboulet, P. (2008). Fiche technique du dosimètre RPL rapport interne SDE/LSDOS – IRSN.
40. Girod, M., Bourgois, L., Cornillaux, G., Andre, S., & Postaük, J. (2004). Study and presentation of a fast neutron and photon dosemeter for area and criticality monitoring using radiophotoluminescent glass. *Radiation Protection Dosimetry*, *112*(3).
41. Gambini, D. J., & Granier, R. (1997). *Manuel pratique de radioprotection*. 2^{e} édition, Tec & Doc.
42. CEI 61526. (2005). Instrumentation pour la radioprotection – Mesure des équivalents de dose individuels Hp(10) et Hp(0.07) pour les rayonnements X, gamma, neutron et bêta – Appareils de mesure à lecture directe et moniteurs de l'équivalent de dose individuel.
43. Texier, C., Itié, C., Servière, H., Gressier, V., & Bolognese-Milsztage, T. (2001). Study of the photon radiation performance of electronic personal dosemeters. *Radiation Protection Dosimetry, 96*(1–3), 245–249.
44. CEI 1323. Instrumentation pour la radioprotection - Rayonnements neutroniques - Moniteur individuel à lecture directe d'équivalent de dose et/ou de débit d'équivalent de dose.
45. Lahaye, T., Cutarella, D., Ménard, S., Rannou, A., & Bolognese-Milsztajn, T. (2000) Dosimètre individuel électronique pour les neutrons: Saphydose-n. *Radioprotection, 35*(2).
46. Lacoste, V., & Gressier, V. (2004). Monte Carlo simulation of the IRSN Canel/T400 realistic mixed neutrons-photon radiation field. *Radiation Protection Dosimetry, 110*(1–4), 123–127.
47. Lacoste, V. (2007). Campagne de mesure, comparaison, perspectives » INSTN: session dosimétrie des neutrons.

48. Tatsuhiko, S., Akira, E., Yasuda, H., & Niita, K. (2011). Impact of the introduction of ICRP publication 103 on neutron dosimetry. *Radiation Protection Dosimetry*, *146*.
49. Pelliccioni, M. (2004). The impact of ICRP publication 92 on the conversion coefficient in use for cosmic ray dosimetry. *Radiation Protection Dosimetry, 109*(4), 303–309.
50. Bourgois, L., & Antoni, R. (2016). Fluence to local skin absorbed dose and dose equivalent conversion coefficients for monoenergeticpositrons using Monte-Carlo code MCNP6. *Applied Radiation and Isotopes, 107*(2016), 372–376.

Chapter 4
Source Evaluation of the External Exposure

Abstract This chapter is devoted to characterize main source terms of primary and secondary particles for external exposure. The assessment of neutron, photon and electron yield is detailed in usual physical process such as: fission reactions, ion interactions, bremsstrahlung on thick targets, induced activity in materials... This characterization allows the access of values of protection and operational quantities previously defined. This prior knowledge is required for designing radiation protection shieldings and, more generally, for developing appropriate radiological counter measures that will be developed in the next chapter. The end of the chapter addresses the study of "exotic facilities" such as klystrons or high intensity lasers.

4.1 Photons Line Spectra

Radioactive nuclei decay releasing gamma line spectra (i.e. photons emitted at discrete energy). We saw in Chap. 3, that it is fairly easy to deduce the ambient dose equivalent rate from the fluence and conversion factors "fluence-ambient dose equivalent" of ICRP [1].

With this technique, for common radionuclides, Table 4.1 gives some ambient dose equivalent rates at one meter distance for a 1 GBq activity isotropic point source.

Thus, it can be deduced the ambient dose equivalent rate from a point source at any distance, using the property of the inverse square law given in Chap. 1. For example, a ^{60}Co source of 1 MBq activity generates at 50 cm distance the following ambient dose equivalent rate:

$$\dot{H}^*(10) = 0.351\left(\frac{1}{1000}\right) \times \left(\frac{1}{0.5}\right)^2 = 1.4\,\mu\mathrm{Sv\,h^{-1}}$$

R. Antoni and L. Bourgois, *Applied Physics of External Radiation Exposure*,
Biological and Medical Physics, Biomedical Engineering,
DOI 10.1007/978-3-319-48660-4_4

Table 4.1 Ambient dose equivalent rate $\dot{H}^*(10)$ at 1 m of a 1 GBq activity point source for different radionuclides

Radionuclide	$\dot{H}^*(10)$ at 1 m ($mSv^{-1}\ h^{-1}\ GBq^{-1}$)
Ytterbium 169	$7 \cdot 10^{-2}$
Technetium 99	$2.2 \cdot 10^{-2}$
Thulium 170	$1.2 \cdot 10^{-3}$
Caesium 137	$8.4 \cdot 10^{-2}$
Iridium 192	$1.3 \cdot 10^{-1}$
Cobalt 60	$3.51 \cdot 10^{-1}$
Selenium 75	$6.6 \cdot 10^{-2}$

The work of Delacroix et al. [2] provides the ambient dose equivalent values at 30 cm distance from a punctual source with 1 Bq activity for 212 radionuclides, for determining the dose equivalent rate at any distance by considering the inverse square law.

For example, for a punctual source of ^{54}Mn, this reference gives a dose equivalent rate of $1.4 \cdot 10^{-6}$ μSv h^{-1} at 30 cm for 1 becquerel. At 1 m and for 1 GBq, then we get:

$$\dot{H}^*(10) = 1.4 \cdot 10^{-6} \times \left(1 \cdot 10^{9}\right) \times \left(\frac{0.3}{1}\right)^2 = 126\,\mu\text{Sv}\,\text{h}^{-1}$$

Moreover, remind that (see Chap. 3) for an isotropic point source with a flux of 1 (γ) s^{-1}, the ambient dose equivalent rate $\dot{H}^*(10)$(in mSv h^{-1}) at 1 m distance can be calculated using the conversion factor "fluence-ambient dose equivalent" from ICRP [1] $h^*_\Phi(10)$ (in pSv cm^2) using (4.1).

$$\dot{H}^*(10) = \frac{h^*_\Phi(10) \times 1 \cdot 10^{-12}}{4\pi(100)^2} \times 3600 \times 1000 = 2.865 \times 1 \cdot 10^{-11} \times h^*_\phi(10) \tag{4.1}$$

Note that the curve described by (4.1) shown in Fig. 4.1, is linear for energies between 80 keV and 2 MeV. Also, in this region, ambient dose equivalent is proportional to energy. A linear interpolation provides a fairly simple expression for ambient dose equivalent expressed in mSv h^{-1} at 1 m distance of a point source, energy E (MeV), activity A (in becquerels) with a branching ratio Γ. This expression is given by (4.2).

$$\dot{H}^*(10)\ in\ \text{mSv/h} = 1.5 \cdot 10^{-10}\text{A} \cdot \Gamma \cdot E \tag{4.2}$$

For a source emitting several rays by decay (4.3) it applies.

$$\dot{H}^*(10)\ in\ \text{mSv/h} = 1.5 \cdot 10^{-10} A \cdot \sum_i \Gamma_i \cdot E_i \tag{4.3}$$

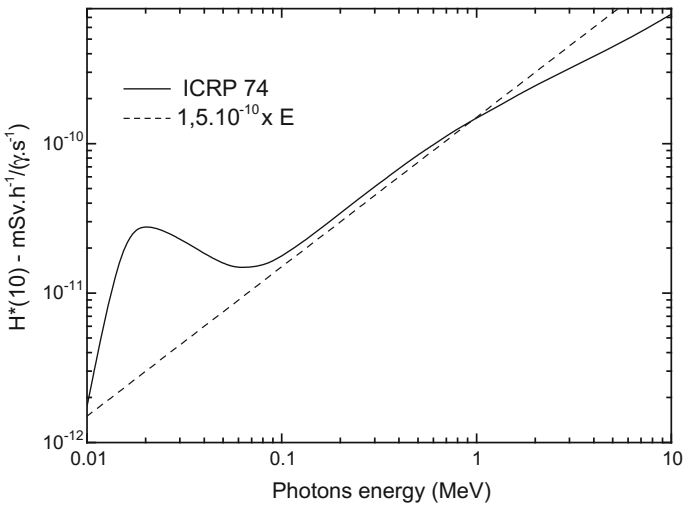

Fig. 4.1 Comparison of ICRP equation method (4.1) and simplified method (4.2)

Note that for photon energy ranging over 80 keV and 2 MeV, the error with this expression is less than 20% compared to the main expression (4.1). Comparison of both methods is shown in Fig. 4.1. Note that this expression can not be extrapolated beyond the energy range 80 keV–2 MeV.

We can illustrate the use of (4.3), considering a ^{58}Co source of 1 MBq activity emitting two photons of 51 and 811 keV energy, respectively, with branching ratio of 0.3 and 0.99. The ambient dose equivalent rate at 1 m for this source is readly obtained:

$$\dot{H}^*(10) = 1.5 \cdot 10^{-10} \times 1 \cdot 10^6 \times (0.511 \times 0.3 + 0.811 \times 0.99) = 143\,\text{nSv/h}$$

Note that this simplified approach is reliable in media without source shielding such as vacuum or air.

4.2 Neutrons

To characterize the dose equivalent due to a neutron field, the approach remains the same, namely weighting a fluence rate by the conversion coefficient of the dosimetric quantity. Also the calculation is dependent on the knowledge of fluence and neutron energies at the observation point.

First, we will discuss nuclear reactions that can generate neutrons.

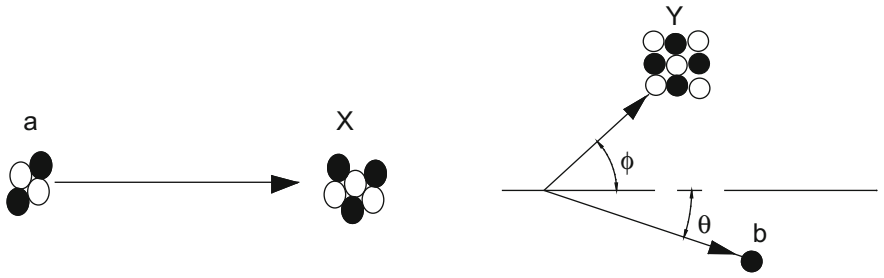

Fig. 4.2 Initial and final steps for a nuclear reaction

4.2.1 Nuclear Reactions

Unlike the radioactive decay process, nuclear reactions consist of transformations resulting from the collision of two nuclei. This reaction occurs by interaction of a moving projectile (proton, neutron, alpha, ion …) on the target nuclei at rest. Figure 4.2 represents initial and final steps resulting from the collision of nucleus (X) with projectile (a) which results in the creation of nucleus (Y) and a light product (b).

Nuclear reaction represented by Fig. 4.2 can be written according to (4.4) and conventionally according (4.5).

$$\mathrm{a} + \mathrm{X} \rightarrow \mathrm{Y} + \mathrm{b} \tag{4.4}$$

$$\mathrm{X}\,(\mathrm{a}, \mathrm{b})\,\mathrm{Y} \tag{4.5}$$

Note that in collision, total energy, momentum, electrical charge and total number of nucleons are conserved.

For lower kinetic energies of 100 MeV per nucleon the classical formalism gives a good approximation. The law of conservation of total energy leads to (4.6), with (m_{X}) the rest mass of the target nucleus X; (m_{a}) the mass of the incident particle; (T_{a}) the kinetic energy of the particle; (m_{Y}) the mass of the resulting nucleus Y; (m_{b}) the mass of the emitted particle b; (T_{b}) the kinetic energy of the particle b.

$$T_a + m_a c^2 + m_X c^2 = T_b + T_Y + m_b c^2 + m_Y c^2 \tag{4.6}$$

By introducing the amount of energy released by the reaction: *Q-value*, the expression (4.6) can be written according to (4.7).

$$Q = (m_a + m_X)c^2 - (m_b + m_Y)c^2 = T_b + T_Y - T_a \tag{4.7}$$

Q-value is the difference between the sums of kinetic energies on the final step and the initial step reaction. So we conclude that if:

- $Q > 0$, the reaction is exothermic; a part of the initial mass, converted into energy, is transmitted as kinetic energy to the particle emitted and the produced nucleus;
- $Q = 0$, the reaction is an elastic collision and does not result in modification of the target nucleus;
- $Q < 0$, the reaction is endothermic; kinetic energy of the projectile is converted into mass or nuclear binding energy. The reaction is possible only above a threshold energy.

Considering the conservation of momentum, the energy of the emitted particle b is given by (4.8). The demonstration of this equation is given in the Further Details 4.1.

$$\begin{aligned} \sqrt{T_b} &= u \pm \sqrt{u^2 + w} \\ \text{with } u &= \frac{\sqrt{m_a m_b T_a}}{m_b + m_Y} \cos(\theta) \\ w &= \frac{m_Y Q + T_a (m_Y - m_a)}{m_Y + m_b} \end{aligned} \tag{4.8}$$

If $Q > 0$, the w term of (4.8) is positive. The kinetic energy of the particle b, T_{b}, is then given by (4.9).

$$\sqrt{T_b} = u + \sqrt{u^2 + w} \tag{4.9}$$

If $Q < 0$, the reaction can occur if the kinetic energy of the particle a, T_{a}, is greater than a threshold energy E_{th}. The threshold energy is given by the expression (4.10).

$$E_{th} = -Q\left(\frac{m_a + m_X}{m_X}\right) \tag{4.10}$$

In what follows, we will focus on reactions for which the emitted particle (b) is a neutron. When projectile energy is low (lower than the lowest excitement of nucleus product), the residual nucleus is set in its ground state after neutron emission. For any direction, neutrons are emitted with a monokinetic energy. This is particularly true when ion energy is close to the production reaction threshold. For higher energies, this energy varies with angle emission of neutrons and the maximum is reached at 0° angle (the direction of the incident ions beam).

4.2.2 Neutrons from the Fusion

The main reactions are given by (4.11)

$$\begin{aligned} &{}^{3}_{1}H(d,n)^{4}_{2}He \\ &{}^{2}_{1}H(d,n)^{3}_{2}He \\ &{}^{2}_{1}H(d,p)^{3}_{2}H \\ &{}^{3}_{1}He(d,p)^{4}_{2}He \end{aligned} \tag{4.11}$$

From (4.8) we can calculate the energy of the emitted particle.

For example, let's calculate the neutron energy for reaction ${}^{3}_{1}H(d,n)^{4}_{2}He$ for a negligible kinetic energy of the deuteron $T_a \sim 0$.

The proposed atomic weights are taken from the publication of Audi and Wapstra [3] (Currently on internet, see reference [3]).

The Q-value according to (4.7) is:

$$Q = (m_a + m_X)c^2 - (m_b + m_Y)c^2 = (2.014101 + 3.016049) - (1.008664 + 4.002603)$$
$$= 0.019\,u.m.a \text{ is } 17.6\,\text{MeV}\,(1\,a.m.u = 931.4943\,\text{MeV})$$

As the *Q-value* is positive, the reaction is exothermic and therefore always occurs. It is noted that the reaction heat can be found currently from the Qtool software on the data viewer nuclear site [4]. In the "Q-values and Thresholds." $T_a = 0$, therefore, $u = 0$

$$\text{and } w = \frac{m_Y Q}{m_Y + m_b} = \frac{4.002603 \times 17.6}{4.002603 + 1.008664} = 14.057\,\text{MeV}$$

For the fusion reaction, the energy of the emitted neutrons is: $T_b = 14.057$ MeV. According to Chap. 3, the conversion factor "fluence-ambient dose equivalent" to this specific neutron energy is $h^*_{\Phi}(10) = 520$ pSv cm^2.

Similarly, let's calculate the energy of the neutron emitted in the second reaction ${}^{2}_{1}\text{H(d,n)}{}^{3}_{2}\text{He}$ for a negligible kinetic energy deuteron $T_a \sim 0$.

The *Q-value* is 3.3 MeV [4]. The *Q-value* is positive so the reaction is exothermic and always occur.

The atomic mass ${}^{3}_{2}$He is 3.016029 amu [3]. Other atomic masses are in Table 4.2.

$T_a = 0$, therefore, $u = 0$.

$$\text{and } w = \frac{m_Y Q}{m_Y + m_b} = \frac{3.016 \times 3.3}{3.016 + 1.008664} = 2.47\,\text{MeV}$$

For the fusion reaction, the kinetic energy of the emitted neutron is: $T_b = 2.47$ MeV. According to Chap. 3, the conversion factor "fluence-ambient dose equivalent" to the neutron energy from this reaction is $h^*_{\Phi}(10) = 415$ pSv cm^2.

Table 4.2 Atomic mass of different elements

Particle/ion	Atomic mass (amu)
$^{3}_{1}$H(X)	3.016049
d(a)	2.014101
n(b)	1.008664
$^{4}_{2}$He(Y)	4.002603

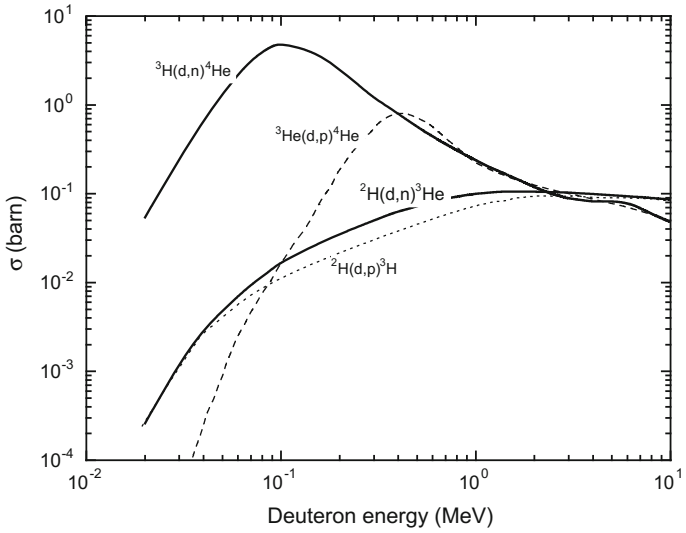

Fig. 4.3 Cross section of fusion reactions (according to data of the site http://www-nds.iaea.org/exfor/endf.htm)

The cross sections of these various reactions depending on the energy of the deuteron are given in Fig. 4.3.

During a fusion reaction, energy is produced. For example, for $^{3}_{1}\mathrm{H(d,n)}^{4}_{2}\mathrm{He}$, 17.6 MeV energy is produced (including 14.1 MeV neutron and provided by the 3.5 MeV by the helium nuclei). Harnessing this source of energy would allow to imagine new reactors without the problems of radioactive waste with long life-time as found in fission reactors. However, controlling fusion reactions remains extremely complex. Indeed, to achieve a continuous fusion requires:

- bring the fuel to a temperature above its flash point (for $^{3}_{1}H(d,n)^{4}_{2}He$ reaction 10 keV energy is necessary, a $1 \cdot 10^{8}$ K temperature);
- require a sufficient fuel mass for losses lower than the energy released and the reaction maintains itself. It is, among others, a challenge of the ITER facility.

It is also possible to get reactions shown in (4.11) from deuteron accelerators. Indeed, it may be observed that the cross section of the reaction ^{2}H(d, n)^{4}He is a

highest at 100 keV energy (see Fig. 4.3). Small deuteron accelerator of 100 keV bombarding tritium targets have been performed to generate monoenergetic 14 MeV neutrons: neutron generator. This device exists also with 2.45 MeV energy using the $^{2}H(d, n)^{3}He$ reaction. This type of reaction is studied in Sect. 4.8.

4.2.3 (α, n) Sources

It is possible to perform an intimate mixture of an alpha source with a light element such as boron, lithium, fluorine and beryllium to generate neutrons from (a, n) reaction.

A wellknown reaction is ${}_{4}^{9}Be(\alpha, n){}_{6}^{12}C$; Q-value of this reaction is 5.7 MeV [4]. For an alpha produced by the ^{241}Am, the neutron energy using the (4.8) is easily calculated. For a 5.5 MeV energy (higher emission of α in ^{241}Am), neutron energy produced range over 11.1 MeV (for an 0° angle θ) and 6.7 MeV (for an 180° angle θ). In addition, the loss of energy by the alpha in solid beryllium and neutron scattering reactions in beryllium are responsible for the emission of a neutron spectrum. Figure 4.4 [5] illustrates the spectrum of a ^{241}Am–Be source. A number of neutron spectra is given in Appendix 1. These spectra may constitute input data, for example, in Monte-Carlo transport calculations.

To calculate the dose equivalent, in addition to energy distribution, we also need the neutron flux emitted by the source. The yield *Y* depends on the geometry of the

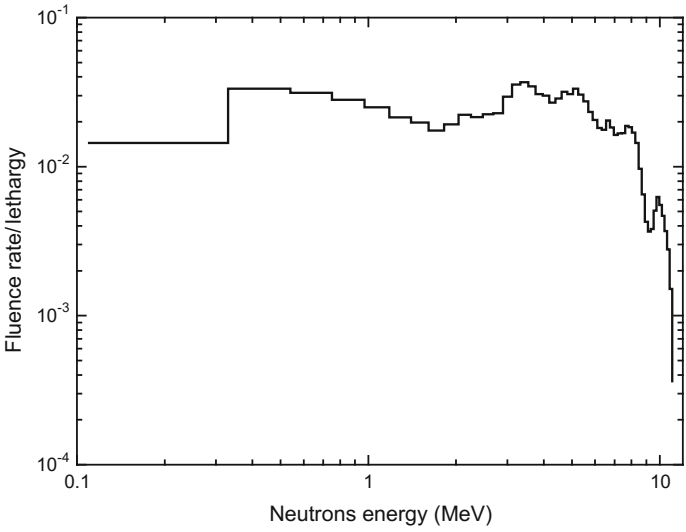

Fig. 4.4 Spectrum neutrons from a ^{241}Am–Be source (from data [5])

source and how emitter and converter materials are mixed or disconnected. For higher performance, corresponding to an optimal intimate mixture, the yield in the most common converter, beryllium, is described by the empirical expression (4.12) [6].

$$Y_{(\alpha,n)} = 0.152E_{\alpha}^{3,56}\left[1+\left(\frac{S_C^e}{S_C^{Be}}\right)\right]^{-1} \tag{4.12}$$

With $Y_{(\alpha,\ n)}$ neutron yield for $1 \cdot 10^6$ α; S_C^e stopping power for emitting material at the alpha energy considered; S_C^{Be} stopping power of beryllium at the alpha energy considered

Let's calculate the Po-210/Be source flux. The ^{210}Po emits alpha of 5.305 MeV; the densities of Be and Po are respectively 1.85 and 9.4 g cm^{-3}. The stopping powers, calculated from expressions of Chap. 2, are:

$$S_C^e = 1425\ \text{MeV cm}^{-1};$$
$$S_C^{Be} = 2006\ \text{MeV cm}^{-1}.$$

According to (4.12), the yield is therefore:

$$Y_{(\alpha,n)}\left(^{210}Po/Be\right) = 0.152 \times (5.305)^{3.56} \times \left[1+\left(\frac{1425}{2006}\right)\right]^{-1} = 34\,(n)/10^6\,(\alpha)$$

In the case of an encapsulated source where the transmitter is disconnected from the converter, assuming that all emitted alphas interact with beryllium converter, the maximum yield for 10^6 alphas can be obtained approximately as a function of the alpha energy, according to the empirical expression (4.13) [6].

$$Y_{(\alpha,n)}(E_\alpha/Be) = \begin{cases} 0.115E_\alpha^{3.82} & 3.5 \le E_\alpha \le 6.5\,\text{MeV} \\ E_\alpha^{2.64} & 6.5 \le E_\alpha \le 10\,\text{MeV} \end{cases} \tag{4.13}$$

Thus, considering the ^{210}Po/Be source into the configuration in which alphas interact only with beryllium converter, the yield is:

$$Y_{(\alpha,n)}(E_\alpha/Be) = 0.115 \times (5.305)^{3.82} = 67\ (n)\ for\ 10^6\ (\alpha)$$

^{210}Po emits alpha with 100% transmission; in other words, for each nucleus decay, an alpha is emitted and consequently the yield $(n) \cdot s^{-1} \cdot Bq^{-1}$ is:

$$Y_{(\alpha,n)}(E_\alpha/Be) = \frac{67}{1.10^6} = 6.7 \cdot 10^{-5}\ (n)/\text{s/Bq}$$

The characteristics of the main neutrons sources processing on this principle are given in Table 4.3. The yield is given for target with thickness greater than the emitted alpha range.

Table 4.3 Sources (α, n). Characteristics

Source (α, not)	Half-life	Energy α main (MeV)	Y (n/s/Bq)	Reference
^{241}Am/Be	432 years	5.486 to 5.443–5.388	$6.6 \cdot 10^{-5}$	[5]
^{241}Am/B			$1.6 \cdot 10^{-5}$	[5]
^{241}Am/Li			$1.1 \cdot 10^{-6}$	[7]
^{241}Am/F			$4.1 \cdot 10^{-6}$	[6]
^{210}Po/Be	138.4 days	5.305	$6.75 \cdot 10^{-5}$	[8]
^{210}Po/B			$1.62 \cdot 10^{-5}$	[8]
^{210}Po/F			$1.1 \cdot 10^{-5}$	[9]
^{210}Po/Si			$1.7 \cdot 10^{-7}$	[9]
^{210}Po/Al			$7.6 \cdot 10^{-7}$	[9]
^{210}Po/C			$1 \cdot 10^{-7}$	[6]
^{210}Po/Na			$1 \cdot 10^{-6}$	[6]
^{226}Ra/Be	1600 years	7.687 to 6.003–5.490	$3.51 \cdot 10^{-4}$*	[8]
+ son		5.304 to 4.785–4.602		
^{238}Pu/Be	87.7 years	5.499 to 5.457–5.358	$6.25 \cdot 10^{-5}$	[8]
^{239}Pu/Be	24,100 years	5.155 to 5.143–5.105	$6 \cdot 10^{-5}$	[6]
^{242}Cm/Be	163 days	6.113 to 6.070	$1.1 \cdot 10^{-4}$	[6]
^{244}Cm/Be	18.1 years	5.805 to 5.763	$1 \cdot 10^{-4}$	[6]
^{227}Ac/Be	28.1	7.386 to 6.819–6.623	$7 \cdot 10^{-4}$**	[6]

*For ^{226}Ra/Be source, note that the yield takes into account both the (α, n) neutron emission and also because of high energy photon production (γ, n)neutron

**For ^{226}Ra/Be and ^{227}Ac/Be sources, the yield depends on the proportion of son within the target. Typically, in the case of [6], the ^{226}Ra/Be is calculated with a 22 years old source

We should note that, today, almost all of these sources are no longer used. Only Am/Be and Am/B are still in use in calibration laboratories. However, we have listed all of these sources for which flux knowledge is especially important for deposit/storage or dismantling studies.

Knowledge of sampled energy spectrum allows to calculate the mean conversion factors "fluence-ambient dose equivalent" $\bar{h}^*_\Phi(10)$ (See Chap. 3). Moreover, from the neutron yield, it is possible to calculate the neutron fluence and to deduce therefrom the neutron ambient equivalent dose rates at a given distance from the source.

With this method, we have calculated for various neutron sources: conversion factors "fluence ambient dose equivalent" and "fluence-effective dose" (in antero-posterior radiation field) and the neutron ambient dose equivalent rate for a point source of 1 GBq activity at 1 m distance in the air. The results are given in Table 4.4.

As we suggested in Chap. 3, it appears in this table that the operational quantity underestimates the ICRP protection quantity to some sources, which modulates the postulate to systematically increase the protection quantity by the operational quantity. However, note that the maximum relative difference does not exceed 12%. Keep in mind that some of these sources emit moreover, photons that can be responsible for an equivalent dose greater than neutron one.

Table 4.4 Average conversion factors "fluence-ambient dose equivalent," "fluence effective dose" and "ambient dose equivalent rate" for (α, n) neutron sources

Source	$\bar{h}^*_\Phi(10)$ (pSv cm^2)	E(AP)/Φ (pSv cm^2)	Neutron ambient dose equivalent rate (μSv h^{-1} GBq^{-1} at 1 m)
Am–B	413	415	$1.89 \cdot 10^{-1}$
Am–Be	391	418	$7.52 \cdot 10^{-1}$
Am–F	417	402	$4.90 \cdot 10^{-2}$
Am–Li	261	172	$8.98 \cdot 10^{-3}$
^{238}Pu–Li	297	191	/
^{242}Cm–Be	411	463	1.29
Po–Be	334	296	$6.46 \cdot 10^{-1}$
^{239}Pu–Be	416	450	$7.15 \cdot 10^{-1}$
Ra–Be	411	447	4.13

4.2.4 (γ, n) Sources

A photon with high energy—beyond the binding energy of the least bound nucleon in the nucleus, can interact by photonuclear inelastic reactions in which secondary particles can be emitted (photonuclear physics reactions developed in Sect. 4.7.4). Some neutron source, based on this reaction, associate a γ emitter and a converter (e.g. Be, D_2O). A significant property of this class of source is the quasi monoenergetic nature of neutrons. Spectra of (γ, n) sources are given in Appendix 1.

Table 4.5 gives the neutron yield for different photoneutron sources. The geometry is considered a γ source surrounded by a cylinder of converter material of 0.79 cm thick [10].

As for (α, n) sources, the energy spectrum of neutron flux allows access to mean conversion factors "fluence-ambient dose equivalent" and "fluence effective dose" and the ambient dose equivalent rate due to neutron to a point source of 1 GBq activity at 1 m distance in the air. They are presented in Table 4.6.

Note that for this class of source, besides the equivalent dose rate neutron, it is necessary to take into account the photon dose equivalent rate.

Table 4.5 Neutron yield of different (γ, n) sources, according to data of [10]

Source (γ, n)	Half-life	Energy γ (MeV)	*Y*-yield (n/s/Bq)
^{140}La–Be	40 h	2.5	$6.21 \cdot 10^{-8}$
^{116}In–Be	54 min	1.8–2.1	$2.21 \cdot 10^{-7}$
^{24}Na–Be	15 h	2.76	$3.8 \cdot 10^{-6}$
^{24}Na–D_2O	15 h	2.76	$7.8 \cdot 10^{-6}$

Table 4.6 Conversion factors "fluence-ambient dose equivalent," "fluence effective dose" and ambient dose equivalent rate for neutron sources

Source	$\bar{h}^*_{\Phi}(10)$ (pSv cm^2)	E (AP)/Φ (pSv cm^2)	$\dot{H}^*_n(10)$ (μSv h^{-1} GBq^{-1} at 1 m)
^{140}La–Be	373.6	237.3	$6.65 \cdot 10^{-4}$
^{116}In–Be	268	155	$1.70 \cdot 10^{-3}$
^{24}Na–Be	346.6	221.9	$3.77 \cdot 10^{-2}$
^{24}Na–D_2O	118.3	76.6	$2.64 \cdot 10^{-2}$

4.3 Fission

Some heavy nuclei, actinides, are likely to be divided into two fragments: the "fission products", releasing significant energy.

This fission occurs spontaneously for naturally unstable nuclei or by absorption of a neutron energy under certain conditions. For example, to ^{235}U, the absorption of a thermal neutron induces fission of the nucleus and in this case the reaction can be written:

$$n_{th} + {}^{235}_{92}U \rightarrow {}^{236}_{92}U^* \rightarrow FP_1 + FP_2 + \bar{\nu}.n \tag{4.14}$$

FP1 with the fission product 1; FP2 the fission product 2; $\bar{\nu}$ the mean number of prompt neutrons emitted per fission.

These reactions are accompanied by emission of photons and neutrons. In a second step these emitting particles may be responsible of interaction with medium nuclei. In fission, two events occur: in the 10 fs after fission photons and neutrons, called prompt are released.

After the fission reaction, it is necessary to take account of the photon emissions from deexcitation fission products.

Almost all neutrons are instantly emitted during the fission. Only a slight fraction of less than 1% is emitted during the fission products evaporation, several seconds to several minutes after the fission these neutrons are called "delayed neutrons". They are one of significant reactivity control elements in reactors. But due to their low percentage and relatively low energy, they are not take into account in the design of shielding.

4.3.1 Source Term from Prompt Fission Reactions

Prompt neutrons

The mean prompt fission neutron yield is noted $\bar{\nu}$. Table 4.7 gives this factor to some common induced fission reactions.

Table 4.8 provides, for spontaneous fission reactions, the fission neutron yield $\bar{\nu}$ and the neutron flux for 1 Bq activity.

Table 4.7 Fission neutrons yield $\bar{\nu}$ for induced fissions (from the data of [11])

Energy of the incident neutron	Fissile isotope	$\bar{\nu}$	Fissile isotope	$\bar{\nu}$	Fissile isotope	$\bar{\nu}$
Thermal	^{235}U	2.414	^{238}U	2.275	^{239}Pu	2.876
1 MeV		2.524		2.43		3.01
10 MeV		3.875		3.827		4.394

Table 4.8 Fission neutrons yield $\bar{\nu}$ and flux per Bq for spontaneous fission (according to data [12])

Radionuclide	$\bar{\nu}$	n/s/Bq
^{242}cm	2.52	$1.6 \cdot 10^{-7}$
^{244}cm	2.69	$3.688 \cdot 10^{-6}$
^{252}cf	3.765	0.1164

Terrell [13] proposes two approaches to fit the spectrum shape of prompt fission neutrons: a Maxwellian distribution—(4.15)—and a more complex distribution, called Watt—(4.16). The Maxwell distribution has already been used in Chap. 1 to illustrate the sampling approach of the ^{252}Cf spectrum. The value of T, "nuclear maxwellian temperature" is given for different reactions in Table 4.9.

$$p(E) = \frac{2}{\sqrt{\pi} T^{3/2}} \sqrt{E} \exp\left(-\frac{E}{T}\right) \tag{4.15}$$

The Watt approach [16] is slightly modified by Cranberg et al. [17]. This distribution is called "Watt-Cranberg distribution" and expressed by (4.16).

$$p(E) = C \exp\left(-\frac{E}{a}\right) \sinh\sqrt{bE} \tag{4.16}$$

Note that in terms of dose calculation, ICRP [12] adopt the formula (4.16) for Watt approach [16]. a and b values for (4.16) are given in Tables 4.10 and 4.11 for spontaneous fission.

The (4.15) and (4.16) can be implemented in the Monte-Carlo transport code with parameters T or a and b as input data.

Figure 4.5 gives the Watt distribution [16] shape according to the formalism (4.16).

Knowing the expression (4.16) completed with Tables 4.10 and 4.11 parameters, we can calculate the mean conversion factors "fluence-ambient dose equivalent"

Table 4.9 T Values from (4.15) for different fission reactions

Radio nucléide	Type fission	T (MeV)	Reference
^{252}cf	Spontaneous	1.42	[5]
^{235}U	Induced E_n = 0.5 MeV	1.37	[14]
^{235}U	Induced E_n = 3.5 MeV	1.42	[14]
^{239}Pu	Induced E_n = 0.5 MeV	1.43	[14]
^{239}Pu	Induced E_n = 3.5 MeV	1.52	[14]
^{238}U	Induced E_n = 14.7 MeV	1.39	[15]

Table 4.10 Values of a and b (4.16) for the induced fission, according from the data [18]

Energy of the incident neutron	Fissile isotope	a	b	Fissile isotope	a	b	Fissile isotope	a	b
Thermal	^{235}U	0.988	2.249	^{238}U	0.88111	3.4	^{239}Pu	0.966	2.842
1 MeV		0.988	2.249		0.89506	3.2953		0.966	2.842
14 MeV		1.028	2.084		0.96534	2.833		1.055	2.383

Table 4.11 Values of at and b (4.16) for spontaneous fission, from data [12]

Fissile isotope	a	b
^{252}Cf.	1.025	2.926
^{242}Cm	0.8873	3.89
^{244}Cm	0.902	3.72

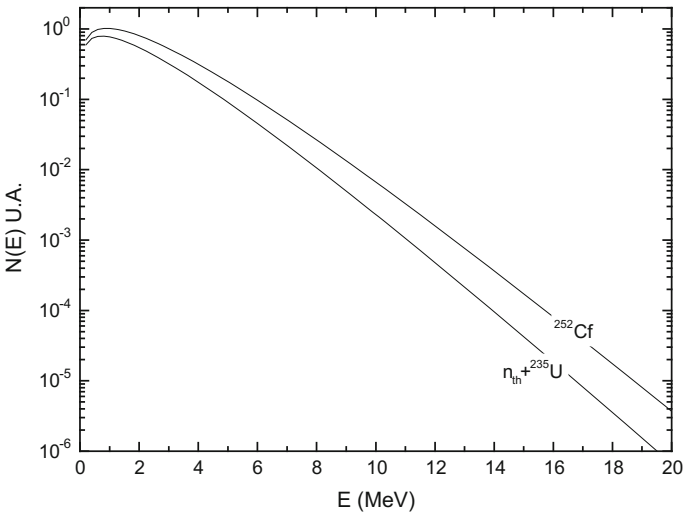

Fig. 4.5 Fission spectrum based on formalism (4.16) for the ^{252}Cf and ^{235}U fission by thermal neutrons

$\bar{h}^{*}_{\Phi}(10)$ (See Chap. 3). Moreover, from the neutron yield (Table 4.8), it is possible to calculate the neutron fluence and therefore the neutron ambient dose equivalent rate at a distance from the point source. Table 4.12 gives these values to various spontaneous fission sources and, Table 4.13 for various induced fission sources.

It is pertinent to note the small differences in mean conversion factors "fluence-ambiant dose equivalent" for all fission reactions.

Prompt photons

When a fission occurs, in addition to prompt neutrons described above, the prompt photons from instant relaxation of fission products are also emitted.

Table 4.12 Mean conversion factor "fluence-ambient dose equivalent" and "fluence effective dose" for different neutron spontaneous fission sources

Sources	$\bar{h}^*_\Phi(10)$ (pSv cm^2)	E(AP)/Φ (pSv cm^2)	Dose equivalent rate a neutron source of activity 1 GBq (μSv^{-1} h^{-1} GBq^{-1} at 1 m)
^{252}cf	385	348.1	1297
^{242}cm	387	340.8	$1.76 \cdot 10^{-3}$
^{244}cm	387	341	$4.08 \cdot 10^{-2}$

Table 4.13 Conversion factor dose equivalent and effective dose for different induced fission neutron sources

Incident neutron energy	Isotope fissionable	$\bar{h}^*_\Phi(10)$ (pSv cm^2)	E(AP)/Φ (pSv cm^2)	Neutron dose equivalent (μSv h^{-1} per fission/s at 1 m)
Thermal	^{235}U	383	332	$2.6 \cdot 10^{-5}$
1 MeV		383	332	$2.8 \cdot 10^{-5}$
14 MeV		384	335	$4.3 \cdot 10^{-5}$
Thermal	^{238}U	383	331	$2.5 \cdot 10^{-5}$
1 MeV		383	331	$3.3 \cdot 10^{-5}$
14 MeV		385	337	$4.2 \cdot 10^{-5}$
Thermal	^{239}Pu	385	337	$3.2 \cdot 10^{-5}$
1 MeV		385	337	$3.3 \cdot 10^{-5}$
14 MeV		387	344	$4.9 \cdot 10^{-5}$

The number of emitted photons by fission is given in Table 4.14.

The prompt photons spectrum of is given by energy bins according to (4.17) [6].

$$\dot{N}_E = \begin{cases} 6.6 & 0.1 < E < 0.6\,\text{MeV} \\ 20.2\,\exp(-1.78E) & 0.6 < E < 1.5\,\text{MeV} \\ 7.2\,\exp(-1.09E) & 1.5 < E < 10.5\,\text{MeV} \end{cases} \quad \textit{photons} \cdot \text{MeV}^{-1} \cdot \textit{fission}^{-1} \tag{4.17}$$

The description of the prompt photon spectrum given by formalism (4.17) is *a priori* representative of U-235 thermal fission. Nevertheless, Shultis and Faw [6] indicates that it is extrapolated to other fission spectra and is usable for calculating radiological shielding for other fissile nuclei.

By weighting the spectrum with mean conversion factors "fluence- ambiant dose equivalent", we obtained an "ambient dose equivalent rate" at 1 m distance $\dot{H}^*(10) = 8 \cdot 10^{-7}$ μSv h^{-1} per (fission) s^{-1}. Note that for prompt fission reactions, the photon dose equivalent is negligible compared to the neutron dose equivalent.

4.3.2 Source Term from the Fission Products

Every fragment fission gets a probability of occurring. Figure 4.6 gives, the frequency of fission fragments yield as a function of mass number,.

Table 4.14 Emitted photons yield per fission for different fission reactions

	Average number of photons per fission	References
^{235}U (n, Fiss)	6.7	[19]
^{239}Pu (n, Fiss)	7.23	[19]
^{252}Cf (Spontaneous fission)	7.8	[19]
^{242}Cm (Spontaneous fission)	6.62	[20]
^{244}Cm (Spontaneous fission)	6.9	[20]

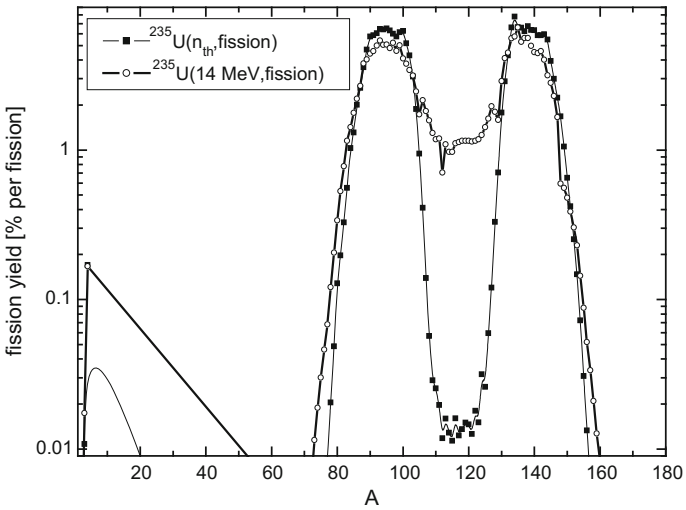

Fig. 4.6 Fission yield as a function of mass number for induced fission on ^{235}U by thermal neutrons and 14 MeV neutrons, from data [21]

After release of fission fragments, radioactive nuclei follow a relaxing process of decay. Thus the activity of each radionuclide shifts over time. The time behaviour of ^{235}U thermal fission fragment normalized to $1 \cdot 10^{20}$ fissions (note that $3.1 \cdot 10^{10}$ f s^{-1} give 1 W) is given in Fig. 4.7. The calculation of the fission products is performed using the decay code Darwin/pepin2 [22] and the time evolution of each of the radionuclides formed is accessed using the compartement model code Erastem [23].

The time evolution of each radionuclides is complex. In addition to their direct production by fission the production can be incresed by daughter products. For example, Fig. 4.8 shows the evolution of $A = 135$ atomic mass radionuclides versus time. ^{135}I production can be performed by direct fission reaction but also by daughter radionuclide of ^{135}Te.

Hunter and Ballou [24] have assessed the time evolution of the total activity of thermal fission products of ^{235}U with time t (in seconds) after the fission reaction by relationships (4.19).

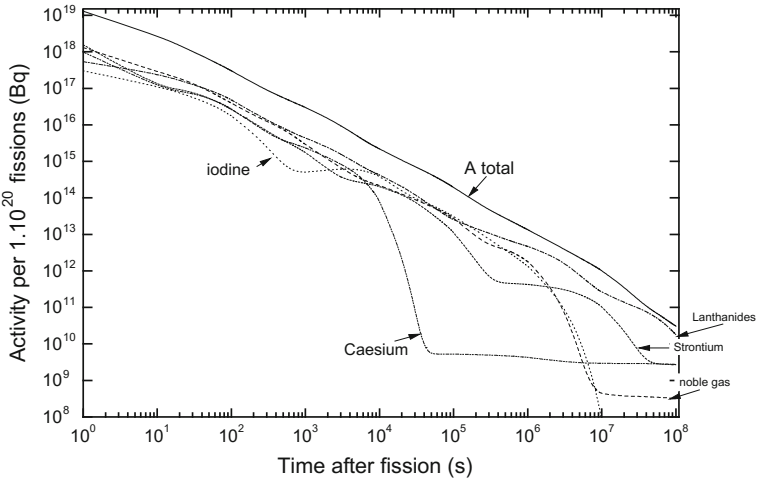

Fig. 4.7 Evolution of total activity for rare gases, iodine, lanthanides, caesium and strontiums for a ^{235}U reaction (nth, fiss) normalized to $1 \cdot 10^{20}$ fissions

$$
\begin{aligned}
A(t) &= k_1 t^{-0.89} \quad 1\,\text{min} \le t < 30\,\text{min} \\
A(t) &= k_2 t^{-1.11} \quad 30\,\text{min} \le t < 1\,\text{day} \\
A(t) &= k_3 t^{-1.25} \quad 1\,\text{day} \le t < 4\,\text{days}\ (t\,\text{in seconds}) \\
A(t) &= k_4 t^{-1.03} \quad 4\,\text{days} \le t < 100\,\text{days} \\
A(t) &= k_5 t^{-1.6} \quad 100\,\text{days} \le t < 3\,\text{years}
\end{aligned}
\tag{4.18}
$$

Figure 4.9 presents the total activity calculated by Darwin/pepin2 and Erastem codes, compared with the assessments of Hunter and Ballou [24].

We can also deduce k_1–k_5 Equation values (4.19). The equation gives the total activity in Bq for a ^{235}U thermal fission.

$$
\begin{aligned}
A(t) &= 0.2 \times t^{-0.89} \quad 1\,\text{min} \le t < 30\,\text{min} \\
A(t) &= 0.7 \times t^{-1.11} \quad 30\,\text{min} \le t < 1\,\text{day} \\
A(t) &= 3.4 \times t^{-1.25} \quad 1\,\text{day} \le t < 4\,\text{days in Bq / Fiss}\ (t\,\text{in seconds}) \\
A(t) &= 0.2 \times t^{-1.03} \quad 4\,\text{days} \le t < 100\,\text{days} \\
A(t) &= 1600 \times t^{-1.6} \quad 100\,\text{days} \le t < 3\,\text{years}
\end{aligned}
\tag{4.19}
$$

The ambient dose equivalent rate is then obtained by weighting the entire spectrum of photons from all fission radionuclides by appropriate conversion factors "fluence-ambient dose equivalent". For simplicity, we considered, for this calculation, a point source without shielding. The time evolution of the ambient dose equivalent rate at 1 m distance is shown in Fig. 4.10.

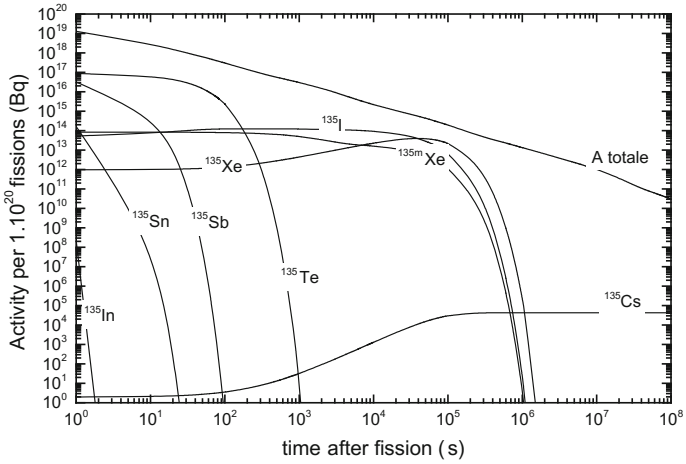

Fig. 4.8 Time evolution of the 135 atomic mass radionuclides for the ^{235}U fission reaction by thermal neutrons on the standardized $1 \cdot 10^{20}$ fissions

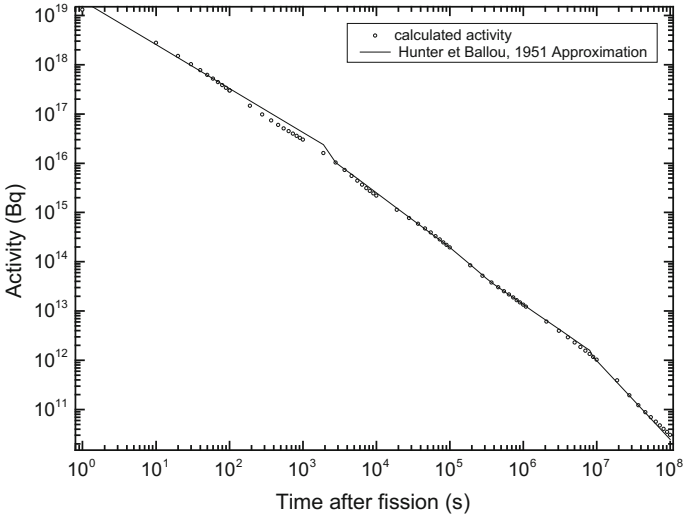

Fig. 4.9 Total activity calculated by Darwin/pepin2 and Erastem codes and Hunter and Ballou formalism [24]

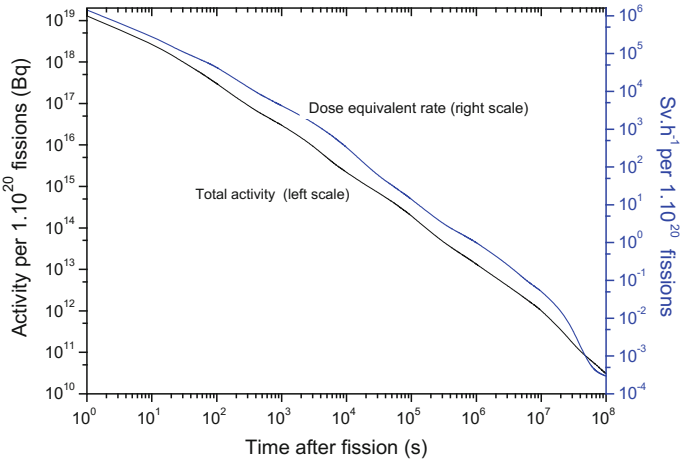

Fig. 4.10 time evolution of total activity and the dose equivalent rate at 1 m distance (source considered as punctual and isotropic) of fission products provided during ^{235}U thermal fission

4.4 Neutron Source from Fuel Cooling

In pressurized water reactors, the fuel assembly is a collection of fuel rods made of zirconium alloys due to its very low absorption cross-section. Uranium oxide so called UOx (with enriched uranium to approximately 4% ^{235}U) is pressed into pellets which are encapsulated within the fuel rod. The core should be added by a mixed uranium-plutonium oxide fuel (U, Pu)O_2, with 5–10% plutonium content so called: MOx.

The neutrons interact with uranium nuclei or plutonium and induce fission reactions for which radiation protection consequences were given previously in Sect. 4.3.

After the reactor shutdown, the fuel going through a cooling process. During this period, in addition to fission products, actinides are present firstly because of fuel component isotope (and daughter products) and secondly because of the (n, γ) radiative captures (for which cross sections are significant at reactors energies) and more marginally (n, 2n) reactions. Figure 4.11 shows a likely way of successive (n, γ) and decays β^- reactions to transmute ^{235}U in ^{244}Cm.

In fact, the number of successive radiative captures depends primarily on the fuels *burn-up*: the more the fuel is "bathed" by thermal neutrons, over a long period, the more radiative captures occur.

The presence of these actinides in cooling fuel produce neutrons by two phenomena: either the actinide emits neutrons by spontaneous fission (e.g. Curium) according to the process discussed above, or by (α, n) reactions on fuel oxygen (or fluorine).

Figure 4.12 shows the neutron flux evolution for both fuel types (UOx and MOx).

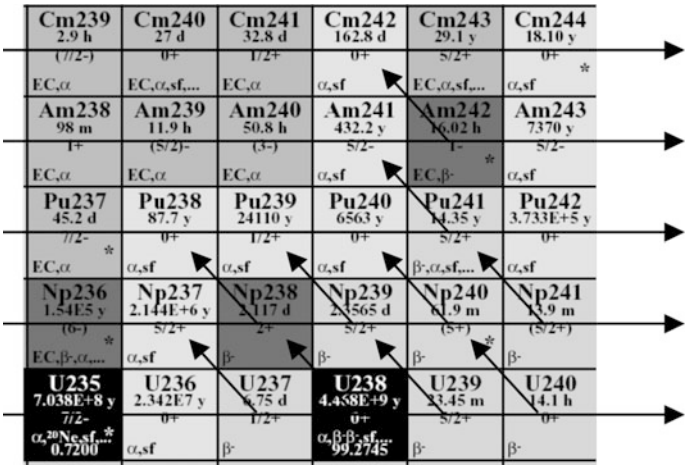

Fig. 4.11 Examples of of a ^{244}Cm production from ^{235}U—*oblique arrows* symbolize β^- decays and the radiative captures *horizontal arrows*

Note that the MOx fuel emits more neutrons than UOx. This difference is explained by a greater presence of ^{239}Pu species in the first type. Also, note that the total flux is mainly due to spontaneous fission of ^{244}Cm and this up to a 100 years of cooling. It is therefore recommended, for calculating the neutron dose equivalent around a spent fuel, a Watt-distribution fission spectrum for neutron component with ^{244}Cm parameters given in Table 4.11.

In fuel or more generally in a material composed of fissile material, the fission release several neutrons, and each of them in turn may induce a fission releasing neutrons and so on. The neutron balance between the number of neutrons produced by fission and the number of neutrons lost by leakage or capture is expressed by the effective neutron multiplication factor: k_{eff}. Thus, the total number of neutrons from a solid compound of the fissile material can be expressed approximately by the (4.20).

$$Y = \left(\frac{1}{1 - k_{eff}}\right)\left(Y_{fiss} + Y_{(\alpha,n)}\right) \tag{4.20}$$

with Y the yield of neutrons; k_{eff} the multiplication factor; Y_{fiss} the neutron flux due to spontaneous fission; $Y_{(\alpha,\text{n})}$ the yield due to (α, n) reactions.

Let's calculate the neutron dose equivalent rate due to UOx and MOx fuel pellets.

In this example, let's consider two pellets of 7 g:

- UOx irradiated enriched to 3.7% with 50 GWd/t burnup, cooled 1 year;
- MOx irradiated enriched to 7.5% with 50 GWd/t burnup, cooled 1 year.

The curves of Fig. 4.12 give a total neutron flux for a fuel of 1 ton weight: $1.5 \cdot 10^9$ n/s/t for UOx or $1 \cdot 10^4$ n/s for 7 g and $1.4 \cdot 10^{10}$ n/s/t for MOX, or $1 \cdot 10^5$ n/s for 7 g.

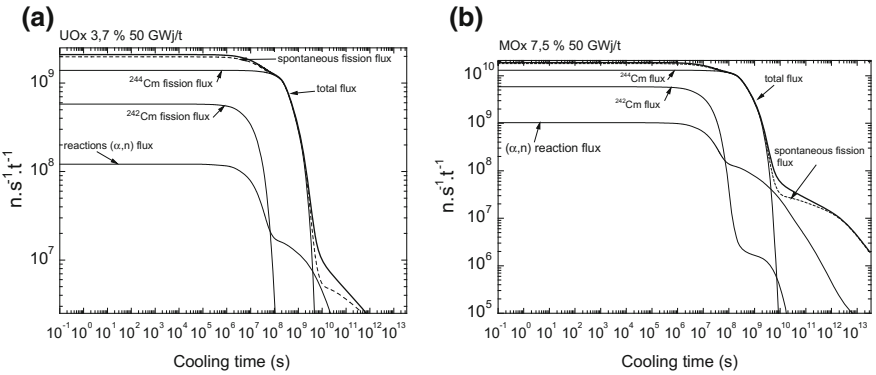

Fig. 4.12 Neutron flux as a function of cooling time. Total flux due to spontaneous fission and (α, n) reactions, the ^{242}Cm and ^{244}Cm for UOx type of fuel enriched to 3.7% with a burnup of 50 GWd/t (**a**) and a type of MOx fuel enriched to 7.5% with burnup of 50 GWd/t (**b**)

In the first case, we consider the neutron emission due to spontaneous fission of ^{244}Cm, which implies a mean conversion factor of fluence-ambient dose equivalent of $\bar{h}^*_{\Phi}(10) = 387$ pSv cm^2 from Table 4.9. The ambient dose equivalent rates 1 m ton each of pellets are:

$$\dot{H}^*(10)_{\mathrm{UOx}} = \frac{1 \cdot 10^4}{4 \times \pi \times 100^2} \times 387 \cdot 10^{-12} \times 3600 \times 1 \cdot 10^6 = 0.1\ \mu\mathrm{Sv/h}$$

$$\dot{H}^*(10)_{\mathrm{MOx}} = \frac{1 \cdot 10^5}{4 \times \pi \times 100^2} \times 387 \cdot 10^{-12} \times 3600 \times 1 \cdot 10^6 = 1\ \mu\mathrm{Sv/h}$$

Due to the small size of pellets, we have considered the point without self-shielding. Similarly, one can consider that the k_{eff} is close to zero because of the low proportion of fissile mass in the pellet. Note that in monte-carlo transport code the neutron multiplication is set by default.

4.5 Photons from Neutron Reactions

4.5.1 Photons Produced by Radiative Captures

Photons emitted in a radiative capture ${}^{A}X(n,\gamma)^{A+1}X$ must be taken into account to assess the exposure risk. These include, for example, the radiative capture on hydrogen by thermal energies whose cross section is about 0.3 barn, with a 2.23 MeV photon emitted (the deuteron binding energy). These reactions are greatly present in the hydrogenated elements surrounding the reactors core (water, concrete …) and constitute significant photon sources.

Table 4.15 [6] synthesizes for many natural elements the cross section and the photon emission yield by energy bins for thermal radiative captures. The case of

Table 4.15 Cross sections of radiative capture with the number of photons emitted by energy bin for inelastic reactions [6], with permission from the American Nuclear Society, La Grange Park, Illinois

	σ_γ(b)	Energy group (MeV)										
		0–1	1–2	2–3	3–4	4–5	5–6	6–7	7–8	8–9	9–10	10–11
H	3.32E−1	0.0000	0.0000	1.0000	0.0000	0.0000	0.0000	0.0000	0.0000	0.0000	0.0000	0.0000
Li	3.63E−2	0.1242	0.0491	0.8933	0.0000	0.0000	0.0000	0.0107	0.0402	0.0000	0.0000	0.0000
Be	9.20E−3	0.2552	0.0000	0.2415	0.4629	0.0000	0.0201	0.6290	0.0000	0.0000	0.0000	0.0000
B	1.03E−1	0.0000	0.0000	0.0000	0.0000	1.1014	0.0000	0.3950	0.4785	0.0000	0.0000	0.0000
C	3.37E−3	0.0000	0.2975	0.0000	0.3240	0.6827	0.0000	0.0000	0.0000	0.0000	0.0000	0.0000
N	7.47E−2	0.1302	0.0000	0.5168	0.4683	0.2284	0.1969	0.2465	0.0000	0.0000	0.0000	0.0000
O^{α}	2.70E−4	1.0000	0.8200	0.8200	0.1800	0.0000	0.0000	0.0000	0.0000	0.0000	0.0000	0.0000
Na	4.00E−1	0.9267	0.2047	0.7265	0.6536	0.0323	0.0633	0.2244	0.0000	0.0000	0.0000	0.0000
Mg	6.30E−2	0.5963	0.6875	0.6404	0.9583	0.0662	0.1077	0.1157	0.0372	0.0474	0.0075	0.0000
Al	2.30E−1	0.2751	0.0877	0.3125	0.2602	0.3709	0.0812	0.1029	0.3874	0.0000	0.0000	0.0000
Si	1.60E−1	0.1172	0.1328	0.3193	0.8266	0.6378	0.0450	0.1361	0.0704	0.0203	0.0000	0.0000
P	1.80E−1	0.4066	0.5411	0.5213	0.5448	0.2690	0.1289	0.1809	0.0789	0.0000	0.0000	0.0000
S	5.20E−1	0.7555	0.0000	0.7718	0.3642	0.1794	0.6348	0.0000	0.0391	0.0266	0.0000	0.0000
CI	3.32E+1	0.3130	0.7353	0.3015	0.2099	0.1379	0.1346	0.3773	0.2037	0.0299	0.0000	0.0000
K	2.10E+0	0.5435	0.4671	0.5927	0.3855	0.2617	0.3736	0.0352	0.0610	0.0000	0.0000	0.0000
Ca	4.30E−1	0.2401	0.9349	0.5187	0.1711	0.2303	0.1254	0.4384	0.0216	0.0000	0.0000	0.0000
Ti	6.I0E+0	0.3097	0.8089	0.0695	0.1249	0.1114	0.0239	0.8495	0.0030	0.0019	0.0000	0.0000
V^{α}	5.04E+0	0.3837	0.2486	0.1335	0.0591	0.0877	0.3158	0.3947	0.1972	0.0000	0.0000	0.0000
Cr	3.10E+0	0.4051	0.1607	0.2067	0.0922	0.0421	0.1103	0.1189	0.2461	0.3766	0.1097	0.0000
Mn	1.33E+1	0.1750	0.1242	0.2421	0.1542	0.1705	0.3134	0.1076	0.3799	0.0000	0.0000	0.0000
Fe	2.55E+0	0.2783	0.2476	0.0954	0.1132	0.1122	0.1093	0.1012	0.5886	0.0082	0.0415	0.0011
Co	3.72E+1	0.9374	0.2054	0.1594	0.1784	0.1566	0.3362	0.3467	0.1139	0.0000	0.0000	0.0000

(continued)

Table 4.15 (continued)

	σ_γ(b)	Energy group (MeV)										
		0–1	1–2	2–3	3–4	4–5	5–6	6–7	7–8	8–9	9–10	10–11
Ni	4.43E+0	0.2616	0.0659	0.0605	0.0365	0.0370	0.0745	0.1704	0.1404	0.5899	0.0000	0.0000
Cu	3.79E+0	0.8175	0.0602	0.0457	0.0496	0.1010	0.1019	0.1621	0.6487	0.0000	0.0000	0.0000
Zn	1.10E+0	0.1600	0.6386	0.5102	0.2837	0.2116	0.1964	0.1820	0.1870	0.0130	0.0111	0.0000
Ge	2.30E+0	1.1018	0.6417	0.6677	0.3826	0.2662	0.1957	0.1806	0.0508	0.0146	0.0001	0.0000
Br^{α}	6.80E+0	0.6347	0.0666	0.0101	0.0030	0.0044	0.0187	0.0318	0.0227	0.0000	0.0000	0.0000
Zr	1.85E−1	0.8078	0.6086	0.8407	0.4718	0.2507	0.1550	0.2200	0.0120	0.0081	0.0000	0.0000
Mo	2.65E+0	0.8289	0.8330	0.8729	0.4635	0.2774	0.1564	0.1065	0.0289	0.0104	0.0000	0.0000
Ag	6.36E+1	0.6831	0.4412	0.7808	0.4241	0.2512	0.1908	0.0593	0.0174	0.0000	0.0000	0.0000
Cd	2.45E+3	1.0399	0.3727	0.9808	0.5940	0.3072	0.2432	0.0558	0.0262	0.0081	0.029	0.0000
In	1.94E+2	0.3357	1.0696	1.0067	0.3758	0.1827	0.0740	0.0093	0.0000	0.0000	0.0000	0.0000
Sn	6.30E−1	0.1410	0.6146	1.0542	0.5974	0.3228	0.1801	0.0994	0.0618	0.0110	0.0029	0.0000
Ba^{α}	1.20E+0	0.3751	0.3971	0.2427	0.0910	0.3210	0.0848	0.0332	0.0088	0.0034	0.0065	0.0000
Ta	2.11E+1	0.4513	0.5841	0.8661	0.4097	0.2039	0.0621	0.0083	0.0000	0.0000	0.0000	0.0000
W	1.85E+1	0.7987	0.2760	0.6804	0.3396	0.1930	0.1354	0.0968	0.0119	0.0000	0.0000	0.0000
Hg	3.76E+2	0.9186	0.4640	0.5811	0.2880	0.3626	0.3682	0.1122	0.0063	0.0000	0.0000	0.0000
Pb	1.70E−1	0.0000	0.0000	0.0000	0.0000	0.0000	0.0000	0.0504	0.9405	0.0000	0.0000	0.0000
Bi	3.30E−2	0.0000	0.0000	0.0000	0.0000	1.1170	0.0000	0.0000	0.0000	0.0000	0.0000	0.0000

thermal neutron capture on iron is emphasized. This reaction causes the most energetic photon component at about 10 MeV.

We will restrict ourselves to quantitatively study photonic spectra for thermal neutron cross sections, much higher than those for more energetic neutrons.

4.5.2 Photons Emitted During Neutron Inelastic Scattering

Following an inelastic scattering, the target nucleus is left in an excited state. This unstable nucleus emits quickly one or more photons (of the order of 10 fs). The cross sections are even more important than the neutron energy and the atomic number Z of the target nucleus are significant. These inelastic scattering will be used to slow the fast neutrons, producing photons that will themselves selfshield in the medium. We will see that because of the low energy photons accompanying such scattering, the risk is low or insignificant compared to that of primary neutrons. However, to characterize these secondary photon yield, it should be consider the neutron flux rate, the energy spectrum thereof and the cross sections of inelastic scattering. For example, Table 4.16 gives to some natural elements, effective photon yield by energy bins as a function of incident neutrons energy. For completeness, these cross sections values integrate photonic emissions by all inelastic reactions could be produced to the energies of neutrons considered, for example: (n, γ).

For the yield of the two-way table, proceed this time according to the relationship (4.21).

$$Y_\gamma = \sum_{E_n} \sum_{\Delta E_\gamma} N\, \sigma\left(E_n, \Delta E_\gamma\right) \dot{\Phi}(E_n) \tag{4.21}$$

with $\sigma(E_\mathrm{n}, \Delta E_\gamma)$ cross section of photon yield in the range ΔE_γ for an incident neutron energy E_n and $\dot{\Phi}(E_n)$ the neutron fluence rate at energy E_n.

For example, let's calculate the yield of decay photons from inelastic reactions on ^{6}Li (density 0.534) per 1 cm^3 of material and a neutron fluence rate of 10^6 cm^2 s^{-1}. The expression (4.21) can also be written as (4.22).

$$Y_\gamma = \frac{\rho\, \eta_A V}{A} \sum_{E_n} \sum_{\Delta E_\gamma} \sigma\left(E_n, \Delta E_\gamma\right) \dot{\Phi}(E_n) \tag{4.22}$$

Consider a trivial case in which the energy distribution of the neutron fluence rate is equally probable in the following energy bin: 4–5 MeV,

Table 4.16 Cross sections of photonic emission for inelastic reactions, which mostly inelastic scattering [6], with permission from the American Nuclear Society, La Grange Park, Illinois

Element or isotope	Gamma energy group (MeV)	Photon production cross section for fast neutrons (mb)									
		Neutron energy (MeV)									
		0.5	1.0	1.5	2	3	4	5	7	10	14
$^{6}Li^{b}$	3.5–4							7.5	5.4	5.0	5.0
$^{7}Li^{b}$	0.45–0.51		147	200	195	217	284	282	226	138	80
$^{10}B^{c}$	4–4.5								3.5	4.0	1.8
	3–4						1.3	3.3	13.4	14.0	6.3
	2–3					3.0	11.5	27.3	33.9	27.1	12.1
	1–1.66				1.2	15.4	34.4	48.3	46.2	31.2	16.2
	0.7–0.8		0.2	4.7	67.9	48.0	72.9	106	87.8	59.4	28.1
^{12d}C	4–4.5							28.2	188	346	221
$^{16}O^{c}$	7–7.5									44	53
	6–7								50	150	178
	4–5										20
	2–3									10	50
	1.66–2									2	10
Si^{c}	10–12										25
	8–10									17	52
	7–8									77	51
	6–7								6	102	112
	5–6								11	85	99
	4–5							2	65	69	77
	3–4						3	8	52	38	73
	2–3					32	40	79	165	141	169
	1.66–2				213	477	543	589	598	469	384
	1–1.66			11	20	19	30	39	42	69	82
Al^{c}	8–10									27	37
	7–8									51	48
	6–7								21	75	66
	5–6								80	132	96
	4–5							27	99	122	113
	3–4						117	139	257	277	265
	2–3					187	272	308	396	444	366
	1.33–2					31	80	77	86	122	116
	1–1.33			141	208	233	225	235	230	182	115
	0.7–10		2.8	94	94	94	135	128	111	90	61
Fe^{b}	8–10									47	60
	7–8									68	42
	6–7								23	129	110
	5–6								74	168	103
	4–5							20	105	220	137

(continued)

Table 4.16 (continued)

Element or isotope	Gamma energy group (MeV)	Photon production cross section for fast neutrons (mb) Neutron energy (MeV)									
	3–4					2.3	166	333	411	475	248
	2–3					86	442	502	634	609	313
	1–2			11	47	291	615	858	1 120	1 270	879
	0.8–2		400	698	865	1 030	1 210	1 280	1 320	1 240	742
	0.45–0.8					97	233	240	120	168	120
Pb[b]	6–7								68	22	7
	5–6							3	172	54	101
	4–5						14	192	329	115	382
	3–4						56	160	407	182	505
	2–3					287	976	1 470	1 860	465	876
	1–2			6	79	300	676	1 050	1 520	1 080	1 610
	0.7–1		105	264	376	575	982	1 250	1 280	1 300	1 210
	0.51–0.7		100	154	252	425	1 070	1 370	1 310	1 280	1 230
	0.4–0.51			6	15	28	89	168	183	178	210
	0.2–0.4			30	31	66	210	310	293	368	320

5–7, 7–10 and 10–14 MeV, which allows us to say that the fluence rate in each of these bins will be a quarter of the total fluence rate. Referring to Table 4.16, we get:

$$Y_\gamma = \frac{0.534 \times 6.02 \cdot 10^{23}}{6} \times \left(7.5 \cdot 10^{-3} + 5.4 \cdot 10^{-3} + 5 \cdot 10^{-3} + 5 \cdot 10^{-3}\right) \cdot 10^{-24} \times \left(\frac{1}{4}\right) \times 1 \cdot 10^{-6} \approx 1.1 \cdot 10^{3}\,\gamma\,\mathrm{s}^{-1}$$

4.6 Electrons—Dark Current Effect

The calculation of dose equivalent due to electrons was discussed in Chap. 3, including using the conversion factors "fluence-ambient dose equivalent" of ICRP.

For example, let's consider an electron accelerator with typical characteristics of industrial radiation, namely energy of 3 MeV and a current of 1 mA to a 10 cm^2

parallel beam section. The "fluence-ambient dose equivalent" conversion factor given in Chap. 3 is 0.336 nSv cm^2 (to 10 mm depth) and therefore we have:

$$\dot{H}(10,0^\circ) = h_\Phi \dot{\Phi} = h_\Phi \cdot \left(\frac{I}{S\,q}\right) = 0.336 \cdot 10^{-9} \times \left(\frac{1.10^{-3}}{10 \times 1.6 \cdot 10^{-19}}\right) = 2.1 \cdot 10^5 \text{ Sv/s}$$

We let it here that the dose equivalent rate due to electron beam from an accelerator is huge. Furthermore, because of their energy, the electrons reach the widely epidermal thicknesses and it is necessary to identify, this time, the dose equivalent generated under 10 mm depth.

To obtain particles with high energy, an accelerator produces a strong electric field (in the case of our example above: an electric field of 3 MV), extracts then accelerates the particles via a "source", constituted for example by free electrons produced with current flux in a cathode. In such a machine, if the source is simply stopped, the electric field is still present and is intense enough to extract "free" electrons at the cathode or the accelerator walls. This current so called "dark current" is a few nA. Considering the above example, with a current of 1 nA, we get $1 \cdot 10^6$ times less dose than with the "electron source" of 1 mA, recalling that the dose is directly proportional to the current. This still creates a residual dose equivalent rate of 210 mSv s^{-1} (756 Sv h^{-1}). Thus, a machine partially stopped, namely that high voltage during operation and standstill current, continuously deliver an extremely high dose equivalent rate: this is the radiological consequences of dark current. Also in radiation safety control procedures, it must be impose to assess this risk in accelerators or X-Rays generators. It is important to guard against this effect that can cause serious radiation injuries including the Forbach accident (France) in 1991 [25].

4.7 Radiation from Bremsstrahlung

4.7.1 Overview

Charged particles, of mass m and charge Ze, penetrating a target material undergo coulomb interactions with orbital electrons and the nucleus (Ze charge). The particles can be subjected to high accelerations. In classical mechanics, when a charged particle is accelerated, it radiates energy in form of an electromagnetic wave and slows. Quantum mechanics it matches the emission of photons.

Acceleration (a) of a charged particle (q *charge*) at a distance (r) from a nucleus is obtained by the coulomb force according to the equality (4.23).

$$m|a| = \frac{qZe}{4\pi\varepsilon_0|r|^2} \quad \Rightarrow \quad |a| \propto \frac{qZe}{m} \tag{4.23}$$

The energy radiated, on the other hand, is proportional to a^2, that is to say the inverse of the mass of the particle to the square, which implies that this radiation is negligible for heavy particles, but significant for electrons. This photon is called *bremsstrahlung radiation*.

Bremsstrahlung differential cross section

The differential cross section, $d\sigma/dk$, depends on energy k[1] of the emitted photon, the kinetic energy of the incident electron T and atomic number Z of the target atom. The cross section can then be written as the sum of two terms as given in (4.24) [28].

$$\left(\frac{d\sigma}{dk}\right) = \left(\frac{d\sigma_n}{dk}\right) + Z\left(\frac{d\sigma_e}{dk}\right) \tag{4.24}$$

with $d\sigma_n/dk$ representing the braking occuring in the nucleus field and $Zd\sigma_e/dk$ that produced in the field of Z electrons (the atom is considered neutral). By posing ξ according to the expression in (4.25), we get the expression of the differential cross section of bremsstrahlung (4.26).

$$\xi = \frac{d\sigma_e}{dk}\left(\frac{1}{Z^2}\frac{d\sigma_n}{dk}\right)^{-1} \tag{4.25}$$

$$\frac{d\sigma}{dk} = \left(1 + \frac{\xi}{Z}\right)\frac{d\sigma_n}{dk} \tag{4.26}$$

Seltzer [28] recommends taking $\xi = 1$. In high Z atomic numbers, the total differential cross-section is equal to the differential section produced by the nucleus.

Many theories on the differential cross section were developed limited by the range of incident electron energy. The expression of the cross section $d\sigma_n/dk$ is given by Koch and Motz [27] and is expressed in (4.27).

$$d\sigma_n = \sigma_0 Z^2\left(\frac{T + m_0c^2}{T}\right)B(T, Z, \theta)\frac{dk}{k} \quad avec\ \sigma_0 = \alpha r_e^2 \tag{4.27}$$

with $\alpha = (137)^{-1}$ and r_e the electron radius ($r_e = 2.818 \cdot 10^{-13}$ cm).

The function $B(T, Z, \theta)$ is a complex formalism including set-dependent energy field considered.

The differential cross section $(k/Z^2) \times (d\sigma_n/dk)$, is shown in Fig. 4.13 for electron energies ranging over 0.05–500 MeV on platinum ($Z = 78$) as a function of the photon energy. In the field of energies below 2 MeV, it is worth mentioning the work of Tseng and Pratt [29], who developed a successful model in this energy range. Cross sections tabulated as a function of Z and of T are published in

[1]In the formalism of this work, we should use the notation E_γ. However, as the notation k has been in widespread in the literature on bremsstrahlung such as [26–28], It is kept in Sect. 4.7.

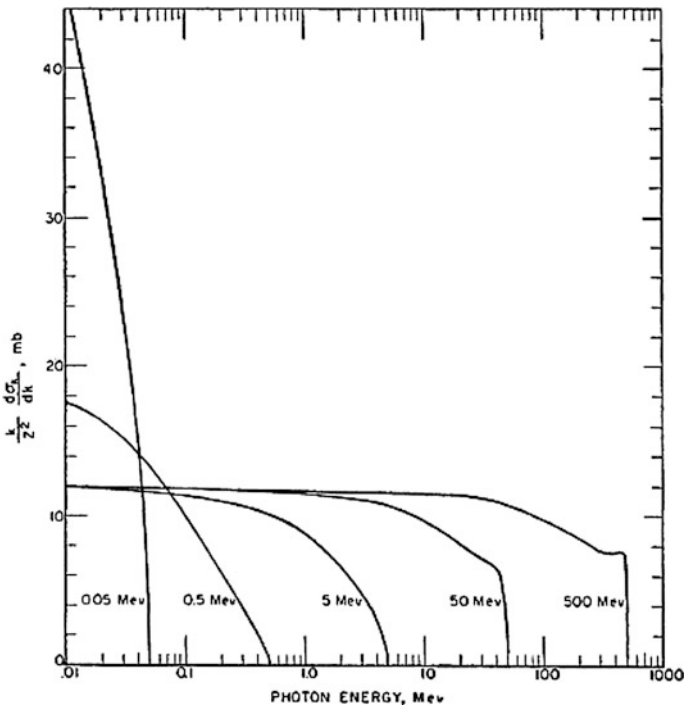

Fig. 4.13 Differential cross section normalized in energy $(k/Z^2) \times (d\sigma_n/dk)$ on platinum as a function of the energy of bremsstrahlung photons, according to [27], with permission from the American Physical Society

references [30, 31]. The differential cross section, $\beta^2(k/Z^2) \times (d\sigma_n/dk)$ (with $1/\beta^2 = (T + m_0c^2)/T)$), is shown in Fig. 4.14 for electron energies in the range 50–500 keV for molybdenum ($Z = 42$) and tungsten ($Z = 74$), depending on energy of photon emitted.

Note that, in Figs. 4.13 and 4.14, the differential cross section range between 0 and the total energy of the incident electrons, which will require continuous spectra between 0 and the maximum energy of electrons. Similarly, it is observed in Fig. 4.14 the dependence of the cross section with the atomic number of the material (Z).

The differential cross section $d\sigma/d\Omega$ angle is shown in Fig. 4.15 for electron energies between 50 keV to 25 MeV.

The differential cross section $d\sigma/d\Omega$ of Fig. 4.15 shows that the emission of bremsstrahlung photons is more and more anisotropic with the energy of electrons.

Bremsstrahlung kerma theoretical expression

As we have assumed, the bremsstrahlung photon spectrum is continuous from 0 to the energy of incident electrons. Also, we can estimate the kerma for a continuous spectrum of photons as defined in Chap. 2. for an electron of energy T, the kerma K at a distance d is assessed according to (4.28).

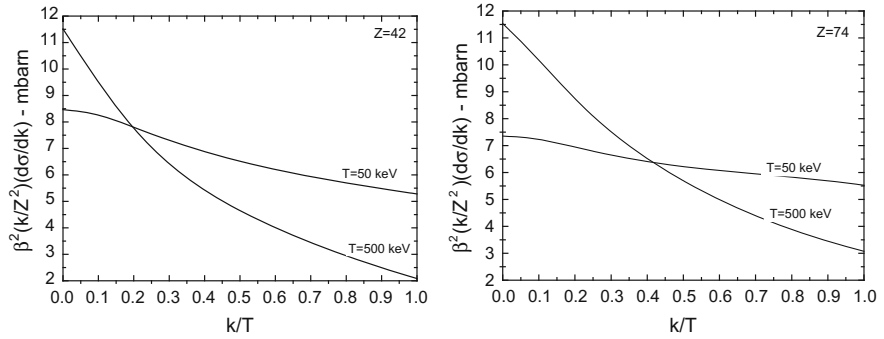

Fig. 4.14 Differential cross section in standardized energy $\beta^2(k/Z^2) \times (d\sigma_n/dk)$ for electron energies range 50–500 keV for molybdenum ($Z = 42$) and tungsten ($Z = 74$), as a function of the energy of the emitted bremsstrahlung photon; from the data of [30]

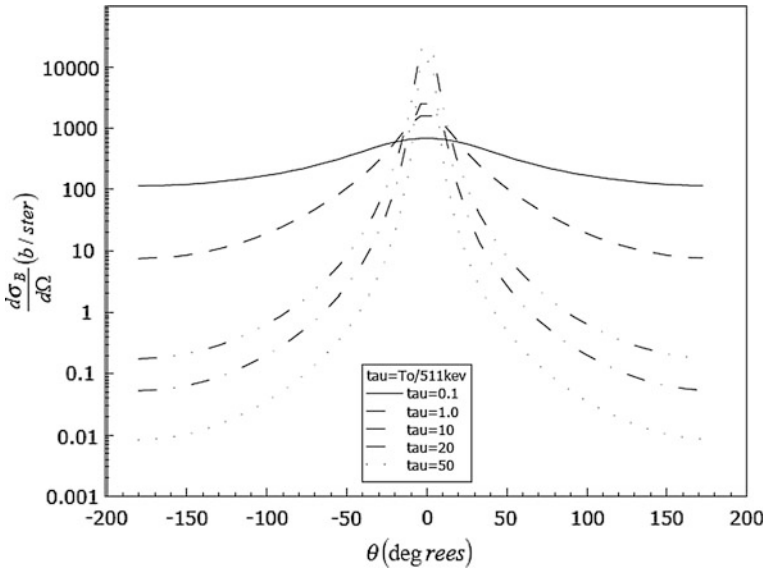

Fig. 4.15 Differential cross section dσ/dΩ for energies between 50 keV and 25 MeV as a function of the emission angle, according to [32]

$$K = \int_0^T \Phi_k k \left(\frac{\mu_{tr}(k)}{\rho}\right) dk = \int_0^T \frac{N(k)}{4\pi d^2} k \left(\frac{\mu_{tr}(k)}{\rho}\right) dk \tag{4.28}$$

Considering that for a thickness x the energy lost by the electron is dT, the ratio T_{rad}/dT gives the fraction of the electron energy converted to energy bremsstrahlung photons k. By integrating, the bremsstrahlung intensity between k and k + dk is according to the (4.29).

$$kN_k dk = \int_k^T \left[\frac{dT_{rad,k}}{dT}\right] dT \tag{4.29}$$

The mean energy released by bremsstrahlung for photons whose energy is between k and $k + dk$ crossing a thickness dx is given by the (4.30).

$$dT_{rad,k} = \left(\frac{\rho}{A}\right) k \, d\sigma \, dx \tag{4.30}$$

Combining (4.27), (4.29) and (4.30), we obtain (4.31).

$$N_k dk = \frac{1}{A}\int_k^T d\sigma \left(\frac{1}{\rho}\frac{dT}{dx}\right)^{-1} dT = \frac{\sigma_0 Z^2}{A}\frac{dk}{k}\int_k^T \frac{T + m_0c^2}{T} B(T, Z, \theta)\left(\frac{1}{\rho}\frac{dT}{dx}\right)^{-1} dT \tag{4.31}$$

The term $\frac{1}{\rho}\frac{dT}{dx}$ is the mass stopping power of electrons described in Chap. 2. Kerma is then obtained by combining (4.31) and (4.28). The terms of the parameters $\frac{\mu_{tr}(k)}{\rho}$, $B(T, Z, \theta)\frac{1}{\rho}\frac{dT}{dx}$ can be approximated by interpolation.

Tucker et al. [33] performed this calculation in order to establish a semi-empirical model for the calculation of X-ray generators kerma with a tungsten target. For this, the forms of interpolation are given in (4.32), (4.33) and (4.34).

$$\frac{\mu_{tr}(k)}{\rho} \propto a_1 + a_2 u^{1.6} + a_3 u^{2.7} + a_4 u^{3.5} + a_5 u^{4.5} \tag{4.32}$$

$$B(T, Z, \theta) \propto [A_0 + A_1 T]\left[1 + \sum_{i=1}^{4} B_i \left(\frac{E}{T}\right)^i\right] \tag{4.33}$$

$$\frac{1}{\rho}\left(\frac{dT}{dx}\right) \propto A + B\exp(-TC) \tag{4.34}$$

Also note that to assess the kerma of photons produced by low energy electrons (<500 keV), the characteristic X-rays emitted during the shuffling of the electron cloud we also be considered. At higher energies, the kerma due to these characteristic lines is negligible due to the continuous background.

Bremsstrahlung radiation yield

Bremsstrahlung radiation yield is defined as the fraction S of the initial energy of an electron converted into bremsstrahlung energy. It is given in (4.35).

$$\eta(T_0) = \frac{1}{T_0}\int_0^{T_0} \frac{S_{rad}(T)}{[S_{coll}(T) + S_{rad}(T)]} dT \tag{4.35}$$

with $S_{coll}(T)$. The stopping power by coulomb interaction defined in Sect. 4.2 and $S_{rad}(T)$. The stopping power by bremsstrahlung is defined as (4.36).

$$-\left(\frac{dE}{dx}\right)_{rad} = S_{rad}(T) = \frac{N}{A}\rho \int_0^{T_0} k\left(\frac{d\sigma}{dk}\right)dk \tag{4.36}$$

With dσ the differential cross section defined by (4.24) and (4.27). The bremsstrahlung stopping power is defined in (4.37) [26].

$$\begin{cases} S_{rad}(T) = \frac{N}{A}\rho\sigma_0 Z^2(T+mc^2)\phi_{rad,n}\left[1+\frac{1}{Z}\phi_{rad,e}/\phi_{rad,n}\right] \\ \phi_{rad,n} = \left[\sigma_0 Z^2(T+mc^2)\right]^{-1}\int_0^{T_0} k\left(\frac{d\sigma_n}{dk}\right)dk \\ \phi_{rad,e} = \left[\sigma_0(T+mc^2)\right]^{-1}\int_0^{T_0} k\left(\frac{d\sigma_e}{dk}\right)dk \end{cases} \tag{4.37}$$

Note that the report $\phi_{rad,e}/\phi_{rad,n}$ can be set to 1 [26].

We see again that the analytic resolution of bremsstrahlung yield calculation is not trivial. Nevertheless there are many tables in which the yield values are available. Examples Pagès et al. [34] or the ICRU [26]. Figures 4.16 and 4.17 provide bremsstrahlung yield values.

For example, for 500 keV electron on a tungsten target, bremsstrahlung yield energy re-emitted by photons formalism is: $E = 500 \times \eta_0 = 500 \times 5 \cdot 10^{-2} = 25$ keV.

Kerma approximation for the bremsstrahlung yield

It is possible to assess the kerma due to bremsstrahlung considering the mean energy of re-emitted photons. According to Chap. 2, we have:

$$\dot{K} = 5.76 \cdot 10^{-4}\left(\frac{\mu_{tr}}{\rho}\right)\dot{\Phi}E$$

In our case, $E = T\,\eta_0$ *and* $\dot{\Phi} = \frac{i}{1.6\cdot 10^{-19}}\frac{1}{4\pi d^2}$ with T electron energy (MeV) and i the electron current in A. This expression is valid for an isotropic photon spectrum, so for low energy electrons. The difficulty lies in the choice of the (μ_{tr}/ρ) value, since the spectral nature of the bremsstrahlung emission. As a first approximation, we can set it for the mean energy of the spectral distribution seen in Chap. 1. The calculation of the mean energy can be provide from the differential cross section defined in 4.7.1 and tabulated by Pratt [31].

For example, let's consider electrons with a current of 1 mA, energy 50 and 500 keV interacting on a tungsten target. Let's calculate the kerma rate in air at 1 m produced by bremsthralung. We have: $\eta_0(500\text{ keV}) = 3.7 \cdot 10^{-2}$ [26]; $\eta_0(50\text{ keV}) = 5.43 \cdot 10^{-3}$ [26]; $\bar{E}_\gamma(500\text{ keV}) = 184$ keV and $\mu_{tr}/\rho = 2.67 \cdot 10^{-2}$ cm^2 g^{-1} (see Chap. 2); $\bar{E}_\gamma(50\text{ keV}) = 23$ keV and $\mu_{tr}/\rho = 0.539$ cm^2 g^{-1} (see Chap. 2).

For the calculation of $\bar{E}$ we applied the weighted average:

$$\bar{E} = \frac{\sum_i \left(\beta^2 \frac{k}{Z^2}\frac{d\sigma_n}{dk}\right)_i E_i}{\sum_i \left(\beta^2 \frac{k}{Z^2}\frac{d\sigma_n}{dk}\right)_i}$$

from tables Pratt et al. of differential cross sections [31]. These cross sections are shown in Fig. 4.14. We then find:

$$\dot{K}_a(500\,\text{kV}) = 240\,\text{mGy/mn}$$
$$\dot{K}_a(50\,\text{kV}) = 70\,\text{mGy/mn}$$

If we compare these results with a numerical Monte Carlo calculation (see Sect. 4.7.2) we can observe that the result of empirical calculation is less than the reference method by a factor of 2–50 and 1.25–500 keV. This gap is due to the large variation in energy of the mass transfer coefficient (μ_{tr}/ρ) at low energy (ratio $1 \cdot 10^5$ between 1 and 50 keV). To improve results, it should be taken into account (μ_{tr}/ρ) on each energy bin. Note that this method is reliable only for isotropic emission and thus low energy.

It is observed in Fig. 4.16 the variation of bremsstrahlung yield particularly at low energy as Z. Figure 4.17 shows that bremsstrahlung yield ranges, particularly at low energy as E. So in first approximation: $\eta \propto ZT$. Recalling that $E = T \cdot \eta$, this suggests that:

$$\dot{K} = 5.76 \cdot 10^{-4}\left(\frac{\mu_{tr}}{\rho}\right)\dot{\Phi}E \Leftrightarrow \dot{K} \propto ZiT^2(\bar{\mu}_{tr}/\rho).$$

Kerma rate due to bremsstrahlung of an electron beam of kinetic energy *T* and intensity *i*, interacting with an atomic number *Z*, varies linearly with *Z*, intensity *i* and with the electron kinetic energy squared.

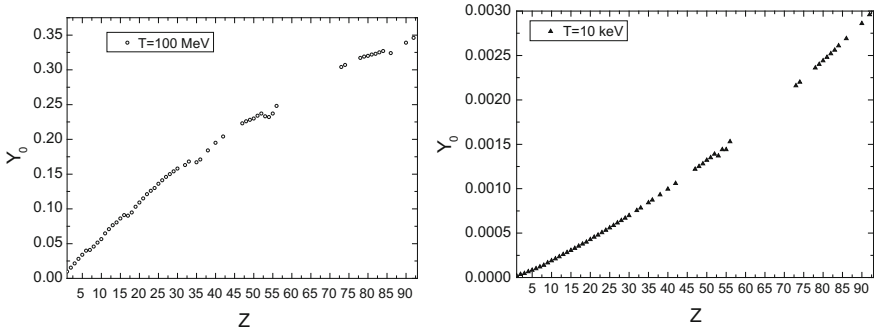

Fig. 4.16 Bremsstrahlung yield according to the atomic number Z for electrons of 100 MeV and 10 keV, from the data of [34]

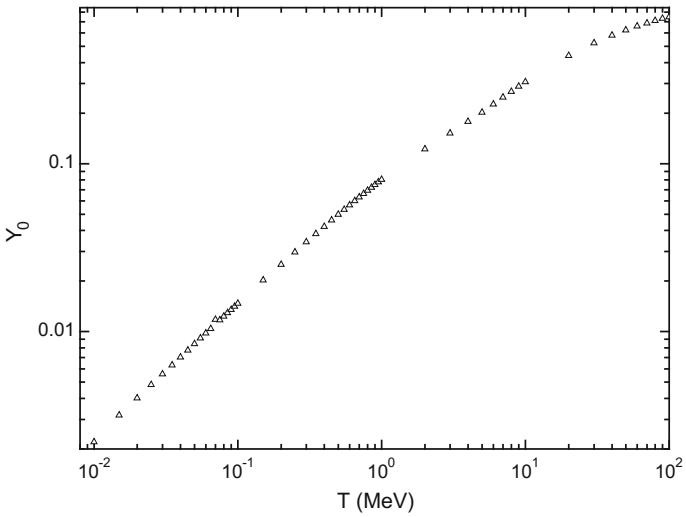

Fig. 4.17 bremsstrahlung yield depending as a function of energy for tungsten (Z = 74), from the data of [34]

There is no simple analytical calculation for assessing the kerma. Also the use of a Monte Carlo method to accurately estimate this quantity is necessary. This method was applied to perform abacus. These results are presented in the following sections.

4.7.2 X-Ray Generators

X-ray generators are used in the fields of medicine (including radiology) or industry (non-destructive testing, crystallography, fluorescence …). The production of radiation by such facilities is still the interaction of electrons produced on a high atomic number target causing the bremsstrahlung. Figure 4.18 gives a sketch of a X-ray generator. The electrons are produced on the cathode by a heated filament. In a vacuum tube, a high voltage is applied between the cathode and the anode inducing an electric field wherein the electrons are accelerated. electrons then interact with the anode producing bremsstrahlung photons. A beryllium window allows the emission of bremsstrahlung photons in a selected direction. Filtration may be added to modify the X-rays spectrum.

The spectrum of Fig. 4.19 is the result of Monte Carlo simulation for 150 keV electron interactions on a tungsten target. It is represented on the one hand energy and the other wavelength. The relationship between the energy and the wavelength is given by the (4.38) (See Chap. 2).

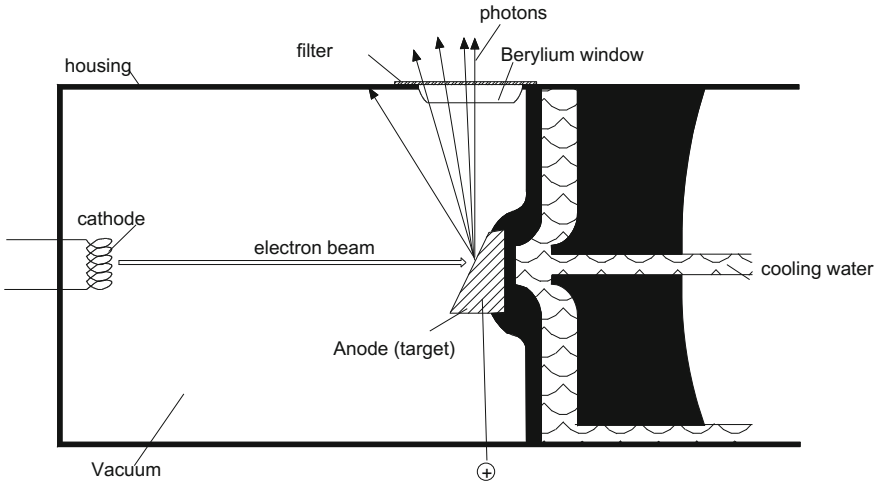

Fig. 4.18 X-ray generator pattern

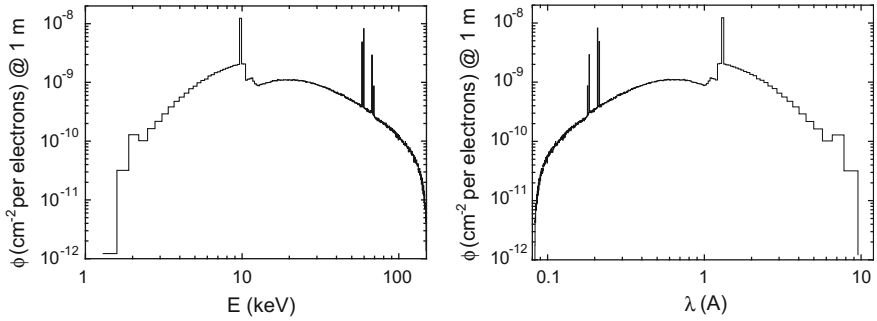

Fig. 4.19 Simulated spectrum of photons for 150 keV electrons interaction on tungsten target. The *left curve* is a representation of energy, the right wavelength (simulation using the MCNPX code)

$$\lambda(\dot{A}) = \frac{12.4}{E_\gamma(\text{keV})} (\lambda \text{ wave length}, E_\gamma \text{ photon energy}) \tag{4.38}$$

As indicated in Sect. 4.7.1, the observed spectrum is a continuous spectrum from 0 to the maximum electron energy (corresponding to the high voltage applied on the tube) on which are superimposed the tungsten characteristic X rays. The maximum value of the photon energy spectrum (thus the energy of electrons), here 150 keV, is also given in terms of "kVp" (kilovolt peak) in publications.

Output of X-ray tube filters may be disposed to cut the low energy component of the spectrum and thus "hardening" the spectrum. Figure 4.20 shows the effect of different filters on the spectrum in Fig. 4.19.

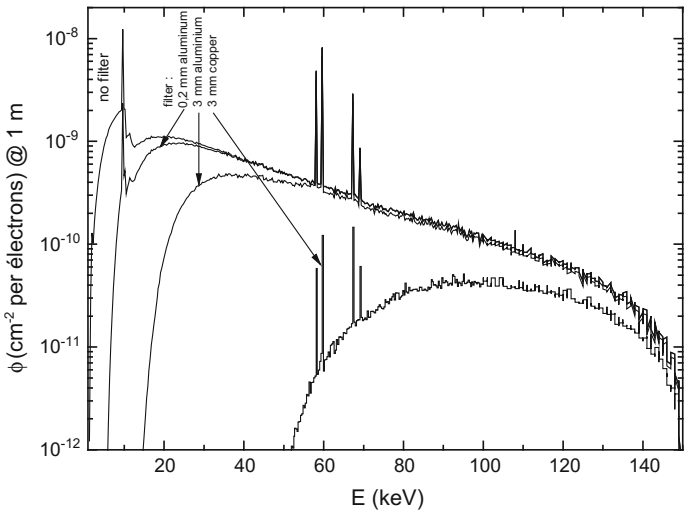

Fig. 4.20 Simulated photons spectra for the 150 keV electrons interaction on a tungsten target with different filtrations (simulation using code MCNPX)

From these spectra, it is relevant to calculate the mean energy of the spectrum depending on the type of filtration. The mean energy is calculated according to the expression 1.24 of Chap. 1. The values of these calculated mean energies are given in Table 4.17.

Note that these photons mean energies vary greatly with the type of filtration, 1/3 (without filtration) and 2/3 of the energy of the electrons (consistent filtration).

Figures 4.21 and 4.22 show respectively air kerma rate and the ambient dose equivalent rate at 1 m from a tungsten target bombarded with energy electron T_{e-} between 50 and 900 keV and for different filtrations. The calculations are performed with the Monte Carlo MCNPX code. Tabulated datas are reproduced in Appendix 2.

These kerma values are compared with the measured values of various generators X. Table 4.18 summarizes these measures. The calculated values are very close to measured values.

Table 4.17 Mean energy of bremsstrahlung spectrum for 150 keV electron interaction on tungsten for different filtrations

Filtration	$\bar{E}_\gamma$ (KeV)
Any	38
0.2 mm aluminum	47
1 mm aluminum	53
2 mm aluminum	57
3 mm aluminum	60
0.3 mm copper	70
3 mm copper	100

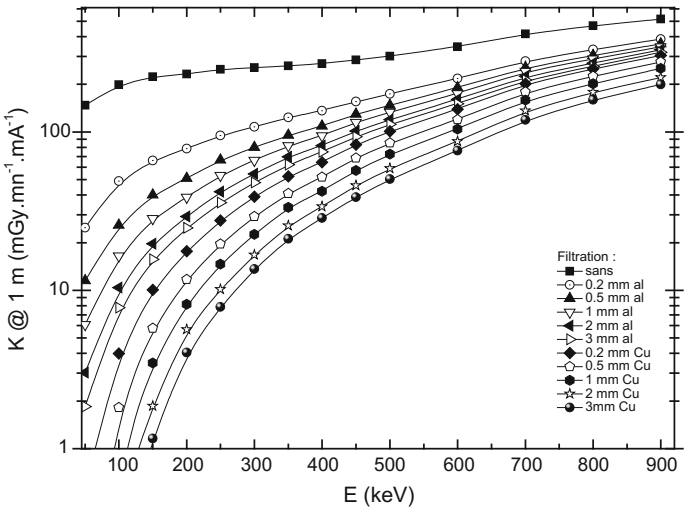

Fig. 4.21 Kerma rate in air at 1 m due to bremsstrahlung photons for a tungsten target bombarded with energy electron T_{e^-}. Values reproduced in Appendix 2

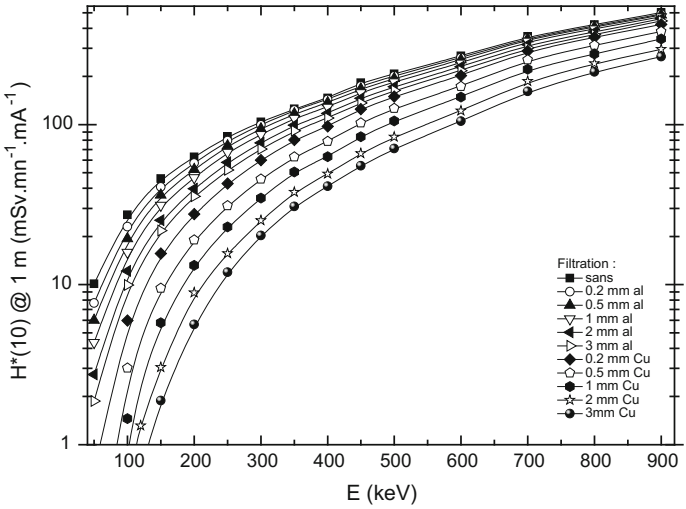

Fig. 4.22 Ambient dose equivalent rate at 1 m due to bremsstrahlung photons of a tungsten target bombarded with energy electron T_{e^-}. Values reproduced in Appendix 2

For example, calculate kerma rates in air and dose equivalent rate at 10 cm to a X-ray generator with a high voltage of 200 kV and a 10 μA intensity with a tungsten anode and a filtration of 0.2 mm aluminum thickness.

Table 4.18 Comparison between measured and calculated kerma values in the air

High voltage (kV)	Current (mA)	Filtration aluminum (mm)	Measured value at 1 m except* [35]	Calculated at 1 m except* (Fig. 4.21)
300	10	3	26 Gy/h	29 Gy/h
450	3.3	3	19.5 Gy/h	18 Gy/h
160	18.75	3	24.5 Gy/h	24.5 Gy/h
50	15	1	0.34 Gy/min*	0.36 Gy/min*

*Value 50 cm

Figures 4.21 and 4.22 respectively give for 200 keV:

$$\dot{K} = 78\,\text{mGy/min/mA at 1 m}$$

$$\dot{H}^*(10) = 57\,\text{mSv/min/mA at 1 m}$$

Either 10 μA:

$$\dot{K} = 78 \times \frac{10 \cdot 10^{-6}}{1 \cdot 10^{-3}} = 0.78\,\text{mGy/mn}$$

and

$$\dot{H}^*(10) = 57 \times \frac{10 \cdot 10^{-6}}{1 \cdot 10^{-3}} = 0.57\,\text{mSv/mn}$$

at 10 cm $\dot{K} = 0.78 \times \left(\frac{100}{10}\right)^2 = 78\,\text{mGy/mn}$ and

$$\dot{H}^*(10) = 0.57 \times \left(\frac{100}{10}\right)^2 = 57\,\text{mSv/mn}$$

4.7.3 Electron Accelerators

Some industrial applications (sterilization, non-destructive testing of thick pieces …), medical (radiotherapy) or research require higher photon energies than those produced by X-ray generators. As seen, the bremsstrahlung of electrons in the material causes continuous spectrum from 0 to the maximum electron energy. Also, to produce high-energy photons, we need high-energy electrons interacting with high atomic number targets. Note that in Europe, the standard definition of "accelerator" is: "A device that accelerates particles, emitting ionizing radiation with an energy greater than 1 MeV" [36]. Thus, photons produced may be sufficiently energetic to be responsible for yielding neutrons from photonuclear reactions. In the following, we will quantify radiation sources provided by both processes.

Ambient dose equivalent due to photons

Figure 4.23 represents the ambient dose equivalent due to bremsstrahlung photons as a function of electron energy, at angles of 0° and 90°. This quantity is calculated with the Monte Carlo MCNPX code for electron between 1 and 100 MeV interacting with a high atomic number target (case inducing the greatest number of photons and therefore equivalent to the highest dose). Hereafter, the target studied is of tungsten, cylindrical. Length and radius are equal to twice the range of the electrons therein, to ensure the total interaction of these electrons.

This figure provides directly photon dose equivalent for electrons bombarding a target of high atomic number ($Z > 73$) in the incidence axis of the electron beam (0°) and perpendicular to this axis (90°). For lower atomic number of targets, the dose equivalent given in Fig. 4.23 must be weighted by the factors in Table 4.19 [37].

As example, to calculate the ambient dose equivalent at 2 m due to photons for a 20 MeV electron accelerator and 2 mA intensity bombarding a lead target. The curve in Fig. 4.23 gives an dose equivalent rate of: $\dot{H}^*(10) = 100$ Sv h^{-1} μA^{-1} at 1 m and 0° and $\dot{H}^*(10) = 1.4$ Sv h^{-1} μA^{-1} at 1 m and 90°.

Either 2 mA: $\dot{H}^*(10) = 100 \times 2000 = 2 \cdot 10^5$ Sv h^{-1} at 1 m and 0° and $\dot{H}^*(10) = 1.4 \times 2000 = 1.4 \cdot 10^3$ Sv h^{-1} at 1 m and 90°.

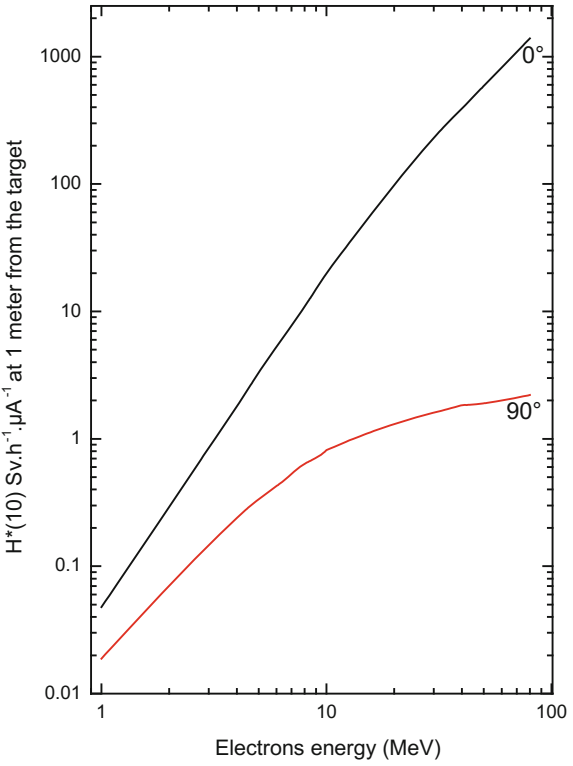

Fig. 4.23 ambient dose equivalent rate due to bremsstrahlung photons at 0° and 90° produced by monoenergetic electrons bombarding a high Z target (calculated using the code MCNPX)

Table 4.19 Weighting factors of the curve in Fig. 4.23 for the low atomic number targets [37]

Target	Z	Weighting factor to 0°	Weighting factor to 90°
Iron or copper	26 or 29	0.7	0.5
Aluminium (concrete)	13	0.5	0.3

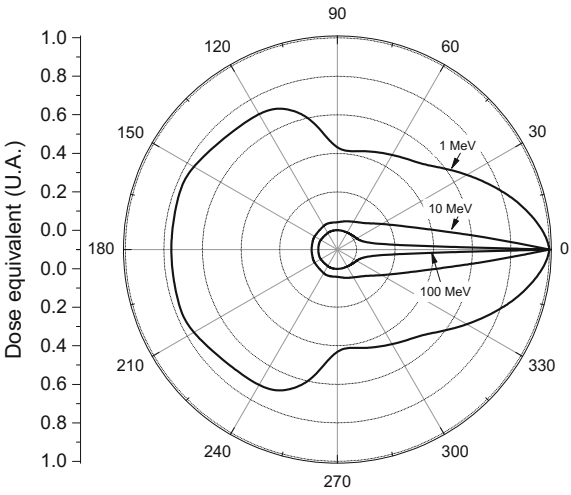

Fig. 4.24 Angular distribution of the dose equivalent of photons produced by electrons of 1, 10 and 100 MeV (the dose equivalents were normalized to 1 in the 0° direction) (calculated using the code MCNPX)

So to 2 m:

$$\dot{H}^*(10) = 2 \cdot 10^5 \times \left(\frac{1}{2}\right)^2 = 5 \cdot 10^4 \,\mathrm{Sv\,h^{-1}\,to\,0°}$$

and $$\dot{H}^*(10) = 2.8 \cdot 10^3 \times \left(\frac{1}{2}\right)^2 = 7 \cdot 10^2 \,\mathrm{Sv\,h^{-1}\,to\,90°}$$

As we have mentioned (Sect. 4.7.1), at high-energy, photon emission is highly anisotropic. Figure 4.24 shows the distribution of the angular dose for photons produced by 1, 10 and 100 MeV electrons. In order to compare them in this representation, the dose equivalents are normalized to 1 in the incident direction.

Note the strong anisotropy at high energy attenuated at low electron energies. The typical shape around 90° is due to the photons selfshielding in the target which does not exist for angles greater than 90°. Figure 4.25 represents the ambient dose equivalent as a function of the observation angle and for various electron energies.

4.7.4 Dose Equivalent Due to Photoneutrons

Overview on photonuclear reactions

A photon with high energy—beyond the binding energy of a nucleon in the nucleus—can interact with nuclei to cause inelastic reactions such as photonuclear wherein secondary heavy particles may occur. Table 4.20 illustrates photonuclear possible reactions and associated thresholds to the isotope ^{186}W tungsten. The datas

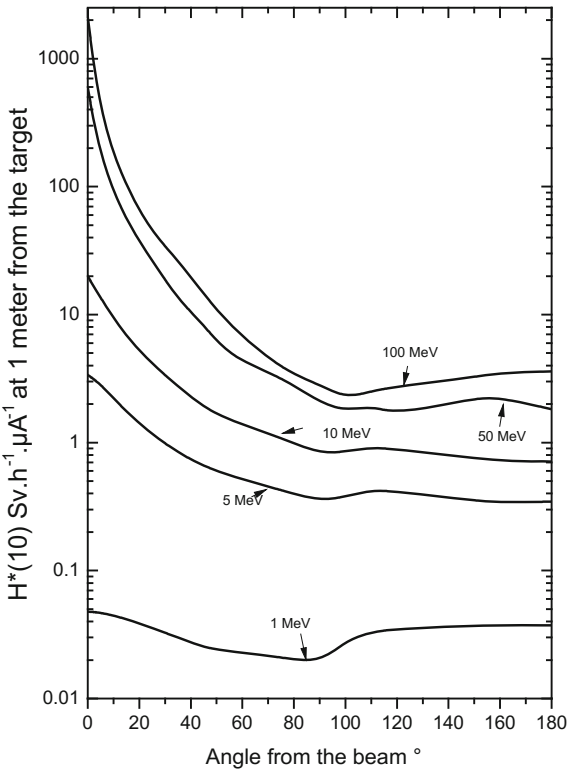

Fig. 4.25 Ambient dose equivalent rate due to bremsstrahlung photons as a function of the angle from incident beam (calculated with MCNPX code)

Table 4.20 Reactions and thresholds for photonuclear reactions on the ^{186}W from [38]

Abundance	Production thresholds (MeV)								
(%)	γ, n	γ, p	γ, t	γ, ^{3}He	γ, α	γ, 2n	γ, np	γ, 2p	γ, 3n
28.60	7.19	8.40	12.17	14.16	1.12	12.95	15.03	15.59	20.36

are from the Handbook of the IAEA [38] listing a large number of data on the photonuclear reactions such as the energy thresholds and reactions cross section for several materials.

The neutron production threshold for this isotope is 7.19 MeV. **Current devices may emit secondary neutron radiation via high energy photons like accelerators encountered in medical and industrial fields**.

The "neutron risk" then becomes significant for energy electrons beyond the photonuclear reactions production threshold, around 6 MeV for medium and low atomic numbers. Note the specific case of beryllium which presents the lowest reaction threshold with a 1.67 MeV.

The difference between the thresholds of (γ, n) and (γ, p) reactions is due to the Coulomb barrier during the emission of the proton. The (γ, 3n) reaction needs about

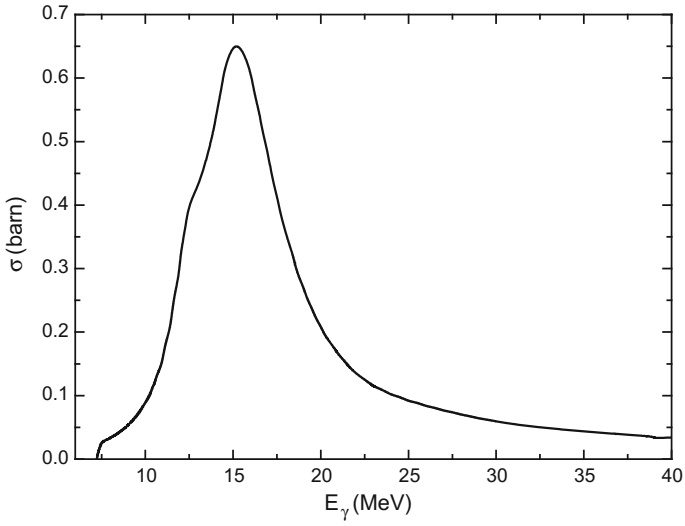

Fig. 4.26 Photonuclear cross section (γ, Xn) on the ^{186}W, according to data of the site http://www-nds.iaea.org/Exfor/endf.html

three times the energy of a reaction threshold (γ, n) to occur, which is intuitive. In these reactions, it must be added the fission induced by photons or "photo-fission". This occurs at about 5 MeV on fissile nuclei and particularly on ^{238}U nuclei. The photofission yield is the same type of that fission induced by fast neutrons on ^{238}U.

Figure 4.26 shows the (γ, Xn) cross sections on the ^{186}W. It is observed in this figure that a resonance peak can be determined for the photonuclear (γ, n) reaction for heavy nuclei ($A \geq 40$) using the semi-empirical relation (4.39) [6].

$$E_\gamma^* = 80 \times (A)^{-1/3} \tag{4.39}$$

Thus, for the ^{186}W this energy is obtained for $E_\gamma^* = 14\,\text{MeV}$, which is in agreement with Fig. 4.26.

We admitted that photonuclear reaction energy threshold appears generally between 6 and 7 MeV; there are nevertheless very light nuclei for which this is not the case and for which thresholds are low; Table 4.21 lists some of them.

Note that besides issues encountered in photoneutrons accelerators for facilities whose energies involved are smaller, the photoneutron reactions may occur when this light material is present. For example, in reactors, the photoneutron production rates are significant in heavy water and beryllium moderators. Remind that deuterium is present at 0.015% in the natural hydrogen, this small percentage becomes significant in concrete shielding. Moreover, as we have admitted, the radiative captures produce high energy photons—from 7 to 11 MeV—and are likely to generate photonuclear reactions, especially in concretes.

In the following, the approach for the estimation of these photoneutron yields and associated dose equivalent rates is described.

Table 4.21 Photonuclear threshold for light nuclei [6], With permission from the American Nuclear Society, La Grange Park, Illinois

Nuclide	Threshold E_t (MeV) (value—Q)	Reaction
^{2}H	2.225	^{2}H (γ, n)^{1}H
^{6}Li	3.698	^{6}Li (γ, n + p)^{4}He
^{6}Li	5.664	^{6}Li (γ, n)^{5}Li
^{7}Li	7.251	^{7}Li (γ, n)^{6}Li
^{9}Be	1.65	^{9}Be (γ, n)^{8}Be
^{13}C	4.946	^{13}C (γ, n)^{12}C

The yield, Y, depending on the energy distribution of the photon fluence rate $\dot{\Phi}_{E,\gamma}$ is described by the (4.40).

$$Y = \int_{E_{Th}}^{E\gamma_{Max}} N\,\sigma_{E(\gamma,n)}\dot{\Phi}_{E,\gamma}dE \tag{4.40}$$

with E_{gmax} the maximum energy of photons; E_{Th} threshold energy; N the atomic density (cm^{-3}); σ(γ, n) cross section of the (γ, n) reaction (cm^{2}); $\dot{\Phi}_{E,\gamma}$ the energy distribution of the fluence of photons (cm^{-2} s^{-1}).

When the incident photon energy is much less than the mass energy of a nucleon (≈931 MeV), the emitted neutrons energy, as a function of its emission angle θ is expressed with the conservation of momentum and energy, with (4.41) from Wattenberg [39].

$$E_n = \frac{A-1}{A}\left[E_\gamma - E_S - \frac{E_\gamma^2}{1862(A-1)}\right] + E_\gamma\left[\frac{2(A-1)(E_\gamma - E_{Th})}{931A^3}\right]^{1/2}\cos\theta \tag{4.41}$$

With A the atomic mass of the target nucleus. Note that the angle θ varies from 0 to π and the second term, regardless θ, does not vary the result of a few percent. In most shielding design, it is conservative to consider that photoneutrons are emitted isotropically with an energy equal to about $E_\gamma - E_{Th}$ and in the case of deuterium, ½($E_\gamma - E_{Th}$).

The curves in Fig. 4.27 provide the yield of neutrons produced on thick targets of various conversion target materials based on the incident electrons energy [40].

Let's determine for example the neutron yield of an electron accelerator delivering 40 MeV energy electrons, bombarding a tungsten target with a 5 mA current. Let's calculate in advance the power of such a device. The electron flux to such intensity is:

$$\dot{N} = \frac{5 \cdot 10^{-3}}{1.6 \cdot 10^{-19}} = 3.12 \cdot 10^{16}\,(\text{electrons})\,\text{s}^{-1}$$

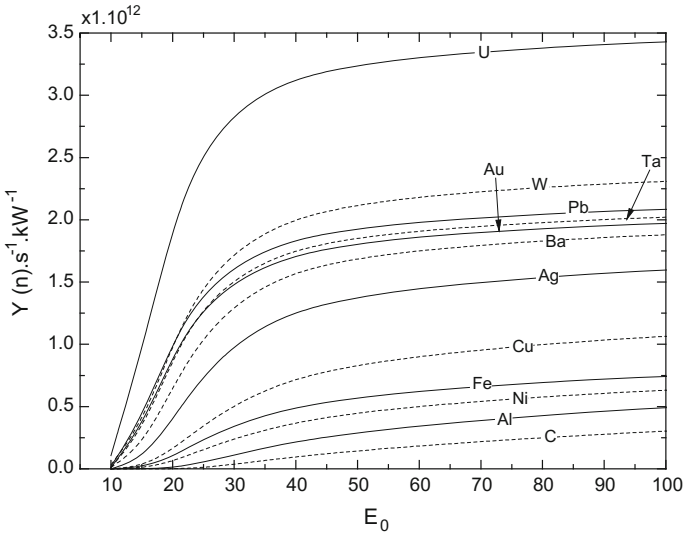

Fig. 4.27 Neutron yield (n) s^{-1} kW^{-1} products by thick targets of various materials as a function of the incident electron energy in MeV (according to the data [40])

With this flux and for 40 MeV electrons, the power is $P = 3.12 \cdot 10^{16}$ [s^{-1}] × $40 \cdot 10^6$ [eV] × $1.6 \cdot 10^{-19}$ [J/eV] = 200,000 [J/s] = 200 kW.

Figure 4.27 indicates for an 40 MeV energy, a yield of about $2 \cdot 10^{12}$ (n) s^{-1} kW^{-1} for tungsten target. Therefore, for a current of 5 mA, we have the following yield:

$$Y = 200 \times 2 \cdot 10^{12} = 4 \cdot 10^{14}\,(\text{neutron})\,\text{s}^{-1}$$

Note: take care to weight results of this abacus by the factor 10^{12} indicated on the curves in Fig. 4.27.

Calculations of dose equivalent due to Photoneutrons

The complexity of the physical parameters to be considered to model yield, and thus the ambient dose equivalent rate around electron accelerators, requires the use of a transport code type Monte Carlo. However, the rest of this section will focus on providing abacus or semi-empirical methods for assessing ambient dose equivalent due to the photoneutrons.

To estimate the dose equivalent due to the photoneutrons around the electron accelerators, we have done calculation using the Monte Carlo code MCNPX. For this calculation, a cylindrical target length and radius equal to five times the electron range in the material was modeled. The set of curves shown in Fig. 4.28 indicates, depending on the energy of incident electrons, the dose equivalent per incident electrons at 1 m of the target.

For example, let's calculate the ambient dose equivalent rate at 2 m due to photoneutrons, around an electron energy of 20 MeV accelerator and 2 mA intensity bombarding a lead target. The curve in Fig. 4.28 gives a dose equivalent to $9 \cdot 10^{-18}$ Sv per electron. The flux of electrons at 2 mA intensity is:

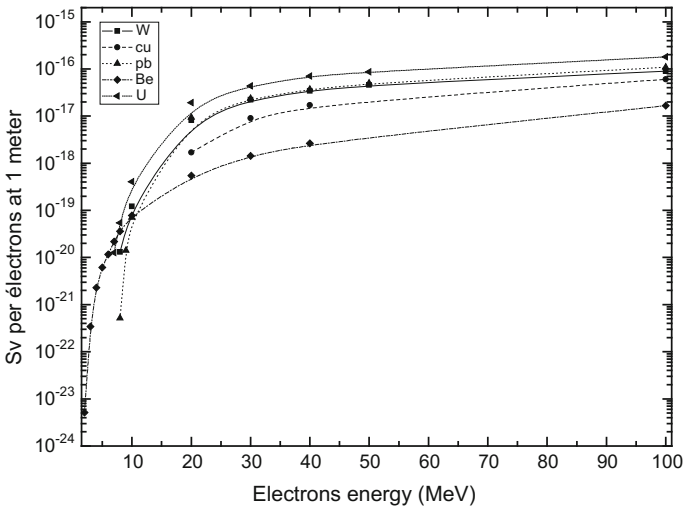

Fig. 4.28 Neutron ambient dose equivalent at 1 m for various thick targets bombarded by electrons depending on the incident electron energy in MeV (calculated using the code MCNPX)

$$\dot{N} = \frac{2 \cdot 10^{-3}}{1.6 \cdot 10^{-19}} = 1.25 \cdot 10^{16}\,(\text{electrons})/\text{s}$$

The ambient dose equivalent rate at 1 m is therefore:

$$\dot{H}^*(10) = 9 \cdot 10^{-18} \times 1.25 \times 10^{16} \times 3600 = \text{Sv/h}$$

to 2 m:

$$\dot{H}^*(10) = 40.5 \times \left(\frac{1}{2}\right)^2 = 10\,\text{Sv/h}$$

Let's compare this neutrons and the previous bremsthralung photons dose equivalent. The example in Sect. 4.7.3 gives similar conditions for an equivalent dose rate of photons 50,000 Sv h^{-1} to 0° and 700 Sv h^{-1} to 90°. We note that the photon component is largely predominant compared to the neutrons dose equivalent.

Figure 4.28 gives the best result. However, it does not offer all types of possible targets. Thus, this section presents an empirical approach to assess the neutron dose equivalent rate around electron accelerators for any target. The neutron dose equivalent rate for this type of reaction can be calculated from the formalism (4.42).

$$\dot{H}^*(10) = \bar{h}^*_{\Phi}(10) \cdot \frac{Y_n}{4\pi d^2} \tag{4.42}$$

Figure 4.27 gives the neutron yield, *Y,* for different electron energies of some targets. The issue is to define the conversion factor "fluence ambient dose equivalent": both photon and neutron spectra are wide. One approach is to consider, as a

first approximation, the photon with monokinetic energy equal to the energy of the photoneutrons resonance peak, given by (4.39). The energy of the emitted neutrons is then calculated for the incident photons energy by (4.41).

The next step is to get the appropriate conversion factor "fluence-ambient dose equivalent" $h^*_\Phi(10)$ proposed in Chap. 3. The difficulty lies in the determination of this factor. Indeed, the calculation of the neutron energy using the formula (4.41) is subject to the prior knowledge of the value of the neutron energy production threshold (these data are available, however, for example in the Handbook IAEA [38]). However, if we study the neutron energy to the photonuclear reactions resonance peaks and factors $h^*_\Phi(10)$, we note that the latter coefficient fluctuates slightly around the mean value of 413 pSv cm^2 for atomic masses between 50 and 210.

Thus the (4.42) can be written:

$$\dot{H}^*(10) = h^*(E) \cdot \frac{Y}{4\pi\, d^2} = 413.10^{-12} \frac{Y}{4\pi d^2} \times 3600$$

$$\dot{H}^*(10) = 1.2 \cdot 10^{-7} \frac{Y}{d^2} \tag{4.43}$$

with $\dot{H}^*(10)$ ambient dose equivalent rate in Sv h^{-1} for 1 kW beam; Y the neutron yield (n) s^{-1}; d target distance observer (cm).

In addition, beyond 30 MeV for thick targets (not fissile) $Z \geq 56$, it is observed that the yield Y is relatively constant and equal to $2 \cdot 10^{12}$ (n) s^{-1} kW^{-1}. Thus, the (4.43) can be simplified for electrons of over 30 MeV bombarding a target with $Z \geq 56$ (non-fissile targets). The dose equivalent rate is given in (4.44).

$$\dot{H}^*(10) = \frac{2.4 \cdot 10^5}{d^2} \tag{4.44}$$

with $\dot{H}^*(10)$ ambient dose equivalent rate in Sv h^{-1} for 1 kW beam and d target distance observer (cm).

Let us take the example of an energy electron accelerator with 30 MeV energy and 10 μA intensity on a tungsten target. It is proposed to calculate the photoneutrons ambient dose equivalent rate at 1 m of this target by the various methods. Then by the reference method (Fig. 4.29) an equivalent dose rate of 5 Sv/h is found. But this method can only be used for a target mentioned in Fig. 4.29. The equation method (4.42) provides meanwhile a dose equivalent rate of 6.3 Sv/h, a difference of 25% compared to the reference method. The (4.43) provides a dose equivalent rate of 6.5 Sv/h, a difference of 30% compared to the reference. Finally, the (4.44) provides a dose equivalent rate of 7.2 Sv/h, a difference of 44% compared to the reference, which is acceptable considering it does not request input data in advance: yield, conversion factors, spectra, etc.

Particular case of medical accelerators for radiotherapy

Medical accelerators for radiotherapy have sufficiently high photon energies to produce secondary neutrons by photonuclear reactions in significant amount. Thus,

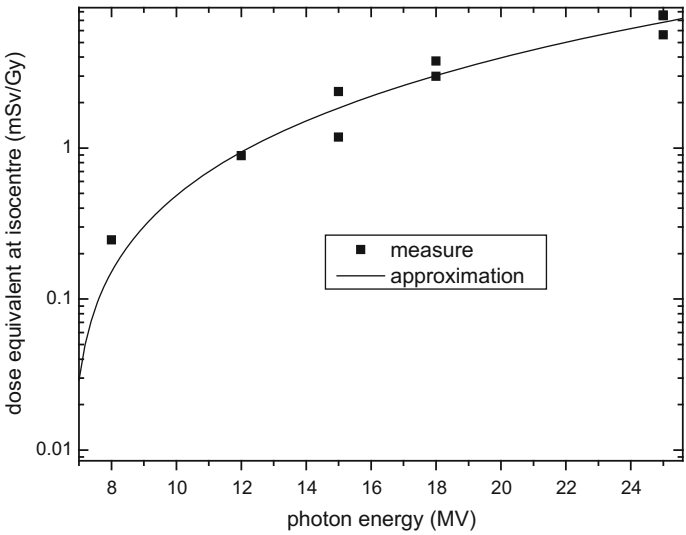

Fig. 4.29 Dose equivalent due to secondary neutrons to 1 Gy photon at the isocenter of a medical accelerator, according to the data of [41]

during treatment, it is necessary to estimate the neutron dose equivalent which exposes the patient. This one is proportional to the photon dose to the isocenter of the accelerator. Bourgois et al. [41] performed and compiled a number of measures for different medical accelerators. Figure 4.29 represents the compilation of these measurements giving the neutron dose equivalent to a dose of 1 gray photon at the isocenter and for different photon energies.

The neutron dose equivalent (H_n) at the isocenter to a gray-photon can be approximated by the relationship (4.45) (See Fig. 4.29) with E_g, the photon energy in MeV (from [41]).

$$\frac{H_n(mSv)}{D_\gamma(Gy)} = 0.015\left(E_\gamma\right)^2 - 0.103E_\gamma + 0.015 \tag{4.45}$$

For example, for a radiotherapy dose of 3 Gy (at the isocentre) for a 20 MeV medical accelerator, the dose equivalent due to the neutrons is approximately 12 mSv.

4.8 Neutrons Produced by Ion Accelerators

The ion interaction with a target may lead to neutron emission via various nuclear reactions. Note that these secondary neutron radiation is the main risk when the accelerator works. To assess the dose equivalent due to the neutrons from this process, it is necessary to know in advance the yield thereof, and its energy distribution.

4.8.1 Neutron Yield by Light Ions

The neutron yield caused by alpha, protons and deuterons bombarding various thick targets are given in Figs. 4.30, 4.31 and 4.32.

Let us calculate the neutron fluence rate to 2 m of a carbon target produced by 10 MeV alphas, protons or deuterons and 10 μAe intensity.

For alpha. In Fig. 4.30, a yield of $2 \cdot 10^{-5}$ (n) alpha^{-1} is obtained, which corresponds for a 10 μAe intensity to the following flux:

$$\dot{N}_\alpha = \frac{10 \cdot 10^{-6}}{1.6 \cdot 10^{-19}} = 6.25 \cdot 10^{13}\ (\alpha)\,\mathrm{s}^{-1}$$

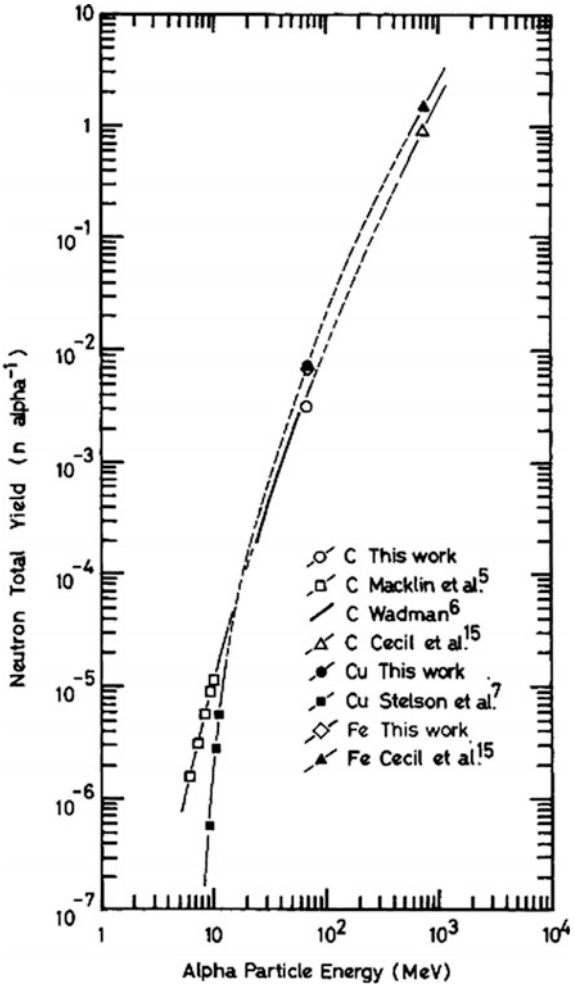

Fig. 4.30 Neutron production yield caused by alpha on various thick targets, according to [42], with permission from the American Physical Society

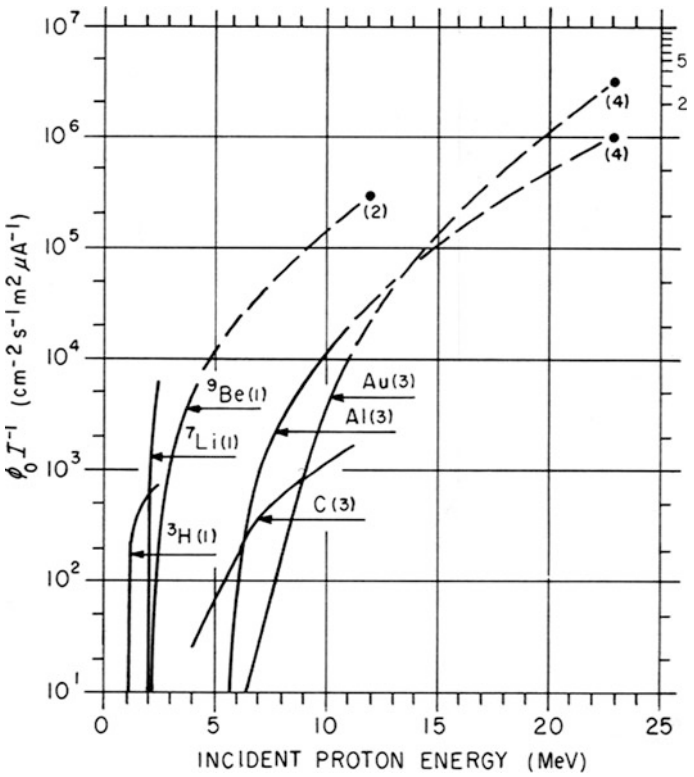

Fig. 4.31 Neutron fluence to 1 m produced by protons of various thick targets, according to [37] with permission from the National Council on Radiation Protection and Measurements, http://NCRPpublications.org

Is a neutron flux of:

$$\dot{N}_n = 6.25 \cdot 10^{13} \times 2.10^{-5} = 1.25 \cdot 10^9 \ (n)\,\mathrm{s}^{-1}$$

And finally a neutron fluence rate:

$$\dot{\Phi} = \frac{1.25 \cdot 10^9}{4 \times \pi \times 200^2} = 2.5 \cdot 10^3 (n)\,\mathrm{s}^{-1}\,\mathrm{cm}^{-2}$$

If protons. In Fig. 4.31, the a fluence rate of $1 \cdot 10^3$ cm^{-2} s^{-1} μA^{-1} to 1 m or a fluence rate to 2 m for 10 μAe is:

$$\dot{\Phi} = 1 \cdot 10^3 \times \frac{10}{4} = 2.5 \cdot 10^3\,\mathrm{s}^{-1}\,\mathrm{cm}^{-2}$$

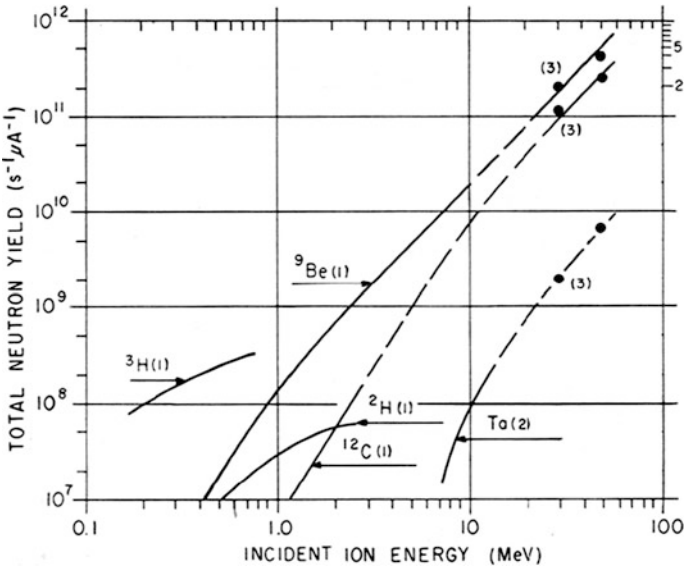

Fig. 4.32 Neutron yield produced by deuterons on various thick targets (according to [37], with the permission of The National Council on Radiation Protection and Measurements, http://NCRPpublications.org)

If deuterons. The yield read on the Fig. 4.32 is $8 \cdot 10^9$ n s^{-1} μA^{-1}, giving a fluence rate to 2 meters for 10 μAe:

$$\dot{\Phi} = \frac{8.10^9 \times 10}{4 \times \pi \times 200^2} = 1.6 \cdot 10^5 s^{-1}\,cm^{-2}$$

Note that the reactions induced by deuterons produce significant neutron fluence, even at low energy. This is due to the low binding energy of two nucleons of the deuteron and its singular character of quasi dual projectile.

4.8.2 Special Case of Deuteron Accelerators: Deuteration Effect

Deuteron accelerators, at low energy, are widely used because of their propensity to generate secondary neutrons. There is a physical phenomenon inherent to deuterons as projectiles: "the Deuteration". This principle can be illustrated by measuring the neutron equivalent dose rate around a copper thick target bombarded with deuterons of 2 MeV at a current of 5 μA, demonstrating increased flux until the stabilization around an asymptote as shown by Bourgois et al. [43] (Fig. 4.33). At this stage, the dose equivalent rate measured is above what expected due to low neutrons

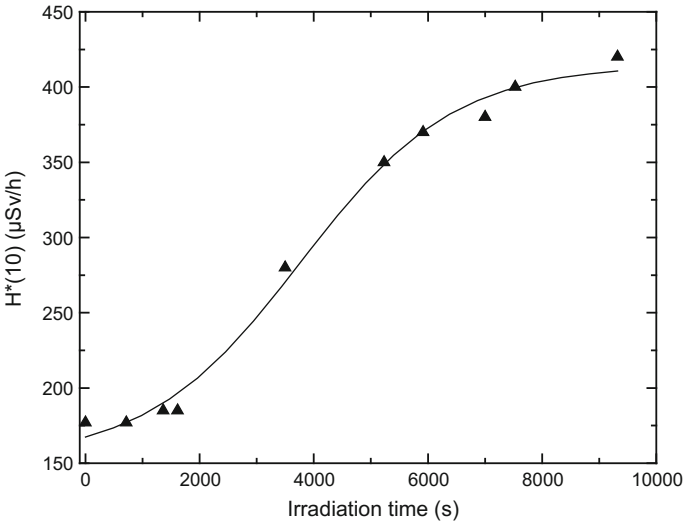

Fig. 4.33 Neutrons dose equivalent rate around a deuteron accelerator, at 2 MeV energy and 5 μA intensity bombarding a copper target, highlighting the deuteration process of a target [43]

production cross sections of deuterons of such energy on a target copper. The explanation is as follows: while accelerator works, deuterons tend to implant themself in the target by adsorption and pill-up to form a layer becoming deuterium target. Then significant fusion reactions ${}^{2}_{1}H(d,n){}^{3}_{2}He$ occur for those energies.

This becomes even more problematic for energies below any neutron production reaction threshold. For example, 40 keV deuterons interacting on a copper target is below any threshold neutron reactions. But the deuteration leads to fusion reactions with a cross section of about 3 mbarn. Comte et al. [45] have demonstrated this phenomenon in an experiment consisting in bombarding a copper target with deuterons. Figure 4.34 shows the rapid increase in the neutron dose equivalent rate from these reactions to quickly reach an asymptote.

Thus, for this configuration, it is important not to omit this physical specificity that may lead to significant dose equivalent due to neutrons.

4.8.3 Neutron Spectra Caused by Light Ions

To assess the dose equivalent due to neutrons produced by ion interactions on a target, in addition to the flux, it is also necessary to determine the neutron energy. This one is given by (4.8).

For example, let us consider the bombing of a target ${}^{7}_{3}Li$ by energy protons T_p = 10 MeV. A probable reaction is: ${}^{7}_{3}Li(p,n){}^{7}_{4}Be$. The Q-value of this reaction is −1.644 MeV [4] (Table 4.22).

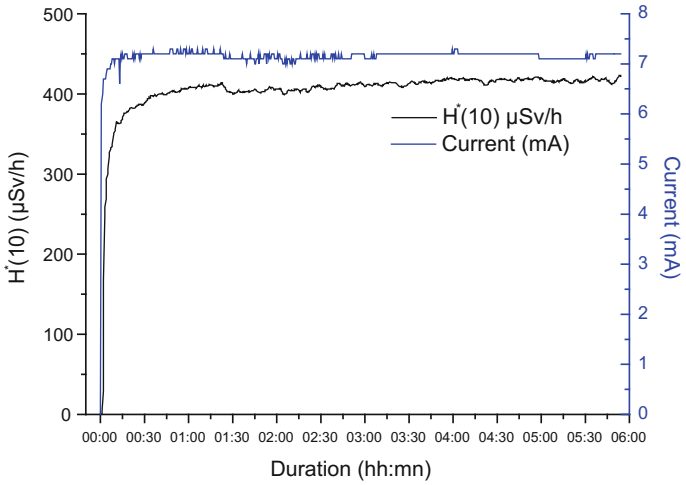

Fig. 4.34 Dose equivalent neutron around a deuteron accelerator 40 keV bombarding a copper target as a function of operating current [45]

Table 4.22 Atomic mass data for reaction $^{7}_{3}\mathrm{Li(p,n)}^{7}_{4}\mathrm{Be}$

Particle/ion	Atomic mass (amu) [3]
$^{7}_{3}$Li (X)	7.016004
p (a)	1.007825
n (b)	1.008664
$^{7}_{4}$Be (Y)	7.016929

The *Q-value* reaction being negative, it shall be ensured that the energy of the incident proton is at least equal to that of the reaction threshold given by (4.10).

$$E_S = -Q \times \frac{M_a + M_X}{M_X} = 1.644 \times \frac{1.007825 + 7.016}{7.016} = 1.9\,\mathrm{MeV}$$

For protons of 10 MeV, the reaction is possible. Let us consider neutrons at 0°. We have according to (4.8):

$$u = \frac{\sqrt{1.007 \times 1.009 \times 10}}{1.009 + 7.055} = 0.4\,\mathrm{MeV}^{1/2}$$

$$w = \frac{7.055 \times (-1.646) + 10 \times (7.055 - 1.007)}{1.009 + 7.055} = 6\,\mathrm{MeV}$$

$$\sqrt{T_n} = u + \sqrt{u^2 + w} = 2.9\,\mathrm{MeV}^{1/2} \quad \text{and } T_n = 8.34\,\mathrm{MeV}$$

Table 4.23 gives neutron energies emitted in forward direction produced by different energies ions on different targets.

Table 4.23 Energy neutrons yield at 0° with ions

Target	^{12}C	^{3}H	^{7}Li	^{2}H	^{9}Be	^{3}H
Accelerated ions	d	p	p	d	α	d
Ion energy (MeV)	MeV energy neutrons generated at 0°					
<1	–	–	–	2.45	5.27	14,05
1	0.69	–	–	4.14	6.68	16.75
2	1.68	1.2	0.23	5.24	7.71	18.26
5	4.64	4.22	3.33	8.24	10.6	21.98
10	9.57	9.23	8.35	13.02	15.23	27.42

For higher energies and higher Z targets, neutron yield ways can be plural and in particular for deuterons: stripping, pick-up, decay in the Coulomb field of the target nucleus, spallation, evaporation … again, the quantitative aspect of the neutron emission is assessed by the mean of appropriate computer codes.

4.8.4 *Neutron Dose Equivalent Caused by Light Ion and Low Energy Accelerators*

The calculation of neutron ambient dose equivalent around the ion accelerators is trivially obtained using the classic formula of Chap. 3.

$$\dot{H}^{*}_{d1}(10) \ = h^{*}_{\Phi}(10) \cdot \dot{\Phi} = h^{*}_{\Phi}(10) \frac{Y}{4\ \pi\ d_1^2}$$

The yield, Y, can be determined from Sect. 4.8 and the conversion factor "fluence-ambient dose equivalent" $h^{*}_{\Phi}(10)$ knowing the neutron energy according to Sect. 4.8.3.

Let us calculate the dose equivalent rate at 2 m of a carbon target bombarded by deuterons of energy 10 MeV and intensity 10 μAe. The energy of the neutron emitted in this reaction is 9.6 MeV (Table 4.23), implying a conversion factor "fluence-ambient dose equivalent" $h^{*}_{\Phi}(10)$ = 430 pSv cm^2. The neutron yield per unit current is obtained by Fig. 4.32. We deduce the neutron fluence rate as:

$$\dot{\Phi} = \frac{8\ \cdot\ 10^9 \times 10}{4 \times \pi \times 200^2} = 1.6 \cdot 10^5 \mathrm{s}^{-1}\,\mathrm{cm}^{-2}$$

Therefore, the ambient dose equivalent rate at 2 m due to neutrons generated by the reaction is:

$$\dot{H}^{*}(10) = 1.6 \cdot 10^5 \times 430 \cdot 10^{-12} = 7 \cdot 10^{-5}\,\mathrm{Sv\,s}^{-1}\ \left(0.25\,\mathrm{Sv\,h}^{-1}\right)$$

4.8.5 Neutron Dose Equivalent Around Accelerators of High Energy Protons

For high energy protons, the approach described above is no longer valid. Indeed, at this energy, the flux at generated neutrons and the mean conversion factor "fluence-ambient dose equivalent" is more difficult to assess. Sullivan [46] provides an analytical expression for calculating the neutron dose equivalent rates due to the interaction of high energy protons on a thick target. The result is obtained by (4.46). This formulation is reliable between 10 and 1000 MeV and has been validated by experimental data for energies between 50 and 800 MeV.

$$H^*(10) = \frac{2 \cdot 10^{-10}\left[1 - \exp\left(-5.7 \cdot 10^{-5}\left(T_p\right)^{1.6}\right)\right]}{\left(\theta + 1265/\sqrt{T_p}\right)^2} \tag{4.46}$$

With $H^*(10)$ the dose equivalent to a distance d (in meters) of the thick target (in Sv per proton); T_p Proton energy (MeV); θ the angle between the incident proton beam and the observer (in degrees).

The curve in Fig. 4.35 indicates this equivalent dose for a proton to one meter of the target for different viewing angles.

For example, consider a therapy proton accelerator (e.g. Etoile). The typical energy is 250 MeV for $1 \cdot 10^{10}$ (p) s^{-1} intensity. To this energy and to an observer located at 90°, the (4.46) gives:

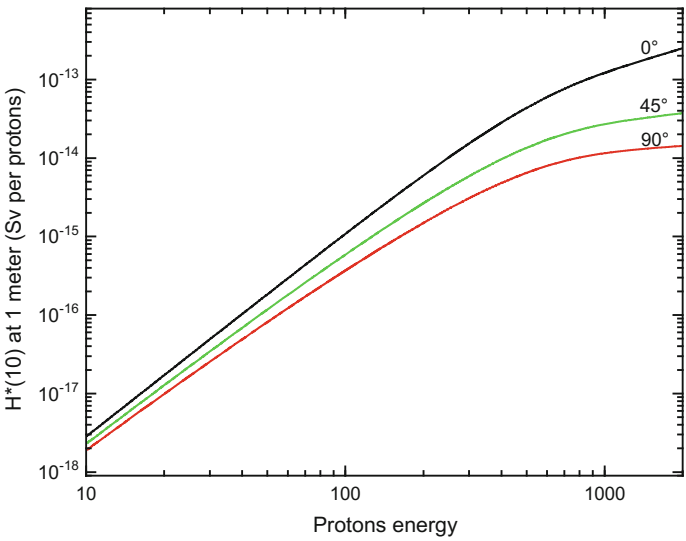

Fig. 4.35 Neutron dose equivalent caused by a proton beam on a thick target

$$H^*(10) = \frac{2 \cdot 10^{-10} \times \left[1 - \exp\left(-5.7 \cdot 10^{-5} \times E^{1.6}\right)\right]}{\left(\theta + 1265/\sqrt{E}\right)^2}$$
$$= \frac{2 \cdot 10^{-10} \times \left[1 - \exp\left(-5.7 \cdot 10^{-5} \times 250^{1.6}\right)\right]}{\left(90 + 1265/\sqrt{250}\right)^2} = 2.25 \cdot 10^{-15}\text{Sv/(protons)}$$

For this case, the neutron dose equivalent rate is $\dot{H}^*(10) = 2.25 \cdot 10^{-15} \times 1 \cdot 10^{10} \times 3600 = 80\,\text{mSv}\,\text{h}^{-1}$ at 90° and 1 m of the target.

4.9 Source Term Associated with Induced Radioactivity

From the standpoint of radiation protection, having interested in instant risk link to bombarded target, the residual activity after stopping the beam, or activity in spent fuel cooling step must be taken into account.

4.9.1 Radionuclides Produced by Induced Radioactivity

In the induced radioactivity process, the activation, is described in Fig. 4.36. A table with radionuclides isotopes and isobars lines diagonally is displayed. It describes it, from a table of isotopes, the residual nucleus is obtained from a given nuclear reaction. For example, a stable nucleus ${}^{A}_{Z}X$ collided with protons during a

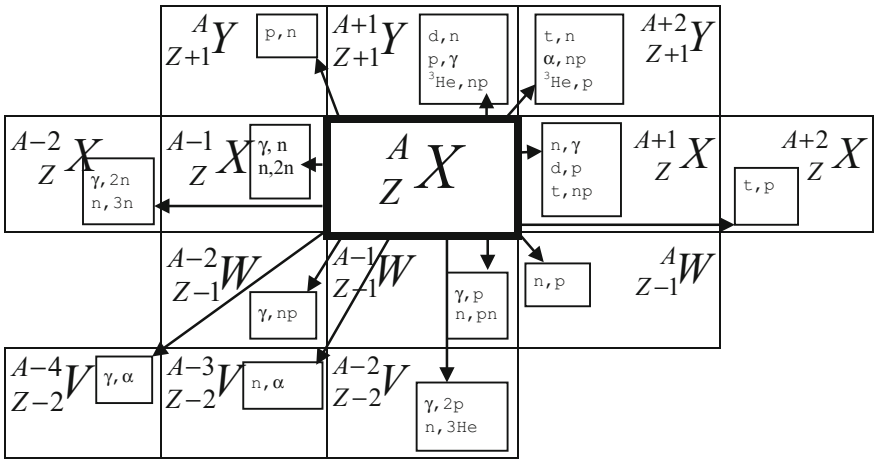

Fig. 4.36 Induced radioactivity process

Table 4.24 Photonuclear reactions on the nitrogen 14

Reactions	γ, n	γ, p	γ, t	γ, 3He	γ, α	γ, 2n	γ, np	γ, 2p	γ, 3n
Threshold MeV	10.55	7.55	22.74	20.74	11.61	30.62	12.50	25,08	46.24

Table 4.25 Photonuclear reactions on oxygen 16

Reactions	γ, n	γ, p	γ, t	γ, 3He	γ, α	γ, 2n	γ, np	γ, 2p	γ, 3n
Threshold MeV	15.66	12.13	25.03	22.79	7.16	28.89	22.96	33.34	52.06

reaction (p, n) is turned into ${}^{A}_{Z+1}Y$. Thus, the yield of ^{18}F for nuclear medicine in a cyclotron is achieved by means of the reaction ${}^{18}_{8}O(p,n)^{18}_{9}F$.

Another case of study could be the possible activation of the ambient air in a radiotherapy facility using 20 MeV photons. The air is predominantly composed with oxygen and nitrogen (we shall not consider the first approach ^{16}O and ^{14}N). At this point, it is appropriate to determine the thresholds of reactions (data in [38]). Possible reactions are given in Tables 4.24 and 4.25.

The shaded parts of the table are not allowed reactions at 20 MeV (higher response threshold for this value). The potential reactions to this energy are as follows: ^{14}N(γ, n)^{13}N (radioactive nucleus of half-live 9.97 min); ^{14}N(γ, p)^{13}C (stable nucleus); ^{14}N(γ, a)^{10}B (stable nucleus); ^{14}N(γ, np)^{12}C (stable nucleus); ^{16}O (γ, n)^{15}O (radioactive nucleus of half-live 2.04 min); ^{16}O(γ, p)^{15}N (stable nucleus); ^{16}O(γ, α)^{12}C (stable nucleus).

Thus, during radiotherapy with 20 MeV photons, the air is activated forming both radioactive elements: ^{13}N and ^{15}O.

4.9.2 Activity Calculation After a Given Reaction

Consider a target having a number N_C of nuclei collied by a fluence rate $\dot{\Phi}$ with a cross section reaction σ, creating N_R nuclei of a radioactive isotope with decay constant λ. The activation process is described by the following differential equation:

$$\begin{aligned} dN_R(t) = {} & N_c \cdot \sigma \cdot \dot{\Phi}(t) \cdot dt \quad : \textit{production by activation} \\ & - \lambda \cdot N_R(t) \cdot dt \quad : \textit{lost by radioactive decay} \\ & - \sigma \cdot \dot{\Phi} \cdot N_R(t) \cdot dt \quad : \textit{lost by activation} \end{aligned} \tag{4.47}$$

Note that this formalism is valid under the condition that the decay of a daughter does not lead to a target isotope.

Solving the differential (4.47) gives the number of target nuclei thus formed to an irradiation time t_i. It is given by the (4.48).

$$N_R(t_i) = \frac{N_C \sigma \dot{\Phi}}{\left(\lambda + \sigma \dot{\Phi}\right)} \left[1 - \exp\left(-\left(\lambda + \sigma \dot{\Phi}\right) t_i\right)\right] \tag{4.48}$$

Neglecting the decay of target nuclei upon irradiation (this is the case when $\sigma\dot{\Phi} \ll \lambda \, et \, \sigma\dot{\Phi}t \to 0$ the activity after a time t_i is then provided by the (4.49).

$$A_R(T_i) = N_C \sigma \dot{\Phi}[1 - \exp(-\lambda t_i)] \tag{4.49}$$

The activity concentration per unit mass is given by (4.50).

$$A_m(t) = f \frac{\eta_A}{A} \sigma \dot{\Phi}[1 - \exp(-\lambda t_i)] \tag{4.50}$$

Thus, after a period of irradiation t_i then stop during t_d, the specific activity is (4.51).

$$A_m(t_i + t_d) = f \frac{\eta_A}{A} \sigma \dot{\Phi}[1 - \exp(-\lambda t_i)] \exp(-\lambda t_d) \tag{4.51}$$

with: η_A Avogadro's number; A the atomic weight number of the target (g); f the isotopic abundance of the target; σ cross section (cm^2); $\dot{\Phi}$ fluence rate (s^{-1} cm^{-2}); λ the decay constant (s^{-1}); t_i irradiation time (s); t_d after the end of irradiation (s).

Figure 4.37 describing the (4.51) schematically shows the time evolution of the activity due to activation. The maximum activity that can be produced, also called "saturation activity", is $N_C \sigma \dot{\Phi}$. When the created radionuclide has short half-life,

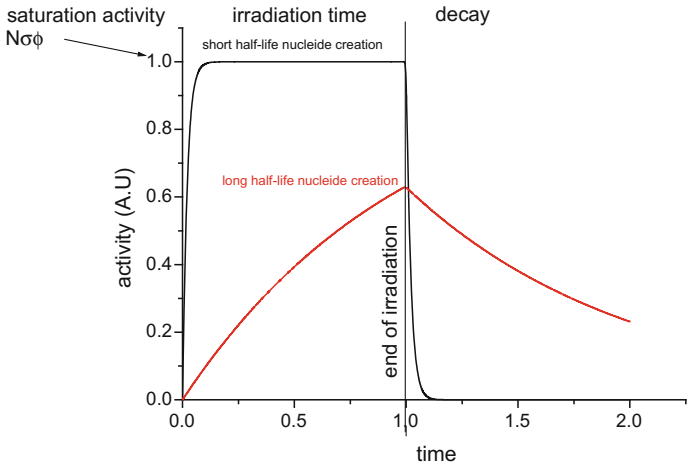

Fig. 4.37 Evolution of activity in the activation step and cooling of a target

the activity rapidly reaches its maximum saturation value; on the other hand, once the activation flux is stopped, the activity decreases rapidly. Conversely when a longer half-life is created, the activity increases slowly to decrease slowly when the flux stops.

Let us calculate for example the activity of radionuclide created by (n,2n) produced on a nitrogen target by neutron of $1 \cdot 10^{12}$ s^{-1} cm^{-2} fluence rate with 14 MeV energy for 1 h irradiation and after 10 min of decay time. Nitrogen is composed of 99.634% ${}^{14}_{7}N$ and 0.366% ${}^{15}_{7}N$ according to the table of isotopes [47]. We focus only on ${}^{14}_{7}N$ activation.

The reaction gives ${}^{14}_{7}N(n,2n){}^{13}_{7}N$· ^{13}N radionuclide has a half-life of about 10 min. The ${}^{14}_{7}N(n,2n){}^{13}_{7}N$ cross section for 14 MeV neutrons is 6.3 mbarn (according to the JEFF library 3.3, data obtained from the Nuclear data viewer website [4]). Therefore the specific activity is:

$$\frac{A(T_i)}{m} = \frac{6.02 \cdot 10^{23}}{14} \times 0.99634 \times 6.3 \cdot 10^{-27} \times 1 \cdot 10^{12} \times \left(1 - \exp\left(-\frac{\ln(2) \times 60}{10}\right)\right) \times \exp\left(-\frac{\ln(2) \times 10}{10}\right)$$

$$\frac{A(T_i)}{m} = 133\text{MBq/g}$$

4.9.3 Radiation Protection Risk Related to the Activation

Some "stopped" devices such as the particles accelerators may emit radiation due to structure activation; this activation has been created by the interaction of primary or secondary particles with the environment pieces. Besides the structures, activation may occur in the surrounding air, which can also induce internal exposure risk from inhalation of radionuclides.

Finally, during the facility decommissioning, having worked with neutron radiation or high-energy particles, we must take into account the radioactive waste produced. For this, the assessment of residual activities by calculation and validation by measures must be undertaken. Such an approach has been made for example to the decommissioning of a high-energy proton accelerator Saturne at CEA Saclay [48].

4.10 Emission of Radiation by "Exotic" Device

In this section, it seemed reasonable to mention device for which the primary function is not to emit radiation, but which by their working principle, can induce significant production of ionizing radiation and consequently radiation protection problems.

Most of these devices are instruments which have a very intense electric field. Under the effect of this field, free electrons are stripped from the walls and accelerated in this field, these electrons interact with matter to produce in turn bremsthralung photons. Among these devices, we can mention the generators of high-power microwave magnetron or klystron type. Another source able to generate high electric fields is the interaction of a short-duration of high-intensity laser pulse in a low-density plasma. We propose to illustrate this part with both devices.

4.10.1 Klystron

Klystrons allows to provide microwaves (on the order of GHz) of very high power (of the megawatt peak). They are commonly used in radar or to create the electromagnetic wave in a particle accelerator like a Linac type. Thus, an accelerator for radiotherapy could not function without this process. A conventional oscillator can generate the high power required for accelerators or radars. Klystrons are therefore high frequency power amplifiers. A classical amplification with transistors or thyristors could not generate the required power. The aim is to transport the energy gain via an electron beam modulated at the desired frequency. Figure 4.38 shows succinctly how a klystron works.

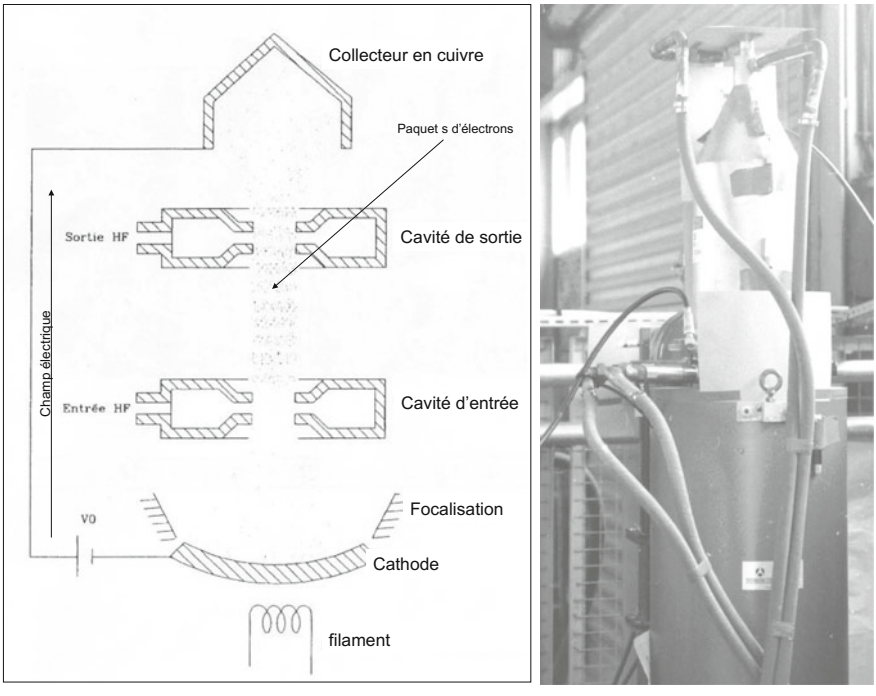

Fig. 4.38 Sketch and photography of a klystron [49]

Focused electrons are accelerated once by a DC voltage V_0. They are modulated by the high frequency signal to be amplified, applied to an input cavity. Some of them, in phase with this signal when they pass within the cavity, acquire additional energy; thus, their energy can be doubled. They catch those, transmitted earlier, which has been slowed: there is a grouping of electrons. These groups excite the output cavity. A part of the kinetic energy of the electrons (≈40%) is converted into high frequency. The other part is converted into photon radiation in the collector where these are finally stopped. In view of the accelerating voltages (several hundred kilovolts) and electron currents (a few hundreds of amperes) klystrons should be considered as X ray generators knowing moreover that most of them have a shielded copper collector with lead. However, it should be checked that the dose equivalent rates are consistent with the controlled areas where they are installed.

For example, Bourgois et al. [49] show that of a klystron with the following characteristics: V_0 = 93 kV; I_0 = 68 A; 40% yield; RF frequency of 1.5 GHz; RF power output of 1 MW peak; the maximum measured dose equivalent rate is 32 mSv h^{-1}. In order to limit this equivalent dose rate at 0.5 mSv h^{-1}, it is necessary to interpose 5 mm lead.

4.10.2 High-Intensity Laser Pulses

The development of High-Intensity Laser Pulses in the early 1980 allowed the study of light-matter interaction in the relativistic field [50]. During the laser-matter interaction, secondary particles (electrons, protons, neutrons …) can be realised and consequently constitutes radiation risks. When propagating in a heavy plasma, a short pulse (a few tens of femtoseconds) and extremely high (above $1 \cdot 10^{18}$ W/cm^2) expels the electrons it encounters and creates in its wake a wave of large electrostatic phase velocity and high amplitude: product fields up to a hundred GV/m [51]. With such an electric field, the charged particles (very few related in this plasma) acquire significant energy similar with those provided by particle accelerators to produce secondary radiation as bremsstrahlung, photoneutron or neutrons from nuclear reactions.

This energy is spread over a range of up to 1 GeV [50] for the more powerful lasers.

Several authors [52, 53, 44] suggest to approach the experimental energy distribution of the emitted electrons, using a relativistic Maxwellian defined according to the (4.52).

$$N(E)dE \propto \exp\left(-\frac{E}{k_B T}\right)dE \tag{4.52}$$

where the temperature T (MeV) is connected to the laser intensity I and its wavelength l by the (4.53) [53].

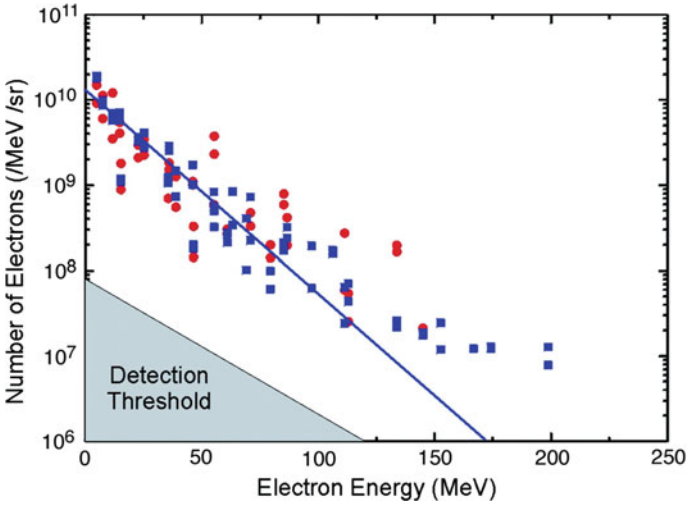

Fig. 4.39 Measured energy spectrum of accelerated electrons in the plasma along the laser axis [44], with the permission of the IAEA

$$T \approx \left(I\lambda^2/1 \cdot 10^{19}\right)^{1/2} \tag{4.53}$$

For example, Lefebvre et al. [44] give the electron spectrum for a laser with an intensity of $3 \cdot 10^{18}$ W cm^{-2} when interacting on a helium target in gaseous form. This spectrum is shown in Fig. 4.39. Similarly, the reference [44] gives the electron spectrum for an intensity of $2 \cdot 10^{19}$ W cm^{-2} to plastic targets of different thicknesses (Fig. 4.40). Note that the Maxwellian temperature depends on the target type and thickness. Similarly, the energy distribution depends on the angle of emission with respect to the axis of the laser beam.

Toupin et al. [54] Show that an ultra-high intensity laser illuminance with a solid target of deuterium generates fusion neutrons from the reaction ${}_1^2H(d,n){}_2^3He$. Figure 4.41 shows the angular distribution of neutrons as a function of the plasma density—$n_c(\text{cm}^{-3}) = 1 \cdot 10^{21}/\lambda_0^2$ and λ_0 the laser wavelength in μm—and the target illuminance (W/cm^2). We show that these two parameters affect the isotropy and the flux of emitted neutrons.

Note in Fig. 4.39 that the electron spectrum extends up to 200 MeV. Thus, the interaction of the electrons with the material will generate high bremsstrahlung energy photons (see Sect. 4.7.3) and photoneutrons (see Sect. 4.7.4). Thus the radiation of this device is studied like an accelerator of high energy particles. However, the input data are difficult to obtain: the flux, spectra, and particles nature emitted depends a lot of laser parameters and target used. Calculation is achieved by coupling a code for high intensity interaction as CALDER with a Monte Carlo

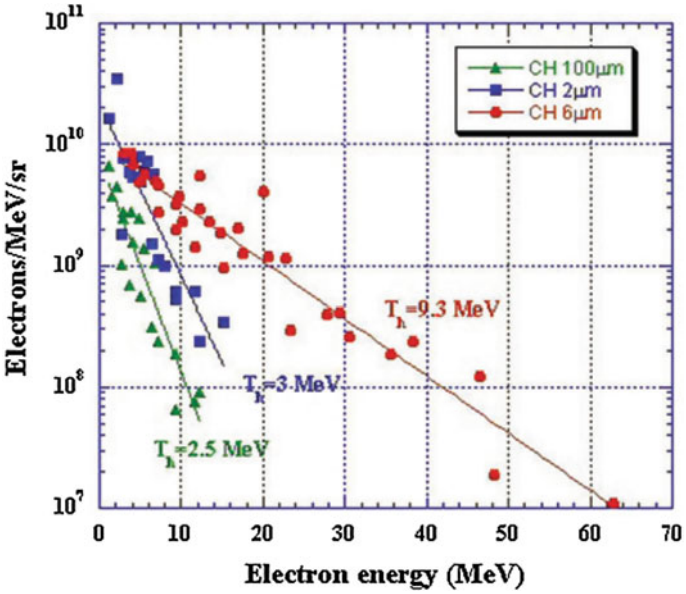

Fig. 4.40 Electron spectrum along the laser axis for three different plastic thicknesses [44], With the permission of the IAEA

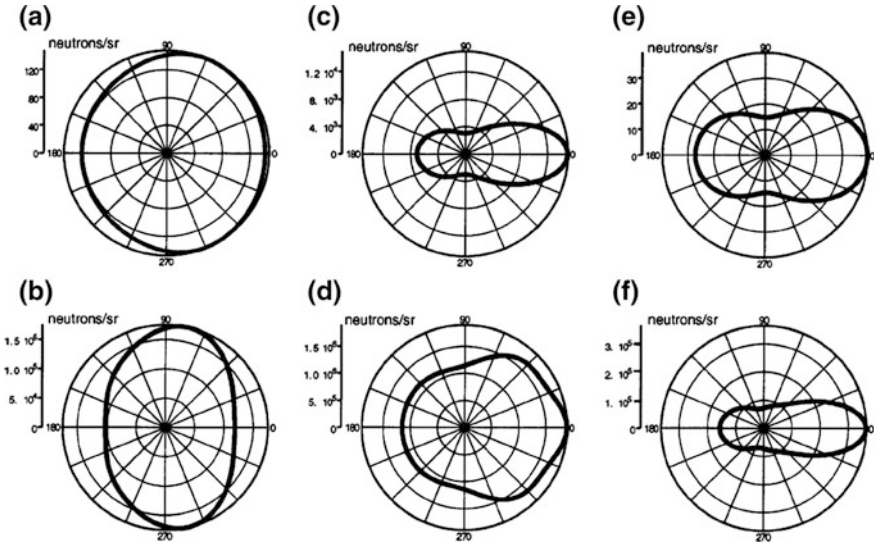

Fig. 4.41 Angular distribution of neutrons due to laser illumination of a deuterium target: **a** $n_{e0} = 4n_c$ $I_0 = 3 \cdot 10^{18}$ W/cm^2; **b** $n_{e0} = 4n_c$ $I_0 = 5 \cdot 10^{19}$ W/cm^2; **c** $n_{e0} = 10n_c$ $I_0 = 1 \cdot 10^{19}$ W/cm^2; **d** $n_{e0} = 10n_c$ $I_0 = 2 \cdot 10^{20}$ W/cm2; **e** $n_{e0} = 50$ n_c $I_0 = 1 \cdot 10^{19}$ W/cm^2; **f** $n_{e0} = 50n_c$ $I_0 = 2 \cdot 10^{20}$ W/cm^2 [54], With permission from the American Institute of Physics

codes such as MCNPX [51]. Nevertheless, this is achievable only with High Performance Computer (HPC).

Similarly, radiation protection measurements were carried out for this device [55] for a laser with an intensity of $3 \cdot 10^{19}$ W cm^{-2}. They show that in contact with the experiment chamber, the dose equivalent is maximum in the 20° direction from the laser axis and can reach 82 mSv for photons and 760 μSv for neutrons for 150 laser shots. Thus, in view of these results, the radiation of this class of facility is not to be underestimated because of huge "flash" dose equivalent. Moreover, as for high-energy electron accelerators, photons are responsible for the major source of external exposure.

Further Details 4.1: Demonstration of the (4.8) The principle of energy conservation is applied to the reaction, and the path of a, b, Y are in the same plane.

$$\overrightarrow{P_a} = \overrightarrow{P_b} + \overrightarrow{P_Y}$$

is:

$$\begin{cases} m_a V_a = m_Y V_Y \cos(\phi) + m_b V_b \cos(\theta) \\ m_Y V_Y \sin(\phi) - m_b V_b \sin(\theta) = 0 \end{cases}$$

or

$$\begin{cases} m_Y V_Y \cos(\phi) = m_a V_a - m_b V_b \cos(\theta) \\ m_Y V_Y \sin(\phi) = m_b V_b \sin(\theta) \end{cases}$$

By squaring the both expressions and summing, we get:

$$m_Y^2 V_Y^2 = m_a^2 V_a^2 + m_b^2 V_b^2 - 2 m_a V_a m_b V_b \cos(\theta)$$

Introducing the kinetic energies T, it comes:

$$m_Y T_Y = m_a T_a - 2\sqrt{m_a T_a m_b T_b}\cos(\theta) + m_b T_b$$

eliminate E_S using (4.7), we obtain:

$$Q = T_b\left(1 + \frac{m_b}{m_Y}\right) - T_a\left(1 + \frac{m_a}{m_Y}\right) - \frac{2}{M_Y}\sqrt{m_a T_a m_b T_b}\cos(\theta)$$

we seek to know the energy of the projectile b. Considering the variable $\sqrt{T_b}$, we are dealing with a quadratic equation whose solution is given by the (4.8).

Appendix 1

Neutron spectra of the main (α, n) and (γ, n) sources

Datas presented are the fluence per unit of lethargy, normalized to a unit fluence.

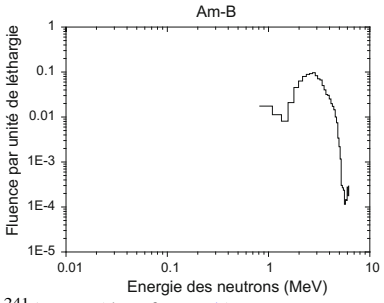

^{241}Am–B (data from [5])

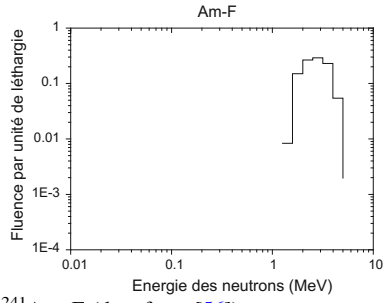

^{241}Am–F (data from [56])

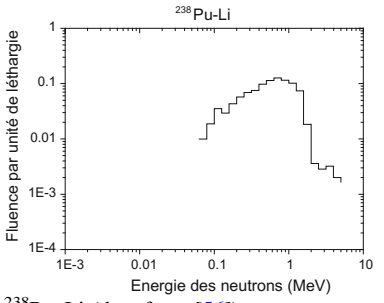

^{238}Pu–Li (data from [56])

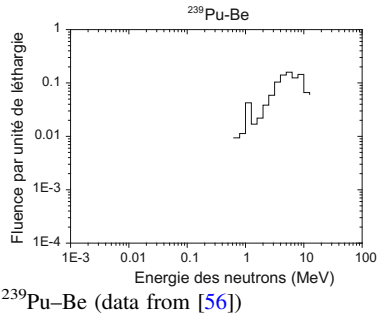

^{239}Pu–Be (data from [56])

(continued)

(continued)

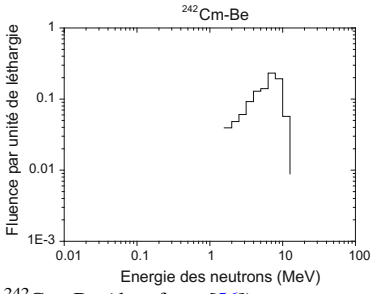

^{242}Cm–Be (data from [56])

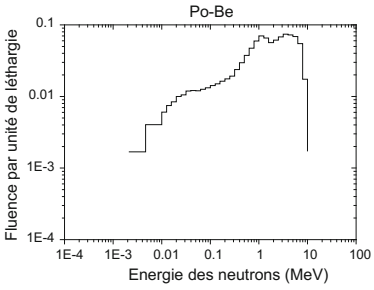

Po–Be (data from [56])

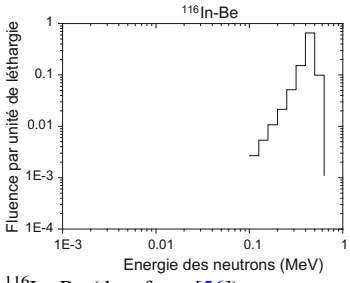

^{116}In–Be (data from [56])

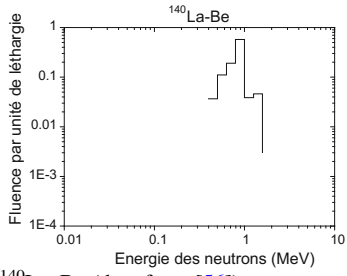

^{140}La–Be (data from [56])

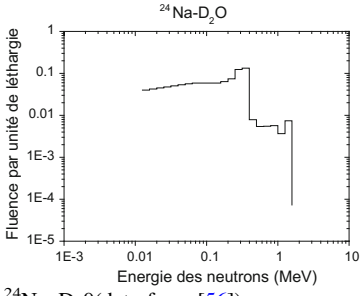

^{24}Na–$D_2$0(data from [56])

Numerical values

Energy (MeV)	Am–B	Energy (MeV)	Am–Be
4.14 E – 07		4.14 E – 07	0
0.82	1.75 E – 02	0.11	1.44 E – 02
1.09	1.13 E – 02	0.33	3.34 E – 02
1.34	8.07 E – 03	0.54	3.13 E – 02
1.56	2.10 E – 02	0.75	2.81 E – 02
1.78	4.54 E – 02	0.97	2.50 E – 02
1.98	6.31 E – 02	1.18	2.14 E – 02
2.17	7.99 E – 02	1.40	1.98 E – 02
2.36	8.90 E – 02	1.61	1.75 E – 02
2.54	9.26 E – 02	1.82	1.92 E – 02
2.72	9.65 E – 02	2.04	2.23 E – 02
2.89	8.31 E – 02	2.25	2.15 E – 02
3.05	7.06 E – 02	2.47	2.25 E – 02
3.22	6.67 E – 02	2.68	2.28 E – 02
3.38	4.99 E – 02	2.90	2.95 E – 02
3.53	4.02 E – 02	3.11	3.56 E – 02
3.68	3.17 E – 02	3.32	3.69 E – 02
3.83	3.03 E – 02	3.54	3.46 E – 02
3.98	2.52 E – 02	3.75	3.07 E – 02
4.13	1.98 E – 02	3.97	3.00 E – 02
4.27	1.72 E – 02	4.18	2.69 E – 02
4.41	1.45 E – 02	4.39	2.86 E – 02
4.55	9.97 E – 03	4.61	3.18 E – 02
4.69	7.46 E – 03	4.82	3.07 E – 02
4.83	3.41 E – 03	5.04	3.33 E – 02
4.96	2.19 E – 03	5.25	3.04 E – 02
5.09	1.16 E – 03	5.47	2.74 E – 02
5.22	3.03 E – 04	5.68	2.33 E – 02
5.35	2.68 E – 04	5.89	2.06 E – 02
5.48	2.36 E – 04	6.11	1.82 E – 02

(continued)

(continued)

Energy (MeV)	Am–B	Energy (MeV)	Am–Be
4.14 E – 07		4.14 E – 07	0
5.61	1.15 E – 04	6.32	1.77 E – 02
5.74	1.45 E – 04	6.54	2.04 E – 02
5.86	1.39 E – 04	6.75	1.83 E – 02
5.98	2.78 E – 04	6.96	1.63 E – 02
6.11	1.78 E – 04	7.18	1.67 E – 02
6.19	2.91 E – 04	7.39	1.68 E – 02
6.25	0.00 E + 00	7.61	1.88 E – 02
		7.82	1.84 E – 02
		8.03	1.69 E – 02
		8.25	1.44 E – 02
		8.46	9.68 E-03
		8.68	6.52 E – 03
		8.89	4.26 E – 03
		9.11	3.67 E – 03
		9.32	3.81 E – 03
		9.53	5.06 E – 03
		9.75	6.25 E-03
		9.96	5.52 E – 03
		10.18	4.68 E – 03
		10.39	3.70 E – 03
		10.60	2.78 E – 03
Data source adapted from [5]		10.82	1.51 E – 03
		11.03	3.63 E – 04
		11.09	0

Appendix 2

Kerma rate in air to 1 m due to bremsstrahlung photons of a tungsten target bombarded with energy electron E and intensity 1 mA.

Filtration	None	0.2 mm Al	0.5 mm Al	1 mm Al	2 mm Al	3 mm Al	0.2 mm Cu	0.5 mm Cu	1 mm Cu	2 mm Cu	3 mm Cu
E(kV)	mGy/min	mGy/min	mGy/min	mGy/min	mGy/min	mGy/min	mGy/min	mGy/min	mGy/min	mGy/min	mGy/min
50	1.48E + 02	2.49E + 01	1.15E + 01	6.08E + 00	3.03E + 00	1.85E + 00	5.62E – 01	9.05E – 02	1.11E – 02	3.62E – 04	1.82E – 05
100	1.99E + 02	4.89E + 01	2.58E + 01	1.65E + 01	1.04E + 01	7.76E + 00	3.99E + 00	1.82E + 00	8.54E – 01	3.73E – 01	1.63E – 01
150	2.23E + 02	6.61E + 01	4.00E + 01	2.85E + 01	1.97E + 01	1.57E + 01	1.01E + 01	5.76E + 00	3.48E + 00	1.86E + 00	1.16E + 00
200	2.32E + 02	7.85E + 01	5.09E + 01	3.87E + 01	2.93E + 01	2.48E + 01	1.77E + 01	1.17E + 01	8.17E + 00	5.66E + 00	4.05E + 00
250	2.4E + 02	9.50E + 01	6.65E + 01	5.33E + 01	4.19E + 01	3.59E + 01	2.76E + 01	1.96E + 01	1.46E + 01	1.02E + 01	7.86E + 00
300	2.55E + 02	1.08E + 02	8.00E + 01	6.62E + 01	5.43E + 01	4.79E + 01	3.90E + 01	2.93E + 01	2.26E + 01	1.67E + 01	1.36E + 01
350	2.62E + 02	1.23E + 02	9.54E + 01	8.19E + 01	6.97E + 01	6.22E + 01	5.25E + 01	4.09E + 01	3.35E + 01	2.56E + 01	2.11E + 01
400	2.70E + 02	1.36E + 02	1.09E + 02	9.48E + 01	8.21E + 01	7.50E + 01	6.45E + 01	5.19E + 01	4.23E + 01	3.37E + 01	2.87E + 01
450	2.86E + 02	1.56E + 02	1.29E + 02	1.15E + 02	1.01E + 02	9.32E + 01	8.33E + 01	6.84E + 01	5.72E + 01	4.58E + 01	3.87E + 01
500	3.02E + 02	1.74E + 02	1.47E + 02	1.33E + 02	1.20E + 02	1.12E + 02	1.01E + 02	8.54E + 01	7.26E + 01	5.88E + 01	5.04E + 01
600	3.45E + 02	2.17E + 02	1.90E + 02	1.75E + 02	1.61E + 02	1.51E + 02	1.39E + 02	1.20E + 02	1.05E + 02	8.73E + 01	7.63E + 01
700	4.16E + 02	2.80E + 02	2.55E + 02	2.41E + 02	2.25E + 02	2.13E + 02	2.02E + 02	1.79E + 02	1.59E + 02	1.36E + 02	1.19E + 02
800	4.69E + 02	3.32E + 02	3.04E + 02	2.89E + 02	2.72E + 02	2.60E + 02	2.50E + 02	2.25E + 02	2.02E + 02	1.79E + 02	1.60E + 02
900	5.17E + 02	3.85E + 02	3.60E + 02	3.45E + 02	3.31E + 02	3.19E + 02	3.04E + 02	2.77E + 02	2.52E + 02	2.21E + 02	2.00E + 02

Ambient dose equivalent rate—H*(10)—to 1 m due to bremsstrahlung photons of a tungsten target bombarded with energy electron *E* and intensity 1 mA

Filtration	None	0.2 mm Al	0.5 mm Al	1 mm Al	2 mm Al	3 mm Al	0.2 mm Cu	0.5 mm Cu	1 mm Cu	2 mm Cu	3 mm Cu
E(KV)	mSv/min	mSv/min	mSv/min	mSv/min	mSv/min	mSv/min	mSv/min	mSv/min	mSv/min	mSv/min	mSv/min
50	1.01E + 01	7.69E + 00	6.00E + 00	4.35E + 00	2.75E + 00	1.87E + 00	6.75 E01	1.28E – 01	1.69E – 02	5.72E – 04	2.92E – 05
100	2.73E + 01	2.31E + 01	1.94E + 01	1.59E + 01	1.22E + 01	9.94E + 00	5.97E + 00	3.02E + 00	1.46E + 00	6.41E – 01	2.79E – 01
120	–	–	–	–	–	–	–	–	–	1.31E + 00	6.91E – 01
150	4.60E + 01	4.07E + 01	3.63E + 01	3.13E + 01	2.53E + 01	2.18E + 01	1.57E + 01	9.50E + 00	5.78E + 00	3.05E + 00	1.89E + 00
200	6.28E + 01	5.74E + 01	5.24E + 01	4.67E + 01	3.97E + 01	3.57E + 01	2.76E + 01	1.90E + 01	1.32E + 01	8.92E + 00	5.63E + 00
250	8.44E + 01	7.95E + 01	7.38E + 01	6.72E + 01	5.82E + 01	5.21E + 01	4.29E + 01	3.11E + 01	2.30E + 01	1.56E + 01	1.20E + 01
300	1.04E + 02	9.97E + 01	9.40E + 01	8.67E + 01	7.68E + 01	7.03E + 01	6.01E + 01	4.56E + 01	3.48E + 01	2.52E + 01	2.02E + 01
350	1.25E + 02	1.23E + 02	1.17E + 02	1.10E + 02	9.93E + 01	9.14E + 01	8.02E + 01	6.28E + 01	5.06E + 01	3.78E + 01	3.08E + 01
400	1.46E + 02	1.44E + 02	1.37E + 02	1.29E + 02	1.18E + 02	1.10E + 02	9.74E + 01	7.86E + 01	6.30E + 01	4.91E + 01	4.12E + 01
450	1.83E + 02	1.74E + 02	1.67E + 02	1.58E + 02	1.46E + 02	1.37E + 02	1.25E + 02	1.02E + 02	8.42E + 01	6.61E + 01	5.52E + 01
500	2.07E + 02	2.02E + 02	1.94E + 02	1.85E + 02	1.72E + 02	1.63E + 02	1.50E + 02	1.26E + 02	1.05E + 02	8.37E + 01	7.09E + 01
600	2.69E + 02	2.62E + 02	2.54E + 02	2.43E + 02	2.30E + 02	2.18E + 02	2.03E + 02	1.73E + 02	1.49E + 02	1.22E + 02	1.05E + 02
700	3.55E + 02	3.48E + 02	3.43E + 02	3.33E + 02	3.17E + 02	3.02E + 02	2.88E + 02	2.54E + 02	2.22E + 02	1.87E + 02	1.61E + 02
800	4.22E + 02	4.15E + 02	4.07E + 02	3.97E + 02	3.79E + 02	3.65E + 02	3.52E + 02	3.13E + 02	2.77E + 02	2.41E + 02	2.14E + 02
900	5.02E + 02	4.91E + 02	4.84E + 02	4.73E + 02	4.59E + 02	4.44E + 02	4.24E + 02	3.81E + 02	3.43E + 02	2.95E + 02	2.66E + 02

References

1. ICRP. (1995). Conversion coefficients for use in radiological protection against external radiation, publication 74.
2. Delacroix, D., Guerre, J. P., & Leblanc, P. (2006). *Radionucléides & radioprotection.* EDP Sciences.
3. Audi, G., & Wapstra, A. H. (1995). The 1995 update to the atomic mass evaluation. *Nuclear Physics A, 595*, 4, 409–480. (data from http://amdc.in2p3.fr/web/mass95.html).
4. Nuclear data viewer Los Alamos Laboratory, http://t2.lanl.gov/nis/data/qtool.html.
5. ISO. (2002). Norme NF ISO 8529-1 Rayonnements neutroniques de référence partie 1: Caractéristiques et méthodes de production.
6. Shultis, J. K., & Faw, R. E. (2000). Radiation shielding. American Nuclear Society, Inc.
7. Tagziria, H., Roberts, N. J., & Thomas, D. J. (2003). Measurement of the 241Am-Li radionuclide neutron source spectrum. *Nuclear Instruments and Methods A, 510*, 346–356.
8. ICRP. (1971). Protection against Ionizing Radiation from External Sources and Data for Protection against Ionizing Radiation from External Sources, publication 15 and 21.
9. Gorshkov, G. V., Zyabkin, V. A., & Tsvetkov, O. S. (1962). Neutron yield from the reaction (α, n) in Be, B, C, O, F, Mg, Al, Si, and granite irradiated with polonium α particles. *Atomic Energy, 13*(1), 654–657.
10. Russel, B., Sachs, D., Wattenberg, A., & Fileds, R. (1948). Yields of neutrons from photo-neutron sources. *Physical Review Second Series, 73*(6), 545–549.
11. Verbeke, J. M., Hagmann, C., & Wright, C. (2010). Simulation of neutron and gamma ray emission from fission and photofission. Lawrence Livermore National Laboratory. UCRL-AR-228518.
12. ICRP. (2007). Nuclear decay data for dosimetric calculations. Publication 107.
13. Terrell, J. (1959). Fission neutron spectra and nuclear temperature. *Physical Review*, *113*, 2.
14. Staples, P., Egan, J. J., Kegel, G. H. R., Mittler, A., & Woodring, M. L. (1995). Prompt fission neutron energy spectra induced by fast neutrons. *Nuclear Physics A, 591*, 41–60.
15. Maslov, V. M., Porodzinskij, Y. V., Baba, M., Hasegawa, A., Kornilov, N., Kagalenko, A. B., et al. (2003). Prompt fission spectra of 238U(n, f) above emissive fission threshold. *European Physical Journal A: Hadrons and Nuclei, 18*, 93–102.
16. Watt, B. E. (1952). Energy spectrum of neutrons from thermal fission of U235. *Physical Review, 87*, 6.
17. Cranberg, L., Frye, G., Nereson, N., & Rosen, L. (1956). Fission neutron spectrum of U235. *Physics Review, 103*, 3.
18. Pelowitz, D. B. (2005). MCNPX User's manual version 2.5.0. LA-CP-05-0369.
19. Verbinsky, V. V., Weber, H., & Sund, R. E. (1973). Prompt gamma rays from ^{235}U(n,¦), 239Pu(n,¦), and spontaneous fission of ^{252}Cf. *Physical Review C, 7*(3), 1173–1185.
20. Valentine, T. E. (2001). Evaluation of prompt fission gamma rays for use in simulating nuclear safeguard measurements. *Annals of Nuclear Energy, 28*, 191–201.
21. IAEA. (2008). Handbook of nuclear data for safeguards: database extensions, august 2008. International Nuclear Data Committee. INDC(NDS)–0534.
22. Tsilanizara, A., Diop, C. M. et al. (2000). DARWIN: An evolution code system for a large range of applications (Proceedings of the 9th International Conference on Radiation Shielding, Tsukuba, Japan, 1999), *Journal of Nuclear Science Technology Supplement 1*, 845–849.
23. Comte, N., Bourgois, L., & Bourion, J. P. (2004). Organisation et schéma de calcul de conséquences radiologiques en situation accidentelle au CEA de Saclay: logiciel SENTINEL. Rapport interne DEN/SAC/SPR/SERD/DF/001.
24. Hunter, H. F., & Ballou, N. E. (1951). Fission product decay rates. *Nucleonics, 9*, 5.
25. Bourgois, L., Zerbib, J. C., & Delacroix, D. (1998). The forbach accident—What is the situation now: do we really use the feedback experience? In *2nd European Alara Network Workshop on Good Radiation Practices in Industry and Research*.

26. ICRU. (1985). Stopping Powers for electrons and positrons. Publication 37.
27. Koch, H. W., & Motz, J. W. (1959) Bremsstrahlung cross section formulas and related data. *Review of Modern Physics*, *31*, 4, 920–956.
28. Seltzer, S. M. (1988). Cross section for bremsstrahlung production and electron impact ionization. In T. M. Jenkins, W. R. Nelson & A. Rindi (Eds.), *Monte Carlo transport of electrons and photons.* New York: Plenum press.
29. Tseng, H. K., & Pratt, R. H. (1971). Exact screened calculation of atomic field bremsstrahlung. *Physical Review A, 3*, 100.
30. Lee, C. M., Kissel, L., Pratt, R. H., & Tseng, H. K. (1976). Electron bremsstrahlung spectrum, 1–500 keV. *Physical Review A, 13*(5), 1714–1727.
31. Pratt, R. H., Tseng, H. K, Lee, C. M., Kissel, L., MacCallum, C., & Riley, M. (1977). Bremsstrahlung energy spectra from electrons of kinetic energy 1 keV £ T £ 2000 keV Incident on neutral atoms 2 £ Z £ 92. *Atomic Data and Nuclear Data Tables,* 20.
32. Leclère, A. S. T. (2001). An evaluation of bremsstrahlung cross-section for keV to GeV electrons. Thesis presented to the graduate school of the University of Florida. University of Florida.
33. Tucker, D. M., Barnes, G., & Chakraborty, D. P. (1991). Semiempirical model for generating tungsten target X-ray spectra. *Medical Physics, 18*(2), 211–218.
34. Pagès, L., Bertel, E., Joffre, H., & Sklavenitis, L. (1972) Energy loss range, and bremsstrahlung yield for 10 keV to 100 MeV electrons. *Atomic Data and Nuclear Data, 4*, 1.
35. Fardeau, F., & Guillo, H. (2010). *Contrôle externe de radioprotection de générateurs de rayonnement X*. Service de protection contre les rayonnements: Trois rapports internes CEA Saclay.
36. Directive 96/29/Euratom du conseil du 13 mai 1996, fixant les normes de base relatives à la protection sanitaire de la population et des travailleurs contre les dangers des rayonnements ionisants, L 159 ISSN 0378-7060.
37. NCRP (1977) Radiation protection design Guidelines for 0.1–100 MeV Particle Accelerator Facilities—NCRP Report n° 51.
38. IAEA. (2000). Handbook on photonuclear data for application. Cross section and spectra. IAEA-TECDOC, 1178, IAEA, Vienna.
39. Wattenberg, A. (1947). Photo-neutron sources and the energy of the photo-neutrons. *Physical Review, 71*(8), 497–507.
40. Swanson, W. P. (1978). Calculation of neutron yields released by electrons near the photoneutron threshold stanford linear accelerator center SLAC-PUB-2211.
41. Bourgois, L., Delacroix, D., & Ostrowsky, A. (1997). Use of bubble detector to measure neutron contamination of a medical accelerator photon beam. *Radiation Protection Dosimetry, 74*(4), 239–246.
42. Shin, K., Hibi, K., Fujii, M., Uwamino, Y., & Nakamura, T. (1984). Neutron and photon production from thick targets bombarded by 30 MeV p, 33 MeV d, 65 MeV 3He, and 65 MeV a ions: experiment and comparison with cascade Monte Carlo calculations. *Physical Review C, 29*, 4.
43. Bourgois, L., Masson, L., & Bertereau, G. (1993). Mesures des niveaux d'exposition auprès du Van de Graaff de la microsonde nucléaire fonctionnant en deutons. Rapport interne CEA DCE-S/DSCE/SRI-A/93-1058.
44. Lefebvre, E., Cochet, N., Fritzler, S., et al. (2003). Electron and photon production from relativistic laser-plasma interactions. *Nuclear Fusion, 43*, 629–633.
45. Comte, N., Gobin, R., Fardeau, F., Bogard, D., Guillo, H., & Leroy, P. A. (2004). Compte rendu d'expérience de mesures neutroniques avec un faisceau intense de deutons (5 mA–40 keV) sur silhi. Rapport interne CEA DEN/SAC/DSP/SPR/SERD/2004-0276.
46. Sullivan, A. H. (1992). A guide to radiation and radioactivity levels near high energy particle accelerators Nuclear Technology Publishing Ashford, Kent, TN23 1JW ISBN 1 870965 18 3.
47. The Lund/LBNL Nuclear Data Search Version 2.0, February 1999 SYF Chu1, LP Ekström and RB Firestone. http://nucleardata.nuclear.lu.se/nucleardata/toi/.

48. Masson, L., & Bourgois, L. (2000). Calculs et mesures de l'activation induite dans les bétons de protection d'un accélérateur d'ions de haute énergie. *Radioprotection, 35*(3), 311–334.
49. Bourgois, L., & Petit, G. (1993). Protection à mettre en place autour du collecteur du klystron prévu pour les cavités supraconductrices à 9 cellules. Rapport interne CEA DCE-S/DSCE/SRI-A/93-327.
50. Malka, V., Faure, J., Gauduel, Y. A., Lefebvre, E., Rousse, A., & Ta Phuoc, K. (2008). Principles and applications of compact laser-plasma accelerators. *Nature Physics, 4*, 447–453.
51. Lefebvre, E., Davoine, X., Beck, A., Rechatin, C., Faure, J., & Malka, V. (2009). Contrôle tout optique des faisceaux d'électrons accélérés par sillage laser. *Revue Chocs* avancées 2009/avancées scientifiques et techniques, CEA, Direction des applications militaires.
52. Belyaev, V. S., Vinogradov, V. I., Matafonov, A. P., Krainov, V. P., Lisitsa, V. S., Faenov, A. Y. et al. (2006) Neutron production in picosecond laser-generated plasma on a be target. *Physics of Atomic Nuclei, 69*, 6, 919–923.
53. Hatchett, S. P., Brown, C. G., Cowan, T. E., Henry, E. A., Johnson, J., Key, M. H. et al. (1999). Electron, photon, and ion beams from the relativistic interaction of petawatt laser pulses with solid targets. LLNL UCRL-JC-135029.
54. Toupin, C., Lefebvre, E., & Bonnaud, G. (2001). Neutron emission from a deuterated solid irradiated by an ultraintense laser pulse. *Physics of Plasmas, 8*(3), 1011–1021.
55. Borne, F., Delacroix, D., Gelé, J. M., Massé, D., & Amiranoff, F. (2002). Radiation protection for an ultra-high intensity laser. *Radiation Protection Dosimetry, 102*, 61–70.
56. IAEA. (1990). Compendium of Neutron Spectra and Detector Responses for Radiation Protection Purposes, Technical Reports Series No. 318, IAEA, Vienna.

Chapter 5
Protection Against External Exposition, General Principles

Abstract This chapter is devoted to biological protection against external exposure. It introduces shieldings against α, β, γ and neutrons radiation and other secondary source term developed previously such as bremsstrahlung photons, neutrons from different reactions (nuclear reactions photoneutrons, …). This chapter also addresses protection against scattered radiation, and the mazes or skyshine. A section is devoted to the production of harmful gases (non-radioactive, e.g. ozone) due to radiation. Finally we are interested in computer codes for calculating shielding.

If in the previous chapters, we saw, from a field of radiation, how to assess useful dosimetric quantities. Biological protections should be defined from these values to be compatible with limits related to radiation protection goal.

ISO standards [1] recommend an iterative method for defining a protection against radiation, including the steps of:

- Choice of radiation protection level and other design criteria;
- Characterization of radiation sources;
- Identification of constraints to implementation and building;
- Choice of shielding materials and arrangement within the shielding;
- Choice of calculation methods;
- Choice of the final solution;
- Experimental check.

Although this standard is devoted to neutrons, the steps to consider are the same for other types of ionizing radiation.

In this chapter a number of these steps are presented. The analytical methods are preferred to develop a first approximation of the shielding to be implemented. As appropriate, for complex cases of geometry, shieldings have to be validated by more sophisticated computer codes such as Monte Carlo codes presented in Chap. 6. Wherever possible, the examples of analytical calculations are compared to codes developed to assess the validity of the methods.

R. Antoni and L. Bourgois, *Applied Physics of External Radiation Exposure*,
Biological and Medical Physics, Biomedical Engineering,
DOI 10.1007/978-3-319-48660-4_5

To understand the concepts detailed in this chapter, we start on a section of definition.

5.1 Definitions

The "primary radiation" is emitted by a radioactive source, an X-ray generator, or by the accelerator beam. The room hosting the radiation source designed with shielding is commonly called "bunker". The shielding designed to attenuate the primary radiation is called "primary barrier".

The "secondary radiation" results from scattering of the primary radiation on the materials. A first scattered radiation can in turn undergo successive scattering. It should be noted that the energy of the primary radiation undergo altering in successive scattering. The shielding designed to attenuate this scattered radiation is called "secondary barrier."

we call "skyshine" a radiation scattered by sky air, outside the radiological shielding.

Figure 5.1 summarizes all of these definitions.

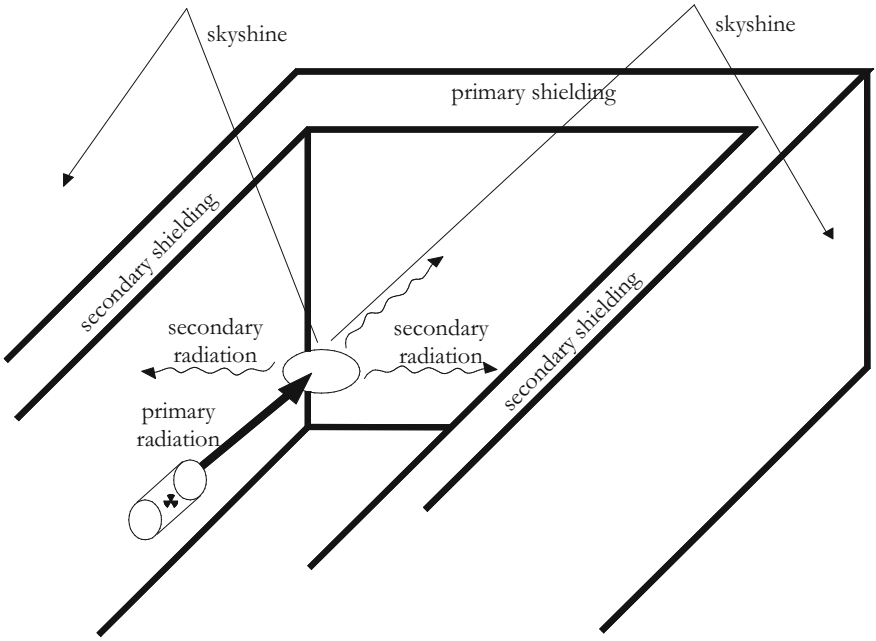

Fig. 5.1 Primary and secondary radiation, sky effect

5.2 Protection Principles

Reducing worker exposure may operate on the following four parameters:

- The intensity of the source: being careful to use the necessary minimum radiation intensity for the operation, in the case of a source such as an X-ray generator, or the minimum amount of a radionuclide as low as achievable;
- Distance: maintaining the greatest possible distance, without undermining the effectiveness of the work involved, between the radiation source and the worker;
- Time: limiting the strictly necessary minimum the time spent near the source;
- Shielding: placing, between the radiation source and the worker, suitable protective shielding and, if necessary, using other shielding to protect people in the vicinity of the source or adjoining areas.

5.2.1 Decay of a Source and Reduction of Exposure Time

An ergonomic approach can reduce the exposure time and therefore the dose integrated by the operators: that is to say study the relationship between the operator and its means, working methods and workplaces. The goal is to gather knowledge to transform existing work situations or to adapt and design the tools, machines and work devices so they can be used with maximum comfort, safety and efficiency.

The activity of a source decreases by a factor of 1000 after 10 half-life, it is the same for the induced dose rate. This economic means will be used whenever circumstances permit.

It is reasonable to expect 150 h before working with a 24 Na (15 h half-life); it is inconvenient to wait 80 days before entering in facility with a source of iodine 131 (8 days half-life), and wait 53 years before working with a cobalt 60 source (5.3 years half-life) is excluded.

The measures to be implemented are of common sense. Typically, preparing an intervention requires:

- To own updated plans of the facility to avoid as much as possible trails on site, or during surgery or operation, leading to unjustified exposures;
- The use of quick release systems;
- To coordinate the interventions and actions of operators;
- Where necessary, to carry out blank tests and use of modern simulation techniques (video …);
- If necessary, share the intervention time between several people;
- Take into account the experience gained in previous handling.

5.2.2 Dose Rate Variation with Distance

Distance is a way to simple, efficient and economic protection to reduce external exposure.

As shown in Chap. 1, for an isotropic point source, the fluence varies as the inverse square of the distance. This remains valid for the ambient dose equivalent as shown by (5.1).

$$\frac{H^*(10)_{d_1}}{H^*(10)_{d_2}} = \left(\frac{d_2}{d_1}\right)^2 \tag{5.1}$$

This law is reliable only if the source view from the observation-point can be considered as punctual. For a non-point source, this law is valid only from a certain distance (around 5–10 times the largest dimension of the source).

The ambient dose equivalent at a distance d is obtained from $H_0^*(10)$ the ambient dose equivalent to 1 m according to the expression (5.2). This is called "inverse square law". Please note that this equation is valid only for an isotropic point source and the distance d must be expressed in meters. This law is also efficient for other quantities such as kerma, absorbed dose …

$$H^*(10)_d = \frac{H_0^*(10)}{d^2} \tag{5.2}$$

For photon emitters, the relationship (5.2) allows use of Delacroix's work et al. [2]. This reference provides the equivalent dose rate at 30 cm from a 1 Bq point source and for 212 radionuclides. Thus, for a source of ^{54}Mn, a dose equivalent rate of $4 \cdot 10^{-6}$ µSv h^{-1} per becquerel at 30 cm is provided. At 1 m and 1 GBq, then we get

$$\dot{H}^*(10) = D_p \times A \times \left(\frac{0.3}{d}\right)^2 = 1.4 \cdot 10^{-6} \times \left(1 \cdot 10^9\right) \times \left(\frac{0.3}{1}\right)^2 = 126\,\mu\text{Sv}\,\text{h}^{-1}$$

warning! attenuation of β particles in the air is important and this formula is no longer suitable.

To easily handle radioactive source, remote handling tongs up to 1 m can be used.

The handling tong consists of few main components and eventual extensions:

- The tong rod with a screw on the back side to limit or reduce the opening of the jaws. The screw can lock the tong squeezing.
- An adaptor for fixing the tight sleeve, transferring tightly the motion between the tong thread and rod.

An illustration of this type of tong is given in Fig. 5.2.

The tong can pass through a shielding, in this case we must be vigilant that no radiation leakage pass through the shielding.

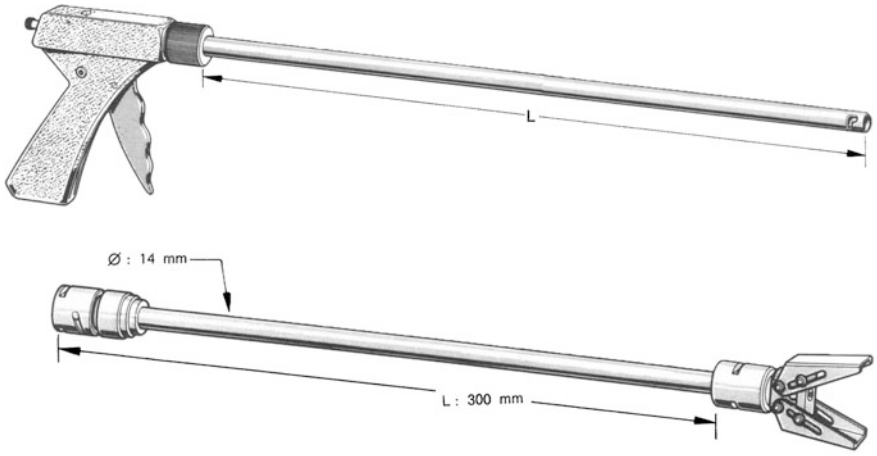

Fig. 5.2 Remote handling tong for handling of radioactive sources [3]

5.3 Shielding Against α and β Radiation

Another method to protect against external exposure is to interpose a shielding between the source and the exposed personnel.

5.3.1 α Particle

α energies emitted during the decay of such radionuclides (about 5 MeV), involve a very small range in matter (see Chap. 2). Just a fraction of a millimeter in any material absorbes these particles (plexiglass, paper, cardboard …). Also, even with the lack of shielding, they do not cause health damage: their range is less than the depth at which the sensitive layer of the skin is located, about 70 μm of tissue (see Chap. 2).

The range of α in dry air at 15 °C and a pressure of the atmosphere is approximately given by the formula (5.3) [4].

$$R_{air}(\text{cm}) = \begin{cases} 0.56E_\alpha & E_\alpha < 4\,\text{MeV} \\ 1.24E_\alpha - 2.62 & 4 \le E_\alpha < 8\,\text{MeV} \end{cases} \tag{5.3}$$

For example, the range of a 5 MeV alpha particle in air is:

$$R = 1.24 \times 5 - 2.62 = 3.6\,\text{cm}.$$

For a material different from air with a atomic mass A, it can be applied [5]:

$$R(\mathrm{mg\,cm^{-2}}) = 0.56\,\mathrm{A}^{1/3} \times R_{\mathrm{air}}$$

For example, for 5 MeV, into the aluminium $R = 0.56 \times (27)^{1/3} \times 3.6 = 6$ mg cm^{-2}. The aluminum having a density of 2.7 g cm^{-3}, there is a range of $R = 6 \cdot 10^{-3}/2.7 = 2.22 \cdot 10^{-3}$ cm.

5.3.2 *β Particle*

We accepted in Chap. 2 that the β particles do not degrade their energy as quickly as the particles α and therefore are more penetrating. For example, in the air, their range varies with the energy of a 50 m–0.5 MeV to about 12 m–3 MeV [6]. Remember that the range for monoenergetic electrons is given by the Katz and Penfold formula [7] presented in Chap. 2.

For β particles, shielding made of low atomic number materials are better suited. Indeed, the β particles lose energy in the shielding by ionization and excitation, but also by producing bremsstrahlung whose yield is proportional to the atomic number (of the material, as shown in Chap. 4).

For the maximum range of β in various materials, we can see Pagès et al. [6].

In conclusion, for a calculation of shielding for β radionuclides, the process is as follows:

- we first try to stop the maximum electron energy of the β using a thick shielding of a low atomic number material and with a thickness equal to the maximum range;
- Dosimetric quantities due to the bremsstrahlung are assessed by considering electron energy equal to the mean energy of the electron spectrum and the shielding is calculated for bremsstrahlung to this energy.

5.4 Shielding Against Photons Radiation

5.4.1 *Calculation of Primary Shielding: Uncollided Radiation*

We consider here a uncollided radiation from the source without interaction in the surrounding medium. It is the case with a narrow parallel beam passing through a relatively thin shield (see Fig. 5.3).

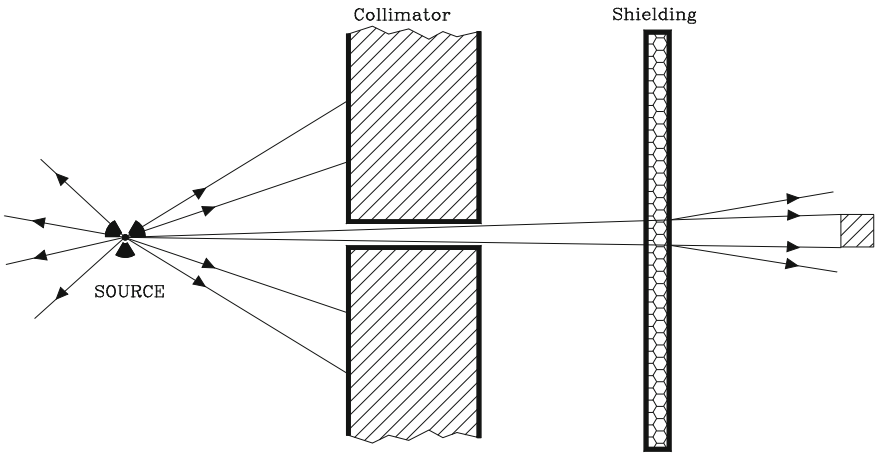

Fig. 5.3 Geometry of uncollided radiation

Chapter 2 shown that:

$$\Phi = \Phi_O \times \exp\left(-\left(\frac{\mu}{\rho}\right)\rho x\right)$$

Chapter 3 shown that the equivalent dose depends on the fluence rate and the conversion factor "fluence/dose equivalent"; therefore the evolution of dose equivalent rate as a function of thickness through shielding is deduced from (5.4).

$$\dot{H} = \dot{\Phi} h_\Phi \exp\left(-\frac{\mu}{\rho}(\rho x)\right) \tag{5.4}$$

For an isotropic point-source at a distance d (in cm) behind a thick shielding, the evolution of the dose equivalent rate according to equation is (5.5).

$$\dot{H} = \frac{\dot{N}}{4\pi d^2} h_\Phi \exp\left(-\frac{\mu}{\rho}(\rho x)\right) \tag{5.5}$$

Note that for a line spectra, the contribution of each one to the equivalent dose is summed according to (5.6).

$$\dot{H} = \frac{1}{4\pi d^2} \sum_{E_i} h_{E_i,\Phi} \dot{N}_{E_i} \exp\left(-\frac{\mu_{E_i}}{\rho}(\rho x)\right) \tag{5.6}$$

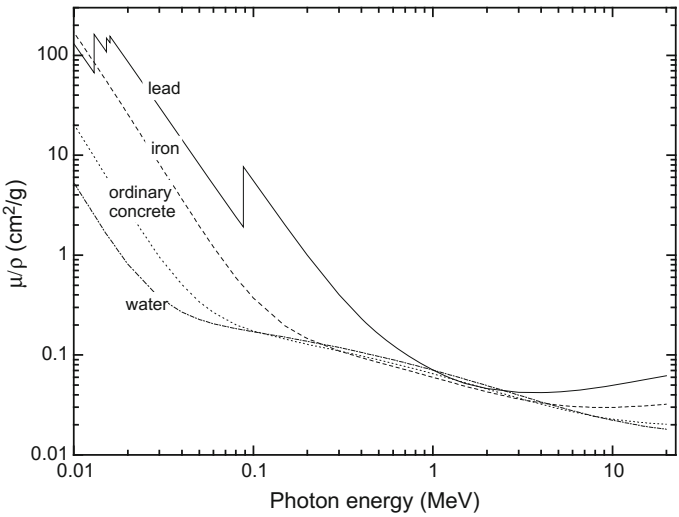

Fig. 5.4 Mass attenuation coefficients as a function of photon energy for the iron, lead, water and concrete (data from [8])

Considering the ambient dose equivalent rate at 1 m from the source, $H_0^*(10)$, we deduce from (5.2) the dose equivalent rate at a distance d (in meters) behind a shielding with a thickness x (in cm) with (5.7).

$$\dot{H}^*(10) = \frac{\dot{H}_0^*(10)}{d^2} \exp\left(-\frac{\mu}{\rho}(\rho x)\right) \tag{5.7}$$

The mass attenuation coefficients values are tabulated by Hubbell and Seltzer [8], in terms of energy for atomic numbers from 1 to 92 and different materials. Remind that Table 2.6 provides the values for a number of chemical elements and compounds. The mass attenuation coefficients of lead, iron, concrete and water are plotted in Fig. 5.4 for energies between 10 keV and 20 MeV.

For non-tabulated value, it is possible to evaluate this parameter by interpolation with the formula (5.8).

$$\frac{\mu}{\rho} = \frac{A_1 \frac{\mu_1}{\rho_1}(Z_2 - Z) + A_2 \frac{\mu_2}{\rho_2}(Z - Z_1)}{A(Z_2 - Z_1)} \tag{5.8}$$

A and Z are the mass and the atomic number of the non-tabulated element, Z_1 and Z_2 the atomic numbers of the elements closest tabulated and framing Z, A_1 and A_2 the atomic masses of the atomic numbers of elements Z_1 and Z_2.

For a mixture, remember that the formula (2.48) of Chap. 2 applies.

For example, let us calculate the linear coefficient for photons of 1 MeV for water. The linear coefficients of Table 5.1 are obtained according to [8].

Table 5.1 Mass attenuation coefficient for hydrogen and oxygen

H	$1.263 \cdot 10^{-1}$ cm^2 g^{-1}
O	$6.372 \cdot 10^{-2}$ cm^2 g^{-1}

Considering the mass fractions of hydrogen and oxygen in a mole of (H_2O): $w_O = 16/18$ and $w_H = 2/18$, we obtain

$$\frac{\mu}{\rho} = \left(\frac{16}{18}\right) \times \left(6.372 \cdot 10^{-2}\right) + \left(\frac{2}{18}\right) \times \left(1.263 \cdot 10^{-1}\right) = 7.07 \cdot 10^{-2}\,\mathrm{cm}^2\,\mathrm{g}^{-1}$$

We can also express the relationship (5.7) in another form, using the "half value layer (HVL)" $x_{1/2}$ or "tenth value layer (TVL)" $x_{1/10}$, meaning the thickness which decrease the initial dose rate respectively by a factor 2 or 10 according to the expression (5.9).

$$\dot{H}^*(10) = \frac{H_0^*(10)}{d^2} \times 10^{-\frac{x}{x_{1/10}}} = \frac{H_0^*(10)}{d^2} \times 2^{-\frac{x}{x_{1/2}}} \tag{5.9}$$

which amounts to the following expressions:

$$x_{1/10} = \frac{\ln 10}{\mu} \quad \text{and} \quad x_{1/2} = \frac{\ln 2}{\mu}$$
$$\text{and} \quad x_{1/2} \cong 0.3 x_{1/10}$$

The TVL as function of incident photons energy exist in publications for several materials. For radionuclides emitting line spectra, it will be more convenient to use the TVL of the radionuclide. These datas are available (e.g. Delacroix et al. [2]). Table 5.2 provides a few TVL of lead and steel, from [2] to some radionuclides.

5.4.2 *Primary Shielding Calculation, the Case of Broad Beam*

The case of broad beam is the most frequent in the field of radiation protection. Photons scattered by Compton effect, in particular, have a probability of scattering

Table 5.2 TVL (in cm) for a few radionuclides, adapted [2]

RN	TVL (in cm)			
	Lead	Steel	Water	Concrete
Na 22	3.6	7.9	35.4	15
I 131	1.1	5.8	23	15.3
Co 60	4.5	8.9	38.3	20.3
Cs-137 (Ba 137 m)	2.4	7.2	27	16.3

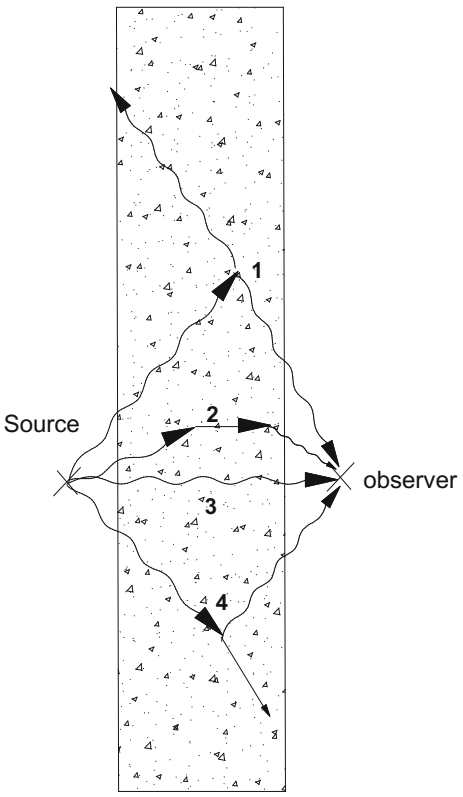

Fig. 5.5 Non-collimated geometry showing the contribution of primary and scattered radiation dose rate at the point observer—examples of interactions: *1* materialization followed by emission of two photons of 511 keV due to positron; *2* photoelectric effect followed by a deexcitation photon from the photoelectron; *3* photons with no interaction; *4* Compton effect

towards the observer thereby increasing the number of photons, and accordingly the fluence. It should, therefore, take into account the scattered photons in the shielding (Fig. 5.5).

To quantitatively illustrate the scattering of photons in the material, 0.1, 1 and 10 MeV photon transport was simulated in water and lead by the Monte Carlo code MCNPX. A graphical display of the scattering phenomenon is given in Fig. 5.6. Take care in these figures, the scales between the different simulations are not comparable.

In figures when comparing the photons path in the primary beam direction (vertical Y axis in the figure) with respect to the scattered photons, the second is almost isotropic at low energy (0.1 MeV case) and become dominant to the primary beam axis at higher energy. The distribution was primarily due to the Compton effect. However, the differential cross section of Klein and Nishina [9] shows that the angular distribution of photons scattered by Compton effect is especially significant in the primary beam axis with high energy beam (see Chap. 2).

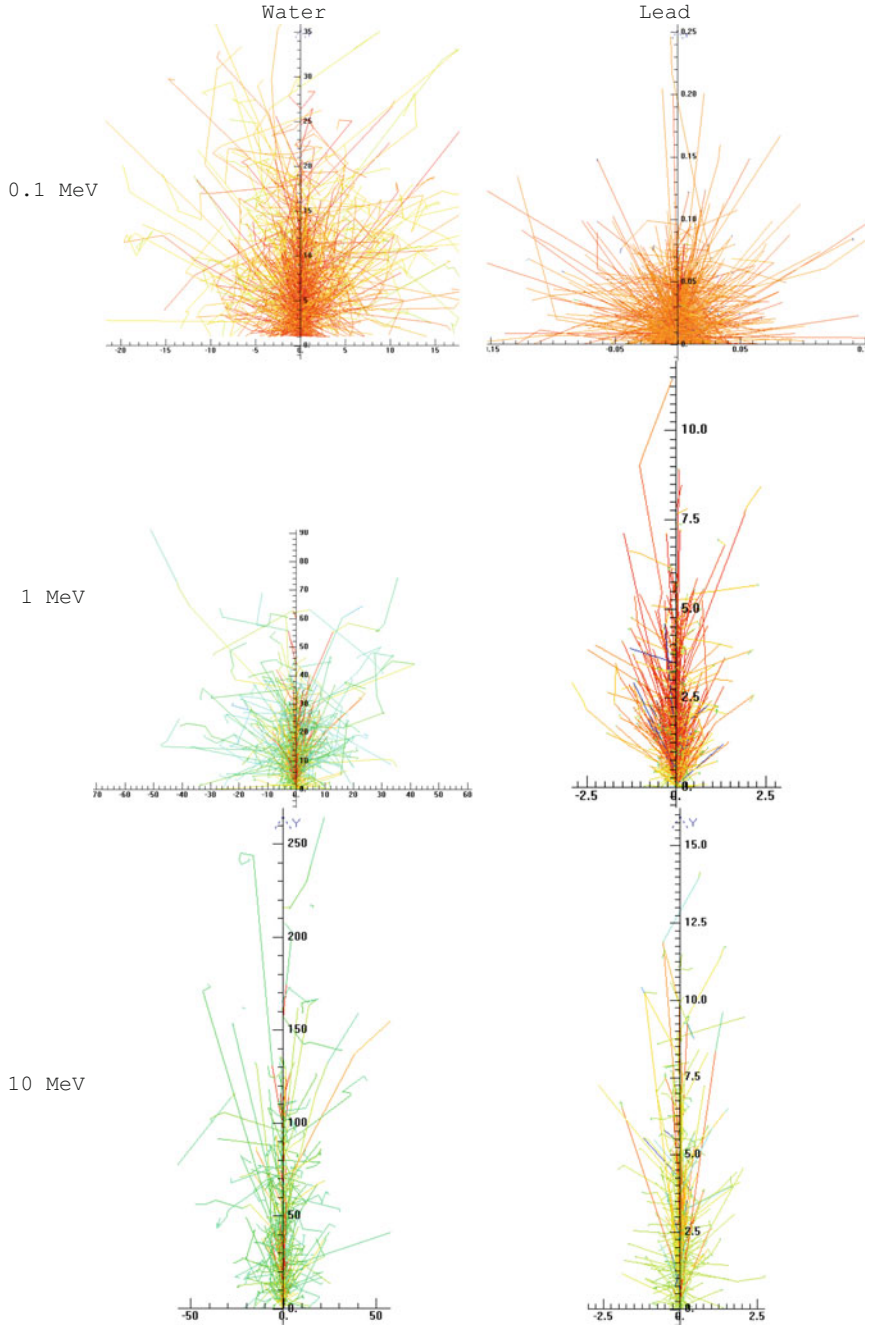

Fig. 5.6 Monte-Carlo simulation of 0.1, 1 and 10 MeV photon transport in lead and water

Calculation of primary shielding with the buildup method

Increasing the number of photons due to scattering increases the fluence and therefore the dose at the observation point. Thus, to estimate the dose equivalent behind protection, (5.5) is not sufficient to take into account photons scattering in the shielding for this increased dose. To maintain simple mathematical relationships for the dose behind shielding, the "build-up factor" was used from 1950 by White [10]. Thus, attenuation is not a pure exponential function, but must be corrected by a multiplication factor B called "*build-up factor*". The build-up is generally dependent on the number of mean free paths, also called "relaxation lengths" (μx), the energy and the shielding thickness. By combining the (5.5) with the increase due to the build-up, the equivalent dose rates in broad beam is obtain for an isotropic point source at a distance d (cm) according to (5.10) for one photon and (5.11) a multi-ray transmission.

$$\dot{H} = \frac{\dot{N}}{4\pi d^2} h_{\Phi} \mathrm{B}(\mu \mathrm{x}, \mathrm{E}) \exp\left(-\frac{\mu}{\rho}(\rho x)\right) \tag{5.10}$$

$$\dot{H} = \frac{1}{4\pi d^2} \times \sum_{E_i} h_{\Phi E_i} \dot{N}_{E_i} \mathrm{B}(\mu_{\mathrm{E_i}} \mathrm{x}, \mathrm{E_i}) \exp\left(-\left(\frac{\mu}{\rho}\right)_{E_i}(\rho x)\right) \tag{5.11}$$

For an isotropic point source at a distance d (in meters) behind a shielding layer x, density ρ, a mass attenuation μ/ρ (5.7) must be completed with the build-up factor B to obtain the dose equivalent rate from (5.12). $\dot{H}_0^*(10)$ is the dose equivalent rate at 1 m unshielded.

$$\dot{\mathrm{H}}^*(10) = \frac{\mathrm{H}_0^*(10)}{\mathrm{d}^2} \times \mathrm{B}(\mu \mathrm{x}, \mathrm{E}) \times \exp\left(-(\mu/\rho)_E \rho \mathrm{x}\right) \tag{5.12}$$

Initially, the build-up was assessed using a Geiger-Müller counter [10]. Since then, many studies have been conducted to calculate this factor. Tanika et al. [11] have identified 51 publications concerning the build-up between 1950 and 1988. If until the 1970s the build-up was estimated by taking into account the Compton scattering in the shielding, calculation methods evolving especially with Monte-Carlo codes, the build-up estimated from the 1980s include all interactions.

Note that, strictly speaking, the build-up factor $B(\mu x, E)$ is dependent on the source-detector distance, the source geometry, and the shielding geometry. In practice, most of these factors are tabulated for the worst case, it means for a source-detector distance equal to the thickness of protection, a point source and an infinite shielding height. It is therefore appropriate to draw reader's attention to the approach limitations: it does not always reflect an accurate characterization of the scattered component, in particular for small dimensions shielding.

Table 5.3 Buildup factors for various energies and materials depending on the number of the MFP, adapted [12]

Material	MeV	MFP									
		0.5	1	2	3	4	5	6	7	8	10
Water	0.1	2.37	4.55	11.8	23.8	41.3	65.2	96.7	137	187	321
	0.2	1.92	3.42	8.31	16	27	42.2	62.5	88.5	121	208
	0.5	1.6	2.44	4.88	8.35	12.8	18.4	25	32.7	41.5	62.9
	1	1.47	2.08	3.62	5.5	7.68	10.1	12.8	15.8	19	26.1
	2	1.38	1.83	2.81	3.87	4.98	6.15	7.38	8.65	9.97	12.7
	5	1.28	1.56	2.08	2.58	3.08	3.58	4.08	4.58	5.07	6.05
	10	1.2	1.37	1.68	1.97	2.25	2.53	2.8	3.07	3.34	3.86
Concrete	0.1	1.89	2.78	4.63	6.63	8.8	11.1	13.6	16.3	19.2	25.6
	0.2	1.78	2.72	5.05	8	11.6	15.9	20.9	26.7	33.4	49.6
	0.5	1.57	2.27	4.03	6.26	8.97	12.2	15.9	20.2	25	36.4
	1	1.45	1.98	3.24	4.72	6.42	8.33	10.4	12.7	15.2	20.7
	2	1.37	1.77	2.65	3.6	4.61	5.68	6.8	7.97	9.18	11.7
	5	1.27	1.53	2.04	2.53	3.03	3.54	4.05	4.57	5.09	6.15
	10	1.19	1.35	1.64	1.93	2.22	2.51	2.8	3.1	3.4	4.01
Lead	0.1	1.51	2.04	3.39	5.6	9.59	17	30.6	54.9	94.7	294
	0.12	1.38	1.7	2.36	3.13	4.19	5.71	7.9	11.2	15.8	32.1
	0.14	1.28	1.48	1.77	1.98	2.1	2.4	2.62	2.87	3.18	3.99
	0.5	1.14	1.24	1.39	1.52	1.62	1.71	1.8	1.88	1.95	2.1
	1	1.2	1.38	1.68	1.95	2.19	2.43	2.66	2.89	3.1	3.51
	2	1.21	1.4	1.76	2.14	2.52	2.91	3.32	3.74	4.17	5.07
	5	1.25	1.41	1.71	2.05	2.44	2.88	3.38	3.93	4.56	6.03
	10	1.28	1.51	2.01	2.63	3.42	4.45	5.73	7.37	9.44	15.4

There are a lot references to build-up tabulated values in the publications, such as ANSI standard [12]. These factors are shown for various materials, for 15 keV–15 MeV photon energies and 0.5–40 mean free path.

For example, Table 5.3 taken from this standard provides, the build-up in terms of energy and the value of the number of mean free path (MFP) (μx) for different materials (water, concrete, lead).

Figure 5.7 provides the buildup curves in water and lead to the energy 0.1, 1 and 10 MeV.

Note that for water, the build-up is all the more important that energy is low. This is consistent with the teachings of Fig. 5.6 showing that the scattering is greater at low energy. For lead, this finding is not verified for 1 and 10 MeV. This is due to the high attenuation of lead which disadvantages the scattering outside the primary beam.

Furthermore tabulated values, analytical expressions buildup from interpolation of various tables exist in publications. The interest of these expressions is their ease of use, especially through numerical deterministic methods.

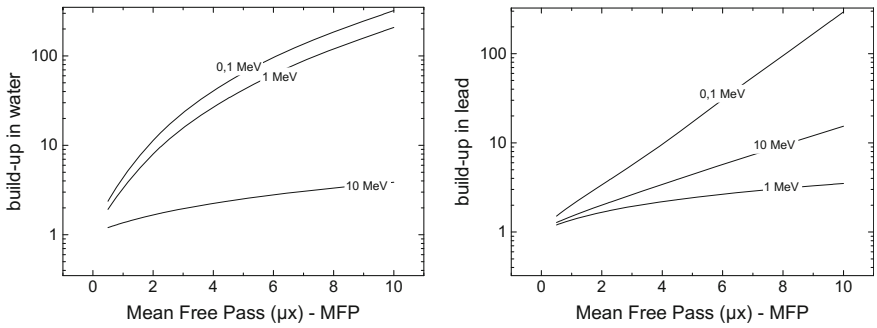

Fig. 5.7 Build-up in water and the lead for 0.1, 1 and 10 MeV (data from [12])

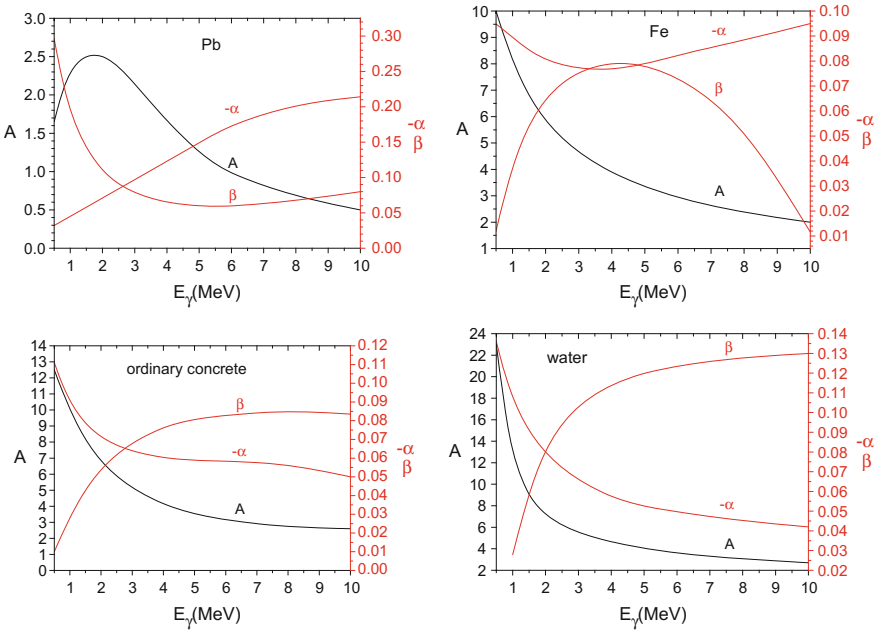

Fig. 5.8 Coefficients A, α and β expression Taylor for lead, iron, water and concrete ordinary function of the energy of the incident photons (data from [13])

One of these expressions used is the Taylor buildup given by (5.13).

$$B(\mu x) = Ae^{-\alpha\mu x} + (1 - A)e^{-\beta\mu x} \tag{5.13}$$

These coefficients are available in [12]. An example of values of A, α and β for lead, iron, water and ordinary concrete is plotted in Fig. 5.8 as a function of the energy of the incident photons.

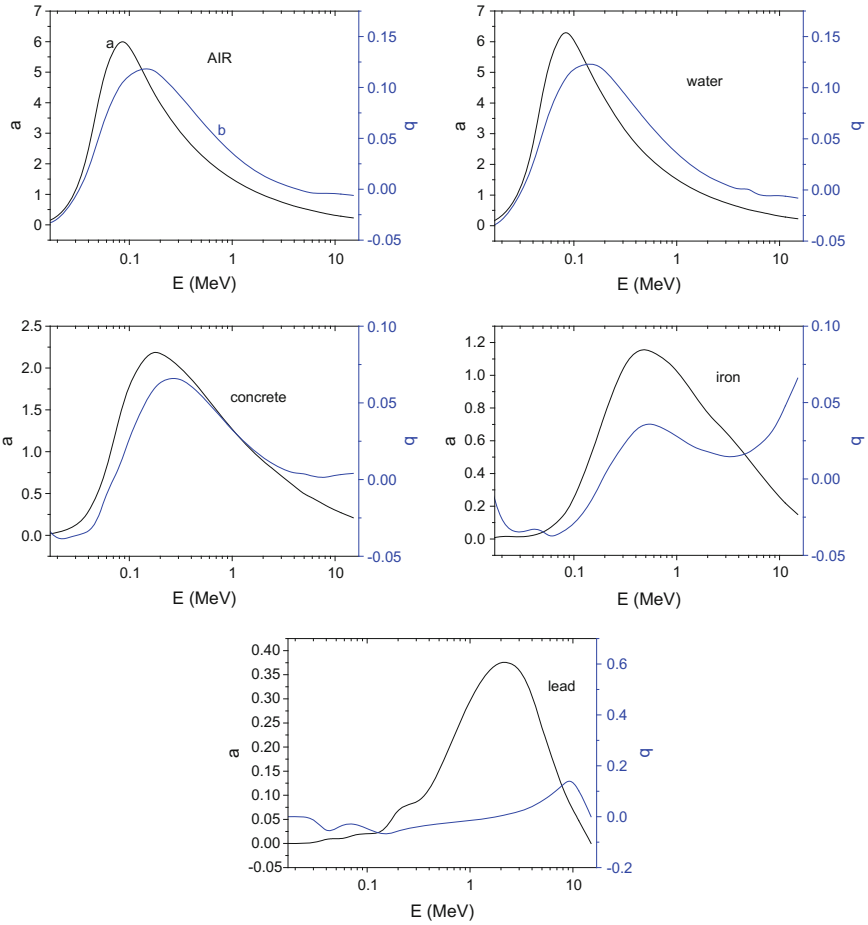

Fig. 5.9 Coefficients *a* and *b* expression Berger for air, lead, iron, water and the ordinary concrete function of the energy of the incident photons (data from [14])

Another analytical approach led to Berger build-up expressions according to (5.14).

$$B(\mu x) = 1 + a\mu x \exp(b\mu x) \tag{5.14}$$

The *a* and *b* values for air, lead, iron, water and ordinary concrete are plotted in terms of the incident photons energy in Fig. 5.9.

For a non-tabulated material of *Z* atomic number the build-up can be assessed by linear interpolation based on atomic numbers according to (5.15).

$$B(Z) = \frac{B(Z_2)(Z - Z_1) + B(Z_1)(Z_2 - Z)}{Z_2 - Z_1} avec\, Z_1 < Z < Z_2 \qquad (5.15)$$

Z_1 and Z_2 are the atomic numbers of the tabulated components whose values are closest to Z.

For example, calculate the dose equivalent rate for an observer located 5 m to a 10 TBq source of ^{60}Co behind a shielding of 1 m of ordinary concrete of density: 2.3 g cm^{-3}.

According to Chap. 4, the equivalent dose rate to 1 m from a ^{60}Co source is 0. 351 mSv h^{-1} GBq^{-1}. Thus, for 10 TBq: $\dot{H}_0^*(10) = 3.51\,\mathrm{Sv\,h^{-1}}$.

To calculate the build-up and the mass attenuation coefficient, a 1.25 MeV photon is considered for ^{60}Co.

The mass attenuation coefficient for 1.25 MeV photon is 5.807 $\cdot 10^{-2}$ cm^2 g^{-1} for the concrete [8].

Figure 5.9 provides, for 1.25 MeV photons and concrete, the following parameters for the calculation of the build-up of Berger: a = 1.14; b = 0.025 then:

$$\begin{aligned} B(\mu x) &= 1 + a\mu x \exp(b\mu x) \\ &= 1 + 1.14 \times 0.05807 \times 2.3 \times 100 \times \exp(0.025 \times 0.05807 \times 2.3 \times 100) = 22 \end{aligned}$$

It therefore comes from (5.12):

$$\begin{aligned} \dot{H}^*(10) &= \frac{H_0^*(10)}{d^2} B(\mu x, E) \exp\left(-(\mu/\rho)_E \rho x\right) \\ &= \frac{3.51}{5^2} \times 22 \times \exp(-0.05807 \times 2.3 \times 100) = 5\,\mu\mathrm{Sv\,h^{-1}} \end{aligned}$$

Note that the build-up calculation for slabs is quite complex: the spectrum is modified in the first shield before releasing the second. Nevertheless, expressions are available to calculating the build-up composed by two Z different slab as presented in Fig. 5.10.

Shultis and Faw [15] propose for this two slabs the build-up expression (5.16).

$$B(\mu_1 x_1, \mu_2 x_2) = B_1(\mu_1 x_1) + [B_2(\mu_1 x_1 + \mu_2 x_2) - B_2(\mu_1 x_1)] \qquad (5.16)$$

with B_1 the Z_1 material build-up and B_2 the Z_2 material build-up.

To illustrate this feature, calculate the dose equivalent rate at 1 m from a 1 MeV photon source and $3.7 \cdot 10^{10}$ (γ) s^{-1} behind a first 1 cm thick lead shielding (density 10.8) and a second of 10 cm thick of water.

For the first material (lead), the mass attenuation coefficients and the relaxation lengths number are [8]:

$$\begin{aligned} &\mu_1/\rho_1 = 7.102 \cdot 10^{-2}\,\mathrm{cm^2/g} \quad \text{also} \\ &\mu_1 x_1 = \mu_1/\rho_1 \times \rho_1 x_1 = 7.102 \cdot 10^{-02} \times 10.8 \times 1 = 0.767 \end{aligned}$$

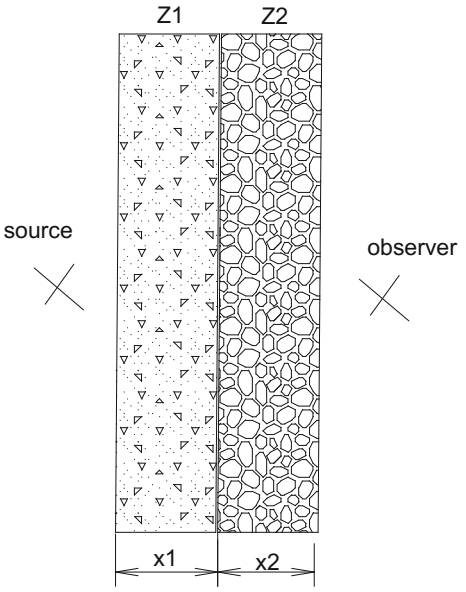

Fig. 5.10 Schematic view of the geometry for two shielding slabs

For water:

$$\mu_2/\rho_2 = 7.072 \cdot 10^{-2}\,\mathrm{cm}^2/\mathrm{g} \quad \text{and}$$
$$\mu_2 x_2 = \mu_2/\rho_2 \times \rho_2 \times x_2 = 7.072 \cdot 10^{-02} \times 1 \times 10 = 0.7072$$

For 1 MeV photons, the Berger build-up parameters are given in Table 5.4. So, the result for the (5.16) is for:

$$\begin{aligned} B(\mu_1 x_1, \mu_2 x_2) &= B_1(\mu_1 x_1) + [B_2(\mu_1 x_1 + \mu_2 x_2) - B_2(\mu_1 x_1)] \\ &= B_{lead}(0.767) + [B_{water}(1.4742) - B_{water}(0.7072)] = 2.45 \end{aligned}$$

From (5.10) is deduced:

$$\begin{aligned} \dot{H}^*(10) &= \frac{\dot{N}}{4\pi d^2} h^*_\Phi(10)\mathrm{B}(\mu_1 \mathrm{x}_1, \mu_2 \mathrm{x}_2, \mathrm{E}) \times \exp\left(-\left[\left(\frac{\mu_{lead}}{\rho_{lead}}(\rho_{lead} x_{lead})\right) + \left(\frac{\mu_{water}}{\rho_{water}}(\rho_{water} x_{water})\right)\right]\right) \\ &= \frac{3.7 \cdot 10^{10} \times 3600}{4 \times \pi \times 100^2} \times 5.2 \times 10^{-12} \times 2.45 \times \exp(-0.767 - 0.7072) = 3\,\mathrm{mSv\,h^{-1}} \end{aligned}$$

Note that a calculation using a Monte Carlo code gives 2.45 mSv h^{-1}.

Table 5.4 *a* and *b* Berger factors for the calculation of the lead and water build-up

	a	*b*
Lead (material 1)	0.3	−0.015
Water (material 2)	1.27	0.032

Let us proceed to the shielding inversion for the previous example and calculate the dose equivalent rate at 1 m from a 1 MeV photon source and $3.7 \cdot 10^{10}$ (γ) s^{-1} behind a first 10 cm thick water shielding and then a second of 1 cm thick of lead. For (5.16). The datas give (the mass attenuation values and parameters for the calculation of Berger's build-up are identical to the previous example):

$$\begin{aligned} B(\mu_1 \times x_1, \mu_2 \times x_2) &= B_1(\mu_1 \times x_1) + [B_2(\mu_1 \times x_1 + \mu_2 \times x_2) - B_2(\mu_1 \times x_1)] \\ &= B_{water}(0.7072) + [B_{lead}(1.4742) - B_{lead}(0.767)] = 2.3 \end{aligned}$$

From (5.10) we have:

$$\begin{aligned} \dot{H} &= \frac{\dot{N}}{4 \times \pi \times d^2} \times h_\varphi \times \mathrm{B}(\mu_1 \mathrm{x}_1, \mu_2 \mathrm{x}_2, \mathrm{E}, \mathrm{shield}) \times \exp\left(-\left[\left(\frac{\mu_{lead}}{\rho_{lead}} \times (\rho_{lead} \times x_{lead})\right) + \left(\frac{\mu_{water}}{\rho_{water}} \times (\rho_{water} \times x_{water})\right)\right]\right) \\ &= \frac{3.7 \cdot 10^{10} \times 3600}{4 \times \pi \times 100^2} \times 5.2 \times 10^{-12} \times 2.3 \times \exp(-0.767 - 0.7072) = 2.7 \ \mathrm{mSv\,h^{-1}} \end{aligned}$$

The Monte Carlo calculation gives 2.15 mSv h^{-1}.

Calculating the primary shielding with the transmission factors.
From a practical point of view, it is common to use the transmission factor T in broad beams, which is defined as $B(x)$ multiplied by $e^{-\mu x}$. Thus (5.12) can be changed into (5.17). The transmission value allows a quick calculation of a shielding thickness.

$$\dot{\mathrm{H}}^*(10) = \frac{\mathrm{H}_0^*(10)}{\mathrm{d}^2} \times \mathrm{T}(\mu \mathrm{x}, \mathrm{E}) \tag{5.17}$$

This factor T is defined in terms of energy and shielding nature. The curves showing the transmission as a function of the thickness of materials for radionuclides or function of energy for concrete or lead, are provided in Figs. 5.11 and 5.12. They were achieved using the software Microshield [16].

It is interesting to amphasize that the shoulder in the first part of the curve is the result of the build-up; without this factor, the curve would be a straight line.

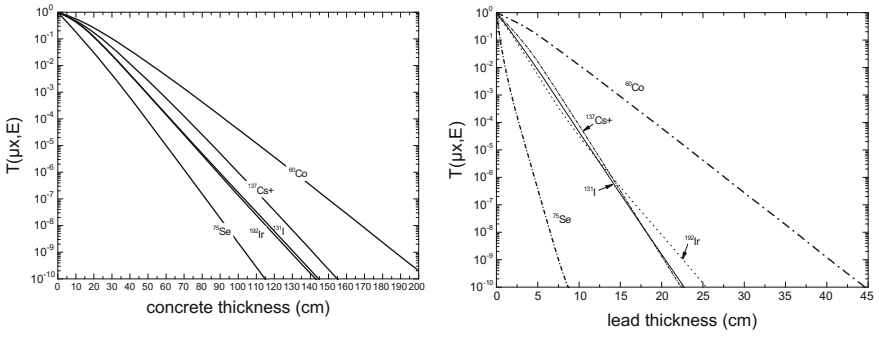

Fig. 5.11 Transmission factors $T(\mu x, E)$ in ordinary concrete and lead for five radionuclides

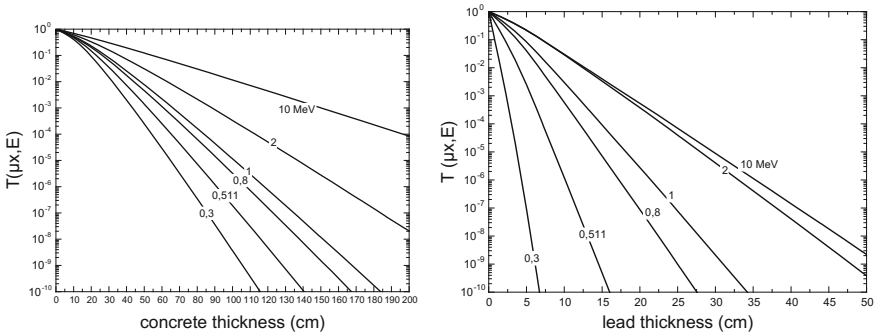

Fig. 5.12 Transmission factors $T(\mu x, E)$ in ordinary concrete and lead to different energies

To illustrate the direct use of transmission, let us calculate the shielding thickness in ordinary concrete (density 2.3) for an ambient dose equivalent rate of 5 mSv h^{-1} for an observer located 5 m to a 10 TBq Co-60 source.

According to Chap. 4, the ambient dose equivalent rate to 1 m from a ^{60}Co source is 0.351 mSv h^{-1} GBq^{-1}. Thus, for 10 TBq, the result is $H_0^*(10) = 3.51\,\mathrm{Sv\,h^{-1}}$.

According to (5.17), the searched transmission factor is

$$\mathrm{T}(\mu x, \mathrm{E}) = \frac{\dot{\mathrm{H}}^*(10) \times \mathrm{d}^2}{\mathrm{H}_0^*(10)} = \frac{5 \cdot 10^{-6} \times 5^2}{3.51} = 3.5 \cdot 10^{-5}$$

From Fig. 5.11 for such transmission, we must interpose a 100 cm thick shielding of ordinary concrete.

Transmission factor for a bremsstrahlung spectrum (X ray generator)
For bremsstrahlung photon spectrum derived from 25 to 150 keV electrons in a conversion target (case of X ray generator), NCRP [17] gives a parametric approach (5.18) for calculating the transmission (Fig. 5.13).

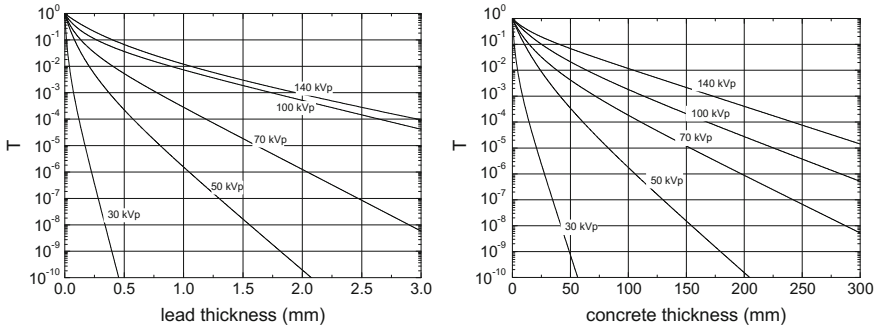

Fig. 5.13 Transmission curves obtained with the NCRP method [17], with (5.18) for lead and concrete

$$T = \left[\left(1 + \frac{\beta}{\alpha}\right) \exp(\alpha\gamma x) - \frac{\beta}{\alpha}\right]^{-\frac{1}{\gamma}} \tag{5.18}$$

Note that the expression (5.19) providing the thickness x can be deduced from (5.18). The settings α, β, γ are given in Table 5.5.

$$x = \frac{1}{\alpha\gamma} \times \ln\left[\frac{T^{-\gamma} + \frac{\beta}{\alpha}}{1 + \frac{\beta}{\alpha}}\right] \tag{5.19}$$

For example, let us calculate the lead thickness required to obtain an ambient dose equivalent rate of 0.5 μSv/h at 1.5 m, for X-ray 50 kV and 5 mA generators with a tungsten anode and a 1 mm thick aluminum filtration.

Chapter 4 provides $\dot{H}^*(10) = 4.35\,\mathrm{mSv/min/mA}$ for this type of X ray generator, to 1 m either to 5 mA and 1.5 m:

$\dot{H}^*(10) = 5 \times 4.35 \times 60 \times \left(\frac{1}{1.5}\right)^2 = 580\ \mathrm{mSv/h}$ from where $T = \frac{0.5 \cdot 10^{-6}}{580 \cdot 10^{-3}} = 8.6 \cdot 10^{-7}$

And

$$x = \frac{1}{\alpha\gamma} \times \ln\left[\frac{T^{-\gamma} + \frac{\beta}{\alpha}}{1 + \frac{\beta}{\alpha}}\right] = \frac{1}{8.801 \times 0.2957} \times \ln\left[\frac{(8.6 \cdot 10^{-7})^{-0.2957} + \frac{27.28}{8.801}}{1 + \frac{27.28}{8.801}}\right] = 1.1\,\mathrm{mm}$$

A lead layer of 1.1 mm cause the ambient dose equivalent rate of 0.5 μSv/h at 1.5 m for an 50 kV and 5 mA X-ray generator with a tungsten anode and a 1 mm aluminum thick filtration.

Transmission factor for a bremsstrahlung spectrum (Electron accelerator)
Transmission factors curves are plotted in Fig. 5.15. For higher electron énergies, photons emitted by bremsstrahlung (case of electron accelerators). They are given for the concrete, iron and lead for 1–100 MeV electron energies (E_0 on the curve[1]).

The view of the calculation geometry is shown in Fig. 5.14. It should be noted that the curves of Fig. 5.15 are valid in forward direction. For 90°, the curve corresponding to E_0 electron must not be choosen but use the 2/3 E_0 energy electron curve [18] in order to take into account the difference of spectrum for both directions.

For example, let us calculate the dose equivalent rate due to bremsstrahlung produced by interaction of a 20 MeV an 10 μA electron beam on a thick target to

[1]Strictly speaking, this should be noted "T_0". Nevertheless, the literature prefers the term E_0 that we retain in this section.

Table 5.5 Values of parameters used in (5.18) and (5.19). *Note* between 25 and 35 kVp molybdenum anode, all other tungsten anode for data (after [17], with the permission of the National Council Radiation Protection and Measurements, http://NCRPpublications.org)

kVp	Lead			Concrete			Plaster		
	α (mm^{-1})	β (mm^{-1})	γ	α (mm^{-1})	β (mm^{-1})	γ	α (mm^{-1})	β (mm^{-1})	γ
25	$4.952 \cdot 10^{1}$	$1.94 \cdot 10^{2}$	$3.037 \cdot 10^{-1}$	$3.904 \cdot 10^{-1}$	1.645	$2.757 \cdot 10^{-1}$	$1.576 \cdot 10^{-1}$	$7.175 \cdot 10^{-1}$	$3.048 \cdot 10^{-1}$
30	$3.88 \cdot 10^{1}$	$1.78 \cdot 10^{2}$	$3.473 \cdot 10^{-1}$	$3.173 \cdot 10^{-1}$	1.698	$3.593 \cdot 10^{-1}$	$1.208 \cdot 10^{-1}$	$7.043 \cdot 10^{-1}$	$3.613 \cdot 10^{-1}$
35	$2.955 \cdot 10^{1}$	$1.647 \cdot 10^{2}$	$3.948 \cdot 10^{-1}$	$2.528 \cdot 10^{-1}$	1.807	$4.648 \cdot 10^{-1}$	$8.878 \cdot 10^{-2}$	$6.988 \cdot 10^{-1}$	$4.245 \cdot 10^{-1}$
40				$1.297 \cdot 10^{-1}$	$1.78 \cdot 10^{-1}$	$2.189 \cdot 10^{-1}$			
45				$1.095 \cdot 10^{-1}$	$1.741 \cdot 10^{-1}$	$2.269 \cdot 10^{-1}$			
50	8.801	$2.728 \cdot 10^{1}$	$2.957 \cdot 10^{-1}$	$9.032 \cdot 10^{-2}$	$1.712 \cdot 10^{-1}$	$2.324 \cdot 10^{-1}$	$3.883 \cdot 10^{-2}$	8.73×10^{-2}	$5.105 \cdot 10^{-1}$
55	7.839	$2.592 \cdot 10^{1}$	$3.499 \cdot 10^{-1}$	$7.422 \cdot 10^{-2}$	$1.697 \cdot 10^{-1}$	$2.454 \cdot 10^{-1}$	$3.419 \cdot 10^{-2}$	8.315×10^{-2}	$5.606 \cdot 10^{-1}$
60	6.951	$2.489 \cdot 10^{1}$	$4.198 \cdot 10^{-1}$	$6.251 \cdot 10^{-2}$	$1.692 \cdot 10^{-1}$	$2.733 \cdot 10^{-1}$	$2.985 \cdot 10^{-2}$	$7.961 \cdot 10^{-2}$	$6.169 \cdot 10^{-1}$
65	6.13	$2.409 \cdot 10^{1}$	$5.019 \cdot 10^{-1}$	$5.528 \cdot 10^{-2}$	$1.696 \cdot 10^{-1}$	$3.217 \cdot 10^{-1}$	$2.609 \cdot 10^{-2}$	$7.597 \cdot 10^{-2}$	$6.756 \cdot 10^{-1}$
70	5.369	$2.349 \cdot 10^{1}$	$5.881 \cdot 10^{-1}$	$5.087 \cdot 10^{-2}$	$1.696 \cdot 10^{-1}$	$3.847 \cdot 10^{-1}$	$2.302 \cdot 10^{-2}$	$7.163 \cdot 10^{-2}$	$7.299 \cdot 10^{-1}$
75	4.666	$2.269 \cdot 10^{1}$	$6.618 \cdot 10^{-1}$	$4.797 \cdot 10^{-2}$	$1.663 \cdot 10^{-1}$	$4.492 \cdot 10^{-1}$	$2.066 \cdot 10^{-2}$	$6.649 \cdot 10^{-2}$	$7.75 \cdot 10^{-1}$
80	4.04	$2.169 \cdot 10^{1}$	$7.187 \cdot 10^{-1}$	$4.583 \cdot 10^{-2}$	$1.549 \cdot 10^{-1}$	$4.926 \cdot 10^{-1}$	$1.886 \cdot 10^{-2}$	$6.093 \cdot 10^{-2}$	$8.103 \cdot 10^{-1}$
85	3.504	$2.037 \cdot 10^{1}$	$7.55 \cdot 10^{-1}$	$4.398 \cdot 10^{-2}$	$1.348 \cdot 10^{-1}$	$4.943 \cdot 10^{-1}$	$1.746 \cdot 10^{-2}$	$5.558 \cdot 10^{-2}$	$8.392 \cdot 10^{-1}$
90	3.067	$1.883 \cdot 10^{1}$	$7.726 \cdot 10^{-1}$	$4.228 \cdot 10^{-2}$	$1.137 \cdot 10^{-1}$	$4.69 \cdot 10^{-1}$	$1.633 \cdot 10^{-2}$	$5.039 \cdot 10^{-2}$	$8.585 \cdot 10^{-1}$
95	2.731	$1.707 \cdot 10^{1}$	$7.714 \cdot 10^{-1}$	$4.068 \cdot 10^{-2}$	$9.705 \cdot 10^{-2}$	$4.406 \cdot 10^{-1}$	$1.543 \cdot 10^{-2}$	$4.571 \cdot 10^{-2}$	$8.763 \cdot 10^{-1}$
100	2.5	$1.528 \cdot 10^{1}$	$7.557 \cdot 10^{-1}$	$3.925 \cdot 10^{-2}$	$8.567 \cdot 10^{-2}$	$4.273 \cdot 10^{-1}$	$1.466 \cdot 10^{-2}$	$4.171 \cdot 10^{-2}$	$8.939 \cdot 10^{-1}$
105	2.364	$1.341 \cdot 10^{1}$	$7.239 \cdot 10^{-1}$	$3.808 \cdot 10^{-2}$	$7.862 \cdot 10^{-2}$	$4.394 \cdot 10^{-1}$	$1.397 \cdot 10^{-2}$	$3.815 \cdot 10^{-2}$	$9.08 \cdot 10^{-1}$
110	2.296	$1.17 \cdot 10^{1}$	$6.827 \cdot 10^{-1}$	$3.715 \cdot 10^{-2}$	$7.436 \cdot 10^{-2}$	$4.752 \cdot 10^{-1}$	$1.336 \cdot 10^{-2}$	$3.521 \cdot 10^{-2}$	$9.244 \cdot 10^{-1}$
115	2.265	$1.021 \cdot 10^{1}$	$6.363 \cdot 10^{-1}$	$3.636 \cdot 10^{-2}$	$7.201 \cdot 10^{-2}$	$5.319 \cdot 10^{-1}$	$1.283 \cdot 10^{-2}$	$3.271 \cdot 10^{-2}$	$9.423 \cdot 10^{-1}$
120	2.246	8.95	$5.873 \cdot 10^{-1}$	$3.566 \cdot 10^{-2}$	$7.109 \cdot 10^{-2}$	$6.073 \cdot 10^{-1}$	$1.235 \cdot 10^{-2}$	$3.047 \cdot 10^{-2}$	$9.566 \cdot 10^{-1}$
125	2.219	7.923	$5.386 \cdot 10^{-1}$	$3.502 \cdot 10^{-2}$	$7.113 \cdot 10^{-2}$	$6.974 \cdot 10^{-1}$	$1.192 \cdot 10^{-2}$	$2.863 \cdot 10^{-2}$	$9.684 \cdot 10^{-1}$
130	2.17	7.094	$4.909 \cdot 10^{-1}$	$3.445 \cdot 10^{-2}$	$7.16 \cdot 10^{-2}$	$7.969 \cdot 10^{-1}$	$1.155 \cdot 10^{-2}$	$2.702 \cdot 10^{-2}$	$9.802 \cdot 10^{-1}$

(continued)

Table 5.5 (continued)

kVp	Lead			Concrete			Plaster		
	α (mm^{-1})	β (mm^{-1})	γ	α (mm^{-1})	β (mm^{-1})	γ	α (mm^{-1})	β (mm^{-1})	γ
135	2.102	6.45	$4.469 \cdot 10^{-1}$	$3.394 \cdot 10^{-2}$	$7.263 \cdot 10^{-2}$	$9.099 \cdot 10^{-1}$	$1.122 \cdot 10^{-2}$	$2.561 \cdot 10^{-2}$	$9.901 \cdot 10^{-1}$
140	2.009	5.916	$4.018 \cdot 10^{-1}$	$3.345 \cdot 10^{-2}$	$7.476 \cdot 10^{-2}$	1.047	$1.088 \cdot 10^{-2}$	$2.436 \cdot 10^{-2}$	$9.964 \cdot 10^{-1}$
145	1.895	5.498	$3.58 \cdot 10^{-1}$	$3.296 \cdot 10^{-2}$	$7.875 \cdot 10^{-2}$	1.224	$1.056 \cdot 10^{-2}$	$2.313 \cdot 10^{-2}$	$9.987 \cdot 10^{-1}$
150	1.757	5.177	$3.156 \cdot 10^{-1}$	$3.243 \cdot 10^{-2}$	$8.599 \cdot 10^{-2}$	1.467	$1.03 \cdot 10^{-2}$	$2.198 \cdot 10^{-2}$	1.013
kVp	Steel			Glass			Wood		
	α (mm^{-1})	β (mm^{-1})	γ	α (mm^{-1})	β (mm^{-1})	γ	α (mm^{-1})	β (mm^{-1})	γ
25	9.364	$4.125 \cdot 10^{1}$	$3.202 \cdot 10^{-1}$	$3.804 \cdot 10^{-1}$	1.543	$2.869 \cdot 10^{-1}$	$2.23 \cdot 10^{-2}$	$4.34 \cdot 10^{-2}$	$1.937 \cdot 10^{-1}$
30	7.406	$4.193 \cdot 10^{1}$	$3.959 \cdot 10^{-1}$	$3.061 \cdot 10^{-1}$	1.599	$3.693 \cdot 10^{-1}$	$2.166 \cdot 10^{-2}$	$3.966 \cdot 10^{-2}$	$2.843 \cdot 10^{-1}$
35	5.716	$4.341 \cdot 10^{1}$	$4.857 \cdot 10^{-1}$	$2.396 \cdot 10^{-1}$	1.694	$4.683 \cdot 10^{-1}$	$1.901 \cdot 10^{-2}$	$3.873 \cdot 10^{-2}$	$3.732 \cdot 10^{-1}$
50	1.817	4.84	$4.021 \cdot 10^{-1}$	$9.721 \cdot 10^{-2}$	$1.799 \cdot 10^{-1}$	$4.912 \cdot 10^{-1}$	$1.076 \cdot 10^{-2}$	$1.862 \cdot 10^{-3}$	1.17
55	1.493	4.515	$4.293 \cdot 10^{-1}$	$8.552 \cdot 10^{-2}$	$1.661 \cdot 10^{-1}$	$5.112 \cdot 10^{-1}$	$1.012 \cdot 10^{-2}$	$1.404 \cdot 10^{-3}$	1.269
60	1.183	4.219	$4.571 \cdot 10^{-1}$	$7.452 \cdot 10^{-2}$	$1.539 \cdot 10^{-1}$	$5.304 \cdot 10^{-1}$	$9.512 \cdot 10^{-3}$	$9.672 \cdot 10^{-4}$	1.333
65	$9.172 \cdot 10^{-1}$	3.982	$4.922 \cdot 10^{-1}$	$6.514 \cdot 10^{-2}$	$1.443 \cdot 10^{-1}$	$5.582 \cdot 10^{-1}$	$8.99 \cdot 10^{-3}$	$6.47 \cdot 10^{-4}$	1.353
70	$7.149 \cdot 10^{-1}$	3.798	$5.378 \cdot 10^{-1}$	$5.791 \cdot 10^{-2}$	$1.357 \cdot 10^{-1}$	$5.967 \cdot 10^{-1}$	$8.55 \cdot 10^{-3}$	$5.39 \cdot 10^{-4}$	1.194
75	$5.793 \cdot 10^{-1}$	3.629	$5.908 \cdot 10^{-1}$	$5.291 \cdot 10^{-2}$	$1.28 \cdot 10^{-1}$	$6.478 \cdot 10^{-1}$	$8.203 \cdot 10^{-3}$	$6.421 \cdot 10^{-4}$	1.062
80	$4.921 \cdot 10^{-1}$	3.428	$6.427 \cdot 10^{-1}$	$4.955 \cdot 10^{-2}$	$1.208 \cdot 10^{-1}$	$7.097 \cdot 10^{-1}$	$7.903 \cdot 10^{-3}$	$8.64 \cdot 10^{-4}$	$9.703 \cdot 10^{-1}$
85	$4.355 \cdot 10^{-1}$	3.178	$6.861 \cdot 10^{-1}$	$4.721 \cdot 10^{-2}$	$1.14 \cdot 10^{-1}$	$7.786 \cdot 10^{-1}$	$7.686 \cdot 10^{-3}$	$1.056 \cdot 10^{-3}$	1.015
90	$3.971 \cdot 10^{-1}$	2.913	$7.204 \cdot 10^{-1}$	$4.55 \cdot 10^{-2}$	$1.077 \cdot 10^{-1}$	$8.522 \cdot 10^{-1}$	$7.511 \cdot 10^{-3}$	$1.159 \cdot 10^{-3}$	1.081
95	$3.681 \cdot 10^{-1}$	2.654	$7.461 \cdot 10^{-1}$	$4.41 \cdot 10^{-2}$	$1.013 \cdot 10^{-1}$	$9.222 \cdot 10^{-1}$	$7.345 \cdot 10^{-3}$	$1.133 \cdot 10^{-3}$	1.116
100	$3.415 \cdot 10^{-1}$	2.42	$7.645 \cdot 10^{-1}$	$4.278 \cdot 10^{-2}$	$9.466 \cdot 10^{-2}$	$9.791 \cdot 10^{-1}$	$7.23 \cdot 10^{-3}$	$9.343 \cdot 10^{-4}$	1.309
105	$3.135 \cdot 10^{-1}$	2.227	$7.788 \cdot 10^{-1}$	$4.143 \cdot 10^{-2}$	$8.751 \cdot 10^{-2}$	1.014	$7.05 \cdot 10^{-3}$	$6.199 \cdot 10^{-4}$	1.365
110	$2.849 \cdot 10^{-1}$	2.061	$7.897 \cdot 10^{-1}$	$4.008 \cdot 10^{-2}$	$8.047 \cdot 10^{-2}$	1.03	$6.921 \cdot 10^{-3}$	$1.976 \cdot 10^{-4}$	3.309
115	$2.579 \cdot 10^{-1}$	1.922	$8.008 \cdot 10^{-1}$	$3.878 \cdot 10^{-2}$	$7.394 \cdot 10^{-2}$	1.033	$6.864 \cdot 10^{-3}$	$-3.908 \cdot 10^{-4}$	$6.469 \cdot 10^{-1}$

(continued)

Table 5.5 (continued)

kVp	Steel			Glass			Wood		
	α (mm^{-1})	β (mm^{-1})	γ	α (mm^{-1})	β (mm^{-1})	γ	α (mm^{-1})	β (mm^{-1})	γ
120	$2.336 \cdot 10^{-1}$	1.797	$8.116 \cdot 10^{-1}$	$3.758 \cdot 10^{-2}$	$6.808 \cdot 10^{-2}$	1.031	$6.726 \cdot 10^{-3}$	$-8.308 \cdot 10^{-4}$	1.006
125	$2.13 \cdot 10^{-1}$	1.677	$8.217 \cdot 10^{-1}$	$3.652 \cdot 10^{-2}$	$6.304 \cdot 10^{-2}$	1.031	$6.584 \cdot 10^{-3}$	$-1.214 \cdot 10^{-3}$	1.192
130	$1.969 \cdot 10^{-1}$	1.557	$8.309 \cdot 10^{-1}$	$3.561 \cdot 10^{-2}$	$5.874 \cdot 10^{-2}$	1.037	$6.472 \cdot 10^{-3}$	$-1.539 \cdot 10^{-3}$	1.285
135	$1.838 \cdot 10^{-1}$	1.44	$8.391 \cdot 10^{-1}$	$3.481 \cdot 10^{-2}$	$5.519 \cdot 10^{-2}$	1.049	$6.306 \cdot 10^{-3}$	$-1.731 \cdot 10^{-3}$	1.465
140	$1.724 \cdot 10^{-1}$	1.328	$8.458 \cdot 10^{-1}$	$3.407 \cdot 10^{-2}$	$5.145 \cdot 10^{-2}$	1.057	$6.191 \cdot 10^{-3}$	$-1.849 \cdot 10^{-3}$	1.53
145	$1.616 \cdot 10^{-1}$	1.225	$8.519 \cdot 10^{-1}$	$3.336 \cdot 10^{-2}$	$4.795 \cdot 10^{-2}$	1.063	$6.115 \cdot 10^{-3}$	$-1.869 \cdot 10^{-3}$	1.498
150	$1.501 \cdot 10^{-1}$	1.132	$8.566 \cdot 10^{-1}$	$3.266 \cdot 10^{-2}$	$4.491 \cdot 10^{-2}$	1.073	$6.02 \cdot 10^{-3}$	$-1.752 \cdot 10^{-3}$	1.483

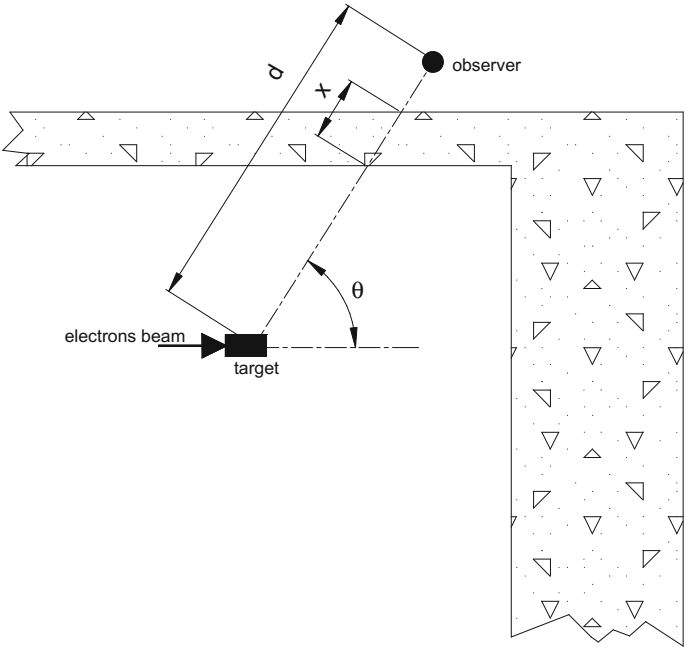

Fig. 5.14 Geometry for calculating the shielding around an electron accelerator

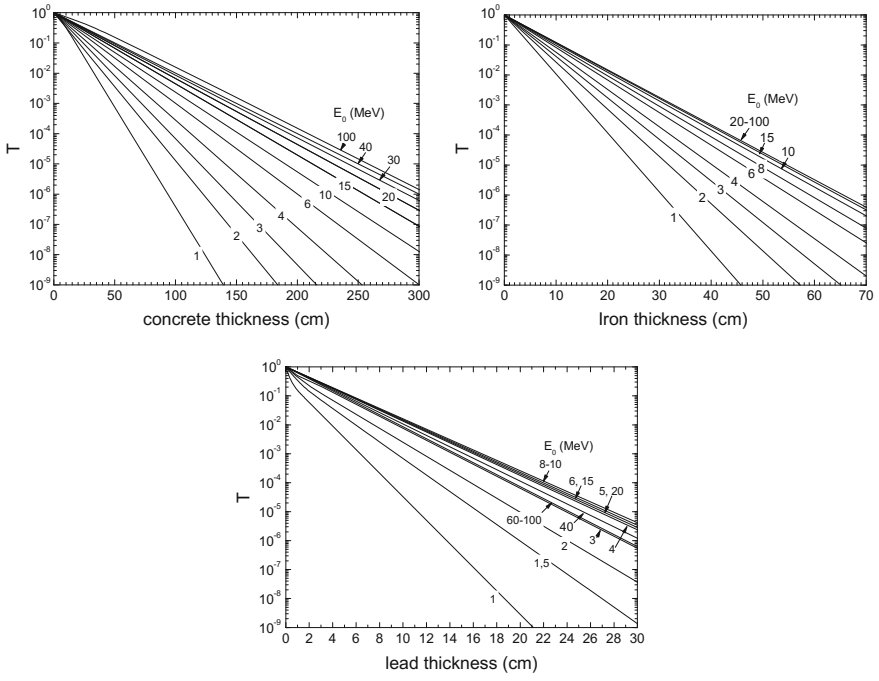

Fig. 5.15 Transmission factor for bremsstrahlung photons product in forward direction of an electron beam of energy E_0 in a thick target: **a** for ordinary concrete (density 2.35 g cm^{-3}); **b** steel (density 7.8 g cm^{-3}); **c** lead (density 11.35 g cm^{-3}) from [18], with the permission of the IAEA

an observer located 5 m behind a shielding of 100 cm of concrete. According to Chap. 4 (Fig. 4.23): $\dot{H}^*(10) = 100\,\mathrm{Sv\,h^{-1}\,\mu A^{-1}}$ at 1 m and in forward direction and 1.4 Sv h^{-1} μA^{-1} at 1 m and 90°. So for 10 μA it reaches 1000 Sv h^{-1} at 1 m and 0° and 14 Sv h^{-1} at 1 m and 90°. From Fig. 5.15, for 100 cm thick of concrete and in forward direction, the transmission is $T = 2 \cdot 10^{-3}$. At 90° on Fig. 5.15 an energy of $2/3E_0$ (E_0 = 20 MeV) is considered, therefore 13 MeV and the factor $T(\mu x, E) = 3 \cdot 10^{-3}$.

So we have from (5.17).

$$\text{At } 0°\ \dot{H}^*(10) = \frac{\dot{H}^*_0(10)}{d^2} \times T(\mu x, E) = \frac{1000}{5^2} \times 2 \cdot 10^{-3} = 8 \cdot 10^{-2}\,\mathrm{Sv\,h^{-1}}$$

$$\text{At } 90°\ \dot{H}^*(10) = \frac{\dot{H}^*_0(10)}{d^2} \times T(\mu x, E) = \frac{14}{5^2} \times 3 \cdot 10^{-3} = 1.7 \cdot 10^{-3}\,\mathrm{Sv\,h^{-1}}$$

Calculation of the dose rate behind a shielding for a volume source

In previous calculations, we considered point sources without self-attenuation. The aim now is to determine the dose equivalent rate behind shielding, with a volume source. It is therefore important to consider in the calculations of self-attenuation in the source, the attenuation in the shielding characterized by μ_2/ρ and the build-up factor generated in the source and the shielding. The schematic set-up view is represented in Fig. 5.16.

As for line or disk sources described in Chap. 1, it is necessary, to calculate the dose equivalent due to a volume source, to sample the source of infinitesimal

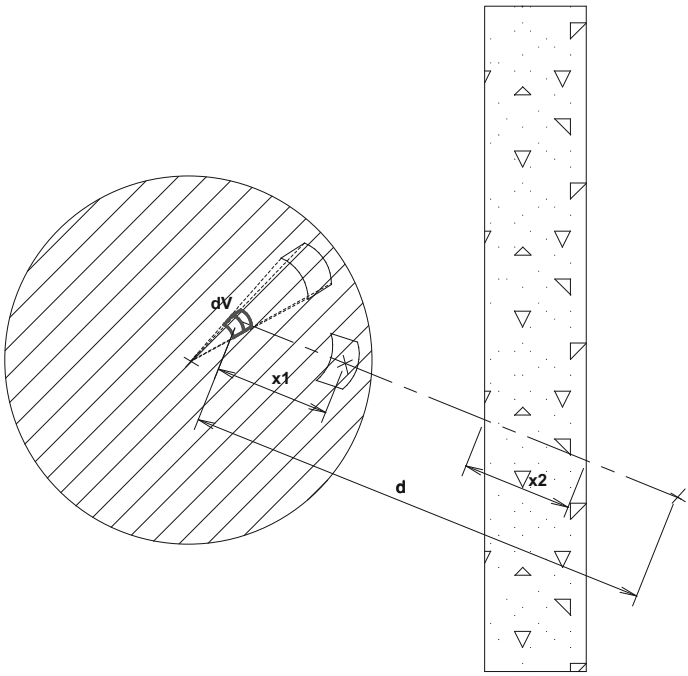

Fig. 5.16 Modelling of the dose rate calculation for a volume source behind a shielding

volume elements dV, punctual for the observer, and therefore to consider a volume flux density defined as:

$$n_{\mathrm{v}} = \frac{\dot{N}}{V}.$$

The element dV emitting $n_{\mathrm{V}}\mathrm{d}V$ particles in the whole space may be treated as a point; thus dose equivalent of each elementary volume is calculated according to (5.11):

$$d\dot{H} = \sum_{E_i} \frac{n_{\mathrm{v}} dV}{4\pi d^2} h_{E_i,\Phi} \left[\mathrm{B_i}\left(\mu_{1,E_i} \mathrm{x}_1; \mu_{2,E_i} x_2, \mathrm{E_i}\right) \times \exp\left(-\left(\frac{\mu}{\rho}\right)_{E_i} (\rho(x_1 + x_2)) \right) \right]$$

It is then necessary to integrated in the entire volume, which leads to formalism (5.20).

$$\dot{H} = \sum_i \iiint_V \frac{\dot{N}/V}{4\pi d^2} h_{E_i,\Phi} \mathrm{B_{E_i}}\left(\mu_{1,E_i} x_1; \mu_{2,E_i} x_2, \mathrm{E_i}\right) \exp\left(-\left(\frac{\mu}{\rho}\right)_{E_i} (\rho(x_1 + x_2)) \right) dV \tag{5.20}$$

This calculation method, called "point kernel method" is widely implemented in deterministic codes algorithms developed in Sect. 5.12.1 (e.g. Microshield, Mercurad).

Example of point kernel calculation

Consider a line source of total flux $\dot{N}$ and length L. Estimate the ambient dose equivalent rate at a distance h from this source behind a thick concrete shielding with a thickness x. Figure 5.17 illustrates the geometry for calculation.

Considering the volume density of flux $n_L = \frac{\dot{N}}{L}$, the dose equivalent due to an infinitesimal element "dl" is given by the following expression:

$$d\dot{H} = \frac{n_L h^*_{\Phi}(10)}{4\pi\rho^2} B(\mu r_1, E) e^{-\mu r_1} dl$$

a change of variable is carried out:

$$\mathrm{h}.\tan(\theta) = 1 \quad \text{so} \quad \mathrm{h}\frac{d\theta}{\cos^2\theta} = dl \quad \text{and} \quad \rho = \frac{h}{\cos\,\theta}$$

We can deduce: $d\dot{H} = \frac{n_L h^*_{\Phi}(10)\left(\frac{h}{\cos^2\theta}\right)}{4\pi\left(\frac{h}{\cos\theta}\right)^2} B(\mu r_1, E)\, e^{-\mu\frac{x}{\cos\theta}} d\theta$

To consider the overall geometry, it is necessary to integrate the expression on the whole line. As a first approximation, we assumed a constant build-up and $B(\mu r_1, E) = B(\mu x, E)$ hence the expression:

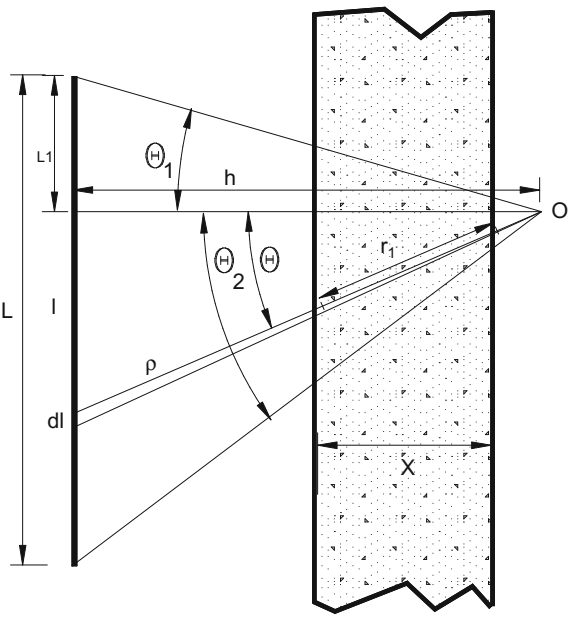

Fig. 5.17 Geometry for calculating the equivalent dose rate of a line behind a wall

$$\dot{H}^*(10) = \frac{\dot{N} h^*_\Phi(10)}{4\pi L h} B(\mu x, E) \int_{-\theta_1}^{\theta_2} e^{-\frac{\mu x}{\cos\theta}} d\theta \tag{5.21}$$

Consider then a ^{137}Cs line source with an activity of 1 GBq (an energy of 660 keV with a branching rate of 0.852), with L = 10 cm, L_1 = 3 cm, h = 20 cm, x = 10 cm and d = 2.35 concrete density.

The concrete mass attenuation factor for 660 keV is $(\mu/\rho) = 8 \cdot 10^{-2}$ g cm^{-2} or, for a 2.35 g cm^{-3} density, a linear attenuation coefficient $\mu = 0.188$ cm^{-1}.

The Berger build-up is considered with datas from [14] which lead to:

$$\begin{aligned} B(\mu x, E) &= 1 + a\mu x \exp(b\mu x) = 1 + 1.5 \times 0.188 \times 10 \exp(0.046 \times 0.188 \times 10) \\ &= 4 \end{aligned}$$

According to (5.21), we have:

$$\begin{aligned} \dot{H}^*(10) &= \frac{A\Gamma h^*_\Phi(10)}{4\pi L h} B(\mu x, E) \int_{-\theta_1}^{\theta_2} e^{-\frac{\mu x}{\cos\theta}} d\theta \\ &= \frac{1 \cdot 10^9 \times 0.852 \times 3 \cdot 10^{-12} \times 3600}{4\pi \times 10 \times 20} \times 4 \times \int_{-Arc\tan(1/20)}^{Arc\tan(9/20)} e^{-\frac{\mu x}{\cos\theta}} d\theta \end{aligned}$$

Note that the integral $\int e^{-\frac{\mu x}{\cos\theta}} d\theta$ has no analytical solution, but can be solved numerically (e.g. the "function calculator" site "http://wims.unice.fr/"). The approximate result is:

$$\int_{-Arc\tan(1/20)}^{Arc\tan(9/20)} e^{-\frac{1.88}{\cos\theta}} d\theta = 0.855$$

hence the dose equivalent rate of $\dot{H}^*(10) = 1\,\mathrm{mSv\,h^{-1}}$.

A sample calculation for a volume source is given in Further Details 5.1. This allows the analytical calculation of the dose equivalent rate for a uniformly contaminated enclosure.

5.4.3 *Calculation of a Secondary Shielding*

Scattered beam on a phantom

Scattering without shielding

In this part, the goal is the assessment of the dose equivalent due to scattered radiation caused by a primary beam. The scattering can be performed on a dosimetry phantom, one person (during a radiography), a primary wall … Figure 5.18 displays the schematic view of a typical geometry.

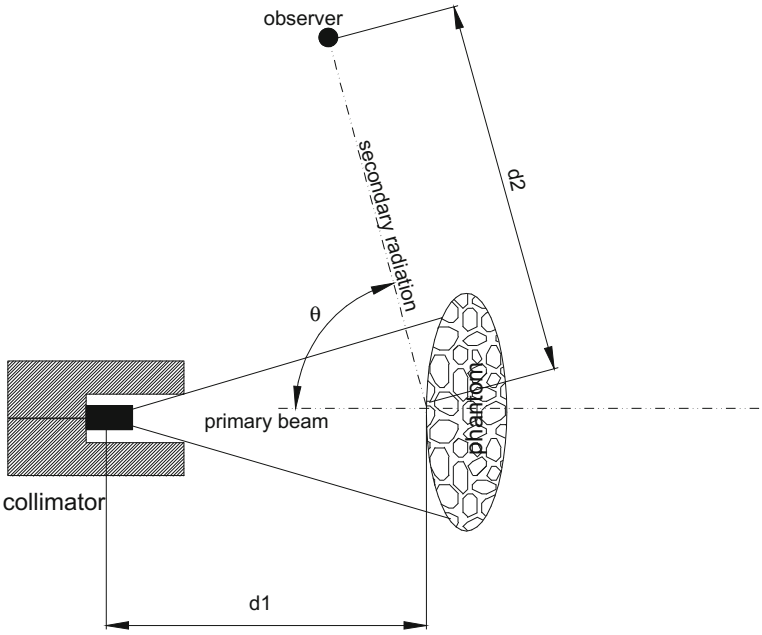

Fig. 5.18 Geometry for calculating a dose equivalent due to scattered radiations

Scattered radiations by various interactions in the phantom, in particular by the Compton effect, is dependent on the angle of observation θ, the fluence at the phantom surface and the beam area interacting with the phantom. To assess the scattered dose, a coefficient α is introduced to calculate the dose equivalent to 1 m of the phantom. This scattering model is described by the NCRP [19].

To calculate the secondary dose equivalent rate, $\dot{H}_s$, scattered by a phantom, in a geometry such as that shown in Fig. 5.18 the following equation can be used:

$$\dot{H}_s = \frac{\dot{H}_0}{d_1^2} \times \frac{\alpha S}{d_2^2} \tag{5.22}$$

where: $\dot{H}_0$ is the dose equivalent rate due to the primary photon beam to 1 m from the source (in the absence of a phantom), and $\frac{\dot{H}_0}{d_1^2}$ is the dose equivalent rate due to the primary beam on the phantom surface (with d_1 being the distance in meters between the source and the phantom centre), d_2 is the distance between the phantom centre and the observer (in m), S is the beam area at the phantom surface and α is the scatter fraction.

The scatter fraction α depends on the scattering angle θ, the energy of primary photons on the phantom and the phantom material. The product αS is dimensionless and α has the reciprocal dimensions of S. Usually, S and α are taken as having the dimensions of cm^2 and cm^{-2}, respectively. Figure 5.19, from Bourgois and Comte [5] provides α coefficients for photon energies between 10 keV and 10 MeV for different angles and on water and steel.

The Fig. 5.20 (from [5]) provides the coefficients for α radiation spectra of X-ray beams (bremsstrahlung), between 30 and 900 kVp.

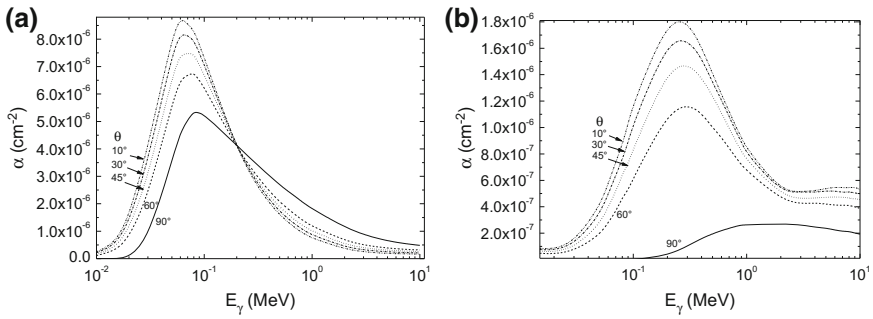

Fig. 5.19 Scatter fraction as a function of energy of monoenergetic photons (10 keV—10 MeV) at various scattering angles (ranging from 10° to 90°) **a** water phantom **b** steel phantom (data from [5])

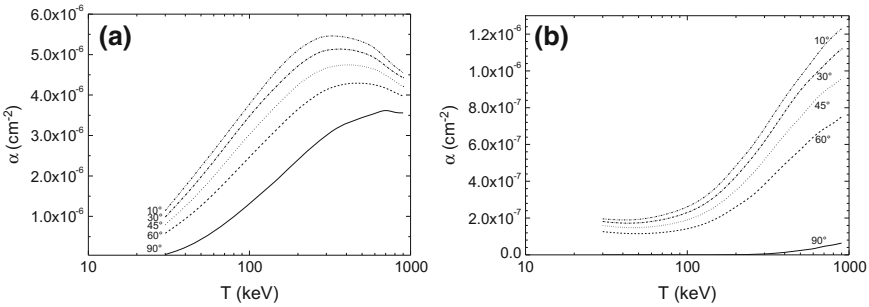

Fig. 5.20 Scatter fraction as a function of scattering angle (ranging from 10° to 90°) for bremsstrahlung photons resulting and from the interaction of electrons (kinetic energy ranging from 30 to 900 keV) is tungsten, without filtering **a** water phantom **b** steel phantom (data from [5])

Figure 5.21, from the IAEA [18], provides α coefficients for bremsstrahlung radiation produced by electrons of energy E_0 between 1 and 100 MeV for different angles and on water, concrete, lead and steel. Take care: in this publication factor is given to a surface, S, of 1 m^2, hence it is necessary to take the area S from (5.22) in same unit.

Calculation of secondary protection

Let us consider a primary beam scattered on a phantom (Fig. 5.22). It is proposed to calculate the dose equivalent rate behind the secondary shielding.

Considering (5.22) and the transmission factor defined in (5.17), then comes the dose equivalent rate due to scattered radiation behind a shielding defined by (5.23).

$$\dot{H}_s = \frac{\dot{H}_0}{d_1^2} \times \frac{\alpha S}{d_2^2} \times T_{\text{sec}}(\mu x, E, \theta) \tag{5.23}$$

$T_{\text{sec}}(\mu x, E, \theta)$ is the secondary shielding transmission for a given scattering angle. Note that the scattered energy is less than the primary one. For primary energy and a given angle, it is possible to calculate the scattered photon energy considering only the Compton effect. It has been shown in Chap. 2 as energy for an angle ranging over 90° and 180° (only possible angle according to Fig. 5.22) is less than 511 keV. The transmission values $T_{\text{sec}}(\mu x, E, \theta)$ in terms of scattering angles are given in ICRP [20]. $T_{\text{sec}}(\mu x, E, \theta)$ for ^{60}Co is plotted in Fig. 5.23 for various θ values.

For example, consider a ^{137}Cs photon source with 10 TBq activity (see Fig. 5.24). The primary beam area irradiating the shielding is 0.16 m^2. Let us consider a 2.5 μSv h^{-1} limit to 50 cm distance behind the shielding. We propose to calculate primary and secondary shielding thickness (ordinary concrete) in order to comply with the limit requirement.

^{137}Cs emits 0.661 MeV photons with an intensity of 85.2%. The dose equivalent rate to 1 m is calculated with (4.2) of Chap. 4. Hence for 10 TBq:

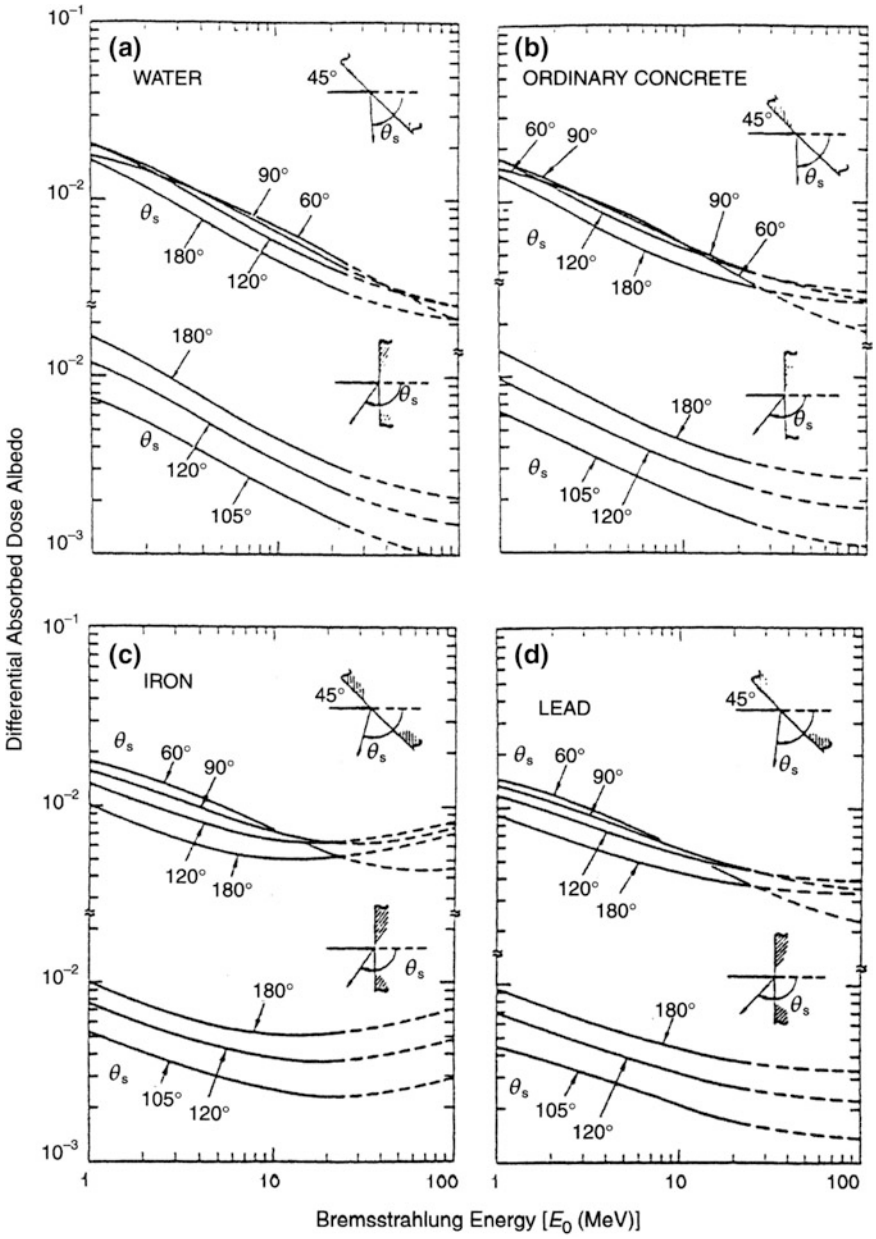

Fig. 5.21 Scattering factors α based in terms of bremsstrahlung photon energy for a phantom in: **a** water; **b** concrete; **c** steel; **d** lead, after [18]. Courtesy of the IAEA

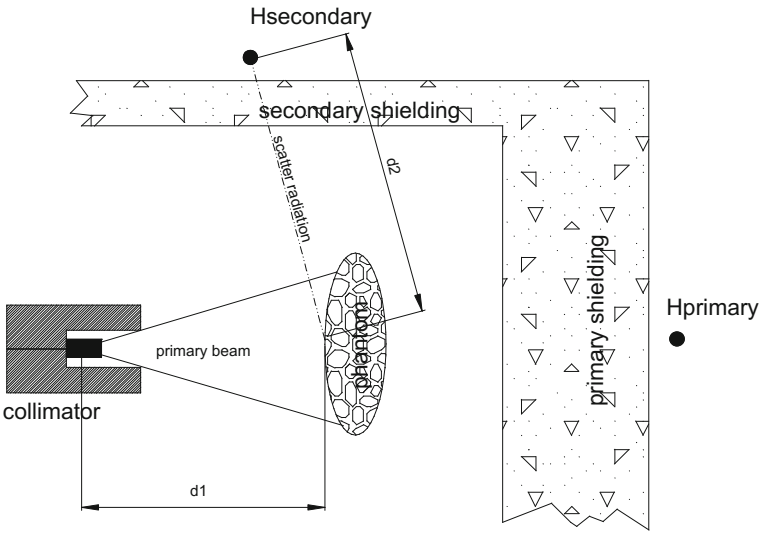

Fig. 5.22 Geometry for calculating a secondary wall

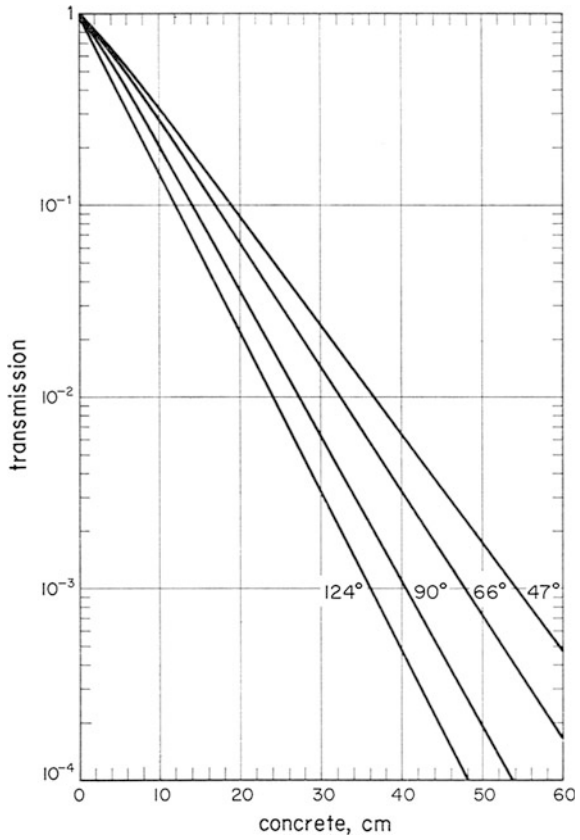

Fig. 5.23 Transmission of secondary radiation ^{60}Co for different scattering angles [20], with the permission of Michiya Sasaki on behalf facility of ICRP

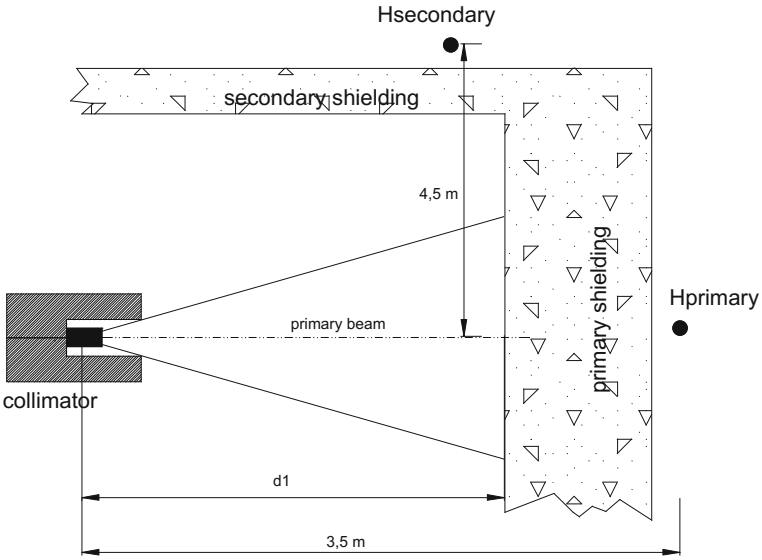

Fig. 5.24 Schematic view of Cs-137 source in a bunker

$$\dot{H}^*(10) = 1.5 \cdot 10^{-10} \times 10 \cdot 10^{12} \times 0.661 \times \frac{85.2}{100} = 780\,\text{mSv}\,\text{h}^{-1}$$
$$= 780{,}000\,\mu\text{Sv}\,\text{h}^{-1}\ (0.78\,\text{Sv}\,\text{h}^{-1})$$

For the calculation of primary shielding, from (5.17), we have:

$\dot{\text{H}}^*(10) = \frac{\text{H}_0^*(10)}{\text{d}^2} \times \text{T}(\text{x}, \text{E}, \text{shielding})$ from where $T = \frac{\dot{H}^*(10) \times d^2}{\dot{H}_0^*(10)}$

The distance between the observer and the source point is 3.5 m, hence:

$$T = \frac{\dot{H}^*(10) \times d^2}{\dot{H}_0^*(10)} = \frac{2.5 \times 3.5^2}{780{,}000} = 4 \cdot 10^{-5}$$

From the curve of Fig. 5.11, a transmission of $4 \cdot 10^{-5}$ for ^{137}Cs requires a concrete shielding thickness of 75 cm.

To calculate the secondary shielding, radiation to consider is the scattered radiation at 90° from the primary shielding. From (5.23), we can write:

$\dot{H}_s = \frac{\dot{H}_0}{d_1^2} \times \frac{\alpha S}{d_2^2} \times T_{\text{sec}}(\theta)$ from where $T_{\text{sec}} = \frac{\dot{H}_s \times d_1^2 \times d_2^2}{\dot{H}_0 \times \alpha S}$

We have $\dot{H}_s = 2.5 \cdot 10^{-6}$ Sv/h (radiation protection's objective); d_1 = 3.5 − (0.5 +0.75) = 2.25 m; d_2 = 4.5 m; α = $2.5 \cdot 10^{-6}$ cm^{-2} (Fig. 5.19: concrete is assimilated to water) beam area S = 1600 cm^2.

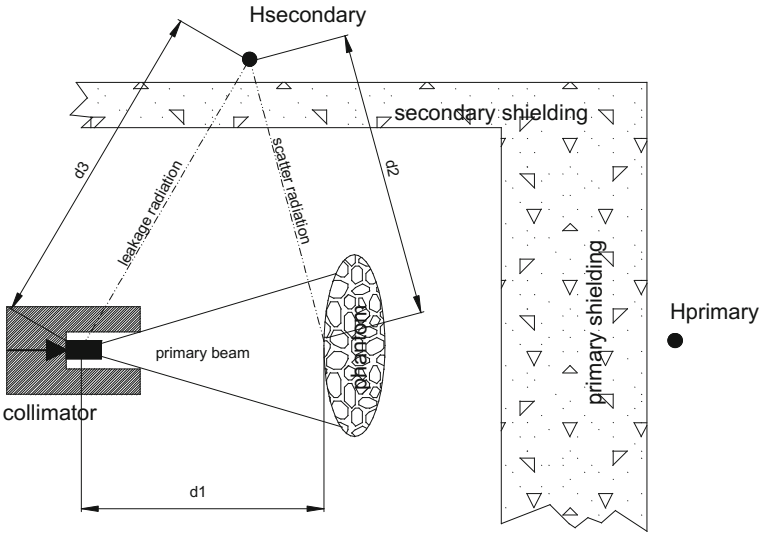

Fig. 5.25 Geometry for calculating the secondary wall with consideration of radiation leakage

$$T = \frac{\dot{H}_s \times d_1^2 \times d_2^2}{\dot{H}_0 \times \alpha S} = \frac{2.5 \times 2.25^2 \times 4.5^2}{780{,}000 \times 2.5 \cdot 10^{-6} \times 1600} = 0.082$$

The scattered photon energy by Compton effect (Chap. 2, 2.31), for 90° and 661 keV, is equal to 300 keV. For a transmission of 0.082 and an energy of 300 keV the concrete thickness is 21 cm (Fig. 5.12).

Leakage radiation

To estimate the secondary shielding, in addition to the scattered radiation, it should take into account the leakage radiation around the collimator (the collimator does not attenuate 100% of radiations). Figure 5.25 illustrates the two radiation sources for the secondary shielding calculation.

In practice, the leakage radiation values must be given by the manufacturer. Note that for radiation accelerators, IEC [21] requires that the dose from the leakage is less than 0.1% of the dose absorbed within the beam.

5.4.4 Maze Calculation

In cases where primary or secondary walls are too thick, it may be too difficult to design a door thickness equal to the shielding thickness. So, a possible alternative is the design of a maze-like structure to attenuate the radiation by successive scattering. Figure 5.26 shows an overview of 1.25 MeV scattered photons in a maze (calculated with the Monte-Carlo code MCNPX). In this model, the source is

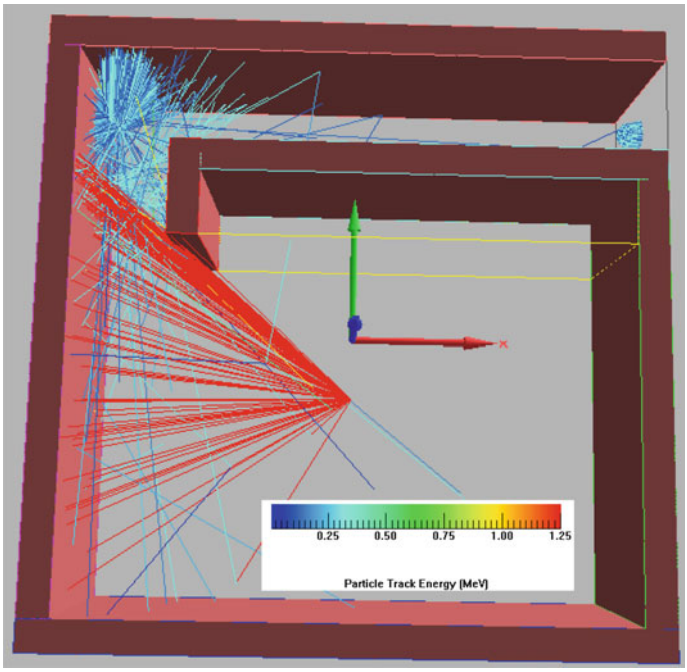

Fig. 5.26 Overview of scattered photons in a maze modeled by Monte Carlo calculation

centered in the bunker. Note that as it get closer the exit, the number of photons decreases with each scattering.

Figure 5.27 gives a view for a maze calculation. The source is located at the point S. First, like in optical's rules, it must be considered geometrically how the scattering radiation reaches the maze exit. The beam is scattered once on the surface S_1, then a second time on the surface S_2. To reach the maze exit, photons travel a distance d_1 (in meters) then d_2 (in meters) then d_3 (in meters). The dose equivalent at the maze exit is the same as a scattering on a phantom by considering scattering surfaces present. Thus, the (5.24) gives the dose equivalent rate at the maze exit by considering two successive scattering surfaces.

$$\dot{H}_{exit\ maze} = \left(\frac{\dot{H}_0}{d_1^2}\right)\left(\frac{\alpha_1 S_1}{d_2^2}\right)\left(\frac{\alpha_2 S_2}{d_3^2}\right) \tag{5.24}$$

Similarly (5.25) provides the dose equivalent rate at maze exit after n successive scattering.

$$\dot{H}_{maze\ exit} = \frac{\dot{H}_0}{d_1^2}\left(\prod_{i=1}^{n}\frac{\alpha_i S_i}{d_{i+1}^2}\right) \tag{5.25}$$

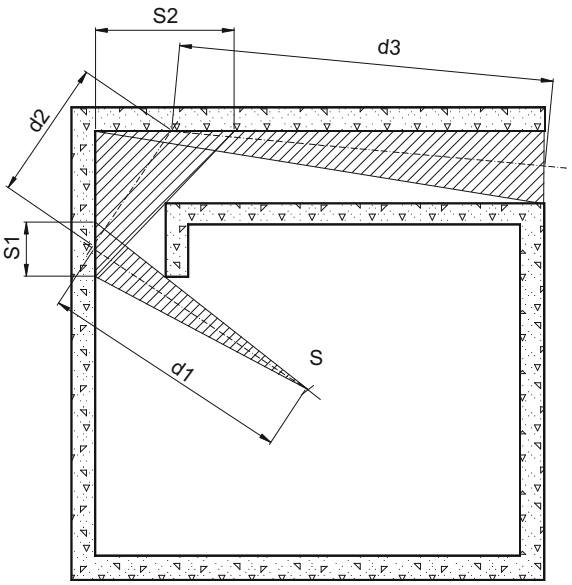

Fig. 5.27 Geometric model for maze calculation

To illustrate this method, let us calculate the attenuation provided by the maze shown in Fig. 5.27 for a ^{60}Co source of 1 TBq. First, we must represent the maze on a scale plan to evaluate different parameters of the calculation, in particular distances and size of scattering surfaces. This is shown in Fig. 5.28. Note that this calculation includes only the dose equivalent due to maze scattering and not those directly transmitted through the shielding. Indeed the dose equivalent can be higher than the scattering one in the maze.

From Fig. 5.28 the following data is obtained: $S_1 = 120 \times 300$ cm^2 (the maze is 3 m height); $S_2 = 300 \times 300$ cm^2; $d_1 = 540$ cm; $d_2 = 300$ cm; $d_3 = 780$ cm.

The value of α_1 is derived from the Fig. 5.19 for 1.25 MeV and an angle $\theta_i = 30°$ (i.e. $\theta_r = 60°$), or $\alpha_1 = 1.5 \cdot 10^{-2}$. The energy of the scattered photon by the surface S_1 is 0.56 MeV (from the Compton diffusion equation see Chap. 2): Factor α_2 is $2 \cdot 10^{-2}$ (Fig. 5.19).

For ^{60}Co source of 1 TBq, the dose equivalent rate at 1 m is $\dot{H}_0 = 0.351\ \mathrm{Sv\,h^{-1}}$ (according to Chap. 4, the dose equivalent rate at 1 m from a ^{60}Co source is 0.351 mSv h^{-1} GBq^{-1}).

At the maze exit, the dose equivalent due to multiple scattering is:

$$\dot{H}_{exit\ maze} = \frac{\dot{H}_0}{d_1^2} \times \left(\frac{\alpha_1 S_1}{d_2^2}\right) \times \left(\frac{\alpha_2 S_2}{d_3^2}\right)$$
$$= \frac{0.351}{(5.4)^2} \times \frac{1.5 \cdot 10^{-2} \times (1.2 \times 3)}{3^2} \times \frac{2 \cdot 10^{-2} \times (3 \times 3)}{7.8^2} = 0.2\ \mu\mathrm{Sv\,h^{-1}}$$

To assess the proposed method performance, the maze considered was simulated using a Monte Carlo code (MCNPX). Note that the calculation considers only the

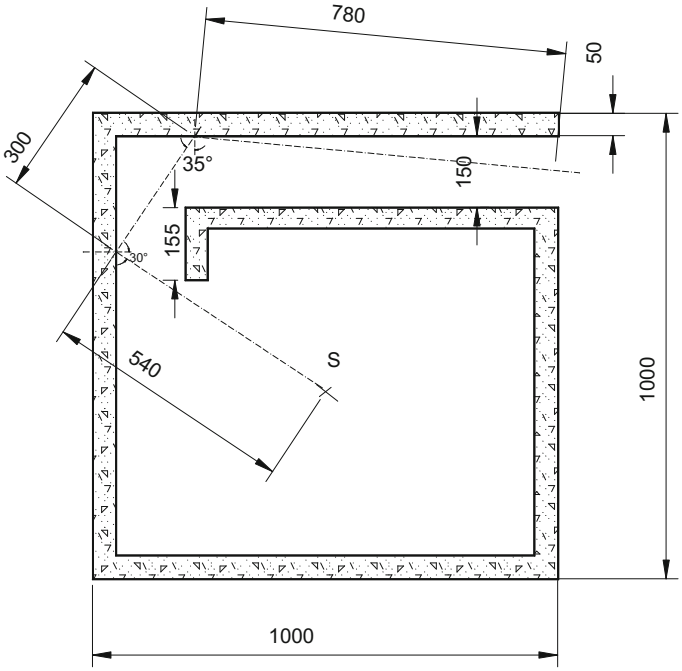

Fig. 5.28 Geometry at scaled dimensions for maze calculation (dimension in cm)

dose equivalent due to scattering in the maze and not those directly transmitted through the shielding.

Figure 5.29 gives point-locations for Monte Carlo maze calculations in the Fig. 5.30 plote Monte-Carlo values according to the maze location (point 1–13). Analytical calculations (5.25) are superimposed.

The difference between the calculation by the Monte Carlo method and the analytical method is less than a factor 2. Hence this trivial method allows a satisfactory dose equivalent assessment. On the maze exit, the dose equivalent calculated by the Monte Carlo method is 0.37 mSv h^{-1} for an analytical estimate of 0.2 mSv h^{-1}.

5.4.5 Skyshine from Photon Radiation

Due to mechanical stress, in some cases, the roof thickness above the source may not be as thick as the primary or secondary shielding. Then, the dose equivalent rate on the roof must be assessed to specify access restrictions if necessary. Radiation scattered through air or "skyshine" (for example, due to a weaker shield on the bunker roof) may cause radiation at remote occupied areas which are not in direct sight of the source. Skyshine may contribute to the public dose beyond the boundary of the facility.

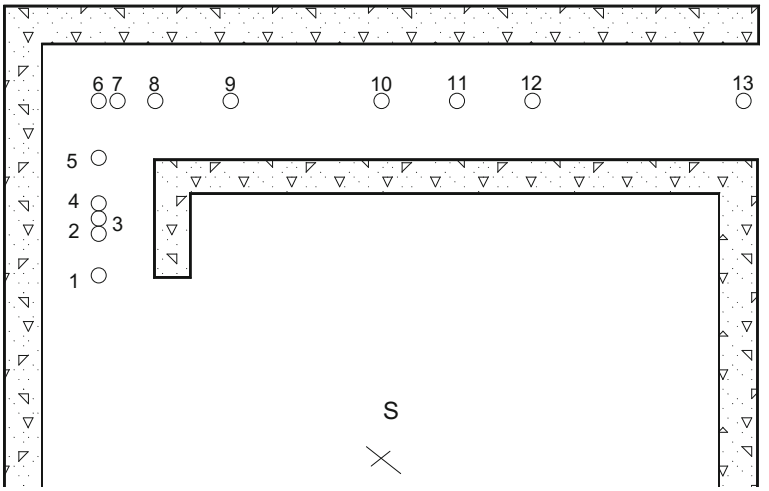

Fig. 5.29 Point locations for the Monte Carlo maze calculation

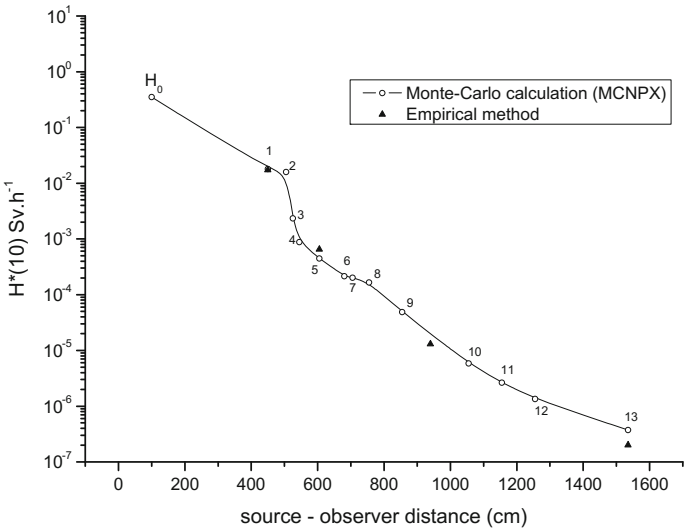

Fig. 5.30 Comparison between Monte Carlo calculations and the semi-empirical method for the assessment of dose equivalent in the maze

The expression (5.26) derived from NCRP [22] to estimate the dose equivalent due to skyshine using a semi-empirical expression. This relationship gives the equivalent dose rate in nSv h^{-1} at a distance d_s in meters.

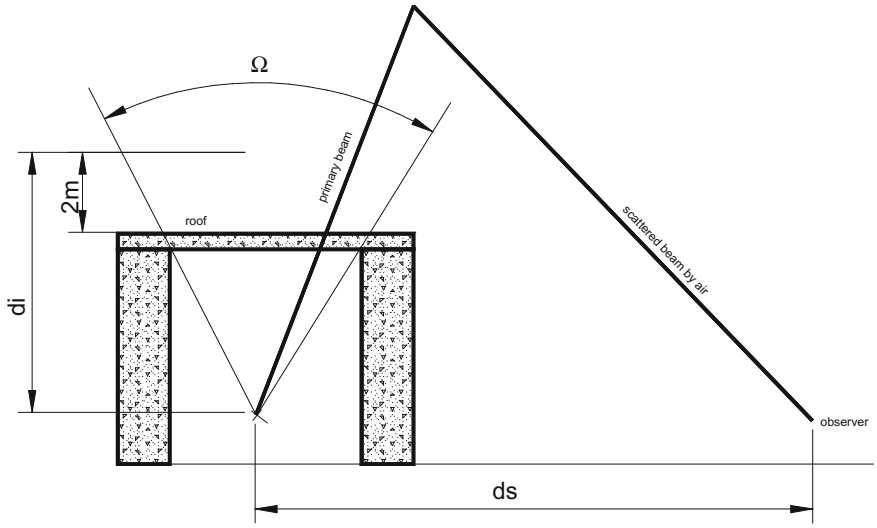

Fig. 5.31 Schematic geometry for the skyshine calculation

Fig. 5.32 Geometry for the calculation example of the skyshine

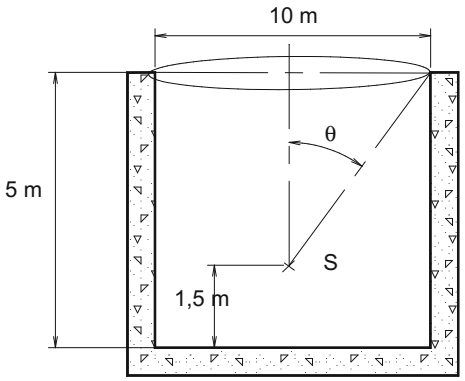

$$\dot{H} = \frac{2.5 \cdot 10^7 T \dot{H}_0 \Omega^{1.3}}{(d_i d_s)^2} \tag{5.26}$$

With d_i the distance (in meters) between the source and 2 m above the roof (see Fig. 5.31); d_s the distance (in meters) between the source and the observer; T the photon transmission through the roof; $\dot{H}_0$ the equivalent dose rate to 1 m the source (Sv h^{-1}) and Ω the solid angle (Sr).

Let us estimate, for example, the dose equivalent rate to 30 m a ^{60}Co source of 10 TBq in a cylindrical bunker of 10 m diameter and 5 m height. The bunker has no roof. The source is at 1.5 m of the ground. Figure 5.32 represents the geometry of this problem.

We have:

$$\Omega = 2\pi(1 - \cos\ \theta) = 2\pi\left(1 - \cos\left(Arc\tan\left(\frac{5}{5 - 1.5}\right)\right)\right) = 2.7\,\mathrm{Sr}$$

$$T = 1; \quad \dot{H}_0 = 3.51\,\mathrm{Sv\,h^{-1}}; \quad di = 5.5\,\mathrm{m}$$

$$\dot{H} = \frac{2.5 \cdot 10^7 T \dot{H}_0 \Omega^{1.3}}{(d_i d_s)^2} = 1.2 \cdot 10^4\,\mathrm{nSv\,h^{-1}}\left(12\,\mu\mathrm{Sv\,h^{-1}}\right)$$

To thirty meters from the bunker, the dose equivalent rate is still 12 μSv h^{-1}. This significant value requires consideration of this radiation component.

5.5 Neutron Shielding

The effectiveness of shielding against neutrons mainly depends on two neutron-matter interaction effects:

- Slowing down of neutrons by successive elastic interaction on other nuclei (scattering), which results in a loss of energy. And, as recognized in Chap. 3, conversion factors "fluence dose equivalent" are lower with low energy neutron;
- Neutron absorption which causes their annihilation with a probable emergence of secondary particles (neutrons, photons).

A neutron shielding calculation is then based on the slowing down of neutrons by successive collision (Chap. 2) and capture (e.g. radiative capture). It is recalled that the radiative capture is responsible for the emission of high energy photons (Chap. 4).

5.5.1 Neutrons Attenuation-Tenth Value Layer

The simplified calculation for neutron shielding is identical to that adopted for photons: an exponential attenuation weighted by build-up factor. Nevertheless, the assessment of this factor is more complex than for photons: it is dependent on neutron scattering, but also secondary particles such as neutrons or photons from radiative captures. However, for small thicknesses of shielding, the attenuation can be fit by an exponential function (like for photons) and tenth value layers can be used (TVL). Thus (5.27) gives an approximation of the neutron dose equivalent behind a shielding of x cm thickness.

Table 5.6 TVL for source neutrons

Sources	TVL (in cm) for various materials			
	Polyethylene	Concrete (2.35)	Water	Lead
^{252}Cf	14	25.5	19.5	53
AmF	11.5	28	–	–
Amli	8	22	–	–
AmBe	23	37	–	–

$$\dot{H}^{*}(10) = \frac{\dot{H}_0^{*}(10)}{d^2} \times 10^{\left(-x/x_{1/10}\right)} \tag{5.27}$$

with $\dot{H}_0^{*}(10)$ the dose equivalent rate at 1 m; d the distance in meters between the source and the observer; $x_{1/10}$ the TVL.

Table 5.6 gives the TVL of some neutron sources for different materials. These values were obtained from publications [20] or measured at CEA Saclay.

For example, let us consider a AmBe source of 111 GBq and calculate the neutron dose equivalent rate at 2 m of this source behind 34 cm thick of polyethylene. In this example, photons emitted by ^{241}Am are not considered.

For a AmBe source, it comes 0.752 mSv h^{-1} GBq^{-1} at 1 m (see Chap. 4).

At 1 m of the source, without shielding, it comes $\dot{H}_0^{*}(10) = 111 \times 0.752 = 83\,\mathrm{mSv\,h^{-1}}$.

Behind 34 cm thick of polyethylene, the equivalent dose rate would be:

$$\dot{H}^{*}(10) = \frac{\dot{H}_0^{*}(10)}{d^2} \times 10^{\left(-x/x_{1/10}\right)} = \frac{83}{2^2} \times 10^{(-34/23)} = 0.7\,\mu\mathrm{Sv\,h^{-1}}$$

We intend to evaluate this semi-empirical method. Figure 5.33 compares the attenuation provided by the relationship (5.27) and a full calculation using a Monte Carlo code for an AmBe source shielded with polyethylene or concrete.

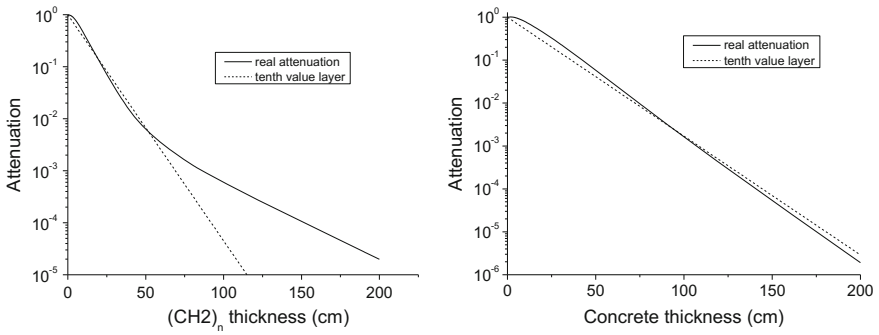

Fig. 5.33 Comparison between relationship (5.27) and a Monte-Carlo calculation for an AmBe source shielded with polyethylene or concrete

For polyethylene, we notice that until 50 cm thick, the TVL provides a good attenuation estimate. however, beyond this thickness, this trivial method rapidly differs from the real attenuation. The explanation is: beyond 50 cm shielding, the dose equivalent is not due to primary neutrons absorbed by radiative capture for a large part, but by the photons emerging from such captures. For concrete, the curves are closer with a ratio between 0.7 and 1.5. This different behavior is due to the strong presence of hydrogen in the polyethylene favoring radiative captures with a large cross section (n, γ) in the energy range of AmBe spectrum (see Chap. 2).

5.5.2 *Transmission Curves for Neutrons*

The performance of the TVL method is limited beyond 50 cm thick for hydrogenated low density materials. So the transmission curves for neutrons must then be calculated using a Monte Carlo code. The calculation will include all components of the primary and secondary radiation from multiple reactions within the shielding for neutrons, "transmission index" concept $I(\Sigma x, E)$ is more efficient. This index is the product of the conversion factor "fluence dose equivalent" and the primary neutron transmission [23]. Hence:

$$H_{behind\ shielding} = \Phi h_{\Phi} T(\Sigma x, E), \quad \text{with } I(\Sigma x, E) = h_{\Phi} T(\Sigma x, E).$$

The dose equivalent behind the protection is given by the relationship (5.28)

$$\mathrm{H} = \Phi\, \mathrm{I}(\Sigma x, E) \tag{5.28}$$

By combining (5.28) and the fluence calculation for an isotropic source (Chap. 1), it comes, the relationship (5.29).

$$\dot{H} = \frac{\dot{N}}{4\pi \mathrm{d}^2}\, \mathrm{I}(\Sigma x, E) \tag{5.29}$$

transmission indexes *in* pSv cm^2 presented in Figs. 5.34, 5.35, 5.36, 5.37 were calculated using MCNPX code for quantity $H^*(10)$ for various neutron spectra and materials. The transmission ratios are tabulated in Appendix 2. In this appendix, besides the transmission indexes for thermal neutrons, 14 MeV, from a source AmBe and ^{244}Cm, indices for the transmission of 0.5, 1, 2.5, 5 and 10 MeV monoenergetic neutrons are added.

Note that, in addition to the neutrons radiation, the contribution of photons created by radiative capture in the materials is considered. The composition of the materials used is given in Appendix 1.

The slope changes in the curves are explained by the contribution of photons from radiative captures that are prevalent with respect to neutrons from a certain shielding layer.

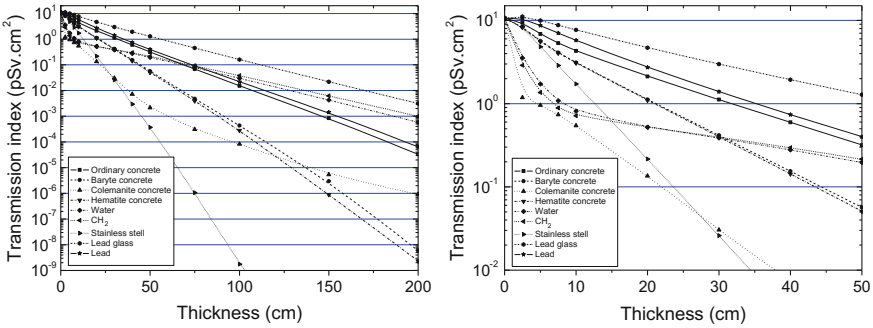

Fig. 5.34 Transmission index for dose equivalent for thermal neutrons (values are reproduced in Appendix 1)

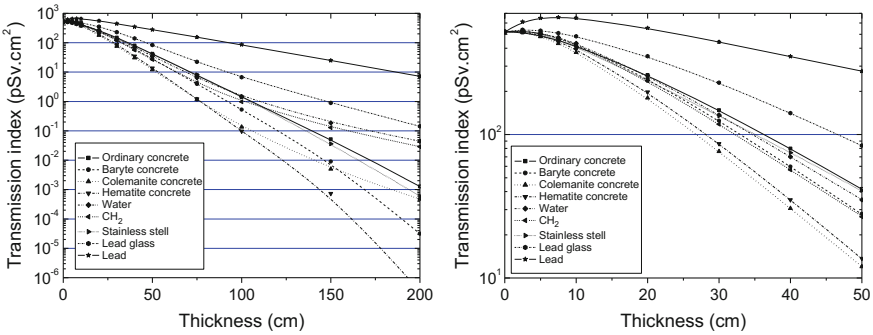

Fig. 5.35 Transmission index for dose equivalent for 14 MeV neutrons (values are reproduced in Appendix 1)

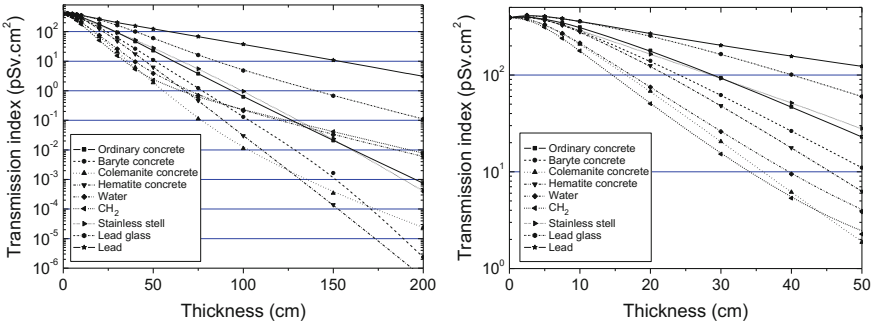

Fig. 5.36 Transmission index for dose equivalent for a ^{241}AmBe source (values are reproduced in Appendix 1)

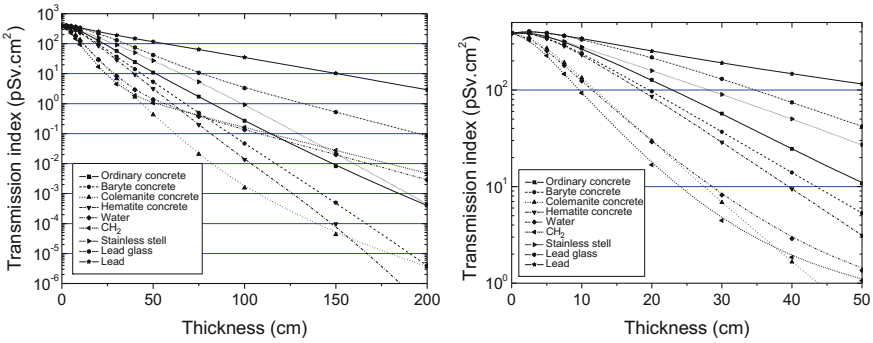

Fig. 5.37 Dose equivalent index in transmission for a ^{244}Cm source (values are reproduced in Appendix 1)

For 14 MeV neutrons, it must be noted for lead, up to about 30 cm depth the dose equivalent is greater with shielding than without. This is due to the (n, 2n) reactions in the shielding that create more neutrons at energies where the conversion factors "fluence-ambient dose equivalent" are equivalent and due to large cross sections at 14 MeV.

Transmission curves allow to quickly choose the material to be used depending on the desired transmission index. Let us consider a spontaneous fission spectrum as ^{244}Cm. The polyethylene provides a good attenuation for thicknesses of less than 50 cm but quickly becomes less efficient beyond.

For ^{241}AmBe source, ^{241}Am photons are not taken into account in calculations. Do not forget to consider this contribution for the shielding compared to radiation protection objectives, especially for light materials.

In order to illustrate the use of the transmission index, let us calculate the shielding with different materials to obtain a neutron ambient dose equivalent rate of 0.5 μSv/h at 2 m of a AmBe source with of 111 GBq.

At 1 m, without shielding, it comes $\dot{H}_0^*(10) = 111 \times 0.752 = 83\,\mathrm{mSv\,h^{-1}}$.

From Table 4.3, an activity of 111 GBq of ^{241}AmBe is responsible for a $7.3 \cdot 10^6$ (n) $\mathrm{s^{-1}}$ neutron flux. The searched transmission index according (5.29) is:

$$\mathrm{I}(\Sigma x, E) = \dot{H} \times \frac{4\pi \mathrm{d}^2}{\dot{N}} = \frac{(0.5 \cdot 10^{-6} \times 1 \cdot 10^{12})}{3600} \times \frac{4\pi (200)^2}{7.3 \cdot 10^6} = 9.5\,\mathrm{pSv\,cm^2}$$

Note the attention that should be given to the units: the dose equivalent rate should be expressed in pSv/s, explaining the presence of factors $1 \cdot 10^{12}$ and 3600 in the above equation.

Thus, using the Fig. 5.36, the thicknesses are obtained depending on the type of material in Table 5.7.

Notice that depending on the material used, the shielding thicknesses range over 34–153 cm. Clearly, lead is the worst performer of materials in this case.

Table 5.7 Shielding thickness required to obtain a neutron ambient dose equivalent rate of 0.5 μSv/h at 2 m from a AmBe source of 111 GBq

Material	Thickness (cm)
$(CH_2)_n$	34
Concrete colemanite	36
Water	40
Concrete hematite	46
Concrete barium	51
Ordinary concrete	61
Stainless steel	66
Lead glass	84
Lead	153

5.5.3 *Calculating a Maze for Neutrons*

Due to the complexity of changes in the neutron energy spectrum within the maze, the dose equivalent calculation for maze exit may not be similarly to photon one, namely-by calculating successive scatterings in the Maze.

The NCRP [24] proposes an analytic approach to dose equivalent rate attenuation issue by multi-legged maze. For the first leg the expression is essentially an inverse square law with an empirical diffusion factor 2. This expression is given in (5.31).

$$H(r_1) = 2 \times H_0(r_0)(r_0/r_1)^2 \quad \text{in the first leg} \tag{5.30}$$

In successive legs, the expression may be written as a sum of two exponential (5.32).

$$H(r_i) = \left(\frac{\exp(-r_i/0.45) + 0.022 \times S_i^{1.3} \times \exp(-r_i/2.35)}{1 + 0.022 \times S_i^{1.3}}\right) \times H_{0i} \quad \text{for the } i_{\text{th}} \text{ legs } (i > 1) \tag{5.31}$$

with r_0 the distance (in meter) from the source to the maze entrance; r_1 the distance (m) from the source in the first leg (in meter); $H_0(r_0)$ dose equivalent form the primary radiation in the maze entrance; S_i the maze area (m^2); H_{0i} dose equivalent in the entrance of *i*th leg; r_i the distance (m) into the *i*th leg (in meter).

Figure 5.38 given the geometry parameters used in expressions (5.31) and (5.32).

To illustrate this approach, we can calculate the 14 MeV neutron dose equivalent with $1 \cdot 10^{11}$ n/s flux in the Fig. 5.28 bunker. Note that the calculation considers only the dose equivalent due to scattering in the maze and not those directly transmitted through the shielding. These dose equivalent may be greater than those released in the maze.

The conversion factor "fluence-equivalent dose" for 14 MeV neutrons is 520 pSv cm^2 (Chap. 3) and r_0 = 4.3 m (Quotations are given in Fig. 5.28) hence we have: r_0 = 4.3 m; r_1 = 5.4 m; r_2 = 3 m; r_3 = 7.8 m and $S_2 = S_3 = 1.5 \times 3 = 4.5$ m^2.

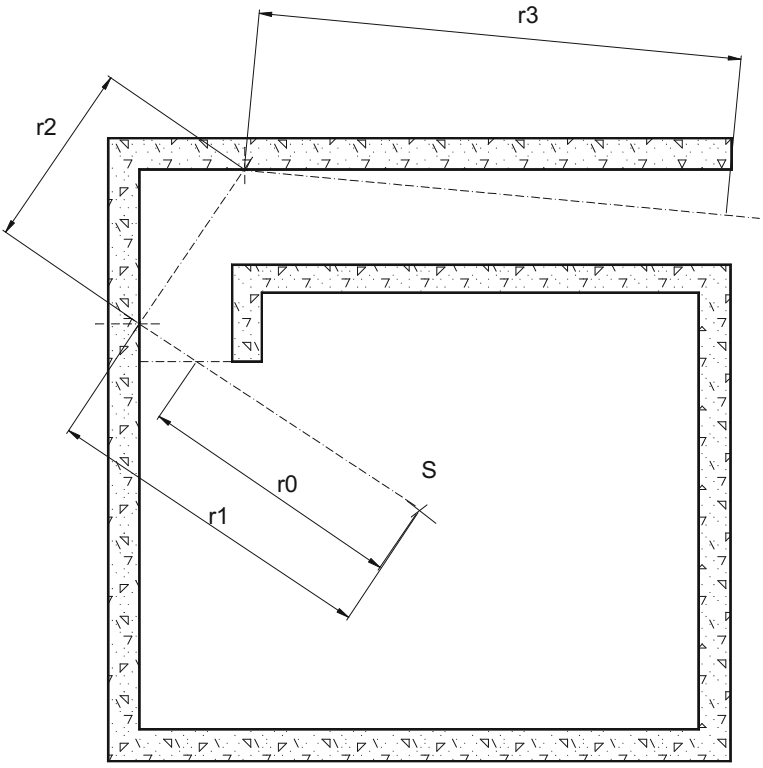

Fig. 5.38 Model for the calculation of expressions (5.31) and (5.32)

$$H_0(r_0) = \frac{520 \cdot 10^{-12} \times 1 \cdot 10^{11} \times 3600}{4 \times \pi \times 430^2} = 80\,\mathrm{mSv\,h^{-1}}$$

$$H(r_1) = 2 \times H_0(r_0)(r_0/r_1)^2 = 2 \times 80 \times (4.3/5.4)^2 = 100\,\mathrm{mSv\,h^{-1}}$$

$$H(r_2) = \left(\frac{\exp(-r_2/0.45) + 0.022 \times S_2^{1.3} \times \exp(-r_2/2.35)}{1 + 0.022 \times S_2^{1.3}}\right) \times H(r_1) = 4\,\mathrm{mSv\,h^{-1}}.$$

$$H(r_3) = \left(\frac{\exp(-r_3/0.45) + 0.022 \times S_3^{1.3} \times \exp(-r_3/2.35)}{1 + 0.022 \times S_3^{1.3}}\right) \times H(r_2) = 19\,\mu\mathrm{Sv\,h^{-1}}$$

The maze section sizes are 1.5 and 3 m height; S_i = 4.5 m^2.

We simulate this maze using a Monte Carlo code (MCNP) to evaluate the model performance. Note that the calculation also considers the dose equivalent due to diffusion in the maze and not those directly transmitted through the shielding.

Figure 5.38 identifies locations (1–13) for Monte Carlo calculations. Figure 5.39 gives the values of the numerical simulation. The figure also displays the results of semi-empirical method proposed above.

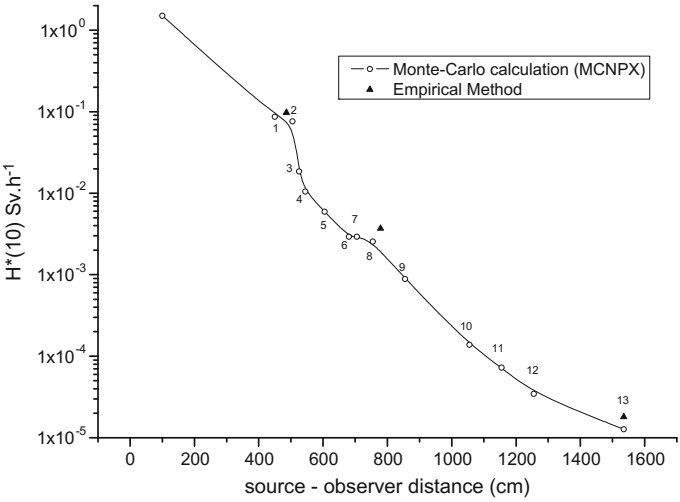

Fig. 5.39 Comparison of Monte Carlo calculations and semi-empirical method for dose equivalents calculation at different location within the maze for a 14 MeV neutron source and $1 \cdot 10^{11}$ n s^{-1} flux

Table 5.8 Comparison of maze calculation methods for various neutron energies

Neutron energy (MeV)	Ratio between analytical and Monte Carlo methods (maze exit)
0.5	2.8
1	1.8
14	1.45
Cf-252 fission spectrum	1.6

Least a factor of 2 is observed between the Monte Carlo calculation and the semi-empirical model at maze locations. Thus, it can be assumed that this model provides a good assessment for this calculation. At maze exit, the ambient dose equivalent rate calculated by numerical simulation resulted in 13 μSv h^{-1} for 19 μSv h^{-1} by the semiempirical method.

Notice that the expressions (5.31) and (5.32) are independent of the neutron energy. The comparison of results from Monte Carlo and analytical methods is presented in Table 5.8 for three neutron energies.

We note that the method is still valid slightly overestimating the result Monte Carlo in the range 0.5–14 MeV, and therefore allows an assessment of the dosimetric quantity at the maze exit for this energy range.

5.5.4 Neutrons Skyshine

The expression (5.32) derived from NCRP [22] allows to assess the dose equivalent rate due to the skyshine. It estimates the equivalent dose rate in nSv h^{-1} at a distance d_s in meters.

$$\dot{H}_n = \frac{0.85 \times 1 \cdot 10^5 I(\Sigma x, E)\dot{\Phi}_0 \Omega}{d_i^2} \quad \text{for } d_s \leq 20\,\text{m} \tag{5.32}$$

With d_i the distance in meters between the source plus 2 m above the roof (see Fig. 5.31); d_s the distance in meters between source and observer; $I(\Sigma x, E)$ The neutron transmission index through the roof (see Sect. 5.5.2 with $I(\Sigma x, E)$ in Sv cm^2); $\dot{\Phi}_0$ the neutron fluence rate at 1 m (n cm^{-2} h^{-1}) and Ω the solid angle of emission (Sr).

5.6 Radiological Protection Around Electron Accelerators

To address the radiological protection calculation within this context, it is worth recalling the lessons of the previous chapters:

- Electron beams are responsible for large ambient dose rates;
- Electron interactions with high material generates bremsstrahlung;
- photon interaction with matter causes a neutron emission beyond an energy threshold T_s.

Indeed, shielding around an electron accelerator will be designed for secondary radiations because of their range: bremsstrahlung or neutrons emerging from photonuclear reactions.

Thus, dose equivalent $\dot{H}^*_{observer}$ to a distance d of the interaction of electron beam on target, with a shielding thickness x as described in Fig. 5.14 can be calculated according to (5.33).

$$\dot{H}^*_{observateur} = \left[\frac{\dot{H}^*_{0,\gamma}(\theta)}{d^2} \times T_\gamma(\theta, \mu x, E_\gamma)\right] + \left[\frac{\dot{H}^*_{0,n}}{d^2} \times T_n(\Sigma x, E_n)\right] \tag{5.33}$$

with $\dot{H}^*_{0,\gamma}(\theta)$ the photon dose equivalent rate without shielding to 1 m of the target. The calculations leading to value are described in Chap. 4; d (in meter) the distance between the beam interaction in target and the observer; θ the angle between the electron beam and the observer; $T_\gamma(\theta, \mu x, E_\gamma)$ the photons transmission for a shielding thickness x, this value can be determined using curves provide Fig. 5.15;

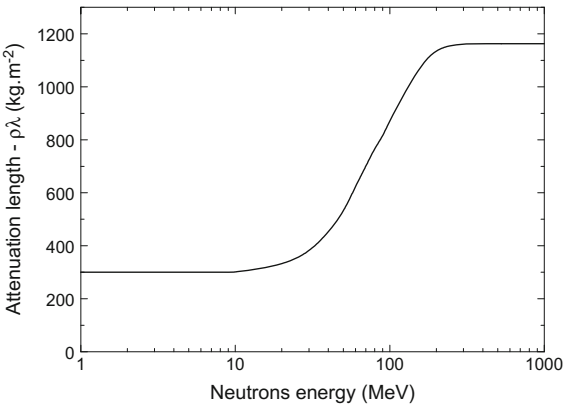

Fig. 5.40 Attenuation length for monoenergetic neutrons for ordinary concrete (from [24], with the permission of the National Council On Radiation Protection and Measurements, http://NCRPpublications.org)

$\dot{H}^*_{0,n}$ the neutron dose equivalent rate at 1 m unshielded interaction point. The calculations for this value are described in Chap. 4. Note that neutron radiation is isotropic, this value is independent of θ; $T_n(\Sigma x, E_n)$ the neutron transmission for a shielding thickness x. The energy of photoneutron is very few dependent with θ (see Chap. 4), the transmission factor follows the same law.

$T_n(\Sigma x, E_n)$ can be estimated according to the relationship (5.34) with the values ρλ (kg m^{-2}) for concrete, given in Fig. 5.40 from NCRP [24].

$$T_n(\Sigma x, E_n) = \exp\left(-\frac{x\rho}{\rho\lambda}\right) \tag{5.34}$$

In Fig. 5.40, we notice that the attenuation length is very few dependent on the neutron energy. Remember that photoneutrons have an energy near $E_n = E\gamma - E_s$ (see Chap. 4); thus, for electron energies less than 50 MeV, an attenuation length value of the order of 300 kg m^{-2} for the concrete is a satisfactory approximation.

It is important to note that in the case of an electron accelerator, all emission sources terms of radiation must be identity. In fact, as soon as the electron beam interacts with matter, bremsstrahlung, or neutrons, are triggered which will be at the origin of several sources terms. All sources will be taken into account for the shielding design. For example, accelerator vessel, deflection magnet, conversion target, etc., can occur photon emissions. Figure 5.41 illustrates the points to consider for a shielding calculation.

To illustrate this approach, let us consider a 40 MeV electron accelerator at 1 mA current interacting with thick tungsten target. We propose to calculate the dose equivalent rate at 5 m of the target in forward and perpendicular direction behind 1 m layer of concrete (density 2.35).

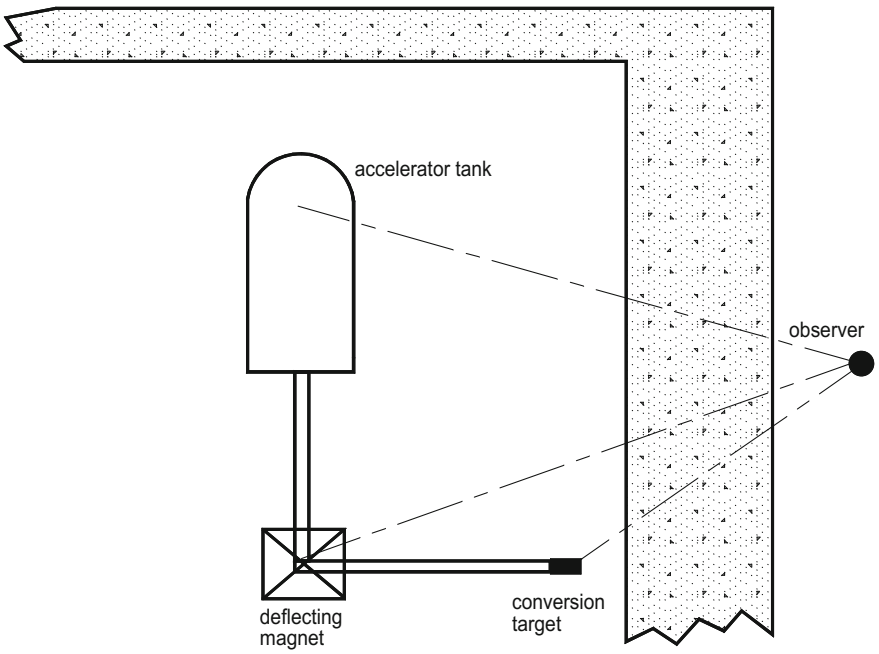

Fig. 5.41 Multiple sources generated by individual loss for an electron beam

First, calculate the dose equivalent rates of photons to 1 m:
Chapter 4 provides:

$$\dot{H}^*_{0,\gamma}(0^\circ) = 600\,\mathrm{Sv\,h^{-1}\,\mu A^{-1}} \rightarrow 600{,}000\,\mathrm{Sv\,h^{-1}} \quad \text{for 1 mA}$$
$$\dot{H}^*_{0,\gamma}(90^\circ) = 2\,\mathrm{Sv\,h^{-1}\,\mu A^{-1}} \rightarrow 2000\,\mathrm{Sv\,h^{-1}} \quad \text{for 1 mA}$$

The (γ, n) reaction threshold on tungsten is 8.41 MeV [25], hence this facility should be responsible of a neutrons' yield. Also, in a second step, let us calculate the dose equivalent rates from this new neutron contribution to 1 m:
Chapter 4 provides:

$$\dot{H}^*_{0,n} = 3 \cdot 10^{-17}\ \mathrm{Sv/e\text{-}\ so}\ 3 \cdot 10^{-17} \times \frac{1 \cdot 10^{-3}}{1.6 \cdot 10^{-19}} \times 3600 = 675\ \mathrm{Sv\,h^{-1}}$$

Thirdly, consider transmissions for photons in forward and perpendiocular direction.

In forward direction, for 100 cm and E_0 = 40 MeV the transmission $T\gamma(0^\circ$, 100 cm) = $1.1 \cdot 10^{-2}$ (Fig. 5.15).

At 90°, for 100 $\mathrm{cm}^2/3E_0$ = 27 MeV the transmission $T\gamma(90^\circ$, 100 cm) = 0.9 10^{-2} (Fig. 5.15).

Finally, in a fourth time, neutron transmission is assessed.

As (γ,n) threshold is 8 MeV [25], the maximum energy will be 40 − 8 = 32 MeV. We can therefore take an attenuation length of 300 kg m^{-2}, or:

$$T_n(1) = \exp\left(-\frac{1 \times 2350}{300}\right) = 4 \cdot 10^{-4}$$

It comes then:

$$\dot{H}^*_{0^\circ} = \frac{600{,}000}{5^2} \times 1.1 \cdot 10^{-2} + \frac{675}{5^2} \times 4 \cdot 10^{-4} = 260 + 1 \cdot 10^{-2} = 260\,\mathrm{Sv/h}$$

$$\dot{H}^*_{90^\circ} = \frac{2000}{5^2} \times 0.9 \cdot 10^{-2} + \frac{675}{5^2} \times 4 \cdot 10^{-4} = 0.7 + 1 \cdot 10^{-2} = 710\,\mathrm{mSv/h}$$

These results must be commented:

A 1 m concrete shielding is not enough to comply with a correct radiation protection objective, the dose equivalent in forward direction ° is higher than 90°, the neutron dose equivalent is negligible compared to that due to photons.

Also, to estimate the radiological protection for a electron accelerator less than 100 MeV, only bremsstrahlung photons must be considered as source term, then checking the neutron equivalent dose is consistent with the radiation shielding objectives.

5.7 Radiation Shielding at Ion Accelerators

5.7.1 Low Energy Ions Accelerators

To address the context of low energy ion accelerator shielding, it is important to remind following knowledgements:

- the dose rates are large in the ion beam;
- Beyond the threshold energy, ion interaction with matter is responsible for monoenergetic neutron emission whose energies depend of the ion beam (i.e. both energy and type), of the target material and the neutron emission angle.

In fact, because of their short range, ions will be stopped by the radiological protections. Thus, radiation shielding for an ion accelerator will be designed for secondary neutron radiation due to nuclear interactions.

In the Chap. 4 we saw how to calculate the dose equivalent rate due to secondary neutrons and their energy. The transmission curves of Sect. 5.5.2 are used to assess the shielding thickness.

For example, let us calculate the ordinary concrete thickness around a deuteron accelerator with a 2 MeV and 1 mA beam interacting with a deuterium target. The limit of radiation protection for an observer to 5 m is 7.5 μSv/h.

The yield for this reaction is $5 \cdot 10^7$ n s^{-1} μA^{-1} (Chap. 4, Fig. 4.32) hence for a 1 mA current, a $5 \cdot 10^{10}$ n s^{-1} flux.

The neutrons energies induced by this reaction is, 5.24 MeV in forward direction (Chap. 4, Table 4.23). We will consider for the rest a 5 MeV energy.

Finally, there is obtained from (5.29):

$$I(\Sigma x, E) = \dot{H} \times \frac{4 \cdot \pi \cdot d^2}{\dot{N}} = \frac{(7.5 \cdot 10^{-6} \times 1 \cdot 10^{12})}{3600} \times \frac{4 \cdot \pi \cdot (500)^2}{5 \cdot 10^{10}} = 0.13\,\text{pSv}\,\text{cm}^2$$

Thus, using the transmission index tables in Appendix 2, the suitable thickness is 130 cm for ordinary concrete.

5.7.2 *High Energy Ions Accelerators*

Like the low-energy ion accelerators, the knowledge the secondary radiation caused by nuclear reactions is required. Shieldings around the accelerator will be designed relative to the secondary neutron radiation. The source term assessment is complex, composed of one hand by the neutron flux generated by the primary ions and secondly by neutrons from the intranuclear cascade produced in the target: a large number of secondary particles are produced with enough energy to generate in turn other particles. Also, because of this complexity, several books are devoted to radiation around particle accelerators. The interested reader may refer to IAEA works [26], NCRP [24] and Sullivan [27].

5.8 Accelerators and Irradiators Safety

At this stage, we have defined tools to design a facility housing a radiation source, responding to a fixed radiation protection limit. Some facilities, such as accelerators, irradiators, operate according two modes:

- "irradiating mode" for which the dose equivalent rate requires the classification of the area as "forbidden zone" with physically unbridgeable barrier within the bunker;
- "safety mode" (irradiation is not possible in the bunker) and the bunker is accessible.

This dual operating mode requires a radiological zoning referred to as "intermittent". Therefore, it is necessary to manage the access prohibition and people presence in the area in operation position and irradiation ban when the area is accessible. As the human factor is not safe, this management process must be completely automated.

The safety position of a stopped accelerator is defined by source and accelerating voltage stopping. This complete stop state avoids cold cathode effect (see Chap. 4).

An irradiator in safety position is defined by the radioactive sources confined in a suited shielded device.

The safety of this facility is based on following principles [28]:

- No irradiation is possible if the bunker is not evacuated and closed;
- The bunker is accessible only if the facility is in safe position (no radiation possibility) and the radiation level is below a set limit.

The authorization of operation (possibility of radiation) is given if the bunker is evacuated and locked.

To allow irradiation, the operator shall:

- Operating a button (search and secure operation) located in the bunker: during this action, the operator ensures that the bunker is evacuated; Soon after he close the heavy door of the irradiator then it turns a key in the control panel;
- If no emergency stop is operated and if ventilation is working, the authorization to operate will be given after a sound evacuation sequence.

Figure 5.42 gives a flow chart of the principle of operation authorization.

As soon as one of the requirements is no longer satisfied (door opening, key removed from the panel, etc.), the operating authorization is canceled and sources are automatically set in safe position.

Authorization to open the bunker door is given if:

- The sources are in safe position;
- The radiation detector is in good working order;
- Dose rate in the bunker, is below the threshold;
- The key which was used for the authorization of operation is turned on a housing near the door.

Figure 5.43 gives a flow chart of principle for the access authorization.

5.9 Shielding Design to Avoid the Radiation Leakage

When designing a bunker, take into account the possible radiation leaks especially at the interfaces between two materials.

If it is planned to implement a door of thickness equivalent to the wall (e.g. the solution of a maze can not be reliable because of the available space), special door design should be considered to prevent radiation leaks at door-wall interface of the bunker.

Figure 5.44 presents poor door design for the wall-door interface of a bunker. Indeed, at the interface, a radiation leak is likely to occur because of the low covering with material at this place.

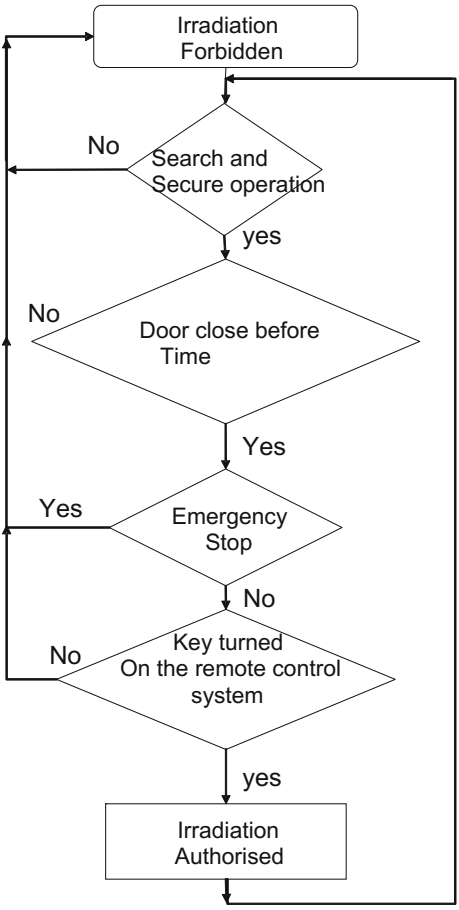

Fig. 5.42 Flowchart principle of irradiation authorization

To hedge against this leak, it is relevant to cover that interface. For example by increasing the door width to get a covering ten times larger than the gap between the door and the bunker wall as suggested in NCRP [24] and shown in Fig. 5.45.

It is also possible to design a concrete-filled radiation shielding door, to attenuate the radiation [24]. Figure 5.46 present this set-up.

Similarly, it is important to treat the interface between the bunker wall and the floor. Indeed if the wall is laid on the ground, the radiation scattered by the ground will cause radiation leakage outside the bunker. Figure 5.47 shows this issue.

To avoid the scattering in soil, it is necessary to reduce the primary radiation so that the radiation can not induce secondary radiation risk outside protection. Figure 5.48 present this design [29].

Similarly, for the lead wall design, the use of interlocking lead bricks is recommended to prevent radiation leakage between sets of two contiguous blocks. Figure 5.49 [3] illustrates such a building with lead bricks.

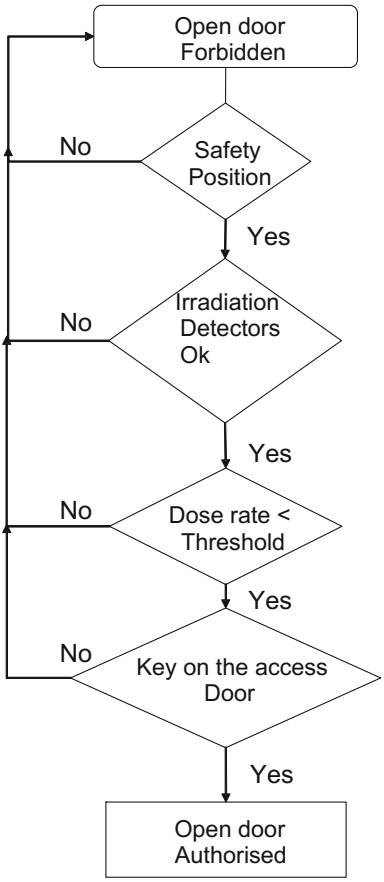

Fig. 5.43 Flowchart of the principle of access authorization

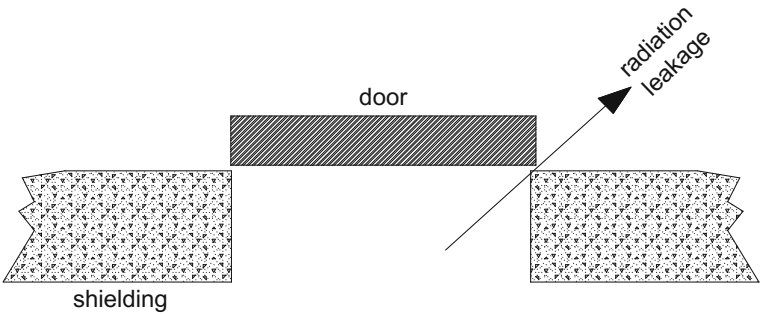

Fig. 5.44 Poor door-wall interface design

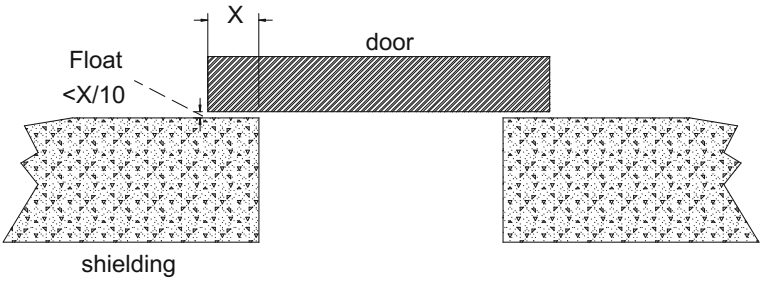

Fig. 5.45 Good design of door-wall interface

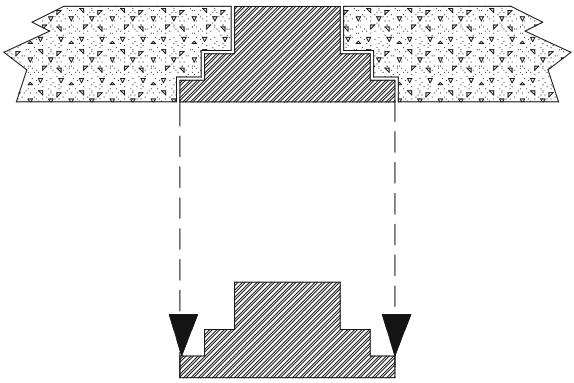

Fig. 5.46 Design of a concrete-filled radiation shielding door

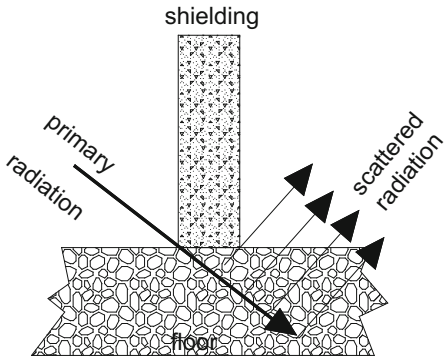

Fig. 5.47 Poor design of wall-ground interface

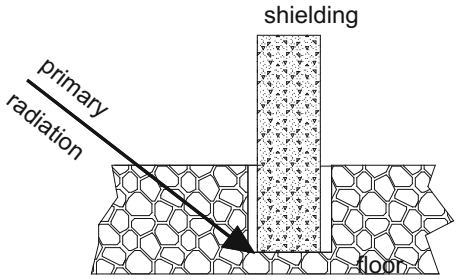

Fig. 5.48 Design of a wall-ground interface avoiding the scattering on the floor

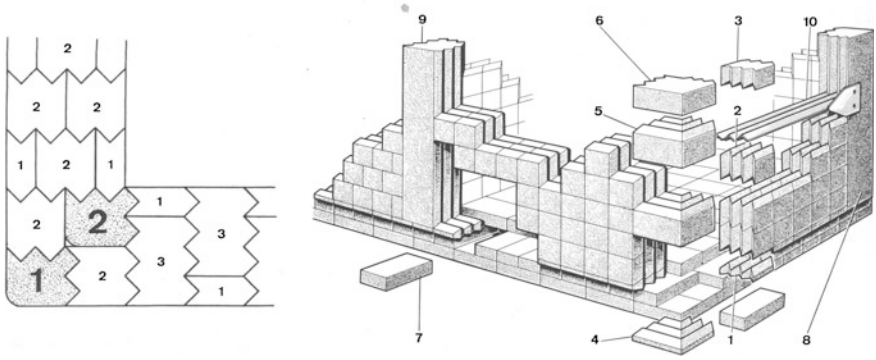

Fig. 5.49 Example of constructing a lead wall with interlocking lead bricks [3]

5.10 Shield Control

Before commissioning a facility, it is necessary to proceed to following checks:

- Monitoring the efficiency of the shielding, i.e. dose rates measurement outside the shield are below the prescribed limits;
- Checking the shield homogeneity, i.e. highlighting attenuation variations because of accidental thickness differences or poor homogeneity of the material, it can also be due to a poor design or a discontinuity when performs.

Figure 5.50 illustrates a lack of homogeneity in an irradiation system containing a ^{60}Co source [30]. This inhomogeneity is evidenced by a digital radiography system. This failure is located at the interface between two pieces of the irradiator and is due to a poor design of the facility.

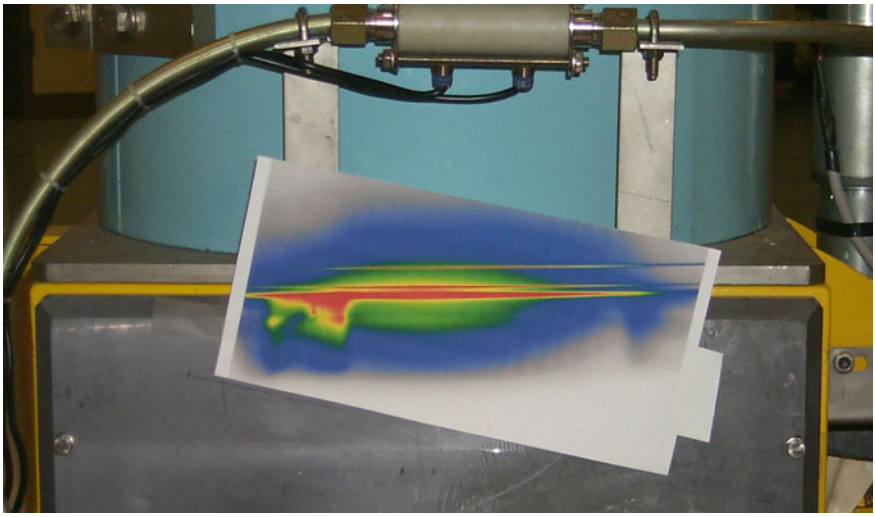

Fig. 5.50 Radiation leak at a poor device containing a radioactive source [30]

5.11 Toxic Gases Production: Ozone, Nitrogen Oxide, Nitrogen Dioxide

In facilities with a high exposure, air radiolysis may cause the production of toxic gases (non-radioactive) such as ozone (O_3) of the nitrogen oxide (NO) or nitrogen dioxide (NO_2). We will focus on the most toxic one: ozone.

For ozone [31], a limit of 0.1 ppm (0.2 mg m^{-3}) is commonly adopted in international literature [24].

In addition, it should be noted that ozone is a strong oxidizing agent producing a rapid corrosion of steel and copper elements.

The NCRP [24] described ozone buildup and destruction during radiation using (5.35).

$$\frac{dN}{dt} = gI - \alpha N - \kappa IN - \frac{Q}{V}N \tag{5.35}$$

With dN/dt production rate of ozone per unit volume and unit time (m^3 s^{-1}); N the number of ozone molecules per unit volume at time t (m^{-3}); I the energy deposited in the air per unit volume (eV m^3 s^{-1}); g the number of ozone molecules formed per unit energy (eV^{-1}); α the rate of decomposition of ozone molecules (s^{-1}); κ the number of destroyed ozone molecules per unit of energy and volume (eV^{-1} m^{-3}); Q the ventilation rate of irradiated volume (m^3 s^{-1}); V the irradiated volume (m^3).

The solution of (5.35) is given by the expression (5.36).

$$N(t) = \frac{gI}{\alpha + \kappa I + Q/V}[1 - \exp(-(\alpha + \kappa I + Q/V)t)] \tag{5.36}$$

Note that saturation (Long irradiation time), the ozone level is given by the solution (5.37).

$$N_{sat} = \frac{gI}{\alpha + \kappa I + Q/V} \tag{5.37}$$

the NCRP [24] proposes a usual value g = 0.074 eV^{-1} or 0.103 m^{-3} s^{-1} eV^{-1} for high dose rates (in excess of $5 \cdot 10^8$ Gy s^{-1} [18]). The value of α is set at $2.3 \cdot 10^{-4}$ s^{-1}. The κ value is very small, of the order of $1 \cdot 10^{-16}$, also $\kappa \times I$ is commonly omitted.

Note that after the end of irradiation, lasting t_i, the ozone levels vary as (5.38).

$$N(t) = N(t_i)[\exp(-(\alpha + Q/V)t)] \tag{5.38}$$

To calculate the energy deposited in the air per unit volume (eV m^3 s^{-1}) two radiation devices may be considered: an electron beam or a photon flux.

5.11.1 Electron Beam in Air [18]

For an electron beam with intensity i (in A) in a volume V (m^3), which reach a distance L (in cm) in the air, the quantity I is calculated using the mass stopping power (S/ρ) as presented in Chap. 2. The (5.39) gives the value of I.

$$I = 1 \cdot 10^6 \times \left(\frac{S}{\rho}\right)_{coll} \times \dot{N} \times \rho \times \frac{1}{V} \times L = 1 \cdot 10^6 \times \left(\frac{S}{\rho}\right)_{coll} \times \frac{i}{1.6 \cdot 10^{-19}} \times 1.29 \cdot 10^{-3} \times \frac{1}{V} \times L$$
$$I = 8 \cdot 10^{21} \frac{i}{V} \left(\frac{S}{\rho}\right)_{coll} L \tag{5.39}$$

As a first approximation (see Table 2.2) the mean value of the stopping power is

$$\left(\frac{S}{\rho}\right)_{coll} = 2 \text{ MeV cm}^2 \text{ g}^{-1}$$

then, the value of I corresponding is provided by (5.40)

$$I = 1.6 \cdot 10^{22} \frac{i}{V} L \tag{5.40}$$

Let us calculate the amount of ozone produced by an electron beam energy of 10 MeV and intensity 1 mA through 300 cm air in a room 4 m × 4 m × 3 m, with a ventilation rate of 10 h^{-1} working 5 min.

According to (5.40) we have

$$I = 1.6 \cdot 10^{22} \frac{i}{V} L = 1.6 \cdot 10^{22} \times \frac{1 \cdot 10^{-3}}{4 \times 4 \times 3} \times 300 = 1 \cdot 10^{20}\,\mathrm{eV\,m^{-3}\,s^{-1}}$$

According to (5.36), the number of ozone molecules per unit volume is:

$$N(t) = \frac{gI}{\alpha + \kappa I + Q/V}\left[1 - \exp(-(\alpha + \kappa I + Q/V)t)\right]$$

$$N(t) = \frac{0.074 \times 1 \cdot 10^{20}}{2.3 \cdot 10^{-4} + 10/3600} \times \left[1 - \exp\left(-\left(2.3 \cdot 10^{-4} + 10/3600\right) \times 5 \times 60\right)\right] = 1.5 \cdot 10^{21}\ \text{ozone molecule/m}^3$$

So

$$m = \frac{1.5 \cdot 10^{21}}{6.02 \cdot 10^{23}/3 \times 16} = 120\,\mathrm{mg\,m^{-3}}\ (60\,\mathrm{ppm})$$

The ozone concentration is greater than 0.1 ppm, so to access the device it is necessary to wait after the shut-down of the machine before entering the bunker.

5.11.2 Photon Beam

The energy deposited calculation in the air by photons is more complex, they do not deposit all their energy in a finite air volume.

Also, to determine the factor I, we have assessed using a Monte Carlo code (MCNPX), the mean energy (E_{dep} in eV m^{-3}) of a photon emitted isotropically in the center of a 3 m height rectangular bunker, square section variable at the ground. The energy deposited in this case is shown in Fig. 5.51, depending on the volume of the room for 1 photon energies, 2, 6, 10 and 20 MeV.

Thus for a beam emitting N photons per second the value I is given by the (5.41).

$$I = E_{dep} \times \dot{N} \tag{5.41}$$

For example, let us calculate the rate of ozone produced by a ^{60}Co industrial irradiator with an activity of 37,000 TBq in a room 4 m × 4 m × 3 m, with a ventilation rate of 10 h^{-1} running 5 min. Then, let us consider the time after which access will be allowed.

From Fig. 5.51, E_{dep} = 170 eV m^{-3} per photon. So, for 37,000 TBq ^{60}Co (emitting two photons per second):

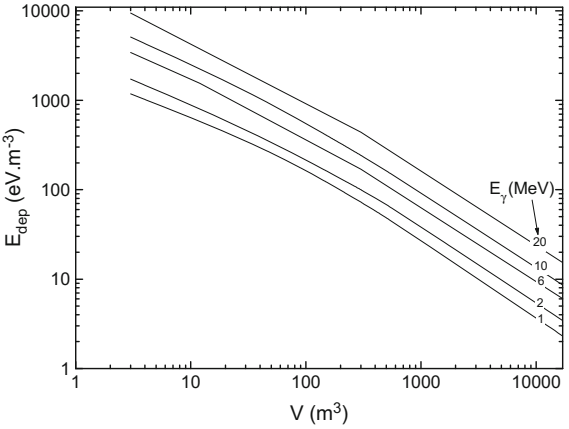

Fig. 5.51 Mean energy deposited by 1, 2, 6, 10 and 20 MeV photon emitted isotropically in the center of a parallelepiped of 3 m height bunker and a square section (variable)

$$I = E_{dep} \times \dot{N} = 270 * 37{,}000 * 1 \cdot 10^{12} * 2 = 2 \cdot 10^{19}\ \text{eV m}^{-3}\ \text{s}^{-1}$$

$$N(t) = \frac{0.074 \times 2 \cdot 10^{19}}{2.3 \cdot 10^{-4} + 10/3600} \times \left[1 - \exp\left(-\left(2.3 \cdot 10^{-4} + 10/3600\right) \times 5 \times 60\right)\right]$$
$$= 3 \cdot 10^{20}\ \text{molecule of ozone/m}^3$$

Is $m = \frac{3 \cdot 10^{20}}{6.02 \cdot 10^{23}/3 \times 16} = 23.3\ \text{mg m}^{-3}$ or $11.6\ \text{ppm}$

To access the bunker, the concentration must be 0.1 ppm. Therefore according to (5.38):

$$0.1 = 11.6 \times [\exp(-(\alpha + Q/V) \times t)],$$

is $t = -\frac{1}{\alpha + Q/V} \times \ln\left(\frac{0.1}{11.6}\right) = 1580\ \text{s}\ (26\ \text{min})$.

For industrial irradiators, it is greatly appropriate to consider this risk in advance of the design.

5.11.3 Bremsstrahlung

The calculation of the energy deposited in the air by bremsstrahlung photons is providing to be more complex for same reasons as previous: they do not deposit all their energy in a finite volume of air.

Thus, to determine the factor *I*, the mean energy deposited by a bremsstrahlung photon spectrum resulting from the reaction of an energy electron beam intensity E0 and 1 μA on a thick tungsten target placed at the center of a parallelepiped bunker 3 m height and a square section (variable), E_{dep} in eV m^{-3} s^{-1} μA^{-1}) was simulated. The energy deposited is presented by the Fig. 5.52, depending on the volume of the room for 1, 5, 10, 15, 20, 50, 80 and 100 MeV electrons.

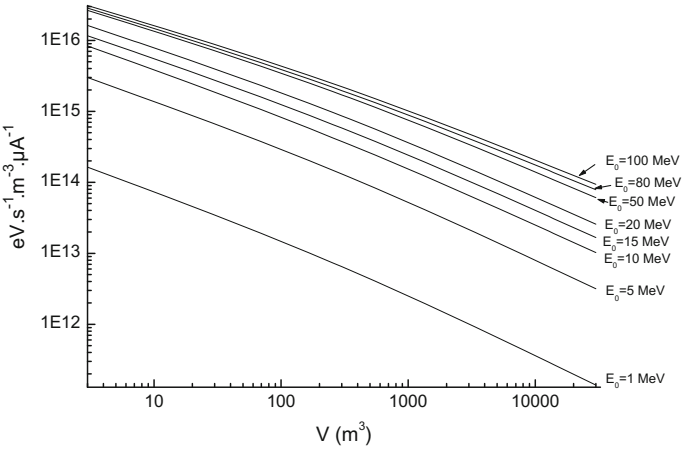

Fig. 5.52 Mean energy deposited for a bremsstrahlung photon spectrum resulting from the reaction of an electron beam energy E0 on a thick tungsten target placed at the center of a parallelepiped bunker (volume V) of 3 m height and square section (variable)

Let us calculate, for example, the rate of ozone produced by a bremsstrahlung spectrum produced by a 10 MeV and 1 mA beam and a volume V = 4 m × 4 m × 3 m, with a ventilation rate of 10 h^{-1} running 5 min (in this case the electron beam remains in the vacuum tube and not through the air of the bunker).

The Fig. 5.52 gives I = 1.3 · 10^{15} eV s^{-1} m^{-3} μA^{-1} and 1.3 · 10^{18} eV s^{-1} m^{-3} for 1 mA.

$$N(t) = \frac{0.074 \times 1.3 \cdot 10^{18}}{2.3 \cdot 10^{-4} + 10/3600} \times \left[1 - \exp\left(-\left(2.3 \cdot 10^{-4} + 10/3600\right) \times 5 \times 60\right)\right]$$
$$= 2 \cdot 10^{19} \text{ molecule of ozone/m}^3$$

Is $m = \frac{2 \cdot 10^{19}}{6.02 \cdot 10^{23}/3 \times 16} = 1.6 \text{ mg m}^{-3}$ or 0.8 ppm

5.12 Calculation Codes Dedicated to Shielding

A number of codes exist for assessing external numerical radiation protection quantities in more or less complex geometries. Remind that the use of a code still requires knowledge of the methods used to properly check their limits and operation fields. The calculation code use requires modeling radiation scene: source term, geometry, and calculation point.

The previous sections offer analytical approaches for delivering this thicknesses and appropriate geometries design for a number of identified conventional cases. When radiological scenes differ from these typical cases studied, these methods can

however provide information on the magnitude of thicknesses. Then, numerical codes consistently take over for more accurate results.

5.12.1 Point Kernel Method

The point kernel method which we have studied the theoretical basis is fairly easy to implement. It is based on a deterministic approach according to the expression (5.20) with a numerical solution of the integral. Note that this method can only deal with the sources of line spectra photons and primary walls.

The relevance of the results of such a code is related to the build-up evaluation and limits for use of this class of code. For a single event (one source, one shielding), it provides satisfactory results. Among the codes using this method, there may be mentioned the US code Microshield [16] or the French code Mercurad [32].

The microshield software [16] is supplied with a human-machine interface (HMI). The geometries are preset, but only 16 basic shapes such as sphere, cylinder, cube … are available. Eight conventional materials such as lead, air, water, iron … are tabulated. The decay/radioactive filiation of a radionuclide can be modeled, allowing from a given activity to calculate the dose equivalent rate at a later date. The code is limited to 25 energy bins, that is to say, for the treatment of radionuclides over 25 lines, the code includes the energy per bin, which can generate significant errors in estimating quantities. There is feature to perform calculations in 6 points simultaneously, but only in one direction. The build-up is based on the Taylor method hence no specific calculation for multilayer shields is implemented. The user must choose the build-up in one of present material to assign to all shielding present in the radiological scene. This approach can generate significant bias on the results.

The software Mercurad is based on the Mercure code developed at CEA [32]. It offers the ability to view 3D complex geometries and features a more developed HMI than Microshield. It is able to manage up to 100 points for calculation. The construction and preservation of new materials are possible. The calculation of the following variables: dose equivalent rate $H^*(10)$ and effective dose rate for anteroposterior (AP) irradiation is available. Mercurad allows, as Microshield, to set source terms from the energy spectra or a list of radionuclides with the corresponding activities. The definition of energy bins is done automatically if the calculations are made from a list of radionuclides. The software can manage up to 195 bins in the energy range 15 keV–10 MeV.

Mercurad performs integration of point kernel by a Monte Carlo method. The sources are spatially mesh (Cartesian grid, cylindrical or spherical) and energy bins are the energy grid.

For each source and each calculation point, Mercurad automatically determines the importance distribution of mesh. The most contributing meshes to result are

sampled more frequently. This therefore enables a numerical calculation considering each sample as punctual and mono-energetic source term.

Unlike Microshield, the buildup factors are determined from transport calculations with computer code Twodant [33]. They take into account the following physical phenomena: the photoelectric effect, coherent and incoherent scattering, pair production, bremsstrahlung and fluorescence.

These factors were calculated for 22 thicknesses between 0.5 and 50 mean free paths and 195 energie bins between 15 keV and 10 MeV.

Unlike Microshield, Mercurad uses a specific method to determine the buildup factor in two successive shielding. This is described by the formula of Suteau et al. [34] given in (5.42).

$$B_{1,2}(X_1, X_2) = \frac{B_1(X_1)}{B_2(X_2)} B_2(X_1 + X_2) F_{1,2}(X_1, X_2) \tag{5.42}$$

The parameters of this equation are: X1 and X2 the respective thicknesses of shielding 1 and 2; B1 and B2 the respective buildup factors shielding 1 and 2; $F_{1,2}$ (X1, X2) depends on many parameters determined from transport calculations with Twodant.

For a shielding series (more than two), Mercurad uses an iterative process. Each iteration consists of two steps: calculation of the buildup factor of the first two shielding of formula (5.42); the two shielding are replaced by an equivalent single shielding composed of a single chemical element (it gets the same buildup factor of the two shielding and its thickness in terms of number of mean free path is the same as that of the two shielding); at the end of the first iteration, the computation can therefore be made to a third shielding using the equivalent shielding and so on.

To illustrate the multi-layer problem, let us take the example of Sect. 5.4.2, allowing the dose rate calculation to a meter of a 1 MeV photon source and $3.7 \cdot 10^{10}$ (γ) s^{-1} behind a first 1 cm lead shielding, and a second 10 cm water and reverse calculation (water and lead).

Taking as reference the Monte Carlo result, we see that the calculation in Table 5.9 Mercurad gives the best result. This is due to the valuation method of build-up, much more efficient in the case of multi-layer problem.

Table 5.9 Results of calculations of various codes for multi-layer simulation

Case	Microshield* (mSv/h)	Mercurad (mSv/h)	Semiempirical method (5.16) (mSv/h)	Monte Carlo (mSv/h)
Lead and water	1.7 or 3	3.2	3	2.45
Water then lead	1.7 or 3	2.2	2.7	2.15

*Depending on the choice of the user settings, two different results are given. The calculation method of Microshield does not take into account the location of the shielding

5.12.2 Other Computer Codes

The point kernel method only partially treat radiological protection issues limited to calculations of primary walls for line spectra photons. What about assessment for protection against neutrons, radiation from particle interactions with matter (accelerators, X generators …), secondary walls, maze …? As it has been widely mentioned throughout the previous chapters, using the Monte Carlo method solves almost all these problems of calculation. This transport method is often regarded as the reference from which the codes with less complex algorithms (such as those with point kernel method) are qualified.

The Monte-Carlo method and codes working with, for the use of dosimetry and radiation protection, are complex and require alone a separate chapter in this book. They are presented in next Chap. 6.

Further Details 5.1: dose equivalent rate for a uniformly contaminated enclosure

Consider a person located at the center of a room, exposed to a noble gas, ^{85}Kr, uniformly distributed in the room. The Room is parallelepiped of floor R^2 and ceiling height R/2. Let us calculate the dose equivalent rate at the location point, neglecting attenuation in the air of gamma ray of 514 keV emitted with a 0.43% intensity and exposure β (add that there is no internal exposure by inhalation for noble gas). The problem amounts to solving a volume integral type:

$$I = \iiint_V \frac{1}{\rho^2} dV \tag{1}$$

The spherical coordinates are used, considering only one twenty-fourth of a cubic R, as shaded in the figure below:

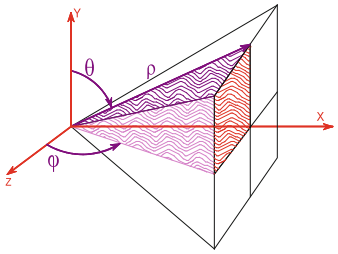

$$\begin{cases} x = \rho \sin\theta \cos\varphi \\ y = \rho \sin\varphi \sin\theta \\ z = \rho \cos\theta \end{cases}$$

avec(2) : $\rho = \frac{R}{2 \sin\theta \sin\varphi}$ *with* (2)/(3) : $\theta = Arc\tan\left(\frac{1}{\sin\varphi}\right)$ and the volume element is:

$$dV = \rho^2 \sin\theta \, d\theta \, d\phi \, d\rho$$

The integral (1) to a volume of half a cube of R × R × R/2 becomes:

$$\begin{aligned}
I &= 12 \int_{\rho=0}^{\rho=R/2 \sin\theta \sin\varphi} \int_{\theta=\arctan(1/\sin\varphi)}^{\theta=\pi/2} \int_{\varphi=\pi/4}^{\varphi=\pi/2} \sin\theta \, d\theta \, d\varphi \, d\rho \\
I &= 12 \int_{\theta} \int_{\varphi} \left[\frac{R}{2 \sin\theta \sin\varphi}\right] \sin\theta \, d\theta \, d\varphi \\
I &= 6R \int_{\theta=\arctan(1/\sin\varphi)}^{\theta=\pi/2} \int_{\varphi=\pi/2}^{\varphi=\pi/2} \frac{1}{\sin\varphi} d\varphi \, d\theta \\
I &= 6R \int_{\theta=\pi/4}^{\theta=\pi/2} \frac{1}{\sin\varphi} \left(\frac{\pi}{2} - \arctan\left(\frac{1}{\sin\varphi}\right)\right) d\varphi \\
I &= 6R \left(\left[\frac{\pi}{2} \ln\left(\tan\frac{\varphi}{2}\right)\right]_{\pi/4}^{\pi/2} - \int_{\pi/4}^{\pi/2} \frac{1}{\sin\varphi} \arctan\left(\frac{1}{\sin\varphi}\right) d\varphi \right) \\
I &= 6R \times (1.38446 - 0.74496) \\
I &= 3.837 \times R
\end{aligned} \tag{5}$$

The fluence rate due to an activity concentration of 1 Bq/m^3 of ^{85}Kr, is obtained by:

$$\dot{\Phi} = \iiint_V \frac{a_v \Gamma}{4\pi r^2} dV = \iiint_V \left(\frac{1}{R^3}\right) \frac{\Gamma}{4\pi r^2} dV = \frac{\Gamma}{4\pi R^3} \iiint_V \frac{1}{r^2} dV$$

Or with the expression (5): $\dot{\Phi} = \frac{0.43 \cdot 10^{-2} \times 3.837 \times R}{4\pi R^3} = \frac{1.31 \cdot 10^{-3}}{R^2}$

The factor "fluence- ambient dose equivalent" of ^{85}Kr is 3 pSv cm^2, the ambient dose equivalent rate in function of R for A Bq/m^3 is given by:

$$\dot{H}^*(10) = h_\Phi^*(10) \frac{1.31 \cdot 10^{-3} A}{R^2} \times 3600 \times 3 \cdot 10^{-6} = 1.418 \cdot 10^{-5} \left(\frac{A}{R^2}\right) \mu\text{Sv/h}$$

Appendix 1. Material Composition

Type of concrete	Ordinary (Bouniol 2001)*	Barium [1]	Colemanite (Bouniol 2001)	Hematite (Bouniol 2001)
Density	2.3	3.3	2.14	4
Composition				
Si	20.68	–	1.56	0.91
Al	0.36	–	4.49	0.12
O	50.85	35.95	60.72	32.82
Ca	21.65	5.07	17.11	4.11
Mg	0.2	–	0.67	–
S	0.14	10.99	–	–
C	4.52	–	0.39	–
H	0.7	0.74	3.25	0.43
Fe	0.66	–	2.5	61.42
Ba	–	47.25	–	–
Ti	–	–	0.31	–
^{10}B	–	–	1.74	–
^{11}B	–	–	7.06	–

Composition of concrete (mass%)
*Based on data Bouniol (2001) *Bétons spéciaux de protection.* Techniques de l'ingénieur. BN 3, 740-1

	Lead glass
Density	4.1
Pb	56.8
O	25.5
Yes	17.7

Lead glass composition (wt%) [21]

	Stainless steel
Density	7.8
Fe	69.25
Cr	18
Or	10
mn	2
Yes	0.75

Composition of the stainless steel type Z2CND1810 (wt%)
Density of lead: 10.8
Density polyethylene $(CH_2)_n$: 0.92

Appendix 2. Neutron Transmission Indexes

Thickness (cm)	Concrete ordinary	Concrete barium	Concrete colemanite	Concrete hematite	Water	CH_2	Steel stainless steel	Glass lead	Lead
0	1.06E+01	1.06E+01	1.06E+01	1.06E+01	1.06E+01	1.06E+01	1.06E+01	1.06E+01	1.06E+01
2.5	9.38E+00	8.36E+00	1.18E+00	8.28E+00	3.54E+00	2.89E+00	8.33E+00	1.11E+01	1.05E+01
5	6.85E+00	5.64E+00	9.58E−01	5.54E+00	1.72E+00	1.36E+00	4.81E+00	9.97E+00	8.67E+00
7.5	5.33E+00	4.10E+00	7.36E−01	4.04E+00	1.08E+00	8.87E−01	2.87E+00	8.76E+00	7.05E+00
10	4.30E+00	3.11E+00	5.43E−01	3.07E+00	8.12E−01	7.15E−01	1.72E+00	7.69E+00	5.74E+00
20	2.12E+00	1.12E+00	1.35E−01	1.10E+00	5.21E−01	5.20E−01	2.16E−01	4.69E+00	2.72E+00
30	1.12E+00	4.16E−01	3.04E−02	3.99E−01	3.87E−01	3.98E−01	2.60E−02	2.99E+00	1.39E+00
40	5.95E−01	1.54E−01	7.27E−03	1.43E−01	2.79E−01	2.96E−01	2.97E−03	1.94E+00	7.36E−01
50	3.16E−01	5.66E−02	2.14E−03	5.09E−02	1.97E−01	2.15E−01	3.70E−04	1.28E+00	3.99E−01
75	6.84E−02	4.82E−03	3.09E−04	3.96E−03	7.85E−02	9.19E−02	1.06E−06	4.52E−01	9.09E−02
100	1.52E−02	4.38E−04	8.25E−05	2.82E−04	3.03E−02	3.80E−02	1.76E−09	1.61E−01	2.17E−02
150	8.37E−04	2.96E−06	5.36E−06	8.94E−07	4.32E−03	6.24E−03	1.83E−14	2.19E−02	1.41E−03
200	3.30E−05	5.95E−09	9.05E−07	2.34E−09	5.79E−04	9.92E−04	1.34E−19	3.15E−03	6.47E−05

Neutron transmission indexes pSv cm^2 for thermal neutrons

Thickness (Cm)	Concrete ordinary	Concrete barium	Concrete colemanite	Concrete hematite	Water	CH_2	Steel stainless steel	Glass lead	Lead
0	3.22E+02	3.22E+02	3.22E+02	3.22E+02	3.22E+02	3.22E+02	3.22E+02	3.22E+02	3.22E+02
2.5	3.19E+02	3.10E+02	2.22E+02	3.15E+02	1.93E+02	1.64E+02	3.16E+02	3.55E+02	3.41E+02
5	2.39E+02	2.21E+02	9.88E+01	2.24E+02	7.97E+01	5.86E+01	2.69E+02	3.15E+02	3.39E+02
7.5	1.61E+02	1.42E+02	3.81E+01	1.42E+02	3.02E+01	1.96E+01	2.24E+02	2.59E+02	3.31E+02
10	1.03E+02	8.70E+01	1.37E+01	8.66E+01	1.16E+01	7.12E+00	1.87E+02	2.04E+02	3.20E+02
20	1.70E+01	1.21E+01	3.19E−01	1.14E+01	1.72E+00	1.61E+00	9.66E+01	7.14E+01	2.74E+02
30	4.60E+00	2.70E+00	4.40E−02	2.02E+00	1.18E+00	1.21E+00	5.16E+01	2.51E+01	2.30E+02
40	2.04E+00	8.93E−01	1.00E−02	5.41E−01	8.60E−01	9.05E−01	2.65E+01	1.01E+01	1.92E+02
50	1.06E+00	3.24E−01	2.79E−03	1.80E−01	6.13E−01	6.60E−01	1.30E+01	5.11E+00	1.57E+02
75	2.18E−01	2.63E−02	3.31E−04	1.35E−02	2.45E−01	2.85E−01	1.86E+00	2.25E+00	8.81E+01
100	4.73E−02	2.30E−03	8.39E−05	9.46E−04	9.40E−02	1.17E−01	2.36E-01	1.24E+00	4.42E+01
150	2.52E−03	1.33E−05	3.36E−06	3.15E−06	1.34E−02	1.92E−02	4.15E-03	2.50E-01	9.51E+00
200	9.30E−05	7.02E−08	1.98E−07	9.36E−09	1.75E−03	3.22E−03	1.40E-04	3.84E-02	2.31E+00

Neutron transmission indexes pSv cm^2 for neutrons of 0.5 MeV

Thickness (cm)	Concrete ordinary	Concrete barium	Concrete colemanite	Concrete hematite	Water	CH_2	Steel stainless steel	Glass lead	Lead
0	4.16E+02	4.16E+02	4.16E+02	4.16E+02	4.16E+02	4.16E+02	4.16E+02	4.16E+02	4.16E+02
2.5	3.42E+02	3.31E+02	2.77E+02	3.16E+02	2.72E+02	2.97E+02	3.55E+02	3.68E+02	4.35E+02
5	2.52E+02	2.34E+02	1.45E+02	2.20E+02	1.38E+02	1.52E+02	2.88E+02	3.00E+02	4.18E+02
7.5	1.81E+02	1.61E+02	7.04E+01	1.52E+02	6.43E+01	6.91E+01	2.42E+02	2.46E+02	3.93E+02
10	1.28E+02	1.10E+02	3.27E+01	1.05E+02	2.89E+01	3.00E+01	2.09E+02	2.04E+02	3.66E+02
20	3.09E+01	2.25E+01	1.38E+00	2.14E+01	2.28E+00	2.41E+00	1.24E+02	9.76E+01	2.69E+02
30	7.67E+00	4.71E+00	7.99E−02	4.11E+00	1.12E+00	1.42E+00	7.46E+01	4.21E+01	1.99E+02
40	2.39E+00	1.17E+00	1.06E−02	8.56E−01	8.07E−01	1.06E+00	4.38E+01	1.74E+01	1.50E+02
50	9.93E−01	3.44E−01	2.62E−03	2.14E−01	5.72E−01	7.73E−01	2.50E+01	7.51E+00	1.15E+02
75	1.83E−01	2.60E−02	2.57E−04	1.21E−02	2.31E−01	3.35E−01	5.24E+00	1.92E+00	6.12E+01
100	3.84E−02	2.00E−03	6.91E−05	8.43E−04	8.83E−02	1.38E−01	9.26E−01	9.56E−01	3.38E+01
150	2.02E−03	1.40E−05	6.32E−06	2.97E−06	1.26E−02	2.32E−02	2.00E−02	2.07E−01	1.09E+01
200	1.12E−04	2.80E−08	1.77E−07	1.82E−08	1.71E−03	3.77E−03	3.34E−04	3.28E−02	3.43E+00

Neutron transmission indexes pSv cm^2 for 1 MeV neutrons

Thickness (cm)	Concrete ordinary	Concrete barium	Concrete colemanite	Concrete hematite	Water	CH_2	Steel stainless steel	Glass lead	Lead
0	4.16E+02	4.16E+02	4.16E+02	4.16E+02	4.16E+02	4.16E+02	4.16E+02	4.16E+02	4.16E+02
2.5	4.39E+02	4.36E+02	4.27E+02	4.42E+02	4.18E+02	4.00E+02	4.30E+02	4.45E+02	4.36E+02
5	4.25E+02	4.17E+02	3.64E+02	4.21E+02	3.46E+02	3.01E+02	3.93E+02	4.39E+02	4.18E+02
7.5	3.95E+02	3.80E+02	2.80E+02	3.79E+02	2.58E+02	2.01E+02	3.48E+02	4.22E+02	3.91E+02
10	3.57E+02	3.33E+02	2.03E+02	3.28E+02	1.81E+02	1.26E+02	3.03E+02	4.01E+02	3.63E+02
20	1.98E+02	1.61E+02	4.38E+01	1.44E+02	3.60E+01	1.60E+01	1.71E+02	2.98E+02	2.66E+02
30	9.49E+01	6.68E+01	8.19E+00	5.18E+01	7.26E+00	3.05E+00	9.66E+01	1.99E+02	2.00E+02
40	4.30E+01	2.60E+01	1.45E+00	1.75E+01	2.22E+00	1.44E+00	5.39E+01	1.24E+02	1.54E+02
50	1.90E+01	9.82E+00	2.54E−01	5.72E+00	1.11E+00	9.81E−01	2.94E+01	7.35E+01	1.21E+02
75	2.55E+00	8.28E−01	4.62E−03	3.64E−01	3.99E−01	4.18E−01	5.85E+00	1.89E+01	6.84E+01
100	3.81E−01	6.94E−02	2.60E−04	2.68E−02	1.54E−01	1.75E−01	1.01E+00	5.41E+00	3.85E+01
150	1.53E−02	5.22E−04	7.14E−06	1.60E−04	2.18E−02	2.85E−02	2.40E−02	7.62E−01	1.15E+01
200	5.91E−04	4.69E−07	2.97E−07	1.73E−07	3.14E−03	4.62E−03	4.17E−04	1.25E−01	3.31E+00

Neutron transmission indexes pSv cm^2 for neutrons of 2.5 MeV

Thickness (cm)	Concrete ordinary	Concrete barium	Concrete colemanite	Concrete hematite	Water	CH_2	Steel stainless steel	Glass lead	Lead
0	4.05E+02	4.05E+02	4.05E+02	4.05E+02	4.05E+02	4.05E+02	4.05E+02	4.05E+02	4.05E+02
2.5	4.12E+02	4.10E+02	4.15E+02	4.18E+02	4.23E+02	4.30E+02	4.26E+02	4.19E+02	4.32E+02
5	4.01E+02	3.93E+02	3.83E+02	4.00E+02	3.93E+02	3.87E+02	3.94E+02	4.15E+02	4.22E+02
7.5	3.82E+02	3.62E+02	3.29E+02	3.65E+02	3.39E+02	3.15E+02	3.50E+02	4.03E+02	4.01E+02
10	3.56E+02	3.25E+02	2.70E+02	3.22E+02	2.78E+02	2.42E+02	3.06E+02	3.87E+02	3.76E+02
20	2.32E+02	1.77E+02	9.55E+01	1.57E+02	1.01E+02	6.60E+01	1.71E+02	2.94E+02	2.80E+02
30	1.31E+02	8.39E+01	2.85E+01	6.37E+01	3.17E+01	1.62E+01	9.64E+01	2.00E+02	2.12E+02
40	6.91E+01	3.74E+01	7.91E+00	2.40E+01	9.99E+00	4.57E+00	5.38E+01	1.27E+02	1.64E+02
50	3.48E+01	1.60E+01	2.10E+00	8.68E+00	3.47E+00	1.84E+00	2.91E+01	7.80E+01	1.29E+02
75	5.75E+00	1.81E+00	7.52E−02	6.29E−01	5.61E−01	5.69E−01	5.73E+00	2.18E+01	7.34E+01
100	9.08E−01	1.91E−01	3.67E−03	4.61E−02	1.89E−01	2.38E−01	9.81E−01	6.37E+00	4.12E+01
150	2.25E−02	1.94E−03	5.02E−05	1.51E−04	2.65E−02	4.06E−02	2.22E−02	8.23E−01	1.21E+01
200	8.44E−04	4.37E−06	1.58E−06	1.96E−07	3.36E−03	7.20E−03	3.93E−04	1.31E−01	3.40E+00

Neutron transmission indexes pSv cm^2 for neutrons 5 MeV

Thickness (cm)	Concrete ordinary	Concrete barium	Concrete colemanite	Concrete hematite	Water	CH_2	Steel stainless steel	Glass lead	Lead
0	4.40E+02	4.40E+02	4.40E+02	4.40E+02	4.40E+02	4.40E+02	4.40E+02	4.40E+02	4.40E+02
2.5	4.34E+02	4.42E+02	4.41E+02	4.41E+02	4.51E+02	4.58E+02	4.47E+02	4.51E+02	5.04E+02
5	4.09E+02	4.16E+02	4.07E+02	4.13E+02	4.33E+02	4.40E+02	4.16E+02	4.39E+02	5.21E+02
7.5	3.78E+02	3.79E+02	3.58E+02	3.73E+02	3.95E+02	4.00E+02	3.74E+02	4.18E+02	5.18E+02
10	3.44E+02	3.36E+02	3.04E+02	3.27E+02	3.50E+02	3.49E+02	3.29E+02	3.92E+02	5.05E+02
20	2.10E+02	1.80E+02	1.32E+02	1.61E+02	1.81E+02	1.65E+02	1.86E+02	2.78E+02	4.15E+02
30	1.15E+02	8.66E+01	5.08E+01	6.78E+01	8.35E+01	6.82E+01	1.04E+02	1.77E+02	3.26E+02
40	6.01E+01	3.95E+01	1.87E+01	2.66E+01	3.72E+01	2.76E+01	5.79E+01	1.07E+02	2.56E+02
50	3.05E+01	1.75E+01	6.81E+00	1.00E+01	1.68E+01	1.13E+01	3.16E+01	6.27E+01	2.01E+02
75	5.35E+00	2.17E+00	5.92E−01	8.26E−01	2.74E+00	1.75E+00	6.32E+00	1.65E+01	1.12E+02
100	9.50E−01	2.59E−01	7.31E−02	6.47E−02	7.01E−01	5.26E−01	1.12E+00	4.93E+00	6.16E+01
150	3.31E−02	3.26E−03	3.46E−03	3.95E−04	1.29E−01	1.01E−01	2.81E−02	6.74E−01	1.78E+01
200	1.48E−03	1.18E−04	2.19E−04	4.10E−07	3.29E−02	2.24E−02	6.17E−04	1.09E−01	5.06E+00

Neutron transmission indexes pSv cm^2 for 10 MeV neutrons

Thickness (cm)	Concrete ordinary	Concrete barium	Concrete colemanite	Concrete hematite	Water	CH_2	Steel stainless steel	Glass lead	Lead
0	5.20E+02	5.20E+02	5.20E+02	5.20E+02	5.20E+02	5.20E+02	5.20E+02	5.20E+02	5.20E+02
2.5	5.15E+02	5.29E+02	5.18E+02	5.24E+02	5.26E+02	5.28E+02	5.33E+02	5.38E+02	6.12E+02
5	4.88E+02	5.08E+02	4.82E+02	4.93E+02	5.09E+02	5.08E+02	5.02E+02	5.30E+02	6.49E+02
7.5	4.54E+02	4.71E+02	4.31E+02	4.46E+02	4.75E+02	4.70E+02	4.57E+02	5.10E+02	6.56E+02
10	4.15E+02	4.27E+02	3.74E+02	3.93E+02	4.33E+02	4.22E+02	4.08E+02	4.84E+02	6.50E+02
20	2.60E+02	2.45E+02	1.80E+02	1.98E+02	2.58E+02	2.37E+02	2.39E+02	3.52E+02	5.53E+02
30	1.48E+02	1.25E+02	7.62E+01	8.63E+01	1.37E+02	1.18E+02	1.35E+02	2.30E+02	4.42E+02
40	7.98E+01	5.98E+01	3.06E+01	3.51E+01	7.00E+01	5.67E+01	7.47E+01	1.41E+02	3.50E+02
50	4.18E+01	2.80E+01	1.20E+01	1.37E+01	3.51E+01	2.67E+01	4.07E+01	8.39E+01	2.77E+02
75	7.81E+00	3.95E+00	1.17E+00	1.22E+00	6.42E+00	4.37E+00	8.13E+00	2.25E+01	1.54E+02
100	1.42E+00	5.25E−01	1.35E−01	9.76E−02	1.46E+00	9.76E−01	1.44E+00	6.70E+00	8.54E+01
150	5.17E−02	8.96E−03	5.02E−03	7.39E−04	1.86E−01	1.28E−01	3.61E−02	8.93E−01	2.48E+01
200	1.28E−03	3.15E−05	4.74E−04	3.52E−07	4.41E−02	2.88E−02	5.98E−04	1.43E−01	7.16E+00

Neutron transmission indexes pSv cm^2 for 14 MeV neutrons

Thickness (cm)	Concrete ordinary	Concrete barium	Concrete colemanite	Concrete hematite	Water	CH_2	Steel stainless steel	Glass lead	Lead
0	3.87E+02	3.87E+02	3.87E+02	3.87E+02	3.87E+02	3.87E+02	3.87E+02	3.87E+02	3.87E+02
2.5	3.92E+02	3.87E+02	3.54E+02	3.87E+02	3.42E+02	3.28E+02	3.95E+02	4.06E+02	4.07E+02
5	3.58E+02	3.44E+02	2.69E+02	3.41E+02	2.55E+02	2.27E+02	3.60E+02	3.89E+02	3.90E+02
7.5	3.13E+02	2.92E+02	1.92E+02	2.86E+02	1.80E+02	1.46E+02	3.18E+02	3.63E+02	3.66E+02
10	2.69E+02	2.40E+02	1.33E+02	2.32E+02	1.24E+02	9.30E+01	2.78E+02	3.34E+02	3.41E+02
20	1.27E+02	9.70E+01	2.97E+01	8.60E+01	2.90E+01	1.68E+01	1.59E+02	2.18E+02	2.52E+02
30	5.69E+01	3.69E+01	6.85E+00	2.88E+01	8.18E+00	4.46E+00	8.99E+01	1.31E+02	1.90E+02
40	2.45E+01	1.40E+01	1.66E+00	9.47E+00	2.90E+00	1.86E+00	5.02E+01	7.46E+01	1.47E+02
50	1.08E+01	5.32E+00	4.27E−01	3.13E+00	1.36E+00	1.06E+00	2.71E+01	4.20E+01	1.15E+02
75	1.70E+00	4.94E−01	2.07E−02	1.97E−01	3.75E−01	3.97E−01	5.33E+00	1.06E+01	6.39E+01
100	2.66E−01	4.65E−02	1.54E−03	1.37E−02	1.35E−01	1.61E−01	9.14E−01	3.31E+00	3.51E+01
150	8.19E−03	4.96E−04	4.28E−05	9.74E−05	1.97E−02	2.76E−02	2.15E−02	5.23E−01	1.01E+01
200	4.00E−04	3.97E−06	3.58E−06	1.49E−07	2.88E−03	4.69E−03	4.41E−04	8.47E−02	2.89E+00

Neutron transmission indexes pSv cm^2 for a neutron spectrum of a source of ^{244}Cm

Thickness (cm)	Concrete ordinary	Concrete barium	Concrete colemanite	Concrete hematite	Water	CH_2	Steel stainless steel	Glass lead	Lead
0	3.92E+02	3.92E+02	3.92E+02	3.92E+02	3.92E+02	3.92E+02	3.92E+02	3.92E+02	3.92E+02
2.5	4.01E+02	4.00E+02	3.86E+02	4.02E+02	3.85E+02	3.78E+02	4.06E+02	4.11E+02	4.16E+02
5	3.79E+02	3.71E+02	3.32E+02	3.72E+02	3.32E+02	3.11E+02	3.74E+02	4.01E+02	4.04E+02
7.5	3.47E+02	3.31E+02	2.68E+02	3.28E+02	2.70E+02	2.39E+02	3.32E+02	3.82E+02	3.83E+02
10	3.12E+02	2.87E+02	2.09E+02	2.80E+02	2.14E+02	1.78E+02	2.90E+02	3.59E+02	3.59E+02
20	1.79E+02	1.40E+02	6.80E+01	1.25E+02	7.49E+01	5.06E+01	1.64E+02	2.55E+02	2.68E+02
30	9.34E+01	6.20E+01	2.05E+01	4.83E+01	2.60E+01	1.52E+01	9.24E+01	1.65E+02	2.02E+02
40	4.68E+01	2.64E+01	6.16E+00	1.77E+01	9.47E+00	5.34E+00	5.15E+01	1.01E+02	1.56E+02
50	2.29E+01	1.10E+01	1.87E+00	6.29E+00	3.87E+00	2.27E+00	2.80E+01	6.01E+01	1.23E+02
75	3.77E+00	1.22E+00	1.12E−01	4.67E−01	6.90E−01	5.89E−01	5.53E+00	1.62E+01	6.79E+01
100	6.21E−01	1.30E−01	1.11E−02	3.00E−02	2.12E−01	2.29E−01	9.57E−01	4.87E+00	3.74E+01
150	2.08E−02	1.64E−03	3.46E−04	1.40E−04	3.26E−02	4.12E−02	2.40E−02	6.80E−01	1.08E+01
200	7.47E−04	2.36E−06	2.37E−05	4.88E−07	5.99E−03	7.77E−03	4.07E−04	1.10E−01	3.10E+00

Neutron transmission indexes pSv cm^2 for a neutron spectrum of a source of ^{241}Am-Be

References

1. ISO. (2002). *Écrans de protection neutroniques—Principes de conception et éléments pour le choix de matériaux appropriés*. Norme NF. ISO 14152.
2. Delacroix, D., Guerre, J. P., Leblanc, P. (2004). *Radionucléides and radioprotection*. EDP Sciences. ISBN 2-86883-704-2.
3. PMDS. (1968). *Catalogue des centres d'études nucléaires—Chapitre I. Éléments constitutifs d'enceintes blindées.* CEA.
4. Cember, H. (1983). *Introduction to health physics* (2nd edition). Pergamon Press.
5. Bourgois, L., & Comte, N. (2014). Monte Carlo method used to determine scatter fractions for estimating secondary gamma-ray and X-ray photons dose equivalent rate. *Radioprotection, 49*, 107–113.
6. Pages, L., Bertel, E., Joffre, H., Sklavenitis, L. (1972). Energy loss, range and bremsstralhung yield for 10 keV–100 MeV electrons. *Atomic data, 4*(1).
7. Katz, L., & Penfold, A. S. (1952). Range energy relations for electrons and the determination on beta-ray end point energies by absorption. *Reviews of Modern Physics, 24*(1), 28–44.
8. Hubbell, J. H., Seltzer, S. M. (1996). Tables of X-ray mass attenuation coefficients and mass energy-absorption coefficients from 1 keV to 20 MeV for elements $Z = 1$–92 and 48 additional substances of dosimetric interest ionizing radiation division, physics laboratory, NIST. http://physics.nist.gov/PhysRefData/XrayMassCoef/tab3.html et http://physics.nist.gov/PhysRefData/XrayMassCoef/tab4.html.
9. Klein, O., & Nishina, Y. (1929). Die Streuung von Strahlung durch freie Elektronen nach der neuen relativistischen Quantendynamik von Dirac. *Zeitschrift für Physik, 52*(11–12), 853–869.
10. White, G. R. (1950) the penetration of Co60 gamma-rays in water using spherical geometry. *Physical Review*, *80*(1).
11. Tanaka, et al. (1988). Annotated bibliography and discussion of gamma–ray build-up factors. *Applied Radiation and Isotopes, 39*(3), 241–252.
12. ANSI/ANS–6.4.3. (1991). *American national standard gamma ray attenuation coefficients and build-up factors for engineering materials.* American Nuclear Society.
13. Jaeger, R. G. (Ed.). (1968). *Engineering compendium on radiation shielding. Volume I. Shielding fundamentals and methods.* Springer.
14. Shultis, J. K., Faw, R. E. (2000). *Radiation shielding*. American Nuclear Society, Inc.
15. PMDS. (1969). *Catalogue des centres d'études nucléaires—Chapitre III. Manipulation, première partie*. CEA.
16. Microshield. (2009). Grove Software Inc. www.radiationsoftware.com.
17. NCRP. (2004). *Structural shielding design for medical X-ray imaging facilities*. NCRP Report 147.
18. IAEA. (1979). Radiological safety aspects of the operation of electron linear accelerators. *IAEA Technical reports series, 188*.
19. NCRP. (1976). *Structural shielding design and evaluation for medical use of X rays and gamma rays of energies up to 10 MeV*. NCRP report no 49.
20. ICRP. (1971). Protection against ionizing radiation from external sources and data for protection against ionizing radiation from external sources. Publication 15 and 21.
21. International Electrotechnical Commission. (1981). Safety of medical electrical equipment part. 2: Particular requirements for medical electron accelerators in the range 1–50 MeV. (Bureau Central de la Commission Electrotechnique Internationale Geneve, Suisse) Publication 601-2-1.
22. NCRP. (2008). *Structural shielding and evaluation for megavoltage X and gamma rays radiotherapy facilities*. NCRP report no 151.
23. Bourgois, L., Comte, N. (2001). *Calcul des facteurs de transmission pour les neutrons en équivalent de dose (CIPR 60) par une méthode de Monte-Carlo*. Congrès SFRP Tours.
24. NCRP. (2003). *Radiation protection for particle accelerator facilities*. NCRP report 144.

25. IAEA. (2000). *Handbook on photonuclear data for applications*. IAEA TecDoc 1178.
26. IAEA. (1988). Radiological safety aspects of the operation of Proton Accelerators. *IAEA Technical reports series, 283*.
27. Sullivan, A. H. (1992) *A guide to radiation and radioactivity levels near high energy particle accelerators*. Nuclear Technology Publishing.
28. Bourgois, L. (1999). Cours régional AIEA sur la notification l'enregistrement et le contrôle des sources de rayonnements. Travaux Dirigés Évaluation de la sûreté d'un irradiateur.
29. IAEA. (1992). *Practical radiation safety manual. Manual on shielded enclosures. Incorporating applications guide procedures guide basics guide*. IEA–PRSM–2.
30. Lelache, H. (2002). Démarche ALARA. Contribution à la diminution de l'exposition radiologique. *Les journées de la propreté radiologique*. CEA Saclay.
31. INRS. (1997). Ozone. *Fiche toxicologique, 43*.
32. Suteau, C., Chiron, M., Luneville, L., Berger, L., Huver, M. (2003). *MERCURE: Un code 3D industriel de propagation des gammas par la méthode d'atténuation en ligne droite. Applications en radioprotection. Codes de calcul en dosimétrie radiophysique et radioprotection*. Congrès de la SFRP Sochaux.
33. Alcouffe, R. E., Brinkley, F. W., Marr, D. R., O'Dell, R. D. (1990). User's guide for TWODANT: A code package for two-dimensional, diffusion-accelerated, neutral-particle, transport, LA–10049–M revised.
34. Suteau, C., Chiron, M., & Arnaud, G. (2004). Improvement of the MERCURE–6's general formalism for calculating γ—ray build-up factors in multilayer shields. *Nuclear Science and Engineering, 147*, 43–55.
35. NCRP. (1977). *Radiation protection design guidelines for 0.1–100 MeV particle accelerator facilities*. NCRP report no 51.
36. NF C 15–160. (2011). Installations pour la production et l'utilisation de rayonnement X— exigences de radioprotection.

Chapter 6
Principle of the Monte-Carlo Method Applied to Dosimetry and Radiation Protection

Abstract In previous chapters, we have seen that it is possible to resolve dosimetric and radiation protection problems with fairly easy analytical approaches. By the way, some of these logics are implemented in deterministic codes (e.g. point kernel method). However, according to circumstances, these methods can lead to significant bias on results especially for complex radiological cases. In order to offset these issues, it may be necessary to switch to a Monte Carlo method. Computational algorithms based on this method rely on repeated random sampling to obtain numerical results. It allows a smooth definition of physical parameters during the particle transport for more accuracy in final results. Furthermore, this method is particularly suitable in multi-particles transport problems and for complex geometries involving multi-materials and various densities. In what follows, the Monte-Carlo method applied to particle transport is detailed in terms of implementation in codes and features for radiation protection and dosimetric problems. The use of computer codes to estimate the various radiometric and dosimetric quantities previously defined in this book has become essential. These operate using methods of numerical calculations with approximations that affect more or less the true value of desired quantities. We chose to detail a particular, which is the reference method for the simulations in the field of dosimetry and radiation protection, and whose evocation staked all previous chapters: the Monte Carlo method.

6.1 Principle of the Monte Carlo Method Applied to the Particle Transport

The flow chart of the calculation process of the Monte Carlo method applied for particles transport is presented in Fig. 6.1. The general principle is: a large number of particles are generated by a random source and their path and their "history" (i.e., the particle interact to give what type of secondary particle, how energy, etc.) will be determined probabilistically.

First, a random selection routine code assigns each particle derived from the source, a set of initial parameters (spatial coordinates x, y, z; release direction u, v, w;

R. Antoni and L. Bourgois, *Applied Physics of External Radiation Exposure*,
Biological and Medical Physics, Biomedical Engineering,
DOI 10.1007/978-3-319-48660-4_6

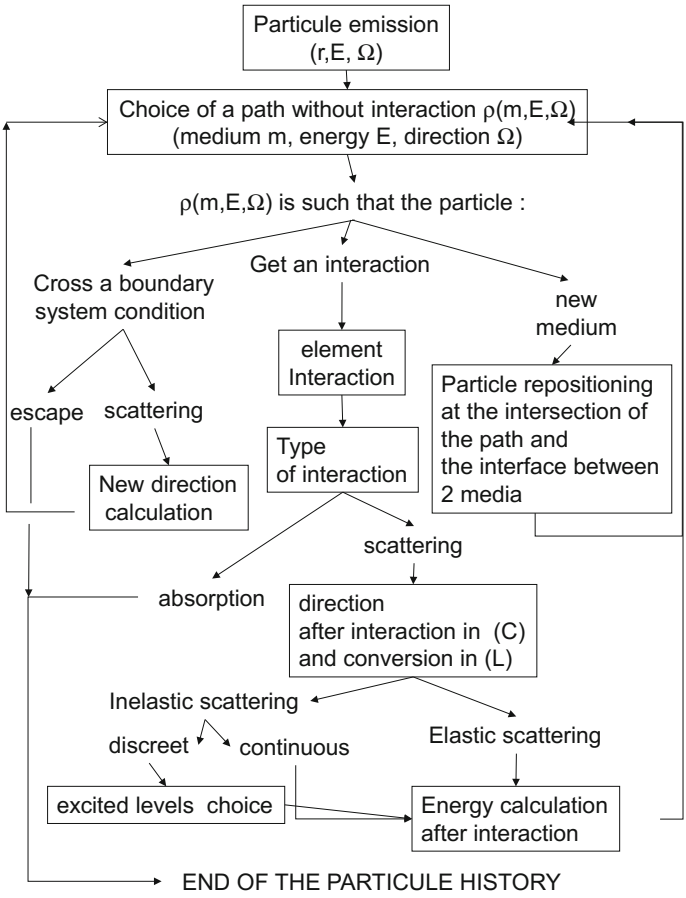

Fig. 6.1 Flow chart of the calculation scheme of the Monte-Carlo method used for the tracking of the particles

energy E; time t if the time dependence is included in the calculation). The values of these parameters are "selected" from the spatial probability distributions, direction, energy, time. The source is thus characterized by a sampling of distributions related to the sampling of random numbers generated by the computer. Such random selection method for characterizing the physical parameters inherent in the transport of the particle is indeed, we shall see, the basis of the Monte Carlo method.

The next step is to select the path length that will reach the particle before interacting with the medium. This length is defined in "mean free path" units or mean length before interaction (see Chap. 2).

The geometry of the source, materialized zones, detectors and system boundaries are specified in an input file. Cross sections and physical models are implemented for various nuclear materials and interactions that may be encountered in the scene.

A path calculation algorithm determines the spatial coordinates of the collision point using the mean free path of the particle obtained from interaction cross sections in the medium. If the interface between two media is crossed, the coordinates are calculated at the point of crossing. If there is an outer boundary of the system, the particle disappears and that's the end of his 'history' (*escape*). A new particle source is then drawn and again tracked until his death. The calculation ends when all the particles from sources and secondary particles generated are tracked.

During transport, the particle may be involved in one or more collisions. A collision algorithm decides whether the particle is scattered or absorbed. The scattering nucleus and scattering reaction type (elastic or inelastic reaction) are in turn sampled. If the distribution is chosen, a collision routine selects the scattering angle using again a random number to calculate the scattered energy, and transforms the direction of the system of fixed laboratory coordinate. The code then returns to the path length calculation algorithm. And history of the particle is continued.

The quantities of calculation: fluence collision density and responses such as the absorbed dose—are determined by a dedicated statistical estimator. The result is obtained by averaging the scoring on all the particles drawn by the source. The result can not be obtained exactly precise and is necessarily accompanied by a statistical uncertainty.

6.2 Random Number Generator

The random selection principle is a cornerstone of the Monte Carlo method. There is need to generate sequences of random numbers to perform the sampling on the different probability densities of the various physical parameters of the transport characteristics of a particle in the material. A common technique for generating these random numbers, there are others, is based on the linear congruence method [1].

In this approach, the idea is to generate a sequence of random integers X_n such that it observes the inequality (6.1).

$$0 \leq X_n \leq m \quad with\ m \in \aleph \tag{6.1}$$

The random number, whose value ranges over 0–1, is then determined according to (6.2).

$$\xi_n = \frac{X_n}{m} \quad 0 \leq \xi_n \leq 1 \tag{6.2}$$

The random sequence of integers is obtained through the recurrence relation (6.3).

$$X_n = (aX_{n-1} + b) \mod m \quad n \geq 0 \tag{6.3}$$

This amounts to:

$$X_n = aX_{n-1} + b - mk_n$$

where k_n is the largest positive integer $\left[\frac{aX_{n-1}+b}{m}\right]$.

m is the upper module 0, a the multiplier is between 0 and m and b the increment, also between 0 and m. The first value of the sequence X_0 called "random seed" is set at an integer value between 0 and m.

For example, let us characterize the module 5 sequence with multiplier, increment and seed set at 3 and the random numbers associated [2].

$$\begin{cases} X_o = 3 & \Rightarrow \xi_0 = \frac{3}{5} = 0.6 \\ X_1 = (3 \times 3) + 3 - 5\left[\frac{(3\times 3)+3}{5}\right] = 2 & \Rightarrow \xi_1 = \frac{2}{5} = 0.4 \\ X_2 = (3 \times 2) + 3 - 5\left[\frac{(3\times 2)+3}{5}\right] = 4 & \Rightarrow \xi_2 = \frac{4}{5} = 0.8 \\ X_3 = (3 \times 4) + 3 - 5\left[\frac{(3\times 4)+3}{5}\right] = 0 & \Rightarrow \xi_3 = \frac{0}{5} = 0 \\ X_4 = (3 \times 0) + 3 - 5\left[\frac{(3\times 0)+3}{5}\right] = 3 & \Rightarrow \xi_0 = \frac{3}{5} = 0.6 \end{cases}$$

A sequence contains $m - 1$ random numbers; to get the highest possible frequency, it takes the largest possible module. Typically, in a computer, one can reach the maximum size of a "word"—in the numerical sense: for a 32-bit machine, the module would be $m = 2^{32}$ or a sequence of $2^{32} - 1 = 4.3 \cdot 10^9$ random numbers.

It more specifically refers to pseudo-random numbers since these are generated via analytical recurring expression.

6.3 Sampling a Discrete Distribution, Application to Choose the Type of Collision

How the random number between 0 and 1 is used for selecting one of a discrete probability distribution event is explained in what follows: it is considered as an example the case of a photon that may interact in the material by photoelectric, Compton or creative pair effects. The probability of interaction by a particular mode are as follows:

$$p_1 = \frac{\sigma_{pe}}{\sigma_t} \quad p_2 = \frac{\sigma_c}{\sigma_t} \quad p_3 = \frac{\sigma_{pp}}{\sigma_t} \quad \text{where} : \sigma_t = \sigma_{pe} + \sigma_c + \sigma_{pp}.$$

It will be noted that:

$$1 = \sum_{i=1}^{n} p_i \tag{6.4}$$

Let us consider arbitrarily a case where $p_1 = 0.2$, $p_2 = 0.5$, $p_3 = 0.3$. The discrete probability distribution of a particular effect can be represented as shown in Fig. 6.2a. It will also define the cumulative probability as (6.5), which could be translated as the probability of getting a value $i < j$.

$$P(i < j) = \sum_{i=1}^{j} p_i \tag{6.5}$$

Figure 6.2b provides a schematic representation of the cumulative probability distribution for the type of photon interaction.

Now, if a random number ξ is generated such as $0 < \xi < 1$ and that is assigned to the result of the cumulative probability distribution: $P = \xi$, the inequality is verified and the k-th interaction is selected:

$$P(k-1) < \xi \leq P(k) \tag{6.6}$$

For example, for our problem, if the random number sampled leads to $\xi = 0.35$, the corresponding interaction is Compton type, as shown in Fig. 6.2b. More generally, according to the value of ξ the following choices will occur:

- $0 < \xi < 0.2$ the interaction is photoelectric;
- $0.2 < \xi < 0.7$ the interaction is Compton;
- $0.7 < \xi < 1$ the interaction is pair creation.

In fact, as ξ is uniformly distributed on the unit interval, each type of interaction is sampled with probabilities $p_1 = 0.2$, $p_2 = 0.5$ and $p_3 = 0.3$. After a large number

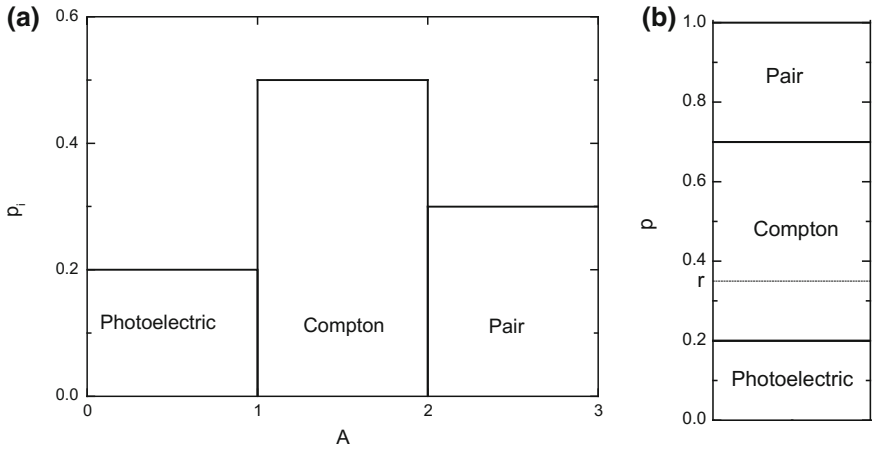

Fig. 6.2 **a** Representation of probability of interaction. **b** Representation of the cumulative probability distribution—in this case leads to the random screening $\xi = 0.35$ and therefore the Compton interaction is chosen, adapted [3]

of samples, the following interaction occurrences should be observed: 50% Compton, 20% photoelectric and 30% pair creation. For low number of samples, statistical fluctuations can be significant and Compton scattering can be selected either above or below 50%. Accordingly, the statistical sampling requires the sampling of a large number of particles to estimate more accurately the true value.

Note that it can be proceed similarly, for the sampling of radionuclide, emitting a line spectrum with N energy rays $E_{\gamma,n}$ and emission percentages Γ_n.

6.4 Sampling of a Continuous Distribution, Application for Calculating Energy and Direction of a Scattering Particle

It exists, for physical models, many continuous probability distributions which are defined by analytical expressions such as emission energy, scattering cross section… To sample these distributions, it necessary to extend the previous discrete approach to a continuous approach. The previous sum sign becomes integral sign and probability $p(x)$ that the variable x has a value x becomes a continuous probability density defined by an analytical expression. The cumulative probability density $P(x)$ associated, which reflects the probability that the variable x is a value less than x, is calculated according to (6.7).

$$P(x) = \int_{x_{\min}}^{x} p(x)dx \quad \text{with} \quad \int_{x_{\min}}^{\infty} p(x)\,dx = 1 \tag{6.7}$$

$x_{\min}$ is the minimum value that can be taken by the variable x. Both terms are respectively the differential extension of continuous expressions (6.4) and (6.5) from the previous discrete approach. For a value of x, a random number ξ is sampled. It is rendered equal to the result of the cumulative probability density $P(x)$ according to (6.8).

$$\xi = P(x) \tag{6.8}$$

We note that the cumulative probability density in the context of the continuous approach is similar to the distribution function for a normal distribution. The desired value x is then determined using the inverse function of $P(x)$ (6.9).

$$x = P^{-1}(\xi) \tag{6.9}$$

This sampling technique is called “method of the inverse of the cumulative probability density”.

For sampling the energy of an emitted particle whose the differential cross section to get an energy between E and $E + \mathrm{d}E$ is ($\mathrm{d}\sigma/\mathrm{d}E$); the probability density of having an emission energy E is then defined by the expression (6.10).

$$p(E) = \frac{1}{\sigma}\left(\frac{d\sigma}{dE}\right) \quad \text{with} \quad \sigma = \int_{E_{\min}}^{E_{\max}} \left(\frac{d\sigma}{dE}\right) dE \tag{6.10}$$

Like the expression (6.7) above, we deduce the expression of the cumulative probability density, which determines the probability of having a lower energy to a certain value E according to (6.11).

$$P(E) = \int_{E_{\min}}^{E} p(E)\, dE = \frac{1}{\sigma} \int_{E_{\min}}^{E} \left(\frac{d\sigma}{dE}\right) dE \tag{6.11}$$

The sampling of a random number then provides the result of E referred to E' by means of the inverse function of the cumulative probability density (6.12).

$$\xi = P(E') \quad \Leftrightarrow \quad E' = P^{-1}(\xi) \tag{6.12}$$

To work correctly, this method requires following three conditions: the integral (6.11) must be defined, it must accept an analytical solution and the inverse function of this solution should also be calculable. However, this "ideal" scenario remains marginal.

Otherwise, when this technique is not applicable, there are a number of alternative approaches to the sampling of the cumulative probability density. In what follows, we will detail a number of them.

6.4.1 *Sampling a Continuous Distribution by a Multi-group Approach*

Continuous probability distribution can be cut into energy bins. The identification of these energy bins can be done in three ways:

- The energy of its upper bound, so that $\Delta E_n = E_{n-1} - E_n$ is identified by E_n;
- The energy of its lower bound, so that ΔE_n is identified by E_n;
- The energy of its midpoint, so that ΔE_n is identified by $E_{n-1} + E/2$.

Each energy bin ΔE_n, with indexing above, correspond to fraction of integrated probability distribution on selected energy bin. Typically, let us take, for instance, the energy probability density of fission neutrons, described by the Watt spectrum (see Chap. 4).

$$p(E_n) = c \exp\left(-\frac{E_n}{a}\right) \sinh\sqrt{bE_n}$$

with *a, b* parameters that depend on the fissile isotope and *c* the normalization term dependent on *a* and *b* defined by:

$$c = \sqrt{\frac{4}{\pi a^3 b}} \exp\left(-\frac{ab}{4}\right)$$

This distribution in the library ENDL (*Evaluated Nuclear Data Library*) [4] is sampled by energy bins. For each higher index E_n of energy bin $\Delta E_n = E_{n-1} - E_n$ corresponds probability $p(E_n)$. All pairs $(E_n, p(E_n))$ are tabulated for fissile radionuclides.

For determining a neutron emission energy, a random number ξ is sampled, then a routine calculates the sum of $p(E_n)$ corresponding to a cumulative probability until equality (6.13) holds.

$$\sum_{E_n=0}^{E_n=E_k} p(E_n) \approx \xi \tag{6.13}$$

Strictly speaking, there is little probability that the value of the sum gives precisely ξ. For the choice of the emission energy, the inequality regarded (6.6).

$$P(k-1) < \xi \leq P(k) \Leftrightarrow \sum_{E_n=0}^{E_n=E_{k-1}} p(E_n) < \xi \leq \sum_{E_n=0}^{E_n=E_k} p(E_n)$$

In this case, the energy E_k is chosen. Note that the approach to describe a continuous distribution in "point by point" mode is applied to a large number of cross sections.

Figure 6.3, gives an overview of Watt spectrum and the cumulative probability density function associated. The latter is logically growing since the more energy increases, the more the probability to sample a lower energy increases.

There are other methods for sampling continuous distributions for which the "method of the inverse of the cumulative probability density" can not be applied.

6.4.2 *Sampling a Continuous Distribution by the Method of Rejection*

When the expression of the cumulative probability density *P(x)* for a known probability density *p(x)* cannot be accessed, and when the probability distribution

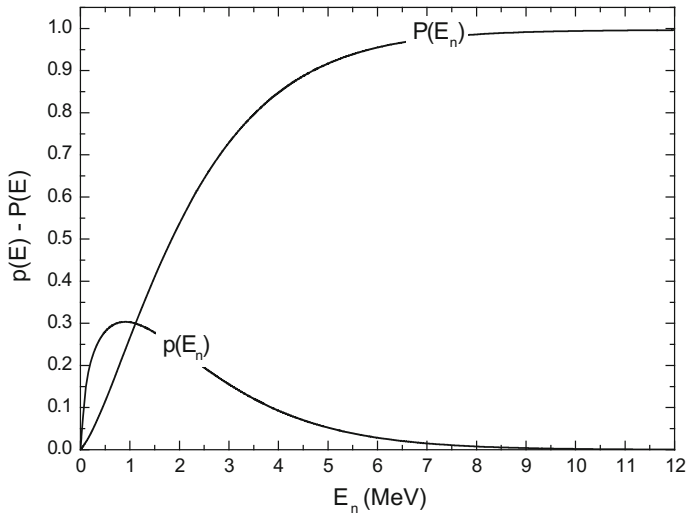

Fig. 6.3 Representation of $p(E)$, the probability density of emitting a neutron of energy E during a fission (Watt Spectrum) and the cumulative probability density $P(E)$

can not be approximated by another function as detailed in Further Details 6.2, the "rejection method" may be used.

To describe this method, let us consider the probability distribution of $p(x)$ describing a semi-circle on an interval [a b]. As shown in Fig. 6.4.

A first random number is drawn ξ_1 determining a random value x over the interval [a b]. According to the expression (6.14).

$$x_t = a + \xi_1 (b - a) \tag{6.14}$$

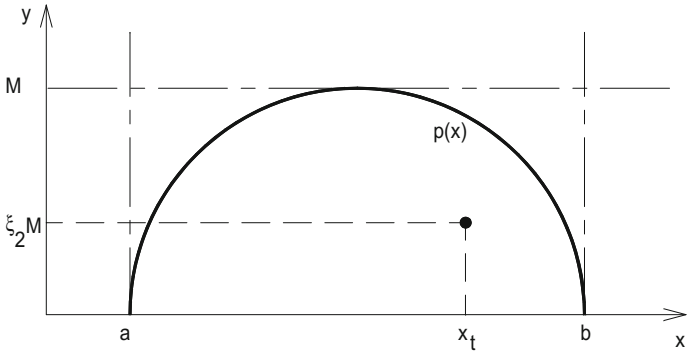

Fig. 6.4 Rejection method—case of a distribution of circular probability over an interval [a b]

A second random number ξ_2 is drawn and the following test is performed:

- if $\xi_2 M > p(x_t)$, then the value of x_t is rejected;
- if $\xi_2 M \leq p(x_t)$, then the value of x_t is accepted.

By performing this operation many times, the probability "acceptance of *xt*" is obtained. This can be simply regarded as the ratio of accepted cases to all tested cases; i.e., in our example, it amounts to the report of the semi-disk from the integration of the semi-circle on [*a b*]. Divided by the area bounded by the rectangle of $M(b-a)$ size. In our case, this ratio is π/ 4, where:

$$\frac{1}{M(b-a)} \int_a^b p(x)\,dx = \frac{\pi}{4}$$

Note that this method can be used to calculate the value of π. In a more general way, to an interval between *a* and *x* and an acceptance probability of $P_{\text{a,}}$ it could be written:

$$\frac{1}{M(x-a)} \int_a^x p(x)\,dx = \frac{P(x)}{M(x-a)} = P_a$$

Thus, drawing a new random number ξ so that $P(x) = \xi$, we finally obtain the random value *x*:

$$\xi = P_a M(x-a) \Leftrightarrow x = \left(\frac{\xi}{P_a M}\right) + a$$

In practice, for better efficiency, it is necessary not to limit to a unique value of *M* but by a function $g(x)$ whose behavior is very similar to that of $p(x)$. This function $g(x)$ must be globally upper bound p(x) and integrable on the same limits as $P(x)$ to provide a function we call $G(x)$. The rejection method is then performed on the composite function $h(x)$ derived from the ratio of $p(x)$ on its upper bound function $g(x)$:

$$h(x) = \frac{p(x)}{g(x)}$$

This time, the test limit value is defined by the maximum of $h(x)$*:* $h_{\max}$ over the interval [*a b*]. The test steps are: first a random number ξ_1 is drawn and a random value is determined to *x*, $x_t = G^{-1}(\xi_1)$; a second random number is drawn ξ_2 and the following test is performed:

- if $\xi_2 h_{\max} > h(x_t)$ then the value of x_t is rejected;
- if $\xi_2 h_{\max} \leq h(x_t)$ then the value of x_t is accepted.

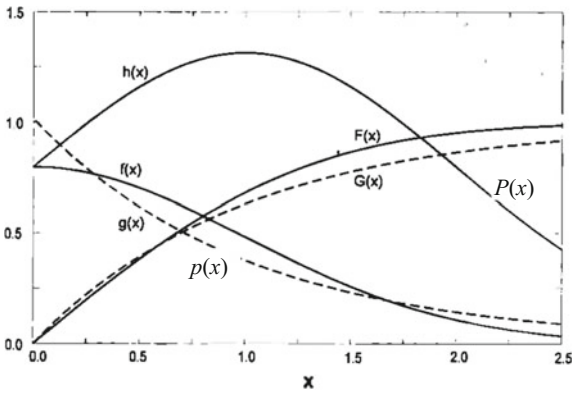

Fig. 6.5 Overview of a probability density $p(x)$, approximated by a function $g(x)$, the ratio $h(x) = p(x)/g(x)$ and the cumulative probability densities $P(x)$ and $G(x)$. The value of h_{max} is a finite limit to $h(x)$, in practice it slightly exceeds the maximum value $p(x)$, adapted from [5]

Figure 6.5, gives an overview of a probability density $p(x)$, approximated by a function $g(x)$, the ratio $h(x) = p(x)/g(x)$ and the cumulative probability densities $P(x)$ and $G(x)$. The value of h_{max} is a finite limit to $h(x)$, in practice it slightly exceeds the maximum value of $p(x)$.

For watt spectrum example, the energy of the fission neutron can be sampled via a rejection method developed by Kalos [6] as follows. A parameter set L, M and N is defined only once as follows:

$$L = 1 + \left(\frac{b}{8a}\right), \quad M = \frac{\left[L + (L^2 - 1)^{1/2}\right]}{a}, \quad N = aM - 1$$

Variable x and y are defined with two random numbers ξ_1 and ξ_2 as following:

$$\begin{cases} x = -Log(\xi_1) \\ y = -Log(\xi_2) \end{cases}$$

Rejection occurs if: $[y - N(x + 1)]^2 > bMx$. Otherwise, the term is accepted and the energy is given as follows:

$$E_n = M\,x = -M\,Log(\xi_1)$$

Performances in terms of computing time provided by this method are significant, typically 0.3 μs per sampling, so approximately 200 million samples per minute.

This rejection method for the determination of $P(x)$ is effective except that a function "close" to $p(x)$ exists. Otherwise, there are particular sampling methods based on mathematical properties of the analytical expression to sample. Further Details 6.1 details the Koblinger method [7] for the sampling of Klein-Nishina distribution applied to the determination of the direction and energy of the Compton photon. Another method based on the sampling of an approaching function, applied to the Watt spectrum, is proposed in the Further Details 6.2.

6.5 Concept of Statistical Weight, Analog and Implicit Tracking

The stochastic nature of the Monte Carlo calculation involves the following specificity: each particle is associated with a statistical weight W (*weight*). To each particle emitted by the source, is by default assigned a weight of 1.

Two approaches are possible for tracking the particle: analog and implicit manners. In the analog approach, in which the "real" physics is "played", a direct simulation is performed. This tracking mode does not induce changes in the statistical weight of the particle. Incidentally, with this approach each particle created in a collision is tracked with the same weight as the particle that gave it birth. To illustrate this approach, consider a flux of neutrons interacting on a hydrogen target. In the analog approach, when the neutron interacts, energy and angle of the recoil proton and scattered neutron are sampled based on the incident neutron inputs (energy, angle …) and conservation laws (time, mass …). So by taking this example, during an elastic scattering, if the incident neutron has a initial energy of 5 MeV and the scattered neutron carries 4 MeV, the created recoil proton has necessarily, by conservation of kinetic energy, an energy substantially equal to 1 MeV. The weight of the recoiling nucleus and scattered neutron is equal to that of the initial neutron.

In the implicit approach, energy and angular deflection of the neutron and the recoil nucleus are both determined randomly, but based on the input data of the neutron incident: for example, the neutron 5 MeV, interacting, can give birth to both 3 MeV proton and a 4 MeV scattered neutron, which is not consistent with the conservation of energy. To overcome the failures of the conservation laws, the statistical weight of secondary released particles are corrected and adjusted.

In general, the implicit method can be recommended as soon as the direct tracking of particles (analog approach) is not efficient for the calculation of an estimator, that is to say, the calculation time is extremely important before leading to a result of which the statistical error is acceptable. This is especially true as we attempt to estimate such a fluence of particles at a point of the space far from the source and which inserted medium is a significant thickness of high Z. In the analog model, for each capture (e.g. radiative capture), the neutron is killed. But if the goal of the estimator is to score neutrons on detector, the disappearance of the neutron represents a loss of information. An alternative solution to the implicit approach is to continue to track the captured particle by weighting the statistical weight W thereof by the probability of non-absorption:

$$p_{na} = \frac{\Sigma_t - \Sigma_a}{\Sigma_t}$$

with Σ_t the total macroscopic cross section to the incident energy, Σ_a the macroscopic absorption cross section. The particle is supposed to scatter each collision, but emerges with the adjusted statistical weight W':

$$W' = p_{\mathrm{na}} W$$

that is called "implicit capture." More generally, when it comes to a problem of scoring the weight of the primary and/or secondary particles, the implicit method may be recommended to speed up the convergence to a statistically reliable result. Adding that in some codes, analog datas do not exist and the treatment is done only in an "implicit" way via use of models.

We just observed that implicit tracking biases particle transport to improve computing performance. Then, appropriate techniques in each case exist to bias energy, transport direction … to improve the computation time and reduce error associated with statistical estimators. These techniques are called "variance reduction" and have in common the change in the statistical weight of the released particle.

When secondary released particles are tracked, it is appropriate, when a secondary particle emerges to generate $k - 1$ other, to increase the population of the latter. If the weight of the emerging secondary particle is W, the weight of each k secondary particles is then W/k (e.g. SPABI card in the MCNP code).

Another, known as "forced collision" allows the following biasing: a particle can be forced to collide every time it enters a cell that is nearly transparent to him, due to small size before the mean free path of the particle. The incident particle is then divided into two "sub-particles": one that collides, the other not, and assign the appropriate statistical weight. This technique is usefull to generate an increasing contribution to the "detector point" type estimators which will be discussed later.

6.6 Definition of Geometry

The first step when creating an input file is to define a source and materialized objects in the modeled scene. Physical objects called 'cells' are previously defined by combinations of surfaces in a cartesian coordinate system. For example, a cylinder filled with polyethylene is previously defined by a mathematical cylinder of infinite height, cut in its top and at its base by two infinite planes. The next step is to describe the material and density that fill this newly created bounded surface.

To define surfaces mathematically, we start from the most general expression of a surface: the quadric form.

$$Ax^2 + By^2 + Cz^2 + Dxy + Eyz + Fzx + Gx + Hy + Jz + K = 0$$

constants *A, B, C, D, E, F, G, H, J, K* are chosen to describe planes, spheres, cylinders, cones, ellipsoids size, desired location and orientation. In recent codes, these simple surfaces are preset and only require to be called in the program with the appropriate setting. For example, the cylinder shown in Fig. 6.6 is defined by two levels: $z = 0$ and $z = 10$ and a cylinder with an axis z and radius 4. Note that in some codes, bounded surfaces can now be set immediately (e.g. Macrobody in

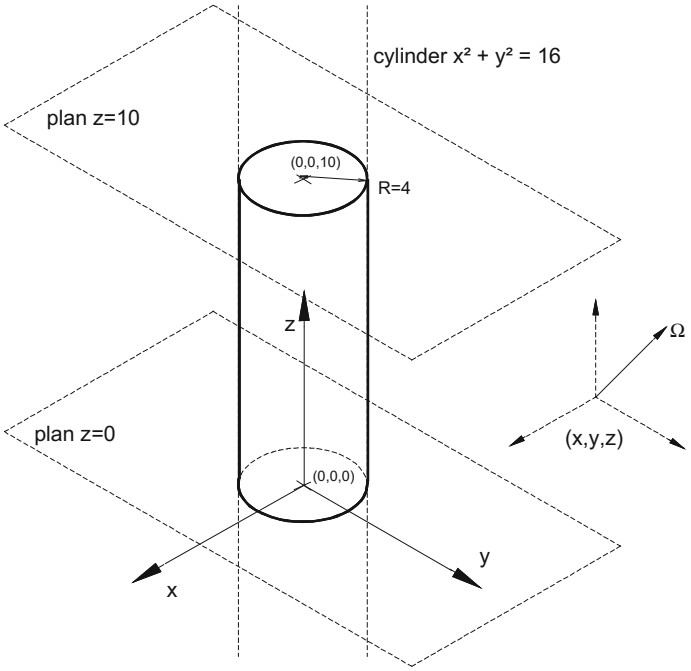

Fig. 6.6 Construction of a geometry in a Monte Carlo code, above a cylinder defined by three surfaces whose generatrix is *Z axis*

MCNP) which automatically generate, for example, the above three surfaces to materialize a cylinder.

Once the closed surface defined, the next step is to "materialize" inside thereof then creates what is called a "cell".

Returning to the case of cylinder, with three surfaces, plans: $z = 0$, $z = 10$ and the cylinder $x^2 + y^2 = 16$. The equation $x^2 + y^2 - 16$ is negative for points inside the cylinder and positive outside and is 0 for points on the surface. therefore this sign convention (−) and (+) is chosen to describe a particular area of space on either side of the surface. To characterize the cell, it is necessary to intersect surfaces covering the portion of the space to materialize. In the case of our cylinder, this is to assign a sign (+) to the plane $z = 0$, a sign (−) to the plane $z = 10$ and a sign (−) to the cylinder. The intersection of these three spatial areas then defines the internal volume of the cylinder and therefore the cell; then remains to assign a material and density to the performed volume.

The definition of surfaces and cells is one of the most difficult issue for performing an input file. It is essential, as far as possible, to have a graphical user interface to display step-by-step the construction of the geometry and to check no errors in geometry.

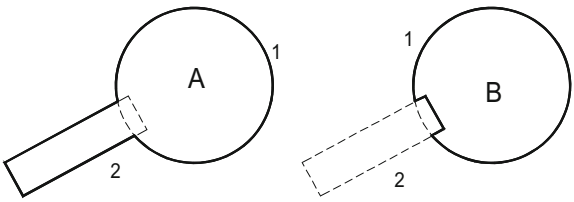

Fig. 6.7 Example of two different cells (A and B) obtained from the same two surfaces (1 and 2) by use of the operator "union" or "intersection"

We have seen that to describe a cell, we used the intersection of spatial areas. The union operator is also useful, similar to Boolean operator "or", in particular to describe a cell from overlapping surfaces. In Fig. 6.7, the B cell is described as an interior of the surface 1 (sphere) intersected with outside the area 2 (cylinder). Which ultimately describe a truncated sphere by a cylinder portion. A cell in turn is the union of all that is in the surface 1 and the surface 2, and finally describes an object with "Maracas" aspect.

Adding that a number of HMI programs exist (Human-Machine Interface) for generating geometries by dispensing with all or some of these difficulties. These may be associated with graphical user interface software.

This combination of geometry therefore has an aspect of "crushing-crushed" which is not only found in Monte Carlo geometry, but also in some deterministic codes (e.g. point kernel code Mercurad [8]. Described in Chap. 5).

6.7 Emission Source

We have already mentioned the sampling of particle source energy including Watt distribution. Let us consider how others physical parameters are treated: emission direction, emission location … It is possible to describe the source separating parameter variables:

$$S(\vec{r},\vec{u},E,t) = W \cdot S(\vec{r}) \cdot q(\vec{u}) \cdot P(E) \cdot f(t) \tag{6.15}$$

From now, include that all results for searched variable are normalized by released source particle. Let us consider a cylinder source of radius R and height H as that defined in Fig. 6.6. Determine where, with what energy, what direction the particle is launched. The densities of cumulative probabilities for the three cylindrical coordinates, considering an equal probability of being launched anywhere in the source volume are:

$$P(z) = \frac{z}{H} \quad P(r) = \frac{r}{R} \quad P(\theta) = \frac{\theta}{2\pi} \tag{6.16}$$

By successively drawing three random numbers, the location of released point $S(\vec{r})$ is sampled:

$$\vec{r}(\xi_1 R,\ \xi_2 H,\ 2\pi\xi_3) \tag{6.17}$$

Then determine the emission direction $q(\vec{u})$ of the emitted particle. Consider a uniformly activated object, the particle release will be isotropic. The cumulative density probability of emitting a particle with a solid angle less than Ω is given by the expression (6.18).

$$P(\Omega) = \int_0^{\Omega} \frac{d\Omega}{4\pi} \tag{6.18}$$

To determine the azimuthal angle θ and polar angle φ, we turn this integral into a product of two independent integrals:

$$P(\Omega) = \int_{\pi}^{\theta} \frac{\sin\theta\, d\theta}{2} \int_0^{\varphi} \frac{d\varphi}{2\pi} \tag{6.19}$$

The first integral characterizes the density of cumulative probability of having a azimuthal angle less than θ and the second one a polar angle less than φ. Two new random numbers are drawn and both angles are:

$$\xi_1 = \int_{\pi}^{\theta} \frac{\sin\theta\, d\theta}{2} \Leftrightarrow \xi_1 = \left[\frac{\cos\theta}{2}\right]_{\pi}^{\theta} = \frac{\cos\theta + 1}{2} \Leftrightarrow \theta = a\cos(2\xi_1 - 1)$$

$$\xi_2 = \int_0^{\varphi} \frac{d\varphi}{2\pi} \Leftrightarrow \xi_2 = \frac{\varphi}{2\pi} \Leftrightarrow \varphi = 2\pi\xi_2$$

The source particle is emitted in the direction defined by the vector with spherical coordinates following (6.20).

$$\vec{u} \begin{cases} \|\vec{u}\| \\ a\cos(2\xi_1 - 1) \\ 2\pi\xi_2 \end{cases} \tag{6.20}$$

Here we took the case of a volume source whose activity is uniformly distributed. In the case of an anisotropic angular distribution, a reference direction is to be defined, as well as the emission probability distribution for each angle then it is similar to the sample of the distribution of cumulative probability, described above for the choice of photon interaction, but this time transposed to the emission angle.

Finally, it is necessary to determine the energy with which the particle will be emitted. We have already had an approach with the study of Watt spectrum sampling for choosing the energy of fission neutrons (Sect. 6.4.1). We also briefly discussed the selection of the emission of discrete photons emitted from a radionuclide which, like the choice of the interaction of the photon, is treated by the method of sampling a discrete distribution (cf. Sect. 6.3) taking into account emission percentages.

In the analog transport, meant reproduce exactly the life of a particle released in a medium, the weight given by default to each source particle is $W = 1$.

However, sampling of the energy spectrum of fission neutrons, for instance, as discussed above, in analog transport may be ineffective in computational problems related to dosimetry and radiation protection. The cross section for fast neutrons, in particular for hydrogen, in general, decreases as the energy of neutrons increases. high energy neutrons penetrate matter further and may therefore contribute more to the depth dose, although the emission rate of these in the energy probability distribution is low. It is therefore appropriate that the calculation code "spend more time" to track these neutrons of higher energy which mainly contribute to the desired response, i.e. the absorbed dose in depth at a great distance from the source. This can be done using a variance reduction technique called "energy importance sampling"; this technique involves sampling on a probability distribution of modified energy: $p^*(E)$ defined to improve the selection of high energies. The weight is then modified $W^*(E)$ so that the average remains unchanged, which roughly requires:

$$W^*(E)\,p^*(E) = W(E)\,p(E) \tag{6.21}$$

For example, let's take the energy distribution of fission spectra of Fig. 6.3 and track preferentially the 6 MeV neutrons.

Initially, in analog sampling, we would have for them:

$$p(6\,\mathrm{MeV}) = 0.02,\ W(6\,\mathrm{MeV}) = 1 \ \Rightarrow\ W(6\,\mathrm{MeV})p(6\,\mathrm{MeV}) = 0.02$$

By lowering the weight of these neutrons to 0.1, the value of the new energy distribution to an energy of 6 MeV would be:

$$W^*(6)\,p^*(6) = W(6)\,p(6) = 0.02 \ \Rightarrow\ p^*(6) = 0.2$$

In other words, emitting 6 MeV neutrons is multiplied by the probability of 10. The immediate effect is the emission and therefore tracking 10 times more 6 MeV neutrons than in the previous case, with statistical weights smaller and readjusted. This technique ultimately allows to reduce the variance while leaving the mean score result, namely, the depth dose unchanged.

However, care must be taken not to bias the distribution of too sharply or eliminated altogether in our case the low energy neutrons, which can be achieved in these codes using a "high-pass filter" for energy (e.g. *cut* card in MCNP), the results

close to the source could be heavily impacted by this choice. Adding that the high-energy gamma emerging from radiative captures that contribute significantly to the dose could be concealed.

Finally, regarding the time dependence, problems of dosimetry and, more generally, of radiation protection involve only very rarely time. However, it is possible in these codes to keep track of the "flight time" between virtual collisions and so characterize a life time of the particle. The time dependence is of interest for pulsed sources, therefor for modeling of particle accelerators.

The variance technique qualified as "increasing importance" based on a similar principle to that described above, allows in high absorption regions and whose detector is also located at a significant distance from the source, to improve the speed of convergence. This method is particularly useful in problems with multiple cells. This consists of assigning increasing importance (I) in adjacent cells. This will have the effect of increasing the number of particles at the interface between two adjacent cells in respect with the following factor:

$$k = \frac{I_{n+1}}{I} \tag{6.22}$$

Always observing "weight-probability" conservation law of the expression (6.21) so that the new weight of these new particles in the new cell after the crossing of the interface it comes:

$$W_{n+1} = k^{-1} W \tag{6.23}$$

Let us take the case, as shown in Fig. 6.8, wherein a first cell 1 has importance of 1 and the particles tracked therein have a weight of 1. Let a contiguous cell 2 having an importance of 3 to increase the population of particles in the cell 2—a lot having been absorbed in the cell 1 and lost to the statistical convergence of the estimator. If

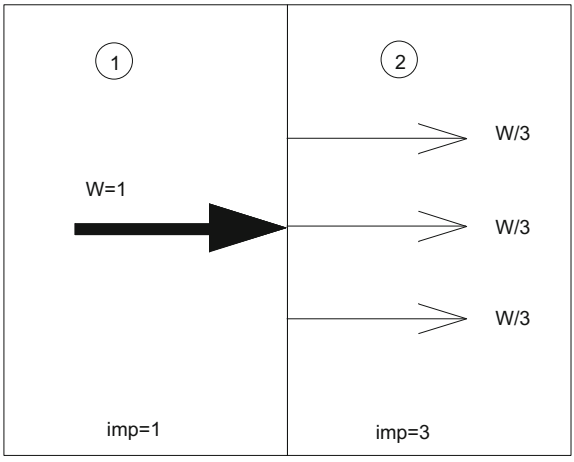

Fig. 6.8 Example of "split" of particles in Monte Carlo tracking

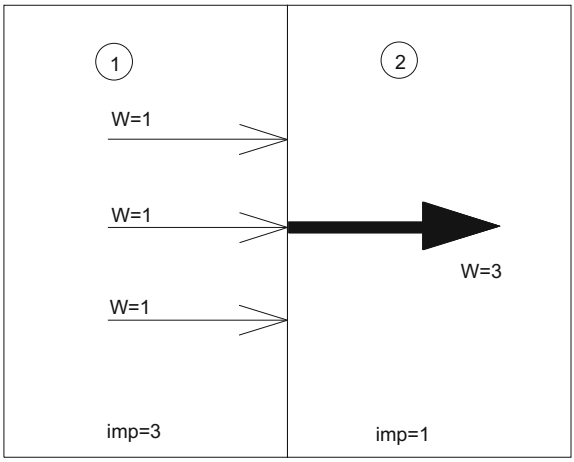

Fig. 6.9 Example of "Russian roulette" of particles in a Monte Carlo code

a particle travels in the cell 1 with a weight W, three new particles will thus be created with each a weight of $W/3$ and the same physical characteristics as the previous ($\vec{r}$, $\vec{u}$ *et* E remain unchanged).

This technique is called "split" *process*. Conversely, the opposite can be performs: removing particles for a multi-particle mode and one or more types of them do not directly concern the calculated estimator then "*Russian roulette*" technique is used, where particles are killed crossing boundaries between two cells. In the example above, but this time with a importance of 3 in cell 1 and 1 in the cell 2. If we consider three particles crossing the interface, two will be killed in random, one will "survive" and will be weighing 3 if the initial weights were 1 as shown in the Fig. 6.9.

Note that it may be worthwhile in some problems causing much absorption (e.g. very thick Z material for biological shielding) to divide the cell into multiple "sub-cells" and increase the importance in each of them in order to increase the number of particles transported to the detector. However, it will ensure that the quantities do not grow too strongly from an adjoining cell to another: the more particles creates, the more these statistics have extremely low weight and their contribution to the desired quantity, if they reach the detector, is statistically low. It is generally recommended to ensure that the population in the cells remains substantially the same; so you have to figure out quantities set for such a simulation. This is achieved through diagnostics on populations of particles carried in each cell.

There is also the possibility in some codes to define a 3D mesh grid wherein the quantities are calculated in each of the meshes (e.g. *Mesh Weight Windows* in MCNP). This evaluation is obtained by means of a first "run" wherein a diagnosis enables to evaluate the regions of the space to which the tracked particles contribute most to the result of the estimator. The code then assigns appropriate importances in each cell of the 3D grid to enhance transport and particle generation in these favorable space regions. At the end of diagnostic "run", an output file put in the

code formalism can be created. It is then inserted into the input dataset and replaces the initial set of importance.

Adding that, in the input file, an initial sphere that surround the entire calculation scene is defined with 0 importance outside. It constitutes the geometric boundary of the system, so that each particle that passes through the surface thereof escape and disappears meaning the end of the history of the particle. The program stops tracking this escaped particle and the new particle is launched by the source. If this sphere of exclusion did not exist, the launched particle would be tracked to infinity and any other particle could be drawn and tracked; This would effectively cause an error and interrupt the calculation.

Finally, another variance reduction technique we briefly mentioned by the term "high pass filter" will kill all particles whose energy is lower than a low limit set (e.g. *cut card in MCNP*). This technique may be relevant, for example, in the case of assessing a photon fluence in the presence of significant absorbent and when the source emits high-energy photons. Only photons of higher energy will contribute to the depth dose. However, a significant number of low-energy photons will be created during reactions processes; nothing thus serves to track them which cause unnecessarily calculation time; this card allows to ignore and kill them.

6.8 Location of Collision

We have shown previously (Koblinger method [7] applied to the Compton scattering) that the angles of the scattered particle (θ and φ) are always calculated from the axis of incidence of the particle before collision and determined by a direction vector $\vec{u}$, not from the coordinate system; each collision causing scattering, it is therefore necessary to recalculate the new direction vector $\vec{u}'$ in the coordinate system. Equation (6.24) characterize the new vector direction.

$$\begin{cases} u'_x = u_x \cos\theta + \dfrac{a}{b}\left(u_x u_w \cos\varphi - u_y \sin\varphi\right) \\ u'_y = u_y \cos\theta + \dfrac{a}{b}\left(u_y u_w \cos\varphi + u_x \sin\varphi\right) \\ u'_z = u_z \cos\theta - ab\cos\varphi \end{cases} \tag{6.24}$$

with: $a = \sqrt{1-\cos^2\theta}$ and $b = \sqrt{1-u_z^2}$.

The scattered particle follows therefore the direction defined by the vector $\vec{u}'$. The next collision point is carried from the macroscopic cross section (Σ_t for neutrons and μ for photons). Remind that the latter is the inverse of the mean free path, that is to say the mean distance traveled by the particle in a medium and at a given energy before interaction.

For energy E and a given direction $\vec{u}$ in space, the probability that a particle (we take here a photon) get not interacted over a distance d is given in terms of the transmission index that we established in Chap. 2.

$$T\left(\mu d, E_\gamma\right) = \exp(-\mu d)$$

The probability that the particle has interacted over the same distance d is 1 minus this expression. In addition, one can explain that probability in different way, by noting that this is also the probability of having interacted on a distance less than d in other words, the density of cumulative probability to interact at a distance d.

$$P(d) = 1 - \exp(-\mu d)$$

With the draw of a new random number and the inverse function $P(d)$, the collision distance d is sampled as:

$$d = -\frac{1}{\mu}\ln(1-\xi)$$

A routine computes the coordinates of the point of collision or intersection with a boundary of the cell, in a homogeneous medium. The new coordinates, knowing that $d = \left\|\vec{d}\right\| = \sqrt{d_x^2 + d_y^2 + d_z^2}$ are then given by the system (6.25).

$$\begin{cases} x' = x + d_x \\ y' = y + d_y \\ z' = z + d_z \end{cases} \tag{6.25}$$

The code performs a test to determine if d is inferior to D, the distance between the last point of the particle location (X Y Z) in the expression (6.25) and the cell boundary in the direction of transport. If this is the case, the coordinates of the particle are $(X'Y'Z')$ according to the expressions (6.25); the parameters of the collision are then calculated (scattering energy, type of collision …). If instead $d > D$ the particle will be assigned the coordinates of intersection with the cell border. At this time, the particle enters a new step of its history. It retains its energy and direction from the previous cell, but the routine for calculating the path and the collision point will integrate new cell characteristics. In particular, the boundaries, as well as the type of material and density of the new medium, thus changing the mean free path of the particle. Remind that if the border crossed belongs to the exclusion sphere then the particle is killed and a new particle is launched at the source.

The sampling of the path length may be biased, in order to facilitate tracking to a detector or along a direction of interest. This biasing method, once more, is corrected on the mean result of the quantity sought by appropriate adjustment of the weight of the particles entering the detector. This technique should reduce the

variance associated with the mean result. In the technique called "exponential transformation", the macroscopic cross section is changed. For the case of photons of energy E we would have:

$$\mu^* = \mu - f(\vec{r}, \vec{u}, E) \tag{6.26}$$

This time the distance d to collision is determined with the new macroscopic section μ*. As before, the adjustment of the statistical weight is calculated according to the principle of "weight-probability" conservation law.

$$W \cdot p = W^* p^* \tag{6.27}$$

Here, p is the density of probability of interacting in point d—in the infinitesimal element slightly higher d; to get it, simply multiply the expression (6.26) not to have interacted to a distance r by the probability μ to interact in an element of length between d and $d + \partial d$:

$$p(d) = \mu \exp(-\mu d)$$

therefore the new adjustment weight is obtained:

$$W^* = W\left(\frac{\mu}{\mu^*}\frac{\exp(-\mu r)}{\exp(-\mu^* r)}\right) = W\left(\frac{\mu}{\mu^*}\right) \exp[-f(\vec{r}, \vec{u}, E)\, d] \tag{6.28}$$

Several expressions of $f(\vec{r}, \vec{u}, E)$ are possible. The use of (6.29), where $\vec{\varepsilon}$ is the unit vector along the direction of interest and B a coefficient setting the "depth" of biasing, improves transport along this direction as μ* > 0.

$$f(\vec{r}, \vec{u}, E) = \vec{\varepsilon} \cdot \vec{u} B \tag{6.29}$$

Function f given by (6.30) enhances transport to the point (x_0 y_0 z_0), while limiting the path d if the transport direction gets away from the detector and increasing it if it approaches the direction toward the detector.

$$f = B\left[(x - x_o)^2 + (y - y_o)^2 + (z - z_o)^2\right]^{\frac{1}{2}} \tag{6.30}$$

6.9 Target Nucleus Sampling

For the choice of target nucleus in the case of a homogeneous mixture, the sampling is performed on the cumulative probability of the macroscopic cross sections of the various components of the mixture. In a mixture, the probability of a target element i is given by:

Table 6.1 Values of the various macroscopic cross sections for the chemical constituents of soft tissue and the density of cumulative probability for the choice of the target nucleus

Component	(μ/ρ) (cm^2 g^{-1})	w (μ/ρ) (cm^2 g^{-1})	$P(j)$
C	0.0636	0.00705	0.10
O	0.0637	0.04846	0.79
H	0.126	0.01272	0.97
N	0.0680	0.00177	1

$$p(i) = w_i \left(\frac{\mu}{\rho}\right)_i \Big/ \left(\frac{\mu}{\rho}\right)_{mélange} \tag{6.31}$$

with w_i the weight percentage of component i in the mixture, (μ/ρ) the mass attenuation coefficient. It is done the same way as in Sect. 6.3; the density of cumulative probability of having a target nucleus below j is as following:

$$P(j) = \sum_{i=0}^{i=j} p(i) = \sum_{i=0}^{i=j} w_i \left(\frac{\mu}{\rho}\right)_i \Big/ \left(\frac{\mu}{\rho}\right)_{tissu}$$

A new random number is assigned to the result of the density and k_{th} nuclide is selected as the target of the collision if the following inequality is satisfied:

$$P(k-1) < \xi < P(k)$$

To illustrate this process, let us consider the example of a nucleus target in human tissue consisting of C (11.1%), O (76.2%), H (10.1%) and N (2.6%), for a 1 MeV photon. Table 6.1 gives the various coefficients for each constituents and the calculated cumulative probability, knowing that (μ/ρ) for a standard tissue is 0.07 cm^2 g^{-1};

Thus, if the drawn random number leads to $P(j) = \xi = 0.8$, the collision impact therefore an oxygen atom.

6.10 Sampling Charged Particle Transport: Electrons Case

At the electron energy range pertinent to this book, the electron transport simulations are usually performed with the "condensed history" method developed by Berger [9].

In the "Class I" condensed history algorithm, all collisions are simulated in a predetermined energy grid in a "step-by-step" approach (i.e. history particle subdivided in equal paths). A disadvantage of the algorithm, as detailed after, is that interpolations are needed when the electron steps do not equal any of the grid energies. Another disadvantage of this approach is that the energy and direction of

the primary particle is not affected by the secondary particles created along its path and therefore energy and momentum are not conserved in a single step [10].

In the "class II" condensed history algorithm, all the interactions are dived into "hard" and "soft" collisons. "Hard" or also so-called "catastrophic" collison are characterised by small number of events and by large energy transfers or large angular deflections. The "soft" collisions are treated like in class I approach, but the hard collisions (inelastic collisions above certain threshold energy of the secondary electrons) are simulated explicitly collision by collision in an analogue manner.

In MCNP code, up to version 5, the class I approach is used to describe multiple-scattering, and consequently energy-loss by collision; the class II approach is used to simulate radiative energy loss. More recently, in version 6, a new feature allows a class II treatment for low-energy electrons. The EGSnrc code employs the class II approach to simulate both radiative and collisional energy loss. PENELOPE code implements class II mixed scheme for electron transport: all interactions that involve changes in the kinetic energy or the direction of flight are simulated in analogue manner above certain threshold values given for scattering angle and energy loss. Below the threshold values, class I multiple scattering methods are applied.

6.10.1 "Step-by-Step" Approach for Multiple Scattering Method (Class I)

Unlike neutrons and photons, electrons and the charged particles cause a large number of interactions in the crossed medium essentially by Coulomb interactions. For example, a neutron in aluminum, to slow down from 0.5 to 0.0625 MeV would need an average of 30 collisions, while at the same time 10^5 electrons cause interactions for the same result. The "collision by collision" approach for electron tracking could therefore be extremely costly in computing time machine. So a "step" approach is used consisting in subdividing the path of the electron in the material into several segments and to perform on each of theme, following calculations:

- Loss of energy of the electron in the segment;
- "overall" scattering angle of the electron;
- Determining of the number of generated photons by bremsstrahlung and energies;
- *Knock-on* electrons released by ionization (*e*);
- Production of fluorescence X rays and Auger electrons.

Note that to limit the computation time, and if these show no interest for results, the last three calculations can be omitted by the user by means of specific cards in the program.

This method of sampling electron parameters by step is called "*Condensed history technique*" [9] and is based on a multi-group approach described in Sect. 6.4.1. The history electron can therefore result in the sequence of the following parameters:

$$\left(0, T_o, t_o, \vec{u}_o, \vec{r}_o\right), \left(s_1, T_1, t_1, \vec{u}_1, \vec{r}_1\right) \ldots\ldots \left(s_n, T_n, t_n, \vec{u}_n, \vec{r}_n\right)$$

where s_n, T_n, t_n, $\vec{u}_n$ and $\vec{r}_n$ are respectively the distance reached by the electron in step (n), energy, time, scattering direction and location. On average, energy and path are linked by the expression (6.32) for the "continuous slowing-down approximation" (CSDA):

$$\left(\overline{\Delta T}\right)_n = T_n - T_{n+1} = -\int_{s_n}^{s_{n+1}} \left(\frac{dT}{dx}\right)_{tot} dx \tag{6.32}$$

where $(\mathrm{d}T/\mathrm{d}x)_{\mathrm{tot}}$ is the total stopping power (bremsstrahlung and collision) that depends on the energy and the crossing area. The difference in energy, which then determines the path length s of the step is set upstream of calculation systematically with the following ratio:

$$k = \frac{T_{n+1}}{T_n} \tag{6.33}$$

The k ratio is set or variable according to codes. For instance, in the MCNP code, this ratio is set (value of CBET) and is $k = 2^{-1/8}$, which leads to a loss of systematic energy of 8.3% step. Note that this value should take into account a number of assumptions inherent to the model. The step should be long enough to allows enough collisions and then apply the "multiple scattering theory" for determining the global angle of scattering. However, it must be short enough so that the energy loss is still small compared to the kinetic energy of the electron that is consistent with the CSDA. Thus, the total energy lost at the end of each step and is set by the expression (6.33) is:

$$\left(\overline{\Delta T}\right)_n = (1-k)T_n$$

Note that in step (n) the electron flights the path portion $s = s_{n+1} - s_n$. Due to the energy dependence of the total stopping power, every step will correspond a different path.

The set of precalculated and tabulated data for the electron transport are stored in an indexed database according to the discrete energie T_n relating to the step (n) and corresponding to the upper bound of the energy bin $\left(\overline{\Delta T}\right)_n = T_n - T_{n+1}$. In this energy grid, previous bound T_{n-1} and following bound T_{n+1} are ruled by the ratio (6.33). At this point, it is important to emphasize that for a given step, calculations

for bin $\left(\overline{\Delta T}\right)_n$ will therefore be made only on the basis of discrete parameters of the upper bound $\left(s_n, T_n, t_n, \vec{u}_n, \vec{r}_n\right)$. This approximation, we shall see, can lead to artifacts calculations and a systematic error in some cases.

However, for more "representativeness" of the real path of the electron in the material and in particular to take into account the property of it to extensively disseminate low-energy during numerous scattering, each step can be subdivided into m substeps. The path length achieved during each substeps is equal to:

$$s_m = \frac{s}{m}$$

If the loss of energy is sampled at the step, the calculations of scattering angles by the multiple scattering theory and the production of secondary particles are in turn sampled at these substeps. The value of m default depends on the Z the material and is empirically determined to be consistent with the range of validity of the different calculation methods: $m = 2$ for $Z = 6$ to $m = 15$ for $Z > 91$ in the MCNP code. Let us add that it is possible to increase this value by means of special cards (e.g. Estep card in MCNP code and Estepe card code in the EGS code). Statistical convergence during calculations can find then improved, but with costly calculation. This can particularly be recommended in small regions of space where the number of sub-steps will not be sufficient to properly simulate electron transport.

As we said, all data related to history calculation for electron—stopping power, path, lengths of sub-steps, probability distribution for the scattering angle, secondary particles production…—are indexed to discrete energy in an energy grid determined by the ratio (6.33). However, the energy lost by collision obtained by sampling the Landau distribution of energy straggling (see example in Further Details 6.3) exceed or do not reach the mean value announced by Bethe-Block, analog transport of bremsstrahlung photons and geometric bounderies (media interface) are that there is little chance that the final energy of the electron at the end of step corresponds to the energy of the lower bound T_{n+1} of the group energy of step (n). Now, logically, following a step (n), there is a transition to the next step $(n + 1)$ related to the energy group $\left(\overline{\Delta T}\right)_{n+1}$. This gap between the energy of the lower bound of a group and the effective final energy calculated is also a source of differences that we will detail later. According to the calculation algorithms, we will discuss how are managed approximations related to this "step by step" method and especially what energy group will be assigned the final energy at the step end, provided that it is different from one bound of an energy bin (see Sect. 6.10.4).

Once the assignment of final energy made, a new calculation step can begin. Although this method allows the restriction in time calculation for electron tracking, be aware that the tracking of electron history for the calculation of an estimator can lead time calculations 1000–10,000 times even more important for the same statistical error. Thus, charged particles are transported only if there actually needs and depending on the degree of accuracy and approximation on estimator's calculation.

6.10.2 Multiple-Scattering Distribution for Energy Loss by Collision (Class I)

As suggested above, calculating the mean energy lost by Coulomb interaction in the segment s in the CSDA approximation considering a continuous and constant energy loss throughout this segment is covered by the Bethe-Block (see Sect. 6.2):

$$\overline{\Delta T}_c = \int_0^s \left(\frac{dT}{dx}\right)_c dx$$

Reminding that the stopping power per collision depends on the initial energy of the electron that begins the segment s, *a priori* T_n for a step (n). The distance s is considered small, the CSDA approximation can be apply meaning that the stopping power remains constant over this interval. In fact, statistical fluctuations are extremely important around the mean value of the loss of energy (all or part of energy can be transferred at one time). To avoid bias this effect can cause to the effective loss of energy, it should take into account the energy straggling around the mean value. Figure 6.10 schematically shows the dispersion of the "effective" loss of energy by collision. We note that the most energy decreases, this straggling is large, which makes sense since most the energy of the incident electron decreases and the most the probability of transferring a large energy at once becomes important.

To overcome the erroneous approximation of mean loss of energy obtained with the Bethe-Block, Landau [12] proposes the probability distribution (6.34) representative of the energy straggling. This distribution is detailed in the Further Details 6.3.

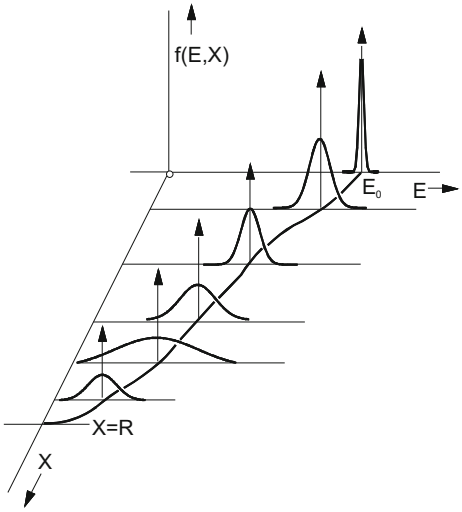

Fig. 6.10 Distribution of energy transferred on each segment x_s by a charged particle of initial energy E_0 [11], with permission from Elsevier

$$p(\Delta) = f\left(s, \bar{\Delta}, \Delta\right) d\Delta \tag{6.34}$$

This expression depends on s and the mean loss of energy calculated by Bethe-Block $\overline{\Delta T}_c$ (note $\bar{\Delta}$ for the occasion). This approach is incorporated into the electron transport algorithm in MCNP code, for example, wherein a sampling on the distribution of cumulative probability that is performed for each step to determine a value Δ_{eff} for effective loss of energy by collision, other than $\overline{\Delta T}_c$ with the CSDA approximation.

6.10.3 *Sampling Bremsstrahlung Photons and Energy Loss (Class I)*

As we mentioned above, the calculation of the number N of bremsstrahlung photons and their energy can be analogically determined in sub-steps. One way to achieve this is: if σ_f is the total microscopic cross section for producing a bremsstrahlung photon from an electron of energy T within a medium of density ρ_a, the mean number of photons emitted on the path segment s is given by (6.35).

$$\overline{N} = \sigma_f s \rho_a \tag{6.35}$$

Considering that the number of bremsstrahlung photons emitted during the path s meets a Poisson distribution, because of few occurrences, independent of each other and that the probability of occurrence on a short distance dx is proportional there to. The Poisson distribution is defined as the mean occurrence of bremsstrahlung photon $\overline{N}$ in expression (6.35). The probability that a result of having N photons released is given by classical Poisson expression:

$$p(N) = \frac{\left(\overline{N}\right)^N \exp\left(-\overline{N}\right)}{N!}$$

The cumulative probability of having a lower number of photons N is then obtained from the following cumulative probability:

$$P(N) = \sum_{n=0}^{n=N} \frac{\left(\overline{N}\right)^n \exp\left(-\overline{N}\right)}{n!}$$

After selection of a random number ξ, the number N is determined by the following inequality: $P(N-1) \leq \xi < P(N)$. For each of these N photons, there is

then necessary to determine the energy. It is reminded that the differential cross section to obtain a photon energy between E_γ and $E_\gamma + dE_\gamma$ for an incident electron energy is roughly the form:

$$\left(\frac{d\sigma_f}{dE_\gamma}\right)_T = \frac{k(T)}{E_\gamma}$$

The probability that the photon is emitted with an energy E_γ and the cumulative probability density associated are then given by:

$$p(E_\gamma) = \frac{1}{\sigma_f}\left(\frac{k(T)}{E_\gamma}\right) \quad \Leftrightarrow \quad P(E_\gamma) = \frac{k(T)}{\sigma_f}\int_{E_{\min}}^{E_\gamma}\frac{dE_\gamma}{E_\gamma} = \frac{k(T)}{\sigma_f}\ln\left(\frac{E_\gamma}{E_{\min}}\right)$$

The energy of ith emitted photon is then obtained by $E_\gamma(i) = P^{-1}(\xi_i)$:

$$E_\gamma(i) = E_{\min}\ln\left(\frac{\xi_i\sigma_f}{k(T)}\right)$$

The bremsstrahlung spectrum starts with a minimum energy $E_{\min}$. Let us add that, unlike the energy lost per collision treated probabilistically, the method developed above is analog. Furthermore, secondary electron production can in turn be treated implicitly or analogically. In the MCNP code for example, it is by default implicitly: the energy and direction of primary electrons are not affected by the creation of these electrons and there is neither energy conservation nor the moment along the way.

The challenge now is to know at what time stops this loop for obtaining energy of bremsstrahlung photons. Upstream, the component of energy lost by collision has been determined. *A priori*, in a step, the energy available for the loss by bremsstrahlung is actually determined by subtracting the energy lost by collision calculated by sampling the distribution of Landau (6.34). Lost to the total mean energy calculated using the total stopping power:

$$\left(\overline{\Delta T}\right)_f = \left(\overline{\Delta T}\right)_t - \Delta_{eff}$$

As we mentioned above, the calculation of the number *of* bremsstrahlung photons and their energy are determined in sub-steps.

Thus, on each of m substeps, a loop performs the sampling of the energy until the sum of the photon energy is approximately equal to the energy available for the loss by bremsstrahlung:

$$\sum_{i=1}^{i=N} E_\gamma(i) \approx \frac{\left(\overline{\Delta T}\right)_f}{m} \tag{6.36}$$

We note that the "substantially equal" may constitute a bias which in practice can have a significant effect for important energies and for high Z materials. For a step wherein a Δ_{eff} energy has been lost by collision, the total effective loss of energy at each substep on the path s_m is:

$$(\Delta T)_{eff,m} = \frac{\Delta_{eff}}{m} + \sum_{i=1}^{i=N} E_\gamma(i) \tag{6.37}$$

The total loss of energy at the end of m substeps and therefore at the end of step is equal to:

$$(\Delta T)_{eff} = \sum_{m} (\Delta T)_{eff,m} \tag{6.38}$$

But it will never match the total energy loss $\left(\overline{\Delta T}\right)_n$ obtained upstream according to expression. Accordingly, the final energy of the electron at the end of this step will not be equal to the energy of the lower limit of considered step (n):

$$T_f = T_n - (\Delta T)_{eff} \neq T_{n+1} \tag{6.39}$$

This is due to several causes: the effective loss of energy by collision Δ_{eff} can far exceed the range of the energy bin, so the total mean energy lost, initially calculated, particularly at low energies. Moreover, to a lesser extent, in the case of interest, the assumption made on the calculation of bremsstrahlung photon energies (see 6.42) also contributes to this gap.

At least, a table-based sampling scheme can be used to sample the photon angular distribution, like in MCNP code.

6.10.4 *Global Deflection Angle According to Multiple Scattering Theory (Class I)*

The calculation of the global deflection angle is also carried out on the substep of path s_m to reproduce at best, especially at low energies, the successive scattering experienced by the electron. The deflection angle of each substep needs a calculation for which a "multi-group analysis" is necessary: the angular distribution is defined by bin according to the probability distribution for having an elementary path s_m a scattering angle θ relative to the direction of s_m as shown in Fig. 6.11.

The complexity of this approach requires a decomposition into Legendre polynomial whose orthogonality property allows to set workable expressions for sampling the cosine of the scattering angle. This probability function can be expressed as the approach of Goudsmit-Saunderson [14] (see Further Details 6.4).

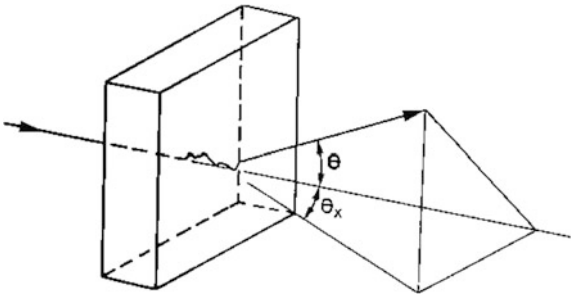

Fig. 6.11 Multiple scattering of an electron. The scales and angles are respected [13]. Courtesy of Springer Heidelberg

6.10.5 *From Step-by-Step to Single-Event Approach Applied to MCNP Code (Class I and II)*

At a step (n) we have seen, there is a good chance that the calculated effective loss of energy $(\Delta T)_{eff}$ differs from the mean loss of energy estimated with the total stopping power $(\overline{\Delta T})_n$. When calculating the effective loss of energy results in a lower mean value, the final energy of the electron T_f at the step end remains higher than the lower bound energy of the energy bin on which was held step. In this case, the m substeps are run and the next step is initiated.

If a media boundary is encountered during a substep, the substep cycle is interrupted and also responds to the triggering of a new step. Note that in the latter case, the path s originally planned, for which the energy loss calculations were made, is not described along its length. This approximation is necessarily responsible for a bias in the deposited energy.

As suggested earlier, the final energy T_f after a step will systematically differ from the lower energy of the energy bin for which unfolds step. Studying more closely how this is then treated gap energy according to the different electron transport algorithms, for example in the case of MCNP code.

First, for readability, an operator $L\left(T, s, \bar{\Delta}\right)$ is defined that, for an electron of energy T preparing to travel the path s by depositing the mean energy $\bar{\Delta}$ by Coulomb interaction. This operator calculates by sampling the Landau distribution, the deposited energy $\Delta_{eff} = L\left(T, s, \bar{\Delta}\right)$.

Nuclear precalculated and tabulated data required to calculate, as mentioned, are classified by energy bin $\left(\overline{\Delta T}\right)_n$. It is important to be aware that the calculations for one step (n) on this energy bin will be made based on physical parameters of the upper bound energy of this bin, namely: $\left(s_n, T_n, t_n, \vec{u}_n, \vec{r}_n\right)$. Thus, the effective energy lost by collision during step (n) will be determined discretely by the operator $L(T_n, s_n, \bar{\Delta}_n)$.

Default assignment in the MCNP code

With the "default" assignment algorithm MCNP code, energy T is assigned to group $\left(\overline{\Delta T}\right)_n$ of step (n) when the following inequality is satisfied:

$$T_n > T \geq T_{n+1} \tag{6.40}$$

where appropriate, T can be an initial incident energy or final energy from the previous step (T_f). The effective energy Δ_{eff} lost is then sampled via the operator $L\left(T_n, s_n, \bar{\Delta}\right)$. Thus, the electron takes m sub-steps of Δ_{eff}/m energy is lost. If m sub-steps are performed, the process is repeated with a new group assignment for final energy $T_f = T - \Delta_{eff}$. However, during a step, if the electron passes through a boundary between cell or that its energy decreases to a value less than the lower limit of the energy bin, the loop m is interrupted and there is a transition to lower energy group, even if the m sub-steps are not performed.

The problem with this approach comes from a high probability of not actually complete the path s for which the lost energy was sampled. In such a case, the loss of energy is connected to a linear interpolation for a theory that is clearly non-linear. Let us add, as we have already suggested, that about 80% of the lost energy is lower than the mean value $\bar{\Delta}$ predicted by Bethe-Block formula which confirms this analysis.

ITS assignment algorithm in the code MCNP

The ITS method (*Integrated Tiger Series*), also called "*nearest-group boundary*" treatment, limits in part the bias mentioned above. The treatment differs from the previous method of assignment. The energy of electron T is assigned to a group (n) since it satisfies the inequality (6.41).

$$\frac{T_{n-1} + T_n}{2} > T > \frac{T_n + T_{n+1}}{2} \tag{6.41}$$

This method makes it possible to affect energy T to a group with an higher energy index closer to T. The operator $L(T_n, s_n, \bar{\Delta}_n)$ induces, in the calculation of the transferred energy, less difference than the previous algorithm, since T is closer to the value of the upper bound T_n.

Other notable differences, if, during a sub-step, the energy of the electron leaves the energy bin, the sequence of m substeps is executed to completion. Furthermore, if crossing an interface, the electron does not automatically switch to a lower energy group. This approach significantly reduces the effects due to previous numerical approximations (see Sect. 6.13.1). In practice, the code activates the ITS mode using the DBCN card with the 18th entry is set to 1.

New algorithms since the code MCNP5

Since the version 5 of MCNP code, it is possible for an electron with energy E about to traverse a step of length s, to sample the straggling from the operator $L\left(T, s, \bar{\Delta}\right)$ without regard to the prearranged energy boundaries E_n. To implement

this "detailed electron energy-loss straggling logic", a FORTRAN90 module has been installed to deal with straggling data. Those parameters that are separate from the individual straggling events are still pre-computed, but each electron transport step can sample its energy loss separately from adjacent steps, and specifically for its current energy and planned step length. Using this new class II approach, the linear interpolations and energy misalignments of the earlier algorithms are largely eliminated [15].

Since MCNP6 version, the ENDF/B VI.8 database provides microscopic cross sections and secondary distributions appropriate to the four fundamental electro-atomic transport processes: atomic excitation, electron elastic scattering, subshell electro-ionization, and bremsstrahlung (library eprdata 12). This new implementation allows a class II treatment for electron transport. In all cases, tabulations of cross sections are given for energies between 10 eV and 100 GeV, and appropriate forms of tabulated distribution functions for secondary particles or energy loss are also provided. These new procedures describe a completely different approach from the condensed-history method that previously was the only available algorithm for electron transport in MCNP. This new single-event method (i.e. class II approach) dispense with the multiple-scattering theories, substep-based approximations detailed above, uncorrelated processes, and other aspects of the condensed-history approach, in favor of direct sampling of microscopic data distributions (according to similar process to those detailed in Sect. 6.3). Single-event electron transport is not intended to replace the condensed-history method in any energy range in which the traditional approach can be used. However, condensed-history electron transport in MCNP fails in the energy range below 1 keV because of specific limitations in the data and semi-analytic methods intended for higher energies. The single-event method now provides an accurate approach to low-energy transport, and it is for this low-energy range that the new method was developed (i.e. the single event method has to be trigged for energie to 10 eV up to a dozen keV, for energy above 1 keV the condensed history method is still used).

To illustrate MCNP6 enhancement in electron transport consider the evolution of a monodirectional, monoenergetic 60-MeV electron beam transporting and diffusing in a large volume of dry air [16]. Here the calculation with three different options for the electron transport is presented. First the standard condensed-history method is used with default values for the various transport controls. The spatial distribution of electron energy flux is shown in Fig. 6.12.

The Fig. 6.12 above display clearly a step-size artifact: the first angular substep occupies a significant part of the geometry of interest, and the condensed-history method in MCNP does not apply multiple-Coulomb energy loss or angular deflection until the end of the substep. We also see artifacts in the apparent ray effects in the angular distribution of the energy flux. As discussed above, the step-size artifacts in the condensed-history method can be improved by increasing the number of angular substeps per energy step. When the calculation is performed with twice the default number of substeps, we see the result in Fig. 6.13.

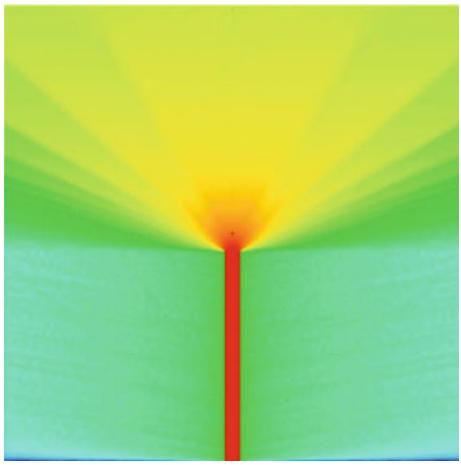

Fig. 6.12 Electron energy flux from 60-MeV electrons in air. Standard condensed-history calculation (from [16])

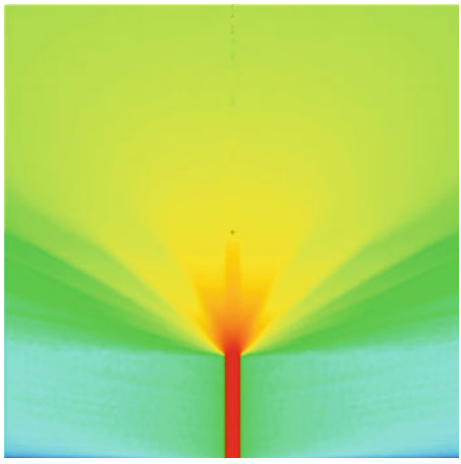

Fig. 6.13 Electron energy flux from 60-MeV electrons in air. Condensed-history with increased number of substeps

In Fig. 6.13, we see an improvement in the spatial artifact (since the initial substep is only half of its original length), but the angular ray effects seem at least as prominent as before. In turn, the single-event method is tried with this calculation and result is show in Fig. 6.14. With the single-event method, both the spatial and the angular artifacts are gone.

Boundary crossing artifacts in depth-dose calculation

Even if problem detailed above show satisfactory results at high energy, as mentioned the single-event method is developed for low-energy range (below 10 keV). Further more, the need at higher energies for the condensed history approximation arises from the fact that an electron with energy of the order of 10 keV experiences several thousand inelastic collisions with small energy transfers and with small angle deflections, plus an even greater number of elastic collisions, before coming

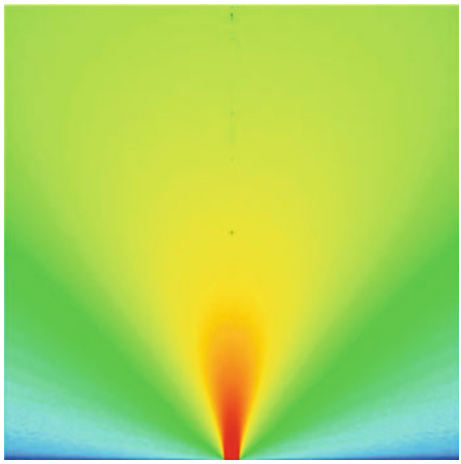

Fig. 6.14 Electron energy flux from 60-MeV electrons in air. Single-event electron transport

to a halt. As electron energy is increased, the number of collisions increases proportionally. This large number of collisions can make the detailed event-by-event simulation prohibitively long when simulating interaction of high-energy electrons with thick targets. Consequently, boundary crossing artifacts can arise especially in depth-dose problem calculations at slightly higher energies than 10 keV. These artefacts are more notable with ITS mode than with detailed electron energy-loss straggling logic, due to the fact that the energy-loss sampling in the method is independent of interfaces. However, in both methods, sampling of the angular deflections and the production of electron induced secondary particles (X-rays and knock-on electrons) are still dependant on cell boundaries. In these cases, the electron step is interrupted at the cell boundaries and interpolation procedures are applied for calculating angular deflection cross sections for partial substeps. Artefact are then more notable for dose distribution with low-energies electron beams due, probably to the fact that the large-angles deflections are more pronounced.

Here we show results from one such test case called the Dose Point Kernel (DPK). The dose point kernels (DPK) reported in the following were obtained for isotropic point sources placed in a water sphere divided in many shells. The energy deposited by the emitted electrons and by all the secondary particles produced along the primary trajectories is then tallied in n spherical shells placed around the radioactive source for distances ranging from 0 to 1.2 * R_0 where R_0 denotes the continuous slowing-down approximation (CSDA) range.

Results are given in terms of "dose point kernel" represented using the dimensionless quantity

$$J(r/R_0, E) = 4\pi r^2 D(r, E) R_0 / E$$

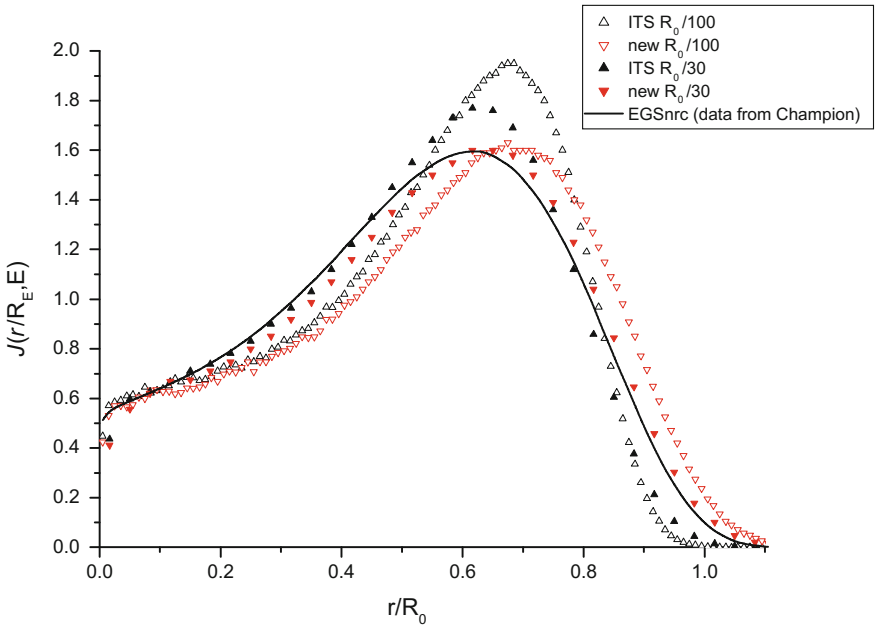

Fig. 6.15 Comparison for the dose profiles at 100 keV, in a water sphere subdivided into thin concentric shells (thickness 1/30 and 1/100 of electron's CSDA range R_0) with MCNP code; for ITS mode and single-event method ("new") turn on at 10 keV. The depth z is normalized by the CSDA range. Results are compared to EGSnrc calculation

where D(r, E) is the absorbed dose per source particle at radial distance r, while R_0 is the nominal CSDA range of electrons with initial energy E. The quantity $J(r/R_0, E)$ represents the fraction of the emitted energy deposited in an infinitesimally thin spherical shell of scaled radius r/R_0 to $r/R_0 + d(r/R_0)$. Figure 6.15 displays comparison for the dose profiles at 100 keV in a water sphere subdivided into thin concentric shells (thickness $R_0/30$ and $R_0/100$) for default ITS mode and single-event [17] ("new" in the figure) algorithm turn on at 10 keV. The depth z is normalized by the CSDA range. The MCNP results are compared to EGSnrc calculation [18].

For ITS algorithm, in both cases, the depth-dose peak is more preminent compared to EGSnrc and the absorbed dose tends to be underestimated at deep depths due to cumulative loss of particles at the interface related to the increase of boundary crossing. While the single-event algorithm follows nearly EGSnrc with 30 shells, a significant peak-shift arise for 100 shells subdivision. The reader will infer that a particular care have to be taken over the choice of adjacent cells amount in geometry design due to boundary crossing artifacts, especially at low-energies.

6.11 Problem Related to the Interface Between Cell for Calculating the Response of an Ionization Chamber

To illustrate the issue of energy deposition linked to the interface crossing in a dosimetry context, consider the problem of an ionization chamber response subjected to a parallel beam of photons ^{60}Co [19]. In this case, the energy is substantially deposited in the gas by the electrons moved in the wall-chamber. We are clearly in situation where the electron tracking is essential for the accuracy of the response.

6.11.1 Response Related to the Use of the Transport Code EGS4 Code (Class I)

The EGS4 code (*Electron Gamma Shower*) is developed at the Stanford Linear Accelerator Center. As we just mentioned, in the electron tracking, there is an "artefect interface", in particular in the case of ionization chamber where particle can switch from a low-density gas to a wall (in this case, carbon) of higher density.

As for the MCNP code, the algorithm Presta EGS4, the path s to move from energy T_n to T_{n+1} is modeled by a straight line segment. So to traverse from point a to point b, the model requires a straight path, when in reality the electron passes through a succession of significant deflection (see Chap. 2). Significant differences may arise in the calculation of the deposited energy due to interface between gas and wall, as shown in Fig. 6.16.

The straight segment between a and b corresponds to the calculated path [19]. Indeed, all paths are possible between point a and point b like curved path (a) in the region (1) or curved path (b) in the region (2). The energy deposited by the electron in the region (1) is correctly calculated from the path (a) and overestimated from the path (b).

We can overcome this issue in part by maximizing the number of steps in the segmentation of the course using the specific card (e.g. Estepe in EGS, Estep in MCNP). However, again, this action will have the effect of significantly increasing

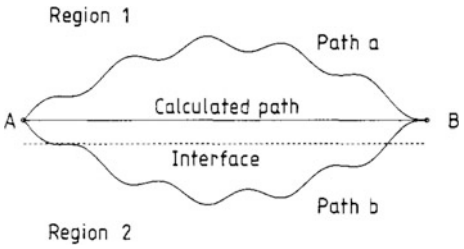

Fig. 6.16 Schematic representation of possible (**a**) and (**b**) paths reach a point B from a point A [19], with permission from IOP Publishing

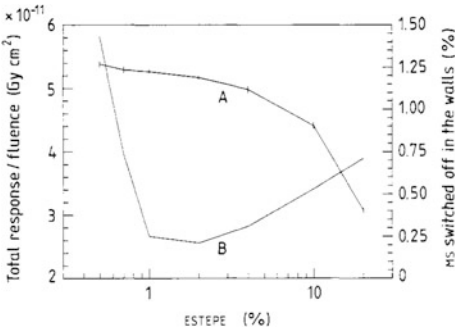

Fig. 6.17 **a** Results of the dose estimator based on the continuing loss of Estepe maximum energy. **b** The curve of the "switch off" percentage, calculated with EGS, in the problem of a cylindrical ionization chamber (2 mm depth and 1 cm diameter for inner radius, carbon wall thickness of 0.5 g cm^{-2}) subject to a parallel beam of photons of ^{60}O [19], with permission from IOP Publishing

the calculation time. Furthermore, limiting the maximum size of the path generates small energy loss $\overline{\Delta T}$, for which from a lower limit, the multiple-scattering algorithm (Molière in EGS) no longer works (not sufficient collisions to apply this theory), an energy-*cut* then takes over and "kills" the lower energy particle. It is therefore to find the right satisfactory compromise between the number of sub-steps without killing too many low energy particles. Figure 6.17 represents the problem of a cylindrical ionization chamber with low sensitive volume (2 mm depth and 1 cm diameter for inner radius, carbon wall thickness of 0.5 g cm^{-2}) subjected to a parallel beam of ^{60}Co photons. Results of the dose estimator based on the continued loss of maximum energy Estepe and the curve of the "switch off" percentage in the multiple-scattering algorithm are displayed when it is relayed by the energy *cut*.

The prediction given by the Bragg-Gray relationship is $5.33 \cdot 10^{-11}$ Gy cm^2. For a low percentage of 0.5%, there is a relatively good agreement between prediction and estimator response.

Then, there was a 70% hit in this response when changing from 0.5 to 20% maximum energy lost on the path segment. The slight curve rise of the "switch off" around 2% Estepe is attributable to the number of electrons transported whose range is interrupted at the interfaces crossing, which increases as the segment size *s* increases.

6.11.2 Improved Response with the Use of Code EGSnrc (Class II)

Recently, enhancements brought to EGS4 computer code have led to a new version: EGSnrc [20]. In this version, all interactions can be simulated in analog manner, so

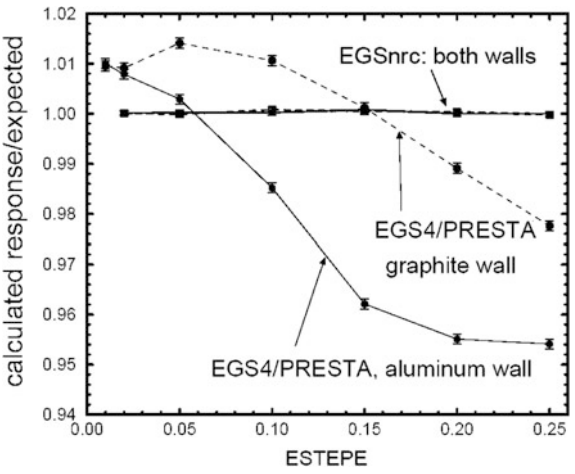

Fig. 6.18 Comparison of different results for the ionization chamber response subjected to a parallel beam of ^{60}Co depending on the number of sub-steps defined by the Estepe card [21], with permission from the National Research Council of Canada

that primary and secondary particles are directly correlated. The impact of secondary electrons creation on the primary electron deflection angle is taken into account.

The new PrestaII algorithm perform calculations on large steps without artifacts in results.

A new multiple-scattering theory based on the Rutherford cross section vanishes the shortcomings of the Molière multiple-scattering theory.

In addition, for a boundary crossing, the algorithm swith to a single-event mode to improve the energy treatment.

EGSnrc proves to be very stable towards the electron transport and is now a reference code for dosimetry calculations related to the electron-photon coupling.

To illustrate the enhancements provided by this code, Fig. 6.18 illustrates the comparison between the results of both version for the previous problem.

It will be noted that EGSnrc provide a satisfactory "response/expected" ratio, regardless of the maximum fraction of energy lost in a sub-step set by Estepe.

This paragraph thus highlights the importance of the awareness in code evolutions. The enhancements are permanent through the implementation of most advanced physical models and algorithms for more accurate calculations, as the computing performance increase.

6.12 Calculated Estimators in Monte-Carlo Codes

In Monte Carlo codes, statistical estimators characteries physical quantities. In this section, we will detail those related to radiometric and dosimetric quantities encountered in previous chapters, namely: the particle fluence Φ, the absorbed dose D and Kerma K. Beforehand, it should clarify two basic elements related to the

Monte Carlo technique: first, these estimators are not *strictly speaking* the particle scoring through the detection region, but more precisely, the sum of the statistical weight of the latter. Secondly, for obvious statistical reasons, all the results are normalized by emitted source particle (i.e. the final score is averaged over all the source particles see Sect. 6.14).

6.12.1 Fluence Estimator

They are of three types:

- The estimator of mean fluence in a volume (a cell) may be interested in, among other, the detection;
- The estimator of the particle fluence traversing a surface, for example, to quantify the particle fields through an interface;
- The estimator so-called "detector point" used to characterize the influence of a radiation field at a point. This may be particularly relevant since the dosimetry punctual quantities are studied. Recall that, by definition, the fluence involves in kerma and dose theoretical calculations is a punctual quantity.

Estimator mean fluence in a volume

To characterize the first of them, the mean fluence in a volume, let's back to the definition of the reaction rate in a given environment: the number of collisions in a volume V to energy E is given by the expression (6.42).

$$\tau_{\mathrm{R}} = \int_{V} \Phi_v(\vec{r}, E)\Sigma(E)\, d\vec{r} \tag{6.42}$$

where $\vec{r}$ is the location vector describing the entire volume V and $\Sigma(E)$ is the total macroscopic collision cross section at energy E. Thus, if the weight of the i-th particle responsible for a collision V is W_i^{coll}. The mean fluence in the volume V is obtained as (6.43).

$$\Phi_v = \frac{\tau_R}{V\Sigma} = \sum_i \frac{W_i^{coll}}{V\Sigma} \tag{6.43}$$

index i indicating the number of particles passing through the volume V. This estimator is fast, in terms of computing time but gives very poor results in terms of statistical convergence to the actual result when there are few collisions, due to a small sensitive volume or low macroscopic cross section. So it is better not to estimate in direct manner the number of collisions, but rather to score the weight of particles that enter, weighted by the probability of a collision once inside the

sensitive volume: $[1 - \exp(-\Sigma d)]$, where d is the path of the particle in the sensitive volume V. So, the above estimator becomes:

$$\Phi_v = \sum_i \frac{W_i^{entré}[1 - \exp(-\Sigma d_i)]}{V\Sigma} \tag{6.44}$$

This method is slower in terms of computing time, but each particle entering the sensitive volume interacts and significantly improves scoring in statistics. Note that if the product Σd is small, which is the case, the exponential can be reduced as $1 - \Sigma d$, simplifying the above expression as follows:

$$\Phi_v = \sum_i \frac{W_i^{entré} d_i}{V} \tag{6.45}$$

We will infer that this provides the appropriate unit of the fluence: cm^{-2}. Strictly speaking, as suggested, the result of this estimator is normalized by the sum of the statistical weights of all the launched source particles N_s. If we consider all sources particles are emitted with a weight of 1 (realistic assumption since no technical variance reduction is performed on the sampling of sources particles), the average estimate of the mean fluence in a volume V finally expressed as (6.46).

$$\sum_{j=1}^{j=N_s} W_j = N_s \Rightarrow \overline{\Phi}_v = \frac{1}{N_s} \sum_i \frac{W_i^{entré} d_i}{V} \tag{6.46}$$

It is also possible to estimate the mean particle fluence across a surface.

Mean fluence estimator across a surface

The estimator of the signal through a surface can be thought of as a limiting case of the previous estimator when one of the dimensions of V becomes infinitely thin, as shown in Fig. 6.19.

In the expression (6.46) $V = \delta A$ and $d = \delta / \left| \vec{\Omega} \cdot \vec{n} \right| \Leftrightarrow d = \delta / |\cos\theta|$ and the estimator of the mean fluence of particles passing through a surface A is obtained as follows:

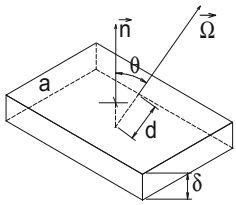

Fig. 6.19 Calculation of surface fluence estimator [22]

$$\overline{\Phi}_s = \frac{1}{N_s}\sum_i \frac{W_i\delta}{|\cos\theta|\delta a} = \frac{1}{N_s}\sum_i \frac{W_i}{|\cos\theta|a}$$

Finally, let's characterise the fluence estimator "point-detector", which will be particularly relevant in dosimetry simulation, since it delivers the mean fluence at a point in space.

Estimator fluence "point-detector"

Recall that the fluence at a point in space is an elementary input data for the theoretical kerma or absorbed dose at the same point (see Chap. 2). This estimator, unlike previous, due to a relatively low occurrence of particles crossing a single point in space and possibly far from the source, is treated deterministically. The method is to calculate the contribution of each particle emitted by a source or following a collision to the point detector, even if these latter have an orientation other than those leading to the point detector during sampling of the emission direction. To do such operation, it is necessary, among others, to balance the weight of each particle by the probability of going through direction of point-detector. This estimator is detailed by Fig. 6.20.

In this previous scheme, we arbitrarily defined a surface *da* as being obtained from a plane passing through the point r_p and limited by the cone defined by the solid angle $d\Omega_p$ around the direction $\overrightarrow{\Omega}_p$, $\overrightarrow{\Omega}_p$ defining the direction to be taken by a particle emitted at point S (from a source or collision) to reach the point detector. We are studying this time the particles that pass through the surface *da*, like the previous surface estimator, but taking care, once the calculation is complete, to tend this surface *a* to 0.

First, let's figure out the probability that a particle passes through the surface *da*. For this to be possible, two conditions are necessary: first, that it goes in the right direction, which occurs with probability $p(\Omega_p)$, secondly, we need this particle does not interact throughout the path from S to p, which results in the transmission factor

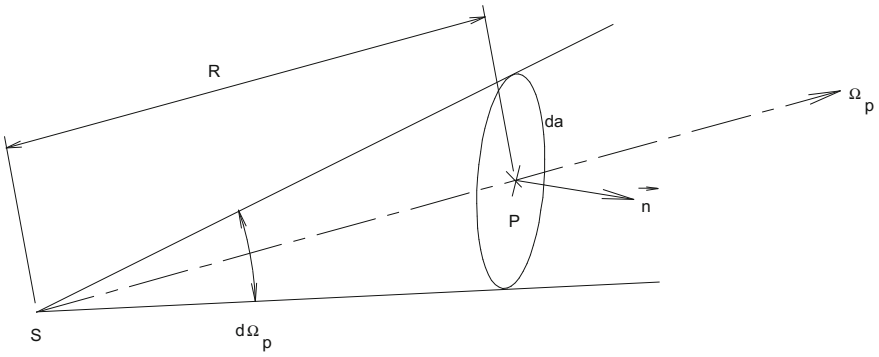

Fig. 6.20 Deterministic calculation of the fluence estimator "point-detector"

$\exp(-\Sigma_t R)$. Thus, the probability that a particle emitted from a point S through the small surface element *da* through p is given by the expression (6.47).

$$p(S \to p) = p\left(\Omega_p\right) d\Omega_p \exp(-\Sigma_t R) \tag{6.47}$$

Like the surface estimator $\overline{\Phi}_s$, if a particle of a weight W crosses the surface *da*, it will contribute to the fluence with the following amount:

$$\frac{W}{\left|\cos\left(\overrightarrow{\Omega}_p, \vec{n}\right)\right| da} \tag{6.48}$$

The expression of the differential element $d\Omega_p$ depending on the element surface *da* is given by (6.49).

$$d\Omega_p = \left|\cos\left(\overrightarrow{\Omega}_p, \vec{n}\right)\right| \frac{da}{R^2} \tag{6.49}$$

The estimator becomes:

$$\begin{aligned}
\Phi_p &= p\left(\Omega_p\right) d\Omega_p \exp(\Sigma_t R) \frac{W}{\left|\cos\left(\overrightarrow{\Omega}_p, \vec{n}\right)\right| da} \\
&= W p\left(\Omega_p\right) \frac{\left|\cos\left(\overrightarrow{\Omega}_p, \vec{n}\right)\right| da}{R^2} \frac{1}{\left|\cos\left(\overrightarrow{\Omega}_p, \vec{n}\right)\right| da} \exp(-\Sigma_t R) \\
\Rightarrow \Phi_p &= W \frac{p\left(\Omega_p\right)}{R^2} \exp(-\Sigma_t R)
\end{aligned}$$

We have $p\left(\Omega_p\right) = p(\varphi) p(\theta)$. In addition, for rotational symmetry $p(\varphi) = 1/2\pi$, then, the final expression of the estimator of the fluence at a point is given by (6.50).

$$\Rightarrow \Phi_p = W \frac{p(\theta)}{2\pi R^2} \exp(-\Sigma_t R) \tag{6.50}$$

Let's apply this expression to an isotropic point source. We know that the probability $p(\theta)$ having a particle source emitted at an angle θ:

$$p(\theta) = \left(\int_0^{\pi} \sin\theta \, d\theta \right)^{-1} = \frac{1}{2} \tag{6.51}$$

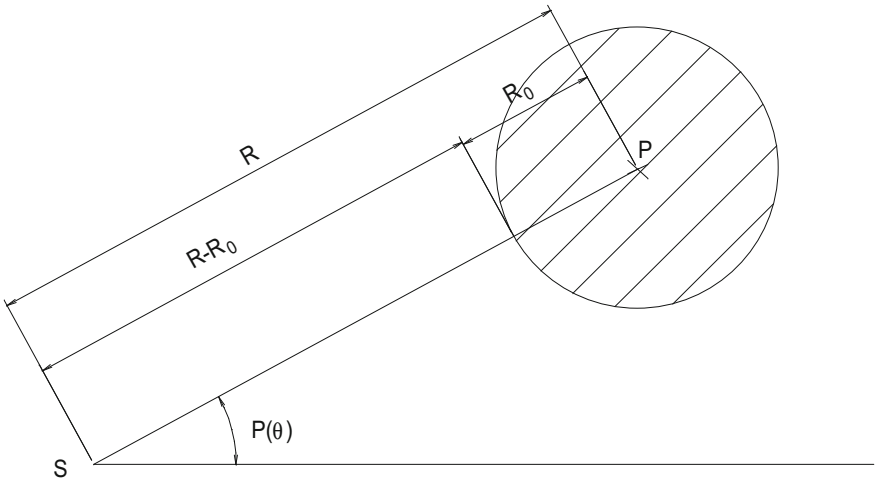

Fig. 6.21 Exclusion Sphere of radius R_0 to calculate the fluence estimator by the point detector

Consequently, expression of the estimator for an isotropic point source becomes:

$$\Rightarrow \Phi_p = W \frac{1}{4\pi R^2} \exp(-\Sigma_t R) \tag{6.52}$$

The term right weight W is common to the calculation of the fluence of photons or neutrons in a thickness R (See Chap. 1). This expression is typical of deterministic calculations of point-kernel type described in Chap. 5.

Note that this estimator presents a singularity due to its R^2 denominator term. Accordingly, if a particle after a collision or of the source is generated in the periphery near point-detector, then R tends to 0 and the fluence to infinity. This causes the effect of significantly slowing the statistical convergence of the estimator, or even make it impossible. One solution is to define an exclusion sphere of radius R_0 and centered on the point-detector as shown in Fig. 6.21.

The estimator is then calculated using the sum of two terms: firstly, the fluence term $\Phi_p(R > R_0)$ is calculated. Taking into account the probability that a particle emitted from S outside the sphere reaches the sphere at a point E:

$$\Phi_p(S \rightarrow E) = W \frac{p(\theta)}{2\pi R^2} \exp(\Sigma_t (R - R_o)) \tag{6.53}$$

Then, the fluence term within the virtual sphere $\Phi_p(R < R_0)$. The latter is then averaged over the entire volume of the sphere.

$$\Phi_p(E \to p) = \frac{\int\limits_V \Phi_p dV}{\int\limits_V dV} = W\,p(\theta)\,\frac{\int\limits_0^{R_o} \exp(-\Sigma_t r) 4\pi\, r^2 dr}{\frac{4}{3}\pi r^3} = \frac{W\,p(\theta)[1-\exp(-\Sigma_t R_o)]}{\frac{2}{3}\pi R_o^3 \Sigma_t} \tag{6.54}$$

It will be noted that this component is free from the R term at the denominator. Therefore, if R_0 is wisely chosen, that avoids the risk of infinite fluence. Typically, the value of R_0 is determined by the user and is equal to a fraction of the mean free path. Finally, the point-detector estimator is given by the sum of these two components (6.55).

$$\Phi_p = \Phi_p(S \to E) + \Phi_p(E \to p) \tag{6.55}$$

It will be observed that the demonstration was conducted for the *score* of a single particle and omitting the normalization term to simplify. So just to sum the above expression on all the sources of particles and divide by the total number of particles emitted by the source to achieve expression (6.56) of the mean estimator $\overline{\Phi}_p$.

$$\overline{\Phi}_p = \frac{1}{N_s}\sum_i \left(\Phi_p\right)_i \tag{6.56}$$

Spatial and energy distribution of estimator response with application to operational quantities

For all the fluence estimators, it is possible to calculate the response of the estimated quantity by energy bins. This response can then be weighted by a function dependent on energy. For example, if the attempted response is air-kerma K_a, simply it is necessary to weight energy bin of point-detector $\Phi_p(E)$ by the corresponding "fluence-air kerma" conversion factor $k_\Phi(E) = (K_a/\Phi)_E$ from publication 74 of the ICRP [23] (see Chap. 3) and sum as following:

$$K_a = \sum_{E_i} \left(\frac{K_a}{\Phi}\right)_{E_i} \Phi_p(E_i : E_{i+1}) \tag{6.57}$$

This energy discrimination of particles counted in assessing the fluence and the possibility *ultimately* to weight the energy spectrum obtained by a function of the energy is also particularly useful for the calculation of the protection quantities. For instance, ICRP [23] provide "fluence-dose equivalent" conversion factors by energy: $(H^*(10)/\Phi)_E$, $(H'(0.07)/\Phi)_E \ldots$ So there is ability to calculate at a point in space, the operational quantities $H^*(10)$, $H'(0.07)$, etc. from the energy bin response of "point-detector".

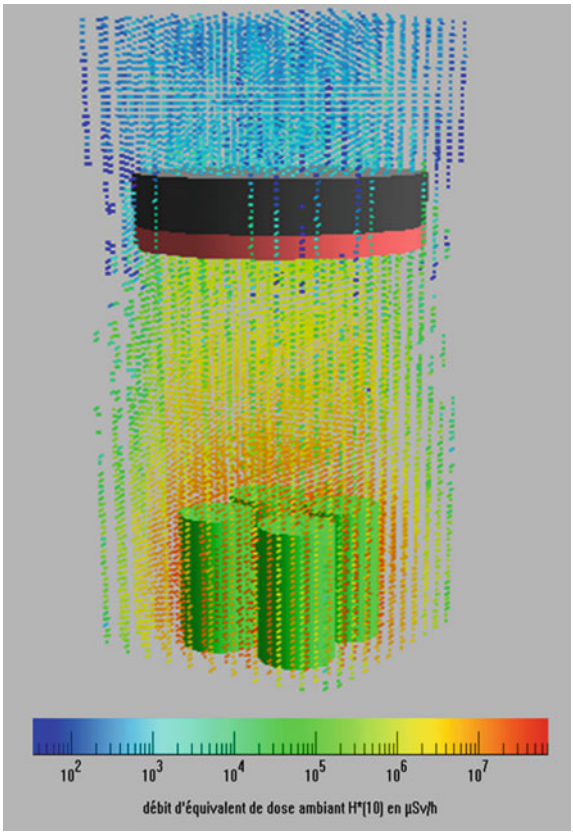

Fig. 6.22 3D representation of ambient equivalent dose $\dot{H}^*(10)$ in a mesh, from the estimator influence through MCNPX 2.6.0 [24]

Adding that in some codes features allow to calculate the estimators in 3D mesh in which responses are calculated in each unit mesh cell (e.g. MESH tally in MCNP).

The problem below summarizes both the use of energy cut and spatialization of the estimator response. The goal is to assess, in a region of space, the ambient equivalent dose $H^*(10)$ due to the presence of irradiating drums stored in wells for a essentially ^{60}Co source term.

In this simulation, a rectangular mesh grid is design to use the fluence estimator with a response by energy bin in each cell, the ambient equivalent dose rates $\dot{H}^*(10)$. Figure 6.22 displays a 3D overview of $\dot{H}^*(10)$ in mesh grid.

Note that the presence of a high Z plug (lead + concrete) strongly smouth results in upper zone.

Determining the response of a dosimeter using a fluence estimator

The mean fluence estimator in volume can also be useful to calculate dosimeters responses and more generally radiation detectors. Some codes allow to calculate

directly from this estimator a reaction rate τ_R (e.g. "fm" card in the MCNP code) in accordance with the usual expression:

$$\tau_R = \rho_a \int_E \overline{\Phi}_v(E)\, \sigma_R(E)\, dE \tag{6.58}$$

For example, to determine the (n, p) reaction rate in a ^{3}He neutron detector or the (n, α) rate in ^{6}Li detector.

We have just detailed below the manner to achieve dosimetric quantities via fluence estimators. In what follows, we will highlight the existence of estimators to obtain directly dose and kerma dosimetric quantities.

6.12.2 Kerma Estimator

It should immediately be noted that the result of the estimators that we will mention in the following is highly subject to checks in set-parameters that the user can specify in the calculation code and in particular, the type of particles chosen to track or not. Recall that the tracking of charged particles is a time consuming calculation —even if they are, a priori managed by "multi-group" approach as detailed in Sect. 6.10. It may be wise for instance not to track the electrons. We will see the impact that this choice can have on the available dose estimators.

The first kerma estimator is achieved by the mean fluence estimator in a volume $\overline{\Phi}_v$ according to the theoretical application of the kerma formula in Chap. 2. Thus, for a type of particle j indirectly ionizing (photon or neutron) having an energy E and evolving in a material, the kerma estimator is defined as (6.59).

$$\overline{K}_j(E) = \overline{\Phi}_v(E) \frac{\rho_a}{\rho} \sigma_t(E) \overline{E}_{tr}(E) \Leftrightarrow \frac{1}{N_s} \sum_i \left(\frac{W_i d_i}{V} \right) \frac{\rho_a}{\rho} \sigma_t(E) \overline{E}_{tr}(E) \tag{6.59}$$

with σ_t the microscopic cross section for the collision energy, $\overline{E}_{tr}$ the mean energy transferred to each collision whose datas are tabulated for each energy and for each material, ρ_a the atomic density (atoms/cm^3) and the ρ density. At least, it will be recognized $m = \rho V$ as the cell mass in which the energy is transferred. Note that for all particles of all energies entering the cell, the result of the estimator is given by the double sum (6.60).

$$\overline{K} = \sum_j \sum_E \overline{K}_j(E) \tag{6.60}$$

It is important to emphasize that in this approach, energy $\overline{E}_{tr}$ transferred to secondary charged particles is deposited locally at the collision point. This approach requires three comments in the particular case of photons: firstly, there is no need to

track the "expensive" electron transport due to the calculation method of energy transferred to the medium in which the energy is deposited in the collision point. On the other hand, it is indeed here a mean Kerma due to its obtaining via the mean fluence estimator in a volume that is opposed to the original Kerma concept as a punctual quantity established in Chap. 2. Finally, it should be very cautious about the analysis of the calculation result. This estimator can characterize the mean absorbed dose as soon as the cell has large dimensions toward the path of secondary electrons set in motion and the electron equilibrium is achieved from a small depth of the cell. Otherwise, the assessed quantity remains a kerma and can over estimate the calculated dose. We can also find the theoretical expression of Kerma from the Estimator Kerma expression (6.59). Indeed, we have shown that the mean spectrum of secondary electrons moved in a medium by a photon fluence is given by:

$$\overline{T}_{e-} = \left(\left(\frac{\mu_{tr}}{\rho}\right)/\left(\frac{\mu}{\rho}\right)\right)E_\gamma \text{ gold, with } \overline{E}_{tr} = \overline{T}_{e-et} \quad \mu = \rho_a \sigma_t$$

Finally, $\overline{K} = \overline{\Phi}_v \frac{\rho_a}{\rho} \sigma_t \overline{E}_{tr} = \overline{\Phi}_v \left(\frac{\mu_{tr}}{\rho}\right) E_\gamma$

For neutrons, the mean value of the energy transferred is also tabulated for each incident energy and for each material; it can be explained according to the following expression:

$$\overline{E}_{tr}(E) = E - \sum_i p_i(E)\left[\overline{E}_{i,n}(E) - Q_i + \overline{E}_{i,\gamma}(E)\right]$$

with E energy of the incident neutron, $p_i(E) = \sigma_i(E)/\sigma_t(E)$ the probability of a reaction to the energy E, $\overline{E}_{i,n}(E)$ the mean energy of neutrons released during the interaction type i, Q_i of the i reaction heat and $\overline{E}_{i,\gamma}(E)$ the mean energy of the photons emitted during type reactions i (Radiative capture photon). Again, the mean energy transferred is deposited to the collision point. So there is no need to track the secondary charged particles (i.e. light ions from capture reactions, recoil nuclei …), which results in gain in computing time.

We note that in the case of neutrons, the calculated quantity via this estimator is the multi-collisions kerma K_{mc}. Indeed, the use in kerma to the mean fluence estimator in a volume $\overline{\Phi}_v$ allows taking into account all of the neutrons passing through the volume V and especially those from multiple-scattering and backscattering in the medium. Finally, remind that because of extremely reduced path of secondary charged particles set in motion, this estimator gives a satisfactory dose approximation (up to neutron energies of tens of MeV: at 20 MeV, the mean energy transferred to the hydrogen recoil proton is 10 MeV, which generates a 1.2 mm range in water). We can write, for neutrons and energy restriction mentioned, the equivalency:

$$\overline{D} \cong \overline{K}_{mc}$$

We see the supply of such a feature to "wring the neck" to the impossibility of calculating theoretically multi-collision kerma.

To assess a mean absorbed dose with accuracy, two others estimators to be described in the following. We will note, in advance, that they have the disadvantage of requiring the transport of secondary charged particles unlike the previous estimators.

6.12.3 *Estimator "Pulse-Dose" for Indirectly Ionizing Radiation and Charged Particles*

The first is derived from "pulse estimator", originally dedicated to the energy deposition within detector (e.g. spectrometry γ). Unlike the previous, it is not based on the use of an mean fluence in the sensitive volume V, but on the individual scoring of each particle which enters the sensitive volume for which a difference is calculated between the incoming and outcoming energy of the particle in the sensitive volume. This approach must spontaneously evoke the theoretical principle of energy imparted ε in a volume V, as shown in Fig. 6.23.

Whenever a particle deposit energy imparted ε in the sensitive volume, its statistical weight is recorded. This process is done for all possible energies and provided for each type of particle. For an incoming particle with energy E_i the "dose-pulse" estimator is deduced by weighting the weight of the latter by the energy imparted into the volume V, all averaged over the mass $m = \rho V$ sensitive volume:

$$D_{imp} = \frac{W\left(E_i - E_f\right)}{\rho\, V} = \frac{W\varepsilon}{m} \tag{6.61}$$

Thus, for all the particles directly and indirectly ionizing passing through the sensitive volume, the estimator in the same volume is described by the expression (6.62).

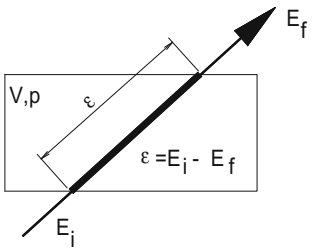

Fig. 6.23 Principle of "dose-pulse" estimator

$$\overline{D}_{imp} = \frac{1}{N_s} \sum_i \frac{W_i \, \varepsilon_i}{m} \tag{6.62}$$

Having to score any type of particles entering the volume V directly and indirectly ionizing, requires the tracking of secondary charged particles. Thus, for a photon source, there is a need to track electrons. Also include it is fundamental that the transport of various particles is tracked in analogue manner. Otherwise, the results obtained are inconsistant. This required treatment also provok time consuming. Finally, note that the pulse-dose estimator provides the exact mean absorbed dose in a volume V. To be convinced, the reader may refer to Sect. 6.13.2, in which a study related to protection quantities, compares this estimator with the previous kerma estimator for photon from 1 to 10 MeV within important sensitive volumes.

6.12.4 Dose Estimator for Charged Particles

This estimator score only the energy deposited by the charged particles in medium. It also requires, by definition, the tracking of charged particles (e.g. transport mode E or NCIA card mode electrons in MCNP to enable the transport of light ions produced during nuclear interactions and recoil nuclei). This estimator is strongly recommended since the photons and electrons are tracked in the problem. Only the energy deposited by the secondary electrons set in motion by the photons will be scored in accordance with the energy deposition calculation method along elementary segments s, developed in previous Sect. 6.10. For an electron, the scoring process is as follows:

$$\overline{D}_{pc} = \overline{\Phi}_v \frac{1}{\rho} \sum_j \frac{\left(\Delta T_{eff}\right)_j}{s_j}$$

This time $\overline{\Phi}_v$ reflects the secondary electron fluence, in accordance with the theoretical expression of the dose calculation for electrons provided in Chap. 2; the right term is also substantially equal to the mass stopping power. The overall expression for electrons is:

$$\bar{D}_{pc} = \frac{1}{N_s} \sum_i \frac{W_i d_i}{\rho \, V} \sum_{j=1}^{j=n_i} \frac{\left(\Delta T_{eff}\right)_j}{s_j} \tag{6.63}$$

with $\rho \, V = m$ and, moreover, given that for the charged particle transport algorithm is:

$$\sum_{j=1}^{j=n_i} s_j = d_i, \quad \sum_{j=1}^{j=n_i} \left(\Delta T_{eff}\right)_j = \varepsilon_i \tag{6.64}$$

the expression is simplified and, at the same time, we demonstrate that the estimator dose for charged particles provides the same result as the pulse-dose estimator.

$$\overline{D}_{pc} = \overline{D}_{imp} = \frac{1}{N_s} \sum_i \frac{W_i \, \varepsilon_i}{m} \tag{6.65}$$

Thus, the case of transport of secondary charged particles can support the use of this estimator.

6.13 Application to MCNP Code

The MCNP code (Monte Carlo *N* particles), we have already widely discussed, tracks neutral particles (photons and neutrons), electrons (negative and positive) and has spread to some heavy charged particles in its MCNPX release. This code is linked directly behind the Manhattan Project. Initially it had only an implementation for the transport of non-charged particles such as neutrons and photons. Thereafter, the transport of the charged particles has been integrated. This code has undergone continuous development since the forties, supported by a quality assurance policy. In addition to modeling the interaction of radiation with matter, it has statistical tools to test the mathematical convergence of the result and integrated variance reduction techniques. It does not require a recompilation of code for each case to be treated as in the EGS code. MCNPX was developed from the MCNP4C version of MCNP and LAHET. It includes, nuclear data tables for the proton transport, physical models to simulate the transport of 30 additional particles (deuterons, tritons, alpha, pions, muons …) and physical models to transport neutrons and protons tabulated when data is available or when the simulated interactions are beyond the energy range (1 keV–150 MeV) for which data tables are saved [25].

In this code, estimators above detailed physical quantities are so-called "*tally*". Note that the choice of transport of a given particle is specified in a special parameter called "mode". The nomenclature definition of an estimator is: an "F" followed by a number indicating the estimator type discussed above, a separator ":", then the type of particles scored.

Table 6.2 provides for easy transport (photon) and mixed (photon + electron) in the case of a simulation involving a photon source, to which correspond the previous estimators *tally*.

We note at the outset that according to the transport mode, simple or mixed, a *tally* can cover different estimators. The most outstanding case being the *tally* F6: p, e which in photon mode of transport, will be consistant with the kerma estimator while for mixed mode this tally coincide with the sum of the estimator Kerma $\overline{K}$

Table 6.2 MCNP estimators versus dosimetry estimators discussed above

Mode p	Mode p e
F4: p = $\overline{\Phi}_{v}(\gamma)$	F4: p = $\overline{\Phi}_{v}(\gamma)$
F4: e = 0	F4: e = $\overline{\Phi}_{v}(e^{-})$
F5: p = $\overline{\Phi}_{p}(\gamma)$	F5: p = $\overline{\Phi}_{p}(\gamma)$
F5: e = 0	F5: e = $\overline{\Phi}_{p}(e^{-})$
*F6: p = $\overline{K}$	*F6: p = $\overline{K}$
F6: e = 0	*F6: e = $\overline{D}_{pc}$
F6: p e = $\overline{K}$	F6: p e = $\overline{K} + \overline{D}_{pc}$
*F8: p e = $\overline{D}_{imp}$	*F8: p e = $\overline{D}_{imp}$

and charged particles dose $\overline{D}_{pc}$. In this case, scoring both energy transferred by the secondary electrons and photons energy transferred locally, substantially double the scoring of same event. This salient example shows that it is necessary to anticipate what is precisely calculated based on the estimator chosen, the type of particles scored and the transport mode.

Concerning *tally* *F8 coinciding with the estimator "pulse-dose", it is worth mentioning it is appropriate to divide the result by the cell mass to homogenize the result to the absorbed dose; this *tally* is dedicated to score in counts the pulse heights.

Also, before calculations, the user should be aware of the nature of nuclear data used. There are both, we said, tabular data (cross sections "point by point" ENDF/B-VI, ENDF/B-VII, Jeff 3.1 …), but also when such data do not exist, codes switch to models that can significantly impact results especially below cut-off or beyond the upper energy limit of the code (e.g. lake of resonances in some models). The models necessarily provide approximations regarding the consideration of different physical phenomena visible especially at low energies: collective effects, influence of molecular structure, the local electric field, etc.

Note that for few Monte Carlo codes, options for choosing a particular model are available. These choices have to be determined by the calculated quantity and can improve the speed convergence to the result.

For example, to emphasize the importance of choosing a model, let us focus on the "phys: p" MCNP card related to photons physical options. According to the second input "IDES" of this card is set to 0 or 1, the physical model of secondary electrons varies. In the first case, to IDES = 0, which is the default template, electron transport is not taken into account; a thick target model is then used to generate, if necessary, depending on the material and the energy of the secondary electrons, Bremsstrahlung photons tracked in turn. In this simplified model, electrons are "virtually" oriented in the direction of the incident photons and stopped locally; they serve as "intermediaries" to the emergence of secondary Bremsstrahlung photons and are not transported.

In the second case, for IDES = 1, the electrons are not created and there is no production of Bremsstrahlung radiation, the energy transferred to the electrons is assigned at the point of interaction. This even simpler model is clearly dedicated to

the approximation "kerma = dose" namely that any energy transferred is imparted locally.

The 'phys: p' card allows also to specifie the analogue or implicit mode (*emcpf)*.

In "mode p e", electrons are created and transported by default according to the process described in Sect. 6.10. Let us add that for electrons, there is also a specific physical options in "phys e" card, which allows among other to choose not to track the Bremsstrahlung photons (*bnum*) and to choose for the energy lost by step, the mean value of the stopping power rather than sampling the Landau energy straggling distribution (*istrg*).

6.13.1 *Calculation of Kerma and Absorbed Dose in Crossing Media Problem, Using the Estimator Kerma with Changes in Transport Mode*

In this problem, illustrating changes in transport mode, and build-up of dose at interface, the considered geometry is a cylinder of 10 cm radius; with a total depth of 2 cm, composed successively of 1 cm of water, 0.2 cm aluminum and 0.8 cm of water. Energy deposition calculations are made at adjacent depths in cylindrical cells of 10 cm radius and 100 microns thick throughout the 2 cm cylinder. The source is described by a parallel beam of 1 MeV photons emitted from a disc of 10 cm radius coaxial with the cylinder. The simulation is performed with the mixed transport mode, namely 'mode p, e', and with ITS algorithm trigged (see Sect. 6.10.5). The calculated energy deposition "tally *F6", expressed in jerks/g (1 jerks/g = 1.10^{12} Gy) gives kerma "*F6:p" and dose "*F6:e" (cf. Table 6.2). The results of the kerma and dose as a function of depth in the cylinder are displayed in Fig. 6.24.

We will mention an interlaboratory measurement of the dose for succesives depths using a multi-cavity ionization chamber (see Chap. 2) with MCNP simulations and EGSnrc which was conducted for successions of Cu/Al circles Cd/Al, Al/Au and Cu/Au. The results show overall minimal gap between experiment and calculation [26].

The analytical approach proposed in Chap. 2 provides the theoretical kerma and dose profiles, in particular at the interfaces.

		from Chap. 2 expression	MCNP
Interface vacuum/water	Kerma (Gy)	$1.6 \cdot 10^{-14}$ (1)	$1.622 \cdot 10^{-14}$
Interface water/aluminium	Kerma (Gy)	$1.49 \cdot 10^{-14}$ (2)	$1.59 \cdot 10^{-14}$
	K_{water}/K_{alu}	1.155 (3)	1.169
	$D_{water}/_{alu}$	1.29 (4)	1.323
Interface aluminum/water	K_{alu}/K_{water}	0.8656 (5)	0.845
	D_{alu}/D_{water}	0.775 (6)	0.816

$$(1)\quad K = 1.6 \cdot 10^{-7} \sum_{E_\gamma} \left(\frac{\mu_{tr}}{\rho}\right)_{E_\gamma} \Phi_{E_\gamma}(x) E_\gamma = 1.6 \cdot 10^{-7} \times 0.031 \times \frac{1}{\pi \times 10^2}$$
$$= 1.6 \cdot 10^{-11}\,\text{mGy} = 1.6 \cdot 10^{-14}\,\text{Gy}$$

$$(2)\quad K = 1.6 \cdot 10^{-7} \sum_{E_\gamma} \left(\frac{\mu_{tr}}{\rho}\right)_{E_\gamma} \Phi_{E_\gamma}(x) E_\gamma \exp(-\mu/\rho\, \rho x)$$
$$= 1.6 \cdot 10^{-26} \exp(-0.07072/1\,1 \times 1) = 1.49 \cdot 10^{-14}\,\text{Gy}$$

$$(3)\quad \frac{K_{water}}{K_{al}} = \left(\frac{\mu_{tr}}{\rho}\right)_{Al}^{water} = 0.03103/0.02686 = 1.155$$

$$(4)\quad \frac{D_{water}}{D_{al}} = \overline{\left(\frac{S}{\rho}\right)}_{Al,800\,\text{keV}}^{water,800\,\text{keV}} = 1.91/1.48 = 1.290$$

$$(5)\quad \frac{K_{al}}{K_{water}} = \left(\frac{\mu_{tr}}{\rho}\right)_{water}^{Al} = 0.02686/0.03103 = 0.8656$$

$$(6)\quad \frac{D_{al}}{D_{water}} = \overline{\left(\frac{S}{\rho}\right)}_{water,800\,\text{keV}}^{Al,800\,\text{keV}} = 1.48/1.91 = 0.775$$

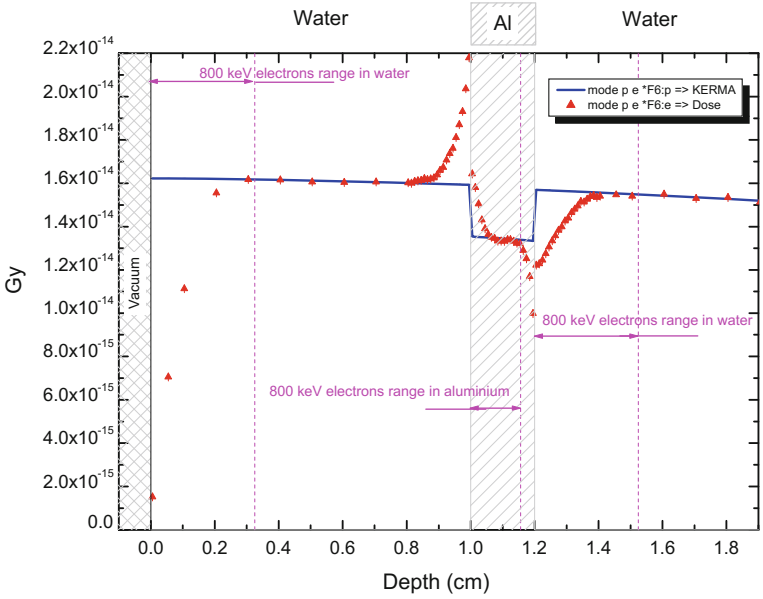

Fig. 6.24 Simulated kerma and dose in an aluminum-water-water medium as a function of depth

The analytical approach also determines the boundary depths from which the electron equilibrium is met in different materials. For example, in water, the maximum energy of 0.8 MeV transmitted by the Compton electron for 1 MeV primary photons, is theoretically completely absorbed in 0.33 cm of water (cf. Chap. 2). The Fig. 6.24 shows that the simulated dose and kerma are equal from an electron equilibrium achieved at 0.3 cm depth.

However the analytical approach proposed in Chap. 2 does not estimate the evolution of the dose in the upstream region of electron equilibrium. Similarly, it does not take into account the potentially important and continuous rise of the dose in the vicinity of an interface, mainly due to the backscattering of the secondary electrons in the second medium. The theoretical model predicts a discontinuity of the dose values at the interface. Note that this growth effect presented in Chap. 2 (2.1.3), proves paramount in radiation therapy, in particular tissue/bone or tissue/implant interfaces [27] to evaluate the "overdose" generated in the healthy tissue.

6.13.2 *Comparison of Kerma and "Dose-Pulse" Estimators for Photons in the Context of Calculating the Effective Dose*

A study using the MCNPX code version 2.5.0 [25] shows notable differences between two dosimetric estimators to calculate mean organ doses D_T in a MIRD anthropomorphic phantom. The estimators compared are kerma (F6: p) in photon transport mode (mode p) and "pulse-dose" (*F8: p, e) in mixed Mode (mode p e). Calculating the relative error between these two estimators was performed for all of the MIRD phantom organs:

$$Er(\%) = \left(\frac{\overline{K}_{F6} - \overline{D}_{*F8}}{\overline{D}_{*F8}} \right) \times 100 \tag{6.66}$$

Knowing, as stated above, the *tally* reference for the calculation is the one coinciding with the dose-pulse estimator namely *F8:p, e. Table 6.3 provides the overall results for AP irradiation for energies 1, 4, 6 and 10 MeV.

From these results above, it therefore finds that the kerma estimator is valid up to about 4 MeV for the assessment of the effective dose. Beyond, overestimation on organ doses become such that the impact on the effective dose can not be overlooked.

Let us add that all the calculations on the MIRD phantom for obtaining conversion coefficients "physical quantity versus dosimetric-quantities" are simulated using MCNP code version 4b with ITS algorithm trigged for electron transport.

Study finally the last available Dose estimator: Dose estimator for the charged particles, this time with an extra-application linked to the simulation of the absorbed dose for a 400 MeV protons beam in a water phantom.

Table 6.3 Relative error E_r for energies of 1, 4, 6 and 10 MeV photon for an AP irradiation fields on a MIRD phantom, on the measurement of the mean dose to the organ D_T [28]

Organs	Relative error to 1 MeV (%)	Error on 4 MeV (%)	Error on 6 MeV (%)	Error on 10 MeV (%)
Brain	0.5	−1.5	−0.5	−1.4
Colon	−2.1	−1.7	−3.8	−0.4
Stomach	−1.9	−1.4	−1.5	1.1
Liver	−1.3	−0.5	−1.4	1.2
Gonads	4.2	3.2	8.6	27.5
Esophagus	5.0	3.7	0.3	0.2
Skin	7.0	68.3	84.8	101.3
Lungs	−1.3	−1.0	−1.9	−0.5
Waist	0.3	−0.7	0.5	0.9
Rest (CIPR60)	−0.5	2.1	5.5	12.1
Rest (subscribe new rec.)	−0.6	2.2	5.6	12.0
Bosom	1.4	21.2	43.0	88.6
Skeleton	−0.3	0.0	2.4	7.4
Thyroid	2.2	3.7	8.3	15.7
Bladder	−3.9	−3.6	−3.5	−2.6

6.13.3 *Dose Profile For a 400 MeV Protons Beam in a Water Cylinder*

In MCNPX, there is also ability to focus on a particular contribution to the dose. For example, Fig. 6.25 gives a display of the absorbed dose in a water phantom for a 400 MeV proton beam. Thus, switch the eighth control input "LCA" at 2, it gets only the contribution due to the Coulomb slowing-down (dotted lines) in the knowledge that, by default, all interactions are taken into account: Coulomb and nuclear (black line) in the energy deposition process. Calculations are performed using the *tally* coinciding with the dose estimator charged particles (F6: h).

We observe clearly the "classic" Bragg curve in dotted line, described in the previous chapter, but completed by nuclear interactions effect in solid line in Fig. 6.23a.

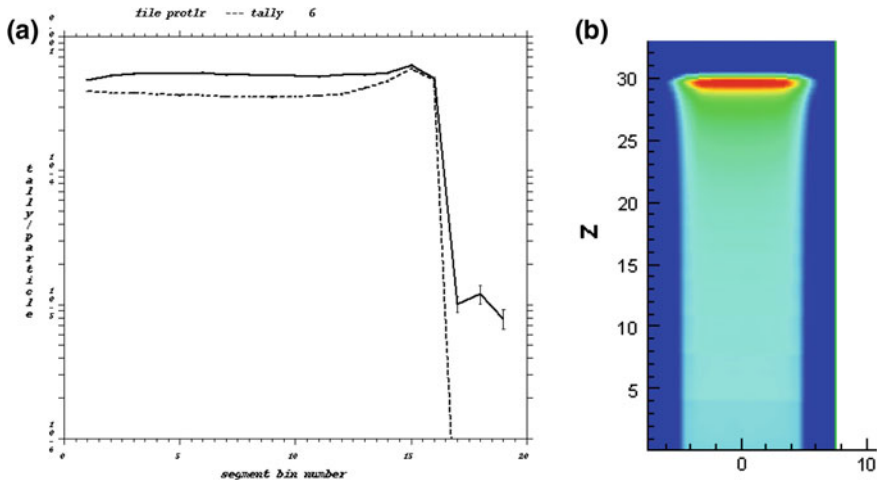

Fig. 6.25 **a** 400 MeV proton beam on a water phantom—dose depth profile calculated using MCNPX, taking into account all interactions (*solid line*) and only Coulomb interactions (*dotted*)—workshop MCNPX Barcelona 2010. **b** longitudinal view of the Bragg peak [29, 30]

6.14 Statistical Error Associated to Estimators

For each particle emitted by the source and consequently for every history, correspond an estimator response. Clearly, it is necessary to generate a number of sources particles to obtain ultimately reliable statistical result.

6.14.1 Calculation of Associated Statistical Error

Consider that N particles are launched (involving tracking N histories) and we investigate the result of the estimator for n batches of N/n particles. First idea for one of these batch, the result of the estimator is provided by the average of all the results of this batch. Thus, if the random variable X_i is the estimator of the dosimetric quantity which we will call G_{d} for the ith of n batch, it has a probability-weighted average $\overline{X}_i$ and a standard deviation σ_{Xi}. The probability law governing the statistical estimator is undetermined at this stage:

$$G_d \neq \overline{X}_i \tag{6.67}$$

However, if the average is performed this time on all n batches:

$$\overline{X_v} = \frac{1}{n}\sum_{i=1}^{i=n} X_i \tag{6.68}$$

And if the number of batch (s) is quite important, the law of large numbers allows us to postulate that:

$$\lim_{n\to\infty} \overline{X_v} = G_p \tag{6.69}$$

The index "v" means that we approach the true mean value of the quantity. The standard deviation associated with the distribution of X_i is classically obtained by the variance estimator as follows:

$$\sigma_{\overline{X_v}} = \frac{1}{(n-1)}\sum_{i=1}^{i=n} \left(X_i - \overline{X_v}\right)^2 \tag{6.70}$$

Moreover, another noteworthy property, in this case the distribution around the true average of the estimator $\overline{X_v}$ follows a normal distribution

$$N\left(\overline{X_v}, \sigma^2_{\overline{X_v}}\right)$$

Applying the Central Limit Theorem, we can thus associate with the estimated mean value $\overline{X_v}$ to the dosimetric quantity G_d with a confidence interval $C(e)$:

$$C(e) = probability\left\{G_d - e \le \overline{X_v} \le G_d + e\right\} \tag{6.71}$$

This, with the distribution function of the normal law $\left(\overline{X_v}, \sigma^2_{\overline{X_v}}\right)$ is equivalent to writing:

$$C(e) = \frac{1}{\sigma_{\overline{X_v}}\sqrt{2\pi}} \int_{G_d-e}^{G_d+e} \exp\left(-\frac{(x-G_d)^2}{2\sigma^2_{\overline{X_v}}}\right) dx \tag{6.72}$$

Thus, "conventionally" for $e = \sigma_{\overline{X_v}}$ we obtain $C(e) = 0.689$, which means that the estimation $\overline{X_v}$ of G_d is reliable to 68.9%; for $e = 2\sigma_{\overline{X_v}}$ we obtain $C(e) = 0.954$, a reliability of 95.4%; finally, for $e = 3\sigma_{\overline{X_v}}$ a reliability of 99.7% is obtained. In practice, the standard deviation of the true mean $\overline{X_v}$ is estimated by $S_{\overline{X_v}}$ as follows:

$$S^2_{\overline{X_v}} = \frac{\sigma^2_{\overline{X_v}}}{n} = \frac{1}{n(n-1)}\sum_{i=1}^{i=n} \left(X_i - \overline{X_v}\right)^2 \tag{6.73}$$

This term characterizes the "statistical error" on the true average; thus, the relative error *Er* at 1σ associated with the result of a normalized calculation is defined as:

$$Er\left(\overline{X}_v\right) = \frac{S_{\overline{X_v}}}{\overline{X_v}} \tag{6.74}$$

Accordingly, for the final result of the required dosimetric quantity, we announce:

$$G_d = \overline{X}_v \pm Er\left(\overline{X}_v\right) \tag{6.75}$$

Typically, the value of *Er* must always be at least less than 10% (more precisely at each estimator is a criterion of acceptability). The challenge will therefore consist in minimize the relative error associated. To illustrate the difficulty of getting a good statistical accuracy, *a fortiori* in agreement with the acceptability criterion of the relative error, let us consider a problem involving a thick biological protection [3]. In this problem, we consider the estimator *X* of the "transmission" quantity (i.e. ratio of incoming to exiting particles). Let us assume that this estimator score the value of 1 when the particle passes through the protection and 0 when it is absorbed (The reader can infer that in a true problem, particle weights should be scored, namely a fraction of unity for collied particle). In this case, we spontaneously have: $\overline{X_v^2} = \overline{X_v}$. When the number of batch n tends to infinity, we assume that $n \approx N$. Another way to express the statistical error similar to the expression (6.73) is:

$$S^2_{\overline{X_v}} = \frac{1}{N}\left(\overline{X_v^2} - \overline{X_v}^2\right) \tag{6.76}$$

With the property set forth above, we can write:

$$S^2_{\overline{X_v}} = \frac{1}{N}\overline{X_v}\left(1 - \overline{X_v}\right) \quad \Leftrightarrow \quad Er\left(\overline{X_v}\right) = \frac{S_{\overline{X_v}}}{\overline{X_v}} = \sqrt{\frac{1 - \overline{X_v}}{N\overline{X_v}}} \tag{6.77}$$

Postulate now, there are very few particles transmitted as may be with a high *Z* thick shielding with high density; in this case, we have $\overline{X_v} \ll 1$ and the above expression is simplified as follows:

$$Er \cong \frac{1}{\sqrt{N\overline{X_v}}} \tag{6.78}$$

Thus, if we take a 10% criterion of uncertainty and that the mean value of the transmission estimator is 10^{-6}, the number of particles from the source to succeed would be 10^8.

In this type of problem, there is slight chance that a particle transported through ultimately the sensitive region of the detector. The analogue approach must be replaced by an implicit approach, using variance reduction techniques such as described in the previous sections, for that the estimator converge to the result with a reasonable computing time related to limited quantities of particles.

6.14.2 Statistical Tests of Reliability

Throughout the simulation, a number of statistical tests are performed by routines. They help provide a trend in the convergence to a statistically reliable result. One of them is the "figure of Merit" test.

FOM factor (Figure of Merit)
The statistical test of FOM is linked to the estimator of the standard deviation and computing time as:

$$FOM \cong \frac{1}{S^2_{\overline{X}_v} T} \tag{6.79}$$

Recall that the variance estimator $S^2_{\overline{X}_v}$ is inversely proportional to the number of particles drawn N and T, the computation time is also proportional to N. The product of the square variance estimator by computing time T is therefore with prior a constant. Furthermore, performance is even better than the variance estimator is small and the computing time per particle too, which means that the FOM should be as high as possible.

This factor therefore optimizes the calculation time by performing several short tests on a small number of particles drawn with, each time, different variance reduction techniques; the preferred option being the one responsible for the highest FOM.

Add that this factor allows to assess the processor time to a statistical precision goal:

$$T = 1/(S^2_{\overline{X}_v} FOM)$$

Finally, this test is also a statistical confidence indicator: the FOM must be relatively constant all n stories, except at the beginning of the calculation, due to the strong statistical fluctuations.

Another statistical test that can be encountered in some codes, is the slope test.

Slope test
One of the issues that may arise with the Monte Carlo simulation is the ability to get a mean estimator result with the expected statistical accuracy even if the result is uncorrect!

A Slope test of "normality", calculates all n particles, a slope of the distribution around the mean value, if the result of a score is far from $\overline{X_v}$ it may be due to a "statistical accident" related to the scoring of a large statistical weight very far from the average. The slope of the distribution tail of estimator values will tend to be flattened and thus put into question the reliability of the final result. Keep in mind, that the calculation of the statistical error is based on a normal law.

Conversely, if no statistical accident arise, all values cluster symmetrically around $\overline{X_v}$ and then the result can be considered reliable towards a normal law and slope value of distribution become preeminent.

Again, it will always ensure a large slope to consider the calculation results as reliable, regardless of the acceptability of the statistical error criterion (e.g. in the MCNP code, a mandatory lower slope of 3 is expected to validate the results).

6.14.3 Result Finalization

At the simulation end, the result of the estimator is, as seen above, an average over all source particles. Therefore, the estimator value is normalized by particle source. To obtain a final result, it will be necessary to weigh the value by the number of drawn particles to achieved an integrated value or a flux to obtain a rate of the estimated quantity.

For example, let us consider a problem with a ^{252}Cf source of 1 MBq. In accordance with Sect. 6.4.1, the energy of the neutron release by spontaneous fission is sampled on the Watt distribution spectrum. Assuming that the mean score of the dosimetric kerma estimator $\overline{K}$ is 0.1 pGy/(particle source), the finalized result would be:

$$\dot{K} = 3600 \times \overline{K} \cdot A \cdot \dot{N}_A$$

with $\dot{N}_A$ the neutron flux by Bq: $1.17 \cdot 10^{-1}$ n^{-1} s^{-1} Bq (see Chap. 4). The 3600 factor converts seconds to hours. So finally we get the following rate:

$$\dot{K} = 3600 \times 0.1 \cdot 10^{-12} \times 10^{6} \times 1.17 \cdot 10^{-1} = 42\,\mu\,\text{Gy/h}$$

By extension, for a problem with i discrete rays of emission percentages Γ_i, the final result should be:

$$\dot{K} = 3600 \times \overline{K} \cdot A \cdot \sum_i \Gamma_i$$

In some codes, there is ability to input a "post processing" weights, which allows immediate finalized result (e.g. "fm" card in MCNP).

6.15 Complexity Levels in Dosimetric Models

The more complex is the model with several cells and the more significantly the computation time is impacted. Adding that following the existence or not of HMI (human-machine interface) design of complex geometry may prove to be tedious. The level of complexity chosen will depend on several factors: type of dosimetric quantity assessed, expected levels of statistical accuracy, time allocated for the study in radiation accident context…. We can identify three approaches with increasing levels of complexity involving in whole or in part human body: the simplified model, the mathematical model with anthropomorphic phantom and voxelised phantom model. For each of these approaches, models are displayed in Chap. 3.

6.16 Application of Monte Carlo Codes for Dosimeters

The problem below, show the value of using a Monte Carlo code in the feasibility study of an atmosphere dosimeter for fast neutrons from a RPL dosimeter (radio-photoluminescent glass) SC-1 type only sensitive to photons [31].

The principle is to develop a conversion-dosimeter: the device consists in a RPL dosimeter surrounded by Cd layer to promote radiative capture (n, γ) with thermal neutrons. The assembly is disposed in the center of a polyethylene cylinder charged to slow the fast neutrons to thermal energy. It is therefore to convert fast neutrons photons into detectable photons by RPL. The Monte-Carlo simulation will serve initially to theoretically assess the detector response to different neutron source terms, to determine whether the latter can be operated to measure the desired operational quantity and that it is independent towards neutron energy. first, simulations of the ambient dose equivalent $H_{\mathrm{n}}^{*}(10)$ at 1 m from different source terms is performed. In a second step, the whole device: RPL + Cd + CH2 is then modeled in the Monte Carlo code (here MCNP code version 4b) at the same location that $H_{\mathrm{n}}^{*}(10)$. The device as modeled in the code is shown in Fig. 6.26.

The ambient equivalent dose due to photons within the RPL (located 1 m from the source) is carried out using the fluence estimator $\overline{\Phi}_{\mathrm{v}}$. The response is generally calculated on the entire spectrum of photons; a ratio R is then estimated:

$$R = \left(\frac{H_n^*(10)}{\sum\limits_{E_\gamma} \overline{\Phi}_v(E_\gamma) h_\Phi(E_\gamma)} \right)_{1\,meter} = \left(\frac{H_n^*(10)}{H_\gamma^*(10)} \right)_{1\,meter}$$

The calculation by the MCNP code photon dose equivalent is performed by weighting the fluence of photons by energy bins by the conversion factor "fluence-ambient equivalent dose". Knowing that the glass answer is constant

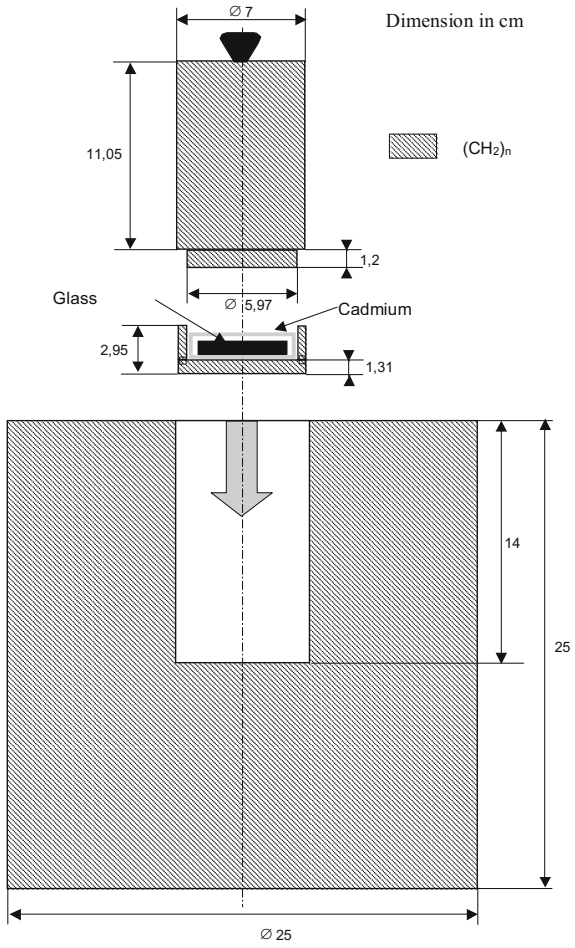

Fig. 6.26 Overview of whole device: RPL + Cd + CH_2 of the ambiant dosimeter for fast neutrons from a RPL, as modeled in MCNP4b [31] (with permission from Oxford University Press)

(±10%) over a range of photon energy of 100 keV to 8 MeV and the energy gammas produced during the radiative capture on the Cd does not exceed this upper energy.

The simulations were performed for various neutron sources, from monokinetic and spectral type: monoenergetic neutron 265 and 565 keV resulting from the reaction ^{7}Li(p, n)^{7}Be and 1.8 MeV resulting from the reaction ^{48}Ti(p, n)^{48}V, as well as (α, n) sources: Am-Be, Am-B and Am-Li (see Chap. 4).

An experimental benchmark was then carried out for all sources. The ratio R_H between simulation and experiments is presented in Fig. 6.27.

The ratio R is noteworthly constant within 30% of the region between 250 keV–10 MeV, which makes it usable for this energy range. Furthermore, we note a significant agreement between MCNP simulations and experiments.

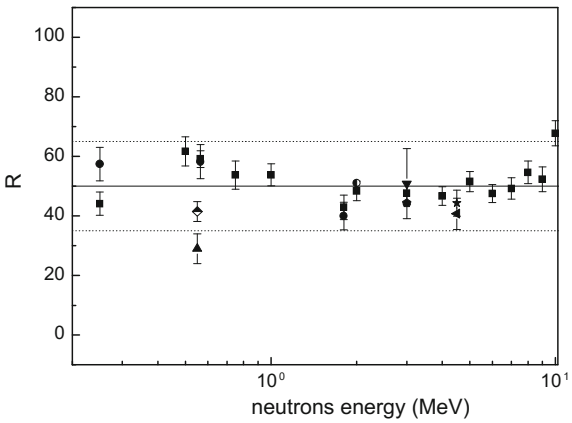

Fig. 6.27 Ratio R as function of the neutron energy for 250 keV to 10 MeV. The *solid line* represents the mean value of $R = 50$, the *dotted lines*, the difference of plus or minus 30% around this value; ■ value calculated by MCNP for mono-energetic neutrons; • value measured around accelerators producing quasi mono-energetic neutrons; ◄ value measured for a ^{241}Am-Be source; ▼ value measured for a source ^{241}Am-B; ▲ value measured for a ^{241}Am-Li source; ✱ value calculated by MCNP for a ^{241}Am-Be source; ⬠ value calculated by MCNP for a source ^{241}Am-B; ◆ value calculated by MCNP for a ^{241}Am-Li source; ◐ value calculated by MCNP for a ^{235}U fission source. According to [31], with permission from Oxford University Press

Let us add that in conjunction with use of the ENDF-B/VI library for neutrons, "special datas" (data $S(\alpha, \beta)$ with mt card) have been set-up, taking into account the molecular specificity for neutron scattering at low energy (below 2 eV), which has the effect of modifying the cross sections of the hydrogen from polyethylene in this case. Note that there exists equivalent for hydogene in water and the carbon in the graphite.

6.17 Application of Monte Carlo Codes for Calculations Relating to Metrology

The metrological use of Monte Carlo codes has grown in recent years for several reasons: implementation of physical models more efficient, cost and power of computers… Nevertheless, the importance of numerical approximations and the inherent uncertainty of cross sections, especially at low energies, do not achieve the absolute precision required in metrology (less than a thousand). Indeed, gray areas remain in the field of interaction cross sections, especially for angular and energy differential cross sections. Transport modeling at low energies sometimes lacks reliability, either for transport photons below a dozen keV or below 1 keV for electrons. Indeed, short of these energies, it is necessary to a have a special care to the collective effects, the influence of the molecular structure, of the overall electric

field, etc. [32]. Further more, relative deficiencies from Condensed technical history method [9]. Developed in Sect. 6.10 with CSDA applied to electron transport can bring significant biases in the metrology-related simulations.

These flaws thus lead to use Monte Carlo codes primarily to calculate or confirm the correction coefficients that are applied to experimental measurements. For obvious mathematical reasons, these coefficients are calculated so far with many simplifying assumptions. The use of Monte-Carlo method thus provides corrective values more accurate or unreachable by traditional methods. Note that these correction factors are normally close to unity.

To illustrate this context, let's take a ionization chamber from which it is accessed the Air Kerma by the following equation (see Chap. 2)

$$K_{air} = \frac{Q_{gaz}}{m_{air}(1-\bar{g}_{air})}\left(\frac{W}{e}\right)_{air}\left(\frac{\overline{S}}{\rho}\right)_{air}^{wall}\left(\frac{\overline{\mu_{en}}}{\rho}\right)_{wall}^{air}\frac{1}{A_{Wall}}\ (\mathrm{Gy})$$

with K_{air} the Air Kerma in the chamber center in the absence thereof. Q_{gas} is released charge in the air mass m_{air} of the sensitive volume, $\bar{g}_{\mathrm{air}}$ is the fraction of electron energy lost by Bremsstrahlung when slowing in the air, $\left(\overline{S}/\rho\right)_{\mathrm{air}}^{\mathrm{paroi}}$ is the ratio of the mass stopping powers in the wall on the air, $(\mu_{en}/\rho)_{wall}^{air}$ is the ratio of the mass absorption coefficients averaged over the energy of the photon spectrum in air on the wall, and finally A_{wall} is the correction factor that takes into account scattering and attenuation of the photon fluence of in the wall. This term close to 1 can be described as the product of two factors [33]: $A_{\mathrm{wall}} = A_{\mathrm{sc}} \cdot A_{\mathrm{at}} \cdot A_{\mathrm{sc}}$ is the factor responsible for the increase of the response due to the photon scattering in the wall (analogy with the build-up factor described in the previous chapter). It is calculated from the total energy imparted in the cavity of the gas $\left(\overline{\Delta\varepsilon}\right)_{air}$ which is expressed as follows:

$$\left(\overline{\Delta\varepsilon}\right)_{air} = \sum_i \left(\varepsilon_i^p + \varepsilon_i^{sc}\right)$$

with $\varepsilon_i^{\mathrm{p}}$ the energy imparted in the first interaction of the photon i, $\varepsilon_i^{\mathrm{sc}}$ the energy imparted by the following interactions of the photon i. the factor A_{sc} is then determined as follows:

$$A_{sc} = \frac{\left(\overline{\Delta\varepsilon}\right)_{air}}{\sum_i \varepsilon_i^p} \geq 1$$

The factor A_{at} is responsible for the attenuation of primary photon field in the chamber. It takes into account the number of mean-free path d_i of each photon i to the point of interaction in the chamber. It is therefore calculated as follows:

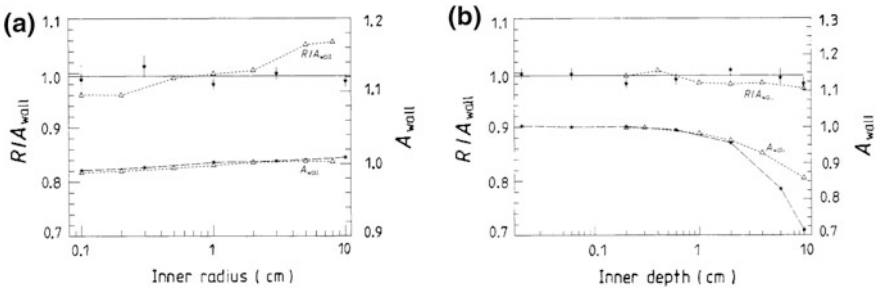

Fig. 6.28 Ratio R/A_{wall} and the correction factor A_{wall} for a parallel beam of ^{60}Co (thickness wall carbon = 0.5 g cm^{-2}) (thickness wall carbon = 0.55 g cm^{-2})—density of carbon = 1.83 g cm^{-3}: **a** to an ionisation chamber of 3 mm deep; **b** an ionization chamber 1 cm inner radius. According to [33]

$$A_{sc} = \frac{\left(\overline{\Delta\varepsilon}\right)_{air}}{\sum_i \left(\varepsilon_i^p + \varepsilon_i^{sc}\right)\exp(d_i)} \leq 1$$

There is a clear similarity with the calculation of transmission $T\left(\mu x, E_\gamma\right)$ based on the point-kernel method we have used to characterize the attenuation of photons in the wall in the previous chapter. These simulations were run using the CAVITY code, dedicated to responses of ionization chambers. To perform these calculations, it is necessary to track in "event-by-event" mode. Note that among other, a variance reduction technique was set-up to force the scattered photons to interact again (forced collision technique cf. Sect. 6.5). Let us add that the two components A_{sc} and A_{at} were calculated separately to limit ultimately statistical uncertainty on product A_{wall}.

By considering an ideally-equivalent air chamber, the Fano theorem provides

$$R_{cav} = \left(\frac{\overline{S}}{\rho}\right)_{air}^{wall} \left(\frac{\overline{\mu_{en}}}{\rho}\right)_{wall}^{air} = 1$$

Now consider the calculated response and incorporate the correction factor A_{wall}: $R = R_{cav}A_{Wall}$. Figure 6.28 give variations in the ratio R/AT_{wall} and A_{wall} depending on the depth and the inner radius for two cylindrical ionization chambers with carbon wall and a parallel beam and a point source of ^{60}Co.

In Fig. 6.28b, for large depths, the difference between A_{wall} originates from the difference in sources. We note that the ratio R/A_{wall} deviates from unit, in particular for the case of ^{60}Co parallel beam.

6.18 Application of Monte Carlo Codes for Scintillator Detectors

Monte Carlo codes also allow the modeling of multiple scintillator detectors: NaI, CZT, CsI, $LaBr_3$, plastic, Ge … The pulses scored in the sensitive volume can be assess by the mean of "pulse-dose" estimator. This feature is, for example, consistent with a common application of the radiation measurement consisting in determining a transfer function of the number of counts per second to becquerels of source or contaminant for geometry and radionuclides considered. The joint knowledge of the self-noise of the detector and the transfer function then determines the minimum detectable activity (MDA).

It is also possible to determine the energy distribution of the pulses scored in the cell modeling the sensitive volume of the detector. This response is typically that of a scintillation detector spectrometer operating mode. In the MCNP code, the estimator "pulse-height" F8 associated with a energy cut option performs this function.

To take into account the energy resolution dependent on the physico-chemical composition of the scintillator, a Gaussian broadening of the absorption peaks can be achieved. Conventionally, the enlargement parameter σ determines the full width at half maximum (FWHM) by the relation FWHM = 2.35σ. In this code, taking account of the mid-height width can be activated by a specific control associated with the estimator F8 (GEB card). This is then supplemented with a set of parameters: a, b and c given in MeV, $MeV^{1/2}$ and MeV^{-1} corresponding to the coefficients of the expression of the mid-height width as a function of energy (MeV):

$$FWHM(E) = a + b\sqrt{E + cE^2} \tag{6.80}$$

The Fig. 6.29 displays a geometry as modeled of a spectrometer with scintillation NaI(Tl) diameter cylindrical Sect. 6.2 "by 2" height, exposed to a ^{60}Co punctual source.

The simulated energy response is that of a conventional spectrometer, or 1024 channels covering a dynamic of 0–3072 keV (switch using the E8 card followed by the parameters 0 1023i 3072). The parameters of the full width at half maximum, corresponding to the resolution type of a crystal NaI are a = −0.00715076 MeV; b = 0.0652825 $MeV^{1/2}$; c = −0.178934 MeV^{-1} (FT8 GEB -0.00715076 0.0652825 –0.178934). The spectrum shape obtained is shown in Fig. 6.30.

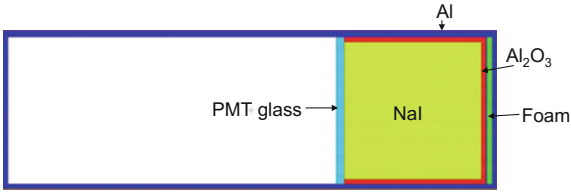

Fig. 6.29 Modeled Geometry of a scintillator NaI

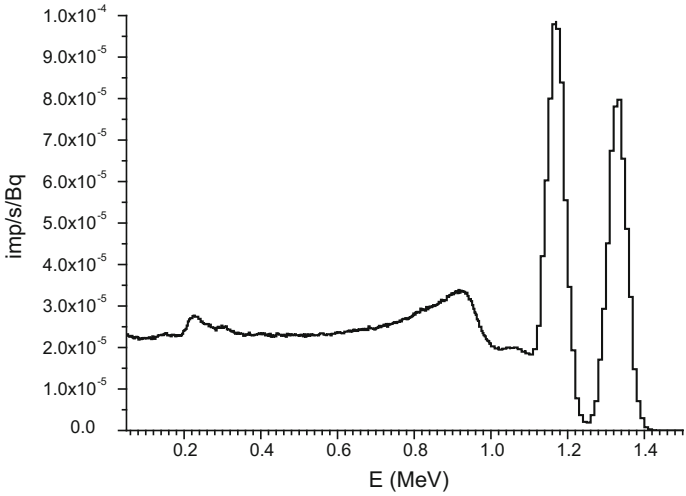

Fig. 6.30 Simulation with MCNP code of a 60_{Co} spectrum with a crystal NaI through the use of the estimator "pulse-dose" F8 type associated with the Gaussian energy broadening card

Further Details 6.1 Sampling a continuous distribution by special method, application to direction and energy of the photon scattered

Let's go back to the transport of photons in Sect. 6.3 and consider that the sampling of cumulative probability leads to the Compton scattering. It is necessary now to calculate the energy and direction of the scattered photon, ditto for the electron Compton released.

This is achieved, strictly speaking, applying the method of the inverse of the cumulative probability density on the energy KN differential cross section. However, the complex analytic form of the latter prevents access to the inverse function. Koblinger et al. [7] propose an alternative method, based on a mathematical peculiarity of the KN analytical expression (for incident energies above 1.4 MeV).

In Chap. 2, the KN differential expression was splitted in four independent terms. The probability that the Compton scattered photon gets an energy between E'_γ and $E'_\gamma + dE'_\gamma$ is obtained by dividing the differential cross section of KN by the total cross section of the Compton interaction:

$$p(x) = \frac{1}{\sigma_c}\left(\frac{d\sigma_c}{dx}\right)$$

$$\text{So}: p(x) = \begin{cases} H\left(A + \frac{B}{x} + \frac{C}{x^2} + \frac{D}{x^3}\right) & \text{if} \quad 1 \le x \le 1 + 2\alpha_o \\ 0 & \text{outside} \end{cases}$$

$$\text{with } H = \frac{K'}{\sigma_c}.$$

As with the previous sampling, it is necessary beforehand to calculate the cumulative probability density:

$$P\left(E'_{\gamma}\right) = P\left(x\right) = \int_{1}^{x} p\left(x\right) dx$$

this integral is calculable but it is not possible to access its inverse function P^{-1} and therefore the desired quantity E'_{γ}. Koblinger method is based on the sum of terms of the KN expression to overcome this failure. The probability density $p(x)$ can be expressed as a sum of partial functions, independent on the interval allowed as follows:

$$p(x) = \phi_1(x) + \phi_2(x) + \phi_3(x) + \phi_4(x)$$

or: $\phi_1(x) = HA, \quad \phi_2(x) = H\frac{B}{x}, \phi_3(x) = H\frac{C}{x}$ and $\phi_4(x) = H\frac{D}{x^3}$.

Note. The restriction on the application of the method is: for all x in the interval $1 \leq x \leq 1 + 2\alpha_o$, the four functions $\phi_i(x)$ must always be positive. However, B and so $\phi_2(x)$ are greater than 0 if: $\alpha_o \geq 1 + \sqrt{3} \Leftrightarrow E_{\gamma} > 1.397\,\text{MeV}$. The Koblinger method involves two steps.

Step 1. First, the partial probability is calculated following probabilities: $\hat{p}_i = \int_{1}^{1+2\alpha_o} \phi_i(x)dx$

Knowing that: $\sum_{i=1}^{i=4} \hat{p}_i = \int_{1}^{1+2\alpha_o} p(x)dx = 1$

Indeed, the integration on the allowable range of the probability density $p(x)$ necessarily leads to 1. The results of integrations are given by the expression:

$$\hat{p}_1 = \hat{p}_3 = H\frac{2}{\alpha_o}, \quad \hat{p}_2 = H\left(1 - \left(\frac{1+\beta}{\alpha_o^2}\right)\right)\ln(\beta) \quad \text{and} \quad \hat{p}_4 = H\frac{\gamma}{2}$$

The next step is to choose one of these four partial probabilities. To do this, the "partial" cumulative probabilities are calculated according to (cf. choice of the photon collision):

$$\hat{P}(j) = \sum_{i=1}^{i=j} \hat{p}_i$$

then the partial probabilities is chosen by drawing a first random number ξ_1. If the number satisfies the inequality, then the kth partial probability $\hat{p}_k$ is selected and therefore the partial function ϕ_k (cf. Fig. 1).

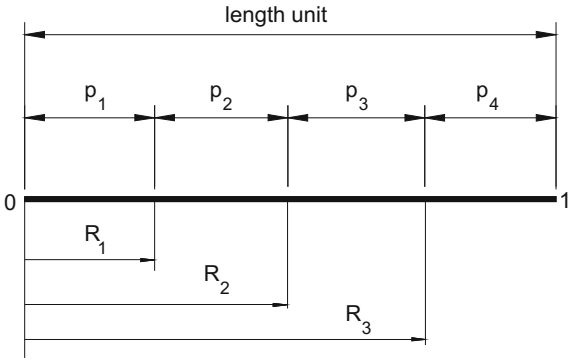

Fig. 1 Distribution of partial cumulative probabilities for the KN sampling by the Koblinger method [7]

$$\hat{P}(k-1) < \xi \leq \hat{P}(k)$$

2nd step. Imagine that the partial probability $\hat{P}(k)$ is chosen, the partial function ϕ_k corresponding is then retained. Again, a cumulative probability density this time is calculated on this function, the value of a new random number is fixed to ξ_2. The inverse function of the latter then allows obtaining x and consequently of E'_γ.

$$\xi_2 = \Phi_k(X) = \frac{1}{\hat{p}_k} \int_1^x \phi_k(x)\, dx$$

$$\Rightarrow x = \Phi_k^{-1}(\xi_2)$$

$$\Rightarrow E'_\gamma = \frac{E_\gamma}{x} = \frac{E_\gamma}{\Phi_k^{-1}(\xi_2)}$$

$(\hat{p}_k)^{-1}$ is the normalization term. Note that the simplicity of the components $\phi_i(x)$ constitutive of $p(x)$ makes it easy to calculate different integrals, and the expressions of inverse functions. For the four components, the values of x are obtained according to:

$$\begin{cases} k = 1 & \rightarrow & x = 1 + 2\alpha_o \xi_2 \\ k = 2 & \rightarrow & x = \beta^{\xi_2} \\ k = 3 & \rightarrow & x = \frac{\beta}{(1+2\alpha_o \xi_2)} \\ k = 4 & \rightarrow & x = (1 - \gamma \xi_2)^{-1/2} \end{cases}$$

For example, let us consider an incident photon of 0.8 MeV. We assume that the calculation of partial probabilities $\hat{p}_i$ and the cumulative probabilities $\hat{P}(j)$ lead to the following results:

$$\hat{p}_1 = 0.1\ \hat{p}_2 = 0.3\, \hat{p}_3 = 0.2\ \hat{p}_4 = 0.4 \Rightarrow \hat{P}(1) = 0.1\ \hat{P}(2) = 0.4\ \hat{P}(3) = 0.6\, et\, \hat{P}(4) = 1$$

the random number is drawn and leads to $\xi_1 = 0.3$ in the range [0, 1] so:

$$\hat{P}(1) = 0.1 < \xi_1 = 0.3 \leq \hat{P}(2) = 0.4 \Rightarrow \hat{P}(2) \qquad \text{(selected!)}$$

The cumulative probability $\hat{P}(2)$ is selected, a second random number ξ_2 is drawn and we take the expression on $k = 2$. Thus, we obtain the energy of Compton scattered photon as follows:

$$E'_\gamma = \frac{E_\gamma}{x} = \frac{E_\gamma}{\Phi_2^{-1}(\xi_2)} = \frac{E_\gamma}{\beta^{\xi_2}} = \left(1 + \frac{2E_\gamma}{0.511}\right)^{-\xi_2} E_\gamma$$

Suppose the draw for a second random number leads to the following result $\xi_2 = 0.6$, the energy of the scattered photon is finally:

$$E'_\gamma = \left(1 + \left(\frac{2 \times 0.8}{0.511}\right)\right)^{-0.6} \times 0.8 = 341 \text{ keV}$$

We get angle θ through the expression linking the energy of the incident photon to photon Compton seen in Chap. 2:

$$\cos\theta = 1 - m_e c^2 \left(\frac{1}{E'_\gamma} - \frac{1}{E_\gamma}\right) = 1 - 0.511 \times \left(\frac{1}{0.341} - \frac{1}{0.8}\right) = 0.1402 \Leftrightarrow \theta$$
$$= a\cos(0.1402) = 82^\circ$$

Finally characterize the direction of the secondary compton photon, remains to determine the azimuth φ. As the emission of the photon Compton responds to a symmetry of revolution, all angles between 0 and 2π have equal probability. Therefore, the probability of an angle between φ and φ + dφ is given by:

$$p(\varphi)d\varphi = \frac{d\varphi}{2\pi}$$

The cumulative probability density of an angle less than φ is given by:

$$P(\varphi) = \int_0^\varphi \frac{d\varphi}{2\pi} = \frac{\varphi}{2\pi}$$

By setting the value of the distribution to a third random number: $P(\varphi) = \xi_3$, it comes: $\varphi = 2\pi\xi_3$. If the draw gives 0.1 for example, we get:

$$\varphi = 2\pi \times 0.1 \times \frac{180}{\pi} = 36^\circ$$

now characterize the parameters of the Compton electron its energy is determined by the following subtraction:

$$T_{e-} = E_\gamma - E'_\gamma - E_L$$

Neglecting the binding energy E_L of the electron in its orbit (a dozen eV), we obtain:

$$T_{e-} \cong 800 - 341 = 459 \text{ keV}$$

Finally, let us calculate the angle ϕ with which the Compton electron is set in movement (see Chap. 2), depending on the energy of the incident photon and the deflection angle θ of the Compton photon:

$$\cot\phi = \left(1 + \frac{E_\gamma}{0.511}\right)\tan\left(\frac{\theta}{2}\right) = \left(1 + \frac{0.8}{0.511}\right)\tan\left(\frac{82}{2}\frac{\pi}{180}\right) = 2.22$$
$$\Rightarrow \quad \phi = a\cot(2.22) = 24^\circ$$

Note that the Monte Carlo codes allow to simulate the whole of the electromagnetic cascade thus, if the electron transport mode is switched, the electrons moved in photonic collisions are in turn tracked. It is the same for the recoil nuclei in the case of neutron interaction. Let us add that X-radiation from the rearrangement of the electron cloud can also be monitored.

For energies of incident photons lower than 1.4 MeV, a method combining the method detailed above with the rejection method is used.

Further Details 6.2 Sampling a continuous distribution by means of an approximating function

A nontrivial analytic expression is approximated by another integrable function and whose inverse function is available. One technique is the series expansion. For example, the Watt spectrum discussed above, by discretization, may be sampled by this method. Indeed, at low energies E_n we have:

$$\sinh(x) = x + \frac{x^3}{3!} + \frac{x^5}{5!}\cdots \Rightarrow p_1(E_n) \approx c\exp(-aE_n)(bE_n)^{1/2}$$

or, when E_n is small $\exp(-aE_n) \approx 1$ and finally gives the following simplified expression:

$$p_1(E_n) \approx k(E_n)^{1/2}$$

with k a constant. Similarly, for higher energies, one of the terms of the distribution can be approximated as follows:

$$\sinh(x) \cong \frac{\exp(x)}{2} \Rightarrow p_2(E_n) \approx \frac{c\exp(-aE_n)\exp(bE_n)^{1/2}}{2} = \frac{c\exp\left(-aE_n + (bE_n)^{1/2}\right)}{2}$$

When a and b are close to 1, for energies above 1 MeV, the term $-aE_n$ dominates; we can thus simplify the initial expression as follows:

$$p_2(E_n) \approx k' \exp(-aE_n)$$

with k' a constant. Indeed, to be convinced, just look at the graph of Watt spectrum in Fig. 6.3: For energies between 0 to about 1 MeV, energy evolves substantially like square root of the energy, i.e. $p_1(E_n)$ approximation, beyond 1 MeV it evolves as a decreasing exponential, i.e. $p_2(E_n)$ approximation.

Both expressions are easily integrated and inverse functions are accessible. So the cumulative probability density is a sum of two partial cumulative probability density valid each on a specific interval. The cumulative probability density over an interval [0, E_c], where E_c is the a limit beyond which we switch from one expression to another (of the order of 1 MeV) is then obtained as follows:

$$P_1(E_n) = k\int_0^{E_n} (E_n)^{1/2} dE_n = \frac{2k}{3} E_n\sqrt{E_n}$$

The cumulative probability density over the interval [E_c, E_{max}] is:

$$P_2(E_n) = k'\int_{E_c}^{E_n} \exp(-aE_n)\, dE_n = \frac{[k'' - k'\exp(-aE_n)]}{a}$$

Sampling can therefore then be achieved trivially, knowing that: $P_1(E_c) + P_2(E_{max}) = 1$:

$$\text{if} \quad \xi < P_1(E_c) \Rightarrow E_n = P_1^{-1}(\xi)$$
$$\text{if} \quad \xi > P_1(E_c) \Rightarrow E_n = E_c + P_2^{-1}(\xi - P_1(E_c))$$

To further illustrate this technique, here is another classical approximation: that of a probability density describing a normal distribution. Again, no analytical solution exists for the integral of the probability density. Khan [34] proposes to approximate this function with another function of equivalent properties. Consider this approach for a standard normal distribution:

$$p(x) = \frac{1}{\sqrt{2\pi}} \exp\left(-\frac{x^2}{2}\right)$$

The latter can be approximated by the following function:

$$p^*(x) = \frac{B \exp(-Bx)}{(1 + \exp(-Bx))^2} \; ; \; -\infty \leq x \leq \infty \; ; \; B > 0$$

We show that this function $p^*(x)$, as the standard normal distribution, has a average to zero and variance to unity since $B = \pi/\sqrt{3}$. It is then possible to calculate the cumulative probability density function of this through the following approximation:

$$P(x) = \int_0^x p(x)dx \cong \int_0^x p^*(x)dx = \frac{\exp Bx}{1 + \exp Bx}$$

We can thus draw a random number ξ and apply the method of the inverse of the cumulative probability density:

$$P(x) = \xi \Rightarrow x = P^{-1}(\xi) = \frac{1}{B} \ln\left[\frac{\xi}{1 - \xi}\right]$$

This type of approach may be, for example, suitable for sampling the particle shot location when the source simulates the Gaussian profile of the cylindrical beam from an accelerator. The figure below shows a visualization of a Gaussian beam profile (Fig. 6.31).

The gradual shift from blue to red reflects an increase in the particle circulation in the beam. Indeed, in a Gaussian beam profile, the particles are preferably shot as the center of the beam is approached. Add that to characterize such a beam, it is appropriate to make two successive draws on Gaussian distributions to characterize in turn, coordinated x and y of shot location.

Further Details 6.3 Landau Distribution of energy straggling [12]. For the calculation of effective energy lost during a step (class I)

Although on average we can calculate the energy lost by collision on a path through the Bethe-Block formula CSDA approximation, significant differences on the energy imparted to the medium (80% energies below this mean value and some rare exceptions where the energy transferred can reach half the energy of the incident electron) gives this approach a highly approximate nature as to the characterization of energy deposition. There is a significant straggling of effective energy lost around this mean value predicted by the stopping power. In the case of thin absorbent (i.e. of the order of s in a step), the limited number of collisions prevents applying the central limit theorem. Moreover, the possibility of having a large energy imparted transmitted to the mean energy involves an asymmetrical

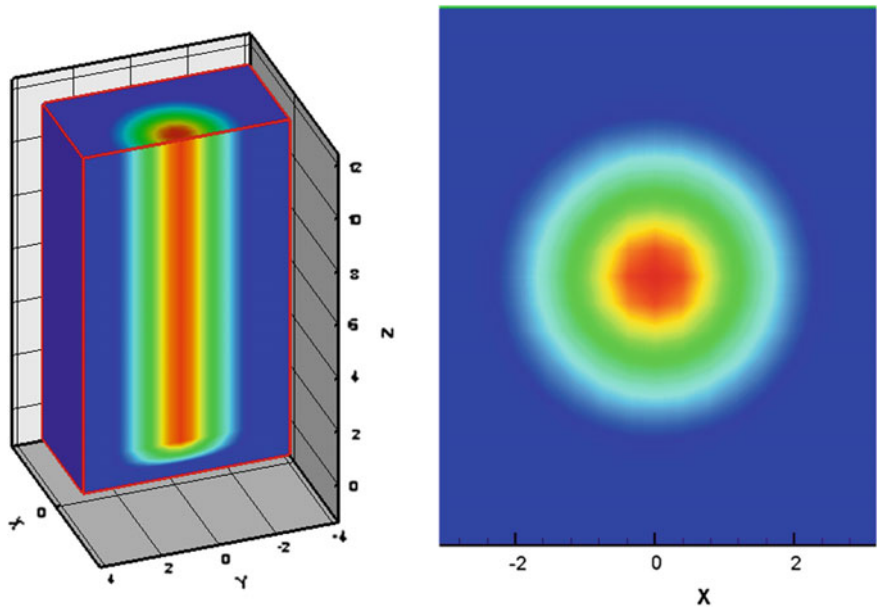

Fig. 6.31 Visualization of a Gaussian beam profile obtained with Monte-Carlo code [29]

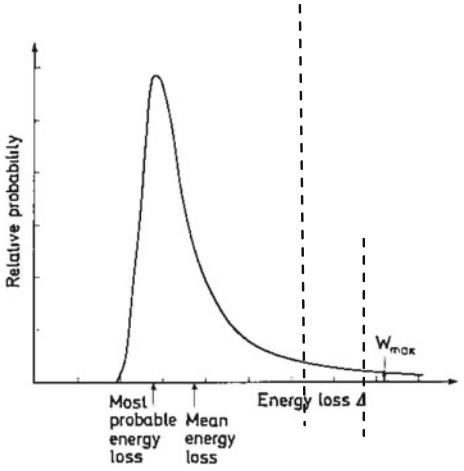

Fig. 1 Typical asymmetrical distribution of the energy loss in collision process, in a thin absorbent [13]

distribution, including the most probable energy is not the mean energy predicted by the stopping power (which we call here $\bar{\Delta}$). Figure 1 shows a typical representation of this straggling distribution.

The exact shape of this distribution, which corresponds to an asymmetric criterion is the ratio:

$$\kappa = \frac{\bar{\Delta}}{W_{\max}}$$

Which is ratio of the mean energy lost by collision and the maximum energy that can be transmitted ($W_{\max} \approx T$). The mean energy is obtained, as we have said, by the Bethe-Block formula to the energy of the electron incident in question, which for practical reasons is "peeled" from its logarithmic term:

$$\bar{\Delta} = 2\pi N_a r_e^2 m_e c^2 \rho \frac{Z}{A} \left(\frac{z}{\beta}\right)^2 s$$

with s the path of step (n) considered. Landau calculated the distribution of energy loss for $\kappa \leq 0.01$ (which is typically the order of magnitude that may be encountered for electrons) upon the following assumptions: (1) the maximum transmitted power is infinite in theory ($W_{\max} \rightarrow \infty \Rightarrow \kappa \rightarrow 0$), (2) the individual energy transfers are sufficiently large to consider electrons as free (3) the decrease in velocity of the primary electron is negligible. The distribution is then expressed as follows:

$$f(s,\Delta) = \frac{\phi(\lambda)}{\Delta} \text{ where } \phi(\lambda) = \frac{1}{\pi}\int_0^\infty \exp(-u\ln u - u\lambda)\sin(\pi u)du$$

$$\text{with: } \lambda = \frac{1}{\Delta}\left[\Delta - \bar{\Delta}\left(\ln\bar{\Delta} - \ln\varepsilon + 1 - C\right)\right] \text{ and } \ln\varepsilon = \ln\left[\frac{\left(1-\beta^2\right)I^2}{2m_e c^2\beta^2}\right] + \beta^2$$

C is the Euler's constant (C = 0.577 …). The amount ε is the minimum energy imparted allowed by assumption 2, function $\phi(\lambda)$ is calculated and tabulated by energy bins for several values of λ. Because of the asymmetry of the Landau distribution, the most probable value is different from the mean value $\bar{\Delta}$ and is found to be:

$$\Delta_{mp} = \bar{\Delta}\left(\ln\left(\frac{\bar{\Delta}}{\varepsilon}\right) + 0.198 - \delta\right)$$

The density effect δ was added. In the MCNP code the binding energy of electrons effect (assumption 2) are taken into account and the Landau approach is slightly modified [35].

Further Details 6.4: Goudsmit-Saunderson Approach for multiple scattering theory (class I)

The ETRANS code and MCNP rely on the Goudsmit-Saunderson theory for the probability distribution of angular deflections. The angular deflection of the electron is sampled once par substep according to the distribution:

$$p(s,\mu) = \sum_{n=0}^{n=\infty} \left(n + \frac{1}{2}\right) \exp(-sG_n) P_n(\mu) \quad \text{with :}$$

$$G_n = 2\pi\rho_a \int_1^{-1} \left(\frac{d\sigma}{d\Omega}\right)(1 - P_n(\mu))d\mu$$

where s is the length of the substep, cosθ is the angular deflection from the direction at the begining of the substep, (dσ/dΩ) Is the differential cross section for an electron to be scattered in a solid angle of between Ω and Ω + dΩ, ρ_{at} is the atomic density. Terms $P_n(\mu)$ are the nth Legendre polynomials defined by the following expression:

$$P_n(\mu) = \frac{1}{n!\,2^n} \frac{d^n}{d\mu^n} \left(\left(\mu^2 - 1\right)^n\right)$$

Note that in practice, an order 5 is typically sufficient to characterize the probability function. A discrete cumulative probability is then calculated and leads to a discreet distribution of angles.

$$P(s, \cos\theta_k) = \sum_{-1}^{\cos\theta_k} p(s, \cos\theta)$$

By means of a new random number, the angular deflection is derived:

$$P(s, \cos\theta_{k-1}) \leq \xi < P(s, \cos\theta_k)$$

In this case, the deflection angle is θ_k for a deflection range between $\Delta\theta_k = \theta_k - \theta_{k-1}$.

References

1. Lehmer, D. H. (1951). *Mathematical methods in large scale computing units*. In Proceedings of the 2nd symposium on large scale digital calculating machinery (141–146). Cambridge, University Press.
2. Métivier, H. (Ed.). (2006) *Radioprotection et ingénierie nucléaire*. EDP sciences.
3. Profio, A. E. (1979). *Radiation shielding and dosimetry*. New York: Wiley.
4. Chadwick, M. B., Oblozinsky, P., Herman, M., et al. (2006). ENDF/B-VII.0: Next generation evaluated nuclear data library for nuclear science and technology. *Nuclear Data Sheets, 107* (12), 2931–3060.
5. Shultis, J. K., & Faw, R. E. (2000). *Radiation shielding*. American Nuclear Society, Inc. The Jeff-3.1.1 Nuclear Data Library—NEA.
6. Kalos, M. (1983). A third Monte Carlo sampler, LA-9721-MS. In C. J. Everett, & E. D. Cashwell (Eds.), Los Alamos National Laboratory.

7. Koblinger, L. (1975). Direct sampling from Klein-Nishina distribution for photon energies above 1.4 MeV. *Nuclear Science & Engineering, 56*(2), 218–219.
8. Suteau, C., Chiron, M., Luneville, L., Berger, L., & Huver, M. (2003). *MERCURE: Un code 3D industrial de propagation des gammas par la méthode d'atténuation en ligne droite. Applications en radioprotection. Codes de calcul en dosimétrie radiophysique et radioprotection*. Congrès de la SFRP Sochaux.
9. Berger, M. J. (1963). Monte Carlo calculation of the penetration and diffusion of fast charged particles. In B. Alder, S. Fernbach, & Rotenberg (Eds.), *Methods in computational physics* (Vol. 1, pp. 135–215). New York Academic.
10. Koivunoro, H., Siiskonen, T., Petri, Kotiluoto P., Auterinen, I., Hippeläinen, E., & Savolainen, S. (2012). Accuracy of the electron transport in mcnp5 and its suitability for ionization chamber response simulations: A comparison with the egsnrc and penelope codes. *Medical Physics, 39*, 1335.
11. Wilken, B., & Fritz, T. A. (1976). Energy distribution functions of low energy ions in silicon absorbers measured for large relative energy losses. *Nuclear Instruments and Methods in Physics, 138*(2), 331.
12. Landau, L. (1944). *J Phys (USSR), 8*, 201.
13. Leo, W. R. (1994) *Techniques for nuclear and particle physics experiments, a how-to-approach*. Springer.
14. Goudsmit, S., & Saunderson, J. L. (1940). Multiple scattering of electrons. *Physical Review, 57*, 24.
15. Howerton, R. J. et al. (1975). *The LLL evaluated nuclear data library (ENDL): Evaluation techniques, reaction, index, and description of individual evaluations, UCRL-50400* (Vol. 15, part A). Lawrence Livermore National Laboratory.
16. Yu, C. X., Mackie, T. R., & Wong, J. W. (1995). Photon dose calculation incorporating explicit electron transport. *Medical Physics, 22*(7).
17. Grady Hughes, H. (2013). *Enhanced electron-photon transport in MCNP6*. LA-UR-13-27632.
18. Champion, C., Incerti, S., Perrot, Y., Delorme, R., Bordage, M. C., Bardiès, M., et al. (2014). Dose point kernels in liquid water: An intra-comparison between GRANT4-DNA and a variety of Monte-Carlo codes. *Applied Radiation and Isotopes, 83*, 137–141.
19. Bielajew, A. F., Rogers, D. W. O., & Nahumt, A. E. (1985). The Monte Carlo simulation of ion chamber response to ^{60}Co-resolution of anomalies associated with interfaces. *Physics in Medicine & Biology, 30*(5), 419–427.
20. Kawrakow, E., & Rogers, D. W. O. (2000). *The EGSnrc code system: Monte Carlo simulation of electron and photon transport, NRCC Report PIRS-701*. National Research Council of Canada.
21. Kawrakow, M. H. E., Rogers, D. W. O., Tessier, F., & Walters, B. R. B. (2010). *The EGSnrc code system: Monte Carlo simulation of electron and photon transport I*. NRCC Report PIRS-701.
22. Briesmeister, J. F. (Ed.). (1997). *MCNP—A general Monte Carlo N—Particle transport code version 4B* (Los Alamos National Laboratory) Report LA-12625-M.
23. ICRP. (1995). Conversion coefficients for use in radiological protection against external radiation, publication 74.
24. Antoni. (2008). Private communication.
25. Hendricks, J. S. (2003). *MCNPX model/table comparison*. Report LA-14030. Los Alamos.
26. Chibani, O., & Allen, L. X. (2002). Monte Carlo dose calculations in homogeneous media and at interfaces: A comparison between GEPTS, EGSnrc, MCNP, and measurement. *Medical Physics, 29*(5).
27. Keall, P. J., Siebers, J. V., JERAJ, R., & MOHAN, R. (2003). Radio therapy dose calculations in the presence of hip prostheses. *Medical Dosimetry, 28*(2), 107–112.
28. Furtoss, C. (2006). *Conception et développement d'un fantôme anthropomorphe équipé de détecteurs dans le but d'évaluer la dose efficace à un poste de travail*. Université Paris XI UFR scientifique d'Orsay, thèse.

29. Agostinelli, S., Allison, J., Amako, K., Apostolakis, J., et al. (2003). Geant4—A simulation toolkit. *Nucl Instrum Meth A, 506*(3), 250–303.
30. Antoni. (2004). Private communication.
31. Girod, M., Bourgois, L., Cornillaux, G., Andre, S., & Postaük, J. (2004). Study and presentation of a fast neutron and photon dosemeter for area and criticality monitoring using radiophoto luminescent glass. *Radiat Prot Dosim, 112*(3).
32. Barthe, J., Gouriou, J., Daures, J., Ostrowsky, A., & Bordy, J. M. (2003). Utilisation des codes de Monte-Carlo en métrologie des rayonnements ionisants. Congrès SFRP sur les codes de calculs appliqués à la radioprotection, radiophysique et dosimétrie.
33. Rogers, D. W. O., Bielajew, A. F., & Nahum, A. E. (1985). Ion chamber response and A_{wall} correction factors in a ^{60}Co beam by Monte Carlo simulation. *Physics in Medicine & Biology, 30*(5), 429–443.
34. Khan, H. (1954). *Applications of Monte-Carlo USAEC Report AECU-3259*. Rand Corp.
35. Blunk O (1950) *Leisgang S Z Phys*.

Index

R. Antoni and L. Bourgois, *Applied Physics of External Radiation Exposure*,
Biological and Medical Physics, Biomedical Engineering,
DOI 10.1007/978-3-319-48660-4